Molecular organization in solid-state using sigma-hole interactions : Exploring the effect of crystalline environment

Vishnu Vijayakumar-Syamala

THÈSE

Présentée et soutenue publiquement pour l'obtention du titre de

DOCTEUR DE l'UNIVERSITE DE LORRAINE

Mention : CHIMIE

Par Vishnu VIJAYAKUMAR SYAMALA

Sous la direction de Prof. Enrique ESPINOSA

Molecular organization in solid-state using sigma-hole interactions: Exploring the effect of crystalline environment

15 Décembre 2022

Membres du jury :

Directeur(s) de thèse :

M. Enrique ESPINOSA	Professor, Université de Lorraine, Nancy
M. Emmanuel AUBERT	Maître de Conférences, Université de Lorraine, Nancy

Président de jury :

M. Marc FOURMIGUÉ	Director of Research (CNRS), Université de Rennes 1, Rennes

Rapporteurs :

M. Deepak CHOPRA	Professor, IISER Bhopal, India
M. Michael PROBERT	Senior Lecturer, Newcastle University, United Kingdom

Examinateurs :

Mme. Ie-Rang JEON	CNRS researcher, Université de Rennes 1, Rennes

Laboratoire de Cristallographie, Résonance Magnétique et Modélisations
UMR CNRS 7036, Institut Jean Barriol
Université de Lorraine

Vishnu Vijayakumar Syamala

December 15th, 2022

Dedicated to my family and friends for unconditional love and support!!!

Acknowledgements

I take this opportunity to thank all the people who helped me directly or indirectly in the realization of this thesis, without whom the realization of this PhD would not have been possible.

First of all, I would like to express my immense gratitude and sincere thanks to my thesis supervisors, Prof. Enrique Espinosa and Dr. Emmanuel Aubert, for offering me this wonderful opportunity to work in the CRM2 laboratory under their guidance. I am extremely grateful and indebted to them for sharing their expertise, their sincere and valuable advice, and their encouragement throughout the course of the thesis. I would also like to acknowledge the contribution of the former postdoctoral fellow, Dr. Rahul Shukla, for his guidance and support early in my PhD, and I am immensely grateful to him for introducing me to the fundamentals of charge density analysis.

I would also like to express my sincere gratitude to Dr. Maxime Deutsch for opening up the world of high-pressure X-ray diffraction to me. His tactical guidance and immense patience helped me learn the basic concepts of high-pressure science from scratch. In addition, his friendly nature and openness to discussion had a great influence on my research work.

I would like to thank Prof. Marc Fourmigué and Dr. Arun Dhaka, from the Condensed Matter and Electroactive Systems group (MaCSE), University of Rennes 1, for providing me with the compounds and crystals necessary for my PhD studies. Their support and suggestions helped me a lot to solve the problems I faced during my PhD work.

I am also grateful to Dr. Christian Jelsch and Dr. Benoît Guillot for troubleshooting the MoPro software whenever required. I feel extremely lucky to have Dr. Christian Jelsch right next to my office, especially when I encountered problems during electron density modeling, he always has a solution.

I am grateful to Dr. Emmanuel Wenger, for always being available to help me manage the data collection in the diffractometers. His tips and shortcuts often worked in my favor. I am also grateful for the freedom he gave me to work independently with the instrument at times, which helped me gain technical skills and confidence.

I express my sincere thanks to Abdelatif Doudouh for sharing his ideas on crystal growth and also for introducing me to the different tools available in our laboratory platform for crystal growth experiments. I am also grateful to Bruno Rock for providing me with timely help with

computer troubleshooting. I also acknowledge the great help offered by other computer technicians Cristian Lordache and Rémi Clausse at different stages of my research work.

I am grateful to Prof. Massimo Nespolo for the in-depth study of the mechanical twinning identified during our diffraction experiments, he is a master in this field.

I would like to thank the secretaries of the CRM2 laboratory - Valérie Richalet and Anne Clausse - for their timely help and kindness, as well as for putting up with my terrible French skills from time to time.

I am grateful to my fellow students Asma Hasil, Amira Ghneim, Hassan Khoder, Akihiro Umayahara, Vedran Vuković, Artem Mikhailov, Eva Mocchetti and Julien Cappele for the memorable moments we shared together, I will always cherish these memories.

I would also like to express my sincere thanks to all the other members of the CRM2 laboratory, for providing me with a great and pleasant working atmosphere. Working at CRM2 has been a great experience, which has helped me a lot both personally and professionally.

I am grateful to my flat mate Aswin Tachambalath for being there for most part of my stay in France, COVID lockdown would have been difficult without his presence. I would also like to thank all my other friends at Nancy Sunija, Aman, Anil, Gagan and Viviana for giving me memorable moments that I will remember for the rest of my life. A special thanks to my neighbors Zita and Isabelle for offering countless bottles of wine, they don't speak English and I don't speak French but we talk almost every day. I would also like to thank Dr. Subhrajyoti Bhandary for his timely suggestions and friendly behavior, I will never forget those IUCr days with you and Arun in Prague.

I express my special thanks to Kaushalya Jhuria, from being a friend and to become an important part of my life. I am grateful to God that you are in my life. I will never forget the support you have provided during the difficult times in my life.

Last but not the least, I would like to extend my gratitude with a deep sense of reverence towards my parents, family members and my friends in India, who have always supported me and been a constant source of inspiration throughout my study abroad.

Thank you all.

Abstract

Understanding the fundamentals of the formation and stabilization of non-covalent interactions is of paramount importance in the field of crystal engineering. In this direction, this thesis reports the crystallographic investigation of a sub-class of non-covalent interactions known as σ-hole interactions. σ-hole interactions are defined as those involving electrophilic sites (also called σ-holes) associated to a covalently bonded atom belonging to either *p*-block (groups 13-18) or *d*-block (groups 8,11 and 12) of the periodic table, and nucleophilic sites coming from either the same or a different molecule. Depending upon the group of the atom on which the σ-hole is present, the interaction can be further classified into various sub-classes. Out of these, we have focused on the cases of halogen bond (HaB) and chalcogen bond (ChB) interactions. As compared to the well-established case of hydrogen bonds (HB), the rationale behind the formation and stabilization of HaB and ChB are still less explored. This thesis is aimed exactly in such a direction, to provide a deeper insight into the characteristics of HaB and ChB interactions, mainly by understanding how the electron density is distributed among the interacting pair of atoms and how it eventually influences the molecular organization in solid-state.

Two main stream topics of crystallography are covered during the course of this thesis: (i) high-pressure X-ray diffraction studies and (ii) charge density analysis. Structural and electronic investigations are carried out based on the data derived from single-crystal X-ray diffraction (SCXRD) experiments performed either at ambient or extreme conditions. The so-obtained crystal structures were used to derive the electron density distribution in the periodic phases. The electron distributions of the molecular systems extracted from their crystalline environments were used to calculate the electrostatic potential in molecular surfaces and to carry out the topological analyses of the electron density and its laplacian function within the framework of the Quantum Theory of Atoms in Molecules (QTAIM) methodology. The effect of crystalline environments in tuning the properties of σ-hole interactions is also explored in detail. The information gathered from such analyses is not only helpful to better understand the molecules in hands, but also to design new molecular patterns with the aim to control the structure-properties relationship in molecular crystals.

Keywords: σ-hole interaction, single-crystal X-ray diffraction, high-pressure crystallography, molecular modelling, electron density analysis.

Introduction Générale

Cette thèse est principalement dédiée à l'étude des interactions intermoléculaires telles que les interactions à trou sigma (σ-hole), dans le contexte de l'ingénierie cristalline pour contrôler efficacement les relations structure-propriété des cristaux moléculaires. En général, les interactions à trou σ sont définies comme celles impliquant des sites électrophiles (également appelés trous σ) associés à un atome des groupes 13-17 avec des sites nucléophiles provenant soit de la même molécule, soit d'une molécule différente. Selon le groupe de l'atome sur lequel ces trous sont présents, ces interactions peuvent être divisées en sous-classes telles que les liaisons halogènes (groupe 17), les liaisons chalcogènes (groupe 16), les liaisons pnictogènes (groupe 15), les liaisons tetrel (groupe 14) et les liaisons triel (groupe 13). Récemment, ces classifications ont été étendues aux éléments du bloc d du tableau périodique (groupes des métaux de transition), où de nouvelles interactions telles que les liaisons spodium (groupe 12), les liaisons régium (groupe 11) et les liaisons osme (groupe 8) ont été introduites. Parmi celles-ci, nous nous sommes concentrés sur les études de cas des liaisons halogènes (HaB) et des liaisons chalcogènes (ChB). Comparé au cas bien établi des liaisons hydrogène (HB), le raisonnement derrière la formation et la stabilisation des HaB et ChB est encore moins exploré. Cette thèse vise précisément à fournir un aperçu plus approfondi des caractéristiques des interactions HaB et ChB, principalement en comprenant comment les densités électroniques sont distribuées parmi les paires d'atomes en interaction. Cela nous conduira finalement à comprendre l'importance de ces interactions dans le contexte de l'organisation moléculaire à l'état solide. Deux thèmes principaux de la cristallographie sont couverts au cours de cette thèse, (i) les études de diffraction des rayons X sous haute pression et (ii) l'analyse de la densité de charge. Les investigations sont menées à la fois d'un point de vue structural et électronique, sur la base des données dérivées d'expériences de diffraction de rayons X sur monocristal (SCXRD) réalisées dans des conditions ambiantes ou extrêmes.

Cette thèse a été divisée en 5 chapitres, (1) Introduction, (2) Méthodologie et procédures expérimentales, (3) Évolution de la liaison halogène dans le co-cristal : couplage de la diffraction des rayons X à haute pression et sur monocristal, (4) Organisation moléculaire des dérivés du sélénocyanate de benzyle à l'état solide : rôle des interactions de liaison chalcogène dans les topologies d'empilement et (5) conclusion générale et perspectives futures.

L'objectif principal de ce travail est de caractériser quantitativement et qualitativement les interactions à trou sigma, qui sont responsables de la directionnalité des assemblages à l'état

solide de molécules spécifiques. Les études de cas comprennent une interaction HaB $N_{donor}\cdots I\cdots N_{acceptor}$ formée dans deux co-cristaux organiques donneur-accepteur, et des interactions ChB Se···N et/ou Se···Se formées dans trois dérivés du sélénocyanate de benzyle. Une série d'expériences SCXRD a été réalisée pour cette étude, soit dans des conditions ambiantes, soit à basse température (100K), soit dans un environnement à haute pression généré dans une cellule à membrane à enclume de diamant (MDAC). Les structures cristallines ainsi obtenues sont traitées dans le cadre de la méthodologie de la théorie quantique des atomes dans les molécules (QTAIM), afin de répartir la densité électronique totale entre les atomes. Ensuite, la distribution de la densité électronique des atomes impliqués dans les interactions à trou sigma est analysée, en particulier comment les sites de concentration de charge (CC) et de dilution de charge (CD) sont placés les uns par rapport aux autres dans le cas d'une interaction CC···CD (scénario le plus fréquent dans HaB et ChB). Les informations recueillies à partir de ces analyses sont non seulement utiles pour mieux comprendre les molécules en question, mais aussi pour concevoir de nouveaux modèles moléculaires en utilisant des composés modèles dans le but de contrôler les relations structure-propriété dans les cristaux moléculaires. Bien que cette thèse soit principalement axée sur les études expérimentales, des calculs théoriques sont également effectués afin de valider les résultats expérimentaux et enrichir les informations disponibles pour les molécules d'intérêt.

Chapitre 1 - Introduction

Dans ce chapitre d'introduction de base, les sujets de recherche qui sont pertinents pour cette thèse sont inclus. Ce chapitre commence par la pertinence des interactions non covalentes dans le domaine de l'ingénierie des cristaux molécualires, en discutant brièvement les cas les plus courants d'interactions non covalentes dans les cristaux organiques. Ensuite, les concepts et la classification des interactions à trou σ sont exposés. Une étude détaillée de la littérature sur la caractérisation structurelle des interactions à trou σ dans les cristaux moléculaires est présentée, fournissant des exemples représentatifs d'architectures supramoléculaires de différentes formes résultant de ces interactions dans les auto-assemblages moléculaires ainsi que dans les cristaux multicomposants. Ensuite, le contexte historique et les caractéristiques électroniques des HaB et ChB sont discutés. Au cours de cette discussion, le mode d'interaction et les différentes perspectives de leur stabilisation sont explorés. De plus, des exemples de la littérature où le HaB révèle un caractère de liaison covalente partielle sont mis en évidence. Un autre sujet d'investigation dans cette thèse est les facteurs accordant la force des interactions à trou σ, où

les aspects de modification synthétique, les bons choix de composés, l'influence des stimuli externes et l'effet de l'environnement cristallin sont détaillés.

Chapitre 2 - Méthodologie et procédures expérimentales

Ce chapitre décrit les méthodes et les outils expérimentaux qui sont utilisés pour la caractérisation structurale et électronique des interactions à trou σ. L'importance de la distribution de la densité électronique $\rho(\mathbf{r})$ dans la caractérisation des interactions non covalentes est discutée, suivie des moyens expérimentaux et théoriques pour l'obtenir dans les cristaux moléculaires. Les principes fondamentaux des différents modèles d'affinement de la densité électronique sont détaillés. En outre, les avantages de l'analyse topologique des densités électroniques ainsi obtenues sont discutés, ainsi que son utilité pour la description des interactions intermoléculaires se produisant dans les cristaux moléculaires. La deuxième partie de ce chapitre présente les méthodes de cristallisation : outils et techniques, qui sont utilisés pour produire des cristaux de bonne qualité des molécules étudiées. Dans la section suivante, la discussion porte sur les concepts des expériences de SCXRD à haute pression : importance et limites associées. Enfin, le chapitre se termine par les détails du dispositif expérimental à haute pression installé au laboratoire CRM2.

Chapitre 3 - Evolution de la liaison halogène dans les cocristaux : couplage de la technique haute pression avec la diffraction des rayons X sur monocristal

L'objectif principal de ce chapitre est de comprendre comment les interactions intermoléculaires dans un cristal moléculaire évoluent sous l'effet d'une pression externe, en utilisant les données obtenues à partir d'une série d'expériences de diffraction des rayons X sur monocristal à haute pression (HP-SCXRD) réalisées avec une cellule MDAC. Deux systèmes de cocristaux donneurs-accepteurs, composés de N-iodosaccharine (NISac) agissant comme donneur de HaB et de deux dérivés de la pyridine [pyridine (Py) elle-même et 4-cyanopyridine (4CYP)] agissant comme accepteurs de HaB, sont utilisés à cette fin. Ce chapitre couvre les voies de co-cristallisation, les expériences HP-SCXRD en laboratoire, la réduction et l'analyse des données, ainsi que les calculs théoriques effectués afin d'étayer ces résultats expérimentaux. Les cocristaux contiennent un important motif HaB $N_{donor}\cdots I\cdots N_{acceptor}$ dans leur unité asymétrique, qui montre des modifications graduelles sous pression en raison des changements dans l'environnement cristallin. Le motif principal de ce travail est d'explorer la possibilité de transition d'un cocristal à une forme ionique de l'adduit binaire sous pression, en modulant la position de l'atome d'halogène entre les parties donneur et accepteur. Une pression externe allant

de 0.00(5) GPa à 5.0(2) GPa est appliquée en utilisant un ou plusieurs monocristaux montés à l'intérieur de la cellule MDAC. L'analyse est effectuée d'un point de vue structural et électronique, en utilisant respectivement le modèle structural obtenu après les expériences de HP-SCXRD et les adduits binaires donneur···accepteur extraits de la géométrie du cristal et traités avec la méthodologie QTAIM à chaque pression.

Les résultats obtenus à partir des expériences HP-SCXRD révèlent que, dans les deux cocristaux, l'atome d'iode initialement trouvé plus près du donneur commence à migrer plus près de l'accepteur en augmentant la pression. Ceci est également vérifié à partir des données théoriques à haute pression et des propriétés électroniques déterminées aux points critiques de liaison N_{donor}···I et I···$N_{acceptor}$. Mais malheureusement, dans les analyses structurales et électroniques, l'environnement électronique différent des atomes N_{donor} et $N_{acceptor}$ est resté un obstacle principal pour conclure à l'état exact du système à haute pression. Cependant, compte tenu des incertitudes sur les distances HaB et les valeurs des propriétés topologiques, il est conclu que les deux adduits binaires à haute pression doivent être considérés comme une seule unité moléculaire plutôt que comme deux entités distinctes.

Chapitre 4 - Organisation moléculaire des dérivés du sélénocyanate de benzyle à l'état solide : rôle des interactions de liaison chalcogène dans les topologies d'empilement.

Ce chapitre est consacré à l'exploration des caractéristiques des interactions Se···N et/ou Se···Se ChB, qui sont responsables de l'organisation moléculaire des dérivés du sélénocyanate de benzyle à l'état solide. Des investigations sont menées avec trois dérivés différents de la famille des sélénocyanates de benzyle, (1) le sélénocyanate de benzyle (SeCN1), (2) le benzène ortho-bis(sélénocyanatométhyle) (SeCN2) et le sélénocyanate de 2-(méthylsélanyle) benzyle (SeCN3). Les structures cristallines de SeCN1 et SeCN2 présentent une topologie de type chaîne 1D dirigée par la formation d'interactions ChB récurrentes ···NC(R)Se···NC(R)Se···NC(R)Se···. L'analyse énergétique des interactions intermoléculaires a montré que ces topologies de type chaîne 1D jouent un rôle décisif dans l'organisation à l'état solide des molécules respectives. Parallèlement, dans SeCN3, un choix supplémentaire d'une base de Lewis sous la forme d'une paire libre de Se dans le groupe -(R)Se-CH_3 entraîne la formation de deux motifs ChB forts dans la structure cristalline, (R)Se···Se et (R)Se···N. Cela conduit finalement à des topologies d'empilement différentes dans SeCN3 par rapport aux deux premières molécules. La raison derrière un tel changement préférentiel dans les interactions ChB est étudié.

Ce chapitre couvre principalement les voies de cristallisation, les expériences de diffraction des rayons X à haute résolution à basse température, l'affinement de la structure à l'aide du modèle d'atomes indépendants et du modèle multipolaire de Hansen-Coppens, ainsi que l'analyse topologique des fonctions de densité électronique $\rho(\mathbf{r})$ et du laplacien de la densité électronique $L(\mathbf{r})$. La force des interactions individuelles des ChB a été estimée en utilisant les propriétés topologiques et énergétiques de $\rho(\mathbf{r})$ déterminées au niveau de leurs BCPs. Ensuite, les interactions ChB locales nucléophiles--électrophiles sont étudiées alternativement comme l'interaction entre les sites CC et CD obtenue à partir de l'analyse topologique de la fonction $L(\mathbf{r})$. L'intensité électrostatique des interactions individuelles CC···CD est évaluée par un paramètre $\Delta(L/\rho)$. En tenant compte de la distance entre les sites CC et CD en interaction, un autre paramètre $\Delta(L/\rho)/d^2_{CC\cdots CD}$ est introduit qui, avec l'angle α (α est l'angle entre les directions CC···CD et atome···atome), indique les interactions CC···CD les plus pertinentes pour les préférences géométriques des atomes en interaction dans les interactions ChB.

L'analyse a révélé des valeurs de $\Delta(L/\rho)/d^2_{CC\cdots CD}$ plus grandes et des angles plus faibles pour les interactions CC···CD qui correspondent aux interactions ChB impliquant des trous forts des atomes de Se, par rapport à celles impliquant des trous faibles. De même, les propriétés électroniques dérivées de l'analyse topologique des fonctions $\rho(\mathbf{r})$ et $L(\mathbf{r})$ suivent la tendance et confirment les résultats obtenus précédemment lors des caractérisations structurales.

Chapitre 5 - Conclusions générales et perspectives futures

Dans ce dernier chapitre, les principales conclusions tirées des analyses ci-dessus sont discutées, en référence à l'importance de ce travail de thèse qui offre un aperçu crucial des interactions à trou sigma, à la fois structuralement et électroniquement.

Enfin, les perspectives futures de ce travail de thèse sont discutées, en ce qui concerne les autres détails qui peuvent être ajoutés au travail actuel pour améliorer la richesse de l'information et pour aborder les situations problématiques rencontrées au cours de cette étude.

CONTENTS

1

Introduction

This chapter aims to give an introductory overview of research topics that are going to be discussed in the follow up of this thesis. This mainly includes the concepts of σ-hole interactions, which are a sub-class of non-covalent interactions playing a significant role in the solid-state assembly of molecules containing *p*-block as well as some *d*-block elements of the periodic table. Out of these, emphasis is given to σ-hole interactions involving halogen (group 17) and chalcogen (group 16) atoms, and to their potential availabilities to act as electrophilic sites while interacting with nucleophilic sites. Other than structural characterizations based on single-crystal X-ray diffraction studies, a strong attempt will be made throughout this thesis to characterize the electronic properties of these σ-hole interactions. In addition, the effect of crystalline environment, as well as other factors potentially tuning the strength of σ-hole interactions, will be explored.

1.1 Crystal engineering and the role of non-covalent interactions

This thesis work is mainly placed in the domain of crystal engineering, which is an inevitable part of crystallography due to its immense applications to multidisciplinary topics ranging from pharmaceuticals to material science and supramolecular chemistry. In this thesis, we will investigate the aspects of crystal engineering related to organic crystals, to understand their structure-properties relationships in solid-state.

The term "crystal engineering" was first introduced by Pepinsky in the American Physical Society meeting of 1955 (Pepinsky, 1955), but it gathered more attention in the scientific world when G. M. J. Schmidt used it again in 1971 to explain the solid-state reactivity of photodimerizable *trans*-cinnamic acid (Schmidt, 1971). However, the current practice of the term is more connected with the seminal definition given by Desiraju in 1989 as "*The understanding of intermolecular interactions in the context of crystal packing and in the utilization of such understanding in the design of new solids with desired physical and chemical properties*" (Desiraju, 1989). Therefore, the field of crystal engineering can be considered as an outcome of interplay between crystallography and chemistry, where chemistry deals with the notion of molecules and crystallography with the extended assemblies resulting from those molecules, known as crystals. The cohesion of molecules in a crystal is accomplished through some forces of attraction known as intermolecular interactions, acting as a connecting bridge between molecules (Novoa, 2018). By definition, these intermolecular interactions are known as non-covalent interactions that occur between atoms of different molecules. At the same time, it is also possible that atoms of the same molecule interact non-covalently. This is known as an

intramolecular interaction and is mainly responsible for constraining the geometry of a molecule in the solid-site, along with the covalent connectivity. In this thesis, we will only focus on non-covalent interactions between molecules, thus notions of intermolecular interactions are only covered in detail.

Individual non-covalent interactions are known to be weaker than covalent bonds in their energy, but they can play a decisive role in driving the molecular arrangement in the solid-state, influencing the properties of the resulting crystal (Batsanov, 2018). Non-covalent interactions also find their importance in various other topics of crystal engineering such as solid-state screening of Active Pharmaceutical Ingredients (API) (He *et al.*, 2008), understanding polymorphism of molecular compounds (Arkhipov *et al.*, 2019), isostructural behaviors observed among different crystal structures (Mondal *et al.*, 2018), designing mechanically flexible molecular crystals (Gupta *et al.*, 2020), etc. Many different types of non-covalent interactions have been identified in molecular crystals thus far, hydrogen bonding (HB) being a classical example among them. The study of HB interactions marks its origin from the very beginning of the crystal engineering field, may be even before that in other domains of crystallography. To date, these interactions have been extensively studied in numerous molecular crystals, in terms of their occurrence, directional preferences, strength and nature (Desiraju, 2011). HB interactions are ubiquitous in organic crystals, and their deep understanding is necessary not only to discuss about the crystal packing of molecules in hand but also to design new molecular frameworks to achieve desirable properties. According to the IUPAC "*The hydrogen bond is an attractive interaction between a hydrogen atom from a molecule or a molecular fragment H-X in which X is more electronegative than H, and an atom or group of atoms in the same or a different molecule, in which there is evidence of bond formation*" (Arunan *et al.*, 2011). Accordingly, this definition points towards the electrostatic origin of HB interactions, where the H-atom covalently bonded to a more electronegative X-atom produces an electrophilic site (HB donor), which interacts with a complementary nucleophilic site coming from another Y-atom of the same or a different molecule (HB acceptor) (**Figure 1.1a**). Depending on the nature of the donor X and acceptor Y atoms, HB interactions can also possess a partial covalent or dispersive-repulsive character in its formation. In addition, based on the interaction energy, HB interactions can be further classified into very strong (63-167 kJ/mol), strong (17-63 kJ/mol) and weak (<17 kJ/mol) types. In general, a very-strong or a strong HB is characterized by a short H···Y distance and a directional (large angle < X-H···Y) contact between atoms (Desiraju and Steiner, 2001). Concerning their importance,

HB interactions find immense applications in many chemically and biologically active systems (Perrin and Nielson, 1997; Steiner, 2002), as well as in the aggregation and functionalities of many molecular materials (Hutchins, 2018).

Another prominent category of non-covalent interaction that is vastly discussed in the literature is the π···π stacking interaction, which is mainly identified in the solid-state array of compounds containing conjugated π electrons (Thakuria *et al.*, 2019). By definition, π···π interactions are the force of attraction or repulsion between π orbitals of a molecular system, and sometimes between π and σ orbitals of the molecular system. For instance, considering the case of a simple benzene ring, this π···π interactions can be of three different types: (i) sandwich, (ii) edge-to-face and (iii) parallel displaced (**Figure 1.1b**). Sandwich interactions (also known as face-to-face interactions or co-facial parallel stacked interactions) are generally repulsive in nature because of the face-to-face orientation of π-electron clouds belonging to benzene molecules. Accordingly, they only have a minor stabilization energy of ~ 4.2 kJ/mol while forming a molecular dimer (Sinnokrot and Sherrill, 2004). On the other hand, edge-to-face and parallel displaced interactions are mostly attractive in nature, in line with the orientation of two opposite charges facing each other. In an edge-to-face interaction (also known as a C-H···π interaction

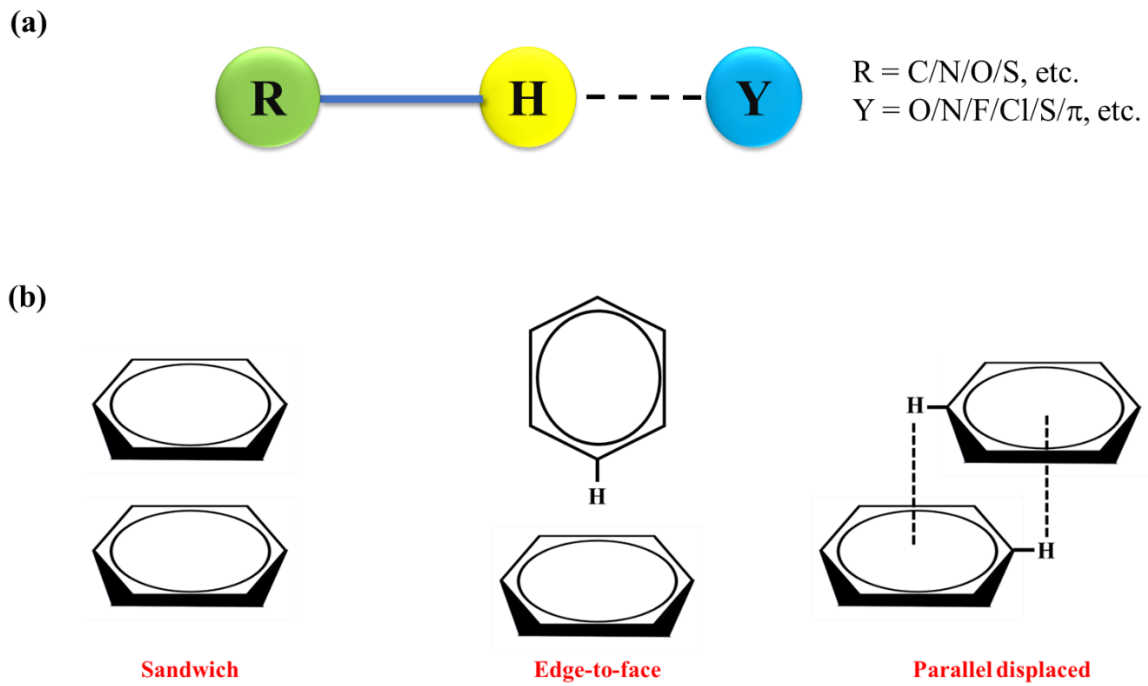

Figure 1.1 (a) schematic representation illustrating hydrogen bonding (HB) interaction, (b) three possible types of π···π stacking interactions found in benzene molecule (H-atoms are shown only if necessary to point the type of interaction).

or a T-shaped interaction) a positively charged region of the H-atom in one benzene ring is facing the π-electron cloud of the other benzene ring, making this interaction stabilizing (11-12 kJ/mol; Sinnokrot and Sherrill, 2004). The third possibility, the parallel displaced interaction (also known as a slip-stacked interaction) is also energetically stabilizing (11-12 kJ/mol; Sinnokrot and Sherrill, 2004), where two simultaneous interactions of positively charged regions of H-atom with the π-electron clouds in the benzene are observed. Considering the case of other aromatic compounds, small and unsubstituted derivatives prefer an edge-to-face orientation, whereas substituted and large derivatives prefer a parallel displaced orientation. At the same time, the occurrence of a face-to-face sandwich orientation is a very rare scenario among molecular crystals, unless the nature of π-electron clouds is altered with functional group substitutions in aromatic rings. A sandwich or a parallel displaced π···π interaction is often causing a layered type of packing in molecular crystals, which finds its importance in topics like mechanical properties (Hayashi, 2020), conductivity (Yao *et al.*, 2018), thermal expansion and thermochromism (Dharmarwardana *et al.*, 2021), etc.

Other than the above discussed interactions, there are multiple other non-covalent interactions frequently found in molecular crystals, such as cation-π interactions (Yamada, 2020), anion-π interactions (Wang and Wang, 2020), methyl···methyl interactions (Sarkar *et al.*, 2019) and dihydrogen interactions (Damodharan and Pattabhi, 2004). However, in this thesis, our main focus will be on another sub-class of non-covalent interactions known as σ-hole interactions. σ-hole interactions are defined as those involving electrophilic regions (σ-holes) associated to a covalently bonded atom (σ-hole donor) from the *p*-block (groups 13-18) of the periodic table with nucleophilic regions (σ-hole acceptor) coming from either the same or a different molecule (Murray *et al.*, 2009). Recently, this terminology was extended to some of the *d*-block elements (transition metal elements) in the periodic table as well, because of similar bonding characteristics appeared among all (Alkorta *et al.*, 2020; Daolio *et al.*, 2021a; Daolio *et al.*, 2021b). σ-hole interactions find very close resemblances with HB interactions in terms of its origin and mode of interaction. The main difference between them is that in a σ-hole interaction the H-atom of a HB interaction is replaced with a heavier atom from either the *p*-block or the *d*-block of the periodic table. Consequently, the additional effect of core electrons needs to be considered. Also, based on the group to which the atom bearing the σ-hole belongs these interactions can be further classified into various types, as shown in **Figure 1.2**. Out of those, in this thesis we will focus on halogen bond (HaB) and chalcogen bond (ChB) interactions.

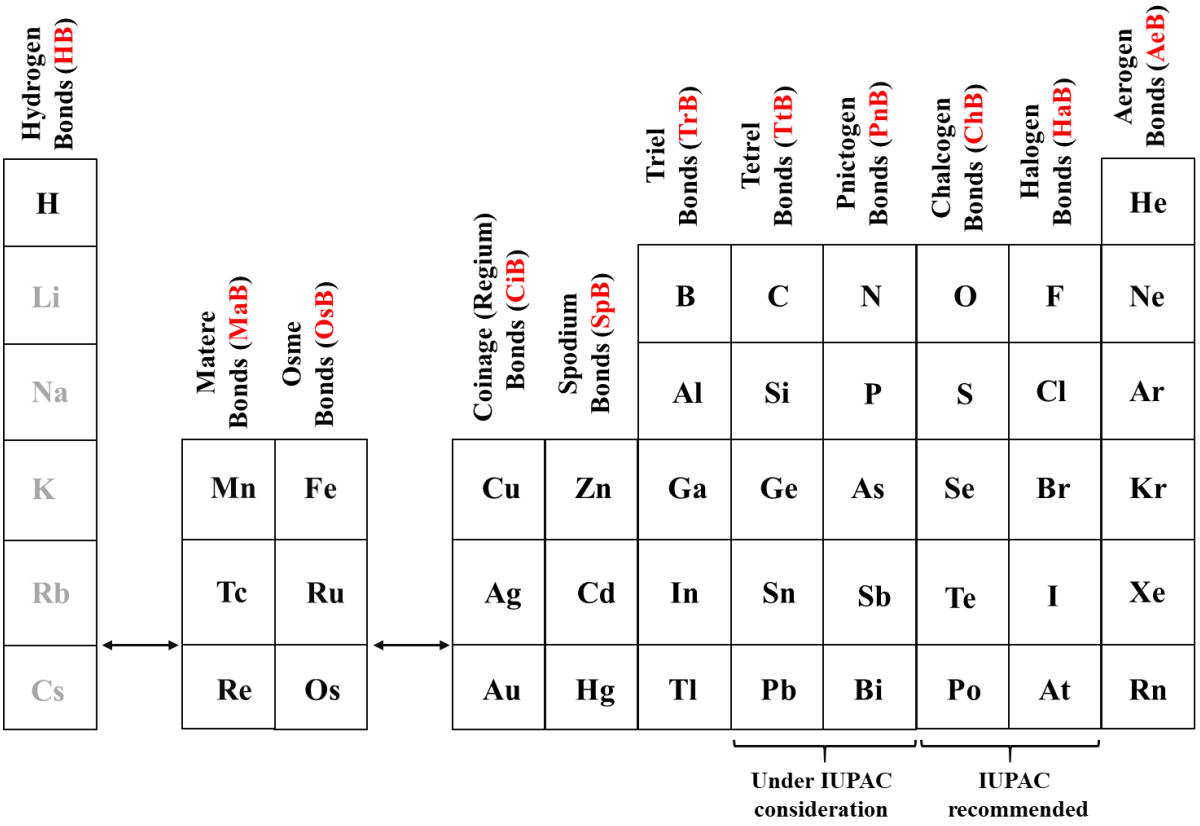

Figure 1.2 Classification of σ-hole interactions based on the group to which the atom bearing the σ-hole belongs. Terminologies and their abbreviations (in bracket) are given corresponding to each group.

As notified in **Figure 1.2,** a formal IUPAC definition is assigned for both HaB and ChB interactions, whereas the cases of pnictogen bond (PnB) and tetrel (TrB) bond are in the consideration. A more detailed discussion concerning the history, definition and electronic origin of HaB and ChB interactions, and their resemblances with HB interactions, is given in the below section.

1.2 Structural characterization of σ-hole interactions: self-assemblies to multicomponent systems

This section will detail the structural characterization of σ-hole interactions in molecular crystals (focusing on HaB and ChB interactions), and their role in directing solid-state assemblies of those associated molecules. In the literature, σ-hole interactions are most often characterized on their atomic geometries obtained from single-crystal X-ray diffraction (SCXRD) experiments. In these studies, the extent of an interaction strength (either σ-hole or other kind) is determined based on a quantity called *reduction ratio* (RR), which is defined as the ratio between the atom···atom distance and the sum of their van der Waals radii.

Accordingly, a lower RR (< 1) implies a stronger interaction. However, sometimes, interactions with RR greater than one (typically < 1.03) are also important in the driving of the crystal packing. In such a way, RR values can be used as a quantitative tool to describe the crystal packing of a molecule, or to identify interactions that are most significant in the construction of the crystal packing. This quantity can also shed light into the significance of σ-hole interactions in the crystal packing and their role in directing solid-state assemblies. Besides RR, the interatomic interaction angle is another important factor that should be considered in case of a σ-hole interaction, because a face-to-face orientation of the involved electrophilic and nucleophilic sites brings a better σ-hole interaction. Thus, along with a lower RR, an interatomic angle close to 180^{o} points to a strong σ-hole interaction.

σ-hole interactions are known to form supramolecular architectures of various shapes in solid-state assemblies, starting from zero-dimensional aggregates to complexes structures such as supramolecular helices or interpenetrated 3D networks. Such examples can be encountered in molecular self-assemblies, as well as in multicomponent systems. Generally, in terms of a σ-hole interaction, the construction of a multicomponent system is done in such a way that one of the constituents acts as a σ-hole donor and the other as a σ-hole acceptor so that they crystallize together to form a single crystalline solid. In the following discussion, some representative examples of supramolecular architectures, featured either in a molecular self-assembly or in a multicomponent system, are highlighted. For the given examples, σ-hole interactions are structurally characterized *via* the RR descriptor and interatomic interaction angles.

1.2.1 Supramolecular architectures directed by σ-hole interactions in molecular self-assemblies

The simplest structural unit that can exhibit evidence of a σ-hole interaction is the molecule itself, where σ-hole donor and acceptor atoms are embedded within the molecule and well oriented in space to form an intramolecular σ-hole interaction. Two such examples are given in **Figure 1.3**, where intramolecular Br···O HaB and Se···O ChB interaction are identified respectively in the molecules 3-(2-((2-Bromo-3,4,5,6-tetrafluorophenyl) ethynyl) phenyl)-1-(4-methoxyphenyl) prop-2-yn-1-one interaction (Widner *et al.*, 2014) and ortho-nitrophenyl selenocyanate (Wang *et al.*, 2018). In both these cases, intramolecular σ-hole interactions act like a conformation lock, which decides the final geometry of the molecule in its crystal phase. Another possible outcome *via* a σ-hole is the formation of a molecular dimer. Here, σ- hole

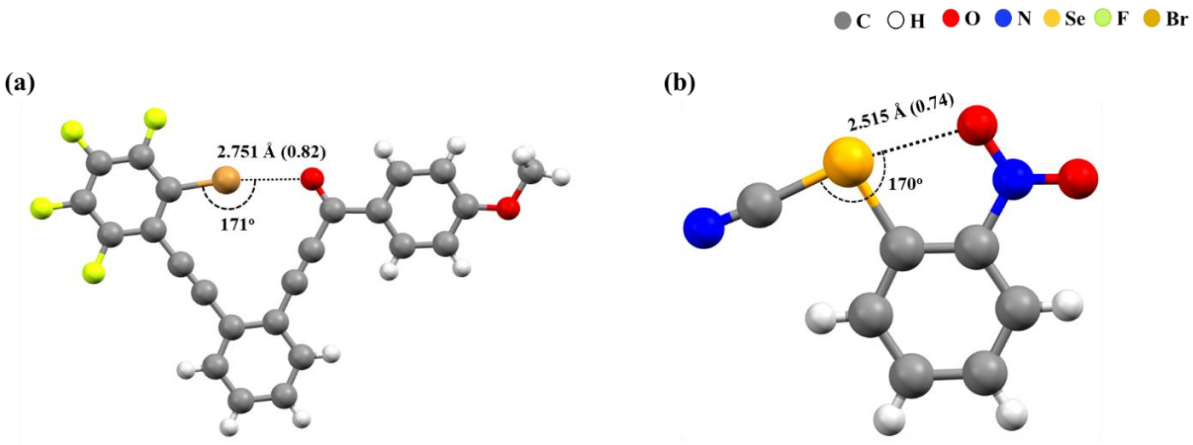

Figure 1.3 (a) intramolecular Br···O HaB interaction found in 3-(2-((2-Bromo-3,4,5,6-tetrafluorophenyl) ethynyl) phenyl)-1-(4-methoxyphenyl) prop-2-yn-1-one, (b) intramolecular Se···O ChB interaction found in ortho-nitrophenyl selenocyanate. Atoms are shown with colouring scheme and intramolecular σ-hole interactions are depicted as black dashed lines with corresponding atomic distances (in Å) and interatomic interaction angles (in degrees). The values within the bracket are the RR of determined distances. Figures are generated from deposited cif files.

donor and acceptor atoms belong to two different molecules and they interact each other to form an intermolecular σ-hole interaction. Later, in the crystal packing, this molecular dimer can exist either as a zero-dimensional aggregate (discrete molecular dimer) or as an extended assembly of larger dimension. Examples of zero-dimensional aggregates are shown in **Figure 1.4**, composed by a symmetry related I···N HaB interaction in the 3-((2,3,4,5-tetrafluoro-6-iodophenyl)ethynyl)pyridine molecule (Oburn *et al.*, 2015) and by a symmetry related Se···N ChB interaction in the 4,5,6,7-tetrachloro-2,1,3-benzoselenadiazole molecule (Prima *et al.*, 2017). In both cases, discrete molecular dimers are further connected through other intermolecular interactions to constitute the entire three-dimensional packing of molecules.

Higher order aggregates resulting from recurrent intermolecular σ-hole interactions (or as a continuous repetition of molecular dimers) can be of several types. One common and frequently observed case among them is the formation of one-dimensional (1D) chain-like architecture, where the σ-hole interaction connecting molecules adopts a linear or a nearly linear geometry. Accordingly, 1D chain-like architectures formed in the molecular self-assemblies of 4-iodo-2,3,5,6-fluoro-benzonitrile (Bond *et al.*, 2001) and benzyl selenocyanate (Maartmann-moe *et al.*, 1984) molecules are depicted in **Figure 1.5**. In both of them, the interatomic interaction angle (167° and 169°, respectively) points a nearly linear geometry of the σ-hole interaction.

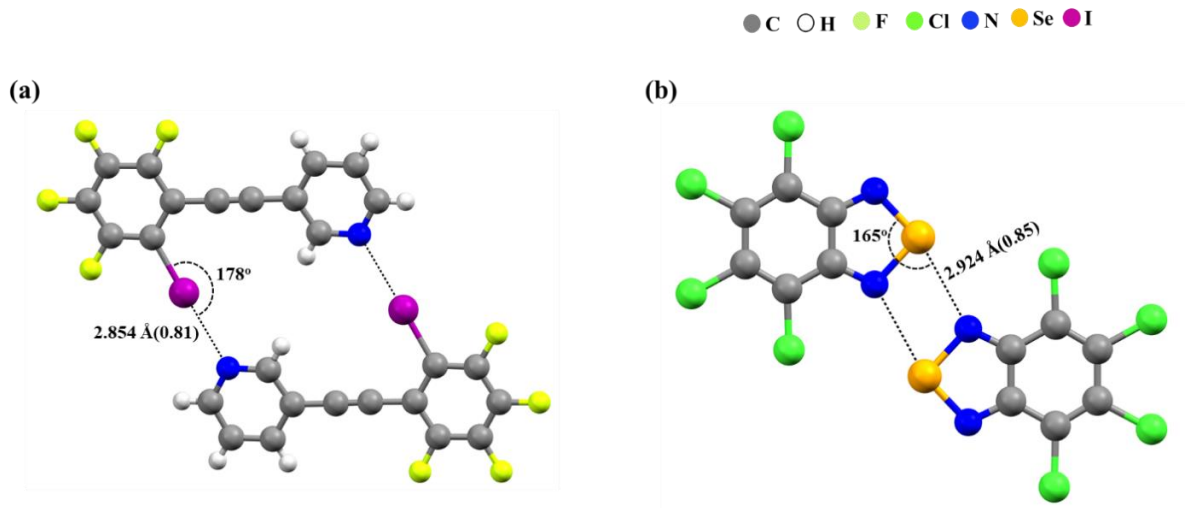

Figure 1.4 (a) intermolecular I···N HaB interaction found in 3-((2,3,4,5-tetrafluoro-6-iodophenyl)ethynyl)pyridine and (b) intermolecular Se···N ChB interaction found in 4,5,6,7-tetrachloro-2,1,3-benzoselenadiazole. Atoms are shown with colouring scheme and intermolecular σ-hole interactions are depicted as black dashed lines with corresponding atomic distances (in Å) and interatomic interaction angles (in degrees). The values within the bracket are the RR of determined distances. Figures are generated from deposited cif files.

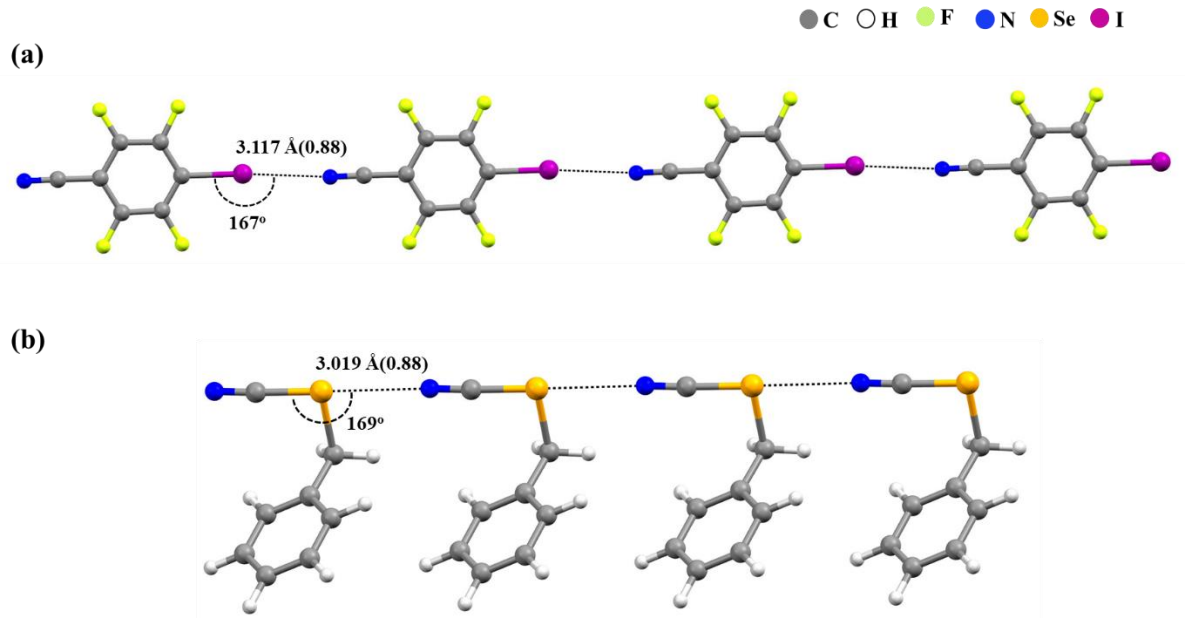

Figure 1.5 Linear 1D chain-like architecture formed *via*: (a) HaB interaction in 4-iodo-2,3,5,6-fluoro-benzonitrile and (b) ChB interaction in benzyl selenocyanate. Atoms are shown with colouring scheme and σ-hole interactions are depicted as black dashed lines with corresponding atomic distances (in Å) and interatomic interaction angles (in degrees). The values within the bracket are the RR of determined distances. Figures are generated from deposited cif files.

Increasing the number of potential σ-hole donor and acceptor sites within the molecular framework can induce aggregation of even higher order supramolecular architectures, such as two-dimensional (2D) and three-dimensional (3D) systems. Even though this approach is sometimes demanding a complex synthetic scheme for the starting block, it has been successfully implemented in many molecular systems during the past years (Cavallo *et al.*, 2016). The 2D sheet-like architecture found in molecular self-assemblies of (5-iodopyridinium-2-yl)([4-bromophenyl]sulfonyl)azanide (Gelbrich *et al.*, 2012) and dicyanoselenide (Klapötke *et al.*, 2008) are shown in **Figure 1.6**. In the case of (5-iodopyridinium-2-yl)([4-bromophenyl]sulfonyl)azanide, the I···Br interactions were identified as the stacking synthon that constitutes the 2D array of molecules, where both I and Br atoms simultaneously act as σ-hole donor and acceptor, exhibiting an amphoteric behaviour (the electronic origin of this behaviour is discussed below). On the other hand, in dicyanoselenide two Se···N ChB interactions of different strengths (different RR values) were found as responsible synthons in constructing the 2D arrangement of molecules.

Most reports concerning the formation of a 3D architecture directed through σ-hole interactions are actually based on a co-crystal rather than a molecular self-assembly, where two separate molecules possessing multiple choices of σ-hole donor and acceptor sites are combined together (discussed below). Nevertheless, the formation of supramolecular helices driven by σ-hole

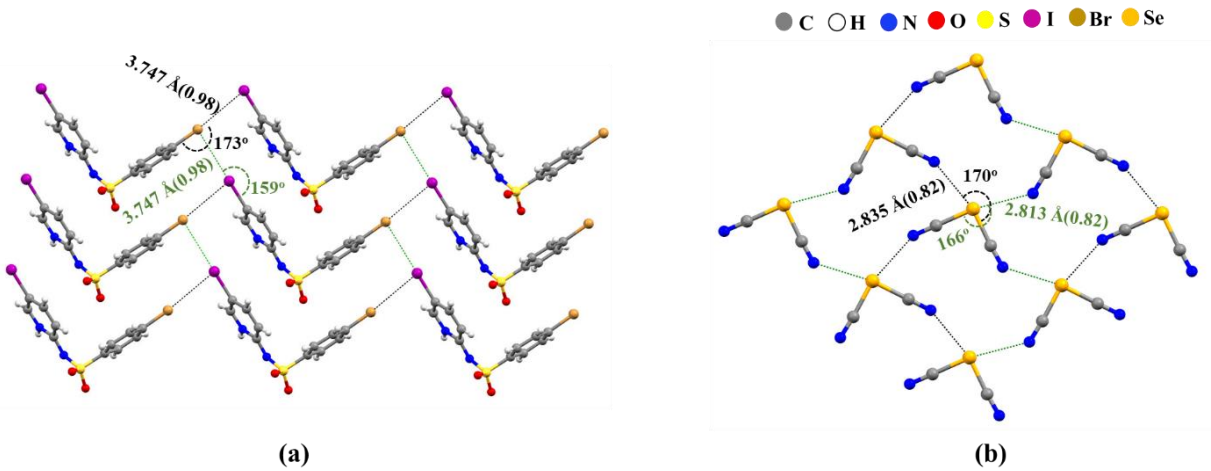

Figure 1.6 2D sheet-like architecture found in, (a) (5-iodopyridinium-2-yl)([4-bromophenyl]sulfonyl)azanide and (b) dicyanoselenide. Atoms are shown with colouring scheme. In (a), I···Br interactions, where I acts as the HaB donor and Br as the HaB acceptor, and vice-versa, are shown respectively as green and black dashed lines. In (b), two types of Se···N ChB interactions are shown as green and blacked dashed lines. Atomic distances (in Å) and interatomic interaction angles (in degrees) are given, values within the bracket are the RR of determined distances. Other interatomic interactions within the 2D network (supporting the synthons) are omitted for better clarity. Figures are generated from deposited cif files.

interactions in peptides can be considered as a sub-class of 3D architectures, even though other type of interactions also are found significant in stabilizing these helical structures. Two such representative examples are highlighted in **Figure 1.7**. In the case of an I-substituted the propagation of the helicity of β-turn structures is achieved through C-I···π HaB interactions (here the π-electron cloud of the benzene ring acts as the nucleophile) (Cao *et al.*, 2017), whereas in another derivative of the same azapeptide (thiophene group attached to *C*-termini) S···O ChB interactions were found responsible for holding the helical structure (Shi *et al.*, 2021).

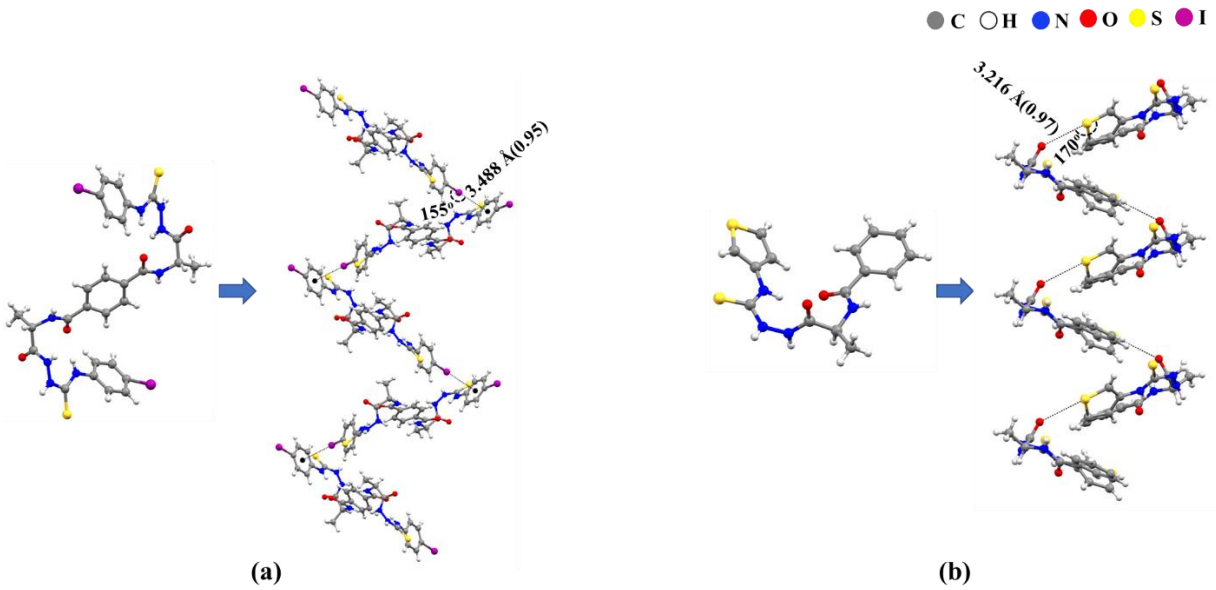

Figure 1.7 Supramolecular helices found in two derivatives of N-amidothiourea (an alanine based azapeptide): (a) I-substituted derivative and (b) derivative in which the thiophene group is substituted at *C*-termini. Atoms are shown with colouring scheme, σ-hole interactions are shown as black dashed lines with corresponding distances (in Å) and angles (in degrees). Values within the bracket are the RR of determined distances. Figures are generated from deposited cif files.

1.2.2 Supramolecular architectures directed by σ-hole interactions in multicomponent crystals

Multicomponent crystals are those solid-state materials where more than one molecular or ionic species are crystallized together to form a single crystalline solid (Tiekink & Zukerman-Schpector, 2017). Formation of multicomponent crystals are often considered as an efficient way to modify properties of a given molecule of interest (often referred as parent compound) in its solid phase. Multicomponent crystals can be further classified into hydrates, solvates, salts and co-crystals, depending upon the species that crystallize along with the parent compound. Hydrates and solvates are the cases where the parent compound respectively crystallizes along

with water and other solvent molecules (Byrn *et al*., 2017). Most often, the occurrence of these hydrates and solvates are unintentional outcomes of crystallization *via* the solvent evaporation method, but yet they find abundant applications in crystal engineering. On the other hand, formation of co-crystals and salts are done with specific aims, mainly to vary physicochemical properties of the parent compound in a desirable manner (Wouters and Quéré, 2012). The species that crystallize along with the parent compound are known as co-formers, and they are generally selected on the basis of the property of the parent compound that we want to vary with. Further, the single crystalline solid resulting from the combination of the parent compound with the co-former can either be called as a salt or a co-crystal. According to IUPAC, a salt is defined as "a chemical compound comprising an assembly of cations and anions" (McNaught and Wilkinson, 1997). This implicitly means that an effective charge transfer takes place from the parent compound to the co-former, or vice-versa, during the formation of the single-crystalline solid, while a definite stoichiometry should be maintained to accomplish charge neutrality. Unlike salts, co-crystals do not have any formal IUPAC definition, but they are mostly considered as a combination of neutral molecular compounds (Bond, 2007). Accordingly, implies that there is no formal charge transfer between the constituents during the co-crystallization process. It should be kept in mind that co-crystals are not just limited to binary compounds, there are other possibilities such as ternary co-crystals (with three components; Tothadi and Desiraju, 2013), quaternary co-crystals (with four components; Rajkumar, 2021), etc. In this thesis, we will cover only the aspects of co-crystals and salts as representatives of multicomponent crystals, formed mainly through σ-hole interactions.

Supramolecular architectures found earlier with molecular self-assemblies can also be encountered with multicomponent crystals, where in general different molecules bearing the σ-hole donor and the σ-hole acceptor are combined together to form a single crystalline solid of desirable property. This property can also be the formation of a molecular assembly of particular shape. Accordingly, some supramolecular architectures directed by σ-hole interactions in two component co-crystals are given below.

Figure 1.8 highlights examples of co-crystals featuring a zero-dimensional aggregate (or a discrete dimeric structure) in their solid-state assemblies: (i) iodopentafluorobenzene with 2,6-dimethy pyridine, formed through the I···N HaB interaction (Wasilewska *et al*., 2007) and (ii) ebselen with 4-dimethyl amino pyridine, formed through the Se···N ChB interaction (Fellowes and White, 2019). In both co-crystals, the number of activated σ-hole donor and acceptor sites (best ones; only one each) restrict the shape of the supramolecular assembly to be a discrete

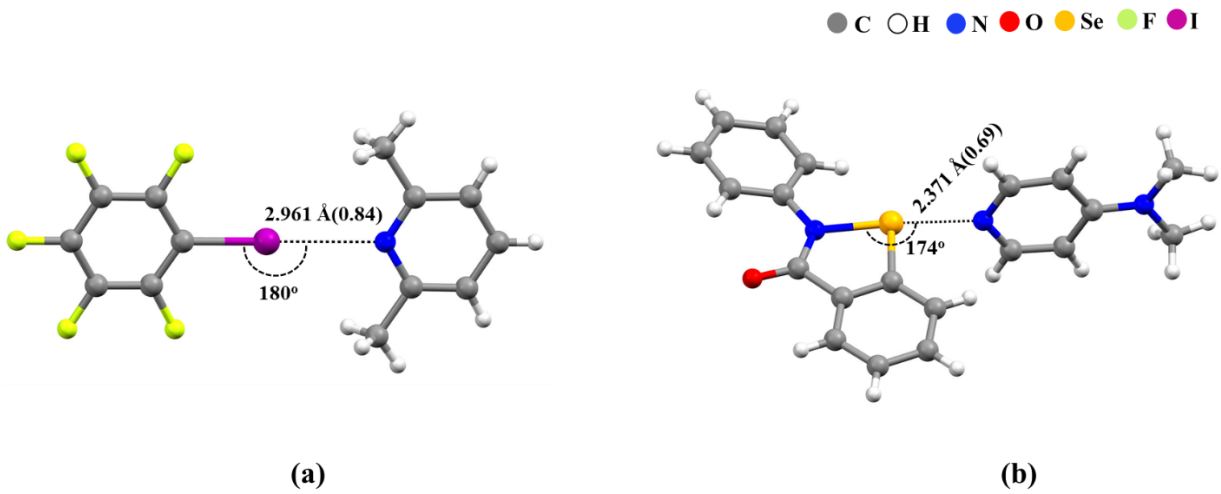

Figure 1.8 Zero-dimensional aggregate (or discrete dimeric structure) formed in the co-crystals of: (a) iodopentafluorobenzene with 2,6-dimethy pyridine and (b) ebselen with 4-dimethylamino pyridine. Atoms are shown with colouring scheme, σ-hole interactions are shown as black dashed lines with corresponding distances (in Å) and angles (in degrees). Values within the bracket are the RR of determined distances. Figures are generated from deposited cif files.

dimer. Also, in both cases, the propensity to form a σ-hole interaction is increased with an adequate functional group substitution in molecular scaffolds of both donor and acceptor entities (more details regarding the tuning of the σ-hole interaction *via* a chemical substitution is discussed in the section below).

In the second set of examples given in **Figure 1.9**, activated bidentate σ-hole donor molecules are combined with activated bidentate σ-hole acceptor molecules to adopt a 1D chain-like architecture. In the first co-crystal (combination of 1,4-diiodotetraflurobenzene with 4,4'-azopyridine), linear recurrent I···N HaB interactions are holding the molecules in 1D architecture (Ravat *et al.*, 2015), whereas in the second co-crystal (1,4-bis(selenomethylethynyl)-perfluorobenzene with 4,4'-bipyridylethane) nearly linear Se···N ChB interactions are serving the same purpose (Dhaka *et al.*, 2021).

As in the case of molecular self-assemblies, supramolecular architectures of even higher dimension can also be achieved in multicomponent crystals by increasing the number of potential σ-hole donor and acceptor sites in the constituent molecules. An evident example is the case of the co-crystal composed by hexamethylenetetramine and triiodomethane (iodoform), where a (6,3) honeycomb 2D network is obtained by combining a tridentate HaB donor with a tridentate HaB acceptor (**Figure 1.10a**). Complementary components are alternatively found at the nodes of this 2D structure and are connected together through two nearly linear I···N HaB

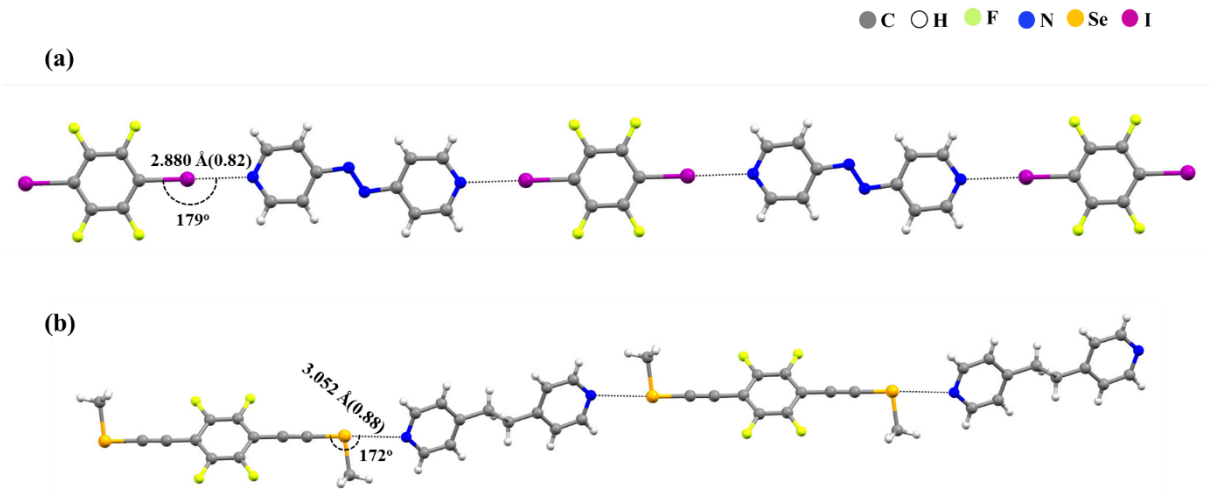

Figure 1.9 1D chain-like architecture formed in the co-crystals of: (a) 1,4-diiodotetraflurobenze with 4,4'-azopyridine and (b) 1,4-bis(selenomethylethynyl)-perfluorobenzene with 4,4'-bipyridylethane. Atoms are shown with colouring scheme, σ-hole interactions are shown as black dashed lines with corresponding distances (in Å) and angles (in degrees). Values within the bracket are the RR of determined distances. Figures are generated from deposited cif files.

interactions (Dahl and Hassel, 1970). Recently, 2D rectangular networks constructed through linear Te···N ChB interactions were reported in co-crystals composed of 1,8-bis(telluromethylethynyl)-anthracene (BTMEA) and ditopic Lewis bases (Dhaka *et al.*, 2021). One of these results is shown in **Figure 1.10b**, where the *U*-shaped morphology of ditopic ChB donor BTMEA and the nearly linear geometry of ditopic Lewis base 4,4'-bipyridyl ethane is inducing the aggregation of 2+2 chalcogen bonded supramolecular rectangles through two distinct Te···N ChB interactions in the crystal packing.

Further increasing the number of activated sites within the molecular scaffolds of donor and acceptor entities in a co-crystal enhances both dimensionality and complexity of the resulting supramolecular networks. One such example is shown in **Figure 1.11**, where the combination of a tetradentate HaB donor tetrakis(4-iodotetrafluorophenyloxymethylene) methane and a tetradentate HaB acceptor tetrapyridylpentaerythritol results to the formation of a rare diamondoid network (Metrangolo *et al.*, 2007). This network exhibits a high degree of translational interpenetration, which eventually induces the aggregation of a complex tenfold network in its crystal packing. Other than the given representative examples, there are several other supramolecular shapes known to exist in solid-state assemblies driven by σ-hole interactions. This includes double-helix structures (Yan *et al.*, 2019), supramolecular ribbons (Guido *et al.*, 2004), supramolecular capsules (Dumele *et al.*, 2015), supramolecular vesicles (Chen *et al.*, 2018), etc.

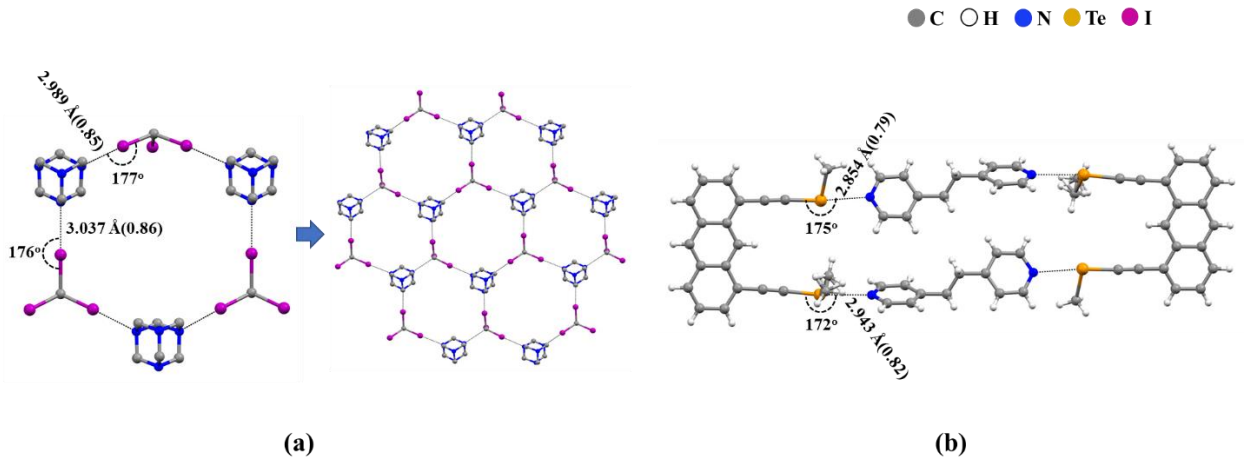

Figure 1.10 (a) Two-dimensional (6,3) honeycomb network constructed in a co-crystal of hexamethylenetetramine with triiodomethane, the building unit and its propagation to honeycomb network are shown as left and right figures, and (b) two-dimensional supramolecular rectangular network obtained in the co-crystal of 1,8-bis(telluromethylethynyl)-anthracene with 4,4'-bipyridyl ethane. Atoms are shown with colouring scheme, σ-hole interactions are shown as black dashed lines with corresponding distances (in Å) and angles (in degrees). Values within the bracket are the RR of determined distances. Figures are generated from deposited cif files.

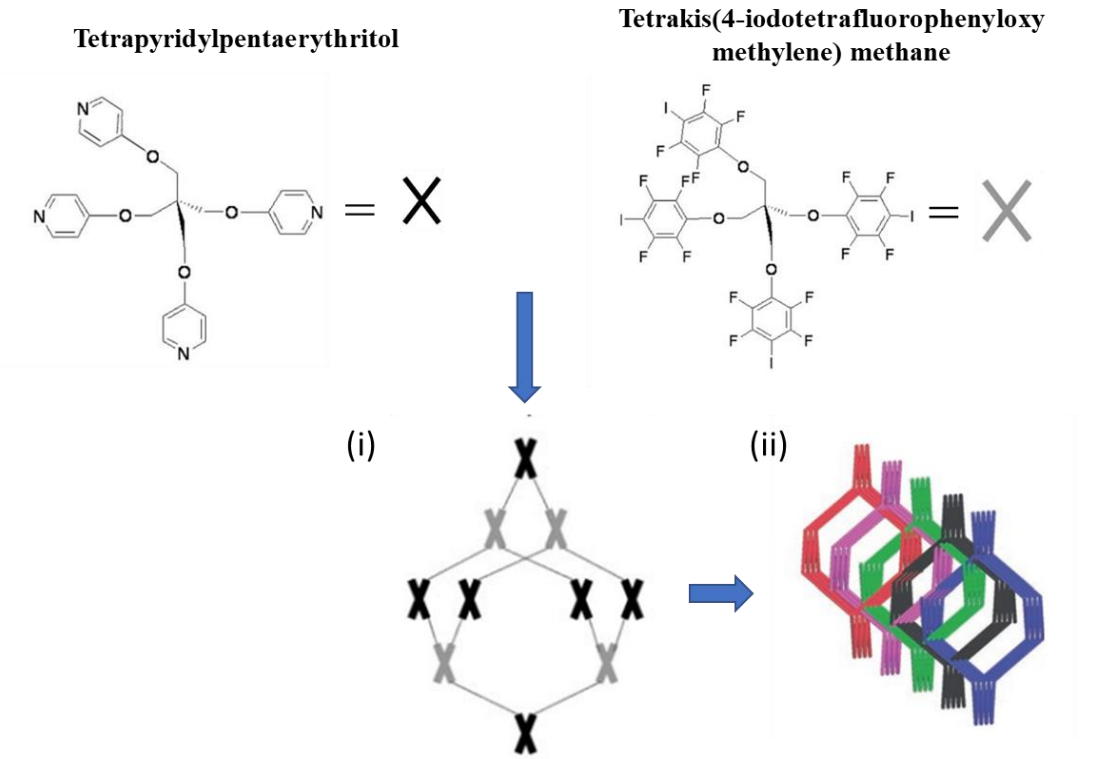

Figure 1.11 Diamondoid network obtained from the co-crystal of tetrakis(4-iodotetrafluorophenyloxymethylene) methane with tetrapyridylpentaerythritol, (i) shows the resulting diamondoid network and (ii) shows the tenfold network generated from translational interpenetration. Figures are taken from Metrangolo *et al.*, 2007.

1.3 Electronic origin of σ-hole interactions

Structural characterization of σ-hole interactions in both molecular self-assemblies and binary co-crystals, based on RR and interatomic interaction angles have been discussed in the previous section. It was also shown that, apart from atom···atom contacts, σ-hole interactions are also responsible for various supramolecular architectures in solid-state assemblies, therefore have a paramount importance in discussing the crystal packing of those molecules or co-crystals. Consequently, it is very important to gather in-depth knowledge about the characteristics of these interactions, not only to understand the crystal packing of molecules in hand but also to design new molecular frameworks utilizing the possibilities open by these interactions. Therefore, the electronic characteristics of σ-hole interactions are discussed below, which along with the structural characterization provide a complete picture of those interactions. This section will cover fundamental aspects of σ-hole interactions from an electronic point of view, from their origin to towards their mode of interaction. The discussion is limited to the cases of HaB and ChB interactions only.

For a halogen atom X (X= F, Cl, Br, I), the valence shell electronic configuration $\mathbf{ns^2np_x^2np_y^2np_z^1}$ (n = 2 for F, 3 for Cl, 4 for Br and 5 for I) exhibits an unpaired electron in the half-filled p_z orbital. Accordingly, during the formation of a covalent bond R-X, this unpaired electron interacts with an electron of opposite spin from atom R, resulting to the rearrangement of the electronic structure within the p_z orbital of the halogen atom and forming a bonding molecular orbital of σ type. This rearrangement induces a higher electron density in the half-lobe of the p_z orbital that is involved in the R-X bond (due to electron pull towards R to make the covalent bond), and conversely the other half-lobe of the p_z orbital become depleted in electron density (Politzer *et al.*, 2007). This depleted half-lobe region is known as the σ-hole and is placed antipode to the R-X covalent bond (**Scheme 1.1a**). Electrostatic potential (ESP) surfaces, which are based on the electrostatic potential function (amount of work done to move a unit positive charge from infinity to a given point in space) in a molecular surface of constant electron density, are commonly used for the identification of these σ-hole regions. Since the σ-hole region possesses a partial positive charge (δ^+), it generally appears as a positive region in the ESP surfaces (Clark *et al.*, 2007). On the other hand, the lone pairs of the halogen atom, which belong to p_x and p_y orbitals, create a belt of negative electrostatic potential in the ESP surfaces, placed perpendicular to the R-X direction of the σ-hole. As a result, an anisotropic distribution of electron density is taking place in the valence-shell of the halogen atom during

the covalent bond formation, as compared to its isolated situation in gas phase where it appears as a spherically symmetric electronegative atom (**Scheme 1.1b**). Apart from the generation of the σ-hole, this anisotropic distribution of electron density is also giving rise to the amphoteric behaviour of the halogen atom, where it can simultaneously act as electrophile and nucleophile (**Scheme 1.1c**). In addition, along with the hybridization rate of *s* and *p* orbitals, this anisotropic distribution of electron density also results in the flattening (or compression) of the halogen along the *z*-axis, known as the polar flattening effect (El Kerdawy *et al.*, 2013). The polar flattening effect leads to a larger atomic radius of the halogen atom in the equatorial region (perpendicular to the direction of covalent bond) and a smaller atomic radius in the polar region (along the extension of covalent bond). Also, this effect usually emerges as the main reason behind a σ-hole interaction in an electronegative halogen atom.

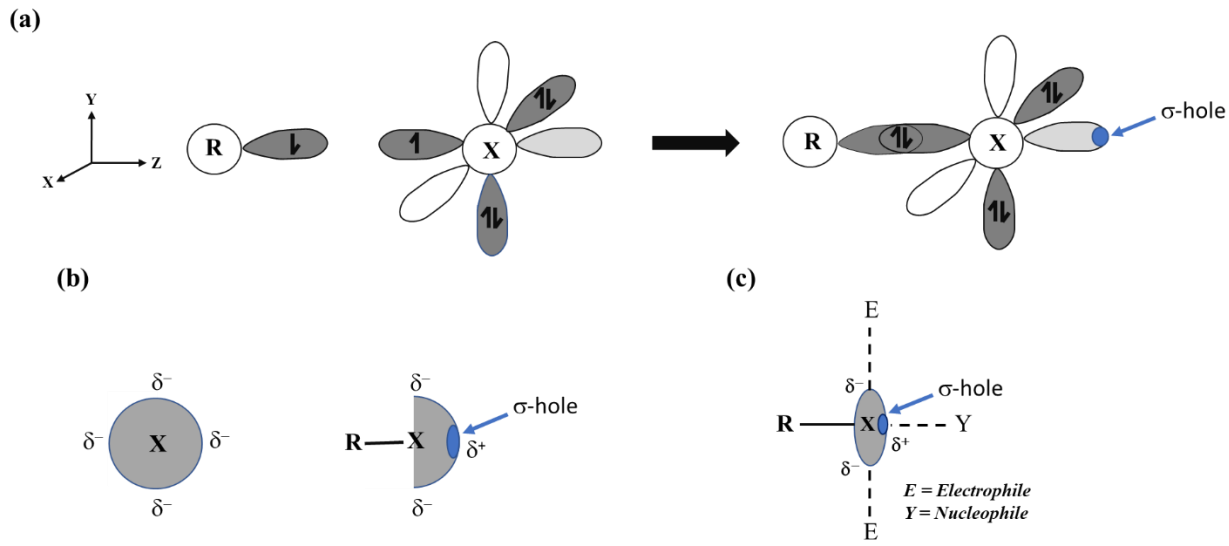

Scheme 1.1. Schematic representations showing: (a) orbital approach of the origin of σ-hole in a halogen atom X, (b) isotropic electron density distribution of an electronegative halogen atom X in gas phase (left) and anisotropic distribution of electron density in a halogen atom X during the covalent bond formation (right), and (c) halogen atom X exhibiting an amphoteric behaviour. X = F, Cl, Br or I.

Similarly, in case of a chalcogen atom, the electronic configuration $\mathbf{ns^2np_x^2np_y^1np_z^1}$ (n = 2 for O, 3 for S, 4 for Se and 5 for Te) indicates two such unpaired electrons in the valence shell, respectively in p_y and p_z orbitals. Here, there are two possibilities for a chalcogen atom during the covalent bond formation, either to adopt a sp^3 hybridization and make two covalent bonds with R and R' atoms (R = R' or R ≠ R') or to make a double bond with an atom R in a sp^2 hybridization. In the former case, two σ-hole regions can be identified, each related to the electron depleted half-lobe of p_y and p_z orbitals, whereas in the second case only one σ-hole region is generated (Wang *et al.*, 2009).

As mentioned earlier, this thesis focuses only on HaB and ChB interactions as representatives of σ-hole interactions. Therefore, a detailed overview of HaB and ChB interactions, starting from their historical backgrounds to the factors affecting their potential use, will be discussed in sections 1.3.1 and 1.3.2 respectively.

1.3.1 Halogen bond

1.3.1.1 Historical background

Non-covalent interactions involving halogen atoms (group 17) as source of σ-hole is known as the halogen bonding (HaB). Even though the HaB interactions carries a history of more than two centuries, it is still an active topic of research in the crystallographic community due to abundant applications it can offer in various disciplines (Metrangolo and Resnati, 2015). The first report involving a halogen atom as an electrophilic site is dated back in 1814, when M. Colin illustrated the formation of a diiodine-ammonia complex during the reaction of iodine with ammonia (Colin, 1814). Later in 1863, the formulation of the same complex was reported as $NH_3{:}I_2$ by F. Guthrie (Guthrie, 1863). However, in both reports, the authors did not explore the nature of the interaction that was responsible for holding the complex together. The first crystallographic study of a halogen containing system, 1:1 molecular complex of dioxane with bromine, was reported in 1954 by O. Hassel, where the evidences of a polarization induced $Br(\delta^+)\cdots O(\delta^-)$ interaction was discussed (Hassel *et al.*, 1954). Later, in his Nobel lecture in 1970, Hassel discussed again on the importance of intermolecular interactions involving halogen atoms as electrophilic sites, and their ability to form molecular self-assemblies with electron pair donors (Hassel, 1970). The term *halogen bond* was first introduced by Dumas in 1978, to indicate the interactions found in C-Hal···LB systems (Hal = halogen atom, LB = Lewis base), involving solvents of type MX_4 (M = C, Si; X = Cl, Br) and polar solutes (oxides, pyridine, benzene, trimethyl-1, 3,5 benzene) (Dumas, 1976; Dumas *et al.*, 1978). In addition, he also ranked the strength of HaB interactions based on the atomic number of the halogen atom (I > Br > Cl) and also found out that the interaction is enhanced when an electron with-drawing group is attached to a more electronegative central atom. Several other authors further documented HaB interactions by exploring halogen atoms as electrophilic sites (Murray-Rust *et al.*, 1983; Ramasubbu *et al.*, 1986; Desiraju and Parthasarathy, 1989). However, a huge turn around in the research of HaB interactions took place in 1994 when Murray *et al.* proposed a valuable tool for the theoretical investigation of HaB interactions, where they identified that the electron density distribution of a covalently bonded halogen atom is anisotropic in nature,

leading to the concept of σ-hole regions (Murray *et al.*, 1994). Over the years, constant efforts were made to expand the concept of σ-hole in multiple molecular systems, both experimentally and theoretically (Metrangolo and Resnati, 2001; Politzer *et al.*, 2007; Clark *et al.*, 2007; Politzer *et al.*, 2008; Murray *et al.*, 2009). After several years of continuous efforts and careful scrutinization, in 2013 the IUPAC published a formal definition of HaB: "*A halogen bond occurs when there is evidence of a net attractive interaction between an electrophilic region associated with a halogen atom in a molecular entity and a nucleophilic region in another, or the same, molecular entity*" (Desiraju *et al.*, 2013). Yet these HaB interactions are considered as an active topic of research mainly because of dubious character in its origin and mode of interaction, which will be discussed in the forthcoming sections.

1.3.1.2 Mode of interaction

HaB interactions are known to exhibit very close resemblances with HB interactions, especially in terms of their electronic origin and mode of interaction. For instance, considering the case of a R-X···Y HaB interaction and R-H···Y HB interaction (**Figure 1.12a**), a clear analogy of their interaction characteristics is visible. In case of HaB interaction (**Figure 1.12a**), the anisotropic distribution of the electron density in a halogen atom X indicates that the positively charged σ-hole region (δ^+) observed along the extension of the covalent bond R-X is interacting with an electron rich center Y (δ^-). In such a way, electrophilic···nucleophilic ($\delta^+\cdots\delta^-$) type of interaction is established. A similar mode of electrophilic···nucleophilic ($\delta^+\cdots\delta^-$) interaction is

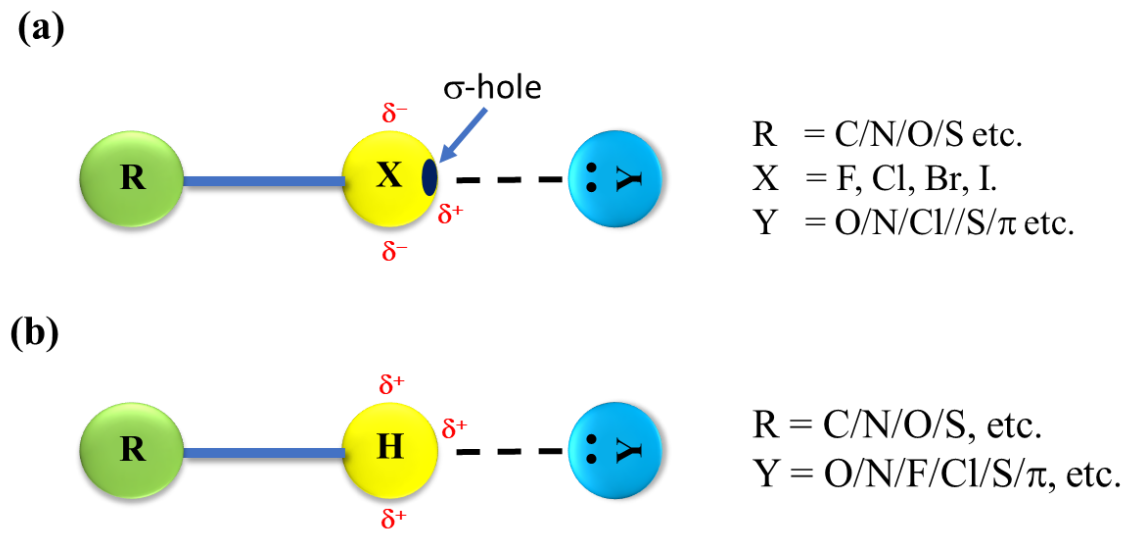

Figure 1.12 Schematic representation of (b) halogen bonding (HaB) and hydrogen bonding (HB) interactions.

also found in the case of a R-H···Y HB interaction (**Figure 1.12b**), where the δ^+ region found in the periphery of the H atom interacts with a δ^- region coming from an electron rich center Y. The main difference between these two interactions is actually found in the region perpendicular to the covalent bond, known as polar region. In the case of the HaB interaction, the lone pairs of the halogen atom present in p_x and p_y orbitals create an accumulation of electron density (δ^-) in the polar region (*xy*-plane), whereas in the case of the HB interaction the whole periphery of H atoms experience a depletion of electron density (δ^+) because of the absence of core electrons. The difference observed in the electron density distribution is also inducing a difference in the directionality of their interactions. For an efficient electrophilic···nucleophilic interaction a face-to-face orientation of δ^+ and δ^- regions is preferred. In the case of the HaB interaction, the best possibility for such an orientation is attained when the nucleophile Y approaches along the extension of the covalent bond, thus the R-X···Y angle for a stronger HaB interaction is expected to be very close to 180°. However, the scenario is a bit different for the HB interaction, since the entire periphery possesses a δ^+ charge distribution it is possible that the nucleophile Y can approach with different angles, which is put forward as the main reason why HB interactions are often bend rather than linear. Therefore, HaB interactions are more linear than HB interactions. Considering the interatomic distances (X···Y and H···Y), they should be smaller than the sum of van der Waals radii of interacting atoms for stronger interactions.

1.3.1.3 Nature of interaction

Traditionally, HaB complexes were considered to be stabilized by charge transfer interactions (Hassel, 1970; Reed *et al.*, 1985), which is also supported by some recent studies (Rosokha *et al.*, 2013; Wang *et al.*, 2014; Robinson *et al.*, 2015; Inscoe *et al.*, 2022). According to the charge transfer notion, the stability of a HaB interaction is mainly driven by the donation of electron charge from the lone-pair region of the nucleophile (HOMO – highest occupied molecular orbital) to the σ^* antibonding orbital of the halogen atom (LUMO – lowest unoccupied molecular orbital). This is also suggesting that, in an R-X···Y HaB system, the donation of electrons from the lone-pair of Y to the σ^* antibonding orbital of R-X would lengthen, weaken and red-shift the covalent bond. These trends have been observed experimentally in many halogen bonded complexes (Murray *et al.*, 2008; Politzer *et al.*, 2013), corroborating the argument that HaB systems are stabilized by a charge transfer process.

In contrast, the IUPAC definition of HaB interactions places electrostatics at the origin of their nature, assigning a paramount importance to the electropositive σ-hole region that is in interaction with an electronegative region from a nucleophile. This electrostatic approach suggests that more depleted is the σ-hole (electropositive) region, more significant (stronger) will be the resulting HaB interaction. This approach also puts forward the observation made earlier with the polarization of the R-X covalent bonds in response to the presence of electron pair donors (Murray *et al.*, 2008; Clark *et al.*, 2015). At the same time, attention has to be paid to the list of features documented along with the IUPAC definition, where a caution note can be found saying "The forces involved in the formation of the halogen bond are primarily electrostatic, but polarization, charge transfer, and dispersion contributions all play an important role. The relative roles of the different forces may vary from one case to the other" (Desiraju *et al.*, 2013). Inclusion of this note is mainly advocated because of the literature inconsistency found in illustrating the nature of HaB interactions. Indeed, the dominant term that contributes to the stabilization and the geometry of HaB interactions varies from system to system. Even in the electrostatically driven σ-hole concept introduced by Politzer and co-workers, a substantial role of induction and dispersion is proposed (Riley *et al.*, 2013). Also, it is not always true that a larger σ-hole output a stronger HaB interaction. One such example can be found in the combination of CX_3I (where X is any of F, Cl, Br, and I) with a halide ion or a trimethylamine molecule, where the binding energy magnitude and the σ-hole size do not appear correlated (Huber *et al.*, 2012). Accordingly, a stronger HaB interaction is observed with CI_4 rather than with CF_3I. The authors propose that it is due to the lowest energy σ* orbital of CI_4, which is acting as the strongest charge acceptor and is enough to overcome the more favorable electrostatics properties of CF_3I (with a dominant charge transfer interaction).

A strong analogy between HaB and HB complexes was also established by Legon and co-workers following some extensive spectroscopic studies (Legon, 1999; Legon 2010). Since HB interactions are mostly driven by an electrostatic origin, the same assumption is also persuaded for HaB interactions. Accordingly, it is acknowledged that the linearity of HaB interactions are attained mainly to enhance the interaction between electrophilic and nucleophilic regions. However, in another study carried out by A.J. Stone, it has been shown that even though electrostatics contribute to the positioning of electrophilic and nucleophilic sites, the linearity of the interaction is mostly accomplished by the exchange-repulsion term (Stone, 2013), being explained in terms of the oblate shape of the bonded halogen atom.

Studies have also shown that an indispensable contribution of dispersion and polarization terms is also important to consider in some HaB complexes, especially if the atoms are of high polarizability (Kozuch and Martin, 2013; Clark *et al.*, 2014). One such example is the case of the CH_3Cl molecule, for which initial studies have shown that the Cl-atom cannot act as a HaB donor due to the completely negative electrostatic potential surface it possesses (Politzer *et al.*, 2007). This trend has been however contracted by the predicted existence of $CH_3Cl\cdots O{=}CH_2$ complex later on (Riley and Hobza, 2008). This inconsistency of results has been explained in terms of induced polarization, modifying the negative electrostatic potential of the Cl-atom upon the approach of the $O{=}CH_2$ molecule. Indeed, a mutual polarization of electron density clouds is happening, due the electric field generated by one component to the other. In such a way, a positive σ-hole is generated on the surface of Cl-atom and it can interact with the O-atom of the $O{=}CH_2$ molecule to establish a halogen bonded complex. Over the years, the importance of polarization and dispersion terms in illustrating the existence HaB complexes have been also addressed in many other studies (Riley and Hobza, 2008; Riley and Hobza, 2013).

In short, all these features suggest that a global conclusion cannot be made on the nature of HaB interactions, it actually varies from system to system. Nevertheless, in most cases, electrostatic forces dictate (to a great extend) the directionality and tunability of HaB interactions, while other attractive terms (charge-transfer, dispersion and polarization) along with electrostatics contribute to the strength of HaB interactions.

1.3.1.4 Partial covalency of halogen bond

In some other studies, it has also been shown that HaB interactions can exhibit a partial covalent bond character along with some other secondary bonding characteristics. This possibility has been mainly explored in the case of halonium ions, where a positively charged halogen atom X^+ is interacting simultaneously with two Lewis bases Y and Y' (Y = Y' or Y ≠ Y') to constitute a three center - four electron (3c-4e) bond (**Figure 1.13a**) (Turunen and Erdélyi, 2020). These halonium ions $[Y\cdots X\cdots Y']^+$ are characterized by short and strong halogen bonds (RR in the range 0.6-0.7), mainly formed through charge transfer and electrostatic interactions. As compared to a halogen atom X of oxidation state 0, which possesses an unpaired electron in the p_z orbital, X^+ shows an oxidation state of +1 and an empty p_z orbital. Indeed, an electrostatic field arising from the Lewis bases is actually inducing a spin paired $\boldsymbol{p_x^2 p_y^2 p_z^0}$ electronic configuration in X^+. This empty p-orbital of X^+ is known as a p-hole that simultaneously

interacts with two Lewis bases, each contributing with a lone-pair of electrons to X^+, resulting to the formation of a linear $[Y\cdots X\cdots Y']^+$ HaB complex (Hakkert and Erdélyi, 2015). Here, each HaB (Y···X and X···Y') possesses a partial covalent character as well as a secondary bonding character. Consequently, the bond distances are in between the sum of van der Waals radii and the sum of covalent radii of the interacting atoms. Also, if the two Lewis bases are of similar electronic nature then $[Y\cdots X\cdots Y']^+$ halonium ions exhibit a static symmetric geometry with similar HaB lengths (typically <10% difference between the HaB distances) (Turunen and Erdélyi, 2020). Electronic analyses performed in the framework of the quantum theory of atoms in molecules (QTAIM) approach again corroborate the high degree of covalency and similarities between the two HaBs (Koskinen *et al.*, 2015). Considering the energetic contributions of the 3c-4e HaBs, covalency is mainly arising from the charge-transfer component whereas the strength of the bonds is accomplished through the electrostatic contribution. Therefore, covalency of the 3c-4e HaBs decreases down the group in the order Cl > Br > I (because the charge transfer component decreases), whereas simultaneously, the strength of 3c-4e HaBs increases down the group (because the electrostatic component increases) (Carlsson *et al.*, 2012; Karim *et al.*, 2014).

A similar kind of covalency in HaB interactions can also be found in some binary co-crystals of type (imide)N–Hal···N'_x (Hal = Br, I, imide = Saccharin, N'_x = 4-picoline, 4-dimethylamino pyridine, Hexamethylenetetramine) (Aubert *et al.*, 2017; Anyfanti *et al.*, 2021). For instance, considering the case of a binary co-crystal composed of N-iodosaccharine (NISac) and 4-dimethylaminopyridine (DAMP), the σ-hole of the I-atom belonging to NISac is interacting with the lone-pair of the N-atom of DAMP to form a $N_{sac}\cdots I\cdots N_{DAMP}$ HaB interaction (Makhotkina *et al.*, 2015). The constitution of this HaB interaction is such that the I atom is placed in between the N atoms of donor and acceptor molecules, thus forming a very similar arrangement as that of halonium ions. Comparing the individual HaB distances, it can be found that the constitution of $N_{sac}\cdots I\cdots N_{DAMP}$ HaB motif is not like a conventional case, where one short and strong covalent bond and another weaker and longer HaB are often identified. Instead, two HaB bonds of comparable length can be found, actually with a shorter $I\cdots N_{DAMP}$ distance and a longer $N_{sac}\cdots I$ distance (**Figure 1.13b**). Therefore, these bond distances indicate a charge separation within the binary adduct where the I-atom is shifted closer to the acceptor N-atom. Nevertheless, since the electronic nature of N-atoms in donor and acceptor moieties is not same, a conclusion about the nature of the system (and of the HaB interactions) cannot be derived from structural distances only. Accordingly, electronic investigations were carried out on these

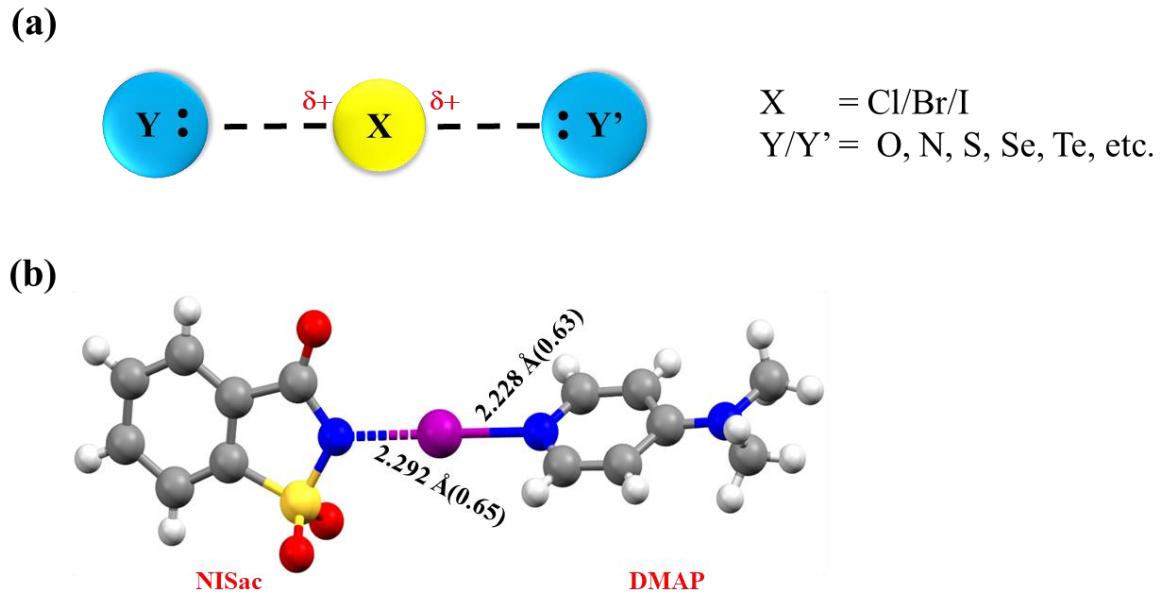

Figure 1.13 (a) schematic representation of halonium ions where a positively charged halogen atom X simultaneously interact with two nucleophile Y and Y', and (b) $N_{sac}\cdots I$ and $I\cdots N_{DAMP}$ HaB interactions found in the co-crystal of NISac and DAMP, values within the bracket are the RR of determined distances.

HaBs and found out that they are very similar in their properties. Also, a partial covalent character of both $N_{sac}\cdots I$ and $I\cdots N_{DAMP}$ were revealed from the electronic properties determined at their bond critical points (BCPs). A similar kind of observation was also made in other co-crystal composed of either N-iodosaccharine or N-bromosaccharine as HaB donor and different derivatives of pyridine as HaB acceptor (Anyfanti *et al.*, 2021; Aubert *et al.*, 2017).

A common observation that can be made from the literature is that, irrespective of the system of consideration, the electrostatic force always plays a vital role in the stabilization and geometry of HaB complexes. Therefore, it is prime importance to have an in-depth knowledge about the electrostatic properties of associated σ-holes. A widely accepted characterization tool that is used for their quantification is the molecular electrostatic potential (MESP) surfaces. In the next section, advantages offered by this characterization are briefly discussed, although a detailed discussion regarding the rationale behind this method can be found in next chapter (section 2.1.1.5).

1.3.1.5 Molecular electrostatic potential surfaces

Analysis of molecular electrostatic potential (MESP) surfaces, based on the electrostatic potential (ESP) function calculated on a molecular surface of constant electron density, is commonly used as a tool to identify the presence of σ-hole regions in a molecule. The ESP function can be calculated from the electron density distribution either measured experimentally

or calculated from a theoretical method. Since the σ-hole is a region of depleted electron density, it is mostly associated with a positive ESP function. Accordingly, a maximal value of the ESP function, denoted as $V_{s,\,max}$, is commonly found in the σ-hole region. The ESP magnitude of a σ-hole characterizes quantitatively the ability of a halogen atom to act as an electrophilic site (Murray and Politzer, 2011). Therefore, a larger positive ESP (larger $V_{s,\,max}$) in the σ-hole region indicates a more depleted electron density, and hence a stronger electrophile in the HaB interaction. Also, once $V_{s,\,max}$ is located on the molecular surface in the σ-hole region, denoted as P ($V_{s,\,max}$), one can measure the orientation of the electrophilic site *via* the R-X⋯ P ($V_{s,\,max}$) angle.

Similarly, a minimal value of ESP function (denoted as $V_{s,\,min}$) can be found in the electron rich center of a nucleophile. Thus, considering both $V_{s,\,max}$ and $V_{s,\,min}$ values, one can have a quantitative measure of the electrophilic and nucleophilic strengths in the HaB interaction. In addition, these MESP surfaces can also give significant information about the interaction preferences of molecules in their solid-state assemblies (Politzer and Truhlar, 2013). At the same time, as discussed in the previous section, one needs to keep in mind that the interaction energy of a HaB interaction is not only decided by electrostatics alone, and this sometimes limit the direct correlation of properties derived from MESP surfaces and the interaction energy.

1.3.1.5.1 Trend down the group

In general, for the same nucleophile magnitude of the σ-hole increases with increasing the size of the halogen atom, following the order F < Cl < Br < I (Politzer *et al.*, 2010; Kolář *et al.*, 2014). This mainly happens because of the increasing polarizability and the decreasing electronegativity of halogen atoms while going down the group. Accordingly, these two properties indicate an easier and enhanced electron density redistribution for a heavier halogen atom than for a lighter one. This redistribution of the electron density is also supported by the fact that in a heavier halogen the outer valence electrons are weakly held to the nucleus due to the screening made by the inner electrons, being therefore easier to reorganize the electron density distribution during the covalent bond formation. As a consequence, the electropositive value of the σ-hole ($V_{s,\,max}$) becomes more important in a heavier halogen atom than in a lighter one.

A misconception was present in initial studies involving the availability of F to generate σ-hole regions. Indeed, the F-atom has the lowest polarizability and the highest electronegativity

among halogen atoms and therefore it cannot straightforwardly form σ-hole regions during the covalent bond formation (Cavallo *et al.*, 2016). For example, considering the case of CF_3X (X = F, Cl, Br or I) molecules (**Figure 1.14**), MESP surfaces generated on 0.001 a.u. (electrons $Bohr^{-3}$) iso-electron density surface reveal that electropositive σ-hole regions can be found in all Cl, Br and I derivatives but not in the F one (Clark *et al.*, 2007). However, later studies have shown that under certain electronic environments F-atoms can also exhibit an anisotropic distribution of the electron density, leading to the formation of σ-holes especially when it is bound to a more electronegative entity (Metrangolo *et al.*, 2011). In such a way, tuning the electrophilic power of the σ-hole of a halogen atom *via* chemical substitution finds vast applications in the field of crystal engineering, which will be discussed in detail in section 1.4.1.

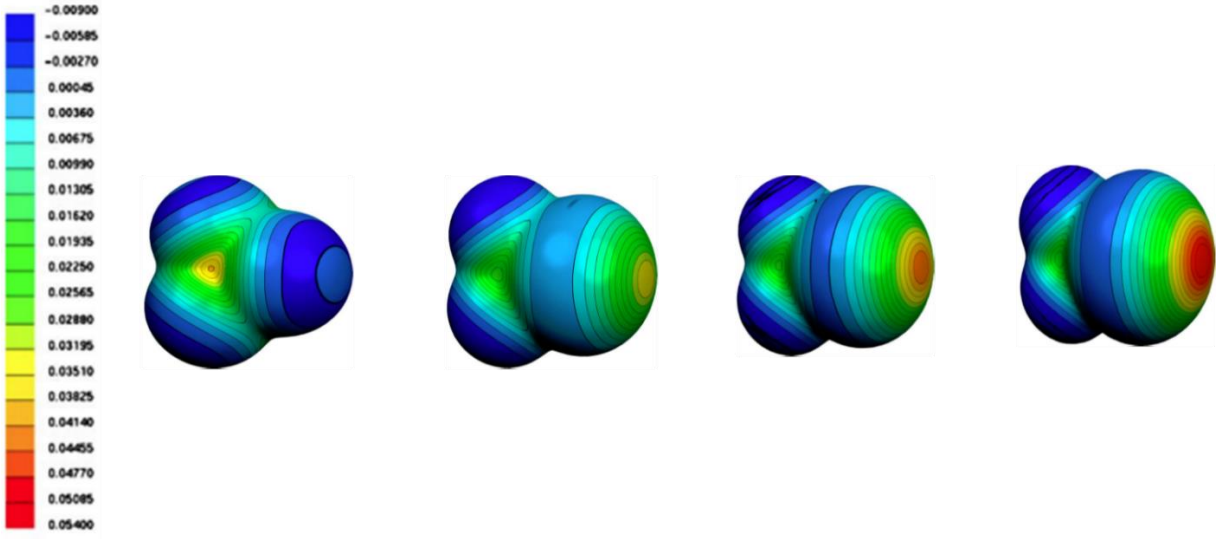

Figure 1.14 Molecular electrostatic potential (MESP) surfaces generated for the CF_3X molecules, X = F, Cl, Br, I from left to right. Figures are taken from Clark *et al.*, 2007.

1.3.1.6 Classification of halogen bonding interactions

It is important to distinguish HaB from other type of interactions involving halogen atoms, especially when a halogen atom acts as the nucleophile and the interaction results to a halogen···halogen contact. Based on the spatial orientation of the interacting pair of atoms, halogen···halogen interactions can be classified into two categories, namely Type-I and Type-II interactions (Desiraju and Parthasarathy, 1989). The symmetrical halogen···halogen contact with θ1≈θ2 is known as Type-I interaction, where θ1 and θ2 are the $R–X_1\cdots X_2$ and $X_1\cdots X_2–R'$ angles respectively (**Figure 1.15a**). On the other hand, the unsymmetrical halogen···halogen contact with $\theta_1 \approx 90°$ and $\theta_2 \approx 180°$ is termed as Type-II interaction, where a closer linear geometry exhibits for the electrophilic site (**Figure 1.15b**). It has to be stated that only Type-II

interactions are included in the category of HaB. The case of Type-I interactions is considered as a short contact mostly arising due to close packing of molecules in space rather than due to a driving attractive interaction.

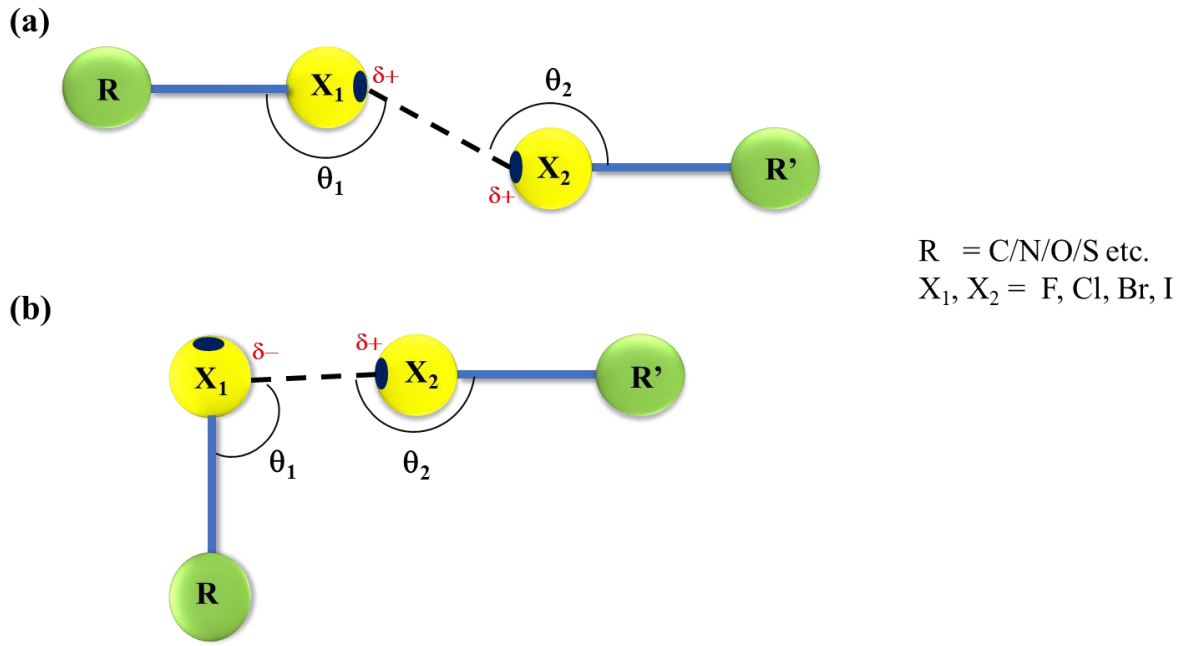

Figure 1.15 Schematic representation showing (a) type-I and (b) type-II halogen···halogen interactions.

1.3.2 Chalcogen bonding

1.3.2.1 Historical background

Non-covalent interactions involving chalcogen atoms (group 16) as source of σ-holes is known as chalcogen bonding (ChB) (Scilabra *et al.*, 2019). ChB interactions are considered to be a sister non-covalent bond of HaB and HB interactions, mainly because of the similarities found in their bonding properties. However, compared to HaB and HB interactions, the fundamentals behind the origin and the stabilization of ChB interactions are still an evolving field of research. Yet, these ChB interactions find immense interest among researchers since it also combines two essential properties of an interaction, strength and directionality. Initial findings concerning ChB interactions are dated back in 1977, when a non-bonded contact involving sulfur atoms was identified for the first time (Rosenfield *et al.*, 1977). Later, in 1981, a crystallographic database study was carried out in order to investigate the directional preferences of S···S interactions in molecular crystals (Parthasarathy and Row, 1981). Initial quantitative investigations of ChB interactions were performed in 1992, using the S···O and Se···O ChB interactions found in thiazole and selenazole nucleoside derivatives (Burling and Goldstein,

1992). Further, while analyzing tubular structures in cyclic tetrachalcogenadiynes, Gleiter and co-workers reported short contacts involving chalcogen atoms (S, Se and Te), which eventually resulted to a zigzag arrangement between molecular stacks (Werz *et al*, 2002a; Werz *et al*, 2002b; Werz *et al*, 2004). However, the main turn around in the history of ChB interactions happened in 2007, when soon after reporting the origin of HaB interactions, Murray *et al.* expanded the concept of σ-holes to chalcogen atoms (Clark *et al.*, 2007). The term *chalcogen bond* was first used by Wang and coworkers in 2009 while exploring the σ-hole sites found in sp^2 hybridized chalcogen atoms (Wang *et al.*, 2009). Later, in 2019, the IUPAC released a formal definition of ChB interaction: "*net attractive interaction between an electrophilic region associated with a chalcogen atom in a molecular entity and a nucleophilic region in another, or the same, molecular entity*" (Aakeroy *et al.*, 2019). As evident from the definition, ChB interactions are showing very close resemblances with HaB interactions, following similar trends and properties pointed earlier for halogen atoms.

1.3.2.2 Mode of interaction

A sp^3 hybridized chalcogen atom possesses two σ-hole regions in its outer periphery, each along the extension of a covalent bond (**Figure 1.16a**). The electrophilicity of these σ-hole regions is strongly dependent on the electronic nature of the substituents R and R' that are covalently bonded to the chalcogen atom (Murray *et al.*, 2014). Accordingly, if the two substituents are of same electronic nature (or even approximately) they output σ-holes of similar electrophilic power. These σ-hole regions R1 and R2 can either interact simultaneously with two nucleophiles Y and Y' or compete with each other to interact with one nucleophile. Therefore, the predictability issue is inherently associated with a sp^3 hybridized chalcogen while designing the molecular core for crystal engineering applications. However, in some recent studies it has been shown that an asymmetric substitution of a chalcogen atom can resolve this issue of predictability by inducing an asymmetry in the generated σ-holes (Huynh *et al.*, 2017; Jeannin *et al.*, 2018; Riel *et al.*, 2019; Huynh *et al.*, 2021). This can be accomplished by choosing substituents R and R' of very different electronic properties. For example, if R is more electronegative than R' then the σ-hole present along the extension of R-Ch covalent bond will show a more depleted electron density than the other present along the extension of R'-Ch covalent bond. In such a way, a stronger ChB interaction is expected with the former σ-hole than the latter, giving a strong element of predictability while designing molecular cores for crystal engineering applications.

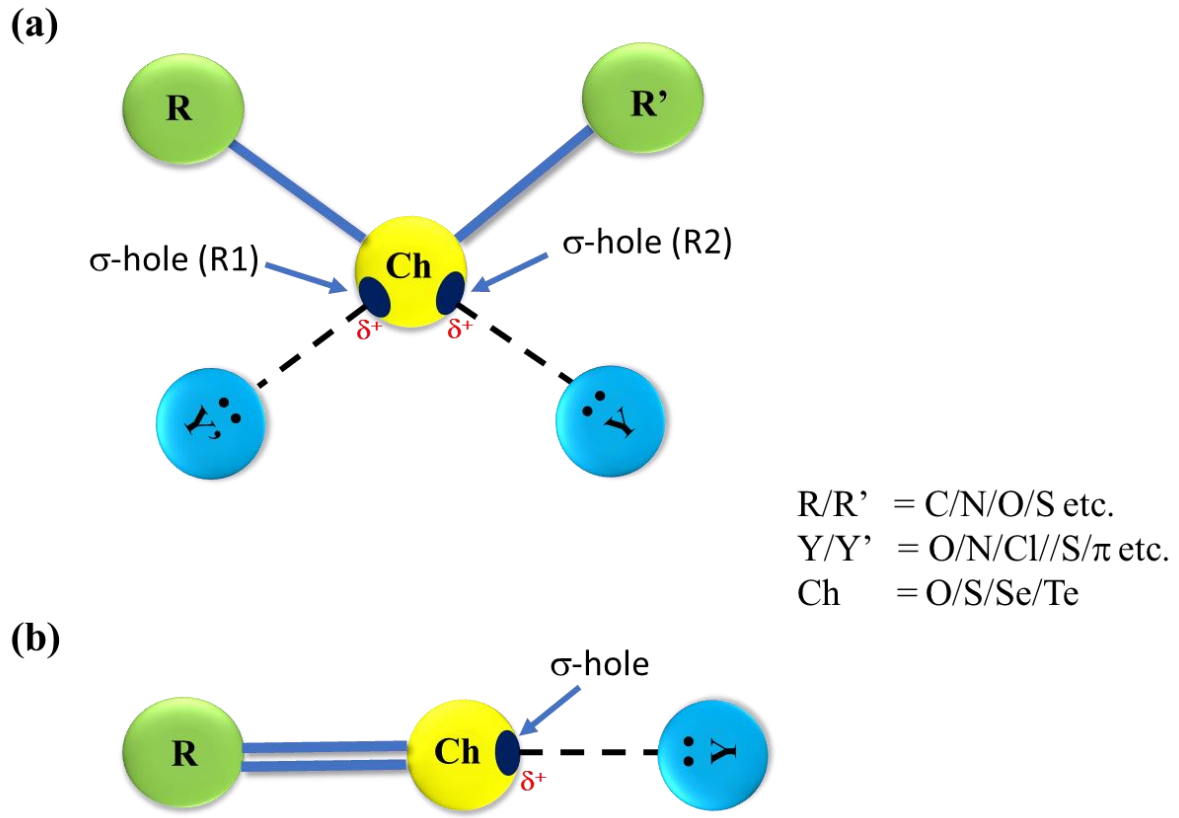

Figure 1.16 Schematic representation of chalcogen bonding interaction when chalcogen atom is of (a) sp^3 and (b) sp^2 hybridizations.

If we consider the nature of the interaction, similar electrophilic···nucleophilic ($\delta^+\cdots\delta^-$) interactions as that of HaB can also be found with ChB. As in HaB, for an efficient ChB interaction, a face-to-face orientation of interacting electrophilic and nucleophilic regions is preferred with the interatomic distances less than the sum of van der Waals radii of interacting atoms. Again, similarly to HaB interactions, a high-directionality is often associated with ChB interactions as well, mostly exhibiting an interatomic interaction angle close to 180°. As mentioned previously, in a sp^3 hybridized chalcogen atom, both p_y and p_z orbitals of the valence shell are involved in the covalent bond formation, whereas the p_x orbital orthogonal to both of them possesses the lone-pair of electrons and therefore acts as the nucleophilic center. Consequently, a chalcogen atom can also simultaneously act as both nucleophilic and electrophilic center (amphoteric behaviour) in solid-state assemblies (Shukla *et al.*, 2020).

On the other hand, chalcogen atoms can also exhibit a sp^2 hybridization when they form a double bond with the substituent R. Hence only one σ-hole is found in the periphery of chalcogen atom with this configuration (**Figure 1.16b**). Experimental studies have shown that the resulting ChB interactions here are quite similar to HaB interactions, with a similar

redistributed electron density cloud and the concomitant weakening of the covalent bond upon interaction (Wang *et al.*, 2009).

1.3.2.3 Other properties

Considering chalcogen atoms down the group, the σ-hole amplitude shows a similar trend than in the case of halogen atoms. Thus, the size of the σ-hole and the $V_{s,\,max}$ magnitude increase with the increasing of the polarizability and the decreasing of the electronegativity of the chalcogen atom (Ibrahim and Telb, 2020).

A similar classification that assigned to halogen···halogen interactions can also be applied to chalcogen···chalcogen contacts, considering that only the type II category is a bonding interaction (chalcogen bond) while the type-I category is rather a van der Waals contact forming due to close packing of molecules (Dhaka *et al.*, 2020).

Regarding the energetic contributions, ChB interactions should also consider as a combination of electrostatics with other attractive terms such as charge-transfer, dispersion and polarization, while the former being the dominant component in most cases (du Mont and Hrib, 2013; Gleiter *et al.*, 2018).

1.4 Factors affecting σ-hole interactions

In the previous sections it has been shown that, for the same nucleophile, the size of the σ-hole can be increased by going from lighter to heavier chalcogen or halogen atoms within their respective group. Thus, for crystal engineering applications, a heavier halogen or a chalcogen atom is preferred in order to enhance the strength of the predicted σ-hole interaction. In addition, the size of the σ-hole in the same atom can also be tuned to control the strength of resulting σ-hole interaction, using the methods discussed below.

1.4.1 Synthetic modification

Synthetic modification of the molecular core is known to be one efficient way to tune the magnitude of resulting σ-holes. It has been shown in literature that the σ-hole is very sensitive to the neighbouring chemical environment. Accordingly, the substituent that is covalently bound to a halogen or a chalcogen atom is very significant for the tuning of the σ-hole properties (Kolář and Hobza, 2016). For example, considering the case of the F-atom, which is the least polarizable and most electronegative atom among halogens and therefore in the past it was

argued that F cannot output a positive σ-hole in its periphery especially the organic fluorine (C-F bonds) (Clark *et al.*, 2007). It was later shown that indeed a positive σ-hole on F can be found in some particular molecules like F_2, C_2F_2, ClF, FCN, etc (Politzer *et al.*, 2007; Metrangolo *et al.*, 2011; Varadwaj *et al.*, 2019). A common feature among these molecules is an electron withdrawing group (EWG) that is covalently bound to F-atom. Further exploration reveals that, for F-atoms, the presence of such covalently bonded EWG appears as a prerequisite to generate positive σ-hole sites (Kolář and Hobza, 2016). This behaviour is not just limited to F, but to any other halogen or chalcogen analogue, for which replacing a less EWG substituent by a stronger one significantly changes the magnitude of σ-hole and eventually leads to a stronger σ-hole interaction. Chemical groups like F, CN, CF_3, C≡C, NO_2, COOH are the common choices of EWGs in crystal engineering applications. On the other hand, instead of an EWG, replacing the substituent with a more electron-donating group (EDG) make the σ-hole less positive and smaller (Bauzá *et al.*, 2011; Kolář *et al.*, 2014). This subsequently leads to comparatively weaker σ-hole interactions. Chemical groups like CH_3, $N(CH_3)_2$, OH, OCH_3 are known to be the common choices of EDGs.

Apart from a direct substitution, the electrophilic power of a σ-hole belonging to an atom bound to the aromatic ring can also be controlled by the substitution of the aromatic hydrogens with electron withdrawing or electron donating groups (Chernysheva *et al.*, 2020). Sometimes, the functional group drastically influences the electronic effect of the aromatic ring and therefore significantly affects the amplitude of associated σ-hole. One such case often found in crystal engineering studies is the substitution of aromatic hydrogens by highly electronegative F atoms. The presence of multiple F atoms makes the aromatic core very electron deficient and hence a halogen (or a chalcogen atom) directly bound to this aromatic core experiences a drastic electron pull. Correspondingly, these electronic effects result to a larger σ-hole within the halogen or the chalcogen atom. An example is the case of 1,4-diiodobenzene and 1,4-diiodotetrafluorobenzene, where a larger σ-hole can be found in the latter molecule as compared to the former (Jaini *et al.*, 2019). In some other instance, it was also revealed that the interaction energy of HaB interactions after F substitution shows a high correlation with the observed $V_{s,max}$ value at the halogen atom (Riley *et al.*, 2011).

As discussed earlier, asymmetric substitution of a sp^3 hybridized chalcogen atom increases the predictability of ChB interactions. This is often achieved through synthetic modification of the molecular core, where two electronically different substituents are attached to a chalcogen atom.

For example, considering the case of benzyl selenocyanate molecule, a strongly electron withdrawing CN group and a comparatively less electron withdrawing benzyl group are covalently bonded to a sp^3 hybridized Se atom (Riel *et al.*, 2019). Consequently, the presence of the strong EWG induces a strong σ-hole along the extension of Se-CN covalent bond. This aspect will be explored more in this thesis, using the benzyl selenocyanate molecule and some of its derivatives.

1.4.2 Right choices of donors and acceptors

Another possibility to enhance σ-hole interactions is by selecting the right choices of partner compounds for crystallization process. For example, in case of a donor-acceptor co-crystal system, if we choose donor and acceptor molecules with activated electrophilic and nucleophilic centres, they are expected to form stronger σ-hole interactions as compared to their inactivated counterparts. Such a case of study has been carried out with a family of complexes involving N-iodosuccinimide (NIS), N-iodosaccharin (NISac) and N-bromosaccharin (NBSac) as HaB donors, and pyridine (Py), 4-picoline (PIC) and 4-dimethylaminopyridine (DMAP) as HaB acceptors (Makhotkina *et al.*, 2015). Here, NISac is the most activated HaB donor among all the imide derivatives, bearing a large positive σ-hole on the I-atom due to an enhanced resonance of the aromatic core and therefore with a large electron pull effect. Simultaneously, DAMP is the most efficient HaB acceptor among all the pyridine derivatives due the presence of strong $N(CH_3)_2$ EDG in the *para* position. Co-crystallization and subsequent structural characterization *via* single-crystal X-ray diffraction (SCXRD) experiments displayed a N-X···N' (N= Nsac/Ns, X = Br/I and N'= Py/PIC/DAMP) HaB interaction in all cases. However, a stronger HaB interaction is observed with the combination of the good HaB donor (NISac) with the good HaB acceptor (DAMP), thus endorsing the importance of right choices of compounds. Some of these compounds and their HaB interactions will be subjected to a detailed analysis in the follow-up sections of this thesis.

Similar types of HaB interactions were also characterized with NIS and NISac as HaB donors and activated pyridine-N-oxides as HaB acceptors (Puttreddy *et al.*, 2016). In the same study, the authors also reported the strongest non-halonium based HaB interaction by selecting the right choices of donor and acceptor molecules.

1.4.3 Influence of external stimuli

Applying external stimuli like temperature, pressure or electric field can also be used as a method to tune the strength of σ-hole interactions (Forni *et al.*, 2004; Giordano *et al.*, 2019; Wang *et al.*, 2019). The variation in temperature is a common method used in many crystallographic studies, where SCXRD experiments are often carried out within a range of temperatures going from room up to low (100K using liquid N_2) or very low (5K using He gas) temperatures. In general, lowering the temperature induces a shrinking in the crystal structure, due to the approach of the relative positions of molecules in space. Most often this effect leads to an enhanced σ-hole interaction, where the σ-hole donor and acceptor molecules approach closer in space (Forni *et al.*, 2004). On the other hand, the application of either pressure or an electric field for tuning the strength of σ-hole interactions is relatively less explored to date, mainly because of the intrinsic experimental limitations. This experimental challenge has been undertaken in this thesis, where we have carried out a series of high-pressure single-crystal X-ray diffraction (HP-SCXRD) experiments to explore the tunability of N···I···N' HaB interactions in some donor-acceptor co-crystal systems.

HB is one of the major class of non-covalent interactions that has been studied in detail under pressure. Since the initial studies dealing with HB in oxalic acid (Putkonen *et al.*, 1985) several works have been reported, illustrating the sensitivity of HB networks towards constrains of pressure (Yan *et al.*, 2012; Mishra *et al.*, 2020). In the literature, it has also been shown that a transition from a neutral to an ionic form of a binary adduct is possible in the case of oxalic acid dihydrate ($H_2C_2O_4.2H_2O$), by the displacement of two H-atoms from oxalic acid to two water molecules upon increasing the hydrostatic pressure (Casati *et al.*, 2009; Macchi *et al.*, 2010). In such studies, the tunability of HB interactions were investigated as a function of external pressure. At the same time, HaB has been less explored than HB by the high-pressure community, even though it could also potentially show significant variations in intermolecular distances and angles under pressure. Since HB and HaB show very close resemblances in their origin and mode of interactions, such a tunability might also be possible with HaB interactions. These details will be explored in the later part of the thesis (Chapter 3).

1.5 Effect of crystalline environment

Along with the factors discussed in the above section, several studies have also shown that crystalline environments play a crucial role in controlling the properties of σ-hole interactions (Riley *et al.*, 2011; Politzer and Murray, 2013; Makhotkina *et al.*, 2015; Lindblad *et al.*, 2021).

The effect of the crystalline environment is often characterized through secondary non-covalent interactions found in the close vicinity of σ-hole interactions, where changes occurring in the former are concomitantly affecting the latter. One such example is the case of 3,5-difluorohalobenzene (X-benz-meta-2F) and 2,6-difluorohalobenzene (X-benz-ortho-2F) derivatives (where X = Cl, Br or I), where computational studies have pointed that meta derivatives possess a larger σ-hole (and therefore a larger $V_{s,\,max}$) as compared to ortho ones for all the three halogen analogues (Riley *et al.*, 2011). However, considering the binding energies of the X···O HaB formed between these derivatives and the acetone molecule, it has appeared that X-benz-ortho-2F derivatives show a larger stabilization than X-benz-meta-2F derivatives. This minor inconsistency was attributed as the possible effect of secondary non-covalent interactions. Indeed, in case of X-benz-ortho-2F derivatives, along with X···O HaB interaction two additional non-covalent interactions can also be found. The positively charged H-atom in the methyl group of the acetone is interacting simultaneously with Br and F atoms, thus forming C-H···Br and C-H···F HB interactions (**Figure 1.17a**). Accordingly, the presence of two additional non-covalent interactions enhances the binding energy of X-benz-ortho-2F derivatives. On the other hand, such HB interactions are not found in X-benz-meta-2F derivatives, because of the absence of the F-atom in the ortho position and the large distance observed between Br and H atoms. Apart from this, a repulson is also conceived between ortho hydrogens and acetone hydrogens in X-benz-meta-2F derivatives, which altogether destabilizes meta derivatives relative to ortho derivatives.

In some other examples, it is also shown that the presence of secondary interactions can affect the linearity of σ-hole interactions as well. For instance, in the HO-Br···Br-OH HaB complex, the computed HaB angle O-Br···Br is only 162° and this deviation from linearity (180°) is attributed to the occurrence of a secondary O···H HB interaction (**Figure 1.17a**) (Politzer *et al.*, 2008).

In another study concerning the N···I···N HaB interaction formed in the co-crystals of N-iodosaccharin (NISac) or N-iodosuccinimide (NIS) imide derivative with 4-dimethylamino pyridine (DMAP) base, it is also shown that secondary non-covalent interactions play a significant role in the halogen atom shift from donor to acceptor moieties (Makhotkina *et al.*, 2015). In the case of *NISac.DMAP*, the structural characterization of the $N_{sac}\cdots I\cdots N_{DMAP}$ HaB interaction reveals that the I-atom is positioned more closer to the acceptor N_{DMAP} than to the donor N_{Sac}. Here, in addition to the strong effect of the acceptor, a favorable $O^{\delta-}{}_{C=O}\cdots I^{\delta+}$ secondary electrostatic interaction formed with a neighboring molecule is found to be one of

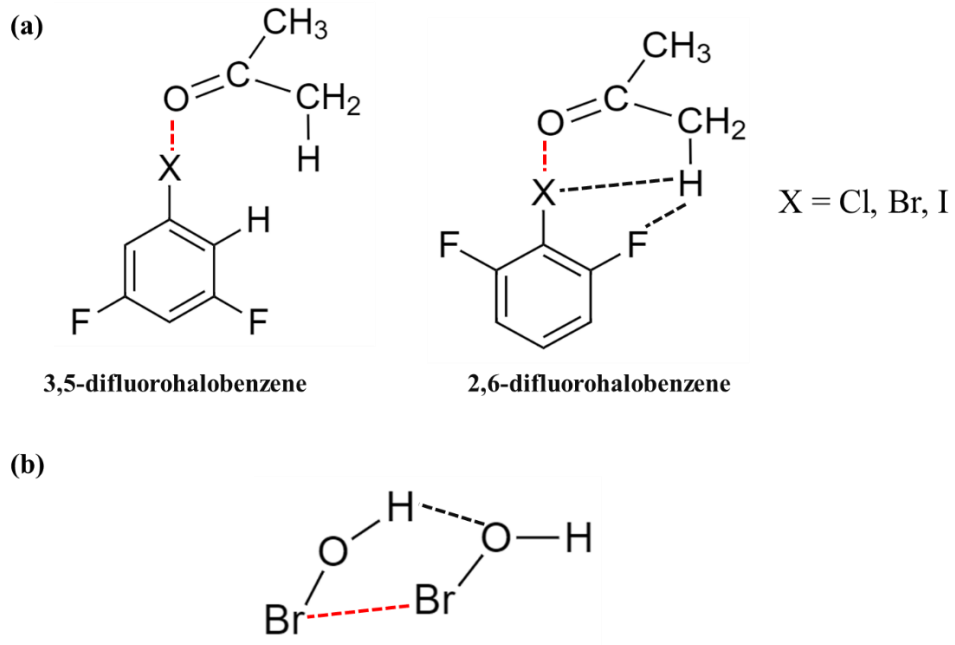

Figure 1.17 (a) HaB complex formed between 3,5-difluorohalobenzene and 2,6-difluorohalobenzene with acetone molecule. HaB interactions are shown as red dashed lines and secondary HB interactions between 2,6-difluorohalobenzene and acetone are shown as black dashed lines (b) HO-Br···Br-OH complex showing a Br···Br HaB interaction (red dashed lines) and a secondary O···H HB interaction (black dashed lines).

the key reasons behind such a halogen atom shift. On the other hand, in the *NIS.DMAP* complex, the position of the halogen atom was determined closer to the donor N_{Sac}, while a least favorable and weaker $O^{\delta-}{}_{C=O}\cdots I^{\delta+}$ secondary electrostatic intreaction was pointed to be the reason for the absence of a halogen atom shift.

On the other hand, cooperativity or anti-cooperativity effects of σ-hole interactions should also be considered in the framework of the crystalline environment. The cooperativity effect is known as the non-additive strengthening of a particular σ-hole interaction upon the formation of a sequence of (linear or cyclic) molecular arrangement. This enhancement in the interaction is mainly attributed to the increasing of charge transfer and polarization components in a larger molecular sequence as compared to the case of a dimer exhibiting the same σ-hole interaction (Esrafili and Mohammadian-Sabet, 2015; Li and An, 2020). Both HaB and ChB interactions are known to show strong cooperativity effects with themselves, as well as in co-existence with other type of non-covalent interactions such as hydrogen bonds (Grabowski, 2013; Li *et al.*, 2008; Ciancaleoni, 2013). The effect of cooperativity in these cases is mainly measured in terms of the analysis of geometrical parameters, binding energy, NBO parameters and electronic properties determined at the bond critical points. So far, several studies have pointed out a strong cooperativity of halogen or chalcogen bonds in 1D-chains, where the strength of the interaction seems to gradually increase with the number of molecules in the chain. Evidence of

cooperativity is found in the infinite chains of halogen cyanides XCN (X = F, Cl, Br, I) and $(OCX)_n$ (X = S, Se; n = 2-8) (George *et al.*, 2014; Esrafili and Mohammadian-Sabet, 2015). A similar enhancement of interactions is also found with some cyclic structures (Parra, 2022). The synergetic effect of HaB in the presence of other non-covalent interactions has been also explored in many systems. One such example is the case of $XCl\cdots FH\cdots F^-$ (X = CCH, CN, OH, NC and F) ternary complex, where a weak Cl···F HaB interaction found in the XCl···FH dimer becomes very strong while adding a third unit F^- that is connected through a strong $H\cdots F^-$ HB interaction. Furthermore, it was also pointed out that whereas both HaB and HB show a mutual enhancement in strength upon ternary complex formation, a larger effect was observed with the former. Another interesting observation made by authors is that, upon ternary complex formation, the nature of the HaB interaction also changes, from a closed-shell to a partially covalent interaction (Li and An, 2020). In some other instances, the modification of HaB interactions from a closed-shell to an ion-pair interaction was also identified (Li *et al.*, 2012).

On the other hand, it should be noted that both HaB and ChB can also show a weakening upon the formation of a larger molecular sequence, which is known as the anti-cooperativity effect. For instance, in case of polytopic HaB donors (donor molecules where multiple halogen atoms can act as potential HaB donor sites), the binding of the acceptor molecule in one donor site reduces $V_{s,\,max}$ values at the other donor sites. Accordingly, this effect decreases the potential power of other donor sites to form HaB interactions (Bedeković *et al.*, 2022). The anti-cooperativity effect of HaB interactions has been also reported with other non-covalent interactions, such as cation-π and anion-π interactions (Razmazma and Ebrahimi, 2018).

Understanding the effect of the crystalline environment on σ-hole interactions is a major focus of this thesis, where the effect of secondary non-covalent interactions will be explored in detail. Also, the changes in the crystalline environment upon the action of an external pressure and their influences on the modification of σ-hole interactions will be investigated in some donor-acceptor co-crystals.

References

Aakeroy, C. B., Bryce, D. L., Desiraju, G. R., Frontera, A., Legon, A. C., Nicotra, F., Rissanen, K., Scheiner, S., Terraneo, G., Metrangolo, P. and Resnati, G. (2019). Pure Appl. Chem., 91 (11), 1889–1892.

Alkorta, I., Elguero, J. and Frontera, A. (2020). Crystals, 10 (3), 180.

Anyfanti, G., Bauzá, A., Gentiluomo, L., Rodrigues, J., Portalone, G., Frontera, A., Rissanen, K. and Puttreddy, R. (2021). Front. Chem., 9, 623595.

Arkhipov, D. E., Lyubeshkin, A. V., Volodin, A. D. and Korlyukov, A. A. (2019). Crystals, 9 (5), 242.

Arunan, E., Desiraju, G. R., Klein, R. A., Sadlej, J., Scheiner, S., Alkorta, I., Clary, D. C., Crabtree, R. H., Dannenberg, J. J., Hobza, P., Kjaergaard, H. G., Legon, A. C., Mennucci, B. and Nesbitt, D. (2011). J. Pure Appl. Chem., 83, 1619-1636.

Aubert, E., Espinosa, E., Nicolas, I., Jeannin, O. and Fourmigué, M. (2017). Faraday Discuss., 203, 389–406.

Batsanov, A. S. (2018). Acta Crystallogr. Sect. E Crystallogr. Commun., 74 (5), 570–574.

Bauzá, A., Quiñonero, D., Frontera, A. and Deyà, P. M. (2011). Phys. Chem. Chem. Phys., 13 (45), 20371.

Bedeković, N., Piteša, T., Eraković, M., Stilinović, V. and Cinčić, D. (2022). *Cryst. Growth Des.*, *22* (4), 2644–2653.

Bond, A. D., Griffiths, J., Rawson, J. M. and Hulliger, J. (2001). Chem. Commun. No. 23, 2488–2489.

Bond, A.D. (2007). CrystEngComm., 9, 833–834 |

Burling, F. T. and Goldstein, B. M. (1992). J. Am. Chem. Soc., 114, 2313-2320.

Byrn, S. R., Zografi, G. and Chen, X. (2017). Solid-State Properties of Pharmaceutical Materials, First Edition, John Wiley & Sons, Inc.

Cao, J., Yan, X., He, W., Li, X., Li, Z., Mo, Y., Liu, M. and Jiang, Y.-B. (2017). J. Am. Chem. Soc., 139 (19), 6605–6610.

Casati, N., Macchi, P., Sironi, A. (2009) Chem. Commun. 19, 2679-2681.

Cavallo, G., Metrangolo, P., Milani, R., Pilati, T., Priimagi, A., Resnati, G. and Terraneo, G. (2016). Chem. Rev., 116 (4), 2478–2601.

Chen, L., Xiang, J., Zhao, Y. and Yan, Q. (2018). J. Am. Chem. Soc., 140 (23), 7079–7082.

Chernysheva, M. V., Bulatova, M., Ding, X. and Haukka, M. (2020). Cryst. Growth Des., 20 (11), 7197–7210.

Ciancaleoni, G. (2018). Phys. Chem. Chem. Phys. 2018, 20 (13), 8506–8514.

Clark T., Hennemann M., Murray J. S. and Politzer P. (2007). J. Mol. Model., 13, 291-296.

Clark, T., Murray, J. S. and Politzer, P. (2014). Aust. J. Chem., 67 (3), 451.

Clark, T., Politzer, P. and Murray, J. S. (2015). Wiley Interdiscip. Rev.: Comput. Mol. Sci., 2015, 5, 169–177.

Colin M. (1814). Ann. Chim., 91, 252.

Dahl, T., Hassel, O. (1970). Acta Chem. Scand., 24, 377 – 382.

Damodharan, L. and Pattabhi, V. (2004). Tetrahedron Lett., 45 (51), 9427–9429.

Daolio, A., Pizzi, A., Calabrese, M., Terraneo, G., Bordignon, S., Frontera, A. and Resnati, G. (2021a). Angew. Chem. Int. Ed., 60 (38), 20723–20727.

Daolio, A., Pizzi, A., Terraneo, G., Frontera, A. and Resnati, G. (2021b). ChemPhysChem, 22 (22), 2281–2285.

Desiraju, G. R. and Parthasarathy, R. (1989). J. Am. Chem. Soc., 111, 8725−8726

Desiraju, G. and Steiner, T. (2001). The Weak Hydrogen Bond: In Structural Chemistry and Biology; Oxford University Press: Oxford and New York.

Desiraju, G. R. (1989). Crystal Engineering. The Design of Organic Solids; Elsevier: Amsterdam.

Desiraju, G. R. (2011). Growth Des. 2011, 11 (4), 896–898.

Desiraju, G. R., Ho, P. S., Kloo, L., Legon, A. C., Marquardt, R., Metrangolo, P., Politzer, P., Resnati, G. and Rissanen, K. (2013). Pure Appl. Chem., 85 (8), 1711–1713.

Dhaka, A., Jeannin, O., Jeon, I., Aubert, E., Espinosa, E. and Fourmigué, M. (2020). Angew. Chem. Int. Ed., 59 (52), 23583–23587.

Dhaka, A., Jeannin, O., Aubert, E., Espinosa, E. and Fourmigué, M. (2021). Molecules 2021, 26 (13), 4050.

Dhaka, A., Jeannin, O., Aubert, E., Espinosa, E. and Fourmigué, M. (2021). Chem. Commun., 57 (37), 4560–4563.

Dharmarwardana, M., Otten, B. M., Ghimire, M. M., Arimilli, B. S., Williams, C. M., Boateng, S., Lu, Z., McCandless, G. T., Gassensmith, J. J. and Omary, M. A. (2021). Proc. Natl. Acad. Sci. 2021, 118 (44), e2106572118.

du Mont, W.-W. and Hrib C. G. in Handbook of Chalcogen Chemistry: New Perspectives in Sulfur, Selenium and Tellurium, Vol.2, 2nd ed. (Eds.: Devillanova, F.A. and du Month W.-W.), RSC Publishing, Cambridge, 2013, pp. 273–316.

Dumas J. M. (1976). Bulletin de la Société Chimique de France.

Dumas J. M., Peurichard H. and Gomel M. J. (1978). Chem. Research, 54-55 Synopses.

Dumele, O., Trapp, N. and Diederich, F. (2015). Angew. Chem. Int. Ed. 2015, 54 (42), 12339–12344.

El Kerdawy, A., Murray, J. S., Politzer, P., Bleiziffer, P., Heßelmann, A., Görling, A. and Clark, T. (2013). J. Chem. Theory Comput., 9 (5), 2264–2275.

Esrafili, M. D. and Mohammadian-Sabet, F. (2015). Struct. Chem., 26 (1), 199–206.

Fellowes, T. and White, J. M. (2019). CrystEngComm, 21, 1539–1542.

Forni, A., Metrangolo, P., Pilati, T. and Resnati, G. (2004). Cryst. Growth Des., 4 (2), 291–295.

George, J., Deringer, V. L. and Dronskowski, R. (2014). J. Phys. Chem. A, 118 (17), 3193–3200.

Giordano, N., Afanasjevs, S., Beavers, C. M., Hobday, C. L., Kamenev, K. V., O'Bannon, E. F., Ruiz-Fuertes, J., Teat, S. J., Valiente, R. and Parsons, S. (2019). Molecules, 24 (10), 2018.

Gleiter, R., Haberhauer, G., Werz, D. B., Rominger, F. and Bleiholder, C. (2018). Chem. Rev., 118 (4), 2010–2041.

Grabowski, S. J. (2013). Theor. Chem. Acc., 132 (4), 1347.

Guido, E., Metrangolo, P., Panzeri, W., Pilati, T., Resnati, G., Ursini, M. and Logothetis, T. A. (2005). J. Fluor. Chem., 126 (2), 197–207.

Gupta, P., Rather, S. A., Saha, B. K., Panda, T., Karothu, D. P. and Nath, N. K. (2020). Cryst. Growth Des., 20 (5), 2847–2852.

Guthrie, F. J. (1863). Chem. Soc., 16, 239-244.

Hakkert, S. B. and Erdélyi, M. (2015). J. Phys. Org. Chem., 28 (3), 226–233.

Hassel, O. (1970). Science, 170, 497-502.

Hassel, O., Hvoslef J., Vihovde E., Hadler E. (1954). Acta. Chem. Scand., 8, 873-873.

Hayashi, S. (2022). Symmetry 2020, 12, 1-20.

He, G., Jacob, C., Guo, L., Chow, P. S. and Tan, R. B. H. (2008). J. Phys. Chem. B, 112 (32), 9890–9895.

Huber, S. M., Jimenez-Izal, E., Ugalde, J. M. and Infante, I. (2012). Chem. Commun., 48, 7708.

Hutchins, K. M. (2018). R. Soc. Open Sci., 5 (6), 180564.

Huynh, H.-T., Jeannin, O. and Fourmigué, M. (2017). Chem. Commun., 53 (60), 8467–8469.

Huynh, H.-T., Jeannin, O., Aubert, E., Espinosa, E. and Fourmigué, M. (2021). New J. Chem., 45 (1), 76–84.

Ibrahim, M. A. A. and Telb, E. M. Z. (2020). ACS Omega, 5 (34), 21631–21640.

Inscoe, B., Rathnayake, H. and Mo, Y. (2021). J. Phys. Chem. A, 125 (14), 2944–2953.

Jaini, A. K. A., Hughes, L. B., Kitimet, M. M., Ulep, K. J., Leopold, M. C. and Parish, C. A. (2019). ACS Sens., 4 (2), 389–397.

Jeannin, O., Huynh, H.-T., Riel, A. M. S. and Fourmigué, M. (2018). New J. Chem., 42 (13), 10502–10509.

Kolář, M. H., Carloni, P. and Hobza, P. (2014). Phys Chem Chem Phys, 16 (36), 19111–19114.

Kolář, M. H. and Hobza, P. (2016). Chem. Rev., 116 (9), 5155–5187.

Kolář, M., Hostaš, J. and Hobza, P. (2014). Phys Chem Chem Phys, 16 (21), 9987–9996.

Koskinen, L., Hirva, P., Kalenius, E., Jääskeläinen, S., Rissanen, K. and Haukka, M. (2015). CrystEngComm, 17 (6), 1231–1236.

Kozuch, S. and Martin, J. M. L. (2013). J. Chem. Theory Comput., 9 (4), 1918–1931.

Legon, A. C. (1999). Angew. Chem., Int. Ed., 38, 2686−2714.

Legon, A. C. (2010). Phys. Chem. Chem. Phys., 12, 7736−7747.

Li, Z. and An, X. (2020). J. Mol. Graph. Model. 2020, 100, 107673.

Lindblad, S., Boróka Németh, F., Földes, T., Heiden, D., Vang, H. G., Driscoll, Z. L., Gonnering, E. R., Pápai, I., Bowling, N. and Erdelyi, M. (2021). Chem. – Eur. J., 27 (55), 13748–13756.

Li, Q., Lin, Q., Li, W., Cheng, J., Gong, B. and Sun, J. (2008). ChemPhysChem, 9 (15), 2265–2269.

Li, Q., Ma, S., Liu, X., Li, W. and Cheng, J. (2012). *J. Chem. Phys.*, *137* (8), 084314.

Maartmann-moe, K., Sanderud, K. A. and Songstad, J. (1984). Acta Chemica Scandinavica A, 38, 187-200.

Macchi, P., Casati, N., Marshall, W. G., Sironi, A. (2010). CrystEngComm. 12, 2596-2603.

Makhotkina, O., Lieffrig, J., Jeannin, O., Fourmigué, M., Aubert, E. and Espinosa, E. (2015). Cryst. Growth Des., 15 (7), 3464–3473.

McNaught, A. D. and Wilkinson, A. (1997). IUPAC Compendium of Chemical Terminology, ed. Royal Society of Chemistry, Cambridge, 2nd edn.

Metrangolo P., Resnati G. (2001). Chem. Eur. J., 7, 2511-2519.

Metrangolo, P. and Resnati, G., Halogen Bonding I, Springer International Publishing: Cham, 2015; Vol. 358.

Metrangolo, P., Murray, J. S., Pilati, T., Politzer, P., Resnati, G. and Terraneo, G. (2011). Cryst. Growth Des., 11 (9), 4238–4246.

Metrangolo, P., Murray, J. S., Pilati, T., Politzer, P., Resnati, G. and Terraneo, G. (2011). CrystEngComm, 13 (22), 6593.

Metrangolo, P., Meyer, F., Pilati, T., Proserpio, D. M. and Resnati, G. (2007). Chem. - Eur. J., 13 (20), 5765–5772.

Metrangolo, P. and Resnati, G. (2014). IUCrJ 1 (1), 5–7.

Mishra, A.K., Murli, C., Pandey, K.K., Sakuntala, T., Poswal, H.K. and Verma, A.K. (2020) J. Phys. Chem. B 124, 373–379.

Mondal, P. K., Shukla, R., Biswas, S. and Chopra, D. (2018). Acta Crystallogr. Sect. B Struct. Sci. Cryst. Eng. Mater., 74 (6), 574–591.

Murray J. S., Lane P. and Politzer P. (2009). J Mol. Model., 15, 723-729.

Murray J. S., Paulsen K. and Politzer P. (1994). Proc. Indian Acad. Sci. Ser. Chim., 106, 267-275.

Murray, J. S. and Politzer, P. (2011). WIREs Comput. Mol. Sci., 1 (2), 153–163.

Murray, J. S., Concha, M. C., Lane, P., Hobza, P. and Politzer, P. (2008). J. Mol. Model., 14, 699–704.

Murray, J. S., Macaveiu, L. and Politzer, P. (2014). J. Comput. Sci., 5 (4), 590–596.

Novoa, J.J. (2018). Intermolecular interactions in crystals: fundamentals of crystal engineering, Cambridge, UK, Royal Society of Chemistry.

Oburn, S. M., Bowling, N. P. and Bosch, E. (2015). Cryst. Growth Des., 15 (3), 1112–1118.

Parra, R. D. (2022). Chem. Phys. Lett., 803, 139825.

Parthasarathy, R. and Row, T. N. G. (1981). J. Am. Chem. Soc., 103, 477-479.

Pepinsky, R. (1955). Phys. Rev., 100, 971.

Perrin, C. L.and Nielson, J. B. (1997). Annu. Rev. Phys. Chem., 48 (1), 511–544.

Politzer P., Lane P., Concha M. C., Ma Y. G. and Murray J. S. (2007). J. Mol. Model., 13, 305-311.

Politzer, P. and Murray, J. S. (2013). ChemPhysChem 2013, 14 (2), 278–294.

Politzer P., Murray J. S. and Concha M. C. (2008). J. Mol. Model., 14, 659-665.

Politzer, P. and Truhlar, D. G. (2013). Chemical applications of atomic and molecular electrostatic potentials: reactivity, structure, scattering, and energetics of organic, inorganic, and biological systems; Springer Science & Business Media.

Politzer, P., Lane, P., Concha, M. C. and Ma, Y.; Murray, J. S. (2007). J. Mol. Model., 13 (2), 305–311.

Politzer, P., Murray, J. S. and Clark, T. (2010). Phys. Chem. Chem. Phys., 12 (28), 7748-7757.

Politzer, P., Murray, J. S. and Clark, T. (2013). Phys. Chem. Chem. Phys., 15 (27), 11178-11189.

Politzer, P., Murray, J. S. and Concha, M. C. (2007). J. Mol. Model., 13 (6–7), 643–650.

Prima, D. O., Vorontsova, E. V., Makarov, A. G., Makarov, A. Yu., Bagryanskaya, I. Yu., Mikhailovskaya, T. F., Slizhov, Y. G. and Zibarev, A. V. (2017). Mendeleev Commun., 27 (5), 439–442.

Putkonen, M.-L., Feld, R., Vettier, C. and Lehmann, M.S. (1985). Acta Cryst. B41, 77–79.

Puttreddy, R., Jurček, O., Bhowmik, S., Mäkelä, T. and Rissanen, K. (2016). Chem. Commun., 52 (11), 2338–2341.

Rajkumar, M. (2021). Cryst. Growth Des., 21, 3547−3553.

Ravat, P., SeethaLekshmi, S., Biswas, S. N., Nandy, P. and Varughese, S. (2015). Cryst. Growth Des., 15 (5), 2389–2401.

Razmazma, H. and Ebrahimi, A. (2018). J. Mol. Graph. Model. 2018, 84, 134–144.

Reed, A. E., Weinhold, F., Weiss, R. and Macheleid, J. (1985). J. Phys. Chem., 89, 2688–2694.

Riel, A. M. S., Huynh, H.-T., Jeannin, O., Berryman, O. and Fourmigué, M. (2019). Cryst. Growth Des., 19 (2), 1418–1425.

Riley, K. E. and Hobza, P. (2008). J. Chem. Theory Comput. 2008, 4 (2), 232–242.

Riley, K. E. and Hobza, P. (2013). Phys. Chem. Chem. Phys., 15 (41), 17742–17751.

Riley, K. E., Murray, J. S., Fanfrlík, J., Řezáč, J., Solá, R. J., Concha, M. C., Ramos, F. M. and Politzer, P. (2011). *J. Mol. Model.*, *17* (12), 3309–3318.

Riley, K. E., Murray, J. S., Fanfrlík, J., Řezáč, J., Solá, R. J.; Concha, M. C., Ramos, F. M. and Politzer, P. (2013). J. Mol. Model., 19 (11), 4651–4659.

Robinson, S. W., Mustoe, C. L., White, N. G., Brown, A., Thompson, A. L., Kennepohl, P. and Beer, P. (2015). J. Am. Chem. Soc., 137, 499–507.

Rosenfield, R. E., Parthasarathy, R. and Dunitz, J. D. (1977). J. Am. Chem. Soc., 99, 4860-4862.

Rosokha, S. V., Stern, C. L. and Ritzert, J. T. (2013). Chem. – Eur. J., 19, 8774–8788.

Sarkar, S., Thomas, S. P., Potnuru, L. R., Edwards, A. J., Grosjean, A., Ramanathan, K. V. and Row, T. N. G. (2019). J Phys Chem Lett, 10, 7224-7229.

Schmidt, G. M. J. (1971). Pure Appl.Chem., 27, 647−678.

Scilabra, P., Terraneo, G. and Resnati, G. (2019). Acc. Chem. Res., 52 (5), 1313–1324.

Shi, D., Cao, J., Weng, P., Yan, X., Li, Z. and Jiang, Y.-B. (2021). Org. Biomol. Chem., 19, 6397–6401.

Shukla, R., Dhaka, A., Aubert, E., Vijayakumar-Syamala, V., Jeannin, O., Fourmigué, M. and Espinosa, E. (2020). Cryst. Growth Des., 20 (12), 7704–7725.

Sinnokrotm, M. O. and Sherrill, C. D. (2004). J. Am. Chem. Soc., 126, 7690-7697.

Steiner, T. (2002). Angew. Chem. Int. Ed., 41, 48 – 76.

Stone, A. J. (2013). J. Am. Chem. Soc., 135, 7005−7009.

Thakuria, R., Nath, N. K. and Saha, B. K. (2019). Cryst. Growth Des., 19 (2), 523–528.

Tiekink E. and Zukerman-Schpector, J. (2017). Multi-Component Crystals, Synthesis, Concepts, Function, Berlin, Boston: De Gruyter, xv+347 pp.

Tothadi, S. and Desiraju, G. R. (2013). Chem. Commun., 2013, 49, 7791-7793.

Turunen, L. and Erdélyi, M. (2020). Chem. Soc. Rev., 49 (9), 2688–2700.

Varadwaj, A., Marques, H. M. and Varadwaj, P. R. (2019). Molecules, 24, 379.

Wang, C., Danovich, D., Chen, H. and Shaik, S. (2019). J. Am. Chem. Soc., 141 (17), 7122–7136.

Wang, C., Danovich, D., Mo, Y. and Shaik, S. J. (2014). Chem. Theory Comput., 10, 3726–3737.

Wang, H., Liu, J. and Wang, W. (2018). Phys. Chem. Chem. Phys., 20 (7), 5227–5234.

Wang, W., Ji, B. and Zhang, Y. (2009). J. Phys. Chem. A, 113 (28), 8132–8135.

Wasilewska, A., Gdaniec, M. and Połoński, T. (2007). CrystEngComm, 9 (3), 203–206.

Wang, D.-X. and Wang, M.-X. (2020). Acc. Chem. Res., 53 (7), 1364–1380.

Werz D. B., Gleiter R. and Rominger F. (2002). J. Am. Chem. Soc., 124, 10638-10639.

Werz D. B., Gleiter R. and Rominger F. (2004). J. Org. Chem., 69, 2945-2952.

Werz D. B., Staeb T. H., Benisch C., Rausch B. J., Rominger F. and Gleiter R. (2002). Org. Lett., 4, 339-342.

Widner, D. L., Knauf, Q. R., Merucci, M. T., Fritz, T. R., Sauer, J. S., Speetzen, E. D., Bosch, E. and Bowling, N. P. (2014). J. Org. Chem., 79 (13), 6269–6278.

Wouters, J. and Quéré, L. (2012). Pharmaceutical Salts and Co-crystals. RSC Drug Discovery Series No. 16, Published by the Royal Society of Chemistry.

Yamada, S. (2020). Coord. Chem. Rev., 415, 213301.

Yan, T., Li, S., Wang, K., Tan, X., Jiang, Z., Yang, K., Liu, B., Zou, G. and Zou, B. (2012). J. Phys. Chem. B 116, 9796-9802.

Yan, X., Zou, K., Cao, J., Li, X., Zhao, Z., Li, Z., Wu, A., Liang, W., Mo, Y. and Jiang, Y. (2019). Nat. Commun., 10 (1), 3610.

Yao, Z.-F., Wang, J.-Y. and Pei, J. (2018). Cryst. Growth Des., 18, 7−15.

2

Methodology and Experimental Procedures

This chapter mainly includes the methods and experimental tools that are used for the structural and electronic characterization of σ-hole interactions. Importance of electron density distribution $\rho(\mathbf{r})$ in characterizing the non-covalent interactions are discussed, followed by experimental and theoretical ways to obtain $\rho(\mathbf{r})$ in molecular crystals. Fundamentals of different electron density refinement models and benefits behind the topological analysis of the so-obtained electron densities are discussed, along with its usefulness for the description of intermolecular interactions occurring in molecular crystals. The second part of this chapter contains crystallization methods: tools and techniques, that are used to produce good quality crystals of the investigated molecules. In the final part, the particulars of experimental set-up that is used for the high-pressure single-crystal X-ray diffraction experiments are detailed.

2.1 Electron density: a tool for investigation of intermolecular interactions

The distribution of electron density $\rho(\mathbf{r})$ in a molecule can be used as the information source to study the characteristics of a bonding interaction, intra or intermolecular. This is a topic of immense research in scientific community since the time when Lewis published his seminar paper entitled *The atom and the molecule* in 1916 (Lewis, 1916). Despite the fact that such bonding interaction analysis between the atoms carries a history of more than one century, there are still continuous efforts to investigate on new modes of describing their interactions.

The concept of description of a chemical bond had a turnaround in the year of 1990 when R.F Bader introduced the *Quantum Theory of Atoms in Molecule* (QTAIM) methodology. This QTAIM is still considered as one of the most powerful and relevant bonding theories of recent decades that links between two cornerstones in chemistry: the atoms and the bonds (Bader, 1990). This thesis will mainly deal with concepts of QTAIM to better understand the bonding interactions, beyond the structural point of view a dedicated effort will be made to look into the electronic descriptors. The sole concept of QTAIM relies on electron density distribution $\rho(\mathbf{r})$ as an information source because of the fact that this function conserves all the ground state properties of a system. This distribution of electron density can be obtained, at least approximately, *via* both experimental and theoretical methods.

This PhD thesis is mainly devoted to the study of bonding interactions, with a particular focus on σ-hole interactions found in the solid-state assemblies of molecular crystals. A dedicated effort will be made to grow single crystals of the interested compounds and to carry out

experimental studies of the same thereafter. Even though there will be a strong inclination towards the experimental methods to obtain the $\rho(\mathbf{r})$ of such compounds, theoretical calculations will also play an important role in this thesis as a counterpart. They will be used in order to account the accuracy of the model obtained experimentally or to obtain a theoretical model that permits to overcome the experimental difficulties which could not permit to derive an experimental model.

In recent times, there has also been lots of efforts made to study the response of molecular crystals under extreme conditions (Lee, 2014). The studies of bonding interactions on response to high-pressure environment is still an evolving field in crystallography. The accurate determination of $\rho(\mathbf{r})$ under high-pressure environment is challenging. There have been conscious efforts made in the past decade to overcome this problem, both technically and theoretically, but still it requires rigorous research to reach complete success. A strong effort will be made to study experimentally the evolution of non-covalent interactions under high-pressure, while theoretical calculations will be employed to cement the results obtained and also to fill the hole left by the limitations associated with high-pressure experimental techniques.

2.1.1 Analysis of electron density ρ(r)

The electron density distribution $\rho(\mathbf{r})$ in a molecular crystal can be obtained from both experimental and theoretical methods. The experimental electron density can be determined through *high-resolution single crystal X-ray diffraction* (HR-SCXRD) experiments, whereas theoretical methods involve *ab-initio* calculations performed on periodic systems and on isolated molecule(s) in gas phase. This thesis will be mainly oriented on the attempt to determine $\rho(\mathbf{r})$ from SCXRD (HR-SCXRD whenever possible) experiments and to analyze it thereafter, accompanied by theoretical counterparts. The so-obtained $\rho(\mathbf{r})$ models will be further utilized to perform the topological analysis of the scalar function $\rho(\mathbf{r})$ within the framework of QTAIM, for characterizing intermolecular interactions (**Figure 2.1**). This will serve the purpose of studying the bonding interactions from the electronic point of view, in addition to the structural analysis.

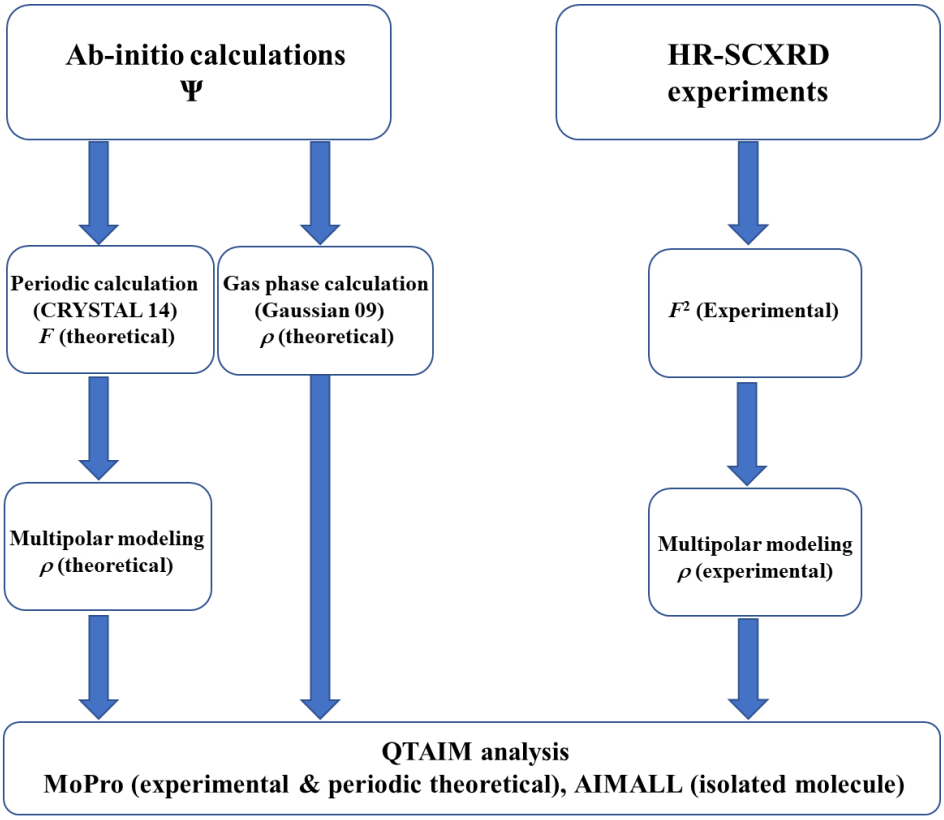

Figure 2.1 Schematic representation illustrating the chemical bonding analysis using QTAIM approach, based on electron density distribution obtained from experimental and theoretical methods.

2.1.1.1 Methods for obtaining the electron density $\rho(\mathbf{r})$ model

Different methods for obtaining $\rho(\mathbf{r})$ are illustrated in this section, accounting their concepts, required tools, challenges and artifacts that have to be identified and treated.

2.1.1.1.1 High-resolution single-crystal X-ray diffraction: an experimental route

High-resolution single crystal X-ray diffraction (HR-SCXRD) is an important tool to experimentally obtain the $\rho(\mathbf{r})$ in a molecular crystal. This method permits to determine the crystal structure, while the utilization scope of the same is not just limited to the crystallographers but it also lies to several other domains of current research such as structural biology, pharmaceutical chemistry, material science, etc. The principle of X-ray diffraction is based on the well-known *Bragg's law* proposed by Sir William Lawrence Bragg and Sir William Henry Bragg in 1913, which eventually leads them to share the Nobel Prize in 1915.

The central concept of the Bragg's law is when a crystal interacts with the X-ray beams, the electrons in the atoms start to oscillate and will get accelerated eventually. This cause the

electrons to emit electromagnetic waves, which can cause either constructive or destructive interferences. Since crystals are three-dimensional array of atoms in periodic order, X-ray diffraction is observed in some specific directions with increased intensities compared to the rest. **Equation 2.1** shows the geometrical condition under which a diffracted X-ray beam undergoes a constructive interference.

$$2\ d\ sin\theta = n\lambda \qquad 2.1$$

where,

n – is an integer corresponding to the order of diffraction (in Bragg's law taken as unity since it deals with only first order reflections)

λ – is the wavelength of the incident beam

d – is the inter plane spacing in the crystal lattice

θ – is the Bragg's angle, which is the half of the angle between the incident and the diffracted beams

Figure 2.2 shows the X-ray beams diffracted by a family of reticular planes (*hkl*) with an interplanar spacing of d_{hkl}. In order to get a constructive interference, the path difference between the diffracted rays should be a whole number of λ.

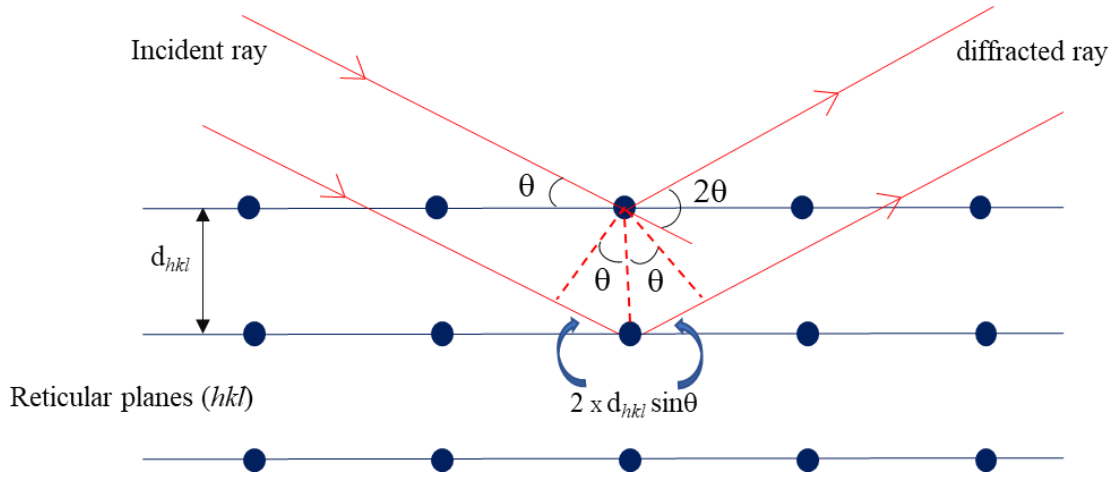

Figure 2.2 Schematic representation of Bragg's law of diffraction

The general idea of X-ray diffraction for structure determination is to collect enough diffraction intensities (diffraction spots) to examine each family of planes with a given resolution. A 4-circles diffractometer equipped with monochromatic X-ray beam source which permit to orient the crystal with three degrees of freedom (ω, Φ, κ) and another one degree of freedom

(2θ) defining the detector position serves the purpose to determine the crystal structure of any given crystal. The position of diffracted X-ray beams allows one to obtain the type of crystal system with the information on the size and shape of the unit cell, but nothing regarding the type and distribution of atoms inside the unit cell. These details can be extracted from the intensity of the diffracted X-ray beams $I(\mathbf{H})$, which gives access to the modulus of the structure factor $F(\mathbf{H})$ as:

$$I(\mathbf{H}) \propto |F(\mathbf{H})|^2$$

As per IUCr "*The structure factor F_{hkl} is a mathematical function describing the amplitude and phase of a wave diffracted from crystal lattice planes characterized by Miller indices h, k, l*" (Coppens, 2006). Therefore, structure factors correspond to the resultant waves scattered by all atoms of the unit cell, giving access to the information of how atoms are arranged inside the unit cell. The modulus sign in the relationship means a phase-less quantity of F. Mathematically, F is obtained by adding together all the waves scattered by individual atoms and the total amplitude is represented as the Fourier transform (FT) of the thermally averaged electron density $\rho(\mathbf{r})$ in the unit cell (**Equation 2.2**).

$$F(\mathbf{H}) = \int_0^V \rho(\mathbf{r})\, e^{2\pi i H.\mathbf{r}}\, d\mathbf{r} \qquad 2.2$$

where $\mathbf{H}$ is the reciprocal lattice vector $\mathbf{H} = h\mathbf{a^*}+k\mathbf{b^*}+l\mathbf{c^*}$ and V is the unit cell volume. Thus, the electron density can be obtained through an inverse FT summation of the structure factors (**Equation 2.3**).

$$\rho(\mathbf{r}) = \frac{1}{V}\sum_{h,k,l} F_{hkl}\, e^{-2\pi i(hx+ky+lz)} \qquad 2.3$$

where x, y and z are fractional co-ordinates defining the position of atom in the unit cell $\boldsymbol{r} = x\mathbf{a}+y\mathbf{b}+z\mathbf{c}$.

One could describe the exact electron density distribution in a crystal using the above equations, but in reality, it is not very straightforward due to the following constraints:

(1) Number of reflections: There is always a limitation in the total number of reflections that can be collected. This is directly related with the wavelength (λ) of the X-ray source, the size of the crystal used and also a strong correlation with the geometry of the diffractometer. One way to overcome this problem is to use a smaller wavelength as possible (of course one

has to compromise the intensity of the diffraction peaks by doing so), a larger crystal as possible (size is limited to the beam size) and considering all possible orientation of the crystals by playing with the four degrees of freedom in the diffractometer.

(2) Scattering problem for heavy atoms: The atomic scattering factor (the amplitude of the ability of an atom to scatter X-ray beams) depends on the number of electrons in that particular atom, which is higher for a heavier element. The atomic scattering factor decreases with increasing the scattering angle. This suggests that the data at low angles must be measured with caution because the scattering due to the valence electrons not only becomes a smaller part of total scattering but also is limited to the low angles in case of heavier elements.

(3) Higher angle reflections: As compared to the low angle reflections, the intensities of diffracted X-ray beams are weaker at high scattering angles. The high angle reflections are very crucial in the accurate determination of the atomic positions and the electron density distribution in a molecular crystal. The possible ways to overcome this issue is to prepare a large good quality crystal and measuring the high angle reflections with a longer exposure time as compared to the one used for the low angle reflections.

(4) Phase problem: This is considered as one of the most important problems in obtaining $\rho(\mathbf{r})$ from experimental measurements. As per the discussion above, it is clear that X-ray intensities yield only structure factor amplitudes not their phases, and one has to obtain the latter from some other means. This can be achieved by using a model that gives information about both the phases and the magnitudes of the structure factors. The model is further refined by minimizing the difference between the calculated structure factors and the experimental structure factors, being suitably weighed using the magnitudes of the experimental uncertainties (this called the structure refinement process).

(5) Absorption effect: It is possible that a sample can absorb X-rays rather than diffracting them. **Equation 2.4** is a relationship showing that for a given wavelength, the level of absorbance of a crystal depends on the absorption coefficient μ. This parameter is directly correlated with the atom types in the crystal, and also with the path length t the X-ray beam travel through the crystal.

$$I_t = I_0 \exp(-\mu t) \qquad 2.4$$

Absorption has also a correlation with the wavelength used for the measurement, longer the wavelength greater is the absorption co-efficient for the crystal, $\mu \alpha \lambda^3$.

In general this problem can be resolved by an accurate absorption correction method, sometimes by indexing the faces of crystal for numerical absorption correction especially for the crystals with heavy elements.

(6) Extinction effect: This problem arises due to the subsequent scattering of the X-rays beam from different parts of the crystal. Hence, firstly scattered by one family of plane, the X-ray beam is further scattered by same family of plane. This effect is known as extinction and it causes the reduction in intensity of the diffracted X-ray beams. In general extinction affects strong and low angle reflections, and it presents a significant correlation with the wavelength used as well. One way to compensate this issue is by including a correction factor, the so-called *extinction co-efficient* parameter, in the structure refinement process.

In conclusion, due to above mentioned problems in the determination of $\rho(\mathbf{r})$ one has to pay attention from the very beginning in an experimental route, that is even from the mode of crystallization. An extreme care should be given to the choice of the X-ray source, the diffracting power of the crystal and the largest resolution that we can achieve with good completeness. Also, the choice of the temperature during the X-ray diffraction experiment is very crucial. At room temperature the atoms in the molecule can undergo relatively large thermal vibration around their equilibrium position. This can hamper the accurate determination of the atomic positions because of the more diffused nature of the electron clouds. Therefore, low temperature (~100K using liquid nitrogen or ~ 5K using Helium) is preferable over the room temperature for the X-ray diffraction experiments. In this thesis, SCXRD experiments are carried out both at room and low temperatures (at ~100K using liquid nitrogen) based on the final requirements.

2.1.1.1.2 Determining the electron density from theoretical methods: gas phase and periodic calculations

Due to the above-mentioned limitations in the experimental methods, theoretical calculations can be a very useful parallel tool in determining $\rho(\mathbf{r})$. This information will be handy for the comparison purposes and also to validate the conclusions made earlier from the experimental results. The experimental data include thermal effects, thus hindering a direct comparison between experimental and theoretical outcomes. Two possible solutions to this problem are (i) convolution of the theoretical electron density with the experimental thermal motion or (ii) deconvolution of the experimental electron density from the thermal effects. The latter solution allows one to compare the static densities derived from theory and experiment, which is a

common practice now a days in the field of charge density analysis and is also used in the course of this thesis.

Theoretical models of $\rho(\mathbf{r})$ can be derived *via* periodic calculations or by gas phase calculations performed on isolated molecule(s), either at optimized or crystal geometries. The electron density function for isolated molecules can be calculated using Gaussian 09 software (Frisch *et al.*, 2016), where the effect of crystalline environment is not considered if the molecular structure is optimized or partially considered if the structure is fixed at the crystalline geometry. The effect of crystalline environment is very crucial in studying the intermolecular interactions, and this can be considered theoretically by performing the periodic calculations using CRYSTAL14 software (Dovesi *et al.*, 2014) or CASTEP (version 19.11) software (Clark *et al.*, 2005).

2.1.1.2 Electron density modelling

The next step is to accurately model the so-obtained electron densities, in order to see how the electronic clouds are distributed among interacting atoms. As discussed before, there are some experimental limitations associated with a full description of $\rho(\mathbf{r})$, mainly arising from the phase problem of the structure factors. This can be resolved by using a theoretical model which gives information about both the phase and magnitudes of the structure factors. In small molecule crystallography Patterson method (Patterson, 1934), direct method (Hauptman, 1997) or charge flipping algorithms (Oszlányi and Sütő, 2008) are used for this purpose. Later, this model is optimized using some iteration or mathematical methods, by adjusting various parameters of the structural model so that the theoretical model coincides with the experimental data. The least square approach is commonly used for this purpose, which fit the electron density model against structure factors. In least-square refinement a set of structure factors are calculated from the atomic models by means of FT, and the parameters of the model are refined further to minimize a mathematical function M (**Equation 2.5**). These refinements can be performed against F or F^2.

$$M = \sum_H \omega_H \left(\frac{1}{k} F_{obs}^2 - F_{calc}^2\right)^2 \qquad 2.5$$

or

$$M = \sum_H \omega_H \left(\frac{1}{k} |F_{obs}| - |F_{calc}|\right)^2$$

where F_{obs} and F_{calc} are structure factors observed (either from experimental or theoretical method) and calculated (from a model), respectively. k is the scale factor and ω_H is the weighting factor which is derived from the standard uncertainty σ of that particular measurement (**Equation 2.6**).

$$\omega_H = \frac{1}{\sigma^2 (F_{obs})} \qquad 2.6$$

2.1.1.2.1 Independent atom model

The independent atom model (IAM) is the most widely used method for structure determination (Stalke, 2011). In IAM the molecular density is described as the superposition of the spherical atomic densities, which corresponds to the spherical atomic scattering factors. The main assumption of this model is that the atoms are considered as neutral, spherical and isolated entities, leading to an atomic electron density distribution only around the nuclei. Therefore, the total electron density distribution can be subdivided into *N* independent atomic densities, each centered at $\mathbf{r_j}$ (**Equation 2.7**):

$$\rho_{IAM}(\mathbf{r}) = \sum_{j=1}^{N} \rho_j^{sph} (|\mathbf{r} - \mathbf{r}_j|) \qquad 2.7$$

The electron density of each atom is further divided into its core and valence electron densities, both are spherically symmetric (**Equation 2.8**):

$$\rho_j^{sph}(\mathbf{r}) = \rho_j^{core}(\mathbf{r}) + \rho_j^{val}(\mathbf{r}) \qquad 2.8$$

In IAM, there can be nine parameters per atom that can be refined which includes three positional (*x*,*y*,*z*) and six anisotropic displacement parameters (U_{ij}). Here, even though atoms are considered as isolated moieties, the connectivity between them is realized by geometrical considerations. IAM is sufficient for determining the crystal structure at low and atomic resolutions, but not for sub-atomic high-resolutions. Bonding effects (intra- or intermolecular) and position of lone pairs cannot be directly derived from IAM. This model is a good approximation for heavy atoms, for which core electrons contribute significantly to the total electron distribution. However, this is not the case for lighter atoms, where valence shells have a significant contribution in total electron density distribution and play a crucial role in bonding interactions. Also, in IAM, the treatment of hydrogen atoms (which have no core electrons) is not so straightforward, causing shortening of the X-H bonds as compared to the real distance.

In reality, molecules can also have net charges, dipoles and higher electrostatic moments, contradicting the assumption of neutral atoms.

In this thesis, all crystal structures are solved by direct methods and refined against F^2 using Olex2-1.3.0 software (Dolomanov *et al.*, 2009). Analysis of the crystal structures are carried out using Olex2-1.3.0, Crystal Explorer – version 17.5 (Turner *et al.*, 2017) and Mercury (version 2020.1) software packages, and the latter is also used to generate crystal structure drawings.

2.1.1.2.2 Multipolar Model

In order to accurately determine the crystalline electron density distribution, several non-spherical atom models have been proposed (Kurki-Suonio, 1968; Hirshfeld, 1971; Stewart and Bentley, 1975; Hirshfeld, 1977). Among them, the most widely used is the multipolar model proposed by Hansen and Coppens in 1978, where multipoles are generated at atomic centers by the superposition of real spherical harmonic functions (Hansen and Coppens, 1978). The level of multipolar expansion is decided based on the size of the atoms and the environment in which the atoms are situated. Currently, the Hansen-Coppens multipolar model is largely used in the field of small molecule charge density analysis, and is incorporated in several software packages (Jelsch *et al.*, 2005; Volkov *et al.*, 2006).

In this Hansen-Coppens multipolar formalism, the total electron density distribution is mathematically expressed as the summation of N-atoms contributions, as indicated in **Equation 2.9**.

$$\rho(\mathbf{r}) = \sum_{i=1}^{N} \rho_i(\mathbf{r}) \qquad 2.9$$

where each of the atomic electron densities $\rho_i(\mathbf{r})$ are further divided into three other terms (**Equation 2.10**).

$$\rho_i(\mathbf{r}) = \rho_{core}(\mathbf{r}) + P_{val} k^3 \rho_{val}(k\mathbf{r}) + \sum_{l=0}^{l_{max}} k'^3 R_l(k'\mathbf{r}) \sum_{m=0}^{l} P_{l\pm m} y_{l\pm m}(\theta, \phi) \qquad 2.10$$

The first term corresponds to core electrons, remaining by hypothesis unperturbed and spherically symmetric even upon the formation of intra or interatomic interactions.

The second and third terms correspond respectively to the spherical and non-spherical distribution of the valence electrons which is directly reflecting the influence of the environment.

The second term describes the atomic charge transfer (P_{val}) and a spherical expansion or contraction parameter (k) of its valence-shell around the atomic position. Since these two parameters are atomic variables, they can be refined in the least square procedure to fit well the electron density distribution around an atom.

The third term is used to describe the asphericity of the valence electron distribution. This is described in terms of real spherical harmonic functions $y_{l\pm m}(\theta,\phi)$ oriented with respect to a local co-ordinate system (*X,Y,Z*) defined by the user. This local co-ordinate system is centered at each atomic position and is oriented on the basis of neighboring atoms. The spherical harmonic functions are parameterized by a multipolar population $P_{l\pm m}$ parameter, which is refined to fit the non-spherical deformation of the electron density. Hence, to accurately describe the electron density distribution a set of multipolar parameters ($P_{val}, k, P_{l\pm m}, k'$) are refined. $R_l(k'\mathbf{r})$ represents the Slater-type radial function (**Equation 2.11**), which is modulated by the expansion or contraction parameter k' and is responsible along with the spherical harmonic functions for the modeling of the non-spherical part of the valence electron density.

$$R_l(\mathbf{r}) = \frac{\xi_l^{n_l+3}}{(n_l+2)!} k'^{nl} r^{nl} e^{-\xi_l k' r} \; ; n_l \geq l \qquad 2.11$$

In the least-square refinement n_l and ξ parameters are kept fixed (sometimes a non-default value is used, details will be discussed in the respective result sections), while the k' parameter is refined in order to account for the expansion or contraction of the multipolar electron densities.

2.1.1.2.2.1 Charge density refinement with MoPro software

The multipolar refinement based on the Hansen-Coppens multipolar formalism is implemented in MoPro software package (Jelsch *et al.*, 2005), which is utilized throughout this thesis for modeling the non-spherical distribution of the atomic electron densities. MoPro uses the local co-ordinate systems centered on atoms for the orientation of the atomic multipoles, with an

optimum representation of the multipoles with respect to the local symmetry. In MoPro, all the parameters of **Equation 2.10** can be either refined manually in a step by step procedure along with structural parameters (*x*,*y*,*z*), U_{ij}'s and the scale factor (SCA) or through an automatic refinement option.

During the fitting procedure, the refined parameters ($P_{val}, k, P_{l\pm m}, k'$) can present sometimes a strong correlation between them, giving rise to unstable or unrealistic results. One way to minimize correlation problems is to introduce some constraints and restraints during the refinement process (if necessary only). The inclusion of constraints is also very useful for improving the data to parameter ratio. The software MoPro itself can create a list of such constraints and restraints, defined by the user, while they can be modified or released during the refinement process based on the requirements.

Another interesting fact to keep in mind during the multipolar refinement process is the consideration of the anharmonic motion of atoms, especially for the heavier atoms. Accounting the anharmonic motion is sometimes essential for an accurate electron density modeling (Herbst-Irmer, 2013). During the multipolar refinement, effects of such anharmonic motions are included using Gram-Charlier expansion coefficients implemented inside MoPro.

2.1.1.3 Validation tools for the model

The process of the refinement is intended to improve the calculated prior model by minimizing the function *M* as small as possible. Therefore, it is very important for the user to get a track of changes in the model in each step of the refinement process. This section will illustrate some validation tools that are available for this purpose.

2.1.1.3.1 Agreement factor

The goal of the least-square refinement process is to minimize the difference between the calculated and the observed structure factors. Two agreement factors can be used to evaluate the statistical quality of the structural model, which are the *R-factor* (**Equation 2.12**) and the *wR*$_2$*-factor* (**Equation 2.13**). The *R*-factor, otherwise known as *Residual or Reliability factor*, is the first criterion that has to be evaluated for commenting about the quality of a refinement model.

$$R = \frac{\sum_H \frac{1}{k}(|F_{obs}| - |F_{calc}|)}{\sum_H \frac{1}{k}|F_{obs}|} \qquad 2.12$$

$$wR_2F = \sqrt{\frac{\sum_H \frac{1}{\sigma^2(F_{obs})}(\frac{1}{\mathrm{k}}|F_{obs}| - |F_{calc}|)^2}{\sum_H \frac{1}{\sigma^2(F_{obs})}(\frac{1}{\mathrm{k}}|F_{obs}|)^2}} \qquad 2.13$$

where k is the scale factor and $\sigma(F_{obs})$ is the standard deviation of the experimental structure factors.

According to **Equation 2.12**, the *R*-factor decreases with that of the difference between $|F_{obs}|$and $|F_{calc}|$. Thus, lower the value better the model. The same is applied for the wR_2-factor, whose numerator is based on the *M* function that has to be minimized during the refinement process.

The *Goodness of Fit (GOF)* is another agreement factor that can also be utilized to analyze the statistical quality of the refinement (**Equation 2.14**):

$$GOF = \sqrt{\frac{\sum_H \frac{1}{\sigma^2(F_{obs})}(\frac{1}{\mathrm{k}}|F_{obs}| - |F_{calc}|)^2}{n_{obs} - n_{par}}} \qquad 2.14$$

Where n_{obs} and n_{par} are the number of observed reflections and the number of parameters used in the refinement process. In an ideal case, for an appropriate refinement of the model carried out with a proper weighing scheme, the value of *GOF* should be close to 1. A GOF < 1 indicates that the standard errors on the measured intensities are overestimated, whereas *GOF* >> 1 usually indicates some problems in the data and/or in the refinement.

2.1.1.3.2 Residual electron density

Another indicator that can be used to check the quality of the model after convergence is the residual electron density map. The residual electron density $\Delta\rho_{res}(\mathbf{r})$ is defined as the difference between the observed [$\rho_{obs}(\mathbf{r})$] and the calculated [$\rho_{calc}(\mathbf{r})$] electron densities (**Equation 2.15**).

$$\Delta\rho_{res}(\mathbf{r}) = \rho_{obs}(\mathbf{r}) - \rho_{calc}(\mathbf{r}) = \frac{1}{V}\sum_{H}\left[\frac{1}{k}|F_{obs}| - |F_{calc}|\right].\exp i(\varphi_{calc} - 2\pi i\boldsymbol{H}.\mathbf{r}) \quad 2.15$$

where $\rho_{calc}(\mathbf{r})$ corresponds to $\rho_{IAM}(\mathbf{r})$ for the spherical atom model, or to $\rho_{MM}(\mathbf{r})$ for the multipolar model. For an ideal case, $\Delta\rho_{res}(\mathbf{r})$ maps should present as less features as possible, with few random distributions coming from experimental noise.

2.1.1.3.3 Deformation density maps

Deformation density maps are calculated to represent the electron density distributions that are resulting from the variation of those of isolated atoms, mainly involved with the valence electrons due to environment effects. In this way, deformation density maps allow one to better understand the features of $\rho(\mathbf{r})$ associated with bonding interactions. For heavier elements, there will be a significant contribution of core electrons that has to be removed in order to well observe the characteristics of bonding interactions.

Mathematically, the deformation density $\Delta\rho(\mathbf{r})$ is defined as the difference between the total $\rho(\mathbf{r})$ and the pro-molecule $\rho_{\text{pro}}(\mathbf{r})$ electron densities (**Equation 2.16**). The Pro-molecule electron density corresponds to the reference electron density of IAM [$\rho_{\text{pro}}(\mathbf{r}) = \rho_{\text{IAM}}(\mathbf{r})$]. Thus, the deformation density maps are calculated by subtracting neutral spherical atom densities from observed electron densities.

$$\Delta\rho(\mathbf{r}) = \rho(\mathbf{r}) - \rho_{pro}(\mathbf{r}) \quad 2.16$$

There are two types of deformation density maps that can be generated:

(1) Dynamic deformation density maps – The observed structure factors F_{obs} are used to compute $\rho(\mathbf{r})$, therefore containing thermal effects (**Equation 1.17**):

$$\Delta\rho_{dyn}(\mathbf{r}) = \frac{1}{V}\sum_{H}\left[\frac{1}{k}|F_{obs}|.\exp(i\varphi_{MM}) - |F_{sph}|.\exp(i\varphi_{sph})\right].\exp(-2\pi i\boldsymbol{H}.\mathbf{r}) \quad 2.17$$

where φ_{MM} are the structure factor phases obtained by multipolar model, whereas φ_{sph} are calculated from the spherical atomic scattering factors.

(2) Static deformation density maps – They are calculated from the multipolar model [$\rho(\mathbf{r}) = \rho_{MM}(\mathbf{r})$], where the multipolar electron density is deconvoluted from thermal smearing. In this case, an important advantage is that it can be directly compared with theoretically calculated maps, since they do not contain the thermal effects (**Equation 2.18**):

$$\Delta\rho_{stat}(\mathbf{r}) = \sum_{i=1}^{N_{at}} \Delta\rho_i(\mathbf{r}) \qquad 2.18$$

where N_{at} represents the number of atoms in the unit cell.

This deformation density map is very important to identify the reliableness of the experimental model that is obtained after refinement process. Additionally, static deformation density maps give a direct representation of the electron density model. Therefore, it can show electron deficient (δ^+) and electron concentrated (δ^-) regions with respect to the non-interacting spherical atoms, thus permit to characterize the accumulation of electron density in bonding regions and lone pairs.

The VMoPro software integrated with MoPro can compute the static electron density, its gradient norm, as well as the laplacian and the electrostatic potential functions. Topological analyses of these scalar functions can help us to better understand the nature of bonding interactions, in-particular the σ-hole interactions that are formed by facing charge concentrated and charge depleted regions.

2.1.1.4 The topology of electron density

In accordance with the QTAIM concept developed by R. F. Bader, the evaluation of the electron density $\rho(\mathbf{r})$ and its topological properties can accurately characterize the concepts of atoms, molecules and then chemical bonds. In the framework of QTAIM, molecular systems are partitioned in regions of the real space *via* the gradient vector field of electron density $\nabla\rho(\mathbf{r})$, known as *atomic basins* Ω. These atomic basins are limited by *zero-flux surfaces* ($\boldsymbol{S}$) in the gradient vector field of the electron density, considered to be the quantum mechanical boundaries of the atoms. They are defined by the points $\boldsymbol{r}$ holding the condition **Equation 2.19**:

$$\nabla\rho(\mathbf{r}).\boldsymbol{n}(\mathbf{r})=\mathbf{0} \quad \forall\ \mathbf{r} \in \boldsymbol{S} \qquad 2.19$$

where $\boldsymbol{n}$ is a unit vector perpendicular to $\boldsymbol{S}$ at any point $\mathbf{r}$ belonging to the surface.

The ending and the starting points of the gradient paths correspond to particular points of the real space where the gradient of electron density vanishes. These points are called *critical points* (CPs) of electron density defined by **Equation 2.20**.

$$\nabla\rho(\mathbf{r}) = \mathbf{i}\frac{\partial\rho(\mathbf{r})}{\partial x} + \mathbf{j}\frac{\partial\rho(\mathbf{r})}{\partial y} + \mathbf{k}\frac{\partial\rho(\mathbf{r})}{\partial z} = \mathbf{0} \qquad 2.20$$

The second derivative of $\rho(\mathbf{r})$ function allow us to study the behavior of the electron density distribution at these CPs, characterizing whether it is a maximum, a minimum or a saddle point. A 3x3 Hessian matrix consisting of all possible partial second derivatives of $\rho(\mathbf{r})$ with respect to the cartesian co-ordinates (x,y,z) is utilized for this purpose. Since the Hessian matrix is real and symmetrical, it can be diagonalized. In such a way, three principal axes and the corresponding curvatures of $\rho(\mathbf{r})$ at a CP are obtained as the eigen vectors and the eigen values (λ_1,λ_2,λ_3) of the diagonalized Hessian matrix (**Equation 2.21**).

$$H = \begin{bmatrix} \lambda_1 & 0 & 0 \\ 0 & \lambda_2 & 0 \\ 0 & 0 & \lambda_3 \end{bmatrix} \qquad 2.21$$

$$\lambda_1 = \frac{\partial^2\rho(\mathbf{r})}{\partial x^2}, \lambda_2 = \frac{\partial^2\rho(\mathbf{r})}{\partial y^2}, \lambda_3 = \frac{\partial^2\rho(\mathbf{r})}{\partial z^2}$$

The Laplacian of electron density $\nabla^2\rho(\mathbf{r})$ function is defined as the sum of the diagonal elements (trace) of the Hessian matrix (**Equation 2.22**):

$$\nabla^2\rho(\mathbf{r}) = \frac{\partial^2\rho(\mathbf{r})}{\partial x^2} + \frac{\partial^2\rho(\mathbf{r})}{\partial y^2} + \frac{\partial^2\rho(\mathbf{r})}{\partial z^2} = \lambda_1 + \lambda_2 + \lambda_3 \qquad 2.22$$

At any position $\mathbf{r}$, $\nabla^2\rho(\mathbf{r})$ determines if $\rho(\mathbf{r})$ is locally concentrated ($\nabla^2\rho(\mathbf{r}) < 0$) or locally depleted ($\nabla^2\rho(\mathbf{r}) > 0$). Its topological analysis (similar in method to that of $\rho(\mathbf{r})$ hence described) will be also explored in this thesis.

The classification of CPs of $\rho(\mathbf{r})$ can be done based on their rank (ω) and signature (σ). The rank (ω) is defined as the number of non-zero curvatures of $\rho(\mathbf{r})$ at the CP, which is equal to 3 for the charge distribution of a stable system. The signature (σ) is defined as the algebraic sum

of the signs of the curvatures at CP. Each CP is thus identified by the pair of numbers (ω, σ). The four possible types of CPs of rank three are:

(1) (3,-3) Nuclear Critical Point (NCP): They are local maxima where all the curvatures (λ_1,λ_2,λ_3) of $\rho(\mathbf{r})$ are negative. These CPs denote the position of a nucleus, and therefore of an atom in most cases. Sometimes non-nuclear attractors of $\rho(\mathbf{r})$ also appear as (3,-3) CPs (Platts et at., 2011), but they will not be treated in this work. The gradient path linking two nuclei is called a *bond path* (BP) and it corresponds to the line where $\rho(\mathbf{r})$ is maximum with respect to any other line connecting between them.

(2) (3,-1) Bond Critical Point (BCP): They are saddle points of $\rho(\mathbf{r})$ where two curvatures (λ_1,λ_2) are negative and one (λ_3) is positive. This means that $\rho(\mathbf{r})$ is a local maximum along two main directions and a local minimum along the third one. These CPs are found at the intersection between a bond path and an interatomic surface (zero flux surface).

(3) (3,+1) Ring Critical Point (RCP): They are also saddle points of $\rho(\mathbf{r})$ where one curvature (λ_1) is negative and two others (λ_2, λ_3) are positive. This means that $\rho(\mathbf{r})$ is a local minimum along two main directions and local maximum along the third one. These CPs are found at the center of topological rings formed by bond paths involving N≥3 atoms (these atoms need not be necessarily covalently bonded).

(4) (3,+3) Cage Critical Point (CCP): They are local minima of $\rho(\mathbf{r})$ where all the curvatures (λ_1,λ_2,λ_3) are positive. These CPs are found in a topological cage formed by bond paths involving at least 4 bonded atoms.

Identification and analysis of these CPs are very vital while studying nucleophilic···electrophilic interactions, that occur between the regions of charge concentration and charge depletion which facing each other.

2.1.1.4.1 Bonding properties

Within the framework of QTAIM, a bonding interaction between two atoms is identified by the presence of a BP and a concomitant (3,-1) BCP. As previously pointed out, a bond path is defined as the gradient path of maximum electron density that connects two nuclei and it crosses the zero-flux surfaces of atoms, whereas a BCP is placed at the intersection between this zero-flux surface and the BP. The length of the bond path can be longer than the internuclear distance. In some systems like the epoxy group, the BP can deviate significantly from the internuclear directions.

The analysis of $\rho(\mathbf{r})$ distribution at BCP open up the possibility to characterize any bonding interaction based on its local topological and energetic properties. The local topological properties of $\rho(\mathbf{r})$ at BCP include the electron density ρ_{BCP}, the magnitudes of the curvatures of the electron density ($\lambda_1, \lambda_2 < 0, \lambda_3 > 0$) and the laplacian of electron density $\nabla^2\rho(\mathbf{r})_{BCP}$, whereas the local energetic properties at BCP include the kinetic $G_{BCP}(\mathbf{r})$, potential $V_{BCP}(\mathbf{r})$ and total $H_{BCP}(\mathbf{r})$ [$H_{BCP}(\mathbf{r}) = G_{BCP}(\mathbf{r}) + V_{BCP}(\mathbf{r})$] energy densities (hereafter, the subscript BCP is omitted for clarity).

The strength of a bond (which parallels the number of shared pairs of electrons, also known as *bond order*) is characterized by the magnitude of charge density at a CP. The larger the ρ value, the stronger the interaction between the atoms. On the other hand, as previously stated, the principal significance of $\nabla^2\rho(\mathbf{r})$ is its sign which reveal whether the charge is concentrated or depleted. In such a way, $\nabla^2\rho(\mathbf{r}) < \mathbf{0}$ corresponds to a *shared-shell* (SS) interaction between two atoms, meaning that charge is concentrated in the interatomic region and the interaction is covalent in nature (negative curvature dominates, $|\lambda_1+\lambda_2|/\lambda_3 > 1$). On the other hand, $\nabla^2\rho(\mathbf{r}) > \mathbf{0}$ corresponds to a *closed-shell* (CS) interaction between the two atoms, meaning the charge is depleted in the interatomic region where two atoms are connected weakly bonded (positive curvature dominates, $|\lambda_1+\lambda_2|/\lambda_3 < 1$). This last feature is typical for an intra- and intermolecular non-covalent interaction.

The local concentration or depletion of $\rho(\mathbf{r})$ in the interatomic space is also related with the features of total electron energy distribution $H(\mathbf{r})$. The local potential energy density $V(\mathbf{r})$ tries to accommodate electrons at **r** while the kinetic energy density $G(\mathbf{r})$ tries to deplete those electrons to minimize the repulsion between the accumulated charges. At the end, the balance between two energetic terms determine the concentration or depletion nature of the electron density at **r**. For a CS interaction, the G, V and H magnitudes can be estimated from ρ and $\nabla^2\rho$ values by applying the functional proposed by Abramov and the local form of virial theorem (**Equation 2.23 and 2.24**). Such a formalism has been used earlier to estimate hydrogen bonding interactions (Espinosa *et al.*, 1998; Espinosa *et al.*, 2001; Espinosa *et al.*, 2002).

$$G = \frac{3}{10}(3\pi^2)^{2/3}(\rho)^{5/3} + \frac{1}{6}\nabla^2\rho \qquad 2.23$$

$$V = \frac{1}{4}\nabla^2\rho - 2\mathrm{G} \qquad 2.24$$

where all magnitudes are calculated at CP and are in atomic units.

Since different valence shell can be involved in the bonding interaction between atoms of different types, it is not always straightforward to compare them by directly using ρ, $\nabla^2\rho$, V and G descriptors. To overcome this problem, one could normalize the quantities per charge density unit, such as $(|V|/\rho)/(G/\rho) = |V|/G$. This $|V|/G$ descriptor permits us to classify the interactions into three regions as follows:

I. $|V|/G < 1$ corresponds to *pure closed-shell* interactions. Here, the kinetic energy density G, which is responsible for the depletion of the electrons is larger than the potential energy density $|V|$, which is responsible for the accumulation of electrons.

II. $1 < |V|/G < 2$ points a situation where the accumulation of electrons due to $|V|$ is larger than the depletion of electrons due to G. However, in this region, the charge is still depleted, as denoted by $\nabla^2\rho > 0$. This is known as a *transition region*.

III. $|V|/G > 2$ corresponds to *pure shared-shell* interactions, where $|V|$ dominates over G in such a way that $\nabla^2\rho < 0$.

Likewise, H/ρ ($H/\rho = V/\rho + G/\rho$) is another parameter, known as *bond degree parameter*, that is normalized to charge density unit (Espinosa *et al.*, 2002). This parameter corresponds to the total energy per electron at BCP and it can give a direct measure of the covalence degree associated with a pairwise interaction. Accordingly, $H < 0$ ($V > G$), corresponds to covalence degree of an interaction. Thus, stronger the interaction more negative the value of H. Similarly, $H > 0$, ($V < G$) corresponds to the softness degree of a pairwise interaction. Here, weaker the interaction more positive is the value of H.

Figure 2.3 shows an example of the calculated values of the function $\nabla^2\rho(\mathbf{r})$ for an H···F interaction as a function of internuclear distance $d_{\mathrm{H}\cdots\mathrm{F}}$ (Espinosa *et al.*, 2002). This study also shows that the nature of the interaction can be associated to three characteristic regions, namely I, II, and II as discussed before. The border between region II (transit closed-shell region) and region III (shared-shell region) is defined by $|V| = 2G$ (or $\nabla^2\rho = 0$), whereas between region II and region I (pure closed-shell region) is defined by $|V| = G$.

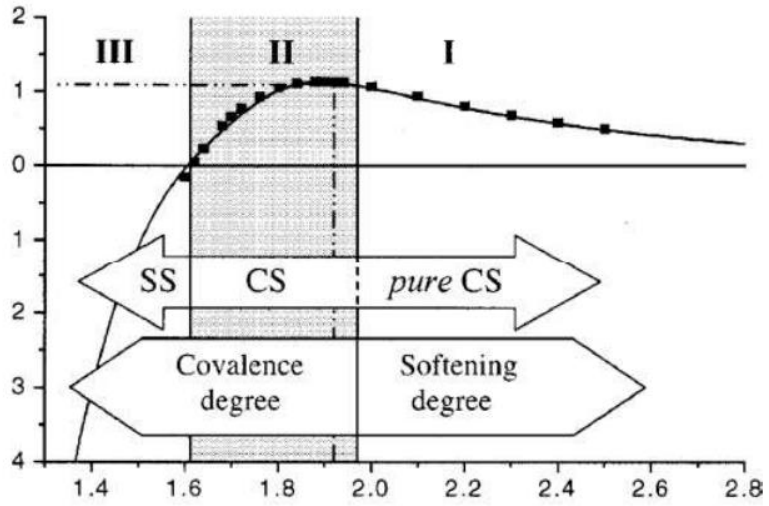

Figure 2.3 $\nabla^2\rho$ **vs** d**(H…F)**

Another important parameter that gives information about the covalent bonding characteristics between two atoms is the *delocalization index* (DI) at the BCP (**Equation 2.25**) (Outeiral *et al.*, 2018). This parameter gives a measure of the number of electron pairs that are being shared between two atoms and is defined as:

$$DI = \delta(A,B) = 2\int_{\Omega_A}\int_{\Omega_B}\rho_{xc}(\boldsymbol{r}_1,\boldsymbol{r}_2)\,d\boldsymbol{r}_1 d\boldsymbol{r}_2 \qquad 2.25$$

where Ω_A, Ω_B are respectively the atomic basins of atom A and B, and $\rho_{xc}(\mathbf{r}_1, \mathbf{r}_2)$ is the probability density of finding a pair of electrons at the volume elements d$\mathbf{r}$1 and d$\mathbf{r}$2.

Figure 2.4 shows an example of delocalization index values associated to various bond in a benzyl selenocyanate molecule. The triple (C≡N) bond corresponds to a larger value of 2.37, whereas the single bonds Se-C(sp), Se-C(sp^3), C(sp^3)-C(sp^2) gives values 1.19, 0.97 and 1.03, respectively. At the same time, the delocalized C=C bonds in the benzene ring shows values in the range 1.33-1.38.

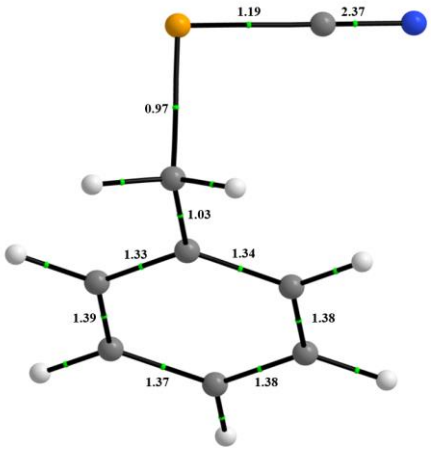

Figure 2.4 The molecular structure and delocalization index (DI) associated to various covalent bonds in benzyl selenocyanate.

2.1.1.4.2 Topological analysis of laplacian of electron density

The Laplacian of $\rho(\mathbf{r})$ function indicates the regions of the space where $\rho(\mathbf{r})$ is locally concentrated ($\nabla^2\rho < 0$) or depleted ($\nabla^2\rho > 0$). Sometimes the $L(\mathbf{r}) = -\nabla^2\rho(\mathbf{r})$ function is used instead of $\nabla^2\rho(\mathbf{r})$ to point charge concentration (CC) regions with positive values ($L > 0$) and charge depletion (CD) regions with negative ones ($L < 0$). In this thesis, $L(\mathbf{r})$ terminology will be followed. This $L(\mathbf{r})$ function fluctuates between positive and negative values quite often in space. In atomic regions, it permits to identify the atomic fine shell structure. According to the QTAIM methodology, $\nabla^2\rho(\mathbf{r}) = 0$ surfaces in the outer valence shell of atoms are defined as the *reactivity surfaces* of a molecule. From the reactivity surfaces one could point possible sites for nucleophilic attack, which is a very important information in many research fields like synthetic organic chemistry, solid-state chemistry, etc. (Shukla *et al.*, 2020). From the analysis of $L(\mathbf{r})$ in the outer valence shell of atoms (mostly responsible for the bonding interactions), *valence shell charge concentration* (VSCC) and *valence shell charge depletion* (VSCD) regions can be identified. The topological analysis of $L(\mathbf{r})$ can also be performed on those VSCC/VSCD regions in order to identify the critical points associated to the $L(\mathbf{r})$ function, known as *laplacian critical points* (LCPs).

Similar to the CPs of $\rho(\mathbf{r})$, LCPs are also classified based on their rank (ω) and signature (σ). In the VSCC of an atom, three types of CPs can appear: local maximum (3,-3) and saddle points (3,-1) and (3,+1), whereas in VSCD regions all possible types of CPs [including local minimum (3, +3) CPs] can be found.

Local electrostatic nucleophilic···electrophilic interactions can be analyzed in terms of CC···CD interactions, where the CC corresponds to the LCP in the charge concentration region (associated to the nucleophilic site) and the CD corresponds to the LCP in the charge depletion region (associated to the electrophilic site). It has been shown in the literature that a good reasoning of HaB and ChB interactions can be derived using the concepts of LCPs, in addition to the traditional plots of the MESP (Brezgunova *et al.*, 2012; Brezgunova *et al.*, 2013). Following this, the nucleophilic···electrophilic power of a CC···CD interactions can be quantified using a $\Delta L/\rho$ [$\Delta L/\rho = (L/\rho)_{CC}$-$(L/\rho)_{CD}$] descriptor, where the normalized magnitudes of $(L/\rho)_{CC}$ and $(L/\rho)_{CD}$ correspond to the nucleophilic and electrophilic power per charge density unit of CC and CD sites (of the LCP). Accordingly, the larger are the positive $(L/\rho)_{CC}$ and the negative $(L/\rho)_{CD}$ magnitudes, the larger is the $\Delta L/\rho$ value and therefore more significant is the local nucleophilic···electrophilic interaction. Very recently, a modified form of this electrostatic descriptor as $(\Delta L/\rho)/d^2_{CC\cdots CD}$ was proposed in order to consider also the distance between CC and CD sites (Shukla *et al.*, 2020). Here, assuming a geometric distribution of a point-source radiation into the 3D space for CC and CD electrostatic sites, a dependence with the distance $\propto 1/(d_{CC\cdots CD})^2$ has been therefore considered. As like the previous descriptor, the larger is the positive value of $(\Delta L/\rho)/d^2_{CC\cdots CD}$ the stronger is the interaction between CC and CD sites. Thanks to the normalization per charge density unit in the descriptor, which allow to compare interactions involving different kinds of atoms at the same time.

Figure 2.5 shows an example where Se···O and Se···Se ChB interactions are observed in the crystal structure of 3H-1,2-benzodiseleno-3-one and are characterized in terms of the $(\Delta L/\rho)/d^2_{CC\cdots CD}$ electrostatic descriptor (Shukla *et al.*, 2020). Here, the Se-atom acts at the same time as a ChB donor with an O-atom and as a ChB acceptor with a Se-atom of the same molecule. As explained in the introduction chapter, a sp^3 hybridized Se atom (for the moment considering only one Se atom of the molecule, which is indicated as Se3A) possesses two σ-hole regions each along the extension of a covalent bond. These σ-hole regions are associated with charge depletion LCPs, which are marked in the **Figure 2.5** as CP4a (resulting from the coalescence of the σ-hole regions of Se2A and Se3A along the C-Se bonding axes) and CP3d. On the other hand, the lone pair of O-atom, which acts as electron donor, is associated to a charge concentration region that results in a LCP denoted by CC1a. Accordingly, the CC···CD interactions between the LCPs are shown as black dashed lines with respective $(\Delta L/\rho)/d^2_{CC\cdots CD}$ values. Here, based on the $(\Delta L/\rho)/(d_{CC\cdots CD})^2$ magnitudes, the CP4a···CC1a interaction is

significantly stronger than the CP3d···CC1a interaction, thus have more importance in driving the relative orientation of atoms in that ChB interaction.

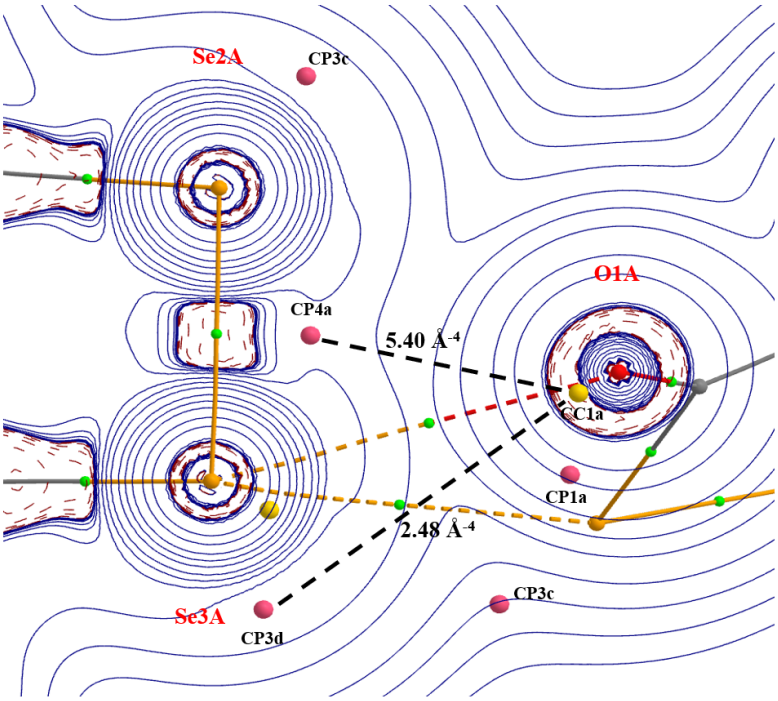

Figure 2.5 Intermolecular bond critical points (BCPs, light green spheres), intermolecular bond paths (dashed lines), and charge concentration (CC) and charge depletion (CD) sites (yellow/pink spheres) involved in the Se···O and Se···Se ChB interactions present in a dimer of the crystal structure of 3H-1,2-benzodiseleno-3-one. CC···CD interactions are denoted by black dashed lines and values corresponding to the electrostatic descriptor are given.

2.1.1.5 Molecular electrostatic potential surfaces

The evaluation of the molecular electrostatic potential (MESP) surfaces is another quantitative tool that can give key insights into charge concentration (CC) and charge depletion (CD) regions associated to a molecule, and therefore to the nucleophilic···electrophilic interactions. We have seen in the previous sections that deformation density maps, QTAIM analysis and $L(\mathbf{r}) = 0$ surfaces can guide us to know about reactivity sites and bonding interactions of a molecule. A careful investigation of MESP surfaces can enrich these information.

In general, MESP surfaces are 3D maps plotted on molecular surfaces, usually of constant electron density known as iso-surfaces of electron density. Mathematically, for a given molecule, the electrostatic potential function $V(\boldsymbol{r})$ at any point $\boldsymbol{r}$ produced by electrons and nuclei is given by **Equation 2.26**:

$$V(\boldsymbol{r}) = \sum_A \frac{Z_A}{|\boldsymbol{r}_A - \boldsymbol{r}|} - \int \frac{\rho(\boldsymbol{r}_e)}{|\boldsymbol{r}_e - \boldsymbol{r}|} \mathrm{d}\boldsymbol{r}_e \qquad 2.26$$

where Z_A is the charge of the nuclei located at $\boldsymbol{r}_A$ and $\rho(\boldsymbol{r}_e)$ is the electronic density of the molecule at $\boldsymbol{r}_e$. A positive $V(\boldsymbol{r})$ indicates the dominance of the first term (nuclei contribution), while a negative one indicates the dominance of the second term (electronic contributions). In general, the iso-surfaces of electron density are considered at 0.001 or 0.002 a.u. (i.e., e/bohr^3) level, because in this limit it is possible to clearly observe the distinction between positive and negative regions that form non-covalent interactions. Accordingly, the MESP function plotted on the molecular surface of constant electron density and the extremum values of the function ($V_{s,\,max}$ or $V_{s,\,min}$) calculated at this surface can give us quantitative measure of electrophilic and nucleophilic power of different sites of a molecule. In addition, a cumulative electrostatic power of a nucleophilic···electrophilic interaction can also be estimated using the individual $V_{s,\,max}$ and $V_{s,\,min}$ values found in the respective regions. In this thesis, MESP surfaces are generated using the GaussView 5.0.9 software (Dennington *et al.*, 2016) and the corresponding extremum points are characterized using the MultiWfn software (version 2.1.2; Lu and Chen, 2012).

Since σ-holes are observed on electron deficient regions, they are generally associated to positive ESP values. Indeed, it has to be kept in mind that sometimes these σ-holes do not exhibit a positive ESP but yet form weaker σ-hole interactions (Varadwaj *et al.*, 2020; Scheiner *et al.*, 2021). Even though this technique offers vital information about nucleophilic···electrophilic interactions, there are some disadvantages involved: (i) MESP function is calculated on an isolated molecule in gas phase, thus do not account the polarization on the electron density distribution that can brought by the presence of neighbouring molecules (ii) ESP function is a long-range function, therefore a $V_{s,\,max}$ or $V_{s,\,min}$ point identified close to an atom will also have contribution from the neighbouring atoms and this questions the quantitative measure of the electrophilic power of an interaction estimated through individual $V_{s,\,max}$ and $V_{s,\,min}$ values.

Figure 2.6 shows an example of MESP function mapped on ρ = 0.002 a.u. molecular iso-electron density surface of 3H-1,2-benzodiseleno-3-one molecule (Shukla *et al.*, 2020). Since the Se-atoms are sp^3 hybridized, two σ-hole regions are expected to be observed for each Se atom along the extension of respective C-Se and Se-Se covalent bonds. They are indicated as R1A, R1B and R2 (in latter case, the σ-holes of two Se atoms are merged into one). The MESP surfaces and $V_{s,\,max}$ values of the corresponding pointed out regions are given in **Figure 2.6b**. The R1B region exhibit a more depleted electron density and therefore shows as the most significant σ-hole among them with largest $V_{s,\,max}$. Relatively, region R1A exhibit the weaker

σ-hole with lowest $V_{s,\,max}$. In this way, MESP can act as a quantitative tool that permit to evaluate the electrophilic power of multiple σ-hole regions present in a molecule, and up to an extent this guides the prediction of possible intermolecular interactions with nucleophilic sites of molecular partners.

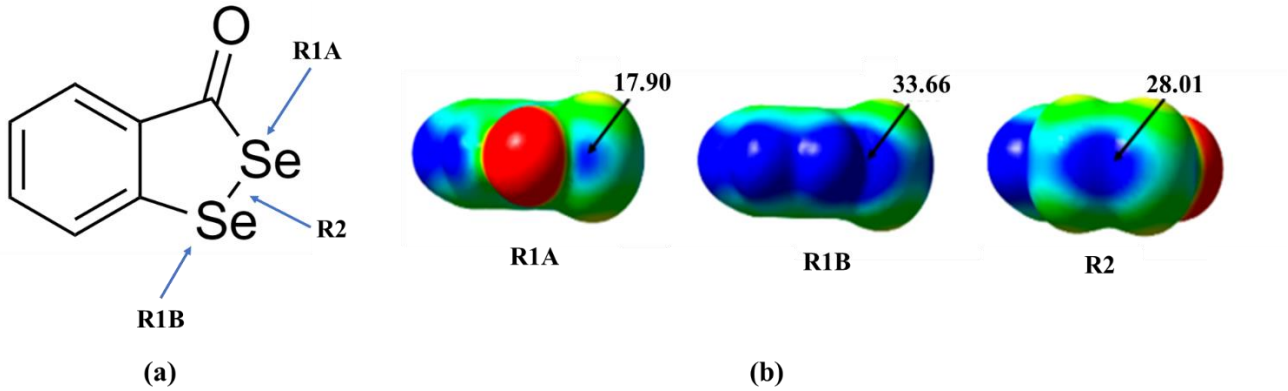

Figure 2.6 (a) The expected σ-hole regions around Se-atoms are indicated with blue arrows in a 3H-1,2-benzodiseleno-3-one molecule (b) MESP function mapped on the ρ = 0.002 a.u. molecular iso-electron density surface with corresponding $V_{s,\,max}$ values indicated in kcal/mol.

2.2 Additional tools for the analysis of intermolecular interactions

In the previous sections we have discussed the usefulness of the QTAIM approach and the MESP tool on the analysis of the intermolecular interactions. The characteristics of such intermolecular interactions can be further analyzed using some other additional tools, helping us to enhance the richness of the information on the nature of chemical bonds. The origin and the mathematical concepts of the tools given below are beyond the scope of this thesis and are not discussed in fine details, but the concepts that are utilized in the subsequent sections to characterize intermolecular interactions are discussed briefly.

2.2.1 Energy calculation

Since the main goal of this thesis is to study the characteristics of intermolecular interactions in molecular crystals, it will be interesting to investigate the binding energies of molecular dimers (linked by intermolecular interactions) at the crystalline geometry. In the course of this thesis, the energy calculation in molecular dimers are carried out using two methods as discussed below:

(1) Binding energy using Gaussian: The binding energy between two molecules A and B can be estimated by using the Gaussian09 software. Molecular dimers can be extracted from the experimental geometry, obtained after the structure determination from SCXRD experiments.

A first co-ordination sphere, which is considered as a molecular shell formed around the central molecule in a radius of 3.80 Å, can be generated and the interaction of each molecule (obtained from symmetry operations) with respect to the reference molecule can be analyzed. Among them, molecular dimers can be chosen to calculate the binding energies as described hereafter:

(i) A single point energy (SPE) calculation of the molecular pair A-B can be carried out with Gaussian by using a desired level of theory, dispersion correction and basis set [for example, B3LYP-D3/6-311++G(3df,3pd)] to obtain the energy E(A-B).

(ii) In the same way, a SPE calculation is also performed on each monomer [E(A) for molecule A and E(B) for molecule B], using the same experimental geometry and level of theory.

(iii) Then, the binding energy B.E. can be calculated as (**Equation 2.27**):

$$\mathrm{B.E.} = \mathrm{E(A)} + \mathrm{E(B)} - \mathrm{E(A-B)} \qquad 2.27$$

A negative binding energy indicates the stabilization on formation of molecular dimers, whereas a positive binding energy indicates their destabilization.

It is important to note that, in this study, a SPE calculation at the crystalline geometry is preferred over full optimization of the molecules (unless there is a specific reason). This is because in crystals molecular pairs are formed upon the influence of the crystalline environment coming from the surrounding molecules, and they do not necessarily correspond with their global minima of energy.

(2) Binding energy using CrystalExplorer: The intermolecular interaction energies in molecular dimers can also be calculated using the CrystalExplorer software (Turner *et al.*, 2017). Likewise, the previous section, a molecular cluster of 3.80 Å in radius around the central molecule can be generated by the GUI of CrystalExplorer. The molecular wavefunctions can be calculated using either TONTO option available in the software or using Gaussian software installed independently. Further, Crystal Explorer will calculate the interaction energy for each molecular dimer among all the crystallographically independent molecules. The total interaction energy between molecules is commonly expressed in terms of four components (**Equation 2.28**):

$$E_{tot} = k_{ele}E_{ele} + k_{pol}E_{pol} + k_{dis}E_{dis} + k_{rep}E_{rep} \qquad 2.28$$

where E_{ele}, E_{pol}, E_{dis} and E_{rep} corresponds to electrostatic, polarization, dispersion and exchange-repulsion contributions and k_{ele}, k_{pol}, k_{dis} and k_{rep} are the respective scaling factors of the energy components, which are dependent on the model used. In the end, by comparing the total interaction energy of individual molecular dimers, a conclusion can be made on their extent and stabilization, that play a role in the constitution of the molecular organization in solid-state.

2.2.2 Hirshfeld surface analysis

The Hirshfeld surfaces are another important tool that is available for the analysis of intermolecular interactions (Spackman and McKinnon, 2002). In this case, a full molecular approach is used rather than considering interactions individually. These surfaces can also be generated by using the CrystalExplorer software while CIF file obtained at the end of crystal structural determination used as the input. Conceptually, Hirshfeld surfaces are defined by the 0.5 iso-surface of the weight function $w(\mathbf{r})$ (**Equation 2.29**):

$$w(\mathbf{r}) = \frac{\rho_{\text{promolecule}}(\mathbf{r})}{\rho_{\text{procrystal}}(\mathbf{r})} = \frac{\sum_{A \epsilon \text{molecule}} \rho_{\text{A}}(\mathbf{r})}{\sum_{A \epsilon \text{crystal}} \rho_{\text{A}}(\mathbf{r})} \qquad 2.29$$

where $\rho_{\text{promolecule}}$ is the spherical atoms densities of the molecule (promolecule) and $\rho_{\text{procrystal}}$ is the spherical atoms densities of the crystal (procrystal).

The electron density of the promolecule dominates the procrystal inside the Hirshfeld surface. Further, two types of distances d_{i} and d_{e}, respectively the distance to the nearest neighbor inside and outside of the Hirshfeld surface, are considered. These quantities, along with the identity of atoms, are used to explore the proximity of intermolecular contacts in a molecular crystal. To overcome the issue related with the different sizes of the atoms involved in the intermolecular contacts, a normalized contact distance d_{norm} is often used (**Equation 2.30**):

$$d_{\text{norm}} = \frac{d_{\text{i}} - r_{\text{i}}^{\text{vdW}}}{r_{\text{i}}^{\text{vdW}}} + \frac{d_{\text{e}} - r_{\text{e}}^{\text{vdW}}}{r_{\text{e}}^{\text{vdW}}} \qquad 2.30$$

where $r_{\text{i}}^{\text{vdW}}$ and $r_{\text{e}}^{\text{vdW}}$ are the van der Waals radii of the internal and the external atoms to the Hirshfeld surface. A contact shorter than the sum of van der Waals radii will result in a negative d_{norm} value, whereas a contact longer than the sum of van der Waals will result in a positive d_{norm} value. These contacts are displayed with a red-white-blue coloring scheme on the d_{norm}

surface. Thus, a red color points shorter contacts, white points contacts around the van der Waals separation, and blue points longer contacts.

Figure 2.7 show the coloring scheme on the d_{norm} surface of a benzyl selenocyanate molecule. The short contact corresponding to a Se···N ChB interaction is indicated with a black arrow and the neighboring molecule constituting this interaction is also shown.

The distances d_{i} and d_{e} can also be used to generate the two-dimensional summary of the intermolecular interactions, which are the so-called 2D fingerprint plots. From these plots one can quantify the percentage of a pairwise atom···atom interaction, which represents relative area of the Hirshfeld surface corresponding to that particular interaction. For each point at the Hirshfeld surface both d_{i} and d_{e} values can be evaluated. Likewise, each point on the 2D fingerprint plot corresponds to a unique $(d_{\mathrm{i}},d_{\mathrm{e}})$ pair, and the color of each point corresponds to the relative area of the surface with that particular $(d_{\mathrm{i}}, d_{\mathrm{e}})$ pair. The points on the 2D fingerprint plot with no contribution to the surface remain uncolored, while a smaller contribution to the surface are colored blue and larger contributions are colored from green to red. **Figure 2.7b** shows the 2D fingerprint plot of the same benzyl selenocyanate molecule, where different colors on the points with respect to the contribution to the Hirshfeld surface are clearly visible.

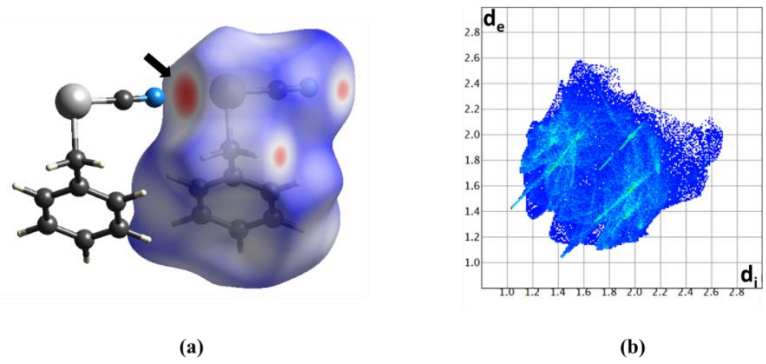

Figure 2.7 (a) d_{norm} surface of the benzyl selenocyanate molecule generated from CrystalExplorer. The Se···N short contact region is indicated with a black arrow along with the generated neighbouring molecule corresponding to the intermolecular interaction (b) 2D-fingerprint plot of the benzyl selenocyanate molecule with characteristic colours.

2.2.2.1 Enrichment ratio

The usefulness of Hirshfeld surfaces and concomitant 2D fingerprint plots in the analysis of intermolecular interactions are discussed in the previous section. Along with these information, an additional quantity called *enrichment ratio* is often used in literature to investigate the preferential atom···atom interaction in the crystal packing (Jelsch *et al.*, 2014). This quantity

also enables us to know which interactions are most significant in constructing the crystal packing of a molecule, through a ranking based enrich ratio values calculated for possible atom···atom interactions. MoProViewer software incorporated in MoPro suite is used for the calculation of this quantity (Jelsch *et al.*, 2014).

Enrichment ratio (ER) for a pair of atoms (X,Y) is defined as the ratio between the proportion of actual contacts seen in the Hirshfeld surface (C_{XY}) to the theoretically calculated proportion of random contacts (R_{XY}) if all types of contacts had equal probability to occur (**Equation 2.31**).

$$\mathrm{ER_{XY}} = \frac{C_{XY}}{R_{XY}} \qquad 2.31$$

An ER value greater than 1 refers to a pair of atoms which have high propensity to form contact in the crystal while an ER value less than 1 refers to the ones which tend to avoid contact between each other.

2.2.3 Non-covalent interaction plots

The non-covalent interaction (NCI) plots allows one to simultaneously analyze and visualize different types of non-covalent interactions as real-space 3D surfaces and 2D plots based on the electron density distribution $\rho(\mathbf{r})$ and its derived functions (Johnson *et al.*, 2010; Contreras-García *et al.*, 2011). One of the most important functions that used in this method is the reduced density gradient S(ρ) given by **Equation 2.32**. The reduced density gradient (RDG) is a fundamental dimensionless quantity that is used in DFT to describe the deviation of the electron density from a homogeneous distribution.

$$s(\rho) = \frac{1}{2(3\pi^2)^{1/3}} \frac{|\nabla \rho|}{\rho^{4/3}} \qquad 2.32$$

The influence of bonding interactions can be visualized by plotting S(ρ) as a function of ρ. The presence of an intra- or intermolecular interaction results the appearance of density critical points between them, where a significant change in S(ρ) is observed. Sudden drop (troughs) in the magnitude of reduced density gradient is a characteristic feature of these density critical points, where S(ρ) try to approaches to zero (**Figure 2.8b**). The regions corresponding to this feature in real 3D space can be visualized as the non-covalent interaction regions in a molecular complex.

As in case of QTAIM analysis, the value of ρ within these troughs points the interaction strength. Therefore, larger the value of ρ stronger is the interaction. However, both attractive and repulsive interactions appear in the same region of ρ or S(ρ). To solve this problem, $\nabla^2\rho$ magnitudes are characterized along the main three axes of variation. As mentioned previously, the analysis of $\nabla^2\rho$ indicates whether the charge is concentrated ($\nabla^2\rho < 0$) or depleted ($\nabla^2\rho > 0$) at a given point in space. Since there is a large contribution from nuclei, one cannot use in a straightforward way the value of $\nabla^2\rho$. Thus, the contributions to the laplacian along the three main axes of its maximal variation are analyzed. These are the eigen values (λ_i) of the Hessian-matrix, such that $\nabla^2\rho = \lambda_1 + \lambda_2 + \lambda_3$ (where $\lambda_1 < \lambda_2 < \lambda_3$). The value of λ_3 vary along the internuclear direction, where λ_1 and λ_2 are the variation of the density in the plane normal to λ_3. The idea of considering these eigen values is that the sign of λ_2 can be either positive or negative, depending on the type of interaction. Attractive bonding interactions leads to the accumulation of the electron density perpendicular to the bonding direction and causes $\lambda_2 < 0$, whereas a non-bonded interaction such as steric repulsion leads to the depletion of the electron density perpendicular to the bonding direction and causes $\lambda_2 > 0$. The van der Waals interactions are identified by $\lambda_2 \sim 0$. Thus, plotting S(ρ) against sign(λ_2)ρ enables one to identify attractive non-covalent interactions and repulsive non-bonded interactions between atoms. Such 2D plots can be generated using the Multiwfn software (version 2.1.2; Lu and Chen, 2012), where the wavefunction obtained for isolated molecule(s) with the Gaussian software can be used as an input to calculate the electron density. **Figure 2.8b** shows such a 2D plot for a dimer composed by the binary adduct formed between N-iodosaccharin (NISac) and pyridine (Py) (**Figure 2.8a**). The low-density and low S(ρ) magnitudes associated to the C-H···O HB interaction is observed in the negative region (shown with a light green circle), whereas a similar trend corresponding to the steric repulsion between the aromatic rings is observed in the positive region (shown with a dark green circle). The 3D surfaces (**Figure 2.8c**) corresponds to the sign (λ_2)ρ descriptor can be also generated with the Multiwfn software in conjunction with the VMD tool (version 1.9.3) (Humphrey et al., 1996), where non-covalent interactions are identified with the same color code.

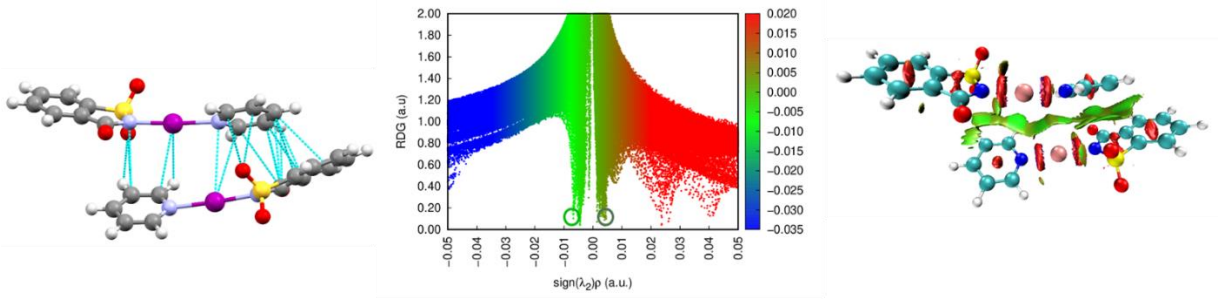

(a) (b) (c)

Figure 2.8 (a) Dimer formed between the binary adduct composed of NISac and Py molecules (b) 2D plot of RDG vs sign(λ_2)ρ with the colour code shown on the right: C-H···O HB interaction and steric repulsion between aromatic moieties are indicated with light and dark green circles, respectively (c) 3D surfaces generated for S(ρ) = 0.7using the same colour code.

2.3 Crystallization – tools and the techniques

Finding a suitable crystallization method to obtain good quality crystals of an investigated compound is an important aspect of this thesis. Various crystallization techniques and tools were utilized for this purpose, in aim to grow good quality single-crystals adequate to perform SCXRD experiments. Even though all the crystallization methods undertaken in this work do not give a fruitful outcome (on the basis of the quality of SCXRD data collected afterwards), all the techniques used are described below. Later, on each chapter, the optimized method to obtain the best crystals for that particular compound will be discussed along with the best data collection strategy undertaken. Thus, this current portion will give a global point of view rather than sample specific cases.

2.3.1.1 Slow solvent evaporation

Slow solvent evaporation is one of the simplest and widely used techniques for growing good quality single-crystals with good success rate in most of the cases. A limitation of this technique concerns however the stability of the compound at room conditions. The sole concept of this method is to prepare a solution by dissolving the compound (solute) in a suitable solvent (with a minimal amount of solvent as possible that can completely dissolve the compound). The choice of the solvent is purely dependent on the solubility of the sample and on most of the cases a rigorous trial and error is required. Solution prepared in such a way can be left behind in a container (a glass vial of 5-10 ml in this study) by covering on top with a parafilm or a sheet of aluminium foil. Perforations can be made on this cover, which will act as a kind of experimental variable that controls the rate of crystallization. The number of perforations made up to an extent also depends on the volatility of the solvent used. Even if we find the right

solvent, it is not always true that the compound will be completely soluble at room conditions. A gentle heating (below the boiling point of the solvent) and stirring is required in some cases for complete dissolution of the compound in the solvent, which can be done with help of a hot plate with magnetic bead inside the container. It is also advisable to filter the solution before keeping it for the crystallization process. This will help to avoid the presence of any impurity left behind, which may act as a nucleation center during crystallization and can affect the crystal quality. The duration of time required for the crystallization procedure is sample specific and is also dependent on the solvent used.

2.3.1.2 Vapor diffusion technique

In this method we have to use two different solvents, one of them being considered as an efficient solvent (solvent I) in which the compound dissolves well, whereas the second one (solvent II) acts as a less-efficient solvent having limited or no solubility of the compound within. This method works better if solvent II is more volatile than solvent I. In this procedure, a solution is prepared in prior with solvent I in a vial and is immersed in a beaker that contains solvent II. An extreme care should be taken not to mix up the saturated solution with solvent II. Thus, advisable to fill the beaker with solvent II in such a way that half of the vial is only immersed in solvent II. Afterwards, the beaker has to be completely closed from the top using a parafilm or an aluminium foil to avoid any solvent vapors going out. Since solvent II is more volatile than solvent I, the vapors of solvent II formed with time diffuse into the vial solution and forces the compound to crystallize due to its insolubility with solvent II. Generally, the duration taken for this crystallization process is a bit longer compared to that of slow solvent evaporation method.

2.3.1.3 Vacuum sublimation

A large number of compounds can be subjected to the process of sublimation to form good quality single-crystals, and this procedure is highly recommended as one efficient way to separate the impurities from a mother crystal (Truong *et al.*, 1995). There are different methods associated with this process, using either a static or a dynamic vacuum. The sublimation technique carried out during the course of this thesis is based on static vacuum and the sublimation set-up used here is developed in-house in our laboratory (**Figure 2.9a**). The mode of operation is described in steps hereafter:

(1) A glass tube (**Figure 2.9b**) open at one end and closed at the other end is first degreased and cleaned perfectly, then rinsed with ethanol solution and placed in an oven at 100°C.

(2) A small amount of compound (limited in mg) is placed in the closed part of the glass tube.

(3) The glass tube is then sealed under vacuum. The vacuum is applied using a pumping unit: a primary vacuum of $3x10^{-2}$ mbar is first applied followed by a secondary vacuum of $5x10^{-5}$ mbar using oil diffusion method (**Figure 2.9c**).

(4) The glass tube sealed under vacuum with the compound on one end is later placed inside a glass bi-temperature furnace (**Figure 2.9a**), also called the sublimation furnace. The latter is equipped with two temperature control knobs placed at both ends of the furnace to create a temperature gradient that facilitates the crystal growth. In such a way, temperature in the two knobs can be raised independently, keeping a temperature gradient in between up to the sublimation temperature of the material in one side. The compound that underwent the sublimation process at the high-temperature end will move to the relatively cooler side and will start its deposition on the glass surface (**Figure 2.9b**). It has been observed during the experiments that the rate of crystallization and the size of crystals formed can be regulated by playing with the temperature gradient, making the deposition procedure slower or faster.

Figure 2.9 (a) Sublimation furnace with the sublimation chamber and the temperature control knobs highlighted with blue arrows (b) glass tube used for the sublimation process, some crystals formed at the end of the process is highlighted with blue arrow (c) independent set-up that is used to generate vacuum inside the glass tube: the primary and secondary vacuum means are highlighted with blue arrows.

2.3.1.4 Crystallization in multi-well apparatus

This dedicated technique allows one to play with a wide-span of temperature range to control the dissolution of the compound and the subsequent crystallization process. The multi-well crystallization apparatus (**Figure 2.10**) used in this work is developed by the company *Anacrismat* (http://www.anacrismat.com/). It permits to reach a maximum temperature of

100°C and a minimum temperature of -10°C. This multi-well crystallization device is equipped with an inverted microscope set-up with two multi-well container blocks (**Figure 2.10b**), each containing 12 cells (alternatively called wells) acting as the support for crystallization. These wells are stored in a container box maintained at constant temperature, which is an experimental variable that can be varied by the user. Each container block can be brought to two different temperatures at a time with independent programs. The blocks are placed on a motorized XY table, above the inverted microscope fitted with a CCD camera. A software based on Labview allows one to monitor the process on a computer screen with a manual or automatic acquisition of images. The image acquisition can be sequential (programmed with a time interval), while the scanning of the wells and/or blocks can be carried out at a selected speed. This acquisition can also be directed to a specific well on choice of the user *via* the programme interface to record the crystal growth in real-time. Thus, this device makes it possible to observe and monitor sequentially the process of crystal growth taking place in different wells with the aid of just one CCD camera.

The first step in the crystallization procedure involves the complete dissolution of the sample in a small glass vial with a suitable solvent. Then the vial is closed with a screw cap on top. It has to be noted that the maximum amount of solvent that can be utilized in this particular vial is limited to 2ml, but it is advisable not to exceed 1.5 ml. This limits the amount of compound that can be crystallized in one go. Later, the vial is placed inside one of the wells in a block (**Figure 2.10b**) and the temperature of the well is raised to a value which is a few degrees below the boiling point of the solvent to ensure the complete dissolution of the compound. The rate of the temperature raise is adjusted to 5°C/min. Once the complete dissolution is made sure with a view via the CCD camera, the temperature is lowered slowly. In our case, the temperature lowering rate is 0.1°C/min. The appearance of crystal seeds is monitored via the recorded images. If multiple seeds (nuclei) are present, then the temperature is raised again to a few degrees and comes back. This procedure can be also repeated in multiple cycles and is mainly intended to dissolve all the nuclei centers except one. In such a way, once the temperature is lowered again, the solute molecules come and deposit on top of this nuclei to obtain a large unique single-crystal. The minimum temperature that one can apply in this crystallization process is determined by the user (up to a minimum of -10°c, specified by the equipment) and the vial can be maintained at this low temperature for few days to ensure complete crystallization.

Once a good quality single-crystal is obtained, the next goal is to carryout SCXRD experiments to collect good quality data that permitting to determine the crystal structure of the compounds, as well as their crystalline electron density distribution. The choice of wavelength, temperature, resolution limit and experimental set-up used for the diffraction experiments is dependent on the final goal of the study.

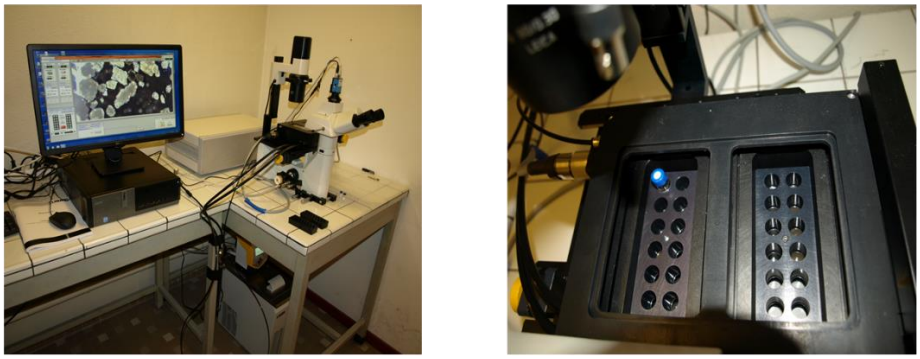

(a) (b)

Figure 2.10 (a) Multi-well crystallization device mounted on an inverted microscope (b) two independently controlled multi-well blocks (each containing 12 blocks), with a sample vial is placed on one of the wells.

2.4 Crystallography under high-pressure

One part of this thesis is dealing with a series of *high-pressure single crystal X-ray diffraction* (HP-SCXRD) experiments and their subsequent analysis, which are carried out to investigate the evolution of HaB interactions upon the modification of crystalline environment in molecular crystals. This includes data collection *via* compression-decompression cycle at various quasi-hydrostatic pressures that are applied to the single-crystals mounted inside a *Membrane Diamond Anvil Cell* (MDAC). Two donor-acceptor co-crystals are chosen for this, each composed by N-iodosaccharin and a derivative of pyridine [pyridine (Py) and 4-cyano pyridine (4CYP)] respectively acting as the HaB donor and acceptor. The rationale behind the choice of these compounds and mode of their co-crystallization will be detailed in the results section. For the time being, this particular section will discuss about the in-house developed experimental set-up that is used for the HP-SCXRD studies. This set-up is a combination of some already existing devices which are modified based on our requirements, along with some other in-house developed devices. This particular experimental set-up is currently installed in the Bruker D8 Venture diffractometer available on the PMD^{2}X platform of CRM2 laboratory.

2.4.1 Requirements

From a simple literature search one can find that carrying out HP-SCXRD study with a single-crystal are available for one to access and easy to follow. There are some common equipments (or devices) available for this technique, including MDAC, and there is no doubt that we could successfully do our need with the same. The HP-SCXRD experimental set-up used in our work, which is mainly based on commercially available supplies and devices that can be machined by a classical university workshop, was made to meet the following requirements:

(i) A high-pressure experimental set-up that can fit inside a diffractometer chamber to consider the whole system as one unit and to carry out all the required procedures within the space of the diffractometer chamber.

(ii) The maximal pressure that can be generated should reach at least 5 GPa. This is a good enough limit for investigations with organic crystals, as in our case.

(iii) The accessible proportion of reciprocal space should be maximal. This is something technical and is highly dependent on the configuration of the MDAC.

(iv) The set-up has to permit to study phase transformations, which are dependent on the pressure increase rate.

The details and technicalities of the above-mentioned points are discussed in several sections hereafter.

2.4.2 Experimental set-up: devices and alignments

As mentioned earlier, the experimental set-up is designed, developed and installed on a Bruker D8 Venture diffractometer. A large X-ray safety enclosure of this diffractometer gave us enough space to install the required devices without any restriction to routine data collection. Any possible collision should be avoided since the high-pressure experimental set-up is considered as an external part of the diffractometer and the run list in a routine data collection do not recognize the presence or the location of this set-up. Thus, this set-up can be permanently placed inside the diffractometer chamber and we do not need to uninstall and remove after every HP-SCXRD data collection. In addition, this diffractometer also allows the possibility to use two different type of X-ray radiation of wavelengths 0.71073 Å and 0.56086 Å, respectively from Mo and Ag anodes.

2.4.2.1 Membrane Diamond Anvil Cell (MDAC)

A Le Toullec-type Membrane Diamond Anvil Cell (MDAC) is used to generate high-pressure environment required for the desired experiments. This MDAC is of a smaller height and a larger opening angle of 100°, designed by BETSA company (**Figure 2.11a**). One of the important limitations with the HP-SCXRD experiment is the completeness of the data collected, especially for low-symmetry crystals where most of the proportion of the reciprocal space will be shadowed by the MDAC body (**Figure 2.11b**). The use of MDAC with a larger opening angle can however improve this experimental constraint upto an extent by increasing the maximal proportion of reciprocal space that can be accessed. Theoretically with this current opening angle of 100° one could access 54% of the reciprocal space upto a resolution of 0.9 Å using Mo wavelength (Merrill and Bassett, 1974). This MDAC is equipped with type IIa diamonds of conical shape and lower birefringence. They are good quality diamonds without any nitrogen impurities, and permit to adapt the system in the future to undertake IR (infrared) spectroscopic studies since type IIa diamond have lower absorption in the infrared region compared to the other types available for the same purpose. The diamonds have the following dimensions: 4 mm diameter, 1.4 mm thickness and a culet size of 600 μm, and they are embedded in Boehler-Almax tungsten carbide backing seat. It has to be noted that, depending on the required pressure and opening angle, several other configurations can also be achieved in our platform. In such cases, only the carbide seats with the diamonds have to be replaced and realigned. In the context of this thesis the same configuration is used throughout during all the HP-SCXRD experiments.

Once the MDAC is ready for use, the next step is the loading of the sample (a single-crystal), that is done in a *sample chamber* (**Figure 2.11c**). This MDAC sample chamber is a hole of 150-400 μm in diameter, drilled at the center of a stainless-steel gasket with an initial thickness of 200 μm, but pre-indented to a desired thickness (90-120 μm) using a BESTA micro-driller (**Figure 2.11d**). The process of pre-indentation is important in the context of our study because the gasket can deform by extrusion of the sample hole on application of pressure (Lee *et al.*, 2014). This extrusion can be inwards or outwards depending on the thickness of the gasket. If the gasket is thin, extrusion can occur inwards, which results in the decrease in the size of the

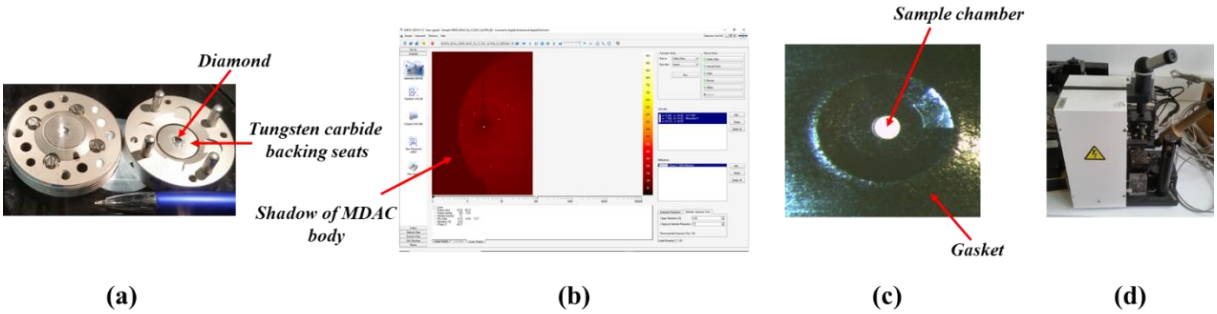

Figure 2.11 (a) Le Toullec-type MDAC used for HP-SCXRD experiments (b) one of the diffraction frames in the GUI interface of APEX3 software, where a portion of the reciprocal space is shadowed by the MDAC body (c) sample chamber (a hole) drilled on the pre-indented gasket surface (d) BESTA micro-driller used for drilling the sample chamber on gasket.

sample hole, causing the easy increase of the pressure inside the sample hole. On the other hand, a thicker gasket causes the extrusion to occur outwards and an eventual enlargement of the sample hole on application of pressure. In this case the pressure inside the sample hole increases comparatively slowly and a larger force has to be applied to reach the same pressure than in the previous case. The gasket is positioned between two diamond anvils. The single-crystal is loaded inside the MDAC sample chamber along with ruby spheres of ~10 μm in diameter for in-situ calibration of the pressure. Another important component of the MDAC is the pressure transmitting media (PTM), which serves the purpose of creating homogeneous pressure inside the sample chamber. It has been reported in the literature that PTMs can have a strong influence in the structural transformation, or in the polymorphism of the single-crystals under pressure, even though they do not interact with the crystal at ambient conditions. These features make the choice of PTM very important and tricky (Zakharov *et al.*, 2016). Another point one has to keep in mind during the selection of a PTM is the solubility of the sample and the hydrostatic limit of the PTM. The most common choice in the literature is a 4:1 methanol-ethanol mixture because of the easy loading and a high hydrostatic limit (~10 GPa) (Angel *et al.*, 2007). As our crystals are soluble in this solvent mixture with time, Daphne oil 7474 was chosen as the PTM, after considering the best compromise between hydrostatic limit and non-solubility of the sample (Murata *et al.*, 2008).

The loading of the crystal inside MDAC can be achieved in two ways. In the first one, a very small drop of vacuum grease is placed on the diamond surface through the sample hole, in order to keep the sample at the same place in the chamber. Later, the crystal is placed manually in the middle, along with one or two ruby spheres. The ruby spheres are supposed to lead to some weak diffraction of X-ray radiations. Therefore, they are kept far from the crystal (on the

periphery of the sample chamber) to avoid any possible merging of the sample peak with the ruby peak (**Figure 2.12a)**. In next step the sample hole is filled with Daphne oil 7474 through a syringe. It is advisable to fill PTM slowly through the inclined surface of the gasket (resulting from the pre-indentation process) rather than filling it directly on the hole, as the sudden movement arising from the direct filling can push the crystal and the ruby from the initial positions and sometimes it can be lost. The loading of the sample can also be done using a home-made micromanipulator, which consists of a clamp fixed on optical micrometric plates, themselves fixed on a strong metallic base equipped with anti-slip pads (**Figure 2.12b**). This configuration allows a great stability for the micromanipulator, and can be brought close to the microscope in order to place the crystal in right place using a needle in the clamp. The process of placing the ruby sphere can also be done with the same procedure.

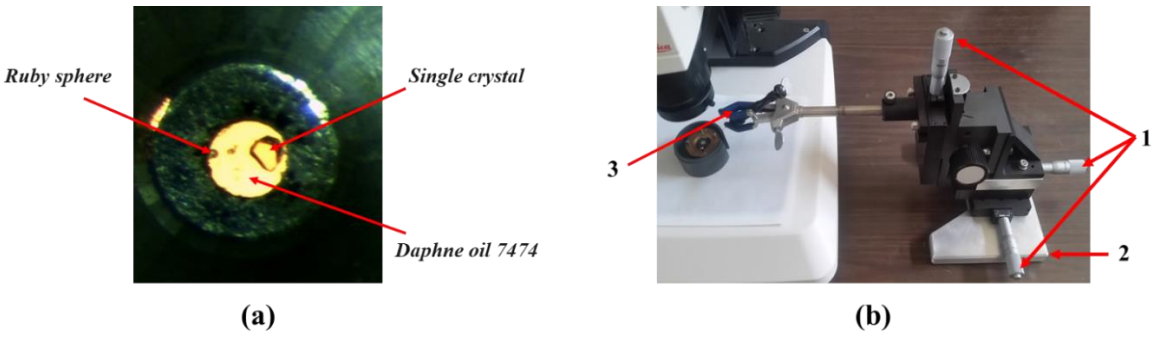

Figure 2.12 (a) A single-crystal mounted inside the sample chamber, along with a ruby sphere on the corner, and filled with Daphne oil 7474 as PTM (b) in-house build micro-manipulator with different parts indicated as: (1) micro-manipulator screw mounted in a *xyz* stage (2) heavy stabilization base (3) tip mounted on the clamp, which allows for the loading and the positioning of the crystal and the ruby sphere inside the sample chamber.

Once the sample loading is done, the next step is the application of external hydrostatic pressure. The force is applied on MDAC by means of a membrane inflated with helium gas, using a pneumatic drive system (**Figure 2.13a**). The flow of the helium gas from the pneumatic drive system to the MDAC is done *via* a metallic capillary (**Figure 2.12c**, shown with red arrow). The inflow or outflow to the MDAC from the capillary can be controlled with a micro-valve system (**Figure 2.13b**). This micro-valve of the MDAC can be opened and closed by using the screw attached. Once the desired pressure is reached the valve can be closed and the pneumatic drive system can be disconnected. This allows the MDAC to be moved in all directions during data collection without any capillary winding problem. An extreme care has to be paid during the rate of inflow or outflow of helium gas, because the change in pressure in the pneumatic drive system is not linearly depend on change in pressure inside the sample chamber. To reach a desired pressure, one has to be patient enough to see the changes in smaller steps rather than

in a sudden variation, which can result in some cracks in the diamonds. With this configuration the maximal pressure achieved in our set-up is 9 GPa, but for being safe with the diamonds the pressure is restricted to 5-6 GPa throughout our study.

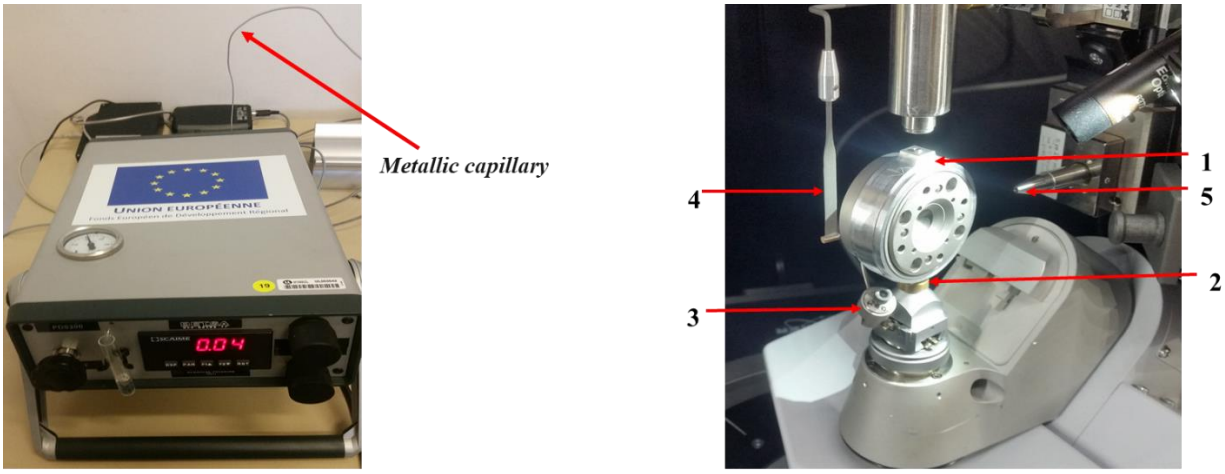

Figure 2.13 (a) Pneumatic drive system used to apply force on the diamonds. The capillary that connects the pneumatic drive system to the micro-valve of MDAC is indicated with a red arrow (b) goniometer head that is used to mount the MDAC for X-ray diffraction experiments. Different parts are indicated: (1) aluminium ring to hold the cell, (2) brass ring used to strengthen the *Z*-stage of the goniometer head, (3) micro-valve that is used to connect the pneumatic drive system to the membrane (the screw on top can be used to open or close the valve), (4) home-made adjustable beam stop and (5) short collimator used during the experiments.

2.4.2.2 Goniometer head

In case of HP-SCXRD experiments, a conventional goniometer head has to be replaced with a modified one, because the goniometer head needs to carry the whole MDAC throughout the diffraction experiment without any kind of misalignment due to its weight. For this purpose, we used a modified goniometer head, consisting of an aluminium ring to hold the cell and brass ring at the *Z*-setting (**Figure 2.13b**). This brass ring is very important to provide the stability to the goniometer head. In our case the weight of the MDAC (including the membrane and the cover) is measured as 324g and that of the MDAC+goniometer head is measured as 459g. To be consistent with the size of the MDAC and thus to avoid any possible collision, we used a homemade adjustable beam stop and a short collimator during the X-ray diffraction experiments.

2.4.2.3 Pressure by Ruby Luminescence: installation and working procedure

The pressure applied on the sample chamber cannot be directly quantified based on the force that we apply on diamonds because of the non-elastic behaviour of the associated screws and

other mechanical parts. This feature marks the importance of an internal standard placed in the sample chamber along with the single-crystal. Ruby spheres (or ruby chips) is a common choice in most of the reported studies, while other internal standards like quartz, gold or sodium chloride are also frequently used (Angel *et al.*, 1997; Pakhomova *et al.*, 2017; Jeffery *et al.*, 1966). In our case, ruby spheres of ~10μm in diameter is chosen as the internal standard for the pressure calibration. Ideally, the fluorescence spectra of a ruby show a doublet of lines, namely R1 and R2 found respectively at 692.7 nm and 694.2 nm at ambient conditions. The position of the peaks shifts linearly to higher wavelengths on application of pressure. The relative shifts in these fluorescence lines can be used as an internal measure to calibrate the change in pressure. This technique of calibration of the pressure inside the sample chamber is known as *Pressure by Ruby Luminescence* (PRL) method, and the whole combination of devices and software used for this purpose is called the *PRL set-up*.

The steps associated with this process is as follows: a Mitutoyo long working distance microscope objective (34 mm), which is a part of the PRL set-up, is used to illuminate the ruby sphere using a blue violet laser diode (λ = 405 nm) through one of the MDAC diamond. The light emitted by the fluorescence of ruby is sent back through the microscope objective and analysed *via* a visible light Ocean Optics HR4000 spectrometer. The transfer is done through an optical fiber. Then, a Labview program, developed at AILES beamline (belonging to the SOLEIL synchrotron facility) allows for the fitting of the fluorescence lines, providing a direct measurement of the pressure inside the sample chamber based on the shift of the R1 peak of the ruby with respect to the position at ambient condition (Voute *et al.*, 2016). This whole set-up is installed on the top of an anodized aluminium rail that is fixed directly on the base of the goniometer, which allows it to move backwards during data collection and forwards during pressure calibration (**Figure 2.14**). The use of the adjustable stops and the clamping screws allows the PRL to be repositioned very precisely. In this experimental set-up pressure can be altered (increased or decreased) by small steps, and the PRL device attached is sensitive enough to record the pressure changes which is even fractions of 1 GPa. Accordingly, this set-up permits us to study molecular crystals that undergoes multiple phase transformations in close by pressure values (with a small gap in between), means the fine control of pressure increase rate allow to reach exact pressure values where the crystal exhibit phase transition process.

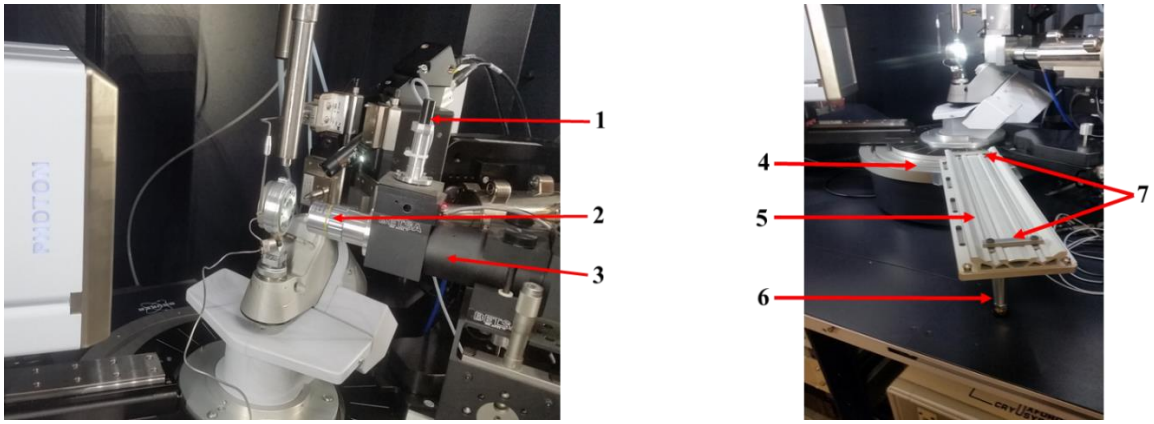

Figure 2.14 The PRL set-up used for the in-situ calibration of the pressure inside the sample chamber with different parts are shown in two figures and are indicated as (1) blue-violet laser diode used to illuminate ruby sphere (2) Mitutoyo long working distance microscope objective (3) body of the PRL that collects the light emitted by the ruby sphere *via* the microscope objective and sending it to the Ocean Optics HR4000 spectrometer (4) goniometer base where the aluminium rail fixed with the diffractometer (5) aluminium rail where the optical parts of the PRL are installed and allowed to move forward and backwards (6) weight supporting stick (7) adjustable stops that limit the movement of optical devices.

It is also important to discuss about the advantages of building a new experimental set-up. This current configuration of the devices enables us to keep the MDAC throughout inside the diffractometer chamber. As mentioned previously, we are interested to carry-out multiple HP-SCXRD experiments, *via* compression-decompression cycle, using the same-single crystal mounted inside the MDAC. This experimental set-up permits to minimize the efforts that one has to put while going from one pressure point to the other. With our configuration, once the sample loading is done and the MDAC is mounted on the goniometer head, the whole MDAC+goniometer can be kept inside the diffractometer chamber and the pressure can be adjusted (by increasing or decreasing its magnitude) in-situ in between X-ray diffraction experiments. In a conventional case after each measurement the MDAC has to be taken out of the diffractometer to adjust the next pressure, which might cause the sample to experience a sudden temperature change. Also, in our case we do not have to start the centering procedure from scratch each time and a quick realignment is sufficient. In the conventional procedure, the centering has to be redone at each time. This saves a lot of time in between the experiments, especially when we have to collect a series of data for the same sample. Another common issue related with this kind of studies is the pressure stability inside the sample chamber. Indeed, an instability in the magnitude of the pressure can arise due to either a He gas leak from the MDAC or a too short stabilization of pressure. However, with our PRL set-up, the pressure can be re-confirmed at any time during the data collection. In addition, the calibration of pressure inside the sample chamber at various point of X-ray diffraction experiment can also provide an estimate of the standard deviation of the applied hydrostatic pressure.

2.4.2.4 Cell alignment and crystal centering

In our study, all HP-SCXRD experiments are carried out using Mo K_α radiations (λ=0.70173 Å) as the X-ray source. The transmission co-efficient of the Mo K_α radiation for a 1.4mm thick diamond is 0.73, whereas in case of the Ag K_α radiation it is 0.83. The use of Ag K_α radiation permits to collect more reflections from the available portion of reciprocal space than Mo K_α radiation, but a compromise with the intensity of the diffraction spots has to be found. Indeed, the Mo source is much more intense than the Ag one, giving rise to higher diffracted intensities, even with larger absorption effects. During the experiments, the X-ray beams are focused on the sample and have a Gaussian profile with a Full Width at Half Maximum (FWHM) of less than 200μm. This value is consistent with the diameter of the sample chamber, which is generally greater than 200μm. Thus, once a crystal (smaller than the sample chamber) placed approximately at the center of the hole and it is under the X-ray beam, it is highly unlikely that one will observe a strong diffraction from the gasket. Due to this reason it is highly advisable to place the crystal far from the gasket periphery, reducing in such a way the diffraction from the gasket ring and eventually reducing the background in the diffraction frames. The accurate alignment of the cell and centering of the crystal is necessary for a successful HP-SCXRD experiment.

Optical centering perpendicular to the cell axis (a conventional cell axis direction is defined perpendicular to the sample hole) can be accurately done with the camera of the diffractometer in combination with the camera of the PRL, since the crystal is clearly visible along these two axes. On doing so, the camera axis should be perfectly perpendicular to the diamonds, because they have a significant optical index (2.417) and this can cause wrong assessment of the crystal position from a misaligned camera. The alignment perpendicular to the diamonds can also be verified with the back reflection of the camera light.

Optical centring along the cell axis is comparatively more difficult, because one could not see the width of the crystal from the side due to the covering of the MDAC body and this is mainly done based on the procedure described by Dawson *et al.* (2004). To follow this procedure, first we have to use two diamonds of same thickness in the anvil, which is true in our case. This centering procedure is mainly achieved through three stages. First, the periphery of the gasket is focused using the PRL camera, which helps to centre the sample approximately. Then the camera is rotated to make sure that the line of view is through the diamond anvils. The PRL camera is mounted on an adjustable platform consisting of micro-metric screws along three

perpendicular directions. The screw that controls the movement along the cell axis is thus turned and adjusted to focus the edges of the crystal and the corresponding micro-meter reading is noted down. The cell is then rotated to 180° and the camera is re-focused on the sample. The new micro-meter reading is also noted down. Further, the camera is moved to the mid-point of the two initial micro-meter reading and the position of the cell is adjusted focusing the edges of the crystal. With this procedure the crystal is focused on both sides of the cell. However, if this is not the case, the same procedure is repeated until we get the crystal focused on both sides.

Once the crystal centering is done and a required pressure is reached, one has to pay attention on the angle settings of the run list, because the diffractometer cannot produce by default the run list considering the crystal portion inaccessible due to the covering of MDAC body. A modified run list defined by the user can be then used to maximize the completeness and the redundancy as much as possible. Afterwards, we could start the X-ray diffraction experiment.

Here, I would like to acknowledge the efforts of Dr. Maxime Deutsch, Dr. Emmanuel Wenger, Dr. El-Eulmi Bendeif and Mr. Cyril Palin on installing the high-pressure experimental set-up in the PMD^{2}X platform of CRM2 laboratory. Dr. Maxime Deutsch conceived the presented idea of the experimental set-up and installation, Cyril Palin designed and machined the parts and others were involved in the development of the presented methods.

References

Angel, R. J., Allan, D. R., Miletich, R. and Finger, L. W. (1997). *J Appl Crystallogr*, *30* (4), 461–466.

Angel, R. J., Bujak, M., Zhao, J., Gatta, G. D. and Jacobsen, S. D. (2007). *J. Appl. Crystallogr.*, *40* (1), 26–32.

Bader R. F. W. (1990). Atoms in Molecules – A Quantum Theory; Clarendon: Oxford, U.K.

Brezgunova, M. E., Aubert, E., Dahaoui, S., Fertey, P., Lebègue, S., Jelsch, C., Ángyán, J. G. and Espinosa, E. (2012). Cryst. Growth Des., 12, 5373–5386.

Brezgunova, M. E. Lieffrig, J., Aubert, E., Dahaoui, S., Fertey, P., Lebègue, S., Ángyán, J. G., Fourmigué, M. and Espinosa, E. (2013). Cryst. Growth Des., 13, 3283–3289.

Clark, S. J., Segall, M. D., Pickard, C. J., Hasnip, P. J., Probert, M. J., Refson, K., Payne, M. C. (2005). *Zeit. für Krist*., 220(5-6) 567-570.

Contreras-García, J., Johnson, E. R., Keinan, S., Chaudret, R., Piquemal, J. P., Beratan, D. N. and Yang, W. (2011). *J. Chem. Theory Comput.*, *7* (3), 625–632.

Coppens, P. (2006**)**. International Tables for Crystallography, Vol. B, Chapter 1.2, pp.10

24.

Dawson, A., Allan, D. R., Parsons, S., Ruf, M. (2004). *J Appl Crystallogr.*, *37* (3), 410–416.

Dennington, R., Keith, T. A. and Millam, J. M. (2016). GaussView, Version 5.0.9, Semichem Inc., Shawnee Mission, KS.

Dolomanov, O.V., Bourhis, L.J., Gildea, R.J., Howard, J.A.K. and Puschmann, H. J. (2009). Appl Crystallogr., 42, 339-341.

Dovesi, R., Orlando, R., Erba, A., Zicovich-Wilson, C. M., Civalleri, B., Casassa, S., Maschio, L., Ferrabone, M., De La Pierre, M., D'Arco, P., Noel, Y., Causa, M., Rerat, M. and Kirtman. B. (2014)**.** Int. J. Quantum Chem., 114, 1287-1317.

Espinosa, E., Alkorta, I., Rozas, I., Elguero, J. and Molins E. (2001). Chem. Phys. Lett., 336, 457-461.

Espinosa, E., Molins, E., Alkorta, I. and Elguero J. J. (2002). Chem. Phys., 117, 5529-5542.

Espinosa, E., Molins, E., Lecomte, C. (1998). Chem. Phys. Lett., 285, 170-173.

Frisch, M.J., Trucks, G.W., Schlegel, H.B., Scuseria, G.E., Robb, M.A., Cheeseman, J.R., Scalmani, G., Barone, V., Mennucci, B., Petersson, G.A., Nakatsuji, H., Caricato, M., Li, X., Hratchian, H.P., Izmaylov, A.F., Bloino, J., Zheng, G., Sonnenberg, J.L., Hada, M., Ehara, M., Toyota, K., Fukuda, R., Hasegawa, J., Ishida, M., Nakajima, T., Honda, Y., Kitao, O., Nakai, H., Vreven, T., Montgomery, J.A., Jr., Peralta, J.E., Ogliaro, F., Bearpark, M., Heyd, J.J., Brothers, E., Kudin, K.N., Staroverov, V.N.. Keith, T., Kobayashi, R., Normand, J., Raghavachari, K., Rendell, A., Burant, J.C., Iyengar, S.S., Tomasi, J., Cossi, M., Rega, N., Millam, J.M., Klene, M., Knox, J.E., Cross, J.B., Bakken, V., Adamo, C., Jaramillo, J., Gomperts, R., Stratmann, R.E., Yazyev, O.A., Austin, J., Cammi, R., Pomelli, C., Ochterski, J.W., Martin, R.L., Morokuma, K., Zakrzewski, V.G., Voth, G.A., Salvador, P., Dannenberg, J.J., Dapprich, S., Daniels, A.D., Farkas, O., Foresman, J.B., Ortiz, J.V., Cioslowski, J. and Fox, D.J. (2013). *Gaussian 09, Revision D.01*, Gaussian, Inc., Wallingford CT.

Hansen N. K. and Coppens P. (1978). Acta Crystallogr., A34, 909-921.

Hauptman, H. (1997). Curr. Opin. Struct. Biol., 7, 672–680.

Herbst-Irmer, R., Henn, J., Holstein, J. J., Hübschle, C. B., Dittrich, B., Stern, D., Kratzert, D. and Stalke, D. (2013). *J. Phys. Chem. A*, *117* (3), 633–641.

Hirshfeld, F.L. (1971). Acta Cryst., B27, 769-781.

Hirshfeld, F. L. (1976). Acta. Cryst., A32, 239-244.

Hirshfeld, F.L. (1977). Theoret. Chim. Acta (Berl.), 44, 129-138.

Humphrey, W., Dalke, A. and Schulten, K. (1996). *Journal of Molecular Graphics*, *14* (1), 33–38.

Jeffery, R. N., Barnett, J. D., Vanfleet, H. B. and Hall, H. T. (1966). *Journal of Applied Physics*, *37* (8), 3172–3180.

Jelsch, C., Guillot, B., Lagoutte, A. and Lecomte, C. (2005). J. Appl. Crystallogr., 38, 38–54.

Johnson, E. R., Keinan, S., Mori-Sánchez, P., Contreras-García, J., Cohen, A. J. and Yang, W. (2010). *J. Am. Chem. Soc.*, *132* (18), 6498–6506.

Kurki-Suonio, K. (1968). Acta Cryst., A24, 379-390.

Lewis, G. N. (1916). J. Am. Chem. Soc., 38, 762-785.

Lee, R., Howard, J. A. K., Probert, M. R. and Steed, J. W. (2014**).** Chem. Soc. Rev., 43,

4300–4311.

Lu, T. and Chen, F. (2012). *J. Comput. Chem.*, *33* (5), 580–592.

Merrill, L. and Bassett, W. A. (1974). *Review of Scientific Instruments*, *45* (2), 290–294.

Murata, K., Yokogawa, K., Yoshino, H., Klotz, S., Munsch, P., Irizawa, A., Nishiyama, M., Iizuka, K., Nanba, T., Okada, T., Shiraga, Y. and Aoyama, S. (2008). *Review of Scientific Instruments*, *79* (8), 085101.

Oszlányi, G. and Sütő, A. (2008). Acta Crystallogr. A, 64, 123–134.

Outeiral, C., Vincent, M. A., Martín Pendás, Á. and Popelier, P. L. A. (2018). Chem. Sci., 9, 5517–5529.

Pakhomova, A., Ismailova, L., Bykova, E., Bykov, M., Ballaran, T. B. and Dubrovinsky, L. A. (2017). *Am. Mineral.*, *102* (3), 666–673.

Patterson, A. L. (1934). Physic. Rev., 46, 517-542.

Platts, J. A., Overgaard, J., Jones, C., Iversen, B. B. and Stasch, A. (2011). *J. Phys. Chem. A*, *115* (2), 194–200.

Scheiner, S. (2021). *J. Phys. Chem. A*, *125* (30), 6514–6528.

Shukla, R., Dhaka, A., Aubert, E., Vijayakumar-Syamala, V., Jeannin, O., Fourmigué, M. and Espinosa, E. (2020). Cryst. Growth Des., 20, 7704–7725.

Spackman, M. A. and McKinnon, J. J. (2002). *CrystEngComm*., *4* (66), 378–392.

Stalke, D. (2011). Chem. - Eur. J., 17, 9264-9278.

Stewart, R.F. (1976). Acta Cryst., A32, 565-574.

Stewart, R.F and Bentley, J. (1975). The Journal of Chemical Physics, 63, 3786-3793.

Truong, K.D., Grenier, P., Houde, D. and Bandrauk. A. (1995). Synthetic Metals, 71, 1707-1708.

Turner, M.J., McKinnon, J.J., Wolff, S.K., Grimwood, D.J., Spackman, P.R., Jayatilaka D. and Spackman, M.A. (2017). CrystalExplorer17, University of Western Australia.

Varadwaj, P. R., Varadwaj, A. and Marques, H. M. (2020). *Crystals*, *10* (3), 146.

Volkov, A., Macchi, P., Farrugia, L. J., Gatti, C., Mallinson, P. R., Richter, T. and Koritsanszky, T. S. (2006). XD2006, University at Buffalo, State University of New York, NY, USA, New York.

Voute, A., Deutsch, M., Kalinko, A., Alabarse, F., Brubach, J. B., Capitani, F., Chapuis, M., Ta Phuoc, V., Sopracase, R. and Roy, P. (2016). *Vibrational Spectroscopy* **2016**, *86*, 17–23.

Zakharov, B. A., Seryotkin, Y. V., Tumanov, N. A., Paliwoda, D., Hanfland, M., Kurnosov, A. V. and Boldyreva, E. V. (2016). *RSC Adv.*, *6* (95), 92629–92637.

3

Evolution of halogen bonding in co-crystal: coupling high-pressure to single-crystal X-ray diffraction

Chapter 3 is devoted to the study of halogen bonding (HaB) interactions under high-pressure, using co-crystals composed of N-iodosacchrin (NISac) acting as HaB donor and two derivatives of pyridine [pyridine (Py) itself and 4-cyanopyridine (4CYP)] acting as HaB acceptors. This chapter will cover co-crystallization routes, high-pressure single crystal X-ray diffraction (HP-SCXRD) experiments, subsequent data reduction and analysis, and the theoretical calculations carried out in order to complement the experimental findings.

3.1 Introduction

The main motivation behind this study and to the choices of the compounds arises from one of the previous reports (Makhotkina *et al.*, 2015), where the co-crystal *vs* salt situation was studied for a family of complexes, involving N-iodosuccinimide (NIS), N-iodosaccharin (NISac) and N-bromosaccharin (NBSac) as HaB donors, and pyridine (Py), 4-picoline (PIC) and 4-dimethylaminopyridine (DMAP) as HaB acceptors. In this study, a set of $N_{donor}\cdots I\cdots N_{acceptor}$ HaB motifs were characterized from the geometrical point of view. Eventually it was observed that a combination of a good donor (NISac) and a good acceptor (DMAP) resulted in I atom being positioned closer to $N_{acceptor}$ than to N_{donor}. On the other hand, a combination of the same donor with a weaker acceptor (PIC) resulted in a co-crystal form where the I remain closer to N_{donor} (**Figure 3.1a**). Additionally, the role of secondary non-covalent interactions in the halogen atom shift has been investigated and a $(C=)O^{\delta-}\cdots I^{\delta+}$ electrostatic interaction found to favour the position of I being closer to the acceptor N in *NISac.DMAP*, thus acting as an additional pulling effect on the halogen atom shift (**Figure 3.1b**).

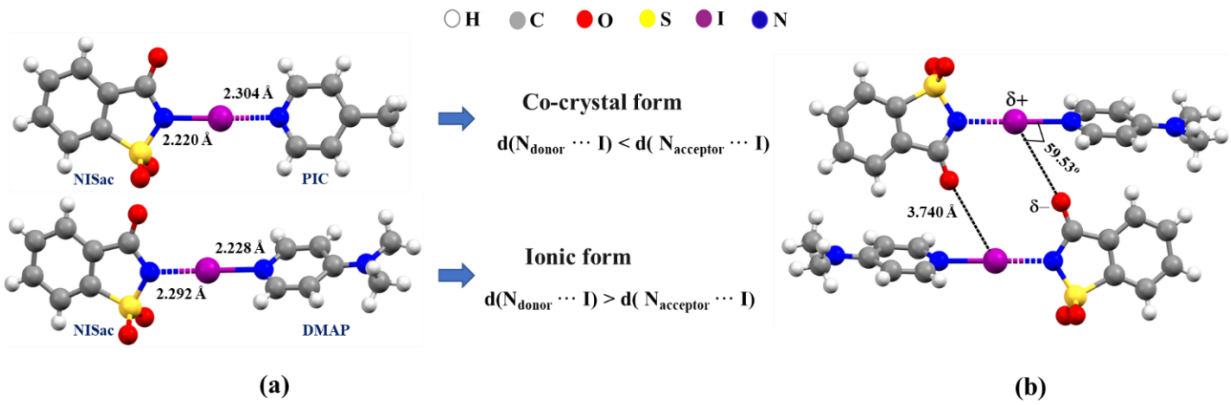

Figure 3.1 Classification of co-crystal *vs* ionic forms under geometrical point of view based on the $N_{donor}\cdots I\cdots N_{acceptor}$ HaB motif (b) Electrostatic $(C=)O^{\delta-}\cdots I^{\delta+}$ secondary interaction found in *NISac.DMAP* co-crystal. Atom types are shown with colouring scheme. Distances and angles are shown in angstroms (Å) and degrees (º).

But in these binary adducts, since the electronic environment of N_{donor} and $N_{acceptor}$ atoms are different (and therefore the middle position between these two nitrogens cannot be considered as the exact transition boundary in the halogen atom transfer), it is however debatable that the geometrical distances can solely conclude about the neutral *vs* ionic form of the system. Consequently, these HaB motifs were studied from the electronic point of view, using the QTAIM analysis. In a previous study, it has been also found that topological and energetic properties of $\rho(\mathbf{r})$ at $N_{donor}\cdots I$ and $I\cdots N_{acceptor}$ BCPs indicate a significant degree of covalency at both sides of I, regardless of the geometrical position of the halogen atom (Aubert *et al.*, 2017). This means that a partial halogen atom transfer has already happened from the donor to the acceptor moiety on co-crystal formation. Overall, these studies reveal the modifications of HaB motifs, both structurally and electronically, on tuning with the electronic properties of the donor and acceptors molecules. Also, it has been clearly demonstrated the importance of crystalline environment (secondary non-covalent interactions) in the migration of halogen atom on such binary adducts, which will be used as the pivotal idea in our current study.

As stated before, HB interaction is one of the major class of non-covalent interactions that has been studied in detail under high-pressure. It has been found that a transition from a neutral to an ionic form is possible in the case of oxalic acid dihydrate ($H_2C_2O_4.2H_2O$) under high-pressure, by the displacement of two H atoms from oxalic acid to two water molecules upon increasing the hydrostatic pressure (Casati *et al.*, 2009). Thus, the neutral oxalic acid dihydrate at 0 GPa becomes an oxalate di-anion with an incipient proton transfer towards two water molecules at 5.3 GPa. An intermediate geometry, where the protons start their migration towards the water molecules but yet in a neutral form, was found at 3.6 GPa (**Figure 3.2**). Limitations on locating the precise position of H atoms in high-pressure data (less precision due to poor completeness) hinders a concrete conclusion out of the experimental findings. However, these results were supported with theoretical calculations. Later on, the authors also performed a combined theoretical simulation with neutron diffraction studies over the same compound, confirming the migration of H atoms and the transition of state from a neutral to an ionic form under high-pressure (Macchi *et al.*, 2010).

However, a similar possibility will also be investigated in this study, where the migration of a halogen atom in between the donor and the acceptor moieties will be investigated in case of two donor···acceptor co-crystal systems under evolving pressure. The subsequent portions of this chapter are split into two, each dedicated to a co-crystal system. The first part deals with the *NISac.Py* co-crystal [combination of N-iodosaccharin (NISac) with pyridine (Py)] while the

second part with the *NISac.4CYP* co-crystal [combination of N-iodosaccharin (NISac) with 4-cyanopyridine (4CYP)]. At the end, results coming from both systems are combined to reach a common conclusion about these donor···acceptor family of compounds, in response to external pressure.

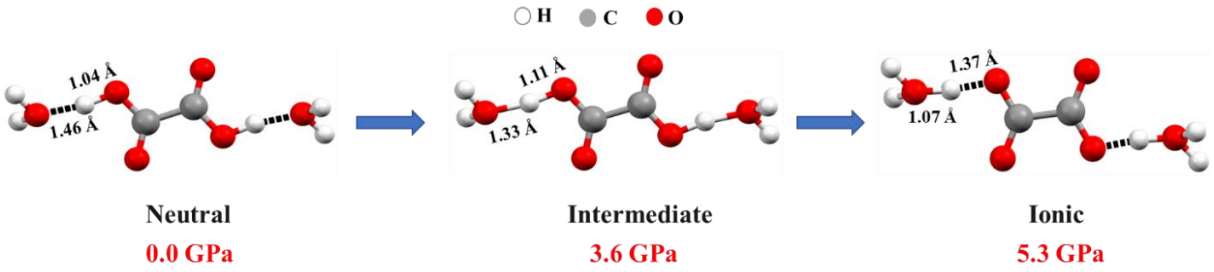

Figure 3.2 Neutral to ionic transition in oxalic acid dihydrate under high-pressure, pressure values are given. Figures are drawn with deposited cif files from Casati *et al*., 2009. Atom types are shown with colouring scheme, O-H···O HBs are shown with black dashed lines along with corresponding distances.

3.2 N-iodosaccharin.Pyridine (*NISac.Py*) co-crystal system

3.2.1 Experimental

3.2.1.1 Synthesis and co-crystallization

I would like to thank *Prof. Marc Fourmigué* and *Dr. Arun Dhaka* [Condensed Matter and Electroactive Systems (MaCSE) group, University of Rennes 1] for the synthesis of the parent compound NISac. This compound was prepared as previously reported, following the classical procedure for the preparation of *N*-haloamides, the reaction of a silver salt of saccharin with iodine (**Scheme 3.1**; Dolenc, 2000). The co-former pyridine (Py) was commercially available (99% from Alfa Aesar) and used as received. A 1:1 stoichiometric co-crystal of N-iodosaccharin and pyridine (*NISac.Py*) was prepared by dissolving 5 mg of NISac (0.016 mmol) in 1 mL of ethyl acetate inside a 5ml glass vial, stirred and gently heated in a hot-plate. Py (0.002 mL, 0.02 mmol) was added slowly to the solution and the mixture was further heated and stirred for another 10 minutes until obtaining a clear solution. Colourless, thin, platey crystals were obtained after two days. In the first batches of crystallization it has been found that some of the crystals obtained were already decayed (on complete solvent evaporation), appearing opaque with random black spots on the surfaces. Covering the vial with aluminium foil and keeping it in a dark chamber for crystallization (for reducing any potential damage that can be caused by light or air), produces comparatively good quality crystals that are stable enough for a few days.

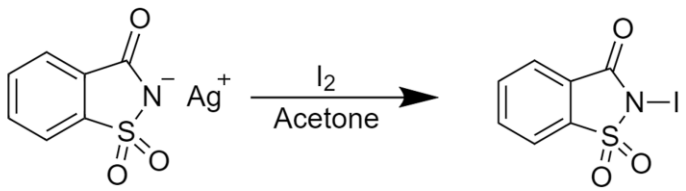

Scheme 3.1. Synthetic scheme of NISac

3.2.1.2 Crystal choice

Crystals of *NISac.Py* grown from ethyl acetate had a similar thin plate morphology but with different crystal habits, making important the choice of the crystals for X-ray diffraction experiments. Crystals were selected using a polarized light microscope. The first type of crystals (**Figure 3.3a**) shown two distinct colours separated by a line on the large face of the crystal, suggesting that the sample may be twinned. Initial unit cell determination on such crystals shows the presence of different orientations for the reciprocal lattice, confirming their twinning. On the other hand, crystals of second type (**Figure 3.3b**) shown a homogeneous colour across the surface, except for the edges (may however be caused by changes in thickness). The diffraction pattern of these crystals indexed at 100% with a single orientation of the reciprocal lattice, excluding at least the possibility of non-merohedric twinning. In such a way, crystals of dimension 0.149×0.122×0.053 mm (crystal-1) and 0.110 × 0.091 × 0.048 mm (crystal-2) were carefully chosen with the aid of a polarized light microscope for the crystal structure determination respectively at room- and high-pressure (both at room temperature).

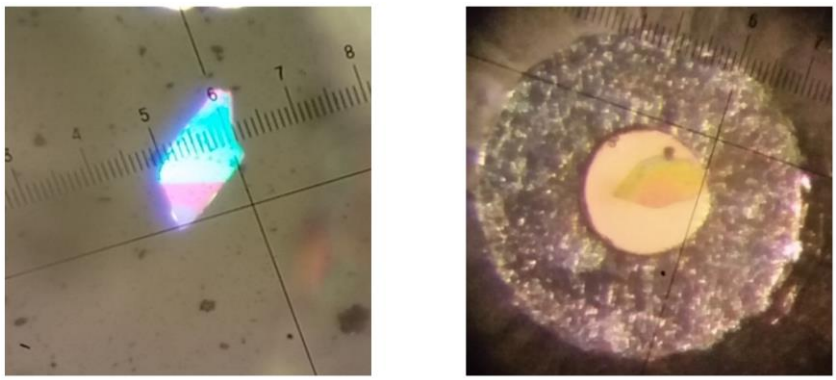

(a) (b)

Figure 3.3 *NISac.Py* crystals showing different crystal habits: (a) two distinct colours are observed on the surface separated by a line (b) homogenous colour observed on the surface except for the edges, photograph being taken after the crystal mounted inside MDAC.

3.2.1.3 Membrane Diamond Anvil Cell (MDAC) loading and centring

A hole of ~280μm in diameter and ~100μm in height drilled at the centre of a stainless-steel gasket acts as the sample chamber in our study. Two crystals were selected: crystal-1 used for data collection at ambient conditions and crystal-2 smaller in dimensions to fit in the MDAC sample chamber. Crystal-2 was placed inside this MDAC sample chamber, with the pressure cell axis quasi-perpendicular to the (100) face of the crystal (in $B2_1/e$ space group setting, see the **section 3.2.3.5.1** below). A ruby sphere of ~10μm in diameter was added for the in-situ measurement of pressure by ruby luminescence (PRL) technique (Piermarini *et al.*, 1975), while the Daphne oil 7474 (Murata *et al.*, 2008) was used as the pressure transmitting media (PTM) (**Figure 3.4**). The initial sealing of the cell does not cause any measurable change in pressure, being thus similar to room pressure. The MDAC was then mounted to the in-house developed high-pressure experimental set-up (see **section 2.4** for details). Quasi-hydrostatic pressures ranging from 0.00(5) GPa to 4.5(2) GPa were applied in a sequential manner, first increasing then decreasing back to ambient pressure.

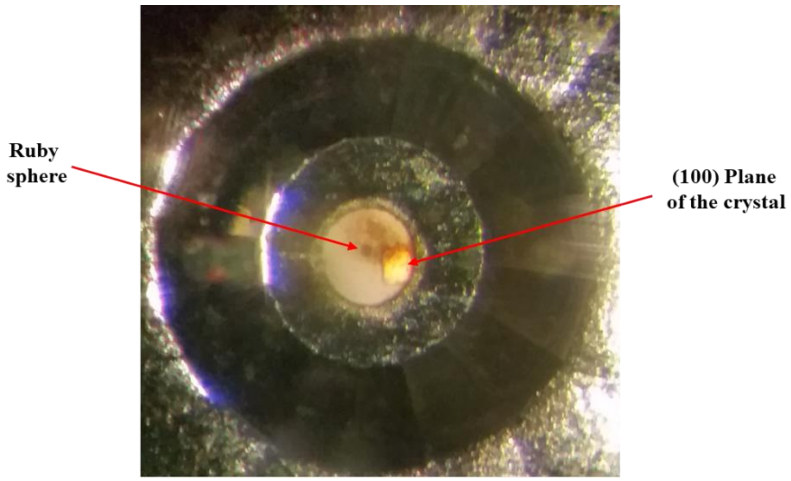

Figure 3.4 *NISac.Py* single-crystal mounted inside the MDAC sample chamber with the cell axis quasi-perpendicular to the (100) plane of the crystal (in $B2_1/e$ space group setting, see text). One ruby sphere (~10 μm in radius) is placed in the middle of the sample chamber for pressure calibration. The sample chamber is filled with Daphne oil 7474 which acts as the pressure transmitting media.

3.2.1.4 Single crystal X-ray Diffraction

Data collection, processing and refinement at ambient conditions: X-ray diffraction data were collected for crystal-1 at ambient conditions outside MDAC, with crystal glued at the extremity of a glass fiber in a goniometer head. A Bruker D8 Venture diffractometer was used, equipped with a molybdenum micro-focus X-ray tube (MoK_α radiation, λ = 0.71073 Å) with mirror optics as a monochromator, and a PHOTON III CMOS detector of size 10 cm x 14 cm.

Data integration and reduction were carried out using the SAINT program incorporated in the APEX3 software (Bruker, 2019). A numerical absorption correction was applied using the crystal shape and face indexing. The crystal structure was solved using the SHELXT (Sheldrick, 2015a) program and refined using the SHELXL (Sheldrick, 2008; Sheldrick, 2015b) program in the Olex2-1.3 (Dolomanov *et al.*, 2009) software suite. All the non-hydrogen atoms were refined anisotropically. Hydrogen atoms were placed at calculated positions and constrained to ride the position with their parent atoms (**Figure 3.5a**). Crystal structure analysis was carried out using Olex2-1.3, Crystal Explorer -Version 17.5 (Turner *et al.*, 2017) and Mercury (version 2020.1) software packages, and the latter is also used to generate crystal structure drawings. The corresponding crystallographic information are gathered in **Table 3.1**.

Data collection, processing and refinement at high-pressure and room temperature. X-ray diffraction data were collected under high-pressure, ranging from 0.00(5) GPa to 4.5(2) GPa at room temperature using the high-pressure experimental set-up installed in Bruker D8 Venture diffractometer. Data integration and reduction were carried out using the SAINT program after excluding the MDAC shadowed regions with a dynamic mask (Dawson *et al.*, 2004). During the integration process, a half-aperture angle of 40° and a φ−offset of -4° is used in the Diamond Anvil Cell section. An empirical absorption correction based on the intensities using SADABS (Krause *et al.*, 2015) was used since the accurate face indexing is not possible inside MDAC because the crystal view is hidden in certain directions due to the metal covering of MDAC. The structure with atomic coordinates determined at ambient conditions were used as the starting model for the refinement of the crystal structure at 0.00(5) GPa (which is the first pressure measured inside MDAC). For all the datasets, only heavier atoms (I1 and S1) could be refined anisotropically (**Figure 3.5b**). Attempts to refine atomic displacement parameters (ADPs) for all other non-hydrogen atoms resulted either non-positive definite or unrealistic behaviour (**Figure 3.5c**). This is happening due to hidden reciprocal space zones and therefore, of missing information in the measured datasets (completeness is only ~40% up to a resolution of 0.56 $Å^{-1}$ for all the data-sets collected with the sample inside MDAC).

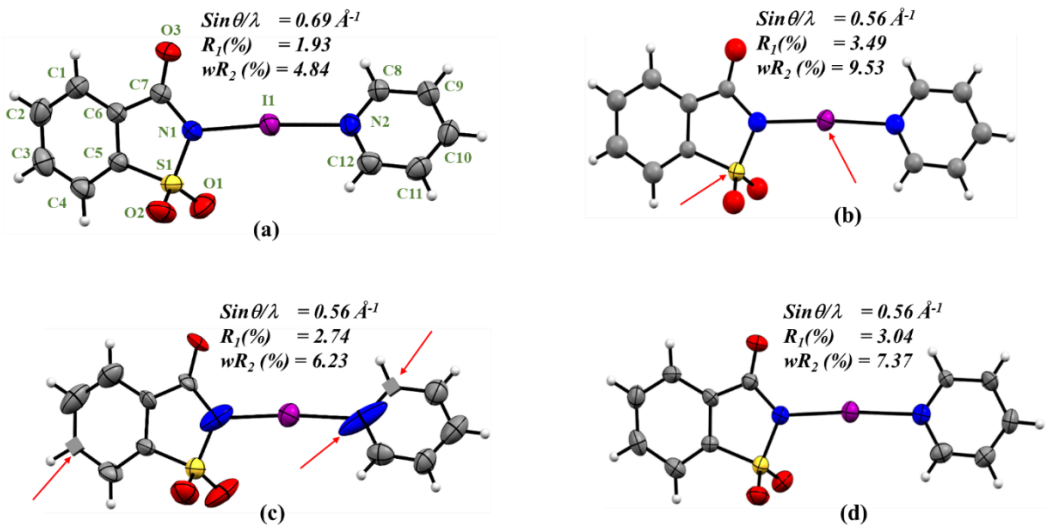

Figure 3.5 (a) Structural model determined at ambient conditions (outside MDAC), atomic labels are given. Representative example of a structural model collected inside MDAC, at 0.5(1) GPa and room temperature, (b) ADPs of I1- and S1-atoms (indicated with red arrows) are only refined, (c) refinemnt of the ADPs of other non-hydrogen atoms showing non-positive definite or unrealistic behaviour (indicated with red arrows) and (d) structural model determined after transferring ADPs from the model at ambient conditions, with a proper scaling. Maximum resolution limit (Sinθ/λ) and agreement factors (R_1 and wR_2) corresponding to each model are shown on the top of respective figures.

To retrieve a good structural model, ADPs for all other non-hydrogen atoms were transferred from the structural model obtained at ambient conditions, assuming that pressure affects U_{ij} in a similar way as U_{iso}. It should be noted here that, ADPs used in this procedure were taken from crystal-2 (namely, the crystal retrieved after the HP-SCXRD experiments, and subjected to a data collection outside MDAC at ambient conditions) rather than from crystal-1 even though the latter had better data statistics and indicators for the structural model at ambient conditions (this is done for using the information coming from crystal-2 consistently in the high-pressure datasets). The crystallographic information corresponding to crystal-2 at ambient conditions can be found in Appendices (**Table 3AP.1**). Further, ADPs of the high-pressure datasets were calculated as $(U_{ij})_{in,P_X} = K * (U_{ij})_{out,P_0}$, where the scale factor $K = (U_{iso})_{in,P_X} / (U_{iso})_{in,P_0}$ is obtained for each pressure X [here $(U_{ij})_{out,P_0}$ corresponds to ADPs obtained with the dataset collected outside MDAC at ambient conditions, $(U_{iso})_{in,P_0}$ and $(U_{iso})_{in,P_X}$ correspond to isotropic displacement parameters obtained with datasets collected with the crystal inside the MDAC at P = 0 and P = X, respectively]. Once obtained, $(U_{ij})_{in,P_X}$ ADPs were kept fixed and not refined further, which eventually leading to the improvement of the refinement parameters in the final model (**Figure 3.5d**). For all the high-pressure datasets H atoms were placed at calculated positions and constrained to ride the position with their parent atoms. In addition, SADI (Same Distance) restraints were applied to the aryl ring of NISac and to the pyridine ring during the

refinements to keep their distortion due to incompleteness as small as possible. The structural model obtained at 0.00(5) GPa was used as the initial reference model for further refinements with high-pressure datasets. Crystallographic information for high-pressure crystal structures can be found in **Table 3.2** and **Table 3.3**.

Table 3.1 Crystallographic information for the data collected at ambient conditions for crystal-1

Crystal data	
Chemical formula	$C_{12}H_9IN_2O_3S$
Formula weight (g/mol)	388.17
Crystal system, space group	Monoclinic, $B2_1/e$
Temperature (K)	298
a, b, c (Å)	27.234 (3), 7.8058 (7), 12.6258 (10)
β (°)	88.606 (2)
V (Å^3)	2683.2 (4)
Z	8
Radiation type	Mo K_α (λ=0.7107 Å)
μ (mm^{-1})	2.55
Crystal size (mm)	0.149 × 0.122 × 0.053
Data collection	
Diffractometer	Bruker D8 Venture
Absorption correction	Numerical (face indexing)
No. of measured, independent, observed [$I > 2\sigma(I)$] reflections	109428, 3759, 3456
Completeness (%)	100
R_{int}	0.034
$(\sin \theta/\lambda)_{max}$ (Å^{-1})	0.694
Refinement	
R [$F^2 > 2\sigma(F^2)$], $wR(F^2)$, S	0.019, 0.050, 1.09
No. of reflections	3759
No. of parameters	173
$\Delta\rho_{max}$, $\Delta\rho_{min}$ (eÅ^{-3})	0.73, -0.29

Table 3.2 Crystallographic information for data collected with increasing pressure for crystal-2. For all data sets: the space group setting is $B2_1/e$ (unconventional setting of $P2_1/c$, No. 14), Z = 8, the formula weight is 388.17 g/mol, the crystal size is 0.110 × 0.091 × 0.048 mm, the radiation type is MoK$_\alpha$, the number of parameters is 71 and the number of restraints is 18.

Pressure (GPa)	**0.00(5)**	**0.20(5)**	**0.4(1)**	**0.5(1)**	**0.9(1)**	**1.5(2)**	**2.0(2)**	**3.3(2)**	**4.5(2)**
a (Å)	27.291 (14)	27.185 (16)	27.108 (16)	26.998 (13)	26.806 (12)	26.653 (12)	26.559 (12)	26.304 (11)	26.020 (12)
b (Å)	7.8228 (16)	7.7444 (19)	7.6595 (19)	7.5869 (15)	7.4450 (14)	7.3257 (13)	7.2336 (13)	7.0512 (11)	6.9618 (13)
c (Å)	12.628 (3)	12.593 (3)	12.539 (3)	12.485 (3)	12.380 (2)	12.284 (2)	12.209 (2)	12.042 (2)	11.937 (2)
β (°)	88.579 (11)	88.608 (12)	88.662 (13)	88.802 (11)	89.057 (10)	89.236 (10)	89.462 (9)	89.932 (9)	89.476 (10)
Volume (Å^3)	2695.1 (16)	2650.4 (18)	2602.9 (18)	2556.7 (14)	2470.4 (13)	2398.2 (12)	2345.4 (12)	2233.5 (11)	2162.3 (11)
μ(mm^{-1})	2.54	2.58	2.63	2.67	2.77	2.85	2.91	3.06	3.16
T_{min}, T_{max}	0.461, 0.563	0.445, 0.563	0.394, 0.563	0.456, 0.563	0.451, 0.563	0.455, 0.563	0.467, 0.563	0.472, 0.562	0.502, 0.563
No. of measured, independent, observed [I >2σ(I)] reflections	10351, 770, 595	9901, 777, 564	8139, 761, 536	9824, 738, 577	9464, 706, 573	9116, 688, 582	8817, 675, 580	8569, 656, 590	7793, 635, 553
Completeness (%)	40	41	41	40	40	40	40	41	40
R_{int}	0.045	0.071	0.080	0.054	0.046	0.044	0.046	0.040	0.046
$(\sin\theta/\lambda)_{max}$ (Å^{-1})	0.555	0.555	0.555	0.556	0.555	0.555	0.556	0.554	0.559
$R[F^2>2\sigma(F^2)]$, $wR(F^2)$, GOF	0.030, 0.080, 1.05	0.036, 0.096, 1.07	0.038, 0.109, 1.17	0.034, 0.091, 1.15	0.033, 0.090, 1.16	0.037, 0.095, 1.13	0.042, 0.107, 1.19	0.020, 0.038, 1.12	0.029 0.049, 1.20
$\Delta\rho_{max}$, $\Delta\rho_{min}$ (eÅ^{-3})	0.46, -0.34	0.39, -0.47	0.51, -0.48	0.53, -0.43	0.82, -0.43	0.85, -0.44	0.70, -0.41	0.22, -0.22	0.29, -0.31
BASF[a] (%)	0.15 (5)	0.15 (6)	0.21 (7)	0.19 (6)	0.23 (7)	0.61 (10)	2.30 (18)	15.02 (9)	14.48 (13)

[a] *BASF(%) corresponds to the batch scale factor parameter obtained during refinement, indicating the percentage of twin domain 2 in respective structures.*

Table 3.3 Crystallographic information for data collected with decreasing pressure for crystal-2. For all data sets: the space group setting is $B2_1/e$ (unconventional setting of $P2_1/c$, No. 14), Z = 8, the formula weight is 388.17 g/mol, the crystal size is 0.110 × 0.091 × 0.048 mm, the radiation type is Mo K_α, the number of parameters is 71 and the number of restraints is 18.

Pressure (GPa)	**2.4(2)**	**1.9(2)**	**1.3(2)**	**0.8(1)**	**0.5(1)**	**0.05(5)**	**0.00(5)**
a (Å)	26.482 (12)	26.581 (13)	26.742 (14)	26.869 (13)	27.035 (13)	27.246 (16)	27.272 (19)
b (Å)	7.1755 (13)	7.2485 (14)	7.3842 (15)	7.4985 (14)	7.6231 (15)	7.819 (2)	7.834 (2)
c (Å)	12.156 (2)	12.220 (2)	12.337 (3)	12.418 (3)	12.507 (3)	12.621 (3)	12.630 (4)
β (°)	89.626 (10)	89.447 (10)	89.154 (11)	88.952 (10)	88.799 (11)	88.538 (13)	88.507 (15)
Volume (Å^3)	2309.9 (12)	2354.4 (13)	2436.0 (15)	2501.5 (14)	2577.1 (14)	2687.7 (19)	2697 (2)
μ(mm^{-1})	2.96	2.90	2.81	2.73	2.65	2.54	2.53
T_{min}, T_{max}	0.485, 0.563	0.490, 0.563	0.488, 0.563	0.479, 0.563	0.486, 0.563	0.470, 0.563	0.470, 0.563
No. of measured, independent, observed [I > 2σ(I)] reflections	8506, 673, 590	8768, 687, 590	8933, 712, 582	9489, 759, 603	9685, 773, 603	10196, 817, 583	8714, 830, 545
Completeness (%)	41	41	41	42	42	42	43
R_{int}	0.046	0.047	0.053	0.049	0.053	0.063	0.069
$(\sin\theta/\lambda)_{max}$ (Å^{-1})	0.556	0.555	0.556	0.555	0.555	0.555	0.555
$R[F^2>2\sigma(F^2)]$, $wR(F^2)$, GOF	0.037, 0.083, 1.15	0.042, 0.102, 1.17	0.043, 0.109, 1.14	0.037, 0.101, 1.14	0.039, 0.100, 1.15	0.041, 0.103, 1.08	0.040, 0.113, 1.08
$\Delta\rho_{max}$, $\Delta\rho_{min}$ (eÅ^{-3})	0.34, -0.33	0.81, -0.43	0.72, -0.41	0.82 -0.49	0.54, -0.39	0.45, -0.37	0.38, -0.51
BASF[a] (%)	8.8 (2)	2.89 (18)	1.00 (14)	0.27 (7)	0.09 (6)	0.16 (8)	0.05 (7)

[a]*BASF(%) corresponds to the batch scale factor parameter obtained during refinement, indicating the percentage of twin domain 2 in respective structures.*

3.2.2 DFT calculations

3.2.2.1 Periodic plane wave calculations

The crystal structure of *NISac.Py* was optimized as a function of isotropic pressure, from -0.25 GPa to 4.5 GPa with 0.25 GPa increments, using the CASTEP software (version 19.11) (Clark *et al.*, 2005). The experimental structure determined at ambient conditions in the $P2_1/a$ setting of the space group [Dolenc & Modec, 2009; CSD reference ID: MUGDAU, a = 12.6184(3) Å, b = 7.8019(2) Å, c = 14.8718(4) Å, β = 113.6530(12)°] was used as the starting point. All atomic positions were allowed to vary, together with cell parameters, while keeping the monoclinic symmetry. The PBE exchange and correlation functional was used, complemented by semi-empirical dispersion corrections (Grimme 2006). A fine plane wave cut-off was used, corresponding to a limit of 625eV. The MP grid size was set to 4 4 4. The optimization convergence criteria were fixed as follow: maximal stress tolerance at convergence: 0.1GPa; energy shift: $1E^{-5}$eV; force: $5E^{-2}$a.u.; displacement: $1E^{-3}$Å. Subsequent analyses on the theoretical data set were performed after transformation of the obtained crystal structures from the $P2_1/a$ setting to the $B2_1/e$ setting of the space group (see **section 3.2.3.5.1** below for more details). **Table 3.4** gathers unit-cell parameters and volume as a function of pressure, along with unit-cell void volumes calculated with the ASV program (Petitjean, 1994).

Here, I would like to thank *Dr. Emmanuel Aubert*, Laboratory of Crystallography, Magnetic Resonance and Modeling (CRM2), University of Lorraine, for the periodic plane wave calculations.

Table 3.4 Unit cell parameters and volume as a function of the pressure for the *NISac.Py* DFT optimized crystal structures (in $B2_1/e$ setting of the space group). Unit cell void volume and percentage were calculated with the ASV program.

P (GPa)	*a*(Å)	*b*(Å)	*c*(Å)	*β*(°)	*V*(Å^3)	Void(Å^3)	% Void
-0.25	27.069	7.828	12.659	88.21	2680.95	771.91	28.79
0.00	26.993	7.720	12.604	88.49	2625.75	718.78	27.37
0.25	26.910	7.564	12.530	88.63	2549.64	644.67	25.28
0.50	26.813	7.492	12.474	88.85	2505.27	602.15	24.04
0.75	26.691	7.413	12.430	88.85	2458.85	557.54	22.67
1.00	26.645	7.348	12.397	88.98	2426.96	527.45	21.73
1.25	26.548	7.276	12.360	88.99	2386.89	488.86	20.48
1.50	26.429	7.240	12.292	89.09	2351.57	455.34	19.36
1.75	26.396	7.194	12.278	89.24	2331.38	436.73	18.73
2.00	26.344	7.155	12.237	89.17	2306.28	412.94	17.91
2.25	26.333	7.120	12.157	89.42	2279.09	387.54	17.00
2.50	26.294	7.085	12.132	89.50	2259.87	369.74	16.36
2.75	26.239	7.050	12.110	89.65	2239.96	351.35	15.69
3.00	26.185	7.028	12.076	89.66	2222.13	334.79	15.07
3.25	26.145	7.004	12.031	89.72	2202.96	316.94	14.39
3.50	26.103	6.977	12.031	89.87	2191.17	306.72	14.00
3.75	26.089	6.954	11.975	89.97	2172.53	289.20	13.31
4.00	26.074	6.926	11.959	90.00	2159.44	277.48	12.85
4.25	26.010	6.909	11.932	90.12	2144.30	263.61	12.29
4.50	25.974	6.883	11.911	90.17	2129.35	250.07	11.74

3.2.2.2 Isolated molecules calculations

Density functional theory (DFT) calculations were performed on the isolated *NISac.Py* adduct, and on NISac and Py molecules, extracted from the crystal structure determined at ambient conditions. Intramolecular C-H bond distances were normalized to standard neutron distances and no geometry optimizations were done. Single point energy (SPE) calculations were performed using the Gaussian09 software (Frisch *et al.*, 2013) and the B3LYP functional, completed with dispersion corrections (Grimme *et al.*, 2010). The Def2TZVP basis set was employed for all atoms, including a pseudo-potential for I (Pritchard *et al.*, 2019). In the framework of the QTAIM methodology, topological calculations were carried out at the crystalline geometry of the adduct by using the AIMALL software (Keith, 2019) in order to characterize atomic charges (**Table 3.5**) and to study the electronic properties at $N_{sac}\cdots I$ and $I\cdots N_{py}$ BCPs. Afterwards, the I atom position was optimized, keeping the rest of the atoms frozen. Further, a full geometry optimization was done (using the same calculation level) for NISac and $[I\text{-}Py]^+$ moieties (the latter is a hypothetical case in which the I atom completely shifts to Py and a positive charge is distributed throughout the I-Py molecule).

Table 3.5 Bader's atomic charges (B3LYP-D3/Def2TZVPP) in *NISac.Py* isolated adduct and in NISac and Py isolated molecules extracted from the crystal structure at ambient conditions.

	NISac.Py	NISac	Py
Atom label	**Q (*e*)**	**Q (*e*)**	**Q (*e*)**
I1	0.48	0.42	
N1	-1.36	-1.29	
S1	3.15	3.15	
O1	-1.36	-1.35	
O2	-1.35	-1.33	
O3	-1.17	-1.14	
C1	0.02	0.03	
H1	0.05	0.06	
C2	0.01	0.02	
H2	0.02	0.03	
C3	0.01	0.02	
H3	0.02	0.03	
C4	0.03	0.04	
H4	0.05	0.06	
C5	-0.18	-0.17	
C6	0.00	0.01	
C7	1.42	1.42	
N2	-1.20		-1.13
C8	0.54		0.55
H8	0.07		0.02
C9	0.01		-0.02
H9	0.05		0.01
C10	0.02		0.00
H10	0.04		0.02
C11	0.02		-0.01
H11	0.05		0.01
C12	0.51		0.52
H12	0.08		0.03

3.2.2.3 Intermolecular interaction energy decomposition

CrystalExplorer (version 17.5; Turner *et al.*, 2017) software was used to calculate intermolecular interaction energies (calculated as total interaction energy between pairs of adducts) and their decompositions into electrostatic, polarization, dispersion and repulsive terms, employing the B3LYP functional and the DGDZVP basis set for all atoms. Intramolecular C-H bond distances were normalized to standard neutron distances. The TONTO option available in the software was used for the wavefunction calculation and a molecular shell of 3.80 Å in radius was generated in each case.

3.2.3 Results

3.2.3.1 Crystal structure description at ambient conditions

The crystal structure of the binary adduct composed of N-iodosaccharin and pyridine was already reported by Dolenc & Modec (2009) at ambient conditions. These authors published the structure in the space group setting $P2_1/a$ (cell choice No. 3 of space-group type No. 14, conventional space group setting is $P2_1/c$), with unit-cell parameters a = 12.6184(3) Å, b =7.8019(2) Å, c = 14.8718(4) Å and β = 113.6530(12)°. The authors collected the X-ray diffraction intensities up to a resolution of 0.65 $Å^{-1}$, for a total number of 5589 reflections (3044 unique reflections). However, the modest quality of the *NISac.Py* crystal resulted in large R_1 and wR_2 values (0.0879 and 0.2702 respectively), and a large residual electron density peak was also found in the final difference electron density map. Later, another attempt of data collection was made by Makhotkina *et al.* (2015), confirming the previously reported unit cell parameters but the structural solution was not accomplished due to the complex diffraction pattern measured.

In the current study, suitable good quality crystals were grown and selected with the aid of a polarized light microscope for the X-ray diffraction experiments at ambient conditions, allowing to obtain a better structural model as compared to the previous reports. Also, the authors of previous reports overlooked the fact that the lattice of their structure is strongly pseudo-orthorhombic (Dolenc & Modec, 2009). Indeed, an *mP* lattice with $-a/2c\cos(\beta)$ ratio of 1 actually corresponds to an *oB* lattice. The unit cell parameters of the $P2_1/a$ structure have a ratio $-a/2c\cos(\beta)$ = 1.06, indicating a strong metric pseudo-symmetry of the lattice. To emphasize this metric pseudo-symmetry, we refined our data in the unconventional setting $B2_1/e$ of the space group (Nespolo & Aroyo, 2016). The transformation of the co-ordinate system from $P2_1/a$ to $B2_1/e$ is **a**+2**c**,**b**,**a** (from the $P2_1/c$ setting, cell-choice No.1 of the space group, the transformation is 2**a**+**c**,**b**,**c**).

The crystallographic information for the data collected at ambient conditions for crystal-1 was given earlier in **Table 3.1**. The corresponding molecular structure (with atomic labels) determined in the asymmetric unit along with the position of first five residual Q-peaks are shown in **Figure 3.6a**. The same information for the crystal-2 collected at ambient conditions is shown in **Figure 3.6b**. In addition to these ambient conditions data collection, a low-

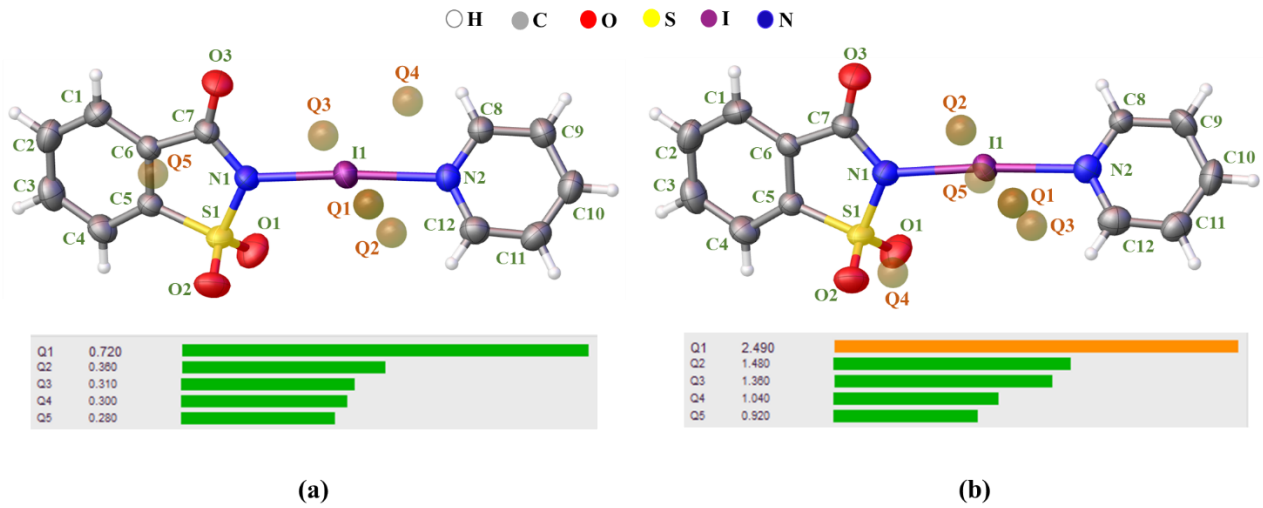

(a) **(b)**

Figure 3.6 First 5 residual density peaks obtained after the final refinement cycle for (a) crystal-1 and (b) crystal-2 data collected at ambient conditions outside MDAC. Atom types are shown with colouring scheme, residual peaks are labelled and the corresponding electron density values (in eÅ^{-3}) are given.

temperature data collection (100 K) was also carried out for crystal-1. The corresponding crystallographic data is given in **Table 3AP.2**.

In case of the *NISac.Py* binary adduct, the I atom lies in between the two N atoms of the parent compounds NISac and Py, resulting to a $N_{sac}\cdots I\cdots N_{Py}$ (alternatively called N1···I1···N2 according to the atomic numbering scheme) HaB interaction. From the analysis of the structural models it has been found that the I1 is located slightly closer to N1 than to N2, both at ambient conditions and at 100K. The corresponding N1···I1/I1···N2 HaB distances determined for crystal-1 at ambient conditions and 100 K respectively are 2.2305(17) Å/2.2876(16) Å and 2.2375(14) Å/2.2722(14) Å, up to a resolution of 0.694 Å^{-1}. Similarly, the HaB distances obtained for the crystal-2 are N1···I1 = 2.245(8) Å and I1···N2 = 2.291(8) Å, up to a resolution of 0.625 Å^{-1}. Therefore, in all these cases, a geometrical position of I closer to the donor moiety is observed. This confirms that, from the structural point of view a neutral co-crystal form of the binary adduct *NISac.Py* is obtained at ambient conditions.

In order to strengthen these geometrical findings, the following calculations were performed to analyse the electron density distribution of the *NISac.Py* binary adduct and thus to provide an electronic point of view of the HaB interactions (**Table 3.6**):

(1) SPE calculation carried out for the *NISac.Py* binary adduct.

(2) Iodine atom position optimization, while keeping all other atoms frozen, for the *NISac.Py* binary adduct.

(3) Full geometry optimization for NISac monomer.

(4) Full geometry optimization for $[I\text{-}Py]^+$ monomer.

In all cases, atomic co-ordinates were extracted from the crystalline geometry [for (3) and (4) the rest of the atoms in the adduct were omitted].

In case of **(1)**, the topological properties at N1···I1 and I1···N2 BCPs confirm that the I1 atom is more strongly bound to the saccharinate donor entity. Indeed, a larger quantity of electron density found in the bonding region of N1···I1 [ρ_{BCP}(N1···I1) > ρ_{BCP}(I1···N2)] with a less depleted character [$(\nabla^2\rho/\rho)_{BCP}$(N1···I1) < $(\nabla^2\rho/\rho)_{BCP}$ (I1···N2), $\nabla^2\rho$ is > 0 in both cases and normalized with respect to ρ because electron density of each nitrogen participating in the HaB are different] substantiate this conclusion. The same can also be concluded from the negative values of total electron energy density [H_{BCP}(N1···I1) < H_{BCP}(I1···N2)], or equivalently from the ratio between the electron potential V and kinetic energy G densities [$|V_{BCP}|/G_{BCP}$(N1···I1) > $|V_{BCP}|/G_{BCP}$(I1···N2)], both measuring the balance between V and G ($H_{BCP}=V_{BCP}+G_{BCP}$) and indicating a stronger bonding interaction at the saccharinate side. The delocalization index (DI) also supports the same situation being DI(N1···I1) > DI (I1···N2).

In case of **(2)**, the position of the halogen atom is determined more closer to the saccharinate moiety. Therefore, indicating the significant role of the crystal environment to the final geometry of the adduct, as previously shown by Aubert *et al.* (2017) with the *NISac.DMAP* adduct (where 4-dimethylaminopyridine acting as the HaB acceptor). In **(2)** also, all the topological and energetic properties at N1···I1 and I1···N2 BCPs suggest a much stronger interaction of I with the saccharinate moiety than with pyridine. The same behaviour of the laplacian function [$(\nabla^2\rho/\rho)_{BCP}$(N1···I1) > $(\nabla^2\rho/\rho)_{BCP}$ (I1···N2)] is occurred here as well.

On the other hand, considering **(3)** and **(4)**, the geometrical distances of I1 to N1 and to N2 are longer in the crystalline geometry than those found in case of the isolated monomers. The corresponding differences Δ(N1···I1) and Δ(I1···N2) found between crystal and gas phases are 0.195 Å and 0.203 Å, respectively.

Another interesting point to note in case of **(1)** concerns the bonding character of N1···I1 and I1···N2 interactions. Indeed, the topological and energetic properties at both BCPs suggest that they exhibit an intermediate character between pure closed-shell ($\nabla^2\rho_{BCP}$ > 0, H_{BCP} < 0, $|V_{BCP}|/G_{BCP}$ < 1) and pure shared-shell interactions ($\nabla^2\rho_{BCP}$ < 0, H_{BCP} < 0, $|V_{BCP}|/G_{BCP}$ > 2). Accordingly, they belong to the intermediate region where the electron density redistributes either to break or to form a chemical bond (Espinosa *et.al*, 2002). In addition, comparing with the corresponding properties of the NISac monomer in gas phase, the NI···I1 bond has been significantly weakened in the adduct as evident from the values of ρ_{BCP} and $|V_{BCP}|/G_{BCP}$ in the

bonding region. Thus, an incipient transfer of the halogen atom is already taken place from the donor to the acceptor moiety within the adduct at ambient conditions. It is also interesting to note that, in the monomers, the properties at N1···I1 and I1···N2 BCPs shows $\nabla^2\rho_{BCP} > 0$ and $1 < |V_{BCP}|/G_{BCP} < 2$, coming as a result of the highly depleted valence electrons of I and the weak N···I bond in both cases.

Thus, in spite I stays slightly closer to NISac than to Py, it can be concluded from the electronic analyses that the *NISac.Py* binary adduct at ambient conditions exhibits a neutral co-crystal character, even though an incipient halogen atom shift within the adduct results into a significant covalent degree both at donor and acceptor sides.

Table 3.6 Internuclear N1···I1 and I1···N2 distances experimentally determined and theoretically calculated. The gathered QTAIM topological properties of the electron density $\rho(r)$ at BCPs are: the electron density(ρ_{BCP}), its laplacian ($\nabla^2\rho_{BCP}$), the total energy density ($H_{BCP} = V_{BCP} + G_{BCP}$) as well as the ratio between the electron potential (V_{BCP}) and kinetic (G_{BCP}) energy densities ($|V_{BCP}|/G_{BCP}$), and its values normalized to ρ_{BCP}. The delocalization index at BCPs is denoted as $(DI)_{BCP}$. (1) – SPE calculation of *NISac.Py*, (2) – iodine atom optimization while keeping all other atoms frozen, (3) – full geometry optimization for NISac monomer and (4) – full geometry optimization for $[I\text{-}Py]^+$ monomer.

	(1)	(2)	(3)	(4)
Distance N1···I1(Å)	2.230	2.124	2.035	-
Distance N2···I1(Å)	2.288	2.398	-	2.085
ρ_{BCP} N1···I1 (eÅ^{-3})	0.578	0.707	0.860	
ρ_{BCP} I1···N2 (eÅ^{-3})	0.510	0.411	-	0.800
$\nabla^2\rho_{BCP}$ N1···I1 (eÅ^{-5})	2.73	3.56	3.52	
$\nabla^2\rho_{BCP}$ I1···N2 (eÅ^{-5})	3.13	2.73	-	3.04
$(\nabla^2\rho/\rho)_{BCP}$ N1···I1(Å^{-2})	4.72	5.04	4.09	
$(\nabla^2\rho/\rho)_{BCP}$ I1···N2(Å^{-2})	6.14	6.63	-	3.80
H_{BCP} N1···I1(a.u.)	-0.029	-0.042	-0.062	
H_{BCP} I1···N2(a.u.)	-0.022	-0.013	-	-0.055
$(H/\rho)_{BCP}$ N1···I1(a.u.)	-0.332	-0.405	-0.482	
$(H/\rho)_{BCP}$ I1···N2(a.u.)	-0.288	-0.218	-	-0.462
$(\|V\|/G)_{BCP}$ N1···I1	1.501	1.535	1.628	
$(\|V\|/G)_{BCP}$ I1···N2	1.401	1.320	-	1.635
$(DI)_{BCP}$ N1···I1	0.749	0.845	1.076	
$(DI)_{BCP}$ I1···N2	0.620	0.525	-	1.023

3.2.3.2 Energetic and electronic analyses of the intermolecular interactions at ambient conditions

The energetic analysis of the intermolecular interactions, performed with CrystalExplorer on the crystal structure determined at ambient conditions, reveals that the crystal packing is mostly governed by two main interactions (**Table 3.7**). The first one (total interaction energy of -80.9 kJ/mol) corresponds to the stacking of the adducts along the [010] direction. It involves π···π stacking interactions between the pyridine and the N-iodosaccharin rings (**Figure 3.7a**), as well as a favourable electrostatic interaction formed between a positively charged halogen atom I1 [Q(I) = +0.48 *e*] and a negatively charged pyridine N atom [Q(N_{py}) = -1.20 *e*] of neighbouring adducts [N2···I1(*1/2-x,1/2+y,1-z*) = 3.890 Å; I1···N2(*1/2-x,-1/2+y,1-z*) = 4.098 Å]. Following the energetic ranking of interactions, the next one corresponds to the formation of a dimer around an inversion centre (-79.4 kJ/mol), involving a couple of symmetry related HBs C10-H10···O1(*1/2-x,1-y,3/2-z*) ($d_{H\cdots O}$ = 2.47 Å, $\alpha_{C\text{-}H\cdots O}$ = 131°). Although of similar interaction energy, the energy decomposition shows that this second interaction is differently formed. Indeed, even showing a similar electrostatic contribution, they differ in dispersion and repulsion contributions, whose variations almost compensate each other. This is in line with the fact that aromatic rings are here observed at a longer distance than in the previous dimer interaction [inter-centroid distance Py···Py(*1/2-x,1-y,3/2-z*) = 4.885 Å] (**Figure 3.7b**).

These two main contacts form (200) *NISac.Py* adduct planes in the $B2_1/e$ setting, whose cohesion is reinforced by three additional interactions of the (*x,y,z*) reference adduct with neighbours (**Figure 3.8**). The first one involves the symmetry related molecule (*1/2-x,1-y,1/2-z*), forming a dimer around an inversion centre and being characterized by the HB C8-H8···O3(*1/2-x,1-y,1/2-z*) ($d_{H\cdots O}$ = 2.52Å, $\alpha_{C\text{-}H\cdots O}$ = 173°) and a relatively close favourable electrostatic interaction between I1 atom and a carbonyl O atom C7-O3··I1(*1/2-x,1-y,1/2-z*) [$d_{O\cdots I}$ = 4.244 Å, $\alpha_{C\text{-}O\cdots I}$ = 148°, Q(I1) = +0.48 *e*, Q(O3) = -1.17 *e*] (**Figure 3.9a**). The second interaction involves the symmetry related molecule (*x,1/2-y,-1/2+z*) through a unique HB C12-H12(*x,1/2-y,-1/2+z*)···O3 ($d_{H\cdots O}$ = 2.41Å, $\alpha_{C\text{-}H\cdots O}$ = 165°) (**Figure 3.9b**). Both of these interactions have a significant dispersion component, resulting in a total interaction energy of -25.9 and -22.6 kJ/mol, respectively.

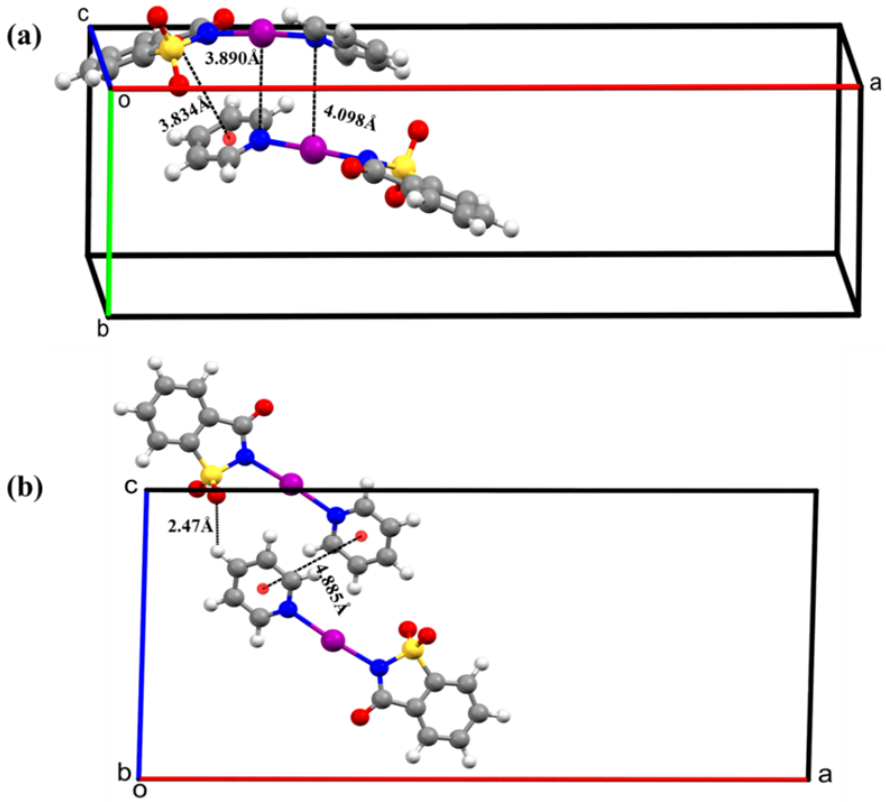

Figure 3.7 Dimers extracted from the *NISac.Py* crystal structure determined at ambient conditions: (a) strongest interaction of *NISac.Py* with its environment, involving a π···π stacking between the symmetry related (*x,y,z*) and (*1/2-x,-1/2+y,1-z*) adducts (b) interaction between the symmetry related (*x,y,z*) and (*1/2-x,1-y,3/2-z*) *NISac.Py* adducts. Characteristic distances (in Å) of relevant interactions (shown with black dashed lines) are depicted in the figures.

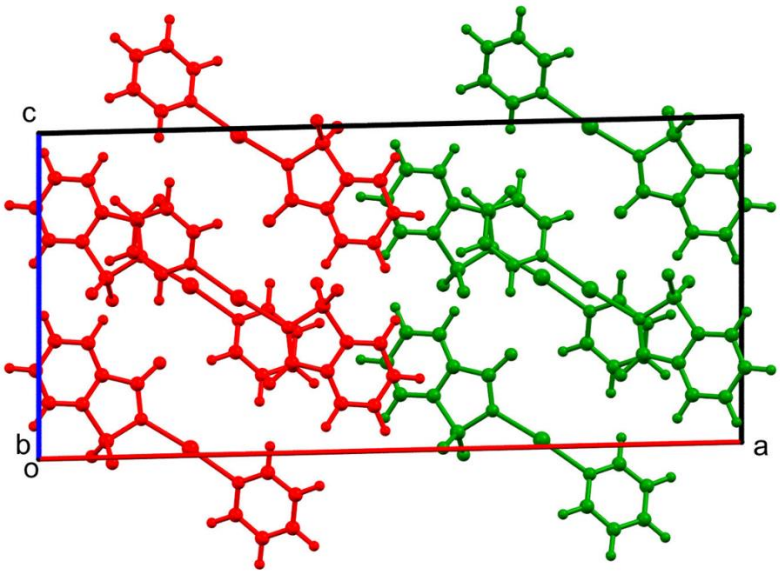

Figure 3.8 Molecular packing in the *NISac·Py* crystal structure determined at ambient conditions, highlighting the formation of (200) molecular planes whose cohesion is driven by the most intense interactions. Two such planes are depicted in green and red and interact through secondary less intense interactions.

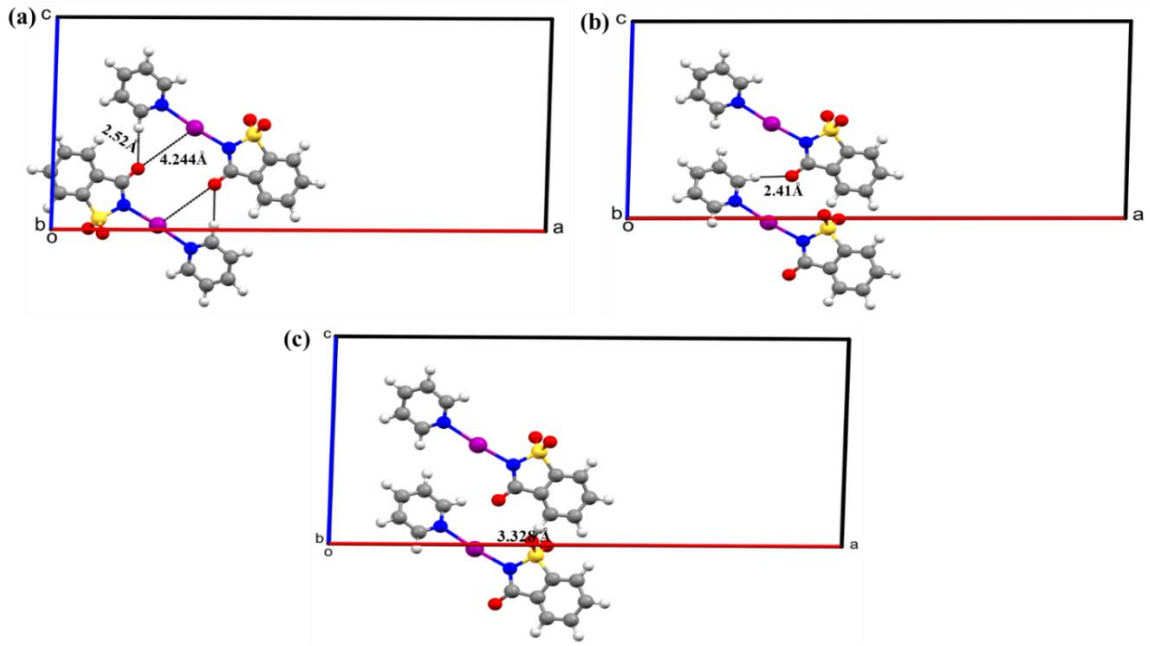

Figure 3.9 Intermolecular interaction formed between (*x,y,z*) and (a) (*1/2-x,1-y,1/2-z*), (b) (*x,1/2-y,-1/2+z*) and (c) (*x,3/2-y,1/2+z*) symmetry generated adducts in the *NISac.Py* crystal structure determined at ambient conditions. Characteristic distances (in Å) of relevant interactions (shown with black dashed lines) are depicted in the figures.

Finally, the third one involves the symmetry related molecule (*x,3/2- y,-1/2+z*), which is barely stabilizing and is characterized by the proximity between atom O1 of the sulfonyl group of the neighboring NISac entity and atom C1 of the π plane of the NISac molecule that is slightly electropositive in the adduct (**Figure 3.9c**) [$d_{C1\cdots O1}$ = 3.328 Å, Q(O1) = -1.36*e*, Q(C1) = +0.02 *e*]. Even though, this dimer interaction has a positive electrostatic component, the stabilization is mainly driven by the dispersion contribution to the total interaction energy.

Adjacent (200) adduct planes interact through two main interactions of moderate intensity (E_{int} = -27.2 and -22.3 kJ/mol). The first one, which has a significant electrostatic component (**Table 3.7**), corresponds to the formation of a cyclic HB between two NISac entities through the sulfonyl O atom and one H atom of the aryl ring C4-H4···O2 (*1-x,1-y,1-z*)($d_{H\cdots O}$ = 2.35Å, $\alpha_{C\text{-}H\cdots O}$ = 160°) (**Figure 3.10a**), whereas the second one involves a long C2-H2(*1-x,-1/2+y,1/2-z*)···O2 contact ($d_{H\cdots O}$ = 2.79 Å, $\alpha_{C\text{-}H\cdots O}$ = 130) with a stabilization that is mainly driven by the dispersion contribution due to the proximity of the aromatic rings (**Figure 3.10b**). Two additional minor interactions (E_{int} ~ -5 kJ/mol) are also present with mainly dispersion contributions, also corresponding to the proximity of aromatic rings (**Figure 3.10c** and **Figure 3.10d**).

The main conclusion derived from this energetic analysis is that the crystal structure of *NISac.Py* at ambient conditions is mainly composed of tightly held (200) planes, which are

largely formed by the interaction of the reference (*x,y,z*) adduct with (*1/2-x,-1/2+y,1-z*) and (*1/2-x,1-y,3/2-z*) symmetry generated adducts. Cohesion of such (200) planes are further supported by two moderately strong and one weak interaction, whereas the interactions across these (200) planes are comparatively weaker. Accordingly, the *NISac.Py* crystal structure exhibits a strong anisotropy of intermolecular interactions at ambient conditions and this might result to different compressibilities along the direction of different crystallographic axes on action of external pressure.

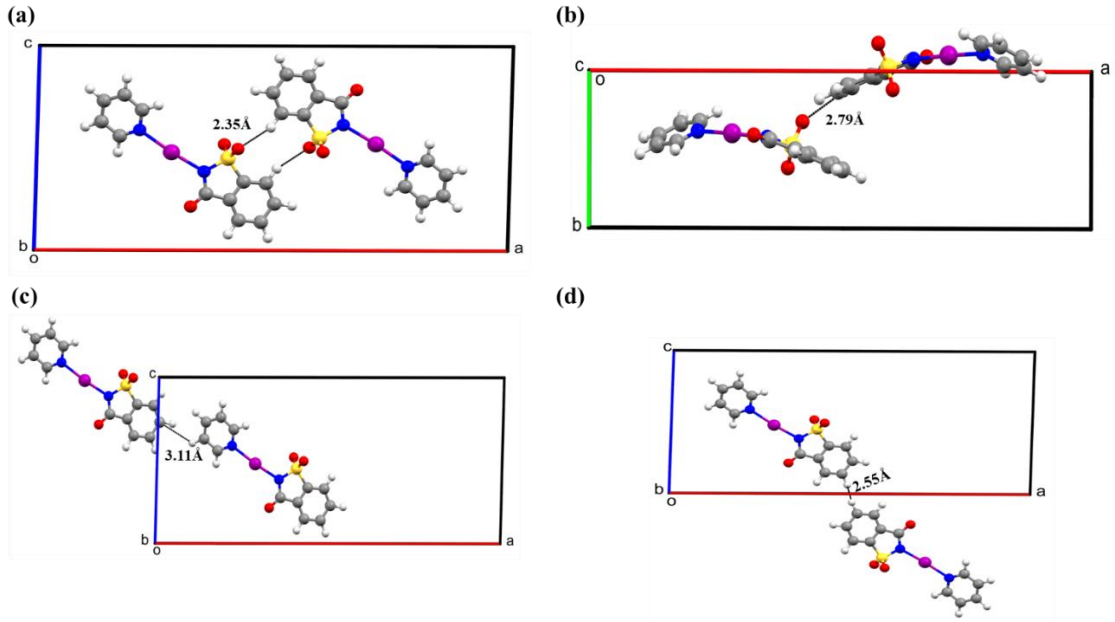

Figure 3.10 Intermolecular interaction formed between (*x,y,z*) and (a) (*1-x,1-y,1-z*), (b) (*1-x,-1/2+y,1/2-z*), (c) (*-1/2+x,y,1/2+z*) and (d) (*1-x,1-y,-z*) adducts in the experimental *NISac.Py* crystal structure at ambient conditions.

Table 3.7 Decomposition of the total interaction energy (E_tot) between dimers of *NISac.Py* adducts in electrostatic (E_ele), polarization (E_pol), dispersion (E_dis) and repulsion (E_rep) terms. Sym. Op denotes the symmetry code of the neighbouring adducts interacting with the reference (*x,y,z*) adduct (R is the intermolecular centroid to centroid distance). All energies are given in kJ/mol.

Sym. Op.	R (Å)	E_ele	E_pol	E_dis	E_rep	E_tot
1/2-x,-1/2+y,1-z [a]	5.74	-60.2	-6.8	-51.5	37.6	-80.9
1/2-x,1-y,3/2-z [a]	8.59	-60.5	-11.9	-29.7	22.7	-79.4
1-x,1-y,1-z	9.75	-23.1	-5.4	-12.7	14.1	-27.2
1/2-x,1-y,1/2-z [a]	6.53	-10.1	-7.9	-23.4	15.7	-25.9
x,1/2-y,-1/2+z [a]	7.01	-7.7	-8.1	-16.9	10.2	-22.6
1-x,-1/2+y,1/2-z	11.39	-12.7	-1.9	-17.4	9.7	-22.3
1/2+x,y,-1/2+z	14.87	0.3	-1.3	-6.4	2.5	-4.8
1-x,1-y,-z	14.66	-1.4	-0.3	-4.9	1.9	-4.6
x,3/2-y,1/2+z [a]	7.9	6.6	-2.6	-7.9	3.2	-0.9
[a] interactions ensuring cohesion of (200) molecular planes						

3.2.3.3 Equation of states (EOS)

Densification of solids under pressure is a main topic of interest among different research communities ranging from material chemistry to planetary science. Here, the fundamental question that one faces is the extent a material responds when subjected to a varying pressure. Numerous efforts have been made in the past to find a universal character to the compressibility of matter when exposed to high-pressure. These efforts eventually resulted to the concept of Equation of States (EOS), in which the intermolecular forces responsible for the resistance to compression are demonstrated with the help of properties determined at (or near to) ambient conditions.

In this study, the evolution of the unit cell volume as a function of pressure has been drawn for the experimental data and fitted with a 3rd order Birch-Murnaghan EOS (Angel, 2000) (the use of a 2nd order Birch-Murnaghan EOS resulted to an improper fitting), using the EosFit7-GUI software (Gonzalez *et al*, 2016). Both compression (blue circle data) and decompression (red circle data) data points can be fitted with the same EOS (**Figure 3.11a**), whereas fitting these two separately leads to equivalent fitting parameters but with larger standard deviations (**Figure 3.11b and Figure 3.11c**). **Figure 3.11a** also shows that the unit cell volume changes monotonically as a function of pressure (without any discontinuities), reducing ~20% in magnitude between the lowest and the highest measured pressures. The resulted EOS parameters are: reference volume V_0 = 2705(11) Å^3, bulk modulus K_{T_0}= 7(1) GPa and first derivative of the bulk modulus K_{T_0}' = 11(3). A small bulk modulus (typically < 10 GPa) is a characteristic of a soft material (like an organic crystal) where the intermolecular interactions are mainly dominated by dispersion forces and/or electrostatic interactions. On the other hand, a larger bulk modulus (typically close to 100 GPa) is often found with minerals (Comodi *et.al*, 2001). Also, considering the uncertainties associated with applied pressures, it is evident that all data points are statistically lying in the EOS curve (black dotted lines in **Figure 3.11a**). Therefore, no hysteresis is found with the compression-decompression cycle. In other words, the shrinking of unit cell volume during the compression process shows a reversible recovery on its expansion *via* the decompression process.

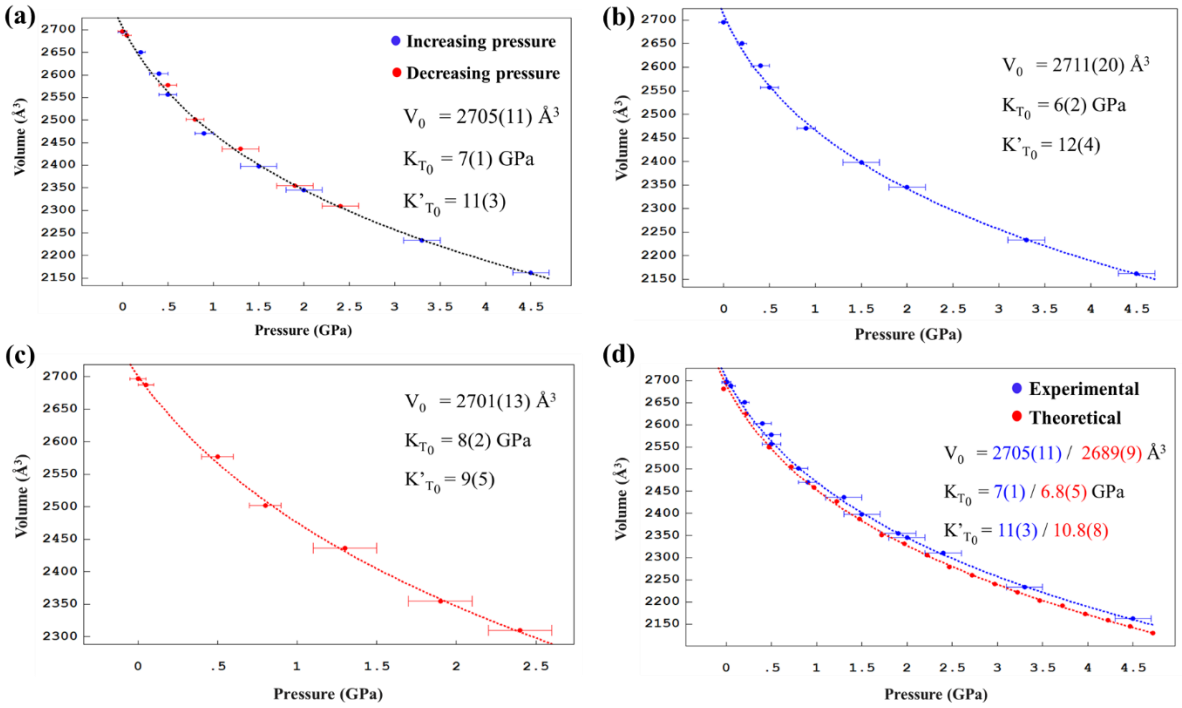

Figure 3.11 Variation of the unit cell volume as a function of pressure fitted with the 3rd order Birch-Murnaghan EOS: (a) experimental dataset with increasing and decreasing pressures (blue circles: increasing pressure data, red circles: decreasing pressure data, black dotted line: EOS fitting curve) (b) experimental dataset with increasing pressures only (blue circles: increasing pressure data, blue dotted line: EOS fitting curve) (c) experimental dataset with decreasing pressures only (red circles: decreasing pressure data, red dotted line: EOS fitting curve) (d) experimental and theoretical data plotted together (blue circles: experimental data, blue dotted line: experimental EOS fitting curve, red circles: theoretical data, red dotted line: theoretical EOS fitting curve). In (d), theoretical pressure values are corrected as described in the text.

In order to validate these experimental findings, EOS is also drawn for the theoretical data using the same 3rd order Birch-Murnaghan EOS (**Figure 3.11d**). The fitting resulted to an overall reduction of ~21% in unit cell volume, with the corresponding EOS parameters V_0 = 2689(9) Å^3, K_{T_0} = 6.8(5) GPa and K_{T_0}'= 10.8(8). All these values show quite good agreement with the experimental results. **Figure 3.11d** also reveals that both the experimental (blue dotted lines) and the theoretical (red dotted lines) EOS curves are in good agreement to each other. The small off-set observed between them might be associated with the temperature effect, considering that all the theoretical data are calculated omitting this thermodynamic parameter. However, to compensate this temperature effect a global pressure shift was applied to theoretical data (while generating EOS) in order to have a similar unit cell volume for experiment and theory at 0GPa.

3.2.3.4 Variations of unit cell parameters with pressure

The plot of relative changes in the unit cell parameters as a function of pressure shows different behaviors (compressibilities) along each crystallographic axis. This feature might be a consequence of anisotropic strain generated in the crystal, resulting from the anisotropy of

intermolecular interactions found in the crystal packing (see **section 3.2.3.2**). For experimental data, **Figure 3.12a** shows the variations with the pressure of the unit cell parameters [relative to the values a_0, b_0 and c_0 determined at 0.00(5) GPa, the starting pressure taken as the reference], indicating that the compressibility along the *b*-direction is more pronounced than along *c*- or *a*-direction. In addition, the percentage compressibilities were calculated along each unit cell axis direction using the ratio $\Delta l/l_0$ (l = *a*, *b* or *c*), where $\Delta l = l_{0.00(5)\,GPa} - l_{4.5(2)\,GPa}$. This resulted to a maximal compressibility of 11% along the *b*-direction, followed by 5.5% along the *c*-direction. The crystal structure is more rigid along the *a*-direction, with a compressibility of only 4.7% between the lowest and the highest achieved pressure. A similar trend is observed with theoretical data (**Figure 3.12a**), where also the maximal compressibility shown along the *b*-direction. Furthermore, the percentage compressibilities obtained from the theoretical dataset are in good agreement with the experimental ones: 12.1% for the *b*-direction, followed by 5.9% and 4% for the *c*- and *a*-directions, respectively. At the same time, the monoclinic angle relative to the value measured at the starting pressure [β_0 at 0.00(5) GPa, taken as the reference] increases as a function of pressure in both experimental and theoretical datasets (**Figure 3.12b**).

However, in case of crystals with lower symmetry (especially monoclinic and triclinic classes) variations in whole set of unit cell parameters (*a*, *b*, c, α, β and γ) are necessary to understand the compression process, thus making individual analysis of the unit cell parameters inadequate. Actually, in those cases, the analysis of principal axes of compression and the corresponding principal compressibility values are required to understand the fundamental mechanical responses of the crystal with pressure. These principal axes of compression are determined as the eigenvectors of the strain tensor matrix, which are not necessarily oriented parallel to the unit cell axes. Accordingly, the principal strains and the principal axes are calculated as the eigenvalues ε_i and eigenvectors X_i of the strain tensor matrix ε. The derivatives of these principal strains with respect to pressure gives the principal compressibility value along each direction K_i (**Equation 3.1**).

$$K_i = -\left(\frac{\partial \varepsilon_i}{\partial p}\right)_T \qquad 3.1$$

In our case, these values were calculated using PASCal (Principal Axis Strain Calculator) web-tool (Cliffe and Goodwin, 2012; **Table 3.8**), for both experimental and theoretical datasets. The first principal axis of compression (denoted as X_1) is placed along the crystallographic *b*-

direction in both cases, while the corresponding compressibility value (denoted as K_1) were calculated respectively as ~27(2) and ~18.9(8) TPa^{-1} for experimental and theoretical datasets. The second and the third principal axes of compression are oriented in the *ac*-plane. **Figures 3.12c** and **Figures 3.12d** respectively shows the compressibility indicatrix for experimental and theoretical data, which is a three-dimensional representation of the compressibilities oriented with respect to the crystallographic axes landmark. In this representation, the origin of the compressibility indicatrix is the same as that of the unit cell, whereas the distance between the origin and any point in the indicatrix surface in a given direction **r** is equal to the magnitude of *K* in that particular direction. In both cases, only positive compressibilities are found in all directions leading to red surfaces only, as evident from compressibility indicatrix plots.

Table 3.8 Principal axes of compression and the corresponding compressibility values determined from the high-pressure datasets of *NISac.Py*: Xi (principal axis-i of compressibility), K_i (principal compressibility value) and $\sigma(K_i)$ (standard deviation of the principal compressibility value, given within brackets). Experimental/ theoretical results are gathered as left/right entries.

Principal axis, X_i	K_i (TPa^{-1})	Components of X_i along the crystallographic axes		
		a	b	c
1	27(2)/18.9(8)	0.0000/0.0000	-1.0000/-1.0000	0.0000/0.0000
2	15(1)/12.5(2)	0.3432/0.2469	0.0000/0.0000	0.9393/0.9691
3	9.1(4)/ 5.7(3)	0.5013/0.6369	0.0000/0.0000	-0.8653/-0.7709

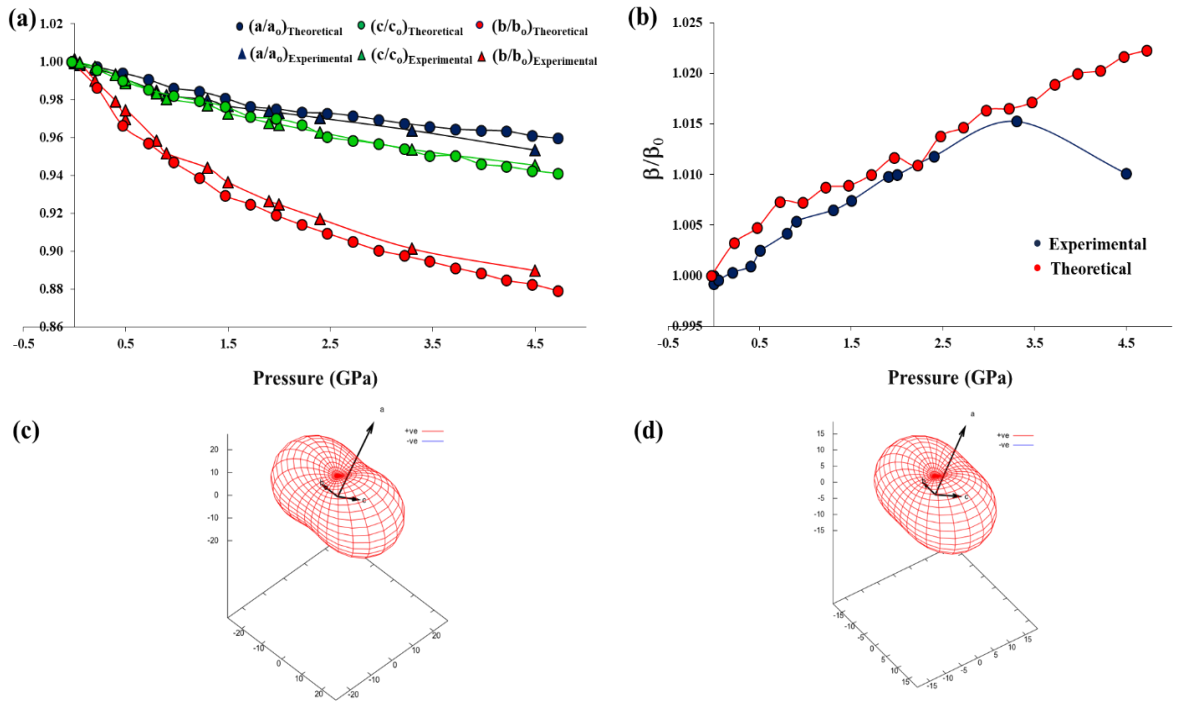

Figure 3.12 Relative variations with pressure of (a) unit cell parameters and (b) unit cell β–angle, for experimental and theoretical datasets, curves connecting data are plotted for guiding eyes. Compressibility indicatrix plots depicted for (c) experimental and (d) theoretical datasets.

3.2.3.5 Mechanical twinning

A mechanical twinning is observed under compression, the twinned sample presenting two domains spanning unequal volumes. Larger and smaller domains are hereafter called domain-1 and domain-2, respectively. The two domains are mapped by a two-fold rotation along the [100] direction of the unit cell, acting as the twin operation. **Figure 3.13** shows the percentage variation in the domain 2 volume as a function of pressure. This percentage is obtained from the BASF (batch scale factor) parameter, which is estimated during the refinement of high-pressure structures (**Table 3.2** and **Table 3.3**). Domain 2 was not detected (~ 0%) at 0.00(5) GPa and gradually increases with pressure, reaching a value of 14.48(13) % at 4.5(2) GPa. The PTM used in this study (Daphne oil 7474) is known to solidify at 3.7 GPa at room temperature (Murata *et al.*, 2008), a feature that may cause non-hydrostatic condition inside the sample chamber. In this respect, it has been observed experimentally that the percentage of domain 2 increases monotonically with compression up to 3.3(2) GPa. Increasing the pressure further, beyond the value at which PTM is expected to solidify, the percentage of domain 2 decreases slightly [15.02(9) % at 3.3(2) GPa and 14.48(13) % at 4.5(2) GPa]. On releasing the pressure, domain 2 reduces to 8.8(2) % at 2.4(2) GPa and finally it disappears (~0%) after the complete removal of the applied pressure. Hence, after a complete cycle of compression-decompression, it can be concluded that the mechanical twinning is reversible and the percentage of domain 2 is dependent on the applied pressure.

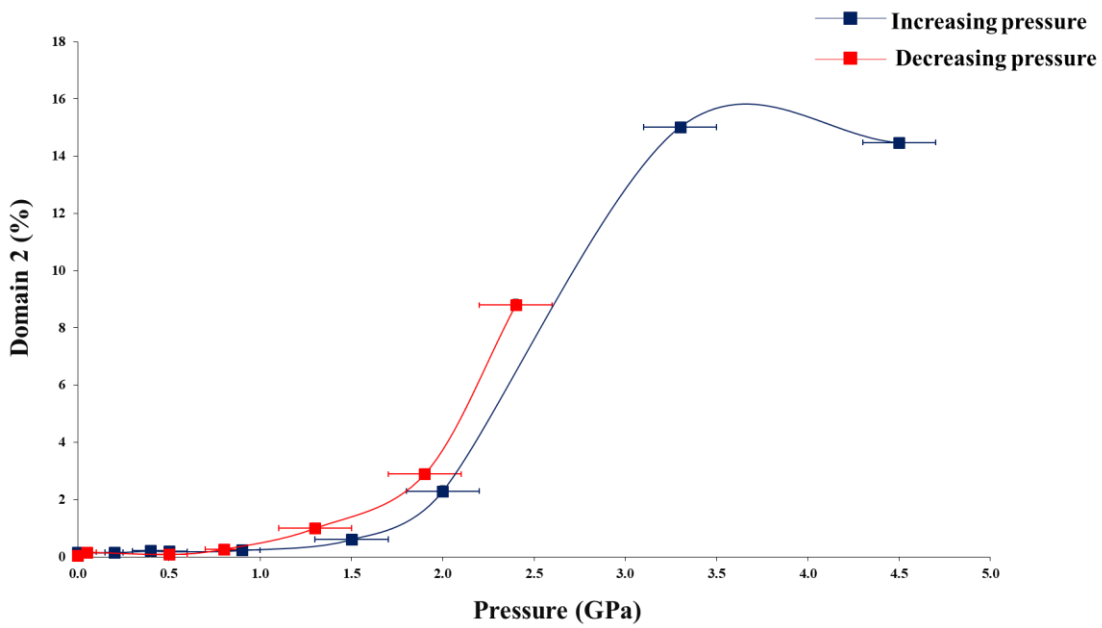

Figure 3.13 The percentage variation of domain 2 plotted as a function of pressure, curves connecting data are plotted for guiding eyes. The error bar corresponding to the percentage variation of domain 2 is small enough to be visible in the plot.

3.2.3.5.1 Structure rationale for twinning

In *NISac.Py*, the structural models were refined in an unconventional setting $B2_1/e$ of the space group to put in evidence the strongly pseudo-orthorhombic symmetry of the lattice, with β angle very close to 90° (**Table 3.2** and **3.3**). In the $B2_1/e$ space group setting, the twin operation is a simple two-fold rotation along the [100] direction of the unit cell, whereas it stands along the [201] direction in the conventional $P2_1/c$ space group setting. Accordingly, the description of twinning becomes comparatively simpler when considering a pseudo-orthorhombic cell. Further, the structure rationale behind this mechanical twinning has been investigated based on the crystallographic orbital approach, in collaboration with *Prof. Massimo Nespolo*, Laboratory of Crystallography, Magnetic Resonance and Modeling (CRM2), University of Lorraine. The details of this analysis can be found in Vijayakumar-Syamala *et al.* (2022).

The main point to note down from this analysis is that, structure of the twinned sample has revealed the continuity of a substantial substructure across the composition plane, where composition plane is characterized as the interface between two twin individuals in case of a mechanical twin [(100) in our case]. The presence of this common substructure in the two orientations of the twinned individuals is interpreted as a structural reason for the formation of the twin and interestingly it is the first observed example in a molecular crystal.

3.2.3.5.2 Energetic analysis of mechanical twinning

In this section, the energetic cost for the formation of a mechanical twin in *NISac.Py* will be discussed. Here, I would like to thank *Dr. Emmanuel Aubert*, Laboratory of Crystallography, Magnetic Resonance and Modeling (CRM2), University of Lorraine for the calculation and analysis of the data.

As described earlier, the crystal structure of *NISac.Py* is mainly composed of strongly held (200) planes bonded through some comparatively weaker interactions. The two-fold rotation twin operation seen along the [100] direction of the unit cell is actually quasi-perpendicular to these (200) planes. Also, (100) composition plane that characterized as the interface between two domains is found quasi-perpendicular to the twin axis (**Figure 3.14**). DFT periodic calculations were performed in order to quantify the energetic cost of twinning at this composition plane. Calculations were carried on the experimental structure obtained at 3.3(2) GPa (which is the best structural model determined among all), H atoms were normalized to neutron distances. Since we are interested in the (100) composition plane, the NISac and Py

molecules closest to the x = 0 and x = 1 are only considered here [that is, molecules interacting across the strongly held (200) are not considered], defining sub-slabs A and B, respectively. Two structural models were then built (**Figure 3.15**). The first one corresponds to the untwinned structure (sub-slabs A and B are from the original structural model), whereas in the second one the sub-slab B is modified by accommodating the molecules coming from the twin two-fold rotation operation along [100], thus creating, due to the periodic boundary conditions of the calculation, the twin composition plane A/B. SPE calculations were performed using identical conditions on these two models, and also on models considering only sub-slab A and B separately. The x = 0 interface in both cases (untwinned and twinned) is observed to be stabilizing, the AB system being lower in energy than that resulting from the addition of those corresponding to the isolated A and B systems. The stabilizing energy difference between the untwinned and the twined interface in only 6.4 kJ/mol in favour to the former structure. In other words, since the interface consists of four *NISac.Py* adducts, the twinning of this structure costs only 1.6 kJ/mol per *NISac.Py* adduct.

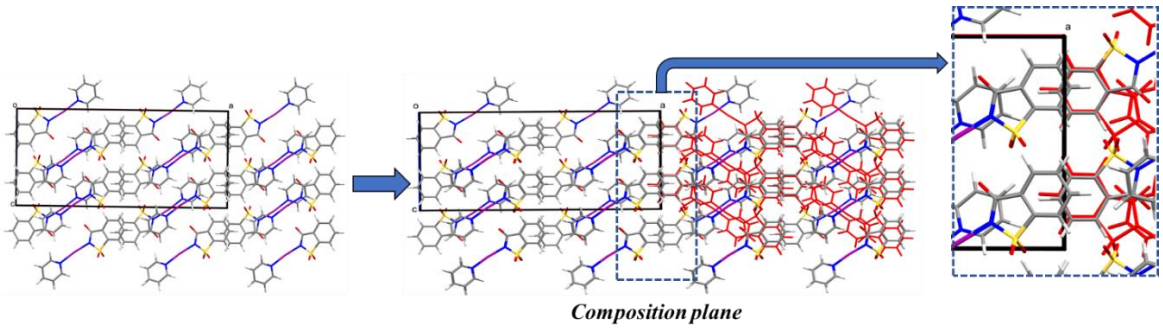

Figure 3.14 Two domains forming at the interface of (100) composition plane, domain 1 is shown with elemental colouring scheme and domain 2 is shown with red colouring. A portion around the interface is highlighted in an enlarged view.

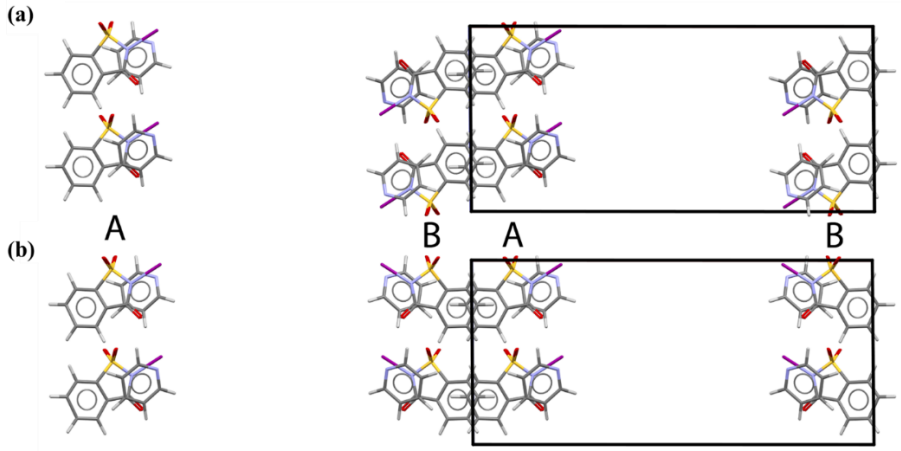

Figure 3.15 Structural models used to calculate the stabilization energy cost of the twining: (a) original (untwinned) *NISac.Py* structure with the central part of the unit cell deleted, described as sub-slabs A and B (b) Twin interface created by appropriate two-fold rotation of sub-slab B.

3.2.3.6 Variation of intermolecular interactions with pressure

It has been observed from the EOS analysis that, on compression, the unit cell volume reduces by ~20% for both experimental and theoretical datasets. This induces a variation in the relative positions of the molecular complexes in space, in most cases approaching towards each other. However, for some of them, either they do not change their relative distances significantly (due to the less compressible behaviour of specific intermolecular interactions) or they separate slightly from each other. Accordingly, these variations can induce changes in the intermolecular interaction patterns, and sometimes at high-pressure new intermolecular interactions are also formed.

One of the most important intermolecular interactions that form *NISac.Py* crystal structure is the N1···I1···N2 HaB motif. The structural modifications of this interaction have been investigated as a function of external pressure, both experimentally and theoretically. It has been observed that, on hydrostatic compression, the N1···N2 distance decreases gradually along with the variation in individual N1···I1 and I1···N2 distances (**Table 3.9**). Thus, in order to determine the relative shift of the I atom from the donor to the acceptor entity, we have followed the evolving behaviour of N1···I1 and I1···N2 distances normalized to that of N1···N2. **Figure 3.16a** shows the variation of the normalized distance (N1···I1)/(N1···N2) as a function of the pressure for both experimental and theoretical data. The horizontal black dotted line indicates the middle position (normalized distance ratio of 0.5) between N1···N2, guiding whether I1 is closer to the donor N atom (N_{sac}) or to the acceptor N atom (N'_{py}) at each pressure. Following the pressure evolution, I atom shifts slightly closer to N2 above 1 GPa, but is still very close to the middle position between donor and acceptor. Therefore, this feature does not permit us to conclude anything about the transfer of the I1 atom from the donor to the acceptor entity, but rather points to an intermediate situation where both donor and acceptor exert a similar interaction strength on the I atom. In addition to the fact that the donor and acceptor entities are electronically different (and therefore the middle position between them cannot be considered as the exact transition boundary in the halogen atom transfer), the large uncertainties associated with these structural distances hinder any conclusion about the precise position of I1 atom within the adduct. These large uncertainties are mainly associated with the poor completeness of the HP-SCXRD data, which is close to 40% up to a resolution of 0.56 $Å^{-1}$ in all datasets (see the **section 3.2.3.7**).

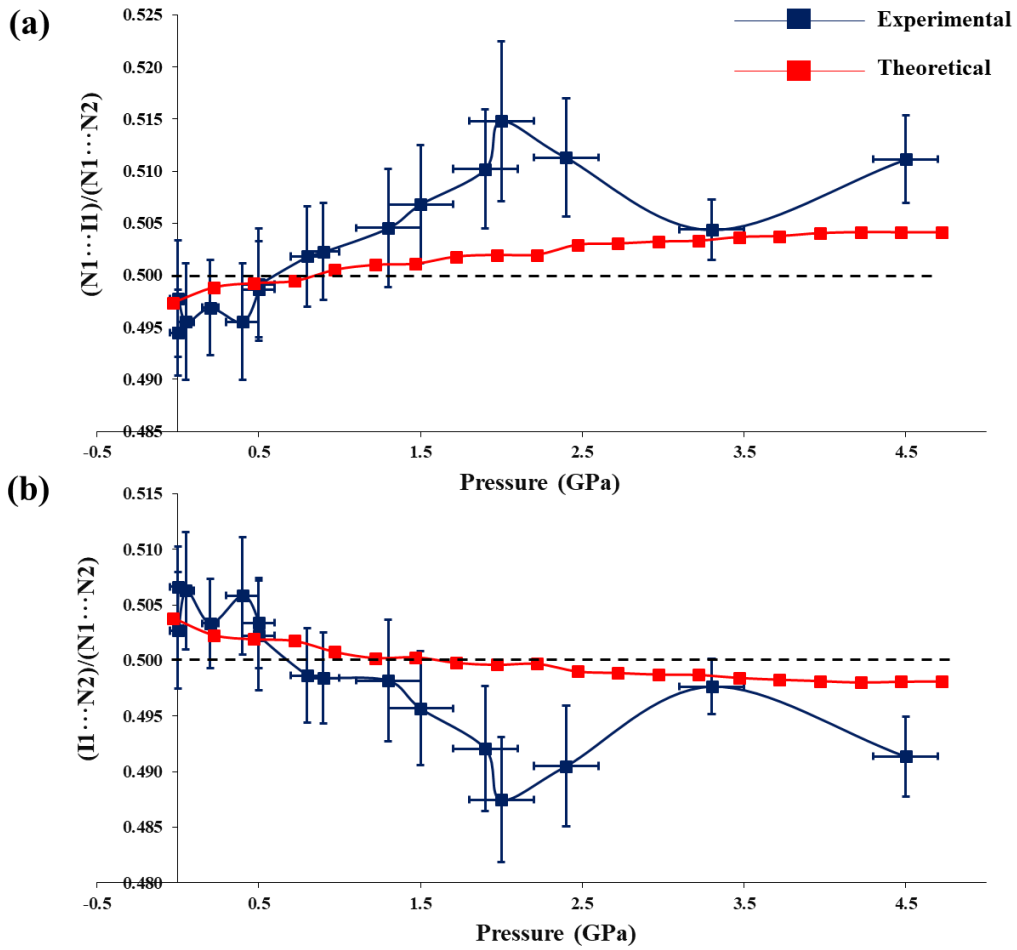

Figure 3.16 Variation of normalized HaB distances (a) (N1···I1)/(N1···N2) and (b) (I1···N2)/(N1···N2), as a function of pressure. Curves connecting data are plotted for guiding eyes. Error bars are shown for experimental data.

The main conclusion that can be derived from this analysis is that *NISac.Py* binary adduct at high-pressure can be considered more as a single molecular unit rather than two separate entities, the latter is resulting in case of a neutral co-crystal or a salt form with complete halogen atom transfer. This argument can be supported by the geometrical position of I atom within the adduct being close to the middle of saccharinate and pyridine moieties at any investigated pressure, exerting similar interaction strength at each side.

To further study this HaB interactions, topological calculations of the electron density distribution was also carried out on the isolated *NISac.Py* adducts extracted from the crystal structure determined at each applied pressure. This is expected to give more insight into the bonding properties of N1···I1 and I1···N2, as well as about the state of *NISac.Py* binary adduct under evolving pressure. The results are discussed in the section below.

Table 3.9 N1···I1···N2 HaB distances and angles, and angle between donor and acceptor molecular planes, determined from the experimental high-pressure datasets of *NISac.Py*. The angle between molecular planes was calculated using the MPLA option in Olex2-1.3. Values within brackets are the standard deviations of the corresponding values.

Pressure (GPa)	**0.00 (5)**	**0.00 (5)**	**0.05 (5)**	**0.20 (5)**	**0.4 (1)**	**0.5 (1)**	**0.5 (1)**	**0.8 (1)**	**0.9 (1)**	**1.3 (2)**	**1.5 (2)**	**1.9 (2)**	**2.0 (2)**	**2.4 (2)**	**3.3 (2)**	**4.5 (2)**
N1···I1 (Å)	2.240 (16)	2.23 (2)	2.21 (2)	2.231 (18)	2.21 (2)	2.214 (18)	2.231 (19)	2.233 (19)	2.220 (18)	2.22 (2)	2.23 (2)	2.25 (2)	2.26 (3)	2.26 (2)	2.248 (11)	2.249 (16)
I1···N2 (Å)	2.295 (13)	2.252 (18)	2.258 (18)	2.26 (15)	2.256 (18)	2.235 (15)	2.245 (16)	2.219 (16)	2.203 (15)	2.192 (19)	2.181 (17)	2.17 (2)	2.14 (2)	2.168 (19)	2.218 (9)	2.162 (13)
N1···N2 (Å)	4.53 (2)	4.48 (3)	4.46 (3)	4.49 (2)	4.46 (3)	4.44 (2)	4.47 (3)	4.45 (2)	4.42 (2)	4.40 (3)	4.40 (3)	4.41 (3)	4.39 (3)	4.42 (3)	4.457 (13)	4.400 (18)
(N1···I1)/ (N1···N2)	0.494 (4)	0.498 (6)	0.496 (6)	0.497 (5)	0.496 (6)	0.499 (5)	0.499 (5)	0.502 (5)	0.502 (5)	0.505 (6)	0.507 (6)	0.510 (6)	0.515 (8)	0.511 (6)	0.504 (3)	0.511 (4)
(I1···N2)/ (N1···N2)	0.507 (4)	0.503 (5)	0.506 (5)	0.503 (4)	0.506 (5)	0.50 3(4)	0.502 (5)	0.499 (4)	0.498 (4)	0.498 (5)	0.496 (5)	0.492 (6)	0.487 (6)	0.490 (5)	0.498 (2)	0.491 (4)
N1···I1···N2 (°)	174.5 (3)	174.1 (5)	174.6 (5)	174.4 (4)	174.5 (5)	174.3 (4)	173.9 (5)	173.7 (5)	173.5 (4)	173.3 (6)	172.9 (5)	172.2 (6)	171.9 (7)	172.3 (6)	172.8 (8)	172.0 (4)
Angle (°)	41.7 (2)	42.4 (3)	41.8 (3)	42.1 (3)	41.5 (3)	41.6 (2)	41.8 (3)	42.0 (3)	41.5 (2)	42.1 (3)	41.6 (3)	41.6 (3)	42.1 (3)	41.6 (3)	41.6 (1)	42.6 (2)

Table 3.10 N1···I1··· N2 HaB distances and angle, and angle between donor and acceptor molecular planes, determined from the theoretical high-pressure datasets of *NISac.Py*. The angle between molecular planes was calculated using Mercury (version 2021.1).

Pressure (GPa)	**-0.03**	**0.22**	**0.47**	**0.72**	**0.97**	**1.22**	**1.47**	**1.72**	**1.97**	**2.22**	**2.47**	**2.72**	**2.97**	**3.22**	**3.47**	**3.72**	**3.97**	**4.22**	**4.47**	**4.72**
N1···I1 (Å)	2.273	2.276	2.274	2.272	2.275	2.274	2.273	2.274	2.271	2.271	2.271	2.271	2.269	2.269	2.269	2.265	2.266	2.265	2.264	2.263
I1···N2 (Å)	2.303	2.292	2.287	2.283	2.276	2.271	2.269	2.265	2.261	2.261	2.253	2.252	2.248	2.248	2.245	2.241	2.240	2.237	2.237	2.236
N1···N2 (Å)	4.570	4.563	4.556	4.549	4.545	4.540	4.536	4.532	4.525	4.525	4.516	4.514	4.508	4.508	4.505	4.497	4.496	4.492	4.491	4.488
(N1···I1)/ (N1···N2)	0.497	0.499	0.499	0.499	0.501	0.501	0.501	0.502	0.502	0.502	0.503	0.503	0.503	0.503	0.504	0.504	0.504	0.504	0.504	0.504
(I1···N2)/ (N1···N2)	0.504	0.502	0.502	0.502	0.501	0.500	0.500	0.500	0.500	0.500	0.499	0.499	0.499	0.499	0.498	0.498	0.498	0.498	0.498	0.498
N1···I1···N2 (°)	174.4	174.7	174.5	174.4	174.2	174.4	174.0	173.6	173.7	173.4	172.9	172.9	172.8	172.8	172.6	172.7	172.4	172.5	172.4	172.4
Angle (°)	42.42	42.06	41.63	41.42	41.01	40.78	40.68	41.73	41.02	41.36	42.20	42.10	42.11	42.21	42.53	42.18	42.86	42.73	43.00	42.92

Once a full cycle of compression–decompression is reached, the unit cell parameters and the unit cell volume regain their initial values, and the *NISac.Py* complex (including I) is back to its initial geometry. The same trend was observed with the theoretical data as well (**Table 3.10**), where the transition of I1 above the middle point between N1 and N2 happened in the same range of pressure, thus validating the experimental results. On the other hand, as the N1···I1···N2 angle is close to 180° at any investigated pressure, the normalized distance (I1···N2)/(N1···N2) evolves in the opposite way to (N1···I1)/(N1···N2) as a function of pressure (**Figure 3.16b**). Within the investigated range of pressures, the N1···I1···N2 angle shows a maximum variations of only 2.70° and 2.34° for the experimental and theoretical data, respectively (**Table 3.9**, **Table 3.10** and **Figure 3.17a**), while the angle between the molecular planes formed by the saccharinate ring (excluding I and H atoms) and the pyridine ring (excluding H atoms) remains mainly unchanged (only very small variations of 1.17° and 2.32° are observed for the experimental and theoretical data, respectively) (**Table 3.9**, **Table 3.10** and **Figure 3.17b**).

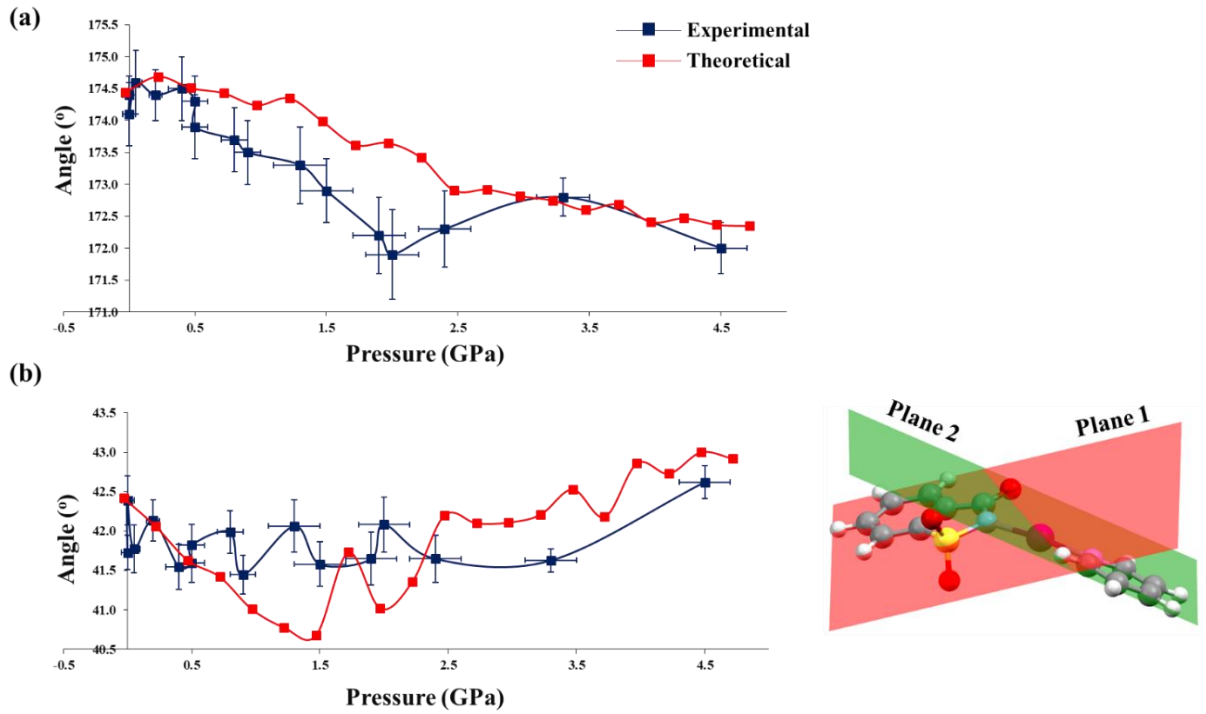

Figure 3.17 Variations of: (a) N1···I1···N2 angle and (b) angle between molecular planes, as a function of pressure. Molecular planes are defined by the saccharinate ring – Plane 1 (excluding I and H atoms) and the pyridine ring – Plane 2 (excluding H-atoms), highlighted with red and green colours, respectively. Error bars are shown for experimental data. Lines connecting data are plotted for guiding eyes.

In order to investigate the effect of crystalline environment on halogen atom shift, selected non-covalent interactions around I1 were studied as a function of pressure. For the structure determined at ambient conditions, four of the nine independent crystallographic dimers exhibit an intermolecular interaction involving I1 [namely, those formed by central (*x*,*y*,*z*) adduct and another one generated by either of the symmetry operations: (i) (*1/2-x*,*-1/2+y*,*1-z*), (ii) (*1/2-x*,*1-y*,*3/2-z*), (iii) (*x*,*1/2-y*,*1/2+z*) or (iv) (*1/2-x*,*1/2+y*,*1-z*)]. The experimental distances of intermolecular interactions involving I1 in the above-mentioned dimers decreases monotonically with increasing pressure, whereas the observed HB angles with I1 show a non-monotonic behaviour and do not deviate significantly from their initial values (**Table 3AP.3**, **Figure 3.18** and **Figure 3.19**).

The theoretical distances are in quite good agreement with the experimental ones, following very similar trends (**Table 3AP.4**, **Figure 3.18** and **Figure 3.19**). Considering the experimental reduction ratio RR values, out of the ten contacts the I1(*x*,*y*,*z*)···C8(*1/2-x*,*-1/2+y*,*1-z*) interaction seems the most significant one at 4.5 (2) GPa [$RR_{4.5\ (2)\ GPa}$ = 0.91], followed by I1(*x*,*y*,*z*)···I1(*1/2-x*,*-1/2+y*,*1-z*) [$RR_{4.5\ (2)\ GPa}$ = 0.96] and then I1(*x*,*y*,*z*)···H8(*1/2-x*,*-1/2+y*,*1-z*) [$RR_{4.5(2)\ GPa}$ = 0.96]. On the other hand, the maximal variation in RR is observed for the I1(*x*,*y*,*z*)···I1(*1/2-x*,*-1/2+y*,*1-z*) interaction [Δ(RR)= 0.14], followed by I1(*x*,*y*,*z*)···O3(*x*,*1/2-y*,*1/2+z*) interaction [Δ(RR)= 0.14]. A similar behavior is observed with the theoretical data as well, where maximal changes occur for I1(*x*,*y*,*z*)···O3(*x*,*1/2-y*,*1/2+z*) [Δ(RR) = 0.15] and I1(*x*,*y*,*z*)···I1(*1/2-x*,*-1/2+y*,*1-z*) [Δ(RR) = 0.14] interactions. Also, for the other intermolecular interactions, RR values at 4.5(2) GPa and ΔRR descriptors show a good agreement between experimental (**Table 3AP.3**) and theoretical (**Table 3AP.4**) results.

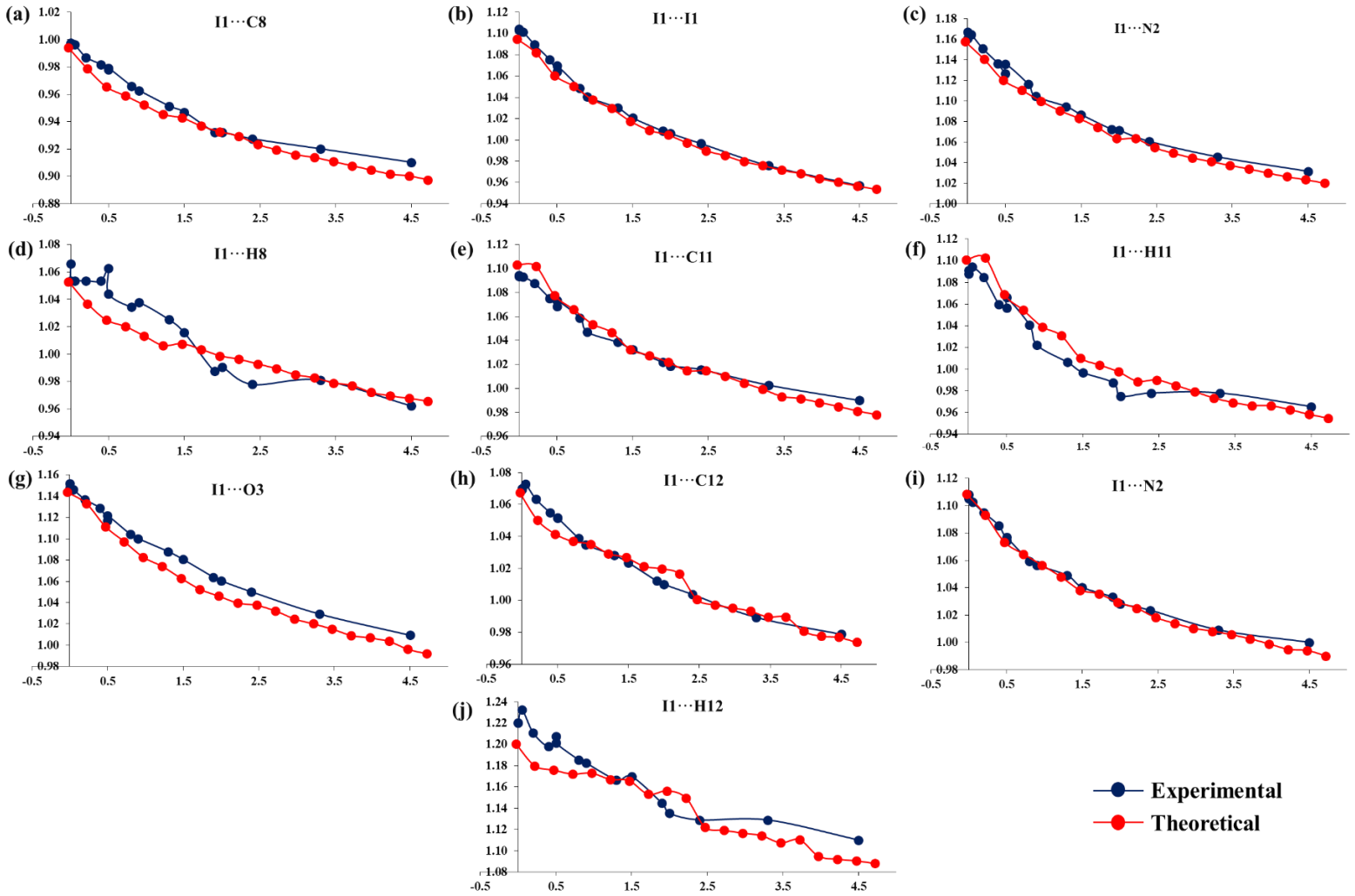

Figure 3.18 Variation of the Reduction Ratio (RR), calculated for intermolecular contacts involving I1(*x,y,z*) and atoms of neighbouring adducts, as a function of pressure. The neighbouring atom belong to: (a)-(d) (*1/2-x,-1/2+y,1-z*), (e)-(f) (*1/2-x,1-y,3/2-z*), (g) (*x,1/2-y,1/2+z*) and (h)-(j) (*1/2-x,1/2+y,1-z*), symmetry generated adducts.

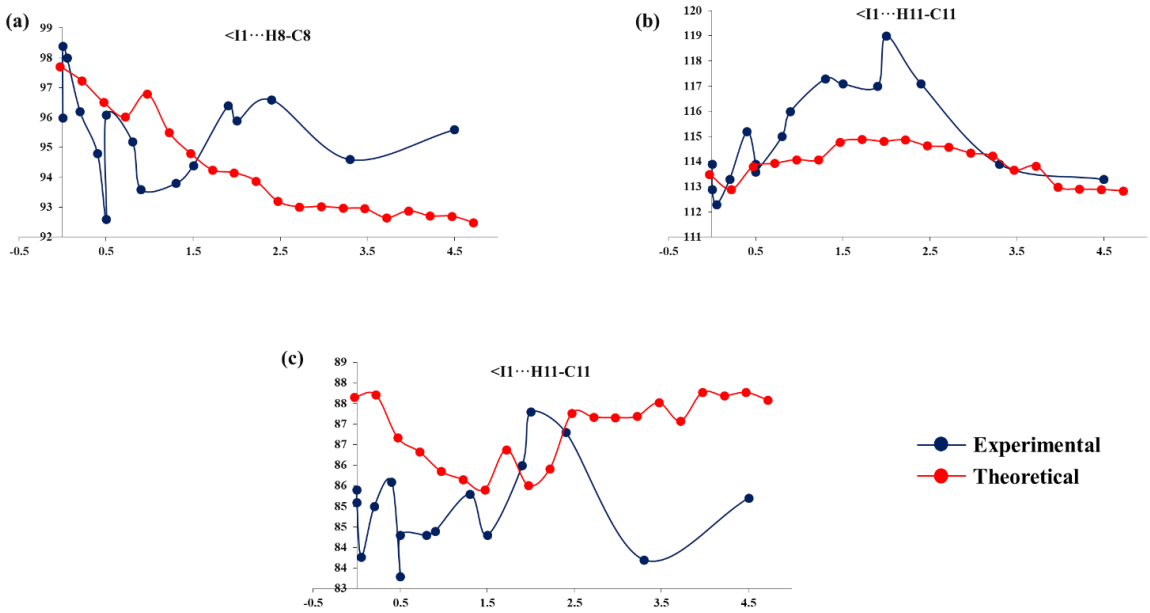

Figure 3.19 Variation of the HB angle, involving I1(*x,y,z*) and atoms of neighbouring adducts, as a function of pressure. The HB acceptor belong to (a) (*1/2-x,-1/2+y,1-z*), (b) (*1/2-x,1-y,3/2-z*) and (c) (*1/2-x,1/2+y,1-z*) symmetry generated adducts.

It is also striking to note that, in both experimental and theoretical datasets I1(*x,y,z*)···O3(*x,1/2-y,1/2+z*) interaction is showing the largest Δ(RR), means it is the interaction most influenced by the change in pressure (in terms of RR). Considering the interatomic distances, I1···O3 interaction show a significant stabilization from low to high pressure with RR ~ 1 at the highest pressure in both cases. From the atomic charges obtained at ambient conditions, it is evident that these I1···O3 interactions are electrostatically attractive [Q(I1) = +0.48 *e* and Q(O2) = -1.17 *e*] and at 4.5(2) GPa atomic charges slightly modifies [Q(I1) = +0.52 *e* and Q(O2) = -1.15 *e*; **section 3.2.3.8**] to make this interaction even stronger, which is also the case with 4.72 GPa in theoretical dataset. In addition, from **Figure 3.20** it is also observed that $I1^{\delta+}\cdots O3^{\delta-}$ secondary interactions are more favorable when I1 atom positioned more closer to the N2 atom, therefore this interaction is expected to have a strong influence on the displacement of I1 atom toward the acceptor while increasing pressure. Modification of other intermolecular interactions, formed by the neighboring adduct with the reference adduct can be found in the appendices (**Table 3AP.5**, **Table 3AP.6**, **Figure 3AP.1-5**). In short, from this analysis it can be concluded that, upon the action of an external pressure the crystalline environment around the HaB motif undergoes a significant modification, especially the I1(*x,y,z*)···O3(*x,1/2-y,1/2+z*) electrostatic interaction. Also, this modification is reversible while going from compression to decompression datasets (the interatomic distances and angles almost regains their initial values back on decompression to ambient pressure), thus favoring the displacement of I1 atom between N1 and N2 atoms within the *NISac.Py* binary adduct.

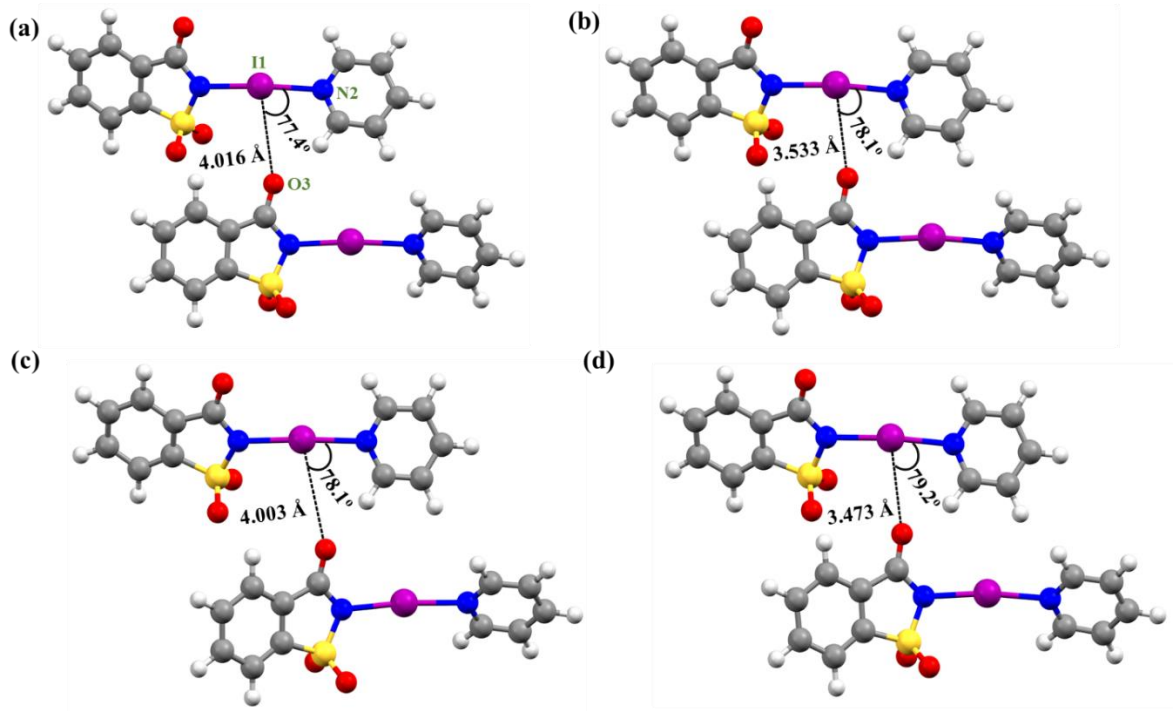

Figure 3.20 I1(*x,y,z*)···O3(*x,1/2-y,1/2+z*) interaction seen: in the experimental dataset at (a) 0.00(5) GPa and (b) 4.5(2) GPa, and in theoretical dataset at (c) -0.03 GPa and (d) 4.72 GPa. The characteristic distance (in Å) and O3···I1···N2 angle [in degrees(º)] are shown in each figure.

From **sections 3.2.3.2** (energetic and electronic analyses of the intermolecular interactions at ambient conditions) and **3.2.3.4** (variation of unit cell parameters with pressure), it has been concluded that the *NISac.Py* crystal structure at ambient conditions reveals an anisotropy in intermolecular interactions which eventually leads to different compressibilities along different crystallographic directions upon the action of external pressure. Maximal compressibility is observed along the crystallographic *b*-direction, followed by *c*- and then *a*- directions, in both experimental and theoretical datasets. In a straightforward scenario, one could expect that this different compressibilities along different directions might be related with the response of intermolecular interactions (to the applied pressure) in those particular directions. Indeed, the results obtained from the analysis of non-covalent interactions (**Tables AP.3-6**) confirm this supposition. In order to simplify further discussion, only the results obtained from the theoretical dataset will be considered. Here, the change in the RR calculated between the lowest and highest pressure (ΔRR) will be used as a quantitative tool to estimate the response of a particular interatomic interaction under pressure.

Considering the variation of interatomic distances within the explored range of pressures, it appears that H1(*x,y,z*)···H2(*1-x,1-y,-z*) interaction experiences maximal change in RR (ΔRR=0.28), followed by the H4(*x,y,z*)···H2(*x,3/2-y,1/2+z*) interaction (ΔRR=0.22). However,

this kind of H···H contacts are occurring as a consequence of crystal packing (due to the dense packing resulting from other intermolecular interactions) rather than any electronic reasons. Therefore, moving to other contacts, O1(*x,y,z*)···H1(*x,3/2-y,1/2+z*) and C8(*x,y,z*)···O1(*1/2-x,-1/2+y,1-z*) are the next two interatomic interactions experiencing maximal ΔRR (0.21 and 0.20, respectively). At 4.72GPa, RR of 0.89 for the former and 0.86 for the latter confirm the importance of these interactions in the overall crystal packing. Now, looking into the orientation of interatomic interaction vectors (formed by interacting atom of reference adduct to the atom of the neighboring adduct) corresponding to above interactions with respect to the crystallographic axes, it is evident that the major component of the vectors are oriented along the crystallographic *b*-direction (**Figure 3.21**). This is consistent with the results obtained earlier, pointing that the maximal compressibility of the crystal is observed along the *b*-direction. Following, the next interactions experiencing maximal ΔRR (ΔRR = 0.17) are cen_1(*x,y,z*)···cen_1(*1-x,1/2+y,1/2-z*) and cen_2(*x,y,z*)···cen_3(*1/2-x,-1/2+y,1-z*). But a final RR of 1.16 and 1.28 respectively make these interactions less important while analyzing the overall crystal structure.

From **section 3.2.3.2** it is also shown that the *NISac.Py* crystal structure is mainly composed of tightly held (200) planes, whereas interactions across these (200) planes are comparatively weaker. Correlating this feature with the variation of interatomic distances, it is observed that the contacts exhibiting larger ΔRR belong to the adducts that are forming the (200) planes rather than the ones interacting across them. This feature indicates that molecular adducts forming (200) planes are more affected with pressure, leading to an even tighter packing of (200) adduct planes at the highest pressure. In this respect, a detailed analysis of the changes in intermolecular interaction energies are discussed in the section below.

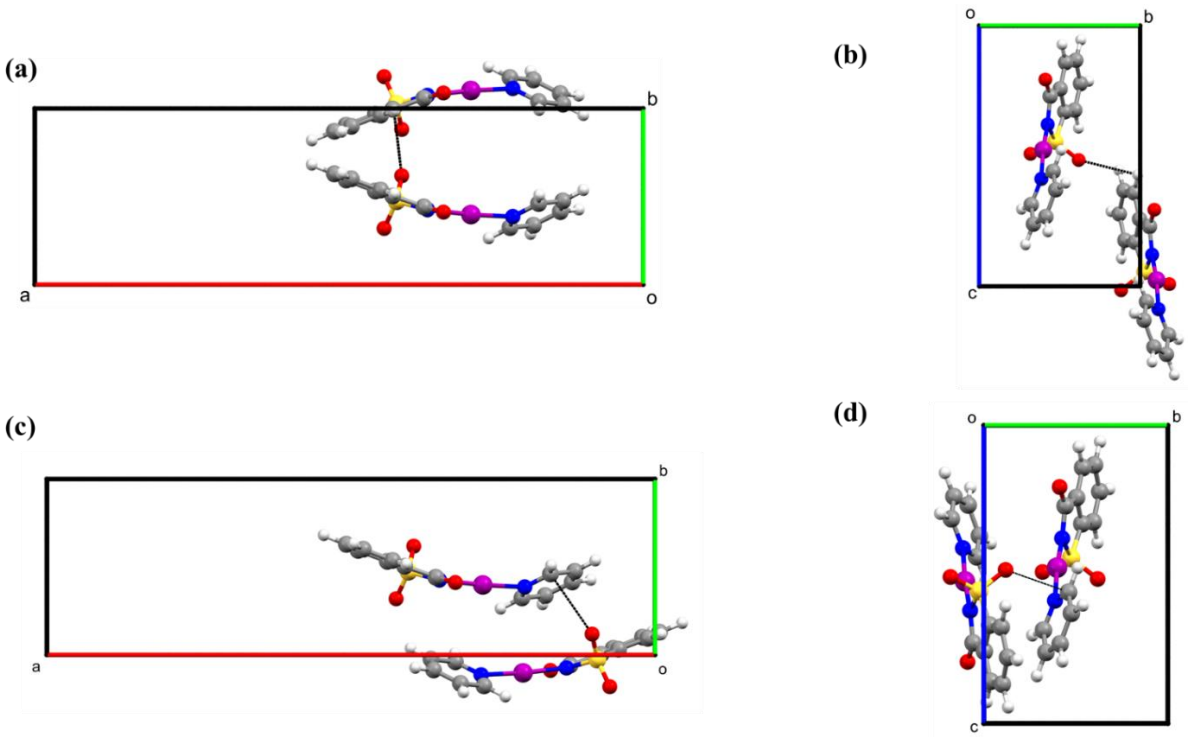

Figure 3.21 Orientation of interatomic interaction vectors (shown as black dashed lines) with respect to the crystallographic axes: projection of O1(*x,y,z*)···H1(*x,3/2-y,1/2+z*) interaction represented in (a) *ab*-plane and (b) *bc*-plane, projection of C8(*x,y,z*)···O1(*1/2-x,-1/2+y,1-z*) interaction represented in (c) *ab*-plane and (d) *bc*-plane. Figures are generated using the structure obtained at 0.00(5) GPa. All the images are depicted to show the contribution of intermolecular interactions along the crystallographic *b*-direction.

3.2.3.7 MDAC mimicking

In order to validate the argument that the poor completeness of the HP-SCXRD data collected inside MDAC is causing the larger uncertainties associated with HaB distances N1···I1 and I1···N2, refinements were carried out by mimicking the MDAC conditions with the dataset collected (with crystal-2) at ambient conditions outside the MDAC. Accordingly, filtered reflections that are common with those of the dataset collected at 0.00(5) GPa inside MDAC were only considered for the new refinement (hence the same number of reflections up to the same maximal resolution of 0.56 $Å^{-1}$). This procedure was carried out to mask the subset of reflections in the ambient dataset that were inaccessible at 0.00(5) GPa due to the shadowing of the MDAC body. Hereafter, **Scheme 3.2** summarizes the steps followed with this procedure. At 0.00(5) GPa, the completeness of the data collected using MDAC was close to 40% up to a resolution of 0.56 $Å^{-1}$. The corresponding HaB distances obtained after the refinement process were N1···I1 = 2.22(2) Å and I1···N2 = 2.285(17) Å with N···N2= 4.50(3) Å. On the other hand, the dataset collected at ambient conditions outside MDAC with a completeness of 100% up to the same resolution resulted to N1···I1 = 2.233(2) Å and I1···N2 = 2.289(2) Å with N1···N2 = 4.517(3) Å. Thus, whereas the standard uncertainties are here associated with the

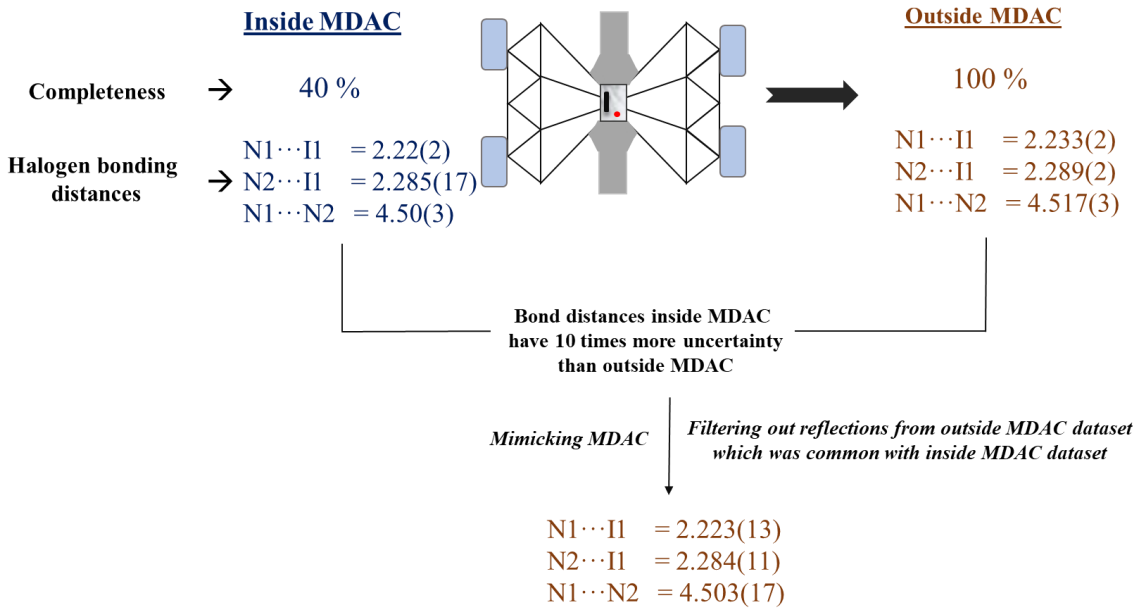

Scheme 3.2. Scheme describing the MDAC mimicking procedure. HaB distances are given in Å.

third digit after the decimal, they were associated with the second digit when using the 0.00(5) GPa dataset, therefore being nearly 10 times higher in the latter case. Later, the independent *hkl* reflections list used for the refinement of 0.00(5) GPa dataset were identified (a total of 822 independent reflections) and the correspondences were filtered from dataset at ambient conditions (accordingly, 822 reflections from a total of 2100 independent reflections). Further, an additional refinement was carried out with the filtered ambient conditions dataset, which resulted to a completeness of ~ 40% as expected, and HaB distances of N1···I1 = 2.223(13) Å and I1···N2 = 2.284(11) Å with N1···N2 = 4.503(17) Å. Considering the standard uncertainties of N1···I1, I1···N2 and N1···N2 distances, it appeared that respectively a nearly 7, 5 and 6 times increment occurred after the new refinement as compared to the one done with the full dataset. Thus, even if it is not necessarily the only reason, these results indicate that larger uncertainties on HaB distances observed with datasets collected at high pressures inside the MDAC are linked to missing reflections, due to the partial accessibility of the reciprocal space.

3.2.3.8 Variation of intermolecular energies with pressure

CrystalExplorer (version 17.5; Turner *et al.*, 2017) was used to calculate the intermolecular interaction energies at each pressure point, employing the B3LYP functional and the DGDZVP basis set for all atoms. Intramolecular C-H bond distances were normalized to standard neutron distances. The TONTO option available in the software was used for the wavefunction calculation, and a molecular shell of 3.80Å in radius was created in each case.

Table 3.11 shows the variation of total intermolecular interaction energies as a function of pressure, revealing that all adduct dimers are getting more stabilized with increasing pressure. Accordingly, an extent of stabilization is calculated each pressure point X using a parameter ΔE [$\Delta E = E_{x\ GPa} - E_{0.00(5)\ GPa}$]. Further, from the ΔE *vs* pressure plot it has been found that the adduct dimer formed with (*1/2-x,-1/2+y,1-z*) experiences maximal modification under pressure (**Figure 3.22a**), characterized with a ΔE of -21.6 kJ/mol (**Table 3.11**). The next adduct dimer experiencing maximal ΔE is formed with (*1/2-x,1-y,3/2-z*) symmetry generated adduct and it exhibit a ΔE value (18.8 KJ/mol) very close to the former. Earlier in **section 3.2.3.2**, we have pointed that these are the two dimers that mainly constituting the crystal packing at ambient conditions. And now, out of all the adduct dimers they itself found to show maximal energy change upon the action of external pressure. In the hierarchy, the next most significant one is the dimer formed with (*1/2-x,1-y,1/2-z*) symmetry generated adduct, showing a lower ΔE of -9.3 kJ/mol as compared to the first two cases. A monotonic increase of ΔE is observed with pressure for the all the three dimers discussed above, indicating that main intermolecular interactions involved in crystal packing are getting more stabilized with pressure leading to a tighter packing. While for all other dimers, the maximal ΔE is found to be below 5 kJ/mol (at any given pressure X), thus considered as less significant cases. **Figure 3.22a** also shows the evolution of ΔE as a function of pressure for all the nine crystallographically independent dimers of adducts. An additional dimer, with (*-x+1/2,-y,-z+3/2*) symmetry code is encountered in the molecular shell from a pressure value of 2.0(2) GPa, but is not included in **Figure 3.22a**.

Now, looking back into the crystal packing at ambient conditions (**Figure 3.23**), the main components of interatomic interaction vectors between (*x,y,z*)···(*1/2-x,-1/2+y,1-z*) adducts are largely oriented parallel to the crystallographic *b*-direction. Similarly, for (*x,y,z*)···(*1/2-x,1-y,3/2-z*) adducts the main interaction components are along *b*- and *c*-directions. Earlier in **section 3.2.3.4** we have pointed that the maximal compressibility of 11% is seen along the crystallographic *b*-direction, which is consistent with the fact that the major components of interatomic interaction vectors corresponding to the adduct dimers that experiencing maximal energy change are oriented in the same direction. Also, at ambient conditions, these two dimers of adducts exhibit significant π···π stacking motifs, which are well-known to show pronounced modifications in response to external pressure. On the other hand, the major components of interaction vectors formed between (*x,y,z*) and (*1/2-x,1-y,1/2-z*) adducts are oriented along the crystallographic *c*-direction, which is direction experiencing maximal compressibility (5.5%) after the *b*-direction.

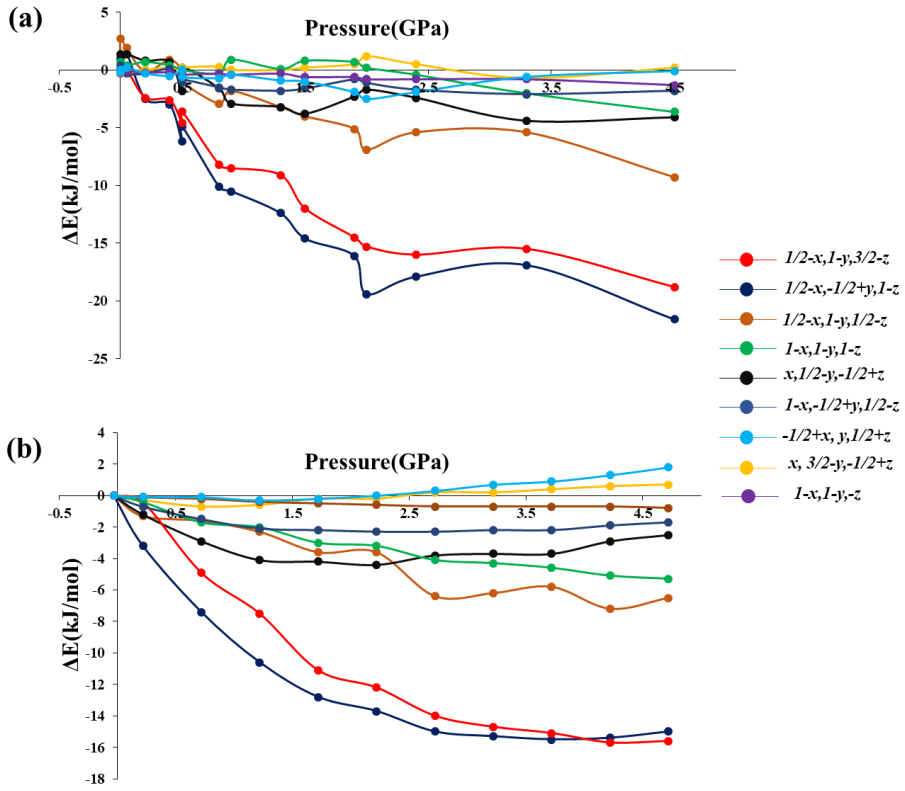

Figure 3.22 Evolution of ΔE *vs* Pressure for (a) experimental and (b) theoretical datasets. Curves connecting data are plotted for guiding eyes.

Also, from the previous discussions, it could conclude that the *NISac.Py* crystal structure at ambient conditions is mainly composed of tightly held (200) planes, which are mainly composed by the interaction of the reference (*x*,*y*,*z*) adduct with (*1/2-x*,*-1/2+y*,*1-z*) and (*1/2-x*,*1-y*,*3/2-z*) symmetry generated adducts. And now from the energetic analysis it revealed that the same dimer adducts modifies most significantly under pressure, getting more stabilized with increasing pressure. Cohesion of these (200) planes are further supported by the dimer formed between (*x*,*y*,*z*) and (*1/2-x*,*1-y*,*1/2-z*) adducts, and this being the next most affected and stabilized interaction in terms of ΔE succeeding the above two cases. Altogether, all these features point out a much stronger cohesion of (200) planes at high-pressure than that identified at low pressure. Also, in a similar way, the intermolecular interactions formed by the molecular adducts across the (200) planes are also getting stronger with pressure (but in a lesser extent), therefore again suggesting an overall tighter packing of crystal structure at high pressure environment as compared to the case of low pressure.

The results obtained from the energetic analysis using the theoretical high-pressure structures are shown in **Table 3AP.7** and **Figure 3.26b**, showing qualitatively the same results and thus the same conclusions as that of experimental data.

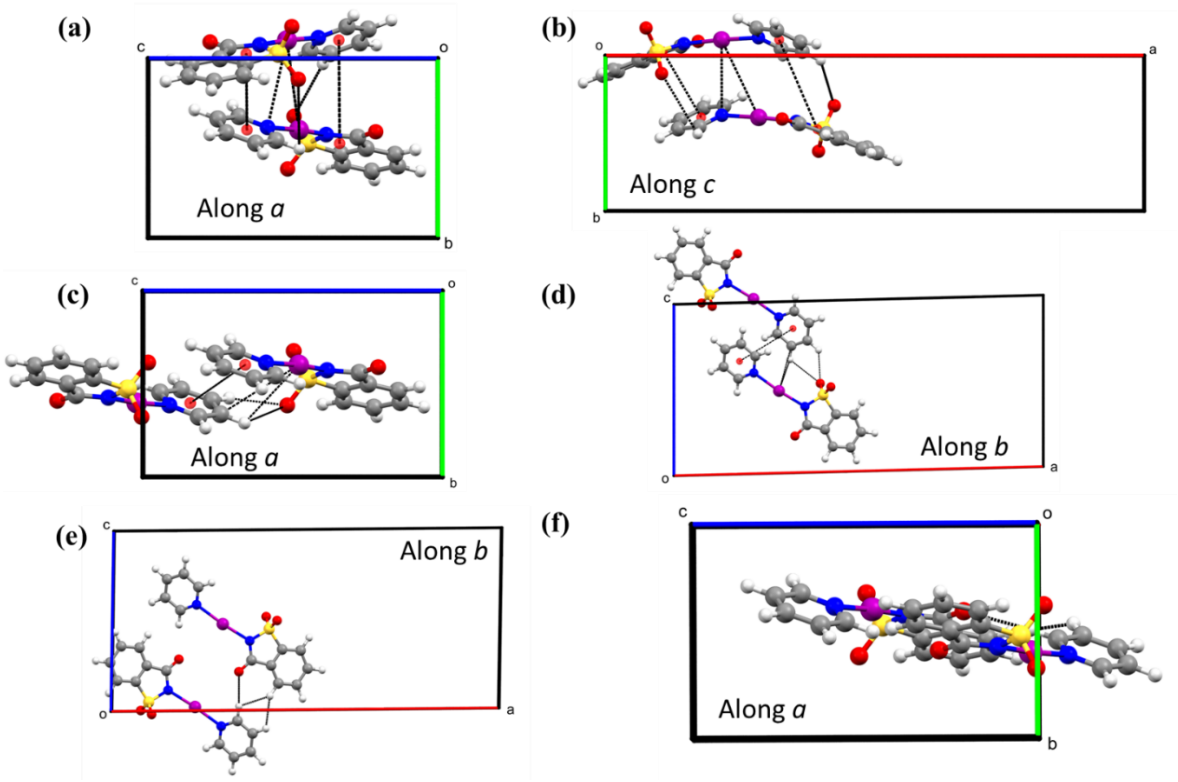

Figure 3.23 Orientation of molecular dimers formed between the reference (*x,y,z*) adduct and (a)-(b) (*1/2-x,-1/2+y,1-z*), (c)-(d) (*1/2-x,1-y,3/2-z*), and (e)-(f) (*1/2-x,1-y,1/2-z*), symmetry generated adducts. projections of major intermolecular interactions (represented as black dashed lines) are shown with respect to the crystallographic axes in each figure. Figures were generated using the structure obtained at 0.00(5) GPa.

Table 3.11 Total intermolecular interaction energies determined from the high-pressure experimental structures. All energies are given in kJ/mol. Total interaction energy and ΔE are gathered as left/right entries. $\Delta E = E_{x\ GPa} - E_{0.00(5)\ GPa}$, whereas for the binary adducts that are coming into the molecular shell at high pressure Y only, $\Delta E = E_{X\ GPa} - E_{Y\ GPa}$.

Pressure (GPa)	**0.00(5)**	**0.00(5)**	**0.05(5)**	**0.20(5)**	**0.4(1)**	**0.5(1)**	**0.5(1)**	**0.8(1)**	**0.9(1)**	**1.3(2)**	**1.5(2)**	**1.9(2)**	**2.0(2)**	**2.4(2)**	**3.3(2)**	**4.5(2)**
1/2-x,-1/2+y,1-z	-81.9/0.0	-80.9/1.0	-80.5/1.4	-84.4/-2.5	-84.9/-3	-88.1/-6.2	-86.8/-4.9	-92/-10.1	-92.4/-10.5	-94.3/-12.4	-96.5/-14.6	-98/-16.1	-101.3/-19.4	-99.8/-17.9	-98.8/-16.9	-103.5/-21.6
1/2-x,1-y,1/2-z	-28/0.0	-25.3/2.7	-26.1/1.9	-28.1/-0.1	-27.1/0.9	-28.1/-0.1	-29/-1	-30.9/-2.9	-29.8/-1.8	-31.2/-3.2	-32/-4	-33.1/-5.1	-34.9/-6.9	-33.4/-5.4	-33.4/-5.4	-37.3/-9.3
x,1/2-y,-1/2+z	-22.4/0.0	-21/1.4	-21/1.4	-21.6/0.8	-21.7/0.7	-24.2/-1.8	-22.2/0.2	-24/-1.6	-25.3/-2.9	-25.6/-3.2	-26.2/-3.8	-24.7/-2.3	-24.1/-1.7	-24.8/-2.4	-26.8/-4.4	-26.5/-4.1
x,1.5-y,-1/2+z	-0.6/0.0	-0.7/-0.1	-0.9/-0.3	-0.6/0	-0.4/0.2	-0.7/-0.1	-0.4/0.2	-0.3/0.3	-0.6/0	-0.6/0	-0.4/0.2	-0.1/0.5	0.6/1.2	-0.1/0.5	-1.3/-0.7	-0.4/0.2
1/2-x,1-y,3/2-z	-79.4/0.0	-79.7/-0.3	-79.4/0	-81.8/-2.4	-82/-2.6	-84/-4.6	-83/-3.6	-87.6/-8.2	-87.9/-8.5	-88.5/-9.1	-91.4/-12	-93.9/-14.5	-94.7/-15.3	-95.4/-16	-94.9/-15.5	-98.2/-18.8
1-x,1-y,1-z	-28.4/0.0	-27.7/0.7	-28/0.4	-27.7/0.7	-28/0.4	-28.4/0	-28.4/0	-28.7/-0.3	-27.5/0.9	-28.3/0.1	-27.6/0.8	-27.7/0.7	-28.2/0.2	-28.8/-0.4	-30.4/-2	-32/-3.6
1-x,-1/2+y,1/2-z	-22.6/0.0	-22.2/0.4	-22.9/-0.3	-22.9/-0.3	-22.5/0.1	-23.7/-1.1	-23.4/-0.8	-24.1/-1.5	-24.3/-1.7	-24.4/-1.8	-24.2/-1.6	-23.4/-0.8	-23.7/-1.1	-24.3/-1.7	-24.7/-2.1	-24.4/-1.8
1-x,1-y,-z	-4.8/0.0	-4.8/0	-4.9/-0.1	-5/-0.2	-5/-0.2	-5.1/-0.3	-5.2/-0.4	-5.1/-0.3	-5.2/-0.4	-5.1/-0.3	-5.4/-0.6	-5.4/-0.6	-5.6/-0.8	-5.6/-0.8	-5.6/-0.8	-6.1/-1.3
-1/2+x,y,1/2+z	-4.7/0.0	-4.9/-0.2	-4.5/0.2	-5/-0.3	-5.2/-0.5	-4.7/0	-5.3/-0.6	-5.4/-0.7	-5.1/-0.4	-5.6/-0.9	-5.7/-1	-6.6/-1.9	-7.2/-2.5	-6.6/-1.9	-5.3/-0.6	-4.8/-0.1
-x+1/2, -y, -z+3/2													-15.0/0.0	-14.9/0.1		-16.7/-1.7

3.2.3.9 Variation of electronic properties with pressure

From the previous **section 3.2.3.6**, it was difficult to conclude about the exact state of the *NISac.Py* binary adduct (neutral co-crystal or ionic form) and the precise location of I1 atom within the adduct solely from N1···I1 and I1···N2 HaB distances. To investigate this system on another point of view, these HaB interactions were electronically characterized by using QTAIM approach. Thus, topological and energetic properties of $\rho(\mathbf{r})$ at the N1···I1 and I1···N2 BCPs were studied as a function of pressure. In this approach we will be able to get a quantitative difference between both the HaB bonds to characterize their interaction strengths. But the main difficulty here is concerning the quality of data that used to determine the atomic positions since we could not collect enough XRD data to derive structural positions with good enough quality. Clearly, such experimental dataset does not permit to undertake an accurate charge density analysis. However, since the periodic calculations show quite good geometrical agreements (in terms of intermolecular interaction distances and angles) with experimental results, we have used the theoretically calculated structures to undertake the charge density analysis in both HaB regions. But still the topological calculations were extended to the experimental dataset for the comparison purpose. Hence, based on quantum chemistry calculations at either experimental or theoretical geometry, we have carried out the topological analysis of the *NISac.Py* adduct to characterize the HaB interactions at different applied pressures and to complement the observations drawn earlier from the geometrical analysis.

For the proceedings SPE calculations were performed using the Gaussian09 (Frisch *et al.*, 2013) software on the isolated *NISac.Py* adducts extracted from the crystal structure at each applied pressure, for either experimental and theoretical dataset. The B3LYP functional was used in all cases. The Def2TZVP basis set was employed for all atoms, including a pseudo-potential for I (Pritchard *et al.*, 2019). Topological calculations were performed using AIMALL software (Keith, 2019).

First, from the topological calculations carried out for the theoretical data (**Table 3.12** and **Figure 3AP.6**), it has been found that $\rho(\mathbf{r})$ at N1···I1 BCP (hereafter, called CP1a) and I1···N2 BCP (hereafter, called CP2a) increases as a function of pressure. Accordingly, CP1a and CP2a show respectively a $\delta\rho(\mathbf{r})$ [calculated as the difference between the largest and lowest $\rho(\mathbf{r})$ values found among all the pressures] of 0.011eÅ^{-3} and 0.069 eÅ^{-3}. Similarly, $\nabla^2\rho(\mathbf{r})$ also shown an increasing behavior upon pressure, with a $\delta\nabla^2\rho(\mathbf{r})$ value of 0.186 eÅ^{-5} and 0.401 eÅ^{-5} for CP1a and CP2a, respectively. Larger $\delta\rho(\mathbf{r})$ and $\delta\nabla^2\rho(\mathbf{r})$ values found at CP2a is actually

pointing to a more significant modification of the HaB interaction at the acceptor side as compared to the donor side while increasing pressure. Thus, whereas the HaB strengthening with pressure is observed at both sides of I, the more important variation is seen with the acceptor side.

It has been previously established that a larger quantity of $\rho(\mathbf{r})$ at BCP represents a stronger interaction (Espinosa *et al.*, 2002). **Figure 3AP.7a** and **Figure 3AP.7b** show the high correlation that exists between $\rho(\mathbf{r})$ and HaB distances, pointing that the strengthening of HaB motifs (by reducing the interatomic distance while increasing pressure) is accompanied by a larger accumulation of charge at BCPs. Additionally, a parameter $\Delta\rho(\mathbf{r}) = \rho(\mathbf{r})_{CP1a} - \rho(\mathbf{r})_{CP2a}$ has been calculated to estimate the difference between the interaction strength of I at donor and acceptor sides. Thus, whereas a positive value of $\Delta\rho(\mathbf{r})$ indicates a stronger interaction at the donor side [$\rho(\mathbf{r})_{CP1a} > \rho(\mathbf{r})_{CP2a}$], a negative value of $\Delta\rho(\mathbf{r})$ indicates a stronger interaction at the acceptor side [$\rho(\mathbf{r})_{CP1a} < \rho(\mathbf{r})_{CP2a}$] at any given pressure. Under compression, $\Delta\rho(\mathbf{r})$ values changes from 0.036 eÅ^{-3} (at -0.03GPa) to -0.026 eÅ^{-3} (at 4.72GPa), thus reversing the significance of the preferential accumulation of charge density at CP1a and CP2a at an intermediate pressure point. The transition from a positive to negative value of $\Delta\rho(\mathbf{r})$ occurs between 1.47 GPa (0.002 eÅ^{-3}) and 1.72GPa (-0.005 eÅ^{-3}), suggesting that I form a relatively stronger interaction with the acceptor side approximately above 1.72 GPa. This observation shows a close agreement with the conclusion made earlier from the geometrical analysis (**Figure 3.16** and **Table 3.10**), that the transition of halogen atom beyond the middle position between the donor and acceptor moieties (0.5 boundary line in normalized distances) happens above 1GPa. At the same time, $\nabla^2\rho(\mathbf{r})_{CP1a}$ and $\nabla^2\rho(\mathbf{r})_{CP2a}$ increase in their positive values with the pressure, whereas $\Delta\nabla^2\rho(\mathbf{r}) = \nabla^2\rho(\mathbf{r})_{CP1a} - \nabla^2\rho(\mathbf{r})_{CP2a}$ shows negative magnitudes and with a monotonic increase of its absolute value ($|(\Delta\nabla^2\rho(\mathbf{r})| \uparrow$) within the investigated range of pressure along with the shortening of the N1···N2 distances. Therefore, this trend indicates an increase in the electron repulsion at both BCPs with pressure (the electron distribution is more depleted in both cases), while a less significant effect is observed at the donor side with respect to the acceptor side due to a more important accumulation of electrons in case of the latter. Similar to $\Delta\rho(\mathbf{r})$, ΔX (where $\Delta X = X_{CP1a} - X_{CP2a}$; X = $|V|/G$ or DI) also show a decreasing behavior in its magnitude with pressure (from 0.083 to 0.036, and from 0.103 to 0.038, respectively for $|V|/G$ and DI; see **Table 3.12**, **Figure 3AP.6a** and **Figure 3AP.6b**), but they do not show any reversal of sign. Therefore, whereas $\Delta(|V|/G)$ and Δ(DI) parameters suggest the strengthening of I1···N2

interaction with pressure, they indicate a stronger interaction of I at the donor side [$(|V|/G)_{CP1a} > (|V|/G)_{CP2a}$ and $DI_{CP1a} > DI_{CP2a}$] at any investigated pressure, as opposite to what is suggested by $\Delta\rho(\mathbf{r})$ at high-pressure (**Table 3.12**). Considering the HaB distances, it is found that I1···N2 is showing a larger shortening (0.067 Å) than N1···I1 (0.010 Å) between the lowest and highest pressure (**Table 3.12**), referring that the volume of the atomic basin of N1 and of N2 atoms at any given pressure (used for the calculation of DI) and the volume of the space in which the accumulation of electrons happens are not same at donor and acceptor sides (might be reason for differences shown by electronic properties).

A similar observation can be also drawn from the topological calculations performed with the experimental dataset, even though the atomic positions are determined with less accuracy (**Table 3AP.8**, **Figure 3AP.6b, c** and **Figure 3AP.7c, d**). In case of the experimental dataset, the transition of $\Delta\rho(\mathbf{r})$ from a positive to a negative value happens in between 0.9(1) GPa (0.005 eÅ^{-3}) and 1.3(2) GPa (-0.018 eÅ^{-3}), showing a good agreement with the theoretical results and with the conclusion made earlier from the geometrical analysis (**Figure 3.16** and **Table 3.9**). A very similar behavior is also observed in the cases of $\Delta(|V|/G)$ (0.098 to 0.031) and Δ(DI) (0.128 to 0.003), both showing no changes in its sign throughout the investigated pressure range and indicating a comparatively stronger interaction at the donor side at any given pressure. In addition, variation in the charges of the atomic/molecular entities were also analyzed as a function of pressure, indicating only a slight modification between the lowest and highest pressure for both experimental and theoretical datasets (see **section 3AP.1** for details).

In conclusion, the topological and the energetic properties of $\rho(\mathbf{r})$ at the N1···I1 and I1···N2 BCPs show a significant modification under pressure, with a potential migration of the halogen atom that shifts closer to the acceptor side upon increasing pressure. This is happening within a range of pressures similar to that observed earlier from geometrical analysis, where it was found that I1 is slightly closer to N2 above 1GPa (even if it located close to the middle position between donor and acceptor at any given investigated pressure). From the topological analysis, the modification of $\Delta\rho(\mathbf{r})$ with pressure indicates a reversal of its sign, pointing the shifting of the strongest interaction at the donor side with lowest applied pressure [$\rho(\mathbf{r})_{CP1a} > \rho(\mathbf{r})_{CP2a}$] towards the acceptor side with highest applied pressure [$\rho(\mathbf{r})_{CP1a} < \rho(\mathbf{r})_{CP2a}$]. However, the different electronic environment of N1 and N2 atoms is still a main hindrance in making a clear distinction in the state of system, in particular when considering the $|V|/G$ and DI parameter.

Table 3.12 Results obtained from the topological calculations of the isolated *NISac.Py* adduct, extracted from the crystal structure at each applied pressure for the theoretical high-pressure dataset. N1···I1/I1···N2 distances are shown as left/right entries. The gathered QTAIM topological and energetic properties of $\rho(r)$ at both N1···I1/I1···N2 BCPs are given as left/right values: the electron density (ρ), its laplacian ($\nabla^2\rho$), the total energy density ($H=V+G$) as well as the ratio between the electron potential (V) and kinetic (G) densities ($|V|/G$), and its values normalized to ρ. The delocalization index at BCPs is denoted as DI. ΔX (X=ρ, $\nabla^2\rho$, $|V|/G$, DI) is the difference between left and right values. Important entries during the discussion are highlighted with red colour. (**Table continues to the next page*)**

Pressure (GPa)	Distance (Å)	$\rho(r)$ (eÅ^{-3})	$\nabla^2\rho(r)$ (eÅ^{-5})	$\nabla^2\rho(r)/\rho(r)$ (Å^{-2})	$\|V\|/G$	H (a.u.)	H/ρ (a.u.)	DI	$\Delta\rho$ (eÅ^{-3})	$\Delta(\nabla^2\rho(r))$ (eÅ^{-5})	$\Delta(\|V\|/G)$	Δ (DI)
-0.03	2.273/ 2.303	0.535/ 0.499	2.475/ 2.987	4.627/ 5.983	1.485/ 1.402	-0.024/ -0.021	-0.305/ -0.282	0.724/ 0.621	0.036	-0.512	0.083	0.103
0.22	2.276/ 2.292	0.531/ 0.510	2.473/ 3.041	4.655/ 5.959	1.481/ 1.409	-0.024/ -0.022	-0.302/ -0.289	0.718/ 0.630	0.021	-0.568	0.072	0.088
0.47	2.274 /2.287	0.532 /0.516	2.490/ 3.071	4.680/ 5.956	1.480/ 1.412	-0.024/ -0.022	-0.303/ -0.292	0.717/ 0.634	0.017	-0.581	0.068	0.083
0.72	2.272/ 2.283	0.535/ 0.519	2.513/ 3.092	4.698/ 5.957	1.481/ 1.414	-0.024/ -0.023	-0.305/ -0.295	0.718/ 0.636	0.016	-0.578	0.067	0.082
0.97	2.275/ 2.276	0.532/ 0.526	2.510/ 3.128	4.718/ 5.944	1.479/ 1.418	-0.024/ -0.023	-0.303/ -0.299	0.714/ 0.642	0.006	-0.618	0.060	0.072
1.22	2.274/ 2.271	0.532/ 0.531	2.524/ 3.154	4.741/ 5.941	1.477/ 1.421	-0.024/ -0.024	-0.303/ -0.302	0.712/ 0.645	0.001	-0.630	0.056	0.067
1.47	2.273/ 2.269	0.534/ 0.532	2.536/ 3.164	4.750/ 5.946	1.478/ 1.421	-0.024/ -0.024	-0.305/ -0.303	0.714/ 0.646	0.002	-0.627	0.057	0.068
1.72	2.274/ 2.265	0.532/ 0.537	2.535/ 3.189	4.763/ 5.941	1.476/ 1.424	-0.024/ -0.024	-0.303/ -0.306	0.711/ 0.650	-0.005	-0.654	0.052	0.062
1.97	2.271/ 2.261	0.534/ 0.542	2.557/ 3.223	4.785/ 5.946	1.476/ 1.426	-0.024/ -0.025	-0.305/ -0.309	0.711/ 0.653	-0.008	-0.666	0.050	0.058
2.22	2.271/ 2.261	0.535/ 0.541	2.560/ 3.219	4.785/ 5.948	1.477/ 1.426	-0.024/ -0.025	-0.305/ -0.309	0.712/ 0.652	-0.006	-0.658	0.051	0.060

2.47	2.271/ 2.253	0.534/ 0.549	2.574/ 3.263	4.817/ 5.941	1.475/ 1.430	-0.024/ -0.026	-0.305/ -0.314	0.709/ 0.659	-0.015	-0.688	0.045	0.050
2.72	2.271/ 2.252	0.535/ 0.551	2.581/ 3.273	4.824/ 5.942	1.475/ 1.431	-0.024/ -0.026	-0.305/ -0.315	0.709/ 0.660	-0.016	-0.692	0.044	0.049
2.97	2.269/ 2.248	0.537/ 0.554	2.600/ 3.297	4.838/ 5.950	1.475/ 1.432	-0.024/- 0.026	-0.307/ -0.317	0.710/ 0.662	-0.017	-0.697	0.043	0.048
3.22	2.269/ 2.248	0.537/ 0.554	2.602/ 3.299	4.844/ 5.949	1.475/ 1.432	-0.024/ -0.026	-0.307/ -0.317	0.709/ 0.662	-0.017	-0.697	0.043	0.047
3.47	2.269/ 2.245	0.537/ 0.558	2.605/ 3.318	4.854/ 5.950	1.474/ 1.434	-0.024/ -0.026	-0.307/ -0.319	0.708/ 0.664	-0.021	-0.712	0.041	0.044
3.72	2.265/ 2.241	0.541/ 0.563	2.636/ 3.354	4.877/ 5.961	1.475/ 1.436	-0.025/ -0.027	-0.309/ -0.322	0.709/ 0.667	-0.022	-0.718	0.040	0.042
3.97	2.266/ 2.24	0.538/ 0.564	2.624/ 3.362	4.879/ 5.958	1.474/ 1.437	-0.025/ -0.027	-0.308/ -0.323	0.707/ 0.669	-0.026	-0.738	0.037	0.039
4.22	2.265/ 2.237	0.539/ 0.567	2.638/ 3.382	4.892/ 5.963	1.474/ 1.438	-0.025/ -0.027	-0.308/ -0.325	0.707/ 0.670	-0.028	-0.744	0.036	0.037
4.47	2.264/ 2.237	0.541/ 0.567	2.650/ 3.379	4.898/ 5.962	1.474/ 1.438	-0.025/ -0.027	-0.310/ -0.325	0.708/ 0.670	-0.026	-0.729	0.037	0.039
4.72	2.263/ 2.236	0.542/ 0.568	2.659/ 3.388	4.907/ 5.964	1.475/ 1.438	-0.025/ -0.027	-0.310/ -0.326	0.708/ 0.671	-0.026	-0.728	0.036	0.038

Finally, all these trends suggest that the *NISac.Py* binary adduct should be considered as a single molecular entity embedded into high-pressure environment rather than two separate units as typically seen with neutral co-crystal or ionic form. Overall, the system is characterized by a very close position of the donor and acceptor moieties, which are linked by a halogen atom making two very strong HaB interactions in both sides (both possessing a significant degree of covalence). In this system, based on the structural distances the halogen atom is located close to the middle position between donor and acceptor moieties at any given pressure. As a result, the system reacts to the external constrains (applied pressures) by reducing the donor to acceptor distance while shifting slightly the position of I towards the acceptor. The question concerning the side to which I preferentially belong cannot be however concluded, because both the HaB interactions being closely similar.

The modification in the non-covalent interactions between the adduct dimers were also studied using NCI (non-covalent interaction) plots and Hirshfeld surfaces, which eventually allow to enrich information derived from the earlier analyses. For the details see **section 3AP.2** and **3AP.3**.

3.3 N-iodosaccharin.4-cyanopyridine (*NISac.4CYP*) co-crystal system

The next part of this chapter will deal with the second co-crystal system in our study, that is the combination of N-iodosaccharin (NISac) with 4-cyanopyridine (4CYP). Here, the HaB donor NISac is taken same as that of *NISac.Py*, whereas the acceptor molecule Py is replaced with a comparatively weaker Lewis base 4CYP, in line with the strong electron withdrawing cyano group in para position. The electrostatic potential (ESP) surfaces depicted in **Figure 3.24** point out the difference between these two molecules as potential HaB acceptors. The 4CYP derivative possesses a less negative ESP value (thus a lesser concentration of electrons) at the N lone-pair position compared to the case of Py derivative. Therefore, from the electrostatic point of view, a weaker HaB motif is expected in *NISac.4CYP* than in *NISac.Py*. These details will be investigated further in the coming sections. Nevertheless, the main reason behind extending the HP-SCXRD studies to another co-crystal system is to examine how the HaB motifs are responding here with pressure, especially when a differently formed HaB motif (in terms of strength) and crystalline environment are in offer.

Since the techniques and the procedures used here are very similar to those of *NISac.Py*, the description and details in common will not be repeated. Instead, the section numbers from the previous part will be indicated.

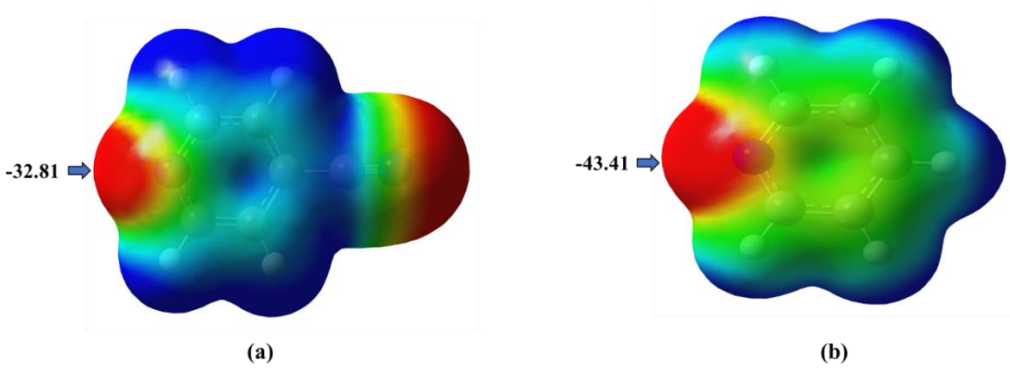

Figure 3.24 Electrostatic potential (ESP) function drawn on the ρ = 0.002 a.u. iso-surface for isolated (a) 4CYP (b) Py molecules, extracted from the experimental geometry at ambient conditions (B3LYP/Def2TZVP). Values are given in kcal/mol, ESP surface colouring: red = -20 kcal/mol to blue = +20 kcal/mol.

3.3.1 Experimental

3.3.1.1 Synthesis and co-crystallization

The same batch of synthesized NISac (**section 3.2.1.1**) is used here as well. The co-former, 4-cyanopyridine (4CYP) was commercially available (98% from Acros Organics) and used as received. A 1:1 stoichiometric co-crystal of N-iodosaccharin and 4-cyanopyridine (*NISac.4CYP*) was prepared by dissolving 20 mg of NISac (0.065mmol) with 6.77 mg of 4CYP (0.065 mmol) in 2 mL of ethyl acetate solution inside a 5ml glass vial, stirred and gently heated in a hot-plate until obtaining a clear solution. Further, the vial was left inside a dark chamber at room temperature for slow solvent evaporation. Colourless block shaped crystals were obtained after 2-3 days. Unlike *NISac.Py*, the single-crystals obtained here do not show any immediate sign of degradation on exposure to atmospheric conditions and are stable enough for several weeks. Also, all the crystals showed similar morphologies and homogenous colour across the surface under polarized light microscope except for the edges (might be a consequence of change in thickness towards the edges).

3.3.1.2 Single crystal X-ray diffraction

Data collection, processing and refinement at ambient conditions. A crystal of dimension 0.118×0.099×0.076 mm (crystal-1) was chosen with the aid of a polarized light microscope for crystal structure determination at ambient conditions, carried out outside MDAC by gluing the crystal at the extremity of a glass fiber on a goniometer head. The same diffractometer configuration and working method was used as previously. *NISac.4CYP* crystallizes in the monoclinic system with a non-centrosymmetric space group *Cc*. An absolute structure

parameter (also called Flack parameter) of -0.047(9) was determined during the refinement, its value close to zero indicates that the *NISac.4CYP* crystal is almost obtained in an enantiomeric pure form. The corresponding crystallographic information are gathered in **Table 3.13**. The molecular structure (with atomic labels) of *NISac.4CYP* determined in the asymmetric unit along with the position of first five residual Q-peaks are shown in **Figure 3.25**. Further crystal structure analysis was carried out using Olex2-1.3 (Dolomanov *et al.*, 2009), Crystal Explorer -Version 17.5 (Turner *et al.*, 2017) and Mercury (version 2020.1) software packages, and the latter is also used to generate crystal structure drawings.

Table 3.13 Crystallographic information for data collected at ambient conditions with crystal-1

Crystal data	
Chemical formula	$C_{13}H_8IN_3O_3S$
M_r (g/mol)	413.18
Crystal system, space group	Monoclinic, *Cc*
Temperature (K)	298
a, *b*, *c* (Å)	7.4806 (8), 23.269 (3), 8.7425 (9)
β (°)	100.336 (3)
V (Å^3)	1497.1 (3)
Z	4
Radiation type	Mo K_α
μ (mm^{-1})	2.29
Crystal size (mm)	0.118 × 0.099 × 0.076
Data collection	
Diffractometer	Bruker D8 Venture
Absorption correction	Numerical (face indexing)
No. of measured, independent, observed [$I > 2\sigma(I)$] reflections	126219, 4570, 4043
Completeness (%)	100
R_{int}	0.042
$(\sin\theta/\lambda)_{max}$ (Å^{-1})	0.714
Refinement	
R [$F^2 > 2\sigma(F^2)$], $wR(F^2)$, S	0.020, 0.049, 1.13
No. of reflections	4570
No. of parameters	190
$\Delta\rho_{max}$, $\Delta\rho_{min}$ (e Å^{-3})	0.31, -0.28
Absolute structure parameter	-0.047 (9)

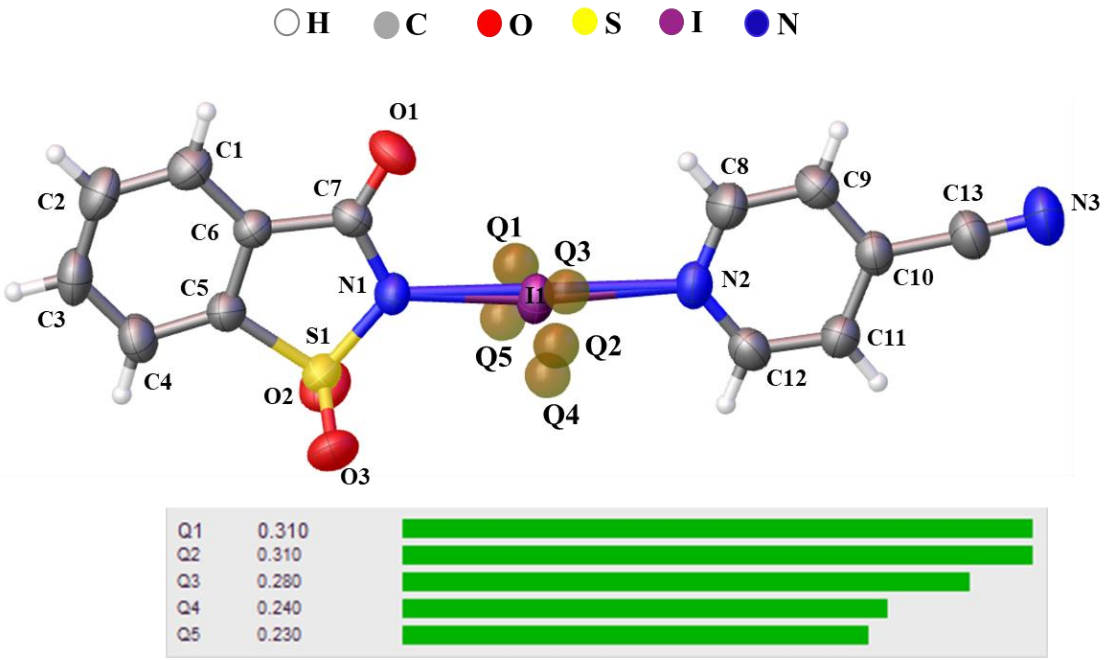

Figure 3.25 First five residual density peaks obtained after the final refinement cycle of *NISac.4CYP* (data collected at ambient conditions outside MDAC with crystal-1). Atom types are shown with colouring scheme, atoms and residual peaks are labelled. Electron density values corresponding to residual peaks are given (in eÅ^{-3}).

Data collection, processing and refinement at high-pressure and room temperature. A hole of ~300μm in diameter and ~100μm in height drilled at the centre of a stainless-steel gasket acts as the sample chamber in this case. The dimensions of crystal-1 (used for data collection at ambient conditions) was suitable enough to accommodate within the MDAC sample chamber, but unfortunately crystal was lost while filling the sample chamber with the PTM. Therefore, another crystal (named crystal-2) was used for HP-SCXRD experiments, without a prior ambient conditions data collection. The pressure cell axis was aligned approximately quasi-perpendicular to the (010) face of the crystal-2 (in the absence of face indexing, the crystal face was identified from the orientation of reciprocal axes with respect to the laboratory co-ordinates, using APEX4 software). A ruby sphere of ~10μm in diameter was placed inside the sample chamber for the in-situ measurement of pressure by ruby luminescence (PRL) technique (Piermarini *et al.*, 1975), while the Daphne oil 7474 (Murata *et al.*, 2008) was used as the PTM (**Figure 3.26**). The configuration of the high-pressure experimental set-up and the alignment of MDAC remains the same as that described in the previous case (**section 3.2.1.3**). During the HP-SCXRD experiments the sample was investigated under various quasi-hydrostatic pressures, ranging from 0.00(5) GPa to 5.0(2) GPa, in a sequential manner by first increasing then decreasing back to room pressure. Unfortunately, the attempt to retrieve crystal-2 out of

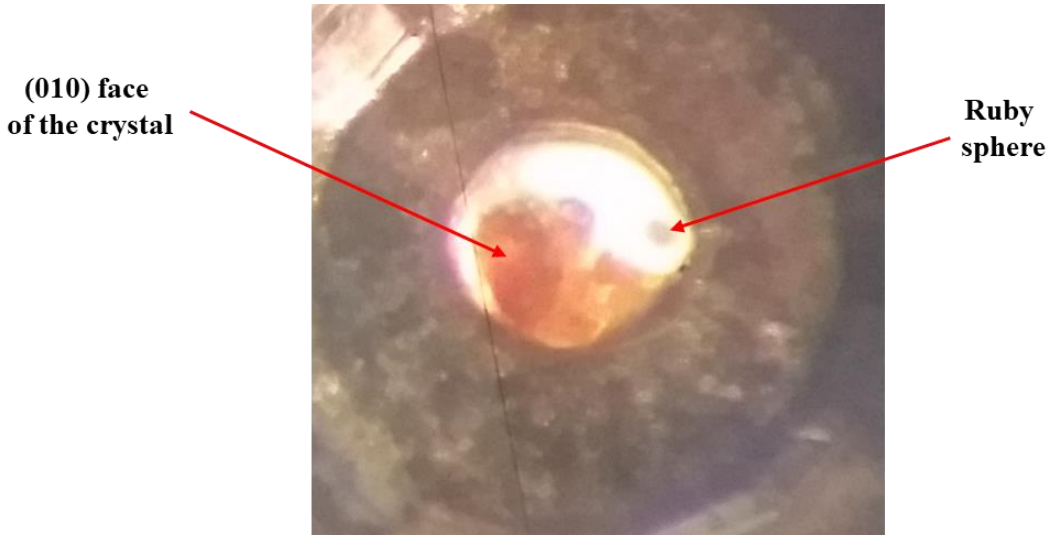

Figure 3.26 ***NISac.4CYP*** **single-crystal mounted inside the MDAC sample chamber with the cell axis quasi-perpendicular to the (010) plane of the crystal. One ruby sphere (~10 μm in radius) is placed in the sample chamber for pressure calibration. The sample chamber is filled with Daphne oil 7474 which acts as the PTM.**

MDAC after HP-SCXRD experiments was also failed, thus ending up with no face indexing (the accurate face indexing is not possible inside MDAC because the crystal view is hidden in certain directions due to the metal covering of MDAC).

High-pressure data integration and reduction were carried out using SAINT program after excluding the MDAC shadowed regions with a dynamic mask. During the integration, a half-aperture angle of 42° and a φ−offset of -4° was used in the Diamond Anvil Cell section for all the datasets. An empirical absorption correction was done based on the intensities using SADABS (Krause *et al.*, 2015). Like the previous case, atomic coordinates of the structure determined at ambient conditions were used as the starting model for the refinement of data collected at 0.00(5) GPa and this structural model obtained at 0.00(5) GPa was then used as the initial reference model for further refinements with high-pressure datasets. Again, during refinement, only the heavier atoms (I1 and S1) could be refined anisotropically. Attempts to refine the ADPs of other atoms resulted to either non-positive definite or unrealistic behaviour. As stated earlier, this feature is linked with the incompleteness of the dataset (completeness being only ~37% up to a resolution of 0.625 $Å^{-1}$ for all the high-pressure datasets). Therefore, to acquire a good structural model, an ADP transfer procedure (similar to **section 3.2.1.4**) was adapted. Here, $(U_{ij})_{out,P_0}$ ADPs were taken from crystal-1 rather than from crystal-2 since we could not collect the ambient conditions data for crystal-2 in order to derive the ADPs outside MDAC.

Table 3.14 Crystallographic information for data collected with increasing pressure for crystal-2. Atomic formula is $C_{13}H_8IN_3O_3S$ and the formula weight is 413.18 g/mol. In the *P*1 space group setting there are two molecular units in the asymmetric unit. (* *Table continues to the next page*)**

Pressure (GPa)	**0.00(5)**	**0.20(5)**	**0.4(1)**	**0.8(1)**	**1.4(2)**	**2.1(2)**	**2.4(2)**	**3.4(2)**	**3.6(2)**	**5.0(2)**
Crystal system, Space group, *Z*	Monoclinic, *Cc*, 4	Monoclinic, *Cc*, 4	Monoclinic, *Cc*, 4	Monoclinic, *Cc*, 4	Monoclinic, *Cc*, 4	Monoclinic, *Cc*, 4	Monoclinic, *Cc*, 4	Monoclinic, *Cc*, 4	Monoclinic, *Cc*, 4	Triclinic, *P*1, 2
a (Å)	7.4933 (5)	7.4367 (8)	7.3619 (8)	7.2735 (8)	7.1338 (8)	7.0386 (8)	7.0051 (8)	6.9115 (9)	6.8876 (8)	6.8346 (10)
b (Å)	23.315 (3)	23.135 (5)	22.913 (5)	22.665 (5)	22.280 (5)	22.013 (5)	21.916 (5)	21.651 (5)	21.582 (5)	8.1775(11)
c (Å)	8.7369 (6)	8.6844 (9)	8.6163 (9)	8.5373 (9)	8.4111 (9)	8.3221 (9)	8.2884 (9)	8.1954 (10)	8.1692 (9)	10.990 (3)
α, β, γ (°)	90, 100.347(2), 90	90, 99.844(2), 90	90, 99.149 (3), 90	90, 98.340 (3), 90	90, 97.029(3), 90	90, 96.043(3), 90	90, 95.668(3), 90	90, 94.560(3), 90	90, 94.265(3), 90	90.786(8), 106.557(8), 94.364 (4)
Volume (Å^3)	1501.6 (3)	1472.1 (4)	1434.9 (4)	1392.5 (4)	1326.8 (3)	1282.3 (3)	1266.2 (3)	1222.5 (4)	1211.0 (3)	586.68(19)
μ(mm^{-1})	2.28	2.33	2.39	2.46	2.58	2.67	2.71	2.81	2.83	2.92
T_{max}, T_{min}	0.563, 0.499	0.563, 0.510	0.563, 0.510	0.563, 0.512	0.563, 0.503	0.563, 0.511	0.563, 0.501	0.563, 0.499	0.563, 0.508	0.563, 0.480
No. of measured, independent, observed [I >2σ(I)] reflections	11697, 1085, 1017	8247, 989, 934	8092, 972, 918	7772, 941, 894	7329, 900, 856	7084, 859, 820	6955, 853, 807	6487, 828, 772	6404, 828, 771	5365, 1218, 1094
Completeness (%)	37	36	37	36	37	36	37	37	37	29
R_{int}	0.022	0.024	0.026	0.025	0.025	0.026	0.028	0.029	0.029	0.030
$(\sin\theta/\lambda)_{max}$ (Å^{-1})	0.624	0.622	0.622	0.623	0.627	0.621	0.622	0.619	0.622	0.626

$R[F^2>2\sigma(F^2)]$, ${}_wR(F^2)$, *GOF*	0.016, 0.035, 1.05	0.017, 0.034, 1.04	0.019, 0.037, 1.02	0.017, 0.036, 1.09	0.019, 0.039, 1.11	0.019, 0.040, 1.16	0.020, 0.041, 1.11	0.023, 0.049, 1.14	0.023, 0.052, 1.14	0.034, 0.077, 1.10
No. of parameters	76	76	76	76	76	76	76	76	76	151
N. of restraints	89	89	89	89	89	89	89	89	89	159
$\Delta\rho_{max},\Delta\rho_{min}$ ($eÅ^{-3}$)	0.14, -0.16	0.14, -0.17	0.18, -0.20	0.22, -0.21	0.29, -0.18	0.20, -0.19	0.24, -0.18	0.29, -0.27	0.27, -0.26	0.37, -0.35
Absolute structure parameter	0.008 (10)	0.007 (11)	-0.001 (10)	0.012 (9)	0.010 (10)	0.015 (10)	0.016 (11)	0.020 (12)	0.015 (13)	0.052 (15)

Table 3.15 Crystallographic information for data collected with decreasing pressure for crystal-2. Atomic formula is $C_{13}H_8IN_3O_3S$ and the formula weight is 413.18 g/mol. In the *P*1 space group setting there are two molecular units in the asymmetric unit. (****Table continues to the next page*****)**

Pressure (GPa)	**4.7(2)**	**4.2(2)**	**4.0(2)**	**2.1(2)**	**1.4(2)**	**1.0(2)**	**0.6(1)**	**0.3(1)**	**0.17(5)**	**0.05(5)**	**0.00(5)**
Crystal system, Space group, Z	Triclinic, *P*1, 2	Triclinic, *P*1, 2	Monoclinic, *Cc*, 4	Monoclinic, *Cc*, 4	Monoclinic, *Cc*, 4	Monoclinic, *Cc*, 4	Monoclinic, *Cc*, 4	Monoclinic, *Cc*, 4	Monoclinic, *Cc*, 4	Monoclinic, *Cc*, 4	Monoclinic, *Cc*, 4
a (Å)	6.8465 (13)	6.8526 (12)	6.8638 (8)	7.0402 (8)	7.1448 (7)	7.1978 (8)	7.2924 (8)	7.3852 (8)	7.4467 (8)	7.4803 (8)	7.4999 (9)
b (Å)	8.1929 (15)	8.1729 (14)	21.530 (5)	22.008 (5)	22.305 (4)	22.452 (5)	22.713 (5)	22.985 (5)	23.167 (5)	23.269 (5)	23.336 (5)
c (Å)	11.074 (4)	11.164 (4)	8.1424 (9)	8.3185 (9)	8.4173 (9)	8.4642 (9)	8.5482 (9)	8.6316 (9)	8.6877 (9)	8.7170 (9)	8.7345 (10)
α, β, γ (°)	90.568 (10), 106.556 (10), 94.433 (5)	90.106 (9), 106.849 (9), 94.287 (4)	90, 93.931(3), 90	90, 96.028(3), 90	90, 97.100(3), 90	90, 97.617(3), 90	90, 98.491(3), 90	90, 99.326(3), 90	90, 99.901(3), 90	90, 100.202(3), 90	90, 100.357(3), 90
Volume (Å^3)	593.3(3)	596.5(2)	1200.4 (3)	1281.8 (3)	1331.1 (3)	1355.8 (4)	1400.4 (4)	1445.8 (4)	1476.5 (4)	1493.3 (4)	1503.8 (4)
μ(mm^{-1})	2.89	2.87	2.86	2.68	2.58	2.53	2.45	2.37	2.32	2.30	2.28
T_{max}, T_{min}	0.563. 0.498	0.563, 0.485	0.563, 0.513	0.563, 0.504	0.563, 0.516	0.563 ,0.511	0.563, 0.511	0.563, 0.515	0.563, 0.516	0.563, 0.510	0.563, 0.515
No. of measured, independent, observed [I >2σ(I)] reflections	4987, 1207, 1068	5552, 1257, 1140	6143, 816, 763	6923, 884, 830	7127, 916, 857	7350, 936, 879	7674, 959, 901	7926, 977, 905	8232, 998, 931	8349, 1023, 933	8455, 1038, 920
Completeness (%)	28	29	37	37	37	37	37	37	37	37	38

R_{int}	0.034	0.029	0.027	0.023	0.021	0.020	0.021	0.023	0.022	0.026	0.028
$(\sin\theta/\lambda)_{max}$ ($Å^{-1}$)	0.622	0.628	0.624	0.630	0.626	0.625	0.621	0.632	0.631	0.630	0.629
$R[F^2>2\sigma(F^2)]$, ${}_wR(F^2)$, GOF	0.042, 0.089, 1.19	0.031, 0.062, 1.17	0.025, 0.061, 1.12	0.019, 0.043, 1.15	0.019, 0.042, 1.10	0.019, 0.041, 1.10	0.019, 0.042, 1.11	0.021, 0.046, 1.09	0.021, 0.049, 1.10	0.024, 0.054, 1.11	0.025, 0.058, 1.17
No. of parameters	151	151	76	76	76	76	76	76	76	76	76
N. of restraints	159	159	89	89	89	89	89	89	89	89	89
$\Delta\rho_{max}$, $\Delta\rho_{min}$ ($eÅ^{-3}$)	0.46, -0.45	0.29, -0.35	0.28, -0.30	0.21, -0.19	0.24, -0.20	0.23, -0.18	0.21, -0.19	0.17, -0.19	0.19, -0.15	0.17, -0.24	0.25, -0.24
Absolute structure parameter	0.066 (16)	0.057 (13)	0.017 (11)	0.017 (10)	0.029 (9)	0.028 (8)	0.007 (10)	0.000 (10)	-0.006 (11)	0.029 (14)	0.007 (14)

Surprisingly, the *NISac.4CYP* crystal undergoes a change in symmetry at an elevated pressure above 4.0(2) GPa, from a monoclinic (*Cc*) to less symmetric triclinic (*P*1) system. This makes the structure solution of the data collected after 4.0(2) GPa less straightforward using the atomic co-coordinates determined in *Cc* at 0.00(5) GPa. Thus, the ambient conditions data was re-integrated and solved again in *P*1 space group to acquire the atomic co-coordinates that can be used as the reference model for any high-pressure dataset collected above 4.0(2) GPa (the reason behind the re-integration rather than a simple transformation using a transformation matrix will be discussed below). Also, from the first set of refinements it has been found that some of the covalent bonds get shorten while increasing pressure, which is not an expected feature especially in a low-pressure regime like 5.0(2) GPa for an organic crystal. This might also be a consequence of poor completeness of the collected dataset, along with the reduction of the crystal quality with time (based on the visual inspection) on increasing the load. Hence, constraints (DFIX, DANG) and restraints (SADI, FLAT) on distances and planarities were applied during the final refinements to keep distortions as small as possible. Crystallographic information for the high-pressure datasets can be found in **Table 3.14** and **Table 3.15**.

3.3.2 DFT calculations

3.3.2.1 Periodic plane wave calculations

Here, I would like to thank *Dr. Emmanuel Aubert*, Laboratory of Crystallography, Magnetic Resonance and Modeling (CRM2), University of Lorraine for the periodic plane wave calculations and the initial inspection of data.

The crystal structure of *NISac.4CYP* was optimized as a function of isotropic pressure, from -0.40 GPa to 6.00 GPa (-0.40, -0.35, -0.30, -0.25, -0.20, -0.05, then 0.00 to 6.00 with 0.25 increments; all in GPa), using the CASTEP software (version 19.11) (Clark *et al.*, 2005). The experimental structure determined at ambient conditions in the *Cc* space group setting was used as the starting point. All atomic positions were allowed to vary, together with cell parameters, while keeping the monoclinic symmetry. The PBE exchange and correlation functional was used, complemented by semi-empirical dispersion corrections (Grimme 2006). A fine plane wave cut-off was used, corresponding to a limit of 625eV. The MP grid size was set to 4 4 4. The optimization convergence criteria were fixed as follow: maximal stress tolerance at convergence: 0.1GPa; energy shift: $1E^{-5}$ eV; force: $5E^{-2}$ a.u.; displacement: $1E^{-3}$Å. The resulted

unit cell parameters and the unit cell volume as a function of pressure are gathered in **Table 3.16.**

Table 3.16 Unit cell parameters and unit cell volume as a function of the pressure for the *NISac.4CYP* DFT optimized crystal structures (in the *Cc* space group setting).

Pressure (GPa)	***a*(Å)**	***b*(Å)**	***c*(Å)**	***β*(°)**	***V*(Å^3)**
-0.40	7.634	24.204	8.948	102.706	1612.727
-0.35	7.606	23.989	8.854	101.479	1583.267
-0.30	7.543	23.895	8.797	100.585	1558.529
-0.25	7.513	23.921	8.772	100.180	1551.707
-0.20	7.467	23.784	8.775	100.697	1531.294
-0.05	7.357	23.701	8.693	99.192	1496.260
0.00	7.324	23.636	8.685	98.986	1484.882
0.25	7.239	23.205	8.585	98.456	1426.509
0.50	7.164	22.932	8.541	97.733	1390.554
0.75	7.093	22.807	8.504	97.281	1364.567
1.00	7.061	22.673	8.431	96.674	1340.638
1.25	7.020	22.537	8.400	96.299	1320.978
1.50	7.003	22.343	8.359	95.770	1301.363
1.75	6.966	22.253	8.336	95.460	1286.305
2.00	6.930	22.168	8.312	95.163	1271.776
2.25	6.918	22.040	8.278	94.796	1257.757
2.50	6.889	21.973	8.253	94.496	1245.310
2.75	6.875	21.877	8.219	94.080	1232.910
3.00	6.854	21.812	8.192	93.769	1222.134
3.25	6.897	21.702	8.081	92.361	1208.503
3.50	6.870	21.658	8.063	92.127	1198.850
3.75	6.856	21.606	8.041	91.877	1190.534
4.00	6.856	21.537	8.000	91.425	1180.972
4.25	6.913	21.477	7.888	90.276	1171.196
4.50	6.888	21.453	7.877	90.132	1163.987
4.75	6.881	21.411	7.854	89.840	1157.118
5.00	6.864	21.382	7.841	89.674	1150.792
5.25	6.877	21.317	7.799	89.192	1143.219
5.50	6.863	21.292	7.785	89.046	1137.543
5.75	6.868	21.244	7.753	88.659	1130.807
6.00	6.861	21.213	7.734	88.452	1125.153

3.3.2.2 Isolated molecules calculations

A similar set of calculations, using the same calculation level as that of *NISac.Py*, were also performed for *NISac.4CYP* (see **section 3.2.2.2** for detailed description). Here, $[I\text{-}4CYP]^+$ (a hypothetical model in which the I atom completely shifts to 4CYP and a positive charge is distributed throughout the I-4CYP molecule) was considered as an isolated moiety.

3.3.2.3 Intermolecular interaction energy decomposition

CrystalExplorer (version 17.5; Turner *et al.*, 2017) was used to calculate intermolecular interaction energies and their decompositions into electrostatic, polarization, dispersion and repulsive terms, employing the B3LYP functional and the DGDZVP basis set for all atoms. Intramolecular C-Hbond distances were normalized to standard neutron distances. A molecular shell of 3.80 Å in radius was generated in each case while the Gaussian09 software (Frisch *et al.*, 2013) was used for wavefunction calculation.

3.3.1 Results

3.3.1.1 Crystal structure description at ambient conditions

The crystal structure of *NISac.4CYP* contains one molecule of NISac and one of 4CYP in the asymmetric unit, held together *via* the same type of $N_{sac}\cdots I1\cdots N'_{4CYP}$ (called N1···I1···N2 according to the atomic numbering scheme) HaB motif (**Figure 3.27**), where the I atom is positioned between the N atoms (N1 and N2) of the parent compounds. The corresponding HaB distances N1···I1 and I1···N2 were determined respectively as 2.167(5) Å and 2.397(5) Å, with N1···N2 = 4.556 Å and $(\widehat{N1\ I1\ N2}) = 172.84(13)°$, for a resolution of 0.714 $Å^{-1}$.

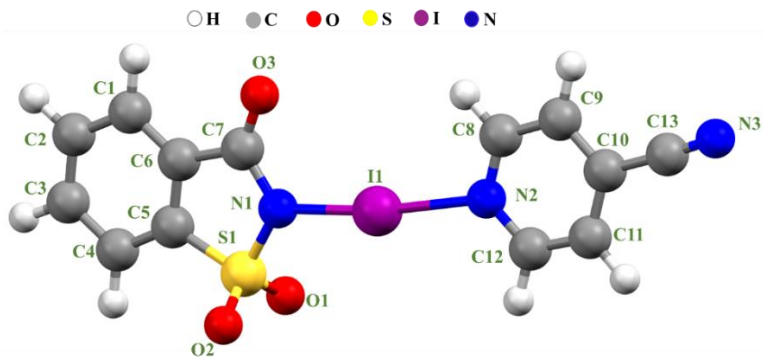

Figure 3.27 Atomic numbering scheme of *NISac.4CYP*, atom types are shown with colouring scheme.

With the same resolution, the HaB distances N1···I1 and I1···N2 obtained for the *NISac.Py* system were 2.2312(15) Å and 2.2865(16) Å, with N1···N2 = 4.513(2) Å and $(\widehat{N1\ I1\ N2}) = 174.88(6)°$. Therefore, the N1···N2 distance is found shorter in *NISac.Py* than in *NISac.4CYP*, suggesting that donor and acceptor moieties come closer to each other in the former thanks to a stronger HaB motif. This is also evident from the individual HaB distances, where a shorter N1···I1 and a longer I1···N2 was found in *NISac.4CYP* compared to the counterpart in *NISac.Py*. Also, this observation is consistent with the assumption made earlier from the ESP surfaces (based on the ESP values found close to the N lone-pair position in each acceptor molecule), pointing that *NISac.Py* is expected to form a comparatively stronger HaB interaction than *NISac.4CYP*.

In order to strengthen these findings regarding the HaB interactions, the electron distribution of the *NISac.4CYP* binary adduct was considered. For this purpose, the following calculations were performed [numbers (1)-(4) were assigned for further discussion] and the results were compared with the counterparts in *NISac.Py* (**section 3.2.3.1**):

(1) SPE calculation carried out for the *NISac.4CYP* binary adduct.

(2) Iodine atom position optimization, while keeping all other atoms frozen, for the *NISac.4CYP* binary adduct.

(3) Full geometry optimization for isolated NISac monomer.

(4) Full geometry optimization for isolated $[I\text{-}4CYP]^+$ monomer.

In all cases, the structures (atomic co-ordinates) were extracted from the crystalline geometry [for **(3)** and **(4)** the rest of the atoms in the adduct were omitted].

In case of **(1)**, a similar conclusion than that of *NISac.Py* can be also be drawn here, the I1 atom remains closer to the saccharinate side at the ambient conditions (**Table 3.17**). This is clearly observed from the topological properties found at N1···I1 and I1···N2 BCPs, showing a greater quantity of electron density in the bonding region of N1···I1[ρ_{BCP}(N1···I1) > ρ_{BCP}(I1···N2)] with a less depleted character [$(\nabla^2\rho/\rho)_{BCP}$(N1···I1) < $(\nabla^2\rho/\rho)_{BCP}$(I1···N2)], while $\nabla^2\rho > 0$ in both cases]. As in the previous co-crystal, this observation is also supported by other properties such as the total electron energy density H_{BCP} [H_{BCP}(N1···I1) < H_{BCP}(I1···N2)], the ratio between the potential V_{BCP} and kinetic energy densities G_{BCP} [$|V_{BCP}|/G_{BCP}$(N1···I1) > $|V_{BCP}|/G_{BCP}$(I1···N2)] and the delocalization index DI [DI(N1···I1) > DI (I1···N2)]. Here also, the N1···I1 and I1···N2 bonds exhibit an intermediate character between pure closed-shell and pure shared-shell interactions, suggesting that incipient halogen atom shift towards the acceptor

in the adduct results into a significant non-negligible covalent degree at both donor and acceptor sides. Considering all these results, the *NISac.4CYP* binary adduct at ambient conditions where the I1 atom is positioned still closer to the donor than to the acceptor, should be rather considered in a neutral co-crystal form.

Table 3.17 Internuclear N1···I1 and I1···N2 distances experimentally determined and theoretically calculated. The gathered QTAIM topological properties of the electron density $\rho(r)$ at BCPs are: the electron density(ρ_{BCP}), its laplacian ($\nabla^2\rho_{BCP}$), the total energy density ($H_{BCP} = V_{BCP} + G_{BCP}$) as well as the ratio between the electron potential (V_{BCP}) and kinetic (G_{BCP}) energy densities ($|V_{BCP}|/G_{BCP}$), its value normalized to ρ_{BCP}. The delocalization index at BCPs is denoted as $(DI)_{BCP}$. Values obtained for *NISac.4CYP* and *NISac.Py* are shown as left/right values. (1) – SPE calculation of *NISac.4CYP/NISac.Py*, (2) iodine atom optimization while keeping all the other atoms frozen, (3) full geometry optimization for NISac monomer (4) full geometry optimization for $[I\text{-}4CYP]^+/[I\text{-}Py]^+$ monomer.

	(1)	(2)	(3)	(4)
Distance N1···I1 (Å)	2.162/2.230	2.102/2.124	2.035/2.035	-
Distance I1···N2 (Å)	2.393/2.288	2.453/2.398	-	2.085/2.085
ρ_{BCP} N1···I1 (eÅ^{-3})	0.662/0.578	0.740/0.707	0.860/0.860	
ρ_{BCP} I1···N2 (eÅ^{-3})	0.412/0.510	0.365/0.411	-	0.798/0.800
$\nabla^2\rho_{BCP}$ N1···I1 (eÅ^{-5})	3.04/2.73	3.65/3.56	3.52/3.52	
$\nabla^2\rho_{BCP}$ I1···N2 (eÅ^{-5})	2.81/3.13	2.63/2.73	-	3.18/3.04
$(\nabla^2\rho/\rho)_{BCP}$ N1···I1 (Å^{-2})	4.59/4.72	4.93/5.04	4.09/4.09	
$(\nabla^2\rho/\rho)_{BCP}$ I1···N2 (Å^{-2})	6.82/6.14	7.20/6.63	-	3.98/3.80
H_{BCP} N1···I1 (a.u.)	-0.037/-0.029	-0.046/-0.043	-0.062/-0.062	
H_{BCP} I1···N2 (a.u.)	-0.013/-0.022	-0.010/-0.013	-	-0.054/-0.055
$(H/\rho)_{BCP}$ N1···I1 (a.u.)	-0.382/-0.333	-0.422/-0.405	-0.483/-0.483	
$(H/\rho)_{BCP}$ I1···N2 (a.u.)	-0.218/-0.288	-0.182/-0.218	-	-0.460/-0.462
$(\|V\|/G)_{BCP}$ N1···I1	1.543/1.501	1.550/1.535	1.628/1.628	
$(\|V\|/G)_{BCP}$ I1···N2	1.313/1.401	1.265/1.320	-	1.623/1.635
$(DI)_{BCP}$ N1···I1	0.827/0.749	0.879/0.845	1.076/1.076	
$(DI)_{BCP}$ I1···N2	0.524/0.620	0.474/0.525	-	1.020/1.023

In comparison with the results obtained for *NISac.Py* (**Table 3.17**), the electron density values at BCPs of *NISac.4CYP* [$\rho_{BCP}(N1\cdots I1)_{NISac.4CYP} > \rho_{BCP}(N1\cdots I1)_{NISac.Py}$ and $\rho_{BCP}(I1\cdots N2)_{NISac.4CYP} < \rho_{BCP}(I1\cdots N2)_{NISac.Py}$] suggest a stronger interaction of I with the donor side (and alternatively, a less stronger interaction of I with the acceptor is also observed). This trend parallels a lesser extent of halogen atom transfer observed in *NISac.4CYP* at ambient conditions, which eventually results in the formation of a comparatively weaker N1···I1···N2 HaB motif.

On the other hand, topological calculations carried out in **(2)**, **(3)** and **(4)** indicate qualitatively the same conclusions as those pointed out for *NISac.Py*. Quantitatively, it should be noted that here the differences Δ(N1···I1) and Δ(I1···N2) found between crystal and gas phases are 0.127 Å and 0.308 Å, respectively.

3.3.1.2 Energetic and electronic analyses of the intermolecular interactions at ambient conditions

The energetic and electronic analysis of the intermolecular interactions are performed with the CrystalExplorer software, using the crystal structure determined at ambient conditions. In such a way, it has been found that the crystal packing is mainly governed by four types interactions, formed by the reference (*x*,*y*,*z*) adduct with (1) (*x*,*y*,*-1+z*), (2) (*-1/2+x*,*3/2-y*,*-1/2+z*), (3) (*x*,*1-y*,*-1/2+z*) and (4) (*-1+x*,*y*,*-1+z*) symmetry generated adducts. Interaction (1), which results to a total interaction energy of -58.6 kJ/mol is mainly formed by π···π stacking motifs oriented along the crystallographic *a*-direction (**Figure 3.28a**), in addition to an electrostatic interaction between a positively charged carbon atom C13 [Q(C13) = +0.94 *e*] and the negatively charged oxygen atom O3 [Q(O3) = -1.17 *e*] C13···O3(*x*,*y*,*-1+z*) = 3.385 Å (**Figure 3.28a**, **Table 3.18** and **Table 3AP.12**). Thus, the decomposition of the total interaction energy suggests that the interaction is equally stabilized by electrostatic (-41 kJ/mol) and dispersion (-43.8 kJ/mol) terms. The second most important interaction is found with the (*-1/2+x*,*3/2-y*,*-1/2+z*) symmetry generated adduct in (2) (-47.2 kJ/mol), which is mainly composed of two HB interactions C4-H4(*-1/2+x*,*3/2-y*,*-1/2+z*)···O2 ($d_{H\cdots O}$ = 2.25 Å, $\alpha_{C\text{-}H\cdots O}$ = 137°) and C12-H12···O1(*-1/2+x*,*3/2-y*,*-1/2+z*) ($d_{H\cdots O}$ = 2.31 Å, $\alpha_{C\text{-}H\cdots O}$ = 153°) and are mainly stabilized by the electrostatic contribution (-40.4 kJ/mol) (**Table 3.18**). From the projection of the interatomic interaction vectors with respect to the crystallographic axes landmark, it is evident that this interaction is largely oriented along the crystallographic *b*-direction (**Figure 3.28b**). Further construction of the crystal packing is mainly led by two other interactions, respectively formed with (3) (*x*,*1-*

y,-1/2+z) and (4) *(-1+x,y,-1+z)* symmetry generated adducts. Interaction (3), which gives rise to a total interaction energy of -44.8 kJ/mol, is mainly composed of three HB interactions C1-H1(*x,1-y,-1/2+z*)···O3 ($d_{H\cdots O}$ = 2.46 Å, $\alpha_{C\text{-}H\cdots O}$ = 124°), C8-H8···O3(*x,1-y,-1/2+z*) ($d_{H\cdots O}$ = 2.38 Å, $\alpha_{C\text{-}H\cdots O}$ = 124°) and C9-H9(*x,1-y,-1/2+z*)···N3 ($d_{H\cdots N}$ = 2.65 Å, $\alpha_{C\text{-}H\cdots N}$ = 135°), being dominated by the electrostatic contribution (**Table 3.18**). Here, the major components of the interatomic interaction vectors are also placed mainly along the crystallographic *b*-direction (**Figure 3.29a**). Following the hierarchy of E_{tot}, the next most significant interaction is formed in (4), resulting into a total interaction energy of -41.5 kJ/mol and mainly composed of π···π stacking motifs running along the crystallographic *a*-direction. In addition, a weak hydrogen contact (resulting from the proximity of H11 and O1 atoms) C11-H11···O1(-1+x,y,-1+z) ($d_{H\cdots O}$ = 2.73 Å, $\alpha_{C\text{-}H\cdots O}$ = 110°) and an electrostatic interaction formed between a positively charged carbon atom C13 [Q(C13) = +0.94 *e*] and the negatively charged oxygen atom O1 [Q(O1) = -1.36 *e*] C13···O1(x,y,-1+z) = 3.294 Å also contribute to the total interaction energy in (4) (**Figure 3.29b**, **Table 3AP.12**). Unlike the previous case, this interaction is mainly stabilized by the dispersion contribution due to the proximity of the aromatic rings.

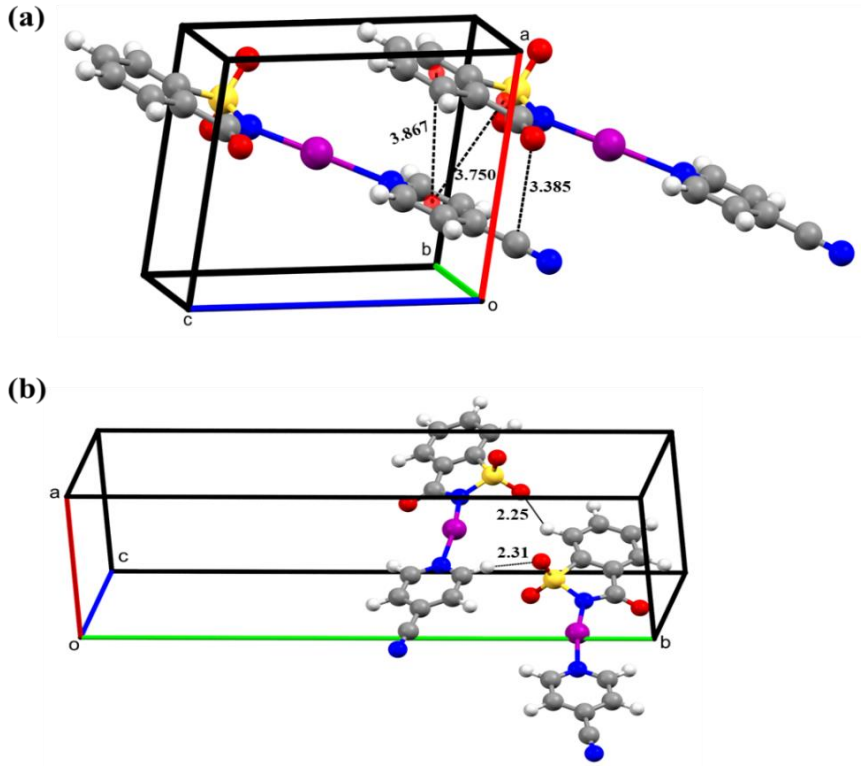

Figure 3.28 Dimers of adducts extracted from the crystal structure of *NISac.4CYP* at ambient conditions. Interactions are formed between the reference (*x,y,z*) adduct and (a) (*x,y,-1+z*) and (b) (*-1/2+x,3/2-y,-1/2+z*) symmetry generated adducts. Characteristic distances (in Å) of relevant interactions (shown as black dashed lines) are shown in each figure.

Table 3.18 Decomposition of the total interaction energy (E_{tot}) between dimers of *NISac.4CYP* adducts in electrostatic (E_{ele}), polarization (E_{pol}), dispersion (E_{dis}) and repulsion (E_{rep}) terms. Sym. Op denotes the symmetry code of the neighbouring adduct interacting with the reference (*x,y,z*) adduct (R is the intermolecular centroid to centroid distance). All energies are given in kJ/mol.

SI.No	Sym. Op.	R (Å)	E_{ele}	E_{pol}	E_{dis}	E_{rep}	E_{tot}
1	*x,y,-1+z*	8.74	-41.0	-4.4	-43.8	30.7	-58.6
2	*-1/2+x,3/2-y,-1/2+z*	7.70	-40.4	-8.4	-18.4	19.9	-47.2
3	*x,1-y,-1/2+z*	7.40	-31.7	-7.5	-24.0	18.5	-44.8
4	*-1+x,y,-1+z*	10.44	-25.9	-3.8	-34.6	22.8	-41.5
5	*-1+x,y,-2+z*	17.74	-6.7	-0.9	-4.4	3.6	-8.3
6	*-1+x,1-y,-3/2+z*	15.11	3.6	-0.8	-5.1	1.9	-0.5
7	*-1/2+x,1.5-y,-3/2+z*	14.16	2.3	-0.6	-2.0	0.1	-0.2

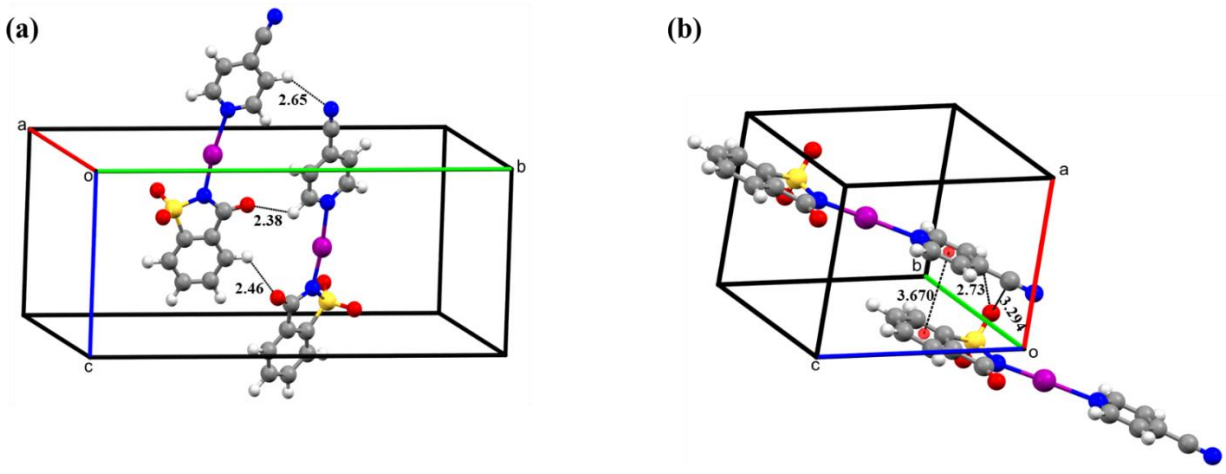

Figure 3.29 Dimers of adducts extracted from the crystal structure of *NISac.4CYP* at ambient conditions. Interactions are formed between the reference (*x,y,z*) adduct and (a) (*x,1-y,-1/2+z*) and (b) (*-1+x,y,-1+z*) symmetry generated adducts. Characteristic distances (in Å) of relevant interactions (shown as black dashed lines) are shown in each figure.

Other interactions are also present in the crystal packing, but comparatively less significant. Among them, the interaction formed with (5) *(-1+x,y,-2+z)* symmetry generated adduct (-8.3 kJ/mol) is the most important one, being mainly stabilized by the electrostatic contribution (**Table 3.18**). Looking at interatomic interactions, this dimer only contains two contacts resulting from the proximity of N3 with H2 and H3 atoms (interatomic distances being long enough to be termed as HB interactions), namely N3···H2-C2(*-1+x,y,-2+z*) ($d_{H\cdots N}$ = 2.79 Å, $\alpha_{C\text{-}H\cdots N}$ = 126°) and N3···H3-C3(*-1+x,y,-2+z*) ($d_{H\cdots N}$ = 2.83 Å, $\alpha_{C\text{-}H\cdots N}$ = 124°), oriented along the crystallographic *c*-direction (**Figure 3.30a**). On the other hand, the interactions formed with (6) (*-1+x,1- y,-3/2+z*) and (7) (*-1/2+x,3/2-y,-3/2+z*) symmetry generated adducts are only offering a very negligible contribution to the overall crystal packing, as indicated by their very small interaction energies (respectively, -0.5 kJ/mol and -0.2 kJ/mol).

In conclusion, motifs formed between the reference (*x,y,z*) adduct and adducts (1)-(4) are the most significant constituents of the crystal packing and are mainly oriented along the crystallographic *a*- and *b*-directions. Including motif (5), the molecular cluster formed around the central (*x,y,z*) adduct develops a tight packing along the crystallographic *c*-direction as well, as shown in **Figure 3.30b**. Overall, the crystal packing of *NISac.4CYP* at ambient conditions is more isotropic than the one found with *NISac.Py*. Accordingly, a different behaviour is expected in response to the action of external pressure. These details will be investigated in coming sections.

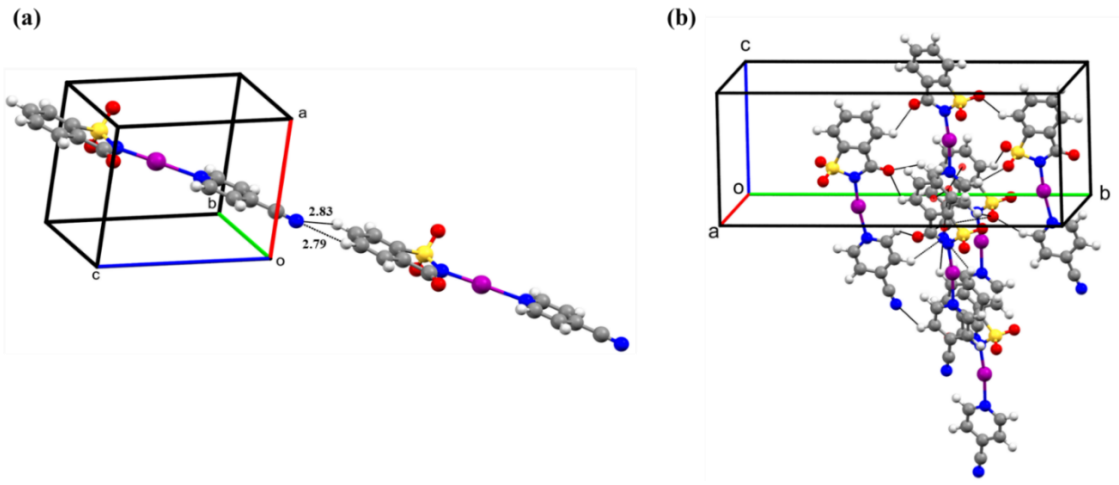

Figure 3.30 (a) Dimer formed between the reference (*x,y,z*) adduct and (*-1+x,y,-2+z*) symmetry generated adduct extracted from the crystal structure of *NISac.4CYP* at ambient conditions. Characteristic distances (in Å) of relevant interactions (shown as black dashed lines) are shown. (b) molecular cluster formed by reference (*x,y,z*) adduct and (1) (*x,y,-1+z*), (2) (*-1/2+x,3/2-y,-1/2+z*), (3) (*x,1-y,-1/2+z*), (4) (*-1+x,y,-1+z*) and (5) (*-1+x,y,-2+z*) symmetry generated adducts.

3.3.1.3 Equation of states (EOS)

The modification of the unit cell volume as a function of pressure was drawn and fitted with a 3rd order Birch-Murnaghan EOS using the EosFit7-GUI software (Gonzalez *et al*, 2016). A continuous compression of the sample was observed till a pressure of 3.6(2) GPa, above which the crystal underwent a change in space group from *Cc* to *P*1. Apart from the maintained single-crystal integrity, this process is reversible and the system regains back its original symmetry on removal of pressure during the decompression process. In such a way, crystal comes back from *P*1 to *Cc* space group at the decompression pressure 4.0(2) GPa. Therefore, we have two distinguishable regions in compression-decompression cycle, namely region-1 and region-2 constituted respectively by the high-pressure structures in *Cc* [0.00(5) GPa to 4.0(2) GPa] and *P*1 [4.2(2), 4.7(2) and 5.0(2) GPa] space groups. In region-1, including the uncertainties associated with the applied pressure, all data (during compression and decompression) can be fitted using a single EOS, ruling out the possibility of a hysteresis. The corresponding resulted EOS parameters are: reference volume V_0 = 1508(7) Å^3, bulk modulus K_{T_0} = 6(1) GPa and first derivative of the bulk modulus K_{T_0}' = 11(3) (**Figure 3.31a**).

In order to characterize if either a continuity or discontinuity appears in the evolution of the unit cell volume during the symmetry change from region-1 to region-2, all the structures obtained at high-pressure were examined in the *P*1 space group setting. This procedure permit to compare the unit cell parameters and the unit cell volume of any two pressure points directly, otherwise being not possible considering different number of molecules in the unit cell for *Cc* (4 molecules) and *P*1(2 molecules) space groups. It has also been found that, the molecules generated by the *c*-glide symmetry operation in the *Cc* space group for the structures in region-1 are no more equivalent in the *P*1 space group for the structures in region-2, even though the molecular packing does not experience any drastic modifications during the space group change (see the below section for more details). However, in order to examine all data together, HP-SCXRD data obtained in *Cc* space group (region-1) were again re-integrated in *P*1 space group. This re-integration is carried out (over a simple transformation of the unit cell parameters, using a transformation matrix) because, during the generation of EOS it is necessary to provide the standard deviations associated with unit cell parameters and unit cell volume. The initial unit cell transformation from *Cc* to *P*1 (necessary for the data re-integration procedure) was performed using the transformation matrix ***A*** obtained from Bilbao crystallographic server (Aroyo *et al*, 2011):

$$A = \begin{bmatrix} 1 & 0 & -1/2 \\ 0 & 0 & -1/2 \\ 0 & 1 & 0 \end{bmatrix}$$

Thereafter, the evolution of unit cell volume was drawn for the whole pressure range (in *P*1) and fitted with a 3rd order Birch-Murnaghan EOS. This resulted in the EOS parameters: reference volume V_0 = 755(4) Å^3, bulk modulus K_{T_0} = 6(1) GPa and first derivative of the bulk modulus K_{T_0}' = 12(3) (**Figure 3.31b**). From the EOS fitting curve, it is evident that all data can be fitted using the same EOS. This trend suggests that the evolution of the unit cell volume does not experience any discontinuity while going from region-1 to region-2, rather showing an overall reduction of ~22% from 0.00(5) GPa to 5.0(2) GPa.

In order to validate these experimental findings, EOS was also represented for the theoretical dataset. Since the monoclinic symmetry was imposed during the calculation, all the theoretical high-pressure data are gathered in *Cc* space group. Therefore, for a better comparison, all the unit cell parameters obtained in *Cc* were transformed to *P*1, using the vector transformation and associated equations given in **Figure 3AP.13**. Afterwards, the theoretical data obtained within the range of experimentally applied pressure were selected and the evolution of the unit cell volume was drawn and fitted with a 3rd order Birch-Murnaghan EOS. The EOS parameters thus obtained are: reference volume V_0 = 756(2) Å^3, bulk modulus K_{T_0} = 6.0(4) GPa and first derivative of the bulk modulus K_{T_0}' = 10.8(6), showing a very close agreement with the experimental values (**Figure 3.31d**).

In this case, while generating the EOS, corrections were made on the theoretical pressure values based on a linear regression relationship, rather than with a constant shift method used in the previous co-crystal system (EOS curve obtained after this method is given in **Figure 3.31c** for comparison purpose). Here, the linear regression relationship is obtained as follow,

(i) A plot of pressure *vs* volume per adduct was drawn and fitted with a polynomial function (6th order; a higher order polynomial is used since a smooth evolution is observed in between the data points), for the whole theoretical dataset (**Figure 3AP.14a**).

(ii) This polynomial function was used to calculate the theoretical pressure values (P_{DFT}) corresponding to the volume per adduct observed at each experimental pressure (P_{Exp}).

(iii) A plot of P_{Exp} *vs* P_{DFT} gives a good linear correlation (R^2 = 0.9974), with an equation $y = 1.1313X + 0.1521$ (**Figure 3AP.14b**).

(iv) This linear correlation was used to correct the theoretically applied pressures, by taking each pressure value as *X* input.

Comparing **Figure 3.31c** and **Figure 3.31d**, it clearly shows that the agreement between theoretical and experimental EOS is better for the case in which the pressure values were corrected based on the linear correlation method.

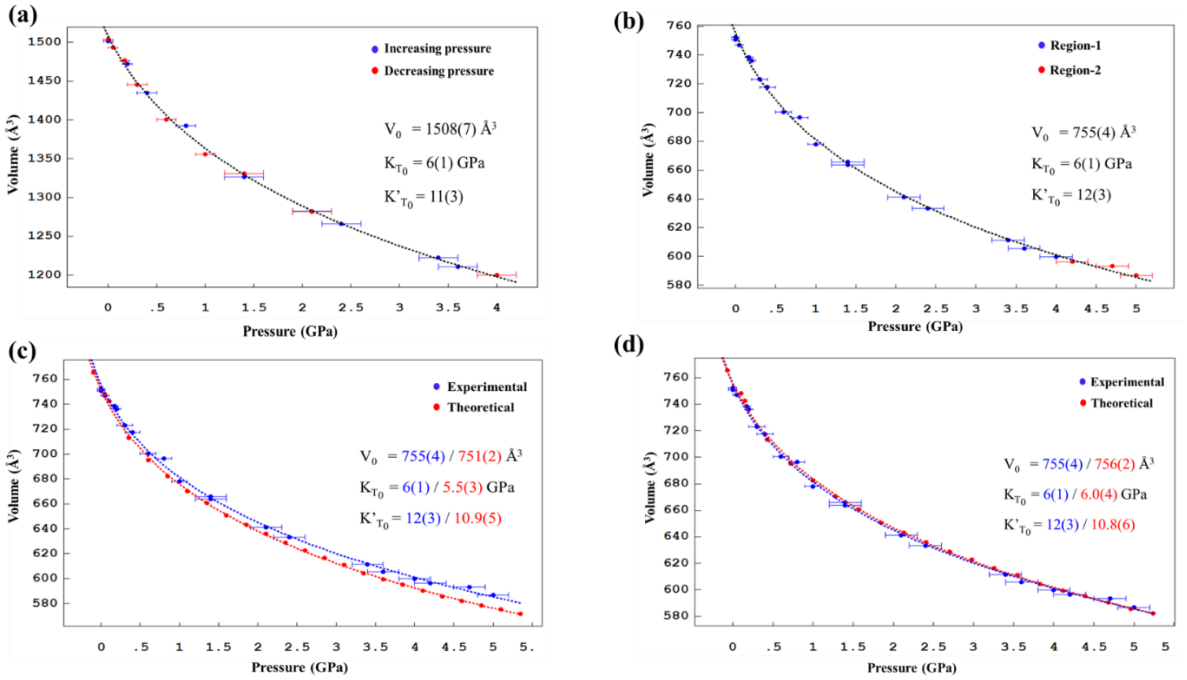

Figure 3.31 Variation of unit cell volume as a function of pressure fitted with a 3rd order Birch-Murnaghan EOS for: (a) compression and decompression data (in *Cc* space group) in region-1 (blue circle: increasing pressure data, red circles: decreasing pressure data, black dotted line: EOS fitting curve), (b) data in region-1 and region-2 (all in *P*1 space group) plotted together (blue circle: pressure data in region-1, red circles: pressure data in region-2, black dotted line: EOS fitting curve), (c) experimental and theoretical data plotted together (theoretical pressure values corrected based on a constant shift method; blue circles: experimental data, blue dotted line: experimental EOS fitting curve, red circles: theoretical data, red dotted line: theoretical EOS fitting curve) and (d) experimental and theoretical data (theoretical pressure values corrected based on a linear correlation method, see text for explanation) plotted together (blue circles: experimental data, blue dotted line: experimental EOS fitting curve, red circles: theoretical data, red dotted line: theoretical EOS fitting curve).

3.3.1.4 Variations of unit cell parameters with pressure

The modifications of unit cell parameters were drawn as a function of pressure for the datasets collected in the *Cc* space group within region-1. It is observed that in region-1 all the four-unit cell parameters (*a*, *b*, *c* and β) exhibit a monotonically decreasing behaviour with increasing pressure (**Figure 3.32a** and **Figure 3.32b**), pointing that a positive compressibility is observed along the direction of each unit cell axis. Further, in order to better visualize the variation in each unit cell length at any given pressure, the evolution of relative changes in the unit cell

lengths [with respect to a_0, b_0 and c_0 values obtained at 0.00(5) GPa, first pressure taken as the reference] were also drawn as a function of pressure (**Figure 3.32c**). In such a way, a maximal compressibility is observed along *a*-axis, followed by *b*- and then *c*-axes. In addition, the percentage compressibility was evaluated along each unit cell axis direction using $\Delta l/l_0$ ($l = a$, b or c) ratio, where $\Delta l = l_{0.00(5)\,GPa} - l_{4.0(2)\,GPa}$. This resulted to a value of 8.4% along *a*-direction followed by 7.7% and 6.8% along *b*- and *c*-directions respectively, indicating that these values are not very different from each other. Earlier, from the analysis of intermolecular interactions, it was found that the *NISac.4CYP* crystal structure at ambient condition is mostly isotropic in nature, meaning that the crystal packing is similarly tightly bound in the direction of each crystallographic axis. And now, the percentage compressibility values suggesting that each unit cell axis directions responds similarly with increasing pressure. A detailed energetic characterization, along with the structural modification of *NISac.4CYP* with pressure, will be discussed in the below section.

In order to validate these experimental findings, the variations of unit cell parameters with pressure were also plotted for the theoretical dataset, using the data selected within the range of experimentally applied pressure in region-1 (that is from -0.07 GPa to 4.39 GPa; the theoretical pressure values being corrected by using the linear correlation, as described above). From **Figure 3.32a**, **b** and **c**, it is observed that the evolution of unit cell parameters in theoretical dataset follows the same trend as that observed in the experimental one, but with some sudden changes appearing after the theoretically applied pressure of 3.55 GPa. These changes are more pronounced in the evolving behaviour of c (or c/c_0), a (or a/a_0) and β parameters. The, percentage of compressibilities show a maximal value of 6.2% along the *b*-direction, followed by 8.4% along *c*- and then 8.2% along *a*-directions, which are very different from those obtained with the experimental dataset. From **Figure 3.32**, it can be argued that these differences are brought by the sudden changes observed in the unit cell parameters after a theoretically applied pressure of 3.55 GPa. Thus, for a better comparison, the percentage compressibilities are recalculated with the theoretical data limited upto 3.55 GPa (that is from -0.07 GPa to 3.55 GPa) and the corresponding range in the experimental data limited upto 3.6(2) GPa [that is from 0.00(5) GPa to 3.6(2) GPa]. In the theoretical dataset, this resulted to a similar compressibility along the *b*- and *a*- directions (respectively of 8.3% and 8.2%), followed by a smaller value of 6.6% along the *c*-direction. On the other hand, the experimental dataset still shows a relatively larger magnitude of 8.1% along *a*-direction, followed by 7.4% along *b*- and 6.5% along *c*-directions.

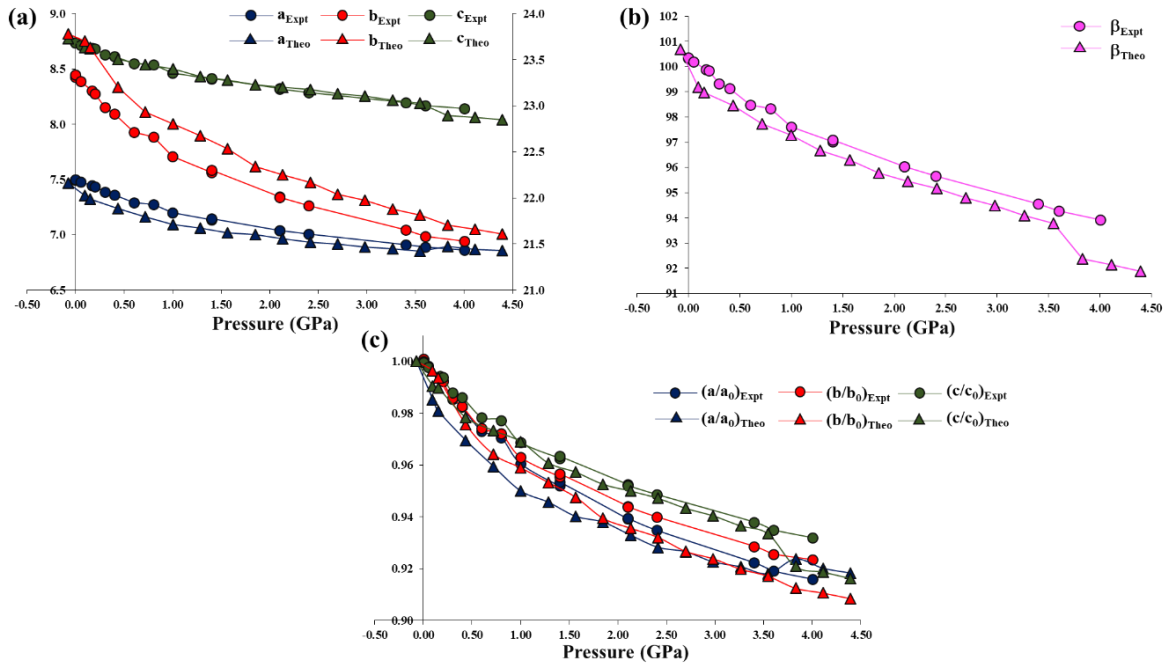

Figure 3.32 Variation of: (a) unit cell lengths, (b) monoclinic angle β and (c) unit cell lengths with respect to a_0, b_0 and c_0 values obtained at 0.00(5) GPa, as a function of pressure for the theoretical and experimental datasets. In (a) the 2nd Y-axis is corresponding to b_{Expt} and b_{Theo} values. Error bars associated with the experimental unit cell parameters are small enough to be visible within the range of plots, whereas the error bars corresponding to the experimental pressures are omitted for better clarity. Curves connecting data are plotted for guiding eyes.

Another interesting point to look concerns how the unit cell parameters are responding during the symmetry change, keeping in mind that the unit cell volume showed a smooth evolution going from region-1 to region-2. For this purpose, the variation of relative changes in the unit cell parameters [with respect to a_0, b_0 and c_0 values obtained at 0.00(5) GPa] were plotted as a function of pressure, actually for the whole pressure range in $P1$ space group. In this manner, using the same convention of space group throughout the explored range of pressures, makes the analysis of unit cell parameters more straightforward. Accordingly, from **Figure 3.33a**, it has been found that all the unit cell parameters except a (or a/a_0) show small discontinuities in their respective evolution during the symmetry change (that is going from region-1 to region-2). Also, the discontinuity of c/c_0 is causing a reversal of trend in region-2. Indeed, while for each pressure in region-1 a/a_0 and c/c_0 are monotonically decreasing with $a/a_0 < c/c_0$, it becomes $a/a_0 > c/c_0$ for each pressure in region-2. At the same time, b/b_0 shows a small increase in its evolution after 4.0(2) GPa, as well as γ/γ_0. On the other hand, α/α_0 and β/β_0 show respectively a sudden increase and decrease in their evolution between 4.0(2) GPa and 4.2(2) GPa. Overall, these modifications of unit cell parameters are not so drastic and they compensate each other in such a way that the evolution of the unit cell volume remains continuous across the boundary between region-1 and region-2 (**Figure 3.31b**).

A similar analysis is also done with the theoretical data set, using the same convention of space group, in order to verify if the unit cell parameters shows a smooth evolution within the whole range of calculated pressures. The analysis is carried out using a filtered dataset ranging from -0.07 GPa (a_0, b_0 and c_0 values are taken from this pressure, considered as the reference) to 5.24 GPa (**Figure 3.33b**). Unlike the experimental data set, here, c/c_0 shows a smooth decreasing behaviour throughout the explored range of pressures, whereas a/a_0 and b/b_0 exhibit some sudden changes after a theoretically applied pressure of 3.55 GPa, very similar to the observation made earlier with the data in *Cc* space group. In such a way, a/a_0 continuously decreasing till 3.55 GPa increases thereafter, whereas b/b_0 experiences a sudden drop in its evolution above 3.55 GPa that eventually makes $b/b_0 < a/a_0$. A similar trend as that of b/b_0 is also observed with γ/γ_0. At the same time, α/α_0 and β/β_0 show a smoothly increasing behaviour (but not deviating too much from its initial value) throughout. Here, it can be also stated that the variations observed in the unit cell parameters above 3.55 GPa compensate each other, making the evolution of the unit cell volume continuous from -0.07 GP to 5.24 GPa (**Figure 3.31d**).

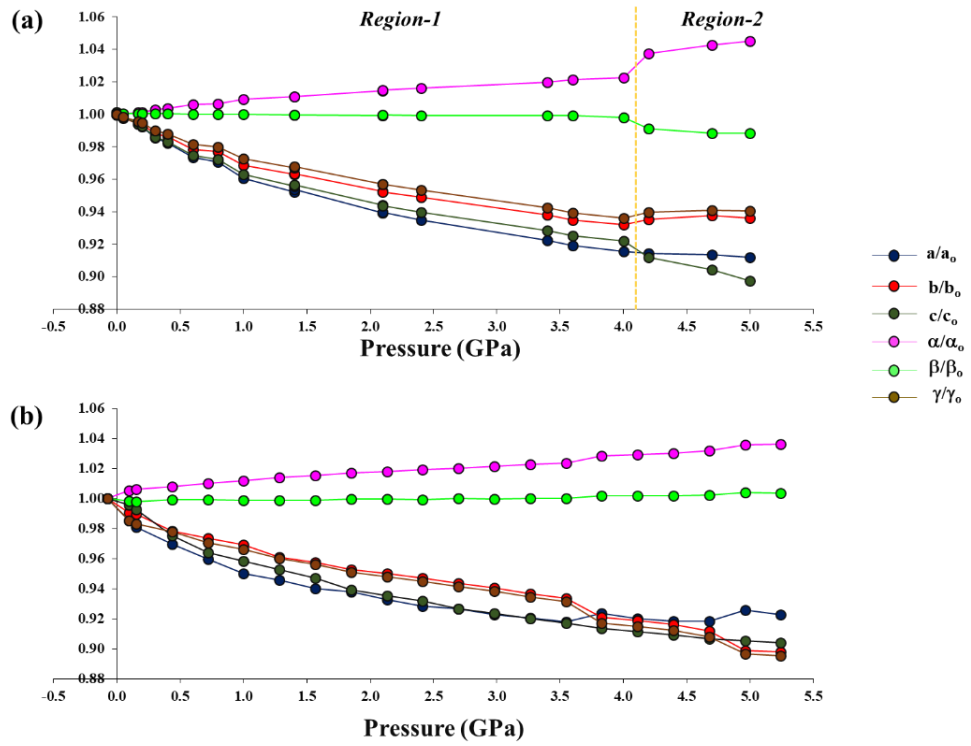

Figure 3.33 Relative variation of the unit cell parameters with pressure for (a) experimental and (b) theoretical data sets. An imaginary boundary is shown with orange dotted vertical line in (a) to distinguish between data in region-1 and region-2. Curves connecting data are plotted for guiding eyes.

As described earlier, in case of crystals with lower symmetry (monoclinic in this case), the simple analysis of the variations in the unit cell parameters might not give a full picture of the compression process. Instead, the principal axes of compression and corresponding principal compressibility values have to be analyzed. Therefore, they were calculated using the PASCal web-tool (Cliffe and Goodwin, 2012; **Table 3.19**). It has to be noted that, since the theoretically calculated unit cell parameters show some sudden changes in their respective evolutions above 3.55 GPa, the theoretical range of pressure used for this analysis was limited from -0.07 GPa to 3.55 GPa (in *Cc* space group). Similarly, for a better comparison, the experimental range of pressures was considered from 0.00(5) GPa to 3.6(2) GPa (also in *Cc* space group).

The results obtained from the experimental and theoretical data sets are qualitatively similar, both having the first principal axis X_1 oriented along the ***c-a*** direction with the corresponding compressibility value (K_1) of 36(1) and 24.0(3) TPa^{-1}, respectively. Similarly, the second principal axis X_2 is placed along the crystallographic *b*-direction, with a compressibility value of 22.4(8) and 19.3(9) TPa^{-1}, respectively for the experimental and theoretical dataset. On the other hand, the third principal axis X_3 showed a smaller compressibility value K_3 in both cases, being oriented along the ***a+c*** direction. Also, the compressibility indicatrix plots given in **Figure 3.34** point a close agreement between experimental and theoretical data, a small difference that is observed along X_1 is due to their different K_1 values. In both cases, only positive compressibilities are found in all directions, leading to the red surfaces only that are depicted in the compressibility indicatrix plots.

Table 3.19 Principal compressibility axes and corresponding compressibility values obtained from the high-pressure experimental and theoretical datasets of *NISac.4CYP* (in *Cc* space group). X_i – Principal axes of compressibility, K_i – principal compressibility value and σK_i - standard deviation of principal compressibility value (given in bracket). Experimental/ theoretical results are gathered as left/right entries.

Principal axis, X_i	K_i (TPa^{-1})	Components of X_i along the crystallographic axes		
		a	b	c
1	36(1)/24.0(3)	-0.8197/-0.8296	0.0000/0.0000	0.5728/0.5584
2	22.4(8)/19.3(9)	0.0000/0.0000	1.0000/1.0000	0.0000/0.0000
3	5.0(2)/2.7(0)	-0.7115/-0.7092	0.0000/0.0000	-0.7027/-0.7050

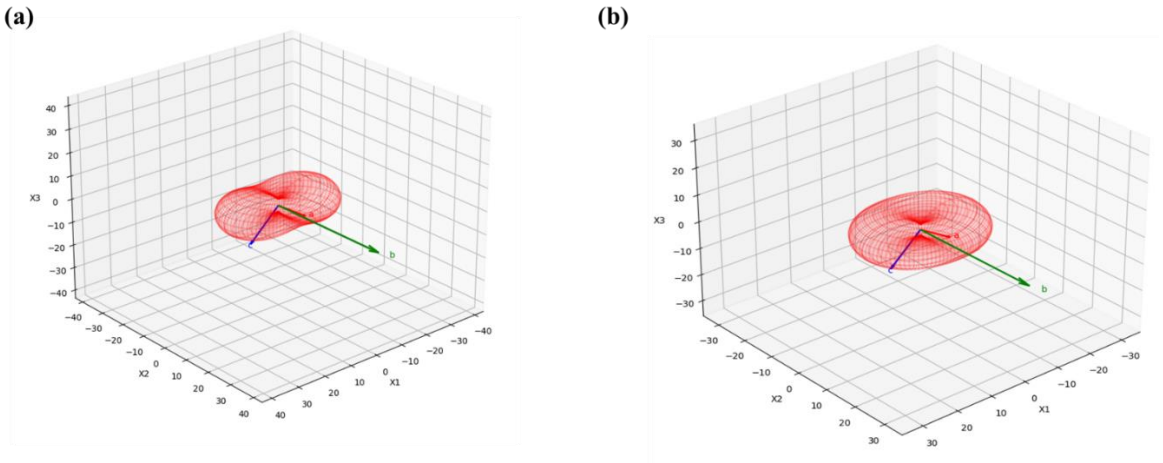

Figure 3.34 Compressibility indicatrix plots drawn for (a) experimental and (b) theoretical data. Positive compressibility values (red surfaces) are observed in all directions in both cases.

3.3.1.5 Phase transition at high-pressure

As mentioned earlier, *NISac.4CYP* crystal undergoes a change in symmetry at an elevated pressure above 4.0(2) GPa, from monoclinic (*Cc*) to triclinic (*P*1) system. During the compression process this transition happens at a pressure above 3.6(2) GPa [5.0(2) GPa being the next measured pressure]. Apart from maintaining the single crystal integrity, this process is also reversible and the crystal regains its initial symmetry back on decompression at 4.0(2) GPa or below, along with the reversible recovery of unit cell parameters and unit cell volume. Unlike the common cases of phase transition involving organic crystals under pressure (Boldyreva *et al.*, 2008), here the packing and the intermolecular interactions are preserved during the change in space group. A small re-orientation of neighbouring adducts with respect to the reference one is only taking place from *Cc* to *P*1, inducing some modifications in the intermolecular distances and angles. Accordingly, this re-orientation is causing a symmetry breakdown of adducts, leading to the low symmetry space group *P*1, that are otherwise equivalent and generated by the *c*-glide symmetry operation in the *Cc* space group (more details are given below).

It is also interesting to note that this reversible change in space group is happening at a pressure very close to that corresponding to the solidification limit of the used PTM (Daphne oil 7474), which is close to 3.7 GPa at room temperature (Murata *et al.*, 2008). Such a scenario has been already discussed in the literature, where the generation of a non-hydrostatic environment within the MDAC sample chamber (as a result of solidification of PTM) is pointed as the main reason behind such a process (Resel *et al.*, 2004). Whereas this might be the case here as well, but unfortunately, we do not have a concrete proof to support this argument since our HP-

SCXRD studies are limited to a single PTM. Thus, unable to verify whether the phase transition is somehow linked with the solidification limit of the PTM that we have used.

Before going to further details, it is important to prove that this phase transition is not resulting from an experimental artifact or a limitation related with data reduction software while judging the symmetry of the crystal structure. One way to crosscheck this possibility is by examining a set of symmetry forbidden reflections in the *Cc* space group, for those datasets originally indexed in the *P*1 space group. The dataset collected at 4.2(2) GPa (which is also the first data available in region-2) was chosen for this purpose. Details of this analysis can be found in **Section 3AP.4**, which confirms that the space group of *NISac.4CYP* changes from *Cc* to *P*1 above 4.0(2) GPa.

3.3.1.5.1 Structural analysis

To understand the structural reasons behind such a change in space group, we have investigated the modifications of molecular arrangements and the resulting intermolecular interactions. During the symmetry change, the molecules generated by the *c*-glide symmetry operation in the *Cc* space group become no more equivalent in the *P*1 space group. Alternatively, this symmetry breakdown (loss of *c*-glide symmetry element) in the *P*1 crystal structure is supposed to cause some changes in intermolecular interactions that are otherwise formed between the reference (*x*,*y*,*z*) adduct and the *c*-glide symmetry generated adducts in the *Cc* crystal structure. The analysis of molecular arrangements in *P*1 at 4.2(2) GPa as compared to the ones in *Cc* at 4.0(2) GPa revealed that they are preserved during the symmetry change, indicating that the modification of the molecular arrangements is minimal while going from region-1 to region-2 (**Figure 3.35**). In this situation, the rationale behind such a symmetry change can be understood by comparing the characteristics of intermolecular interactions, using the structure obtained in *Cc* and *P*1 space groups at any given pressure in region-2. This method will give a direct access to the modifications in intermolecular interactions from one space group to the other. Unfortunately, the attempts to refine the structure in the *Cc* space group for any dataset collected in region-2 was unsuccessful, hindering a direct comparison between the intermolecular interactions in the crystal structure obtained in *P*1 and *Cc* space groups at the same pressure. However, it is possible to examine the difference in the packing between the crystal structure obtained in *Cc* at 4.0(2) GPa and *P*1 at 4.2(2) GPa, but the constrain is that it is difficult to confirm whether the changes in intermolecular interactions are brought by the effect of symmetry lowering or it is simply a consequence of increase in pressure. In addition, the

completeness of the experimental datasets in *Cc* and *P*1 space groups are different for the same resolution, which can induce some differences (even though minor) in the structural distances and angles. Therefore, in this regard, it will be more appropriate to hypothetically generate a structure in the *Cc* space group at any given pressure in region-2 and directly compare with the actual structure obtained in the *P*1 space group at the same pressure. This possibility will rule out the differences in structural distances caused by the effect of pressure. Here, a hypothetical structure was generated in the *Cc* space group at 4.2(2) GPa, using an extrapolation of the polynomial fitting method. Accordingly, the modification of the x,y,z structural co-ordinates of each atom (of the reference adduct) was drawn as a function of pressure, from 0.00(5) GPa to 3.6(2) GPa in the *Cc* space group, and fitted with a 3rd order polynomial function. This polynomial fitting resulted to a good statistical R^2 value in most cases, suggesting that the evolution of structural co-ordinates actually follow a particular trend with pressure. Further, these 3rd order fitting equations were utilized to generate the x,y,z co-ordinates of each atom at 4.0 GPa and 4.2 GPa. In both these hypothetical structures the unit cell parameters were derived from the equation given earlier in **Section 3AP.4**. The idea behind generating a hypothetical structure first in the *Cc* space group at 4.0 GPa is to verify whether this extrapolation method is working or not, by comparing between the hypothetical and the actual experimental structures obtained in *Cc* at 4.0 GPa. Accordingly, the molecular overlay diagrams drawn using these two structures at 4.0 GPa suggest the goodness of this extrapolation method (**Figure 3.36**). Therefore, in order to investigate the structural modifications occurred due to the change in symmetry, this method was used to generate the hypothetical structure in the *Cc* space group at 4.2 GPa and was compared with the actual *P*1 structure.

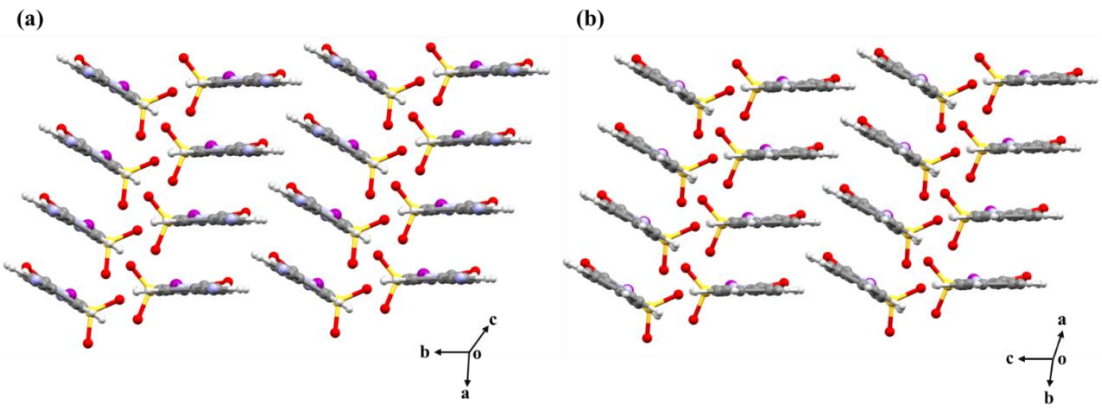

Figure 3.35 Similarity of the molecular packing observed in the crystal structures that determined in (a) *Cc* space group at 4.0(2) GPa and (b) *P*1 space group at 4.2(2) GPa.

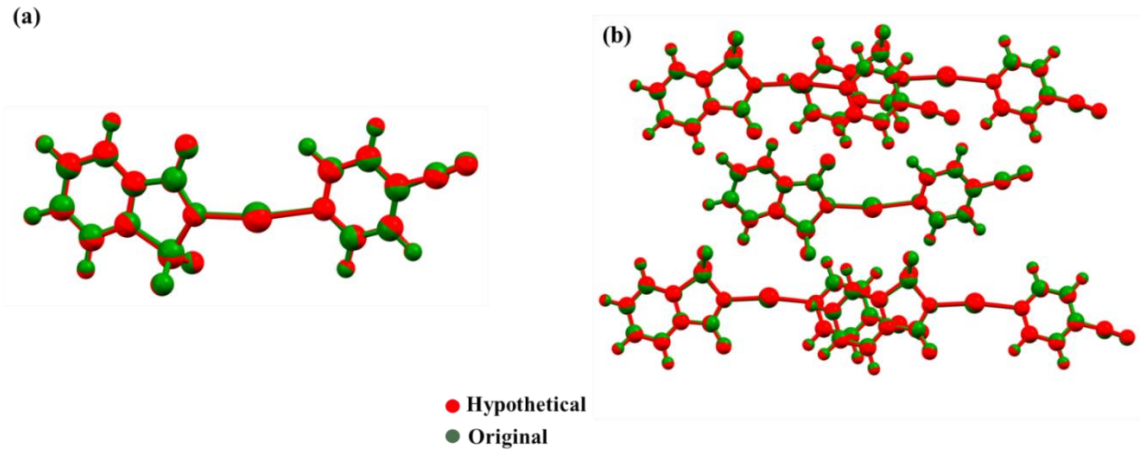

Figure 3.36 Molecular overlay diagrams, of (a) (*x,y,z*) reference adduct and (b) the reference adduct surrounded by the neighbouring adducts generated by the *c*-glide symmetry operation. Hypothetical and actual structures (in different colours) are determined at 4.0 GPa in the *Cc* space group.

If we consider the orientation of neighboring adducts (generated by the *c*-glide symmetry operation in *Cc* and those found in similar positions in *P*1) with respect to the reference one as well as the molecular centroid···centroid distance measured between them, it is found that no drastic rearrangement of molecules happens during the symmetry change (**Figure 3.37**). Rather, small molecular rotations are only observed from the selected interatomic distances and angles (**Table 3.20**), measured in *Cc* and *P*1 space groups at the same pressure of 4.2 GPa.

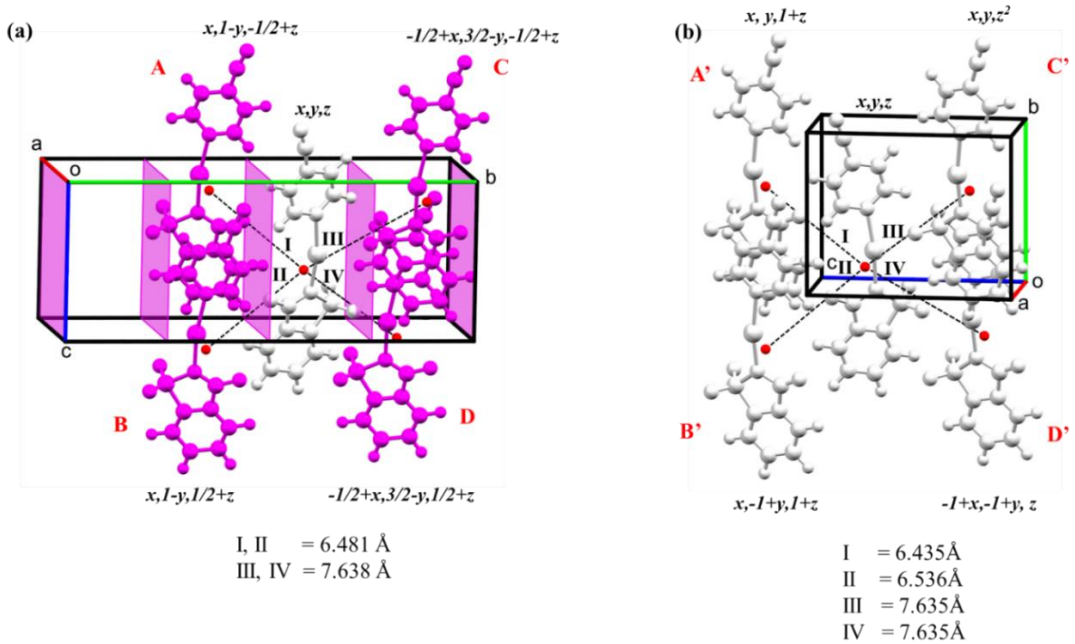

Figure 3.37 Molecular arrangement of the reference adduct with its neighbours (a) generated by *c*-glide symmetry operation for the crystal structure (hypothetical) in the *Cc* space group at 4.2 GPa and (b) adducts found in equivalent position for the crystal structure in the *P*1 space group at 4.2(2) GPa. Symmetry codes and centroid···centroid distances (using roman numbering) are shown in each figure. In (a), *c*-glide planes perpendicular to *b*-axis and molecules generated by the glide operation along the *c*-axis direction are shown in pink colour.

Unfortunately, for the hypothetical structure in *Cc* at 4.2 GPa, the e.s.d's (estimated standard deviations) associated with the atomic positions could not be generated. Therefore, the corresponding structural distances are left without e.s.d's, while the latter are given for the experimental structure in *P*1.

If we consider the centroid···centroid distances between dimers, the distances formed by A' and B' adducts (6.435 Å and 6.536 Å, respectively) with respect to the reference one in case of the crystal structure in *P*1 are not very different from the distance found with A (6.481 Å) in the crystal structure in *Cc*. This feature indicates that the adducts have not shifted much from each other in space as a consequence of the symmetry change. The same applies to the resulted interatomic distances and angles between these adducts, some minor differences (HB angles and H8···O3 distances) being only observed between the crystal structures in *Cc* and *P*1. On the other hand, the centroid···centroid distances found with C' and D' in *P*1 are very similar to the one obtained with C in *Cc*, even if the interatomic distances and angles exhibit some differences between each other. These differences are more pronounced in the case of I···O-S contacts. For the structure in *Cc* at 4.2 GPa, I1(*x,y,z*)···O2-S1(*-1/2+x,3/2-y,-1/2+z*) and I1(*x,y,z*)···O1-S1(*-1/2+x,3/2-y,-1/2+z*) distance/angle were determined respectively as 3.408 Å/98.2° and 3.743 Å/82.7° [which is also same for (*-1/2+x,3/2-y,1/2+z*) ; both the adducts being generated by the same *c*-glide symmetry operation]. In the case of the *P*1 crystal structure, the corresponding distances and angles measured for the adducts found in similar position show some differences: for C' I2(*x,y,z*)···O1-S1(*x,y,z*^{2}) and I2(*x,y,z*)···O2-S1(*x,y,z*^{2}) distance/angle are respectively 3.39(2) Å/104.5(7)° and 3.84(3) Å/84.7(10)°, whereas for D' S2(*x,y,z*)···O4-I1(*-1+x,-1+y,z*) and S2(*x,y,z*)···O5-I1(*-1+x,-1+y,z*) distance/angle are respectively 3.62(3) Å/94.0(12)° and 3.58(2) Å/95.2(7)°. This means that the (*-1+x,-1+y,z*) symmetry generated adduct (D') slightly rotated in space to make the S2(*x,y,z*)···O4-I1*(-1+x,-1+y,z*) and S2(x,y,z)···O5-I1(*-1+x,-1+y,z*) angles almost equal to each other compared to the case of C' or C (in both cases one angle is larger than the other) (**Table 3.20**). These molecular rotations are however not drastic enough to break the existing intermolecular interactions. In addition, one O···H-C HB is also showing some differences in their interatomic distances: O2···H3 (*-1/2+x,3/2-y,-1/2+z*) = 2.69 Å [in (*C*)] as compared to O5···H3 (*x,y,z*^{2}) = 2.57 Å [in (C')] and H16···O1 (*-1+x,-1+y,z*) = 2.72 Å [in (D')] (**Table 3.31**). In short, from the structural analyses it could be concluded that the types of intermolecular interactions are preserved during the symmetry change, the resulting symmetry breakdown from *Cc* to *P*1 space group being only the consequence of a small molecular rotation. This could be also the reason behind the small

discontinuities observed for the unit cell parameters while going from region-1 to region-2, as the types of intermolecular interactions are the same before and after symmetry change with minor differences observed in their interatomic distances and angles.

The symmetry change happening in our case from region-1 to region-2 is very different from the common cases of phase transitions previously reported for organic crystals under pressure (Boldyreva *et al.*, 2008). In most of those cases, phase transitions were accompanied with a rearrangement of the molecules in space and sometimes to the appearance of new intermolecular interactions that were not existing before. These rearrangements resulted to significant discontinuities in the evolution of the unit cell parameters and unit cell volume, and therefore they were classified as first order phase transitions. However, in the case of *NISac.4CYP*, the symmetry changes are mainly brought by some smaller molecular rotations in space, preserving the type of intermolecular interactions and therefore the crystalline environment around the reference molecule. Accordingly, these structural similarities before and after the symmetry change is only causing a small discontinuity in the evolution of in unit cell parameters while keeping the variation in unit cell volume continuous throughout the investigated range of pressure. This observation suggests that the symmetry change happening in the case of *NISac.4CYP* can be classified as a single-crystal to single-crystal second-order structural phase transition, which is reversible in nature (Landau and Lifshitz, 1980). This case is very similar to one of the phase transitions previously reported with L-threonine, from phase II to Phase III. There, the symmetry reduction was mainly caused by a change in the orientation of the hydroxyl group in half of the molecules, resulting only in small discontinuities in the unit cell parameters and unit cell volume (Giordano *et al.*, 2019).

Table 3.20 Intermolecular interactions formed between the reference (*x*,*y*,*z*) adduct and (i) the neighbouring adducts generated by the *c*-glide symmetry operation for the structure (hypothetical) in the *Cc* space group at 4.2 GPa, (ii) the adducts found in similar positions in the crystal structure determined with the *P*1 space group at 4.2(2) GPa. Distances are given in Å and angles are in degrees(º). Values within brackets are the standard deviations of the corresponding values. Distance and reduction ratio (RR) values are gathered as left/right entries.

Space Group	Pressure (GPa)	*x*,1-*y*,-1/2+*z* (A)						-1/2+*x*,3/2-*y*,-1/2+*z* (C)									
		N3···H9	N3···H9-C9	H8···O3	C8-H8···O3	O3···H1	O3···H1-C1	I1···O2	I1···O2-S1	I1···O1	I1···O1-S1	O2···H3	O2···H3-C3	O2···H4	O2···H4-C4	H12···O1	C12-H12···O1
Cc	4.2	2.24/0.81	136	2.14/0.79	123	2.20/0.81	109	3.408/0.97	98.2	3.743/1.07	82.7	2.67/0.98	106	2.07/0.76	128	1.92/0.71	151
Symmetry change																	
		x,*y*,1+*z* (A')						*x*,*y*,*z*[2] (C')									
		N6···H9	N6···H9-C9	H21···O3	C21-H21···O3	O6···H1	O6···H1	I2…O1	I2…O1-S1	I2…O2	I2…O2-S1	O5…H3	O5…H3-C3	O5…H4	O5…H4-C4	H25…O2	C25-H25…O2
*P*1	4.2(2)	2.23/0.81	141	2.21/0.81	117	2.21/0.81	115	3.39(2)/0.97	104.5(7)	3.84(3)/1.10	84.7(10)	2.57/0.94	108	2.04/0.75	128	1.88/0.69	154
		x,-1+*y*,1+*z* (B')						-1+*x*,-1+*y*,*z* (D')									
		H22…N3	C22-H22…N3	O6…H8	O6…H8-C8	H14…O3	C14-H14…O3	O4…I1	S2-O4…I1	O5…I1	S2-O5…I1	H16…O1	C16-H16…O1	H17…O1	C17-H17…O1	O4...H12	O4...H12-C12
*P*1	4.2(2)	2.24/0.81	137	2.21/0.81	120	2.19/0.81	116	3.62(3)/1.03	94.0(12)	3.58(2)/1.02	95.2(7)	2.72/1.00	104	2.07/0.76	128	1.92/0.71	141

[2] *there are two crystallographically independent adducts present in the asymmetric unit of P1 structures since the c-glide symmetry is broken from Cc to P1*

3.3.1.6 Variation of intermolecular interactions with pressure

In the previous case of *NISac.Py* we have seen that the N1⋯ I1⋯N2 HaB motif modifies as a result of changes in the crystalline environment in response to external pressure. In such a way, a halogen atom shift is happening within the adduct, where the position of I1 atom changes from being closer to N1 at low pressure to being slightly closer to N2 at high pressure, but still adjacent to the middle position between donor and acceptor moieties at any given pressure. Therefore, from the structural distances it has been concluded that the *NISac.Py* adduct at high-pressure becomes a single molecular unit (rather than two separate entities) in which both donor and acceptor exert a similar interaction strength to the I atom.

Actually, the same kind of N1⋯I1⋯N2 HaB motif is also present in the crystal structure of *NISac.4CYP*, but with a different crystalline environment around the I atom. The structural and electronic analysis of *NISac.4CYP* at ambient conditions revealed that the HaB interaction is weaker in nature and the I atom is bound closer and strongly to the donor moiety as compared to the case of *NISac.Py*. Thus, a slightly different response of the N1⋯I1⋯N2 HaB motif is expected on action of external pressure. Here also, in order to locate the relative position of I1 atom in between the donor and acceptor moieties, both N1⋯I1 and I1⋯N2 distances were normalized with respect to that of N1⋯N2 at each pressure (because both donor and acceptor moieties approach each other in space while increasing pressure). Due to the symmetry change happened above 4.0(2) GPa, the further analysis of the experimental datasets is limited from 0.00(5) GPa to 4.0(2) GPa. Also, the completeness of the collected datasets drops from ~37% (in *Cc*) to ~29% (in *P*1) after the symmetry change, for the same resolution of 0.625 $Å^{-1}$. Therefore, it is not convenient to compare the HaB distances in region-1 and region-2 directly.

By following the evolution of the normalized HaB distances with pressure in region-1, it is observed that the position of the I1 shifts in response to the external pressure, from its closer position to the donor nitrogen N1 at 0.00(5) GPa towards the acceptor nitrogen N2 at 4.0(2) GPa. However, even at the highest pressure, it is still far below the 0.5 transition boundary (**Figure 3.38a**). The corresponding individual and normalized HaB distances at each pressure can be found in **Table 3.21**. Therefore, based on these structural distances it can be argued that the I atom is bound closer to the donor at any given pressure, even though a slight shift is observed towards the acceptor side with increasing pressure. Unfortunately, here also, different electronic environments of donor and acceptor moieties along with the large uncertainties associated with the structural distances hinder to conclude about the precise position of I atom

within the adduct. Nevertheless, from the structural point of view, which clearly points the position of I closer to the donor, the *NISac.4CYP* adduct can be considered in its neutral co-crystal form throughout the investigated pressure range. For the high-pressure data collected in region-2 [that is at 4.2(2) GPa, 4.7(2) GPa and 5.0(2) GPa], there are two crystallographically independent adducts present in the asymmetric unit as a consequence of the symmetry breakdown happened from *Cc* to *P*1. These two crystallographically independent adducts exhibit almost identical values of normalized HaB distances (considering the uncertainties), while the corresponding values are found to be below the 0.5 transition boundary at any given pressure in region-2 (**Table 3.21**). Hence, the state of *NISac.4CYP* is still considered to be in its neutral co-crystal form till 5.0(2) GPa from the structural point of view. It is also interesting to note that, in region-2 these normalized HaB distances do not show significant modifications in its magnitude from 4.2(2) GPa to 5.0(2) GPa.

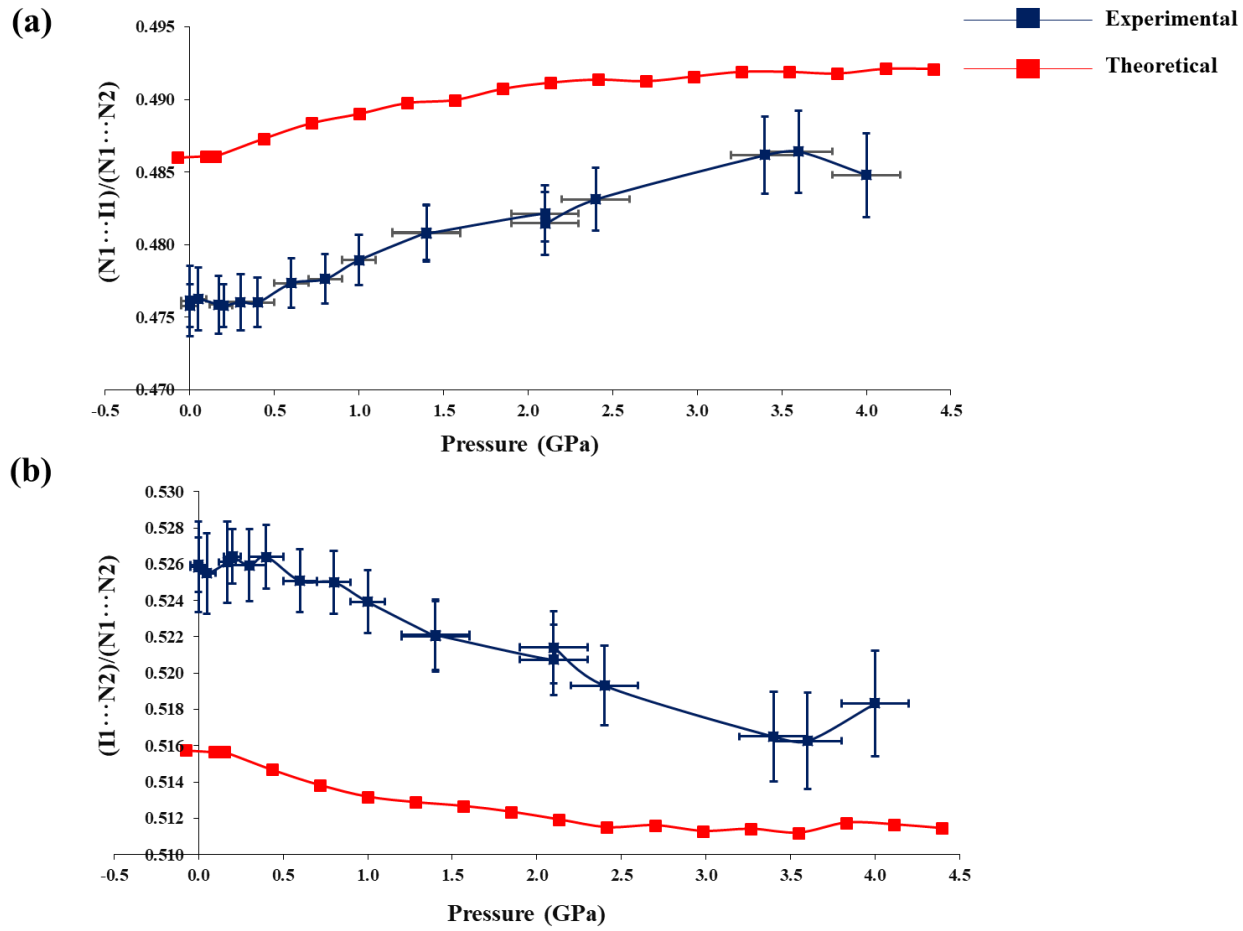

Figure 3.38 Variation of the normalized HaB bonding distances (a) (N1···I1)/(N1···N2) and (b) (I1···N2)/(N1···N2), as a function of pressure. Curves connecting data are plotted for guiding eyes. Error bars are shown for experimental data.

Table 3.21 N1···I1···N2 HaB distances and angles, and angle between the molecular planes, determined from the experimental high-pressure datasets of *NISac.4CYP*. The angle between molecular planes was calculated using the MPLA option in Olex2-1.3. The values determined for the two crystallographically independent adducts in region-2 are gathered as left/right entries (for the last three pressure points) and highlighted with red colour. Values within brackets are the standard deviations of the corresponding values.

Pressure (GPa)	0.00(5)	0.00(5)	0.05(5)	0.17(5)	0.20(5)	0.3(1)	0.4(1)	0.6(1)	0.8(1)	1.0(1)	1.4(2)	1.4(2)	2.1(2)	2.1(2)	2.4(2)	3.4(2)	3.6(2)	4.0(2)	4.2(2)	4.7(2)	5.0(2)
N1···I1 (Å)	2.162 (6)	2.173 (10)	2.176 (9)	2.168 (8)	2.161 (6)	2.166 (8)	2.163 (7)	2.170 (7)	2.168 (7)	2.172 (7)	2.172 (8)	2.175 (8)	2.174 (8)	2.170 (9)	2.176 (9)	2.180 (11)	2.183 (12)	2.169 (12)	2.160(15)/ 2.186(16)	2.149(19)/ 2.20(2)	2.166(18)/ 2.200(17)
I1···N2 (Å)	2.390 (6)	2.40 (1)	2.401 (9)	2.397 (9)	2.391 (6)	2.393 (8)	2.392 (7)	2.387 (7)	2.383 (7)	2.376 (7)	2.358 (8)	2.362 (8)	2.348 (8)	2.350 (8)	2.339 (9)	2.316 (10)	2.317 (11)	2.319 (12)	2.317(15)/ 2.308(13)	2.312(19)/ 2.314(18)	2.329(16)/ 2.302(15)
N1···N2 (Å)	4.544 (6)	4.564 (10)	4.569 (9)	4.556 (9)	4.542 (6)	4.550 (8)	4.544 (7)	4.546 (7)	4.539 (7)	4.535 (7)	4.517 (7)	4.524 (7)	4.509 (7)	4.507 (8)	4.504 (8)	4.484 (9)	4.488 (9)	4.474 (10)	4.460(19)/ 4.483(19)	4.45(3)/ 4.50(3)	4.48(2)/ 4.49(2)
(N1···I1)/ (N1···N2)	0.476 (1)	0.476 (2)	0.476 (2)	0.476 (2)	0.476 (1)	0.476 (2)	0.476 (2)	0.477 (2)	0.478 (2)	0.479 (2)	0.481 (2)	0.481 (2)	0.482 (2)	0.481 (2)	0.483 (2)	0.486 (3)	0.486 (3)	0.485 (3)	0.484(4)/ 0.488(4)	0.483(5)/ 0.489(6)	0.483(5)/ 0.490(4)
(I1···N2)/ (N1···N2)	0.526 (1)	0.526 (2)	0.525 (2)	0.526 (2)	0.526 (1)	0.526 (2)	0.526 (2)	0.525 (2)	0.525 (2)	0.524 (2)	0.522 (2)	0.522 (2)	0.521 (2)	0.521 (2)	0.519 (2)	0.517 (2)	0.516 (3)	0.518 (3)	0.520(4)/ 0.515(4)	0.520(6)/ 0.514(5)	0.520(4)/ 0.513(4)
N1···I1···N2 (º)	173.2 (4)	172.8 (5)	173.1 (5)	172.9 (5)	172.7 (4)	172.4 (5)	172.2 (4)	172.1 (4)	171.7 (4)	171.4 (4)	171.5 (4)	171.5 (5)	171.4 (5)	171.3 (5)	171.7 (5)	171.4 (6)	171.6 (6)	170.7 (7)	170(1)/ 172(1)	170(1)/ 172(1)	169(1)/ 173(1)
Angle b/w planes(º)	4.724 (185)	4.489 (290)	4.172 (280)	4.012 (272)	4.131 (206)	3.775 (281)	3.895 (232)	3.542 (255)	3.467 (240)	3.421 (249)	3.474 (266)	3.469 (254)	3.132 (285)	3.358 (279)	3.326 (296)	3.221 (352)	3.075 (369)	3.053 (422)	2.981(510)/ 2.266(616)	3.251(754)/ 2.962(867)	2.941(643)/ 3.725(746)

Table 3.22 N1···I1···N2 HaB distances and angles, and angle between the molecular planes, determined from the theoretical high-pressure dataset of *NISac.4CYP*. The angle between molecular planes was calculated using Mercury (version 2021.1).

Pressure (GPa)	-0.07	0.10	0.15	0.43	0.72	1.00	1.28	1.57	1.85	2.13	2.41	2.70	2.98	3.26	3.55	3.83	4.11	4.39
N1···I1 (Å)	2.222	2.220	2.220	2.225	2.226	2.225	2.224	2.223	2.225	2.225	2.223	2.222	2.221	2.221	2.219	2.218	2.217	2.215
I1···N2 (Å)	2.358	2.355	2.355	2.350	2.342	2.335	2.329	2.326	2.323	2.319	2.314	2.314	2.310	2.309	2.306	2.308	2.305	2.302
N1···N2 (Å)	4.572	4.567	4.567	4.566	4.558	4.550	4.541	4.537	4.534	4.530	4.524	4.523	4.518	4.515	4.511	4.510	4.505	4.501
(N1···I1)/ (N1···N2)	0.486	0.486	0.486	0.487	0.488	0.489	0.490	0.490	0.491	0.491	0.491	0.491	0.492	0.492	0.492	0.492	0.492	0.492
(I1···N2)/ (N1···N2)	0.516	0.516	0.516	0.515	0.514	0.513	0.513	0.513	0.512	0.512	0.511	0.512	0.511	0.511	0.511	0.512	0.512	0.511
N1···I1···N2 (º)	173.5	173.3	173.2	172.8	172.3	172.1	171.7	171.6	171.4	171.3	171.2	171.2	171.0	170.9	170.9	170.4	170.3	170.3
Angle b/w planes (º)	6.02	4.99	4.88	4.55	4.27	4.18	3.72	3.76	3.90	3.82	3.75	3.63	3.57	3.47	3.39	3.12	3.13	3.11

Similarly, the normalized HaB distances were also analyzed as a function of pressure for the theoretical data, with pressures ranging from -0.07 GPa to 4.39 GPa (**Table 3.22**). **Figure 3.38a** shows that theoretical data follows the same trend as the experimental one, the normalized (N1···I1)/(N1···N2) HaB distance increasing gradually with pressure. Accordingly, the theoretical dataset is also pointing the shift of I atom towards the acceptor moiety while increasing pressure. On the other hand, since the N1···I1···N2 angle is close to 180° at any given pressure, the normalized (I1···N2)/(N1···N2) HaB distances evolves in an opposite way (gradually decreases) than that of (N1···I1)/(N1···N2) with pressure, for both experimental and theoretical data sets (**Figure 3.38b**, **Table 3.21** and **Table 3.22**). Within the investigated pressure range the N1···I1···N2 angle shows a maximum variation of only 2.5º and 3.2º for the experimental and the theoretical data, respectively (**Table 3.21, Table 3.22** and **Figure 3AP.17a**), while the angle between the molecular planes formed by the saccharinate (excluding I and H atoms) and the 4-cyanopyridine ring (excluding H atoms) remains mainly unchanged (only very small variations of 1.67º and 2.91º are observed for experimental and theoretical data, respectively) (**Table 3.21**, **Table 3.22** and **Figure 3AP.17b**).

In order to investigate the modification of crystalline environment with pressure and how it eventually influences the shift of I atom between donor and acceptor moieties, we have selected the intermolecular interactions around the I atom and analyzed as a function of the pressure (**Table 3AP.13**). Out of the seven symmetry generated neighboring adducts found in the molecular shell (3.80 Å in radius) at ambient conditions, only three of them are involving intermolecular interactions with I1, namely (i) (*x,y,-1+z*) (ii) (*x,y,-1+z*) and (iii) (*-1/2+x,3/2-y,-1/2+z*). By analyzing these intermolecular interactions, it appears that in all cases the interatomic distances decrease monotonically as a function of pressure, most of them showing significant variations in their RR between the lowest and highest pressure considered (**Table 3AP.13** and **Figure 3.40**). Based on the RR values determined at 4.0(2) GPa, the I1···C3(*x,y,-1+z*) (RR = 0.93) interaction is found to be the most significant one, followed by I1···C2(*x,y,-1+z*) (RR = 0.97) and then I1···O2(*-1/2+x,3/2-y,-1/2+z*) (RR = 1.01) interactions, whereas the other interactions show RR values significantly greater than 1, even at 4.0(2) GPa. Simultaneously, tracing ΔRR (ΔRR= $RR_{0.00(5)\,GPa}$ - $RR_{4.0(2)\,GPa}$), I1···O2(*-1/2+x,3/2-y,-1/2+z*) interaction shows the largest values (ΔRR = 0.22) followed by I1···C3(*x,y,-1+z*) (ΔRR = 0.13) interaction. From the atomic charges determined at ambient conditions, it appears that the I1···O2*(-1/2+x,3/2-y,-1/2+z*) interaction is electrostatically attractive with Q(I1) = +0.48 *e* and Q(O2) = -1.36 *e*, while at 4.0(2) GPa these atomic charges modify slightly [Q(I1) = +0.50 *e* and

Q(O2) = -1.38*e*], making these interactions a bit more attractive. Considering the intermolecular interactions around the I atom under pressure, the same I1···O2 interaction shows significant stabilization from low to high pressure, with RR ~1 at 4.0(2) GPa and ΔRR = 0.22. In addition, the $I1^{\delta+}\cdots O2^{\delta-}$ secondary interaction is more favorable in a situation where the I atom is positioned closer to the acceptor side and therefore expected to play a crucial role on the shift of the I atom towards the acceptor moiety while increasing pressure (**Figure 3.39**). At the same time, among the selected interatomic angles, two of them shows monotonically increasing behaviour with pressure, while the other exhibits a continuous decrease with increasing pressure (**Table 3AP.13** and **Figure 3.41**). In order to validate these experimental findings, similar kind of analyses were also carried out with theoretically calculated structures, showing a very good agreement with the experimental results (**Table 3AP.14**, **Figure 3.39**, **Figure 3.40** and **Figure 3.41**). Modification of the other intermolecular interactions, formed by the atoms of the reference (*x*,*y*,*z*) adduct with the atoms of neighboring symmetry generated adducts can be found in appendices (**Table 3AP.15**, **Table 3AP.16** and **Figure 3AP.18-20**). Overall, this structural analysis reveals that the crystalline environment around the N1···I1···N2 HaB motif modifies significantly in response to external pressure, and this modification is mostly acting as a triggering force behind the shift of the I atom between donor and acceptor moieties.

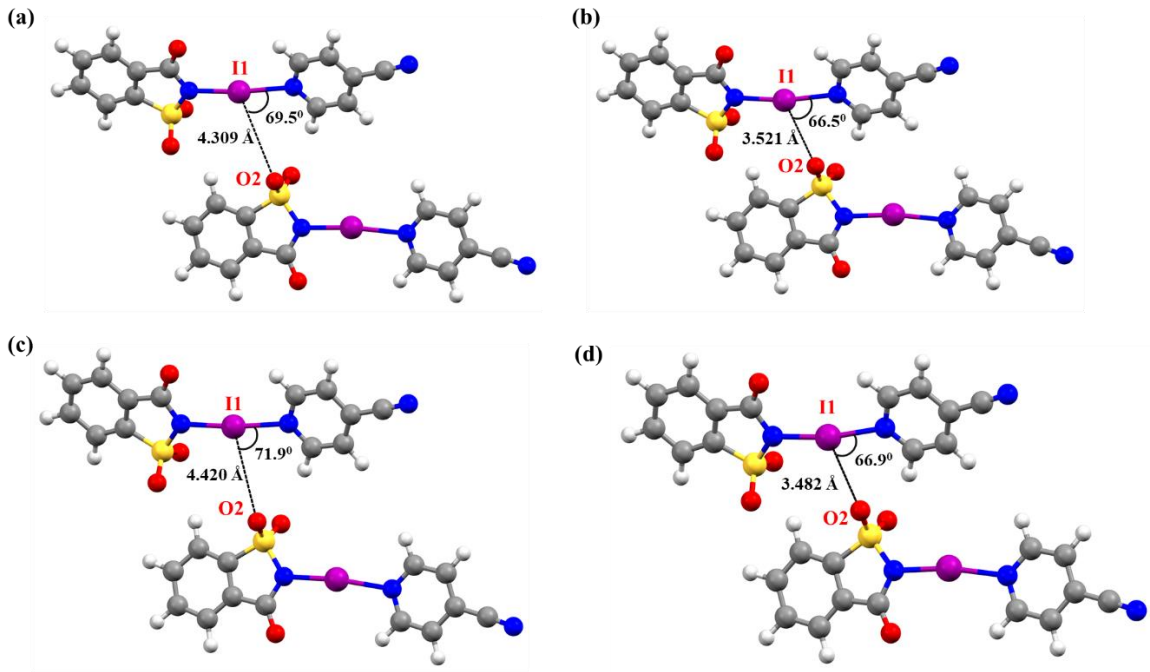

Figure 3.39 I1(*x*,*y*,*z*)···O2(*–1/2+x*,*3/2-y*,*-1/2+z*) interaction determined from the experimental dataset at (a) 0.00(5) GPa and (b) 4.0(2) GPa, and from the theoretical dataset at (c) -0.07 GPa and (d) 4.39 GPa. The characteristic distance (in Å) and O2···I1···N2 angle [in degrees(⁰)] are shown in each figure.

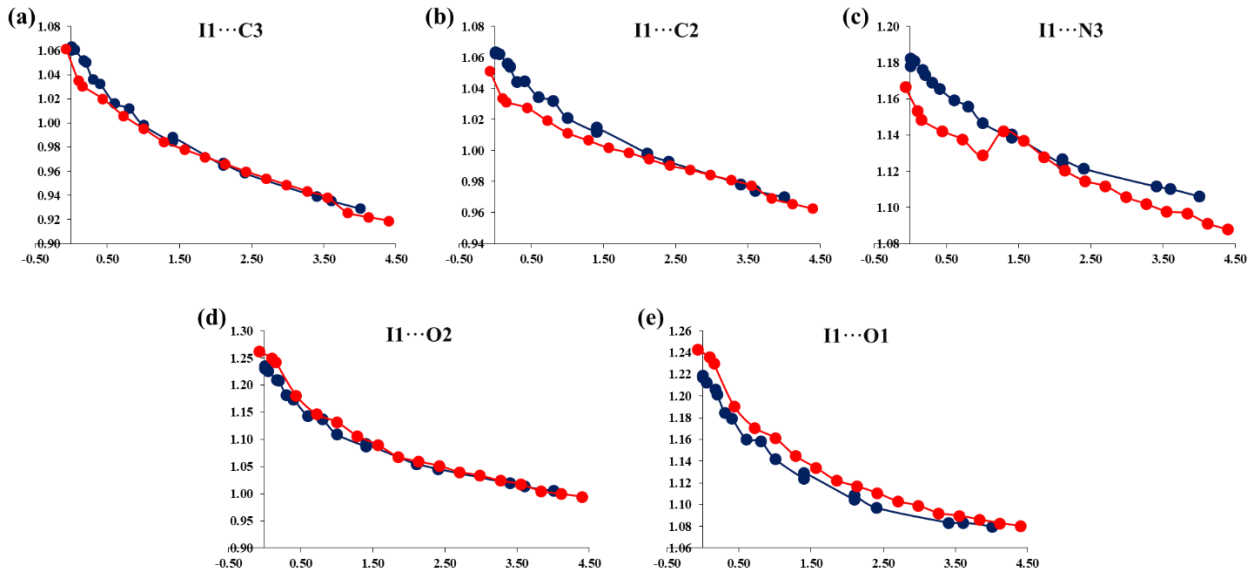

Figure 3.40 Variation of RR values as a function of pressure, calculated for interatomic contacts involving I1(*x,y,z*) and atoms of neighbouring adducts. The neighbouring atom belongs to: (a)-(b) (*x,y,-1+z*), (c) (*x,y,1+z*) and (d)-(e) (*-1/2+x,3/2-y,-1/2+z*) symmetry generated adducts.

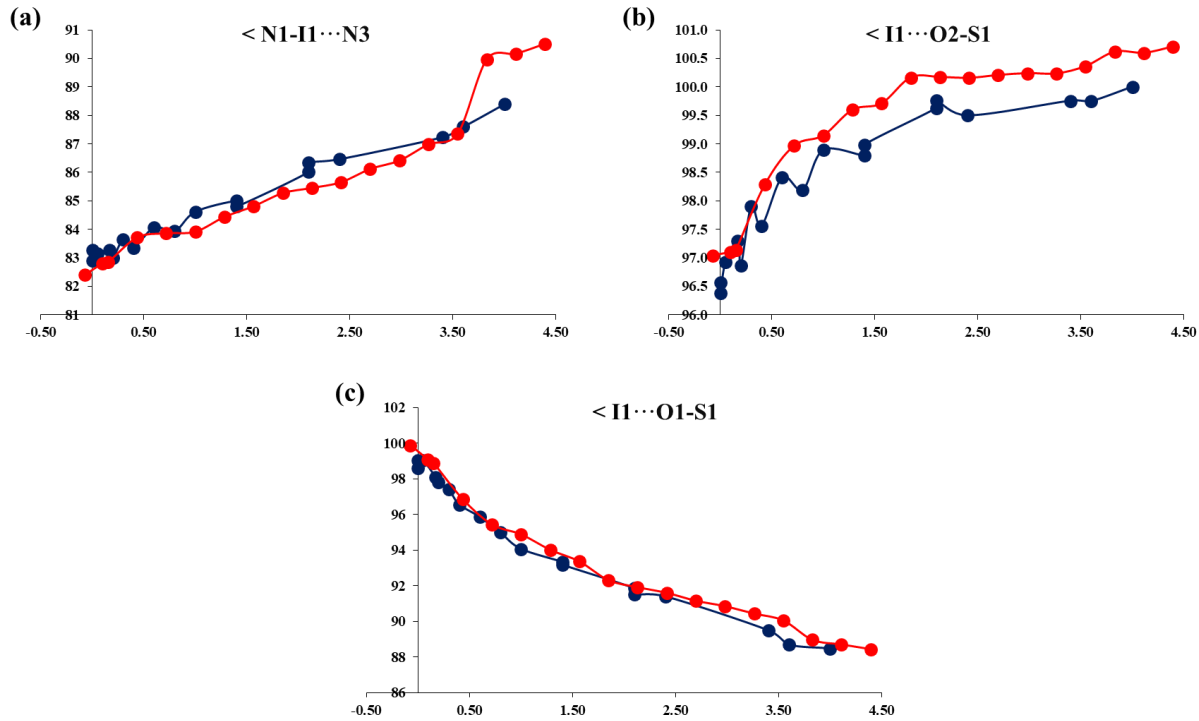

Figure 3.41 Variation of the interatomic angle as a function of pressure, involving I1(*x,y,z*) and atoms of neighbouring adducts. The acceptor atom belong to (a) (*x,y,1+z*) and (b)-(c) (*-1/2+x,3/2-y,-1/2+z*) symmetry generated adducts.

In order to find an eventual correlation of interatomic distances with the compressibility values determined along the directions of the unit cell axes, we have used the theoretical dataset ranging from -0.07 GPa to 3.55 GPa (as the unusual modifications seen in the theoretical unit cell parameters above 3.55 GPa are also expected to affect the resulting intermolecular interactions and therefore the interatomic distances in the same way). Accordingly, the analysis of the experimental dataset is also limited to the same range [from 0.00(5) GPa to 3.6(2) GPa]. Considering all intermolecular interactions (not just around I) formed by the reference adduct with the neighbouring ones in the experimental dataset, the I1···O2(*-1/2+x,3/2-y,-1/2+z*) interaction shows the largest value of ΔRR (ΔRR = 0.22), followed by N3···H9 (*x,1-y,-1/2+z*) (ΔRR = 0.15) and then I1···O1(*-1/2+x,3/2-y,-1/2+z*) (ΔRR = 0.14) interactions (only the first three interactions with maximal ΔRR values are chosen here, as representative examples). From the orientation of the interatomic interaction vectors of the above interactions with respect to the crystallographic axes landmark, it appears that these interactions exhibit major components oriented along the crystallographic *a*- and *b*-directions. Accordingly, **Figure 3.42** shows that the major component of the I1···O2(*-1/2+x,3/2-y,-1/2+z*) interaction is largely placed along *a*- and *b*- directions, whereas the major components of N3···H9(*x,1-y,-1/2+z*) and I1···O1(*-1/2+x,3/2-y,-1/2+z*) interactions are mostly oriented along *b*-direction. Earlier, it has been observed that, these are the crystallographic directions that experiencing maximal compressibility from low to high pressure in the experimental dataset. Therefore, this analysis points that the interatomic interactions experiencing maximal change in RR from low to high pressure have also their major component oriented along crystallographic *a*- and *b*-directions, which are the crystallographic axes directions showing maximal compressibilities among the three. Similarly, the I1···O2(*-1/2+x,3/2-y,-1/2+z*) interaction is also showing a maximal value of ΔRR= 0.15 in the theoretical dataset, followed by O2···H3(*-1/2+x,3/2-y,-1/2+z*) (ΔRR = 0.15), N3···H9(*x,1-y,-1/2+z*) (ΔRR = 0.15) and then I1···O1(*-1/2+x,3/2-y,-1/2+z*) (ΔRR = 0.15) interactions. The interatomic interaction vector corresponding to the O2···H3(*-1/2+x,3/2-y,-1/2+z*) interaction is also largely oriented along the crystallographic *b*-direction.

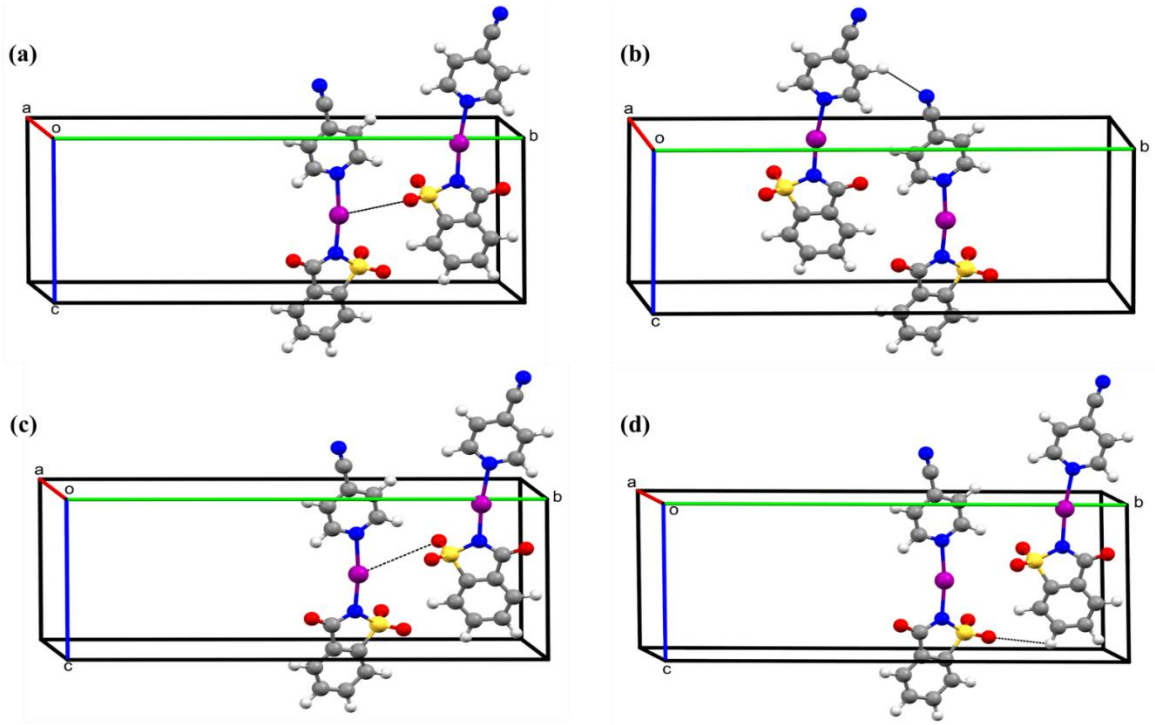

Figure 3.42 Plots of the interatomic interaction direction of: (a) I1···O2(*-1/2+x,3/2-y,-1/2+z*) (b) N3···H9(*x,1-y,-1/2+z*), (c) I1···O1(*-1/2+x,3/2-y,-1/2+z*) and (d) O2···H3(*-1/2+x,3/2-y,-1/2+z*) interactions, within the crystallographic axes landmark. Figure (a)-(c) were generated using the structure determined at 0.00(5) GPa, whereas figure (d) was generated using the structure calculated at -0.07 GPa. The interatomic interactions are shown with black dashed lines.

3.3.1.7 Variation of intermolecular energies with pressure

CrystalExplorer (Turner *et al.*, 2017) was used to calculate the intermolecular interaction energies at each pressure, employing the B3LYP functional and the DGDZVP basis set for all atoms. Intramolecular C-H bond distances were normalized to standard neutron distances. The Gaussian09 software (Frisch *et al.*, 2013) was used for the wavefunction calculation, and a molecular shell of 3.80 Å in radius was created in each case.

Total intermolecular interaction energy calculated for the experimental crystal structure determined at each pressure shows that all dimers of adduct stabilize further while increasing pressure (**Table 3AP.17** and **Figure 3.43a**). In addition, the interaction energy difference ΔE ($\Delta E = E_{x\ GPa} - E_{0.00(5)\ GPa}$) was calculated for the dimers at each pressure X, in order to characterize the modifications (extent of stabilization) happened with respect to the starting pressure 0.00(5) GPa. The analysis was carried out for experimental dataset in the range of pressure from 0.00(5) GPa to 3.6(2) GPa (due to the same reason mentioned in the previous section). The plot of ΔE *vs* pressure (**Figure 3.43a**) shows that the adduct dimers formed between (*x,y,z*) and (i) (*x,y,-1+z*), (ii) (*-1+x,y,-1+z*) and (iii) (*-1/2+x,3/2-y,-1/2+z*) symmetry generated adducts are only

displaying significant modifications under pressure, whereas the others show ΔE < 2 kJ/mol. The dimer formed with (*x*,*y*,*-1+z*) exhibits the maximal value of ΔE = -16.3 kJ/mol. Earlier, from the analysis of intermolecular interactions at ambient conditions, it has been observed that the same dimer of adducts had the largest contribution to the construction of the crystal packing (largest E_{tot}). Looking back into the interatomic interactions, this dimer is mainly constituted by π···π stacking interactions running along the *a*-direction, along with an electrostatic interaction formed between a positively charged carbon atom (C13) and the negatively charged oxygen atom (O3), whose interatomic interaction vector is also largely oriented along *a*-direction. Before, it was also noted from the experimental dataset that the ~c-*a*-direction is experiencing the maximal compressibility (8.1%) in region-1. Therefore, combing all these observations it can be deduced that, the adduct dimer whose interatomic interaction components largely oriented along the unit cell axis direction of maximal compressibility also experiencing the maximal energy change between the lowest and highest pressure considered. Further, the dimer formed between the reference (*x*,*y*,*z*) adduct with that generated by the symmetry operation (*-1+x*,*y*,*-1+z*) showing the second largest ΔE value (ΔE = -10.2 kJ/mol), which is also mainly constituted by π···π stacking interactions running along the *a*-direction. In addition, a weak C11-H11···O1 HB interaction and an electrostatic interaction formed between a positively charged carbon atom (C13) and the negatively charged oxygen atom (O1) is also observed in this dimer with components mostly along the *a*-direction. Hence, a similar conclusion derived for (i) can also be deduced here. Comparing the dimers obtained with adducts (i) and (ii), the larger ΔE value found with (i) might be in phase with its comparatively larger contribution of π···π stacking interaction (because π···π stacking interactions are known to display very significant sensitivity under pressure). The next one in the hierarchy of ΔE is the dimer formed with *(-1/2+x*,*3/2-y*,*-1/2+z*). Unlike the first two cases there is no π···π stacking interaction found with this dimer, and is mainly formed by two HB interactions (C4-H4···O2 and C12-H12···O1) whose major components are oriented along the crystallographic *b*-direction. This adduct dimer shows a comparatively smaller ΔE value (ΔE = -4.1 kJ/mol), mainly because the major component of the HBs are placed here along the *b*-direction whose compressibility (7.43%) is less than that along the *a*-direction. Now, going back into the ranking of dimers based on the E_{tot} at ambient conditions, the third most significant dimer was formed with the (*x*,*1-y*,*-1/2+z*) symmetry generated adduct (E_tot = -44.8 kJ/mol). Even though the major components (interatomic interaction vectors) of this dimer are lying along the *b*-direction, they do not experience significant modification in its energy with pressure (a maximal ΔE of -2.7 kJ/mol in

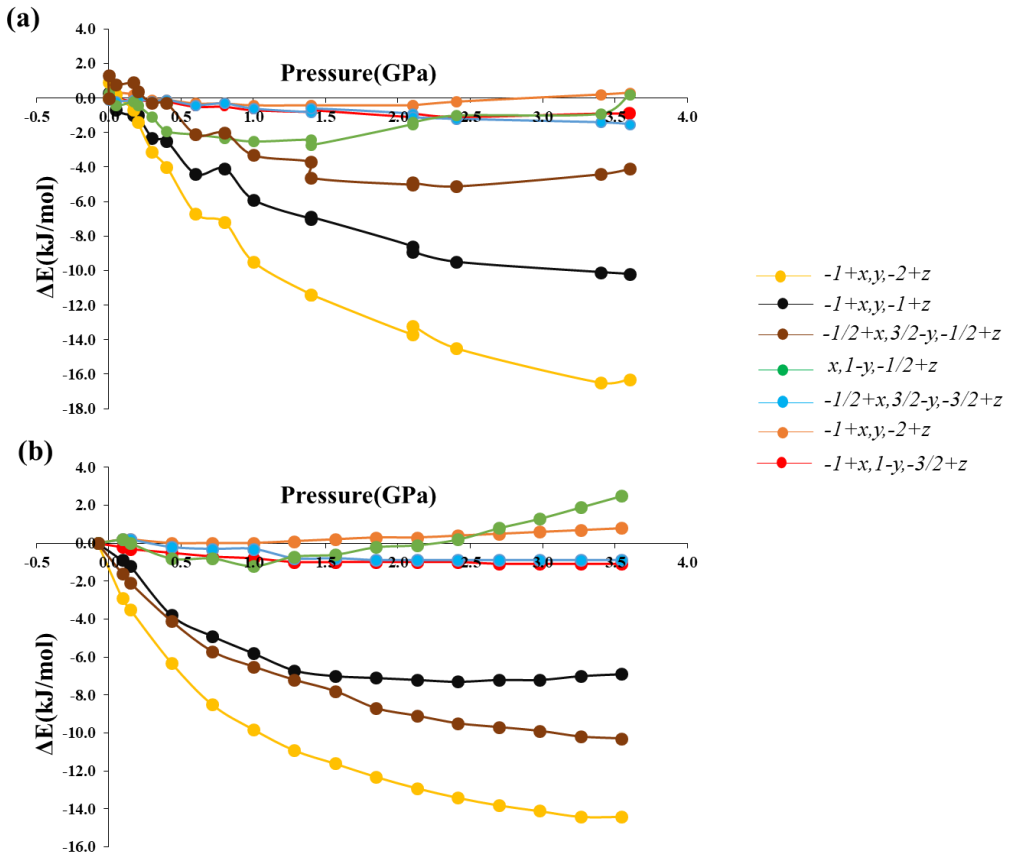

Figure 3.43 Evolution of ΔE *vs* Pressure for (a) experimental and (b) theoretical datasets. Curves connecting data are plotted for guiding eyes.

only observed among all the pressures). This trend is due to the fact that the HB interactions assembling the dimer are already very strong at 0.00(5) GPa, and therefore they only show a limited compressibility (change in RR) with pressure.

The same kind of analysis was also performed with the theoretical dataset (from -0.07 GPa to 3.55 GPa), showing qualitatively the same results (**Table 3AP.18** and **Figure 3.43b**), except the observation that here the dimer formed with (*-1/2+x,3/2-y,-1/2+z*) adduct shows larger ΔE (-10.3 kJ/mol) than that formed with (*-1+x,y,-1+z*) (where ΔE = -6.9 kJ/mol). This reversal of trend can be brought close to the fact that with the theoretical dataset both *a*- and *b*- directions show almost equal compressibilities (8.2% for *a*-direction and 8.3% for *b*-direction) upto 3.55 GPa, while this was not the case with the experimental dataset where a difference of 0.7% is observed between *a*- and *b*- directions.

3.3.1.8 Variation of electronic properties with pressure

As stated earlier, the different electronic environment of donor and acceptor moieties and larger uncertainties associated with the normalized HaB distances hinder to conclude about the precise position of the I atom within the adduct at any measured pressure. Therefore, to investigate this system on another point of view, both N1···I1 and I1···N2 HaB interactions were electronically characterized using the QTAIM approach, for both experimental and theoretical datasets. Accordingly, topological and energetic properties of $\rho(\mathbf{r})$ at N1···I1 and I1···N2 BCPs were studied to gather more insight into the HaB interactions, and to determine whether the I atom is strongly bounded to the donor or to the acceptor while increasing pressure. As in the previous co-crystal, not enough XRD data could be collected to derive the structural position of atoms with good enough quality to undertake an accurate experimental charge density analysis. However, the good geometrical agreement observed between the theoretically calculated and the experimentally determined crystal structures in the same range of pressure allowed to undertake the charge density analysis using the theoretical data. Nevertheless, the quantum chemical calculations and the topological analyses were carried out for the crystal structures in both experimental (for the comparison purpose and to complement the observations drawn earlier from the geometrical analyses) and theoretical datasets.

For the proceedings, SPE calculations were performed using the Gaussian09 software (Frisch *et al.*, 2013) on the isolated *NISac.4CYP* adduct extracted from the crystal structure at each pressure, for both experimental or the theoretical datasets. The B3LYP functional was used in all cases. The Def2TZVP basis set was employed for all atoms, including a pseudo-potential for iodine (Pritchard *et al.*, 2019). Topological calculations were performed using AIMALL software (Keith, 2019).

From the topological calculations carried out with the theoretical dataset, it is observed that the electron density $\rho(\mathbf{r})$ at both N1···I1 BCP (hereafter, called CP1a) and I1···N2 BCP (hereafter, called CP2a) increases as a function of pressure (**Table 3.23** and **Figure 3AP.21a**). Accordingly, CP1a and CP2a show respectively a $\delta\rho(\mathbf{r})$ [calculated as the difference between the largest and the lowest $\rho(\mathbf{r})$ values found out within the range of applied pressures] of 0.010 eÅ^{-3} and 0.048 eÅ^{-3}. Similarly, $\nabla^2\rho(\mathbf{r})$ also shows an increasing behavior with pressure in both cases, and a $\delta\nabla^2\rho(\mathbf{r})$ value [calculated similarly than for $\delta\rho(\mathbf{r})$] of 0.150 eÅ^{-5} and 0.261 eÅ^{-5} was determined at CP1a and CP2a, respectively. As compared to CP1a, larger $\delta\rho(\mathbf{r})$ and $\delta\nabla^2\rho(\mathbf{r})$ values at CP2a indicate a more significant modification of the HaB interaction at the

acceptor side while increasing pressure. Hence, even though the HaB interactions increase their strength at both sides of I on increasing pressure, the most significant changes are occurring at the acceptor side. This is also observed with the individual HaB distances, where NI···I1 shows a shortening of 0.006 Å between the lowest and the highest pressure, whereas the corresponding value in I1···N2 is 0.053 Å (**Table 3.23**). In addition, with increasing pressure, the I atom keeps shifting closer to the acceptor side while the donor and the acceptor moieties approach to each other. Further, a high correlation is also observed between the values of $\rho(\mathbf{r})$ and HaB distances, confirming the strengthening of HaB motifs by a larger accumulation of charge while reducing the interatomic distance on increasing pressure at BCPs (**Figure 3AP.22a** and **Figure 3AP.22b**).

As in the previous case of *NISac.Py*, a parameter $\Delta\rho(\mathbf{r}) = \rho(\mathbf{r})_{CP1a} - \rho(\mathbf{r})_{CP2a}$ has been also calculated here. A positive value of $\Delta\rho(\mathbf{r})$ indicates a stronger interaction at the donor side [$\rho(\mathbf{r})_{CP1a} > \rho(\mathbf{r})_{CP2a}$], whereas a negative value of $\Delta\rho(\mathbf{r})$ indicates a stronger interaction at the acceptor side [$\rho(\mathbf{r})_{CP1a} < \rho(\mathbf{r})_{CP2a}$], for any applied pressure. From **Table 3.23**, it is observed that under compression the magnitude of $\Delta\rho(\mathbf{r})$ monotonically decreases from 0.147 eÅ^{-3} (at -0.07 GPa) to 0.102 eÅ^{-3} (at 4.39 GPa), without any reversal of sign as compared to *NISac.Py* (see the general conclusion section for more discussion). The positive value of $\Delta\rho(\mathbf{r})$ at 4.39 GPa indicates that the I atom is still bound stronger to the donor side even at the highest considered pressure. The constantly decreasing value of $\Delta\rho(\mathbf{r})$ also suggests that the interaction of I with the acceptor is getting stronger while increasing pressure. Similarly to $\Delta\rho(\mathbf{r})$, ΔX (where $\Delta X = X_{CP1a} - X_{CP2a}$; X=$|V|/G$ or DI) also shows a decreasing behavior with pressure (from 0.177 to 0.134, and from 0.216 to 0.165, respectively; **Table 3.23**, **Figure 3AP.21a** and **Figure 3AP.21c**). Therefore, in addition to $\Delta\rho(\mathbf{r})$, the positive values of these two parameters point that the I atom is strongly bound with the donor at any applied pressure. At the same time, $\nabla^2\rho(\mathbf{r})_{CP1a}$ and $\nabla^2\rho(\mathbf{r})_{CP2a}$ increase in their positive values with the pressure (pointing the increase in electronic repulsion due to larger quantity of electrons at the BCPs), whereas $\Delta\nabla^2\rho(\mathbf{r}) = \nabla^2\rho(\mathbf{r})_{CP1a} - \nabla^2\rho(\mathbf{r})_{CP2a}$ shows a negative value and an increase of its absolute value ($|\Delta\nabla^2\rho(\mathbf{r})| \uparrow$) throughout the investigated range of pressures (**Table 3.23**). On the other hand, the individual $|V|/G$ values at both CP1a and CP2a show an intermediate situation between shared-shell and closed-shell interactions with $1<|V|/G<2$, suggesting that the *NISac.4CYP* adduct should be considered as a single molecular unit rather than two separate entities at any applied pressure.

The net charges of saccharinate (N_{sac}), 4-cyanopyridine (4CYP) and I atom were also studied as a function of pressure, but showing only a slight modification under pressure (**Table 3AP.20** and **3AP.21**).

The analyses were also extended to the experimental dataset, even though the atomic positions were determined without good enough accuracy to perform the topological calculations and the subsequent charge density analysis. In the process, it has been found that $\rho(\mathbf{r})$ at both N1···I1and I1···N2 BCPs increases as a function of pressure, along with the reduction of the individual HaB distances (**Table 3AP.19**, **Figure 3AP.21b**, **Figure 3AP.21c** and **Figure 3AP.22**). At the same time, $\Delta\rho(\mathbf{r})$ changes its magnitude from 0.241 eÅ^{-3} [at 0.00(5) GPa] to 0.172 eÅ^{-3} [at 4.0(2) GPa], but with a particular increment in $\Delta\rho(\mathbf{r})$ observed between 3.6(2) GPa and 4.0(2) GPa. This increment in $\Delta\rho(\mathbf{r})$ might be the consequence of the poor data quality, because 4.0(2) GPa is very close to the phase transition pressure and within the solidification limit of the PTM (causing inhomogeneity of pressure within the MDAC sample chamber). Similarly, $\Delta(|V|/G)$ and Δ(DI) also show a decreasing behavior with pressure (from 0.230 to 0.158, and from 0.297 to 0.212, respectively; **Table 3AP.19**, **Figure 3AP.21b** and **Figure 3AP.21c**). All these features are again indicating a comparatively stronger interaction of I atom with the donor. On the other hand, the data measured in region-2 (after phase transition) are treated in the *P*1 space group, with two crystallographically independent adducts present in the asymmetric unit, while the completeness for these data is only ~29% for a resolution of 0.625 Å^{-1}. This poor completeness affects the precision of the atomic positions in a large extent, being probably the reason of the large deviation with respect to the trends of the parameters observed in region-1 (**Table 3AP.19**).

In spite of this feature, topological and energetic properties of $\rho(\mathbf{r})$ calculated at N1···I1 and I1···N2 BCPs clearly show a significant modification of HaB interactions under pressure, for both experimental and theoretical datasets. Hence, values $\Delta\rho(\mathbf{r})$, $\Delta(|V|/G)$ and Δ(DI) calculated at each pressure indicate a continuous strengthening of the interaction formed between I atom and the acceptor moiety while increasing pressure, therefore corroborating the shift of the I atom towards the acceptor as previously observed from the geometrical analysis. Furthermore, at the same time, the values obtained at the highest pressure also point that, even though the interaction of I with the acceptor increase with pressure the I atom is strongly bound to the donor at any investigated pressure

Table 3.23 Topological parameters obtained for the isolated *NISac.4CYP* adduct, extracted from the crystal structure at each applied pressure using the theoretical dataset. N1···I1/I1···N2 distances are given as left/right values. The gathered QTAIM topological and energetic properties of ρ(r) at both N1···I1/I1···N2 BCPs are given as left/right values. They are electron density (ρ), its laplacian ($\nabla^2\rho$), the total energy density ($H=V+G$) and the ratio between the electron potential (V) and kinetic (G) densities ($|V|/G$), as well as their values normalized to ρ. The delocalization index at BCPs is denoted as DI. ΔX (X=ρ, L, |V|/G, DI) is the difference between left and right values.

Pressure (GPa)	Distance (Å)	ρ(r) (eÅ^{-3})	$\nabla^2\rho$(r) (eÅ^{-5})	$\nabla^2\rho$(r)/ρ(r) (Å^{-2})	|V|/G	H(a.u.)	H/ρ (a.u.)	D.I	Δρ (eÅ^{-3})	Δ$\nabla^2\rho$(r) (eÅ^{-5})	Δ($\nabla^2\rho$(r)/ρ(r)) (Å^{-2})	Δ(|V|/G)	Δ (DI)
-0.07	2.222/2.358	0.593/0.446	2.620/2.906	4.417/6.512	1.524/1.348	-0.030/-0.016	-0.341/-0.243	0.780/0.564	0.147	-0.286	-2.095	0.177	0.216
0.15	2.220/2.355	0.594/0.446	2.624/2.903	4.420/6.515	1.525/1.347	-0.030/-0.016	-0.341/-0.243	0.780/0.563	0.148	-0.279	-2.096	0.177	0.217
0.43	2.225/2.350	0.588/0.451	2.600/2.922	4.425/6.481	1.521/1.352	-0.029/-0.016	-0.337/-0.246	0.774/0.569	0.137	-0.322	-2.056	0.170	0.206
0.72	2.226/2.342	0.586/0.457	2.604/2.955	4.442/6.458	1.520/1.357	-0.029/-0.017	-0.337/-0.251	0.772/0.574	0.129	-0.351	-2.016	0.163	0.198
1.00	2.225/2.335	0.587/0.463	2.620/2.986	4.466/6.447	1.519/1.361	-0.029/-0.017	-0.337/-0.255	0.771/0.579	0.124	-0.366	-1.981	0.158	0.192
1.28	2.224/2.329	0.588/0.469	2.636/3.019	4.486/6.431	1.518/1.365	-0.029/-0.018	-0.337/-0.259	0.769/0.584	0.118	-0.383	-1.945	0.152	0.186
1.57	2.223/2.326	0.588/0.472	2.647/3.033	4.499/6.431	1.517/1.367	-0.029/-0.018	-0.338/-0.261	0.769/0.585	0.117	-0.386	-1.932	0.151	0.184
1.85	2.225/2.323	0.587/0.475	2.647/3.049	4.509/6.420	1.516/1.369	-0.029/-0.018	-0.337/-0.263	0.767/0.588	0.112	-0.401	-1.911	0.147	0.179
2.13	2.225/2.319	0.587/0.479	2.653/3.075	4.522/6.414	1.515/1.372	-0.029/-0.019	-0.337/-0.266	0.766/0.592	0.107	-0.421	-1.892	0.143	0.174
2.41	2.223/2.314	0.589/0.482	2.671/3.091	4.538/6.413	1.515/1.373	-0.029/-0.019	-0.338/-0.268	0.766/0.594	0.107	-0.420	-1.875	0.142	0.172
2.70	2.222/2.314	0.589/0.483	2.675/3.099	4.545/6.411	1.515/1.374	-0.029/-0.019	-0.338/-0.268	0.766/0.595	0.105	-0.424	-1.866	0.141	0.171
2.98	2.221/2.310	0.591/0.486	2.692/3.118	4.558/6.413	1.515/1.376	-0.030/-0.019	-0.339/-0.270	0.766/0.597	0.104	-0.427	-1.855	0.139	0.169
3.26	2.221/2.309	0.590/0.488	2.694/3.124	4.563/6.408	1.515/1.377	-0.030/-0.020	-0.339/-0.271	0.765/0.598	0.103	-0.430	-1.844	0.138	0.167
3.55	2.219/2.306	0.591/0.490	2.705/3.140	4.574/6.405	1.514/1.378	-0.030/-0.020	-0.339/-0.273	0.765/0.600	0.101	-0.435	-1.831	0.136	0.166
3.83	2.218/2.308	0.593/0.488	2.723/3.132	4.588/6.414	1.515/1.377	-0.030/-0.020	-0.340/-0.272	0.767/0.598	0.105	-0.409	-1.826	0.138	0.169
4.11	2.217/2.305	0.595/0.492	2.736/3.158	4.600/6.417	1.515/1.379	-0.030/-0.020	-0.341/-0.274	0.767/0.600	0.103	-0.421	-1.817	0.136	0.167
4.39	2.215/2.302	0.596/0.494	2.750/3.164	4.614/6.408	1.514/1.380	-0.030/-0.020	-0.342/-0.275	0.767/0.602	0.102	-0.414	-1.794	0.134	0.165

3.4 Summary

In this chapter we have studied two donor-acceptor co-crystals *NISac.Py* and *NISac.4CYP* under external pressure ranging from 0-5 GPa, in aim to investigate the modification of $N_{donor}\cdots I\cdots N_{acceptor}$ HaB motif in response to the application of external pressure. It has been shown previously that, in these complexes the position of the halogen atom can be modulated by modifying the electronic properties of the constituents (individual donor and acceptor), however, this study reveals that the same purpose can also be achieved through applying pressure as an external constraint.

Structural and electronic analyses of *NISac.Py* carried out at ambient conditions revealed a neutral co-crystal form of the binary adduct, where I was bound closer and stronger to the donor side even though an incipient halogen atom shift towards the acceptor was happened within the adduct as compared to the isolated monomers. This feature is resulting to a significant covalent degree of HaB both at donor and acceptor sides, suggesting that individual $N_{donor}\cdots I$ and $I\cdots N_{acceptor}$ HaB bonds are not very different from each other. On compression, I atom initially found closer to the donor starts migrating closer to the acceptor, but adjacent to the middle position between the donor and the acceptor at any investigated pressure. These experimental findings were also supported with theoretical high-pressure data. Accordingly, even though both experimental and theoretical data seem to indicate a monotonic shift of I from the donor to the acceptor with increasing pressure, the system cannot be considered as a salt (with a fully transferred I) but rather as a co-crystal in a frozen transferal process. These geometrical findings were then complemented with electronic descriptors derived within the framework of QTAIM, for both $N_{donor}\cdots I$ and $I\cdots N_{acceptor}$ BCPs. Evolution of $\Delta\rho(\mathbf{r})$ parameter calculated with pressure indicates a shift in the preferential affinity I from the donor to the acceptor side with increasing pressure. Unfortunately, in both structural and electronic analyses, the different electronic environment of N_{donor} and $N_{acceptor}$ atoms remained as a main hindrance in concluding the exact state of system at high- pressure. However, considering the uncertainties of HaB distances and other topological properties [$\Delta(|V|/G)$, Δ(DI)] one could conclude that *NISac.Py* binary adduct at high-pressure should be considered more as a single molecular unit rather than two separate entities. Interestingly, *NISac.Py* crystal structure was also shown a reversible recovery upon the decompression process, as evidenced by the evolving behaviour of unit cell parameters, unit cell volume and interatomic interactions. This reversibility of the crystal structure also implied a reversibility in the position of I atom within the adduct. In addition to the electronic influences of donor and acceptor moieties these changes are also partially driven by secondary interactions.

In addition, under pressure a reversible mechanical twinning was also observed in *NISac.Py*, which later rationalized using the crystallographic orbital approach, being the first example for a molecular crystal.

A similar but weaker $N_{donor}\cdots I\cdots N_{acceptor}$ HaB motif was also observed in *NISac.4CYP*. Even though, in *NISac.4CYP* the crystalline environment around the I atom is differently formed (as compared to *NISac.Py*), a similar movement of the halogen atom towards the acceptor was observed during the compression process. Here, the position of the I atom was found very far below the middle point between the donor and the acceptor at any investigated pressure. But the features observed from the electronic analysis revealed that both $N_{donor}\cdots I$ and $I\cdots N_{acceptor}$ HaBs are not very different from each other, therefore *NISac.4CYP* at high-pressure should also be considered as a single molecular unit rather than two separate entities. An interesting feature found with *NISac.4CYP* at high-pressure is the single-crystal to single-crystal 2^{nd} order structural phase transition happened at an elevated pressure of 4.0(2) GPa, driven by small molecular rotations in space. This process is happening close to a pressure in which the PTM is expected to solidify, however, a link between them cannot be conclusively stated.

In summary, this study reveals that the $N_{donor}\cdots I\cdots N_{acceptor}$ HaB motif in both *NISac.Py* and *NISac.4CYP* can be modified by using pressure as an external force. The secondary interactions immediate to these HaB motif and their evolution with pressure plays a crucial role in the halogen atom shift. However, the shift of halogen atom in the studied co-crystals are not sufficient enough to conclude about the state of system at high-pressure. With this respect, it should be kept in mind that interatomic distances of the $N_{donor}\cdots I\cdots N_{acceptor}$ HaB motif are difficult to characterize accurately using the experimental data (because of the constraints associated with the data collection and processing). In such a situation, DFT periodic calculations performed by applying isotropic external pressures can be used as a complementary tool, considering a good geometrical agreement between the theoretically calculated and the experimentally determined crystal structures. Further, a deeper insight on these $N_{donor}\cdots I\cdots N_{acceptor}$ HaB motifs can be gathered from the topological and the energetic properties of $\rho(\mathbf{r})$ at $N_{donor}\cdots I$ and $I\cdots N_{acceptor}$ BCPs, performed within the framework of QTAIM.

References

Angel R. J. (2000), High-pressure structural phase transitions. In: Transformation Processes in Minerals (Eds. S. A. T. Redfern, M. A. Carpenter), Reviews in Mineralogy & Geochemistry, Vol. 39, pp. 85–104. Mineralogical Society of America and Geochemical Society, (Washington, DC)

Aroyo, M. I.; Perez-Mato, J. M.; Orobengoa, D.; Tasci, E. (2011) Crystallography Online: Bilbao Crystallographic Server, Bulg. Chem. Commun. 43(2), 183-197.

Aubert, E., Espinosa, E., Nicolas, I., Jeannin, O. and Fourmigué, M. (2017). Faraday Discussion, 203, 389–406.

Boldyreva, E. V., Sowa, H., Ahsbahs, H., Goryainov, S. V., Chernyshev, V. V., Dmitriev, V. P., Seryotkin, Y. V., Kolesnik, E. N., Shakhtshneider, T. P., Ivashevskaya, S. N., Drebushchak, T. N. (2008). J. Phys. Conf. Ser. 121 (2), 022023.

Bruker (2019). APEX3 v2019.11. Bruker AXS Inc., Madison, Wisconsin, USA.

Casati, N., Macchi, P., Sironi, A. (2009) *Chem. Commun.* 19, 2679-2681.

Comodi, P., Gatta, G. D., Zanazzi, P. F. (2001). *Eur. J. Mineral.*, 13 (3), 497–505.

Clark, S. J., Segall, M. D., Pickard, C. J., Hasnip, P. J., Probert, M. J., Refson, K. and Payne, M. C. (2005) *Zeit. für Krist.*, 220(5-6) 567-570.

Cliffe, M. J., Goodwin, A. L. (2012). *J. Appl. Cryst.* 45, 1321-1329.

Dawson, A., Allan, D.R., Parsons, S. and Ruf, M. (2004). *J. Appl. Crystallogr.* 37, 410–416.

Dolenc, D. (2000). *Synlett* 2000, 544-546.

Dolenc, D. and Modec, B. (2009). *New J.* Chem. 33, 2344-2349.

Dolomanov, O.V., Bourhis, L.J., Gildea, R.J., Howard, J.A.K. and Puschmann, H. (2009). *J Appl Crystallogr.* 42, 339-341.

Espinosa, E., Alkorta, I., Elguero, J., Molins, E. (2002). *J. Chem. Phys.* 117, 5529–5542.

Frisch, M.J., Trucks, G.W., Schlegel, H.B., Scuseria, G.E., Robb, M.A., Cheeseman, J.R., Scalmani, G., Barone, V., Mennucci, B., Petersson, G.A., Nakatsuji, H., Caricato, M., Li, X., Hratchian, H.P., Izmaylov, A.F., Bloino, J., Zheng, G., Sonnenberg, J.L., Hada, M., Ehara, M., Toyota, K., Fukuda, R., Hasegawa, J., Ishida, M., Nakajima, T., Honda, Y., Kitao, O., Nakai,

H., Vreven, T., Montgomery, J.A., Jr., Peralta, J.E., Ogliaro, F., Bearpark, M., Heyd, J.J., Brothers, E., Kudin, K.N., Staroverov, V.N.. Keith, T., Kobayashi, R., Normand, J., Raghavachari, K., Rendell, A., Burant, J.C., Iyengar, S.S., Tomasi, J., Cossi, M., Rega, N., Millam, J.M., Klene, M., Knox, J.E., Cross, J.B., Bakken, V., Adamo, C., Jaramillo, J., Gomperts, R., Stratmann, R.E., Yazyev, O.A., Austin, J., Cammi, R., Pomelli, C., Ochterski, J.W., Martin, R.L., Morokuma, K., Zakrzewski, V.G., Voth, G.A., Salvador, P., Dannenberg, J.J., Dapprich, S., Daniels, A.D., Farkas, O., Foresman, J.B., Ortiz, J.V., Cioslowski, J. and Fox, D.J. (2013). *Gaussian 09, Revision D.01*, Gaussian, Inc., Wallingford CT.

Giordano, N., Beavers, C. M., Kamenev, K. V., Marshall, W. G., Moggach, S. A., Patterson, S. D.; Teat, S. J., Warren, J. E., Wood, P. A., Parsons, S. (2019). CrystEngComm. 21 (30), 4444–4456.

Gonzalez-Platas, J., Alvaro, M., Nestola, F. and Angel, R. (2016). *J. Appl. Crystallogr.* 49 (4), 1377–1382.

Grimme, S. (2006). *J. Comput. Chem.* 27, 1787-1799.

Grimme, S., Antony, J., Ehrlich, S. and Krieg, H. (2010). *J. Chem. Phys.* 132, 154104.

Keith, T. A. AIMAll (Version 19.10.12), TK Gristmill Software, Overland Park KS, USA, (2019).

Krause, L., Herbst-Irmer, R., Sheldrick, G.M. and Stalke, D. (2015). *J. Appl. Crystallogr.* 48, 3-10.

Landau, L.D. and Lifshitz, E.M. Statistical Physics.vol.5 Course of Theoretical Physics, Part1, 3rd ed. Pergamon Press, Oxford, 1980.

Macchi, P., Casati, N., Marshall, W. G., Sironi, A. (2010). *CrystEngComm*. 12, 2596-2603.

Makhotkina, O., Lieffrig, J., Jeannin, O., Fourmigué, M., Aubert, E. and Espinosa, E. (2015). *Cryst. Growth Des.* 15 (7), 3464–3473.

Mishra, A.K., Murli, C., Pandey, K.K., Sakuntala, T., Poswal, H.K. and Verma, A.K. (2020) *J. Phys. Chem. B* 124, 373–379.

Murata, K., Yokogawa, K., Yoshino, H., Klotz, S., Munsch, P., Irizawa, A., Nishiyama, M., Iizuka, K., Nanba, T., Okada, T., Shiraga, Y. and Aoyama, S. (2008). *Rev. Sci. Instr.* 79, 085101.

Nespolo, M. and Aroyo, M.I. (2016). *Acta Cryst.*, A72, 523-538.

Petitjean, M. (1994). *J. Comput. Chem*. 15, 507-523.

Piermarini, G.J., Block, S., Barnett, J.D. and Forman, R.A. (1975). *J Appl. Phys*. 46, 2774-2780.

Pritchard, B.P., Altarawy, A., Didier, B., Gibson, T.D. and Windus, T.L. (2019). *J. Chem. Inf. Model.* 59, 4814-4820.

Putkonen, M.-L., Feld, R., Vettier, C. and Lehmann, M.S. (1985). *Acta Cryst*. B41, 77–79.

Resel, R., Oehzelt, M., Shimizu, K., Nakayama, A., Takemura, K. (2004). Solid State Commun. 129 (2), 103–106.

Sheldrick, G. M. (2008). *Acta Cryst*. A64, 112-122.

Sheldrick, G.M. (2015a). *Acta Cryst*. A71, 3-8.

Sheldrick, G.M. (2015b). *Acta Cryst*. C71, 3–8.

Turner, M.J., McKinnon, J.J., Wolff, S.K., Grimwood, D.J., Spackman, P.R., Jayatilaka D. and Spackman, M.A. (2017). CrystalExplorer17. University of Western Australia.

Vijayakumar-Syamala, V., Aubert, E., Deutsch, M., Wenger, E., Dhaka, A., Fourmigué, M., Nespolo, M. and Espinosa, E. (2022). Acta Crystallogr B Struct Sci Cryst Eng Mater. 78 (3), 436–449.

Yan, T., Li, S., Wang, K., Tan, X., Jiang, Z., Yang, K., Liu, B., Zou, G. and Zou, B. (2012). *J. Phys. Chem. B* 116, 9796-98.

4

Molecular organization of benzyl selenocyanate derivatives in solid-state: role of chalcogen bonding interactions in packing topologies

This chapter is devoted to explore the characteristics of Se···N and/or Se···Se ChB interactions that are responsible for the molecular organization of benzyl selenocyanate derivatives in solid-state. Investigations are carried out with three different derivatives of benzyl selenocyanate family, (1) benzyl selenocyanate (SeCN1), (2) ortho-bis(selenocyanatomethyl) benzene (SeCN2) and (3) 2-(methylselanyl) benzyl selenocyanate (SeCN3). This chapter mainly covers crystallization routes, low-temperature high-resolution X-ray diffraction experiments (HR-SCXRD), structure refinement using both the independent atoms model and the Hansen-Coppens (HC) multipolar model, and the topological analyses of the electron density $\rho(\mathbf{r})$ and its laplacian $L(\mathbf{r})$ function applied to the latter HC model. These topological analyses are done in order to investigate the electrostatic intensity of individual nucleophilic···electrophilic ChB interactions and thereby by understanding their role in the geometrical preferences of interacting atoms in a molecular assembly.

4.1 Introduction

Benzyl selenocyanate derivatives (Bz-SeCNs) are considered as strong ChB donors in crystal engineering, in line with the highly electron withdrawing nitrile group (CN) covalently attached to the sp^3 hybridized Se-atom. The presence of this CN group is leading to the formation of a strong σ-hole in the Se-atom along the extension of the CN-Se covalent bond, whereas a weaker σ-hole is found along the extension of the other Bz-Se covalent bond due to the smaller electronegativity of the benzyl group. In such a way, a dissymmetry in the substitution of a sp^3 hybridized Se atom in Bz-SeCNs is causing a dissymmetry between the σ-holes generated along the extension of each covalent bond. This dissymmetry also brings a significant degree of predictability while designing molecular blocks for crystal engineering applications utilizing ChB interactions. For example, when a strong nucleophile (ChB acceptor) approaches Bz-SeCNs (ChB donor) it prefers to interact with the molecule along the direction of stronger σ-hole rather than the weaker one (excluding other factors such as steric bulkiness) to enhance the extent of the nucleophilic···electrophilic interaction. In the past decade, this feature has been wisely utilized by the crystal engineering community to control the structure-property relationship in various molecular solids (Fourmigué & Dhaka, 2020; Riel *et al.*, 2017; Huynh *et al.*, 2017). These studies were mostly done based on the crystal structures obtained from SCXRD experiments, which were carried out at either room- or low-temperature.

Another advantage with Bz-SeCNs family concerns the large variety of synthetic derivatives that are already known. Most of them can be crystallized at room conditions, following standard

crystal growth procedures, and the so-obtained crystals are stable enough for several weeks or months. Therefore, this large library of compounds gives us an opportunity to study how the ChB formation can be tuned with the modifications in chemical composition and how it eventually affects the preferential nucleophilic and electrophilic sites in associated ChB interactions.

Another interesting feature characterizing Bz-SeCNs is the similar molecular pattern found in solid-state assemblies, mainly directed by strong and linear ChB interactions. Thus, recurrent NC(R)Se···NC(R)Se ChB interaction between selenocyanate groups leads to the formation of infinite 1D chain-like motifs ··· NC(R)Se···NC(R)Se···NC(R)Se··· within the crystal packing, as for instance in the case of simple benzyl selenocyanate molecule (**Figure 4.1a**). Here, the ChB is formed by the interaction of the N lone-pair in the CN group of one molecule with the strong σ-hole found in the Se-atom on another molecule. Therefore, the molecule acts itself as ChB donor and ChB acceptor (known as amphoteric behaviour). Further, adjacent 1D chains are connected through other intermolecular interactions, such as HBs. Formation of these 1D chains are also identified in many other benzylic selenocyanate derivatives (Jeannin *et al.*, 2018). In the literature, it is also shown that within this Bz-SeCNs family, the molecular packing can be adapted by changes made on the chemical composition of the benzyl core. This way, a 1D chain-like motifs found in benzyl selenocyanate can be extended to a 2D sheet-like topology in 1,2,4,5-tetrakis(selenocyanatomethyl) benzene (Jeannin *et al.*, 2018; **Figure 4.1b**). However, robustness of these 1D chain-like motifs is questioned when multiple choices of ChB acceptors are present, as for instance in the case of 4-nitrobenzyl-selenocyanate and 2-(methylselanyl) benzyl selenocyanate where either the O-atom of a $–NO_2$ group or the Se-atom of a $–Se-CH_3$ group act as the ChB acceptor in the interaction with the strong σ-hole of the Se-atom (Maartmann-Moe *et al.*, 1984; Lari *et al.*, 2009). This results to the formation of a tetrameric unit in 4-nitrobenzyl-selenocyanate where both σ-holes of Se-atom are involved in short Se···O ChB interaction (**Figure4.1c**). On the other hand, a centrosymmetric dimer is found in the case of 2-(methylselanyl) benzyl selenocyanate involving a strong Se···Se ChB interaction (**Figure 4.1d**).

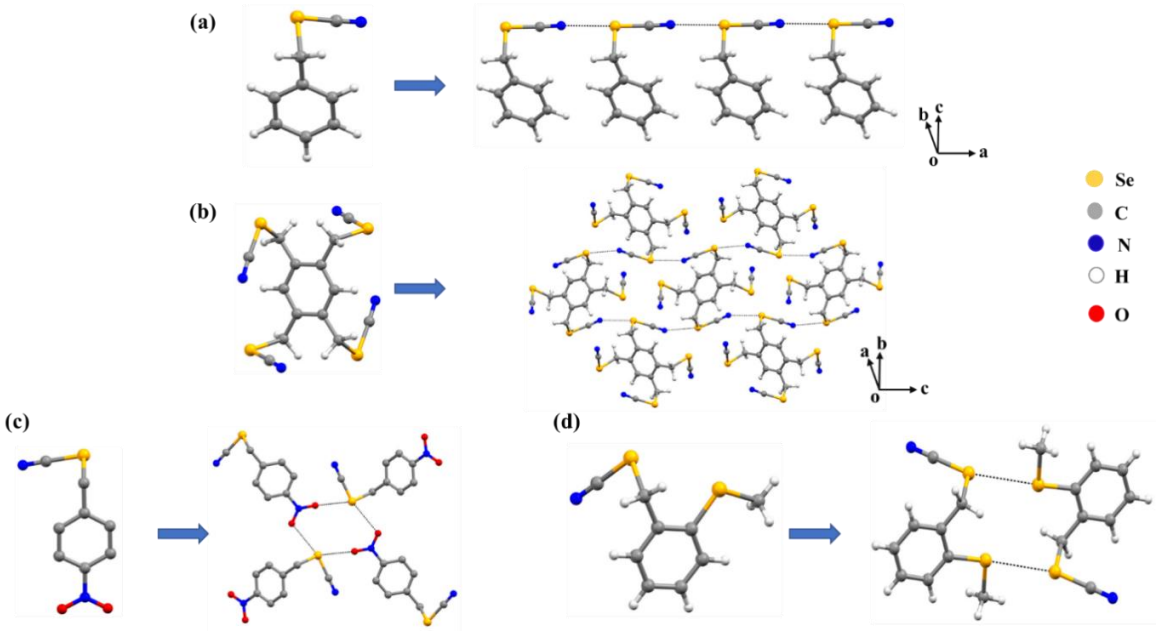

Figure 4.1 Crystal packing of (a) benzyl selenocyanate forming 1D chain-like motifs along the crystallographic *a*-axis, (b) 1,2,4,5-tetrakis(selenocyanatomethyl) benzene forming 2D sheet-like motifs in the *bc*-plane, (c) 4-nitrobenzyl-selenocyanate forming supramolecular tetrameric unit (H-atoms are omitted) and (d) 2-(methylselanyl)-benzyl selenocyanate forming a centrosymmetric dimer. Atoms are shown with colouring scheme and ChB interactions are depicted as back dashed lines. Figures are generated from deposited cif files.

Beyond molecular self-assemblies, Bz-SeCNs are also known to form bimolecular adducts where potential possibilities with other Lewis bases acting as ChB acceptors have been explored. Among these examples, it is found the co-crystal formed by para-bis(selenocyanatomethyl) benzene and 4,4'-bipyridine (Huynh *et al.*, 2017). Interestingly, a recurrent 1D chain-like motif were observed in the co-crystal as well, but here the lone-pair of N in the 4,4'-bipyridine takes the role of the ChB acceptor instead of the lone-pair of N in the CN group (**Figure 4.2a**). Also, there are other instances where bimolecular adducts obtained with anions (in search for anion binding capabilities) or with solvent molecules (formation of solvates). Two such representative examples are given in **Figure 4.2b** and **Figure 4.2c** (Riel *et al.*, 2019). In almost all of those cases, the presence of strong and linear ChB interactions was evident.

Overall, all these examples are indicating a crucial role of ChB interactions in the solid-state assemblies of Bz-SeCNs. This is exactly the main aim of this chapter, to better understand how important is the role of ChB interactions in the solid-state assemblies of Bz-SeCNs and how exactly are these interactions taking place between specific ChB donor and ChB acceptor atoms. At the same time, along with these ChB interactions, we also describe the effect of other non-covalent interactions in the formation of the molecular packings. In addition to the

structural descriptions, a rationalization of ChB interactions based on electronic descriptors that are obtained from the topological analysis of $\rho(\mathbf{r})$ and $L(\mathbf{r})$ functions will also be discussed. These analyses will permit to characterize interatomic interactions, as well as the local nucleophilic···electrophilic interactions, based on the electron density distribution of interacting atoms. For this purpose, we will use the data collected from HR-SCXRD experiments and the Hansen-Coppens (HC) multipolar formalism to derive the $\rho(r)$ multipolar model. Periodic and gas phase theoretical calculations are also performed either to corroborate the information derived from experimental data or to use in case some problematic situations are found with experimental models.

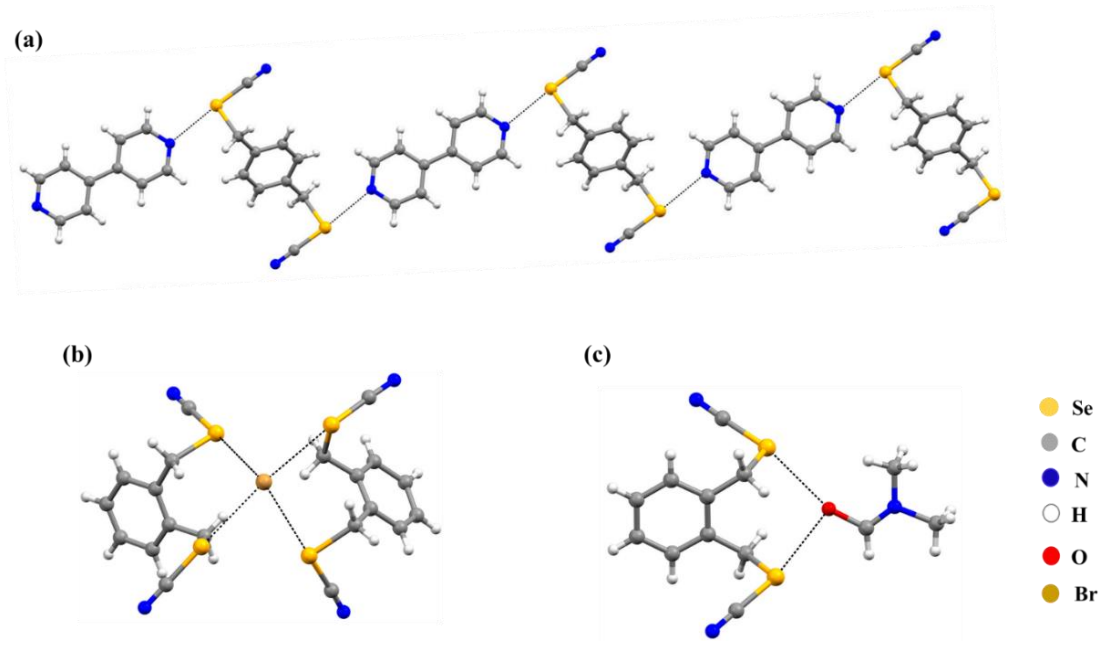

Figure 4.2 (a) 1D chain-like motifs formed by recurrent Se···N ChB interaction in the co-crystal of para-bis(selenocyanatomethyl) benzene with 4,4'-bipyridine, (b) Se···Br^- ChB motifs found in the bimolecular adduct, formed in the salt of ortho-bis(selenocyanatomethyl) benzene with PPh4Br ($PPh4^+$ is omitted for clarity) and (c) Se···O ChB motifs found in the bimolecular adduct formed by ortho-bis(selenocyanatomethyl) benzene with DMF solvent molecule. Atom types are shown with colouring scheme, ChB interactions are shown as black dashed lines. Figures are generated from deposited cif files.

4.2 Choice of compounds and crystallization methods

The compounds chosen for this work are benzyl selenocyanate (SeCN1), ortho-bis(selenocyanatomethyl) benzene (SeCN2) and 2-(methylselanyl) benzyl selenocyanate (SeCN3) (**Figure 4.3**). Crystal structures of these compounds are already reported. The first two compounds, SeCN1 and SeCN2, are known to form 1D chain-like motifs directed by recurrent ···NC(R)Se···NC(R)Se···NC(R)Se··· interactions (Maartmann *et al.*, 1984; McWhinnie *et al.*, 1998). In case of SeCN3, an additional choice of Lewis base, in the form of the Se lone-pair within the –Se-CH_3 group, leads to the formation of a discrete centrosymmetric

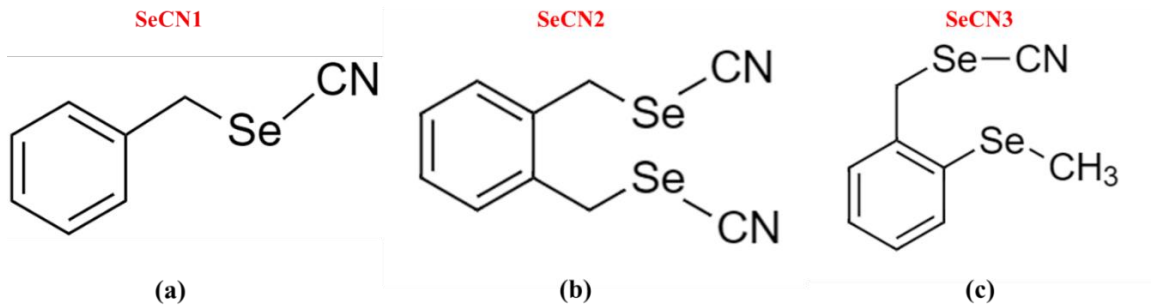

Figure 4.3 (a) molecular structures of (a) benzyl selenocyanate (SeCN1), (b) ortho-bis(selenocyanatomethyl) benzene (SeCN2) and (c) 2-(methylselanyl) benzyl selenocyanate (SeCN3). H-atoms are omitted for better clarity.

dimer (Lari *et al.*, 2009). In such a way, a preferential change in the ChB acceptor causes the absence of 1D chain-like motifs in the crystal structure of SeCN3 that were found in the case of the two former molecules. Another advantage of the selected molecules concerns their size and therefore the practicality for carrying out the experimental multipolar modelling. Indeed, the number of parameters to be refined in the multipolar modelling increases significantly with the number of atoms in the asymmetric unit. Thus, a larger molecule with a greater number of atoms in the asymmetric unit might cause a poor data/parameter ratio, which eventually causes difficulties in the precise modelling of the electron density distribution. In the case of three given molecules, other than the functional groups of interest (-CH_2-Se-CN or -Se-CH_3), only the benzene core is remaining, being relatively easy to model using experimental data.

Here, I would like to thank *Prof. Marc Fourmigué* and *Dr. Arun Dhaka* Condensed Matter and Electroactive Systems (MaCSE) group, University of Rennes 1 for the synthesis of the above three molecules. The synthesis of respective compounds was done based on previously reported procedures (Nasim *et al.*, 2019; Lari *et al.*, 2009a; Lari *et al.*, 2009b). Several crystallization methods were attempted to produce good quality crystals of the molecules. The method that resulted with the best quality crystals in each case is given in **Table 4.1**. Initial crystallization of the samples was done *via* the slow solvent evaporation method, by using ethanol solution. However, the quality of the crystal was not good enough to collect X-ray diffraction data at high resolution [$(\sin\theta/\lambda)_{max} \sim 1.00$ Å^{-1}]. Therefore, in the second step, the so-obtained crystals were subjected to the sublimation method (as described in **section 2.3.1.3**). After sublimation, SeCN1 and SeCN3 produced better quality crystals (as evident from the separation of impurities, appearing as black precipitates), whereas the attempts to obtain good quality crystals of SeCN2 were unsuccessful (even after trying with different ranges of temperature gradient in the sublimation process).

In conclusion, the crystals obtained after the sublimation method for SeCN1 and SeCN3, and the slow solvent evaporation method for SeCN2, were used for subsequent HR-SCXRD experiments.

Table 4.1 Crystallization methods adapted for SeCNi (i=1,2,3) molecules. In all three cases, a slow solvent evaporation was done from ethanol solution. For both crystallization methods, the obtained crystal shape/quality are indicated as left/right entries. The sublimation temperature/temperature gradient (both in degrees) are given as left/right entries within the bracket.

Compounds	Slow solvent evaporation method	Sublimation method
SeCN1	Block/Moderate	Block/Moderate (45/5)
SeCN2	Needle/Good	Unsuccessful
SeCN3	Block/Moderate	Block/Moderate (55/5)

4.3 Experimental details

4.3.1 High-resolution single-crystal X-ray diffraction experiments

High-resolution single-crystal X-ray diffraction (HR-SCXRD) experiments are carried out at 100K to precisely determine the crystal structures and subsequently to attempt the charge density analyses of the investigated molecules. In case of SeCN1 and SeCN2, X-ray diffraction data is collected using a Bruker D8 Venture diffractometer, equipped with a molybdenum micro-focus X-ray tube (MoK_α radiation, λ = 0.71073 Å) with mirror optics as a monochromator and a two-dimensional PHOTON III CMOS detector. Data integration and reduction have been performed using the SAINT program incorporated in the APEX III software (Bruker, 2019). For SeCN3, X-ray diffraction data is collected using an Agilent Supernova Microfocus diffractometer equipped with a two-dimensional ATLAS detector, using the MoK_α radiation. Here, data integration and reduction are carried out using the CrysAlisPRO program suite (Rigaku, 2020). In all cases, a suitable single-crystal is selected with the aid of a polarized light microscope and glued at the extremity of a glass fiber in a goniometer head. A numerical absorption correction is applied using the crystal shape and face indexing. Equivalent Bragg reflections are merged and the resulted datasets are sorted out using SORTAV option of WinGX software package (Blessing, 1986; Farrugia, 1999). The crystal structures are solved and refined respectively using the SHELXT (Sheldrick, 2015a) and the SHELXL (Sheldrick, 2008; Sheldrick, 2015b) programs incorporated in the Olex2-1.3

(Dolomanov *et al.*, 2009) suite. All the non-hydrogen atoms are refined anisotropically. H-atoms are placed at calculated positions and constrained to ride the position with their parent atom using the riding hydrogen model.

4.3.2 Independent atoms modelling

Multiple data collections are performed on each derivative by choosing single-crystals gathered from different batches of crystallization, and using various data collection strategies (choosing different combinations and limits of diffractometer angles). Below, for each molecule, the dataset that is leading to the best result is only discussed.

All the three datasets are subjected to an initial structure refinement using the independent atoms model (IAM), primarily to assess the data quality in order to proceed further with the multipolar modelling. The information of the crystallographic data obtained by employing the above-mentioned method are mentioned in **Table 4.2**. In all three molecules, data collection is done up to a maximum resolution of $(\sin\theta/\lambda)_{max}$ = 1.00 Å^{-1}, which is adequate to perform the experimental multipolar modelling and to obtain an accurate description of electron density distribution in the crystal. The molecular structures obtained after IAM, along with the position of highest five residual Q-peaks are shown for each derivative in **Figure 4.4**.

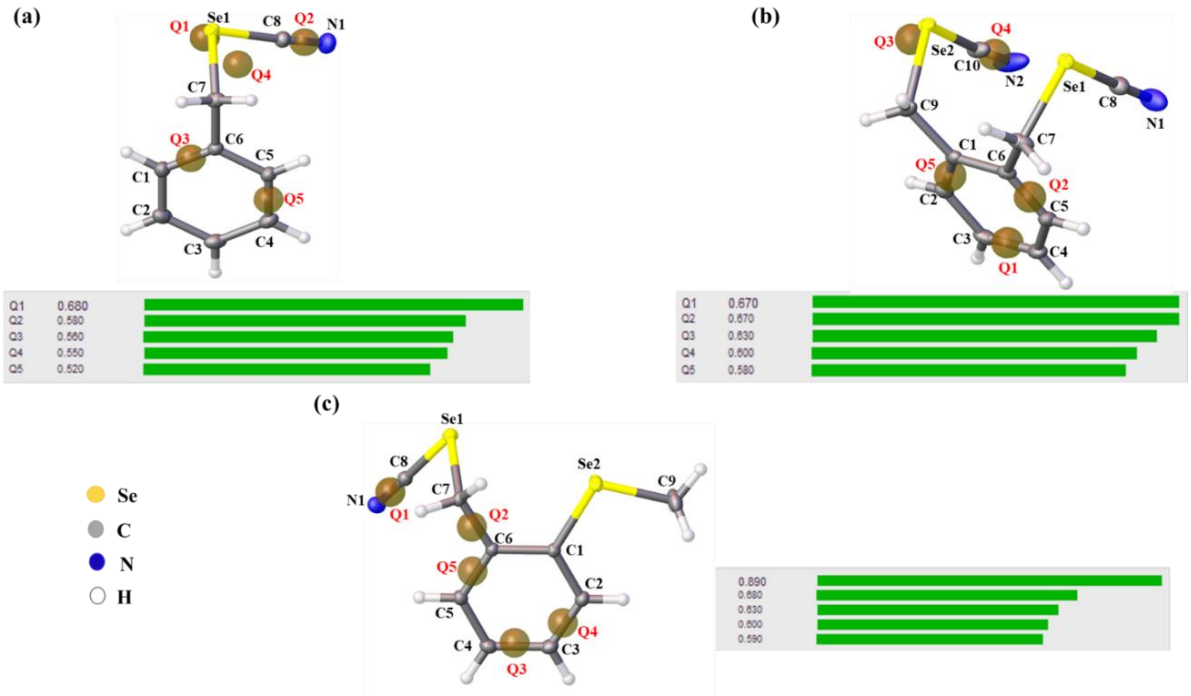

Figure 4.4 First five residual Q-peaks observed after IAM for (a) SeCN1, (b) SeCN2 and (c) SeCN3. The corresponding Q-peaks values (in eÅ^{-3}) are given in each figure along with labels. Atom types are shown with colouring scheme and atomic labels are shown for each molecule.

Table 4.2 Crystallographic data obtained for SeCNi (i = 1,2,3).

ID	SeCN1	SeCN2	SeCN3
Crystal data			
empirical formula	C_8H_7NSe	$C_{10}H_8N_2Se_2$	$C_9H_9NSe_2$
formula weight (g/mol)	196.11	314.10	289.09
crystal system, space group, *Z*	Monoclinic, $P2_1/c$, 4	Monoclinic, $P2_1/c$, 4	Monoclinic, $P2_1/c$, 4
a, *b*, *c* (Å)	5.9942 (14), 7.4504 (19), 17.478 (5)	7.9346 (7), 5.9006 (5), 22.381 (2)	8.7877 (1), 16.5522 (2), 7.1433 (1)
β (°)	96.159 (7)	91.629 (3)	112.587 (2)
V (Å^3)	776.1 (3)	1047.42 (16)	959.34 (2)
μ (mm^{-1})	4.76	7.02	7.65
crystal size(mm)	0.18 × 0.16 × 0.16	0.12 × 0.12 × 0.08	0.08 x 0.10 x 0.12
Data collection			
$(\sin\theta/\lambda)_{max}$ (Å^{-1})	1.00	1.00	1.00
no. of measured, independent, observed [I > 2σ(I)] reflections	119683, 6477, 5526	88790, 8767, 7049	185370, 8043, 6663
R_{int}	0.0411	0.0486	0.0530
completeness to $(\sin\theta/\lambda)_{max}$ (%)	100	100	100
absorption correction	Numerical	Numerical	Numerical
T_{min}/T_{max}	0.519/0.654	0.339/0.433	0.731/0.513
Refinement data – IAM Model			
refinement method	F^2	F^2	F^2
data/restraints/parameters	6477/0/91	8767/0/159	8043/0/110
R [$F^2 > 2\sigma(F^2)$], $wR(F^2)$	0.021, 0.056	0.025, 0.053	0.025, 0.059
GOF on F^2	1.054	1.058	1.073
peak/hole (eÅ^{-3})	0.68/-1.03	0.68/-0.74	1.32/-1.19
Refinement data - Multipolar model (theoretical) [a]			
refinement method	*F*	*F*	*F*
no. of reflections	6478	8772	6663
GOF	0.072	0.087	0.080
R(F), wR(F)	0.0023, 0.0024	0.0020, 0.0021	0.00192, 0.0020

[a] *information given here concerns theoretical multipolar models obtained at experimental geometry. A low GOF for theoretical calculation is due to the use of theoretical structure factors, for which the associated standard deviations are set to 1 and in that case the GOF should go to 0 rather than to 1 at the convergence.*

The points to note here are, (i) presence of a large Q-peak of > 0.6 eÅ^{-3}, found very close to Se-atom in SeCN1 and SeCN2, and (ii) comparatively larger magnitude of peak/hole ratio [1.32/-1.19 eÅ^{-3}] found in SeCN3. Another surprising feature is the difference between the ADPs of N1 and N2 atoms found in SeCN2, where for the latter they seemed to be more elongated (perpendicular to the covalent bond) than for the former. All these features are indicating relatively not so good quality of the data obtained after diffraction experiments. However, none of the other data collection attempts produced a better data set quality than the above ones. Therefore, these datasets are used for the further proceedings.

4.3.3 Experimental multipolar modelling

Experimental multipolar electron density refinements (based on *F*) are performed using the HC multipolar formalism implemented in the MoPro software package (Jelsch *et al.*, 2005). The refinements are performed up to a resolution of $(\sin\theta/\lambda)_{max}$ = 1.00 Å^{-1} for reflections with I > 2σ(I). During the experimental multipolar modelling (EMM), all the parameters are refined in a least-square procedure against the experimental structure factors (F_{exp}) in order to fit the deformation of the electron density distribution. A local axes system is assigned for each atom in order to define the orientation of multipolar harmonic functions. For this purpose, the default suggestion of MoPro (based on crystallographic symmetry and atom environments) has been taken into consideration. Restraints (*SIMPVM* – similar valence and multipolar populations) are applied for all H atoms in the final model (reasons are specified in the discussion section below). Also, in the final refinement model, modified values of Slater-type radial function parameter n_l are used for specific atoms with the aim to improve the quality of the model (**Table 4.3**). Since the three derivatives of Bz-SeCNs are very similar in their chemical composition (in terms of functional groups and connectivity of atoms), orientation of the local axes system and values of Slater-type radial function parameters (n_l and ξ) are kept the same for the same type of atoms from one molecule to the other.

Table 4.3 n_l and ξ values of the Slater-type radial function used in multipolar modelling. Default parameter values are given in parenthesis if those are modified in the final model.

Atom	ξ (bohr^{-1})	n_l (l = 1)	n_l (l = 2)	n_l (l = 3)	n_l (l = 4)
Se	4.4	4(6)	6	8(6)	8(6)
N	3.839	2	2	3	-
C	3.176	2	2	3	-
C_x	3.176	3(2)	2	4(3)	-
C_y	3.176	3(2)	3(2)	5(3)	-
H	2.0	1			

C_x is the sp^3 hybridized carbon atom of the -CH_2- group and C_y is the sp hybridized carbon atom of the -C≡N group, both are covalently bonded to the Se-atom.

In EMM, the following model parameters are introduced: scale factor (SCA), atomic positional coordinates (*XYZ*), thermal displacement parameters (U_{ij}/U_{iso}), valence (P_{val}) and multipolar ($P_{l\pm m}$) populations, expansion/contraction coefficients (k, k') and anharmonicity correction factor (ANH). Each parameter is introduced in a step-by-step manner, as given below:

1. SCA, 0.0 < S < 1.0 Å^{-1}
2. SCA + *XYZ* U_{ij} NOH, 0.0 < S < 1.0 Å^{-1}
3. *XYZ* U_{ij} NOH, 0.7 < S < 1.0 Å^{-1}
4. U_{iso} HYD, 0.0 < S < 0.7 Å^{-1}
5. SCA
6. SCA P_{val}
7. SCA + k NOH
8. SCA P_{val} + k NOH
9. SCA $P_{l\pm m}$
10. SCA P_{val} $P_{l\pm m}$ + k NOH
11. SCA + *XYZ* U_{ij} NOH
12. SCA P_{val} $P_{l\pm m}$ + k *XYZ* U_{ij} NOH
13. SCA + k' NOH
14. SCA P_{val} $P_{l\pm m}$ + k *XYZ* U_{ij} NOH
15. SCA + k' NOH
16. SCA P_{val} $P_{l\pm m}$ + k k'*XYZ* U_{ij} NOH

17. SCA P_{val} $P_{l\pm m}$ + k $k'XYZ$ U_{ij} (U_{ij}'s of H atoms are included)
18. ANH (4th order), 0.7 < S < 1.0 Å^{-1}
19. SCA P_{val} $P_{l\pm m}$ + k $k'XYZ$ U_{ij}, 0.0 < S < 1.0 Å^{-1}

where S = sinθ/λ (resolution). NOH and HYD abbreviations correspond respectively to non-hydrogen and only hydrogen atoms. During the refinement, step 5-17 are carried out for the full resolution range [0.0 < S < 1.0 Å^{-1}] and a *RESKP2* restraint is used from step 14 onwards. In addition, during the refinement, k and k' values of H-atoms are fixed to 1.2 since this atom is expected to be electron deficient and therefore contracted in its electron density distribution. Also, C-H distances are constrained to the values observed either from standard neutron diffraction experiments or from periodic theoretical calculations.

In the first step, the scale factor SCA is refined for the whole resolution range of data (0.0 < S < 1.0 Å^{-1}), with I > 2σ(I) intensity cut-off. In the next step, atomic positional (*XYZ*) and anisotropic displacement parameters (U_{ij}) are refined for non-H atoms with the same resolution limit. This is followed by the refinement of *XYZ* and U_{ij} parameters for non-H atoms using only the higher-order reflections (0.7 < S < 1.0 Å^{-1}). Refinement using only the higher-order reflections is important because it allows the estimation of best atomic positional and thermal displacement parameters of non-H atoms since they are strongly depending on the core electrons that dominate the diffraction contribution at high-resolution. This procedure also enables to minimize the correlation of *XYZ* and U_{ij} parameters with the multipolar parameters, which is very important for the proper modeling of electron density distribution (Guillot *et al.*, 2021). In the next step of EMM, the isotropic displacement parameters (U_{iso}) of H-atoms are refined using only the low-order reflections (0.0 < S < 0.7 Å^{-1}), since they do not possess any core electrons. In 17th step of the given procedure, U_{ij}'s are included for H-atoms by means of a constraint and using the values estimated from SHADE3 server (Madsen, 2006). Anharmonicity (ANH) corrections are only applied to Se-atoms, which is also the heaviest element in these molecules. ANH refinements are only done with high-order reflections (0.7 < S < 1.0 Å^{-1}) using the 4th order Gram-Charlier correction (as introduced in MoPro). From the second attempt to refine k' parameters (that is from 15th step), a *RESKP2* restraint is introduced for all the atoms. *RESKP2* is a restraint applied on k' values, using the values obtained in the first refinement step (13th step; as the reference) along with a default standard uncertainty of 0.01. This is done mainly because of two reasons, (i) the model convergence is not reached at the ending step when all the parameters are refined together (due to the high correlation between k' and other parameters) and (ii) k' values of atoms gradually go far from 1.0 if the

parameters are further refined in multiple cycles. The same refinement procedure is repeated in a cyclic manner if the convergence is not reached in the first attempt.

At each step of refinement, residual, static deformation density and laplacian of electron density maps are plotted and monitored to assure the refinement quality or to identify the appearance of any unexpected feature.

Initial experimental refinement models, done using default n_l and ξ parameters for all atoms with H-atom positions normalized to standard neutron diffraction values resulted to some potential problems (discussed below). Therefore, periodic theoretical multipolar modelling (TMM) are also carried out for each derivative, initiated with atomic co-ordinates extracted from the best EMM at each stage. Best choices of n_l parameter for all atoms are also estimated from these TMMs (default ξ parameters kept intact for all atoms) (**Table 4.3**). Further, EMM is repeated again using these newly estimated n_l parameters with optimized C-H distances determined from theoretical periodic calculation and required restraints or constraints. These new models are found to be of better quality than the first ones.

4.3.4 Theoretical multipolar modelling

Periodic theoretical calculations and subsequent theoretical multipolar modelling (TMM) can be used to resolve complicated situations arises during the experimental modeling, especially when SCXRD data are not of very high-quality and the derived EMM does not reach very good standards. As shown earlier, IAMs of all three molecules resulted to large residual densities close to Se-atoms, even after numerical absorption corrections done based on crystal shape and face indexing. These limitations in the data quality are also propagated to EMMs, where residuals of positive and negative magnitudes can be found close to Se-atom(s) after the fitting (shown below in results section). In this situation, it has been recommended to use TMM as a complementary tool to enrich the electron density information which can be later utilized to guide EMM to a better standard. For example, from the TMM, we can know about the similarities between the multipolar parameters of atoms which are in similar chemical and crystalline environment. Thus, applying such similarities as a constraint (or restraint) in EMM can improve the data/parameter ratio and eventually lead to a better modeling.

For periodic theoretical calculations, unit cell parameters and atomic co-ordinates are taken from the best EMM. Further, optimization of H-atom positions is carried out in the periodic system using the CRYSTAL09 software package (Dovesi *et al.*, 2005). The B3LYP functional

and POB-TZVP basis set is employed for all atoms during this process. It is important to mention here that, attempts to optimize all the atoms (rather than only H-atoms) at the same calculation level resulted to some striking differences in the molecular packing (therefore to the intermolecular interactions), and this was more or less pronounced among all three molecules. Therefore, only the optimization of H-atoms is preferred during periodic theoretical calculations. During the calculation, the shrinking factors IS1, IS2 and IS3 are kept to 6 with 80 k-points in the irreducible Brillouin zone. The truncation criterion for bielectronic coulomb and exchange integrals for the calculations are set as ITOL1_ITOL4 = 8 and ITOL5 = 18. The eigenvalue level shifter is set to 0.4 Hartree and a SCF convergence limit of the order of 10^{-7} Hartree is used. From the periodic wavefunction, structure factors are calculated upto a resolution of $(\mathrm{Sin}\theta/\lambda)_{max} = 1.00$ Å^{-1}. Missing reflections (100% given in **Table 4.2** is a rounded value) in the experimental dataset are identified from SORTAV option of WinGX software and added to the reflections list prior to the corresponding structure factor calculation. During TMM, U_{ij}'s of atoms are not accounted and the structure factors are assigned with unit weight. The refinement strategy used for the TMM is given below:

1. P_{val}
2. k NOH
3. P_{val} + k NOH
4. $P_{l\pm m}$
5. $P_{val}\ P_{l\pm m}$ + k NOH
6. k' NOH
7. $P_{val}\ P_{l\pm m}$ + k NOH
8. $P_{val}\ P_{l\pm m}$ + $k\ k'$ NOH

Here also, k and k' values of H-atoms are fixed to 1.2. All parameters (in all the above steps) are refined in the whole resolution range of data ($0.0 < S < 1.0$ Å^{-1}). A similar *RESKP2* restraint than in case of EMM is used here as well (from step 7 onwards) due to the same reasons mentioned previously. Again, each step of the refinement is monitored with the aid of residual, static deformation density and laplacian of electron density maps.

The same local axes orientations than those applied in EMM is used here for all atoms. Initial refinements are done with default values of n_l and ξ parameters. Unfortunately, these models left with large positive residuals (of spherical shape) around Se-atoms. Therefore, a new refinement strategy is adapted for Se-atoms, considering their core electrons to follow a

spherical contraction/expansion that is translated in terms of an additional k parameter in the refinement procedure (called core-valence split strategy hereafter) (Guillot *et al.*, 2021). Accordingly, spherical residual densities around Se-atoms are taken into the model with a significant improvement shown in residual maps. Later, n_l parameters are modified for specific atoms, mainly based on the features observed in residual electron density maps (to minimize the appearance and spreading of residuals). These values are the same used for final EMMs (**Table 4.3**), and one should also notice that default ξ values kept intact for all atoms in final EMMs and TMMs. Crystallographic information obtained after final TMMs (models generated with experimental geometry and optimized H-atom position) are given in **Table 4.2**.

4.4 Tools utilized

This section will discuss about the main tools that are going to be utilized in the later part of this study. The main focus is to rationalize the characteristics of ChB interactions in the crystalline phase and to reckon how important are these interactions in the constitution of respective crystal packings.

4.4.1 Intermolecular interaction energies

Analysis of intermolecular interaction energies, calculated as the total interaction energy (E_tot) in crystallographically independent molecular dimers, is widely accepted as an efficient tool to describe the crystal packing of a molecular crystal (Turner *et al.*, 2014; Spackman *et al.*, 2021). In the context of the present study, this analysis is intended to provide the following information: (i) intermolecular interactions that are most significant in constituting the crystal packing, (ii) among them, identify the significance of molecular dimers that are connected by ChB interactions, and (iii) how modifications in intermolecular interactions bring different packing topologies among the three investigated molecules (mainly concerning the absence or presence of 1D chain-like motifs).

CrystalExplorer (version 17.5; Turner *et al.*, 2017) software is used to calculate E_tot and their decompositions into electrostatic, polarization, dispersion and repulsive terms. The B3LYP functional and DGDZVP basis set are used for all atoms. Intramolecular C-H bond distances determined from periodic theoretical calculations are used. The Gaussian09 software (Frisch *et al.*, 2013) is used for the wavefunction calculation (for more details refer **section 2.2.1**).

4.4.2 Molecular electrostatic potential (MESP) surfaces

Once we are aware of the importance of ChB interactions in the crystal packing, the next goal is to understand how these interactions are taking place between donor and acceptor atoms, that is to identify the regions of atoms that are involved in ChB interactions. Most often, ChB interactions are identified as electrostatic interactions between the σ-hole of the chalcogen atom acting as electrophilic site and the electron rich center of the Lewis base acting as the nucleophilic site. In order to understand the characteristics of these nucleophilic···electrophilic interactions, it is important to identify first all such regions in associated atoms (and also in other atoms of the molecule). In this respect, molecular electrostatic potential (MSEP) surfaces are successfully used as a quantitative tool to provide key insights into electrophilic and nucleophilic regions of a molecule (more details of this technique can be found in **section 2.1.1.5**).

In this study, MESP surfaces are generated using the GaussView 5.0.9 software (Dennington *et al.*, 2016), plotted on a 0.001 a.u iso-electron density molecular surface calculated at B3LYP-D3/6-311++G(3df,3pd) level (SPE calculation using molecules extracted from crystal geometries). In parallel, all extremal points ($V_{s,\,max}$ and $V_{s,\,min}$ points) of the MESP function are characterized using the MultiWfn software (version 2.1.2; Lu and Chen, 2012).

Even though, this technique can offer vital information about the regions of atoms that could interact each other in a molecular assembly, there are some disadvantages involved with this technique (as discussed in **section 2.1.1.5**) that eventually demand the need for another complementary tool.

4.4.3 Topological analysis of $\rho(r)$ and $L(r)$ functions

The topological analysis of electron density $\rho(\mathbf{r})$ and its associated laplacian function $L(\mathbf{r})$ can act as a complementary tool to enrich the information gathered earlier with MESP surfaces. Unlike ESP function, both $\rho(\mathbf{r})$ and $L(\mathbf{r})$ functions are considered to be local functions that can give a closer (more local) picture to specific nucleophilic···electrophilic interaction (for more details see section **2.1.1.4**).

In this study, BCPs between any pair of atoms (either it be interacting or covalently bonded) is searched for the structure: (i) obtained after multipolar modelling (only theoretical; reasons are specified below) by using VMoPro software (Jelsch *et al.*, 2005), and (ii) extracted from the

crystal geometry and subjected to SPE calculation (monomers, dimers and trimers; in gas phase) by using *AIMALL* software (Keith, 2019). Meanwhile, SPE calculations are performed with Gaussian09 software (Frisch *et al.*, 2013) using the B3LYP functional and 6-311++G(3df,3pd) basis set for all atoms completed with dispersion corrections (Grimme *et al.*, 2010).

Simultaneously, individual nucleophilic···electrophilic interactions (ChB interactions, in particular) are quantitatively characterized by using the laplacian of electron density function $L(\mathbf{r})$ and its associated critical points (LCPs), as discussed in **2.1.1.4.2**. Due to some technical barriers, critical points search of the $L(\mathbf{r})$ function are just limited to gas phase structures (monomers, dimers and trimers) by using *AIMALL* software.

4.5 Results

4.5.1 Multipolar electron density modeling

As mentioned earlier, for each derivative several attempts of data collection are performed by choosing single-crystals obtained from different batches of crystallization. All these datasets are used in the refinements with independent and multipolar atoms models (IAM and MM). However, whereas IAM models are of good quality, in most cases they end up with a low quality of the multipolar model. Therefore, in the below discussion, for each derivative, multipolar refinement models generated from the best quality dataset is only discussed.

4.5.1.1 Benzyl selenocyanate (SeCN1)

Multipolar modelling of SeCN1 is not straightforward. A final model is derived only after interplay between multiple EMMs and TMMs. An initial EMM is generated from the experimental data, which resulted with some unusual features in residual, static deformation density and laplacian of electron density maps. Therefore, efforts are made to tackle this problematic situation by generation of TMMs and incorporation of the information derived from TMM to EMM. At the end, all this information is gathered to generate a comparatively better multipolar model.

All EMMs and TMMs are generated using HC multipolar formalism, based on the refinement strategy respectively described in **sections 4.3.3** and **4.3.4**. In all cases, the Slater-type radial functions are expanded up to the hexadecapolar level (l = 4) for Se-atoms and up to octupole

level (l = 3) for N-, and C-atoms, whereas only a dipole oriented in the bonding direction is refined for H-atoms.

EMM-1

This model starts with the unit cell parameters and atomic co-ordinates taken from the best IAM. C-H distances are normalized to the mean standard neutron diffraction values (1.089 Å). The same number of independent reflections and intensity cut-off [$I > 2\sigma(I)$] than of IAM are used. In each step of the refinement the convergence of the model is ensured; if not, the refinement is repeated from the beginning to that particular step. Maps generated after the multipolar modelling are shown in **Figure 4.5**, which reveals that the quality of fitting is not good as observed from the large residual densities around the Se-atom. **Figures 4.5a** and **4.5d** respectively show the residual electron density map drawn in the plane containing the Se-atom (plane defined by C7, Se1 and N1 atoms; called *plane-1* hereafter) and the bisecting plane containing the Se lone-pairs (bisecting the C7-Se1-N1 angle; called *plane-2* hereafter). These maps give a clear indication that there are still residual densities left unmodelled, especially close to the Se-atom. Another unexpected feature is displayed in **Figure 4.5b**, which concerns the laplacian of electron density map drawn in *plane-1*. Here, two charge concentration regions can be found each along the extension of the covalent bond connected to the Se-atom. They appear in the positions where one expects the appearance of σ-holes. This clearly points a potential issue that has to be resolved while studying ChB interactions involving the Se-atom. Apart from this, **Figures 4.5e** and **4.5f**, which respectively corresponds to the laplacian of electron density and the static deformation density maps drawn in *plane-2*, show two not equivalent lone-pairs of the sp^3 hybridized Se-atom, where one of them seems to be more concentrated in electron density than the other. This is not an ideal situation since the crystal packing analysis (discussed below) shows that the crystalline environment around these two lone-pairs are very similar. Also **Figure 4.5i**, which shows the static deformation density map drawn in the benzene plane, indicates that the electron depletion observed along the extension of C-H bonds is not similar. For example, a larger electron depletion exhibits along C2-H2 as compared to C1-H1. Again, the crystal structure analysis (discussed below) reveals a similar crystalline environment immediate to all C-H bonds.

In short, there are several unexpected features found in this EMM that have to be resolved properly to derive an accurate modelling of the electron density distribution. In addition, refinement attempts were also made by changing the reflection cut-off criterion [that is from I

> 2(σ) to I > 3(σ); in case problems are brought by some dominant background noise] and also by re-orientating the local co-ordinate system assigned to specific atoms (for instance, the Se-atom, in order to see if the re-oriented multipoles could take into account the unmodelled electron densities). Unfortunately, none of these models produced better results than EMM-1.

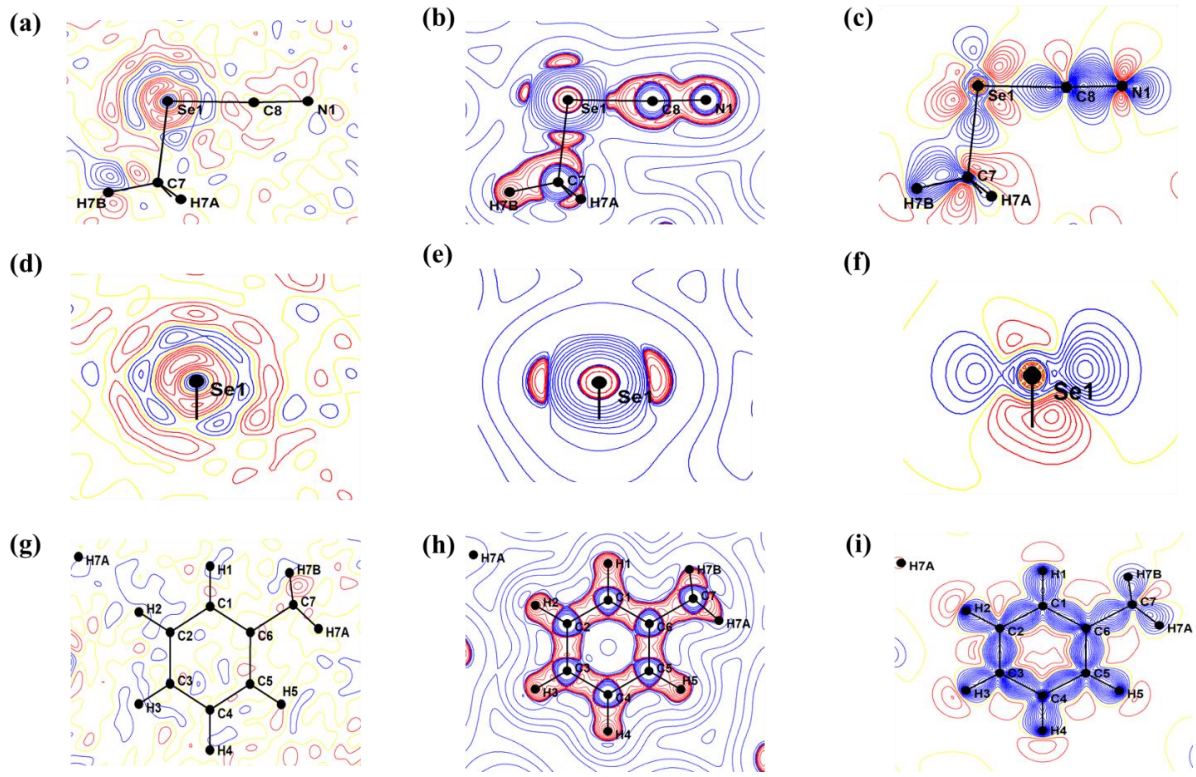

Figure 4.5 Residual, laplacian of electron density and static deformation density maps drawn after EMM-1 of SeCN1 in, (a)-(c) *plane-1* [containing C7, Se1 and N1 atoms], (d)-(f) *plane-2* [plane bisecting C7-Se1-N1 angle], (g)-(i) plane containing the benzene ring. Contours of residual maps (drawn for the resolution range 0.0 < sinθ/λ < 0.8 Å^{-1}) and static deformation density maps are at ±0.05 eÅ^{-3} level: blue - positive, red - negative. Laplacian of electron density maps contours (eÅ^{-5}) are in logarithmic scale: red - positive, blue - negative.

TMM-1

A theoretical model was generated aiming to resolve the difficulties found in EMM-1. The same n_l and ξ parameters, and local axes system, applied in EMM-1 were used here. Interestingly, maps given in **Figure 4.6** reveal that the unusual features found in EMM-1 are not observed with TMM-1, except for the appearance of a large negative residual density approximately of spherical shape, around the Se-atom (**Figures 4.6a** and **4.6d**). There is also a positive contour of electron density found in the middle of C7-Se1 and Se1-C8 covalent bonds (**Figures 4.6a**). Therefore, both of these features are suggesting the requirement for a new theoretical model that could consider the unmodelled electron densities observed with TMM-1.

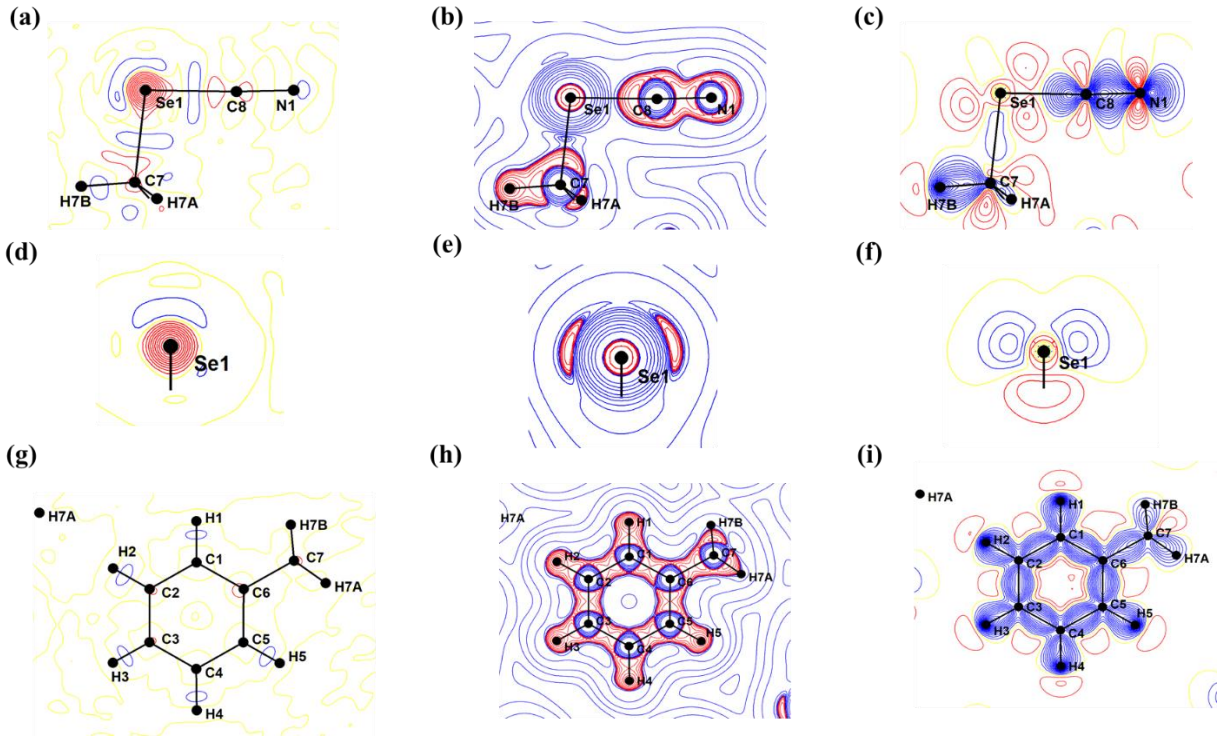

Figure 4.6 Residual, laplacian of electron density and static deformation density maps drawn after TMM-1 of SeCN1 in, (a)-(c) *plane-1* [containing C7, Se1 and N1 atoms], (d)-(f) *plane-2* [plane bisecting C7-Se1-N1 angle], (g)-(i) plane containing the benzene ring. Contours of residual maps (drawn for the resolution range 0.0 < sinθ/λ < 0.8 Å^{-1}) and static deformation density maps are at ±0.05 eÅ^{-3} level: blue - positive, red - negative. Laplacian of electron density maps contours (eÅ^{-5}) are in logarithmic scale: red - positive, blue - negative.

TMM-2

In order to account for the large negative residual densities found in TMM-1, a core-valence split refinement strategy is adapted for the Se-atom. Thus, including an additional k parameter in the refinement process, which corresponds to the expansion/contraction of core electrons of the Se-atom. This new model shows a significant improvement in the final residual density maps, even though two negative contours (~-0.1 eÅ^{-3}) are still remain close to the Se-atom (**Figures 4.7a** and **b**). However, the positive contours observed earlier in the middle of C7-Se1 and Se1-C8 covalent bonds remain after this modelling (**Figure 4.7a**).

TMM-3

In order to further improve the quality of TMM-2, n_l parameters of Se1, C8 and C7 atoms (the C-atoms covalently bonded to Se) were modified, while the default values of ξ parameters were kept the same as they seemed adequate (**Table 4.3**). This model also shows very low residuals around the Se-atom (with only two negative contours; **Figures 4.7c** and **4.7d**). Interestingly,

the positive contours found previously in the middle of C7-Se1 and Se1-C8 covalent bonds are disappeared, meaning that they are taken into account in the model. Consequently, among the three TMM models, TMM-3 is considered to be of the best quality.

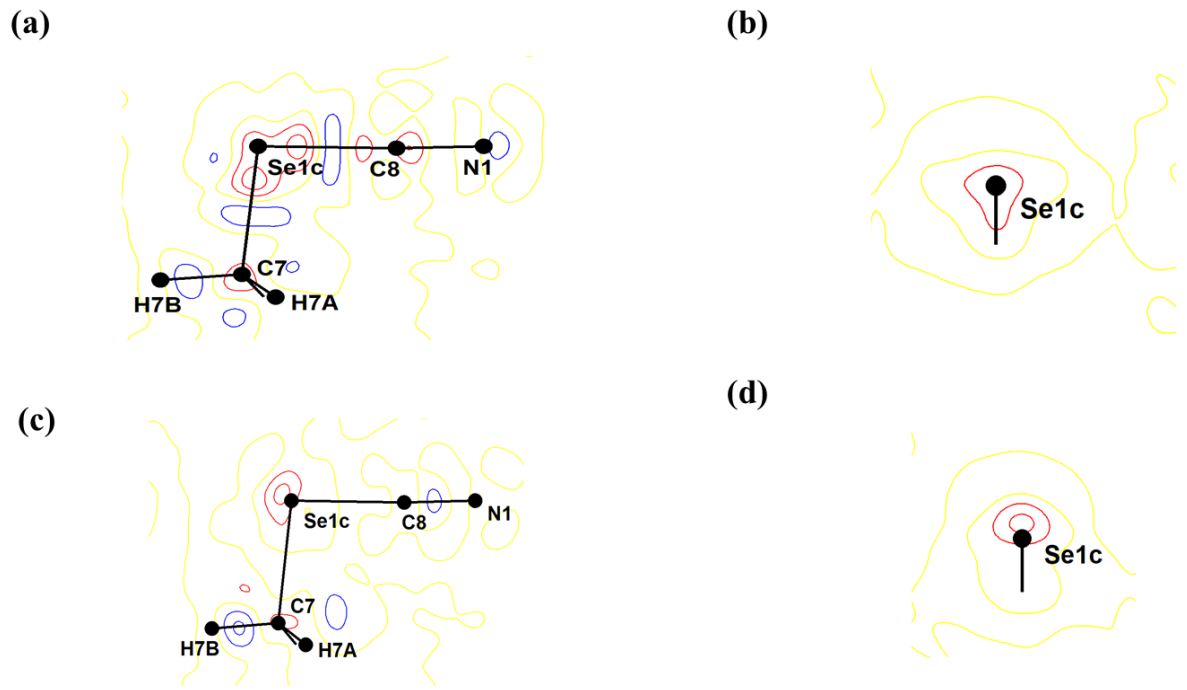

Figure 4.7 Residual maps drawn after: TMM-2 of SeCN1 in (a) *plane-1* and (b) *plane-2*, TMM-3 of SeCN1 in (c) *plane-1* and (d) *plane-2*. Contours of residual maps (drawn for the resolution range $0.0 < \sin\theta/\lambda < 0.8$ Å^{-1}) are at ±0.05 eÅ^{-3} level: blue – positive, red – negative. All other maps corresponding to these two models are given in appendices.

EMM-2

The information gathered from previous theoretical models is translated to a new experimental model, in order to derive an EMM of better standard. Accordingly, in EMM-2: (i) optimized values of C-H distances determined from the theoretical periodic calculation, (ii) similarity restraint *SIMPVM* on the valence and dipolar populations of the H atoms (while declaring restraints, H2-H5 atoms are considered in one set and H7A, H7B are considered in another) and (iii) best choice of n_l and ξ parameters for Se1, C7 and C8 atoms, are used. Even then, the model again displayed two charge concentration regions, each close to the σ-hole of the Se-atom (**Figure 4.8a**). Also, the electron density distribution of the two lone-pairs of the Se-atom were again found to be very different (**Figure 4.8b** and **c**). These features clearly indicate that the introduced modifications are not enough to improve the quality of EMM-1.

EMM-3

In another attempt, multipolar populations of the Se-atom derived from TMM-3 are transferred to the experimental model, keeping the same local axes systems, n_l and ξ parameters. Since TMM-3 is a core-valence split refinement, multipolar populations corresponding to the Se valence electrons are transferred. These transferred values are kept intact without any further refinement while all other parameters are refined as in previous models. After convergence, it has been found that charge concentration regions observed closer to Se-atom are not present anymore (**Figure 4.8d**).

Also, the two lone-pairs of the Se-atom are now showing similar electron density features (**Figure 4.8e** and **4.8f**). However, this new model still persists with large residual densities around the Se-atom (**Figure 4.8g** and **4.8h**), and cannot be considered of high quality to further proceed with the analysis of intermolecular interactions. Rather, a theoretical model is more preferred for this purpose since it shows only minimal features in residual density maps.

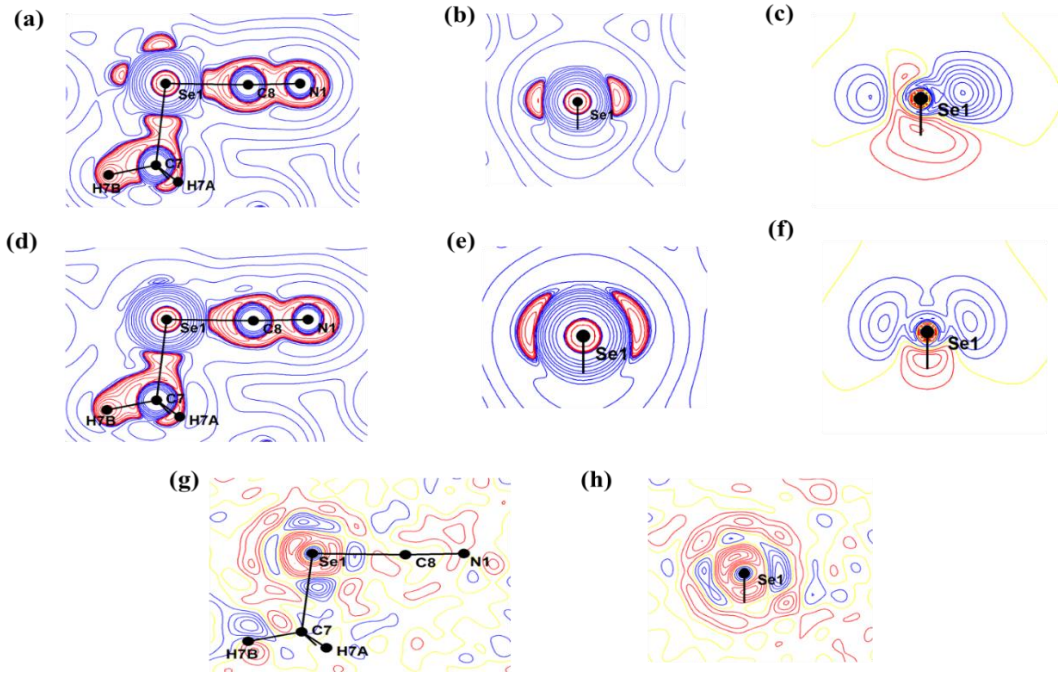

Figure 4.8 Laplacian of electron density map in (a) *plane-1* and (b) *plane-2*, (c) static deformation density map in *plane-2*, drawn after EMM-2 of SeCN1. Laplacian of electron density map in (d) *plane-1* and (e) *plane-2*, (f) static deformation density map in *plane-2* and residual density map in (g) *plane-1* and (h) *plane-2*, drawn after EMM-3 of SeCN1. Contours of residual maps (drawn for the resolution range 0.0 < sinθ/λ < 0.8 Å^{-1}) and static deformation density maps are at ±0.05 eÅ^{-3} level: blue - positive, red - negative. Laplacian of electron density maps contours (eÅ^{-5}) are in logarithmic scale: red - positive, blue - negative. All maps corresponding to these two models are given in appendices.

TMM-4

Now, the goal is to reproduce a theoretical model, similar to TMM-3, but using the new atomic co-ordinates determined from EMM-3. Therefore, a new periodic theoretical calculation is performed by optimizing the position of H-atoms, using the same calculation conditions as in the previous case but with the new atomic co-ordinates extracted from EMM-3. Afterwards, a new TMM is generated from the newly obtained theoretical structure factors, employing the same refinement strategy, n_l and ξ parameters as that of TMM-3 (**Table 4.3**). Features of the maps obtained with TMM-4 are quite close to the ones in TMM-3 (**Figure 4.9**).

Static deformation density maps given in **Figures 4.9c, f** and **i** indicate that electron densities are mainly concentrated in the covalent bonds and lone-pair regions of Se- and N-atoms. The charge distribution in the benzene ring is mostly symmetric, with an electron density value of ~0.5 eÅ^{-3} on the $C_{sp^2} - C_{sp^2}$ aromatic bonds. The C– H bonds (including C7-H7A/H7B bonds) exhibit similar peaks of electron densities. At the same time, Se1-C7 and Se1-C8 covalent bonds are characterized by relatively smaller electron density peaks, respectively of ~0.1 and ~0.4 eÅ^{-3}. A comparatively larger electron density value of ~0.8 eÅ^{-3} is located in the C8-N1 triple bond and the N lone-pair positions, whereas the Se lone-pairs are much more diffused with an electron density value of only ~0.1 eÅ^{-3}. Another interesting feature is the anisotropic distribution of the electron density found in the Se-atom, resulting to regions of charge concentration and charge depletion in the periphery of the atom. The lone-pair regions correspond to charge concentrated sites, while a charge depletion is observed elsewhere. Regions with two positive contours of electron density can be found close to the Se-atom (indicated with green arrows), approximately along the extension of Se-C7/C8 covalent bonds, which correspond to the σ-hole regions of the Se-atom (**Figure 4.9c**). It is also important to note here that these σ-hole regions are not placed along the direction of the Se-C7/C8 covalent bonds (this point will be discussed in following sections). The maps of the laplacian of electron density (**Figures 4.9b, e** and **h**) are also revealing the same information, corroborating again the anisotropic electron density distribution of the Se-atom.

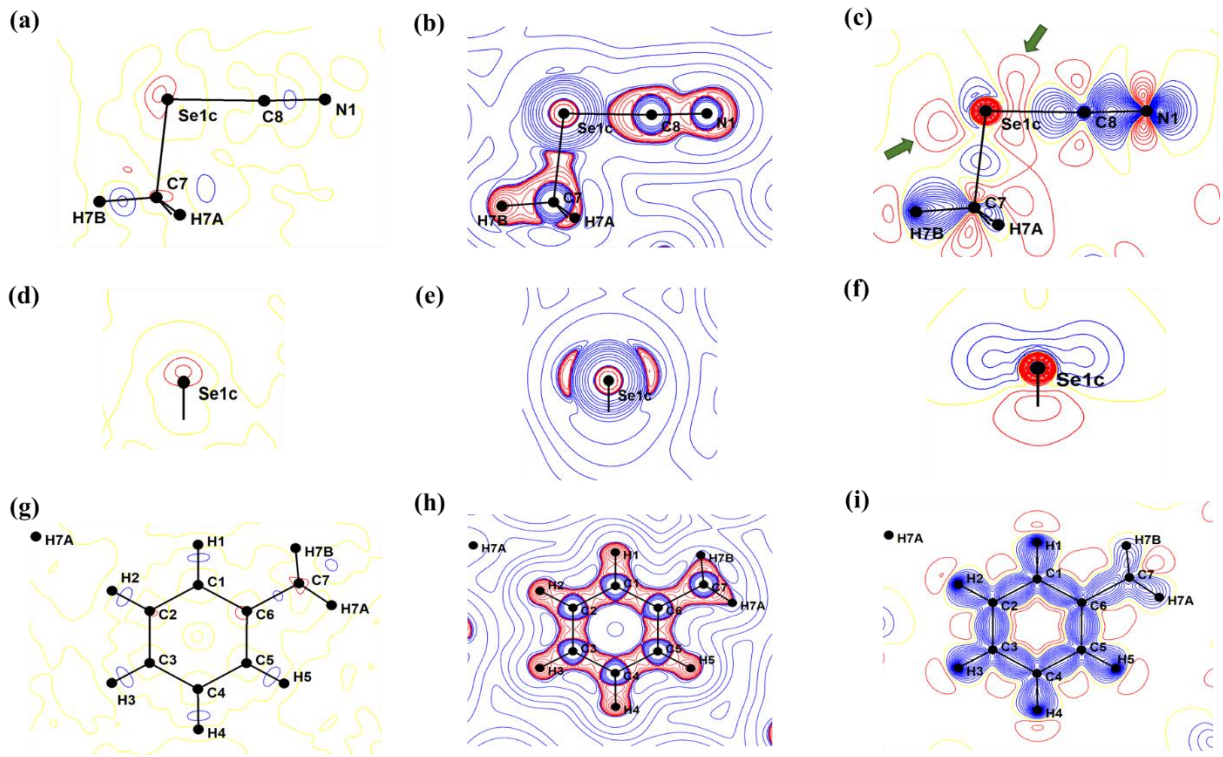

Figure 4.9 Residual, laplacian of electron density and static deformation density maps obtained after TMM-4 of SeCN1 in, (a)-(c) *plane-1* [containing C7, Se1 and N1 atoms], (d)-(e) *plane-2* [plane bisecting C7-Se1-N1 angle], (g)-(i) plane containing the benzene ring. Contours of residual maps (drawn for the resolution range $0.0 < \sin\theta/\lambda < 0.8$ Å^{-1}) and static deformation density maps are at ±0.05 eÅ^{-3} level: blue - positive, red - negative. Laplacian of electron density maps contours (eÅ^{-5}) are in logarithmic scale: red - positive, blue - negative.

4.5.1.2 ortho-bis(selenocyanatomethyl) benzene (SeCN2)

Modelling of SeCN2 was very similar to SeCN1 since both these molecules possess the same functional groups, with the only difference being that the H in the ortho-position in SeCN1 is replaced with another -CH_2-SeCN group in SeCN2. Accordingly, the same number of EMMs and TMMs were also generated for this molecule, using the same strategies. Here also, the initial experimental multipolar model (EMM-1; shown in the appendices) displayed some unusual features around Se-atoms, along with some striking differences observed between N1 and N2 atoms considering that these two N-atoms have a similar chemical environment. The electron density distribution observed for N1 is very similar to that of the N-atom in SeCN1, suggesting that the issue can be related to N2. Residual maps obtained after the first theoretical model (TMM-1; shown in the appendices) gather exactly the same features as those for SeCN1 (large negative residuals of spherical shape are found around both Se-atoms), thus demanding for another theoretical model. In addition, the close electron density distributions observed for N1 and N2 atoms in TMM-1, corroborate the need for an additional similarity restraint *SIMPVM* (between N1 and N2 atoms) in new experimental models. Afterwards, TMM-2 and

TMM-3 models are created, respectively using core-valence split strategy for Se atoms and modified n_l parameters for Se and C atoms covalently bonded to Se. In TMM-3, the same values of n_l and ξ parameters than those of SeCN1 are used for Se and C atoms in the same chemical environments (**Table 4.3**). Later, EMM-2, EMM-3 and TMM-4 models are generated following the same strategy, but with an additional *SIMPVM* restraint between N1 and N2 atoms for the experimental models. Results obtained from TMM-4 are shown below, while maps derived from other refinement models are given in appendices.

TMM-4

Residual, laplacian, and deformation density maps drawn in *plane-1* (containing the S- atom; defined either by C7, Se1, and N1 atoms, or by C9, Se2, and N2 atoms) and *plane-2* (bisecting either C7-Se1-N1 or C9-Se2-N2 angles) are shown in **Figure 4.10**. They are quite similar to those obtained earlier with SeCN1. In addition, electron density peaks found in covalent bonds and lone-pair regions display the same magnitudes than those found in SeCN1. Further, in SeCN2, the atoms of the two selenocyanate groups are displaying identical features in all maps, pointing out a similar crystalline environment in the vicinity of each group. Apart from this, σ-hole regions of both Se-atoms are found with similar features, identified by two positive contours of the electron density deformation that are placed almost in the extension of the

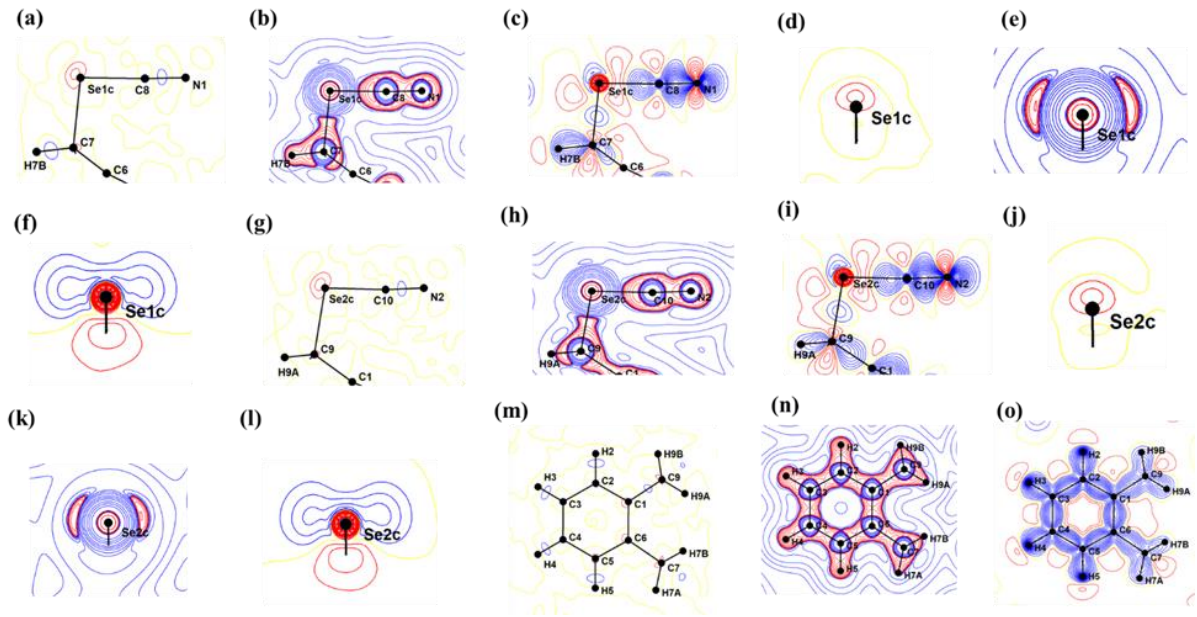

Figure 4.10 Residual, laplacian of electron density and static deformation density maps obtained after TMM-4 of SeCN2 in, (a)-(c), (g)-(i) *plane-1* [containing either C7, Se1 and N1 atoms or C9, Se2 and N2 atoms], (d)-(f), (j)-(l) *plane-2* [plane bisecting either C7-Se1-N1 or C9-Se2-N2 angle] and (m)-(o) plane containing the benzene ring. Contours of residual maps (drawn for the resolution range $0.0 < \sin\theta/\lambda < 0.8$ Å^{-1}) and static deformation density maps are at ±0.05 eÅ^{-3} level: blue - positive, red - negative. Laplacian of electron density maps contours (eÅ^{-5}) are in logarithmic scale: red - positive, blue - negative.

covalent bonds (but not linear as in the previous molecule) (**Figure 4.10c** and **i**). This might be an indication that both Se-atoms are involved in ChB interactions of similar strength in the crystalline environment (this will be verified in the crystal packing analysis later on).

4.5.1.3 2-(methylselanyl) benzyl selenocyanate (SeCN3)

Even though the chemical composition of SeCN3 is slightly different from the first two molecules, the multipolar modelling followed the same pathway. Here, in EMM-1, the same problematic situation also occurred for Se2 (corresponding to the Se-atom of the -Se-CH_3 group) along with Se1 (corresponding to the Se-atom of the -CH_2-SeCN group). The Se2 atom is covalently attached to the electron donating CH_3 group and to the aromatic ring. Therefore, in addition to the quite visible difference in chemical environment, a different electronic distribution is expected for Se2 in comparison to Se1. The same number of EMMs and TMMs are also generated here, and in each case the maps displayed approximately similar features than those observed for the first two molecules. In TMM-4, the same n_l and ξ parameters are used for both Se-atoms, even though they are of different chemical and electronic environments (they are also the same than for the first two molecules; **Table 4.3**). Results obtained with TMM-4 are given below, while maps corresponding to other models are given in appendices.

TMM-4

Both Se-atoms show very close features in residual maps (with two negative contours, also similar to the first two molecules) (**Figures 4.11a** and **g**). Even though the CH_3 group attached to Se2 atom is electron donating and the CN group attached to Se1 atom is electron withdrawing in nature, both Se atoms show equivalent electron density peaks in their lone-pair regions (~0.1 eÅ^{-3}) with almost identical features (**Figures 4.11f** and **l**). In addition, the σ-hole regions of Se1 and Se2 atoms reveal close similarities, with two negative contours of electron densities positioned slightly out of the extension of the covalent bonds (again, very similar to SeCN1 and SeCN2). The main difference is found in the Se2-C9 and Se2-C1 covalent bonds, here the electron density peaks respectively display ~0.1 and~0.2 eÅ^{-3} (**Figures 4.11c** and **i**). At the same time, all the C-H bonds in the CH_3 group (C9-H9A/H9B/H9C) show identical electron density peaks (~0.5 eÅ^{-3}) than those observed in other C-H bonds.

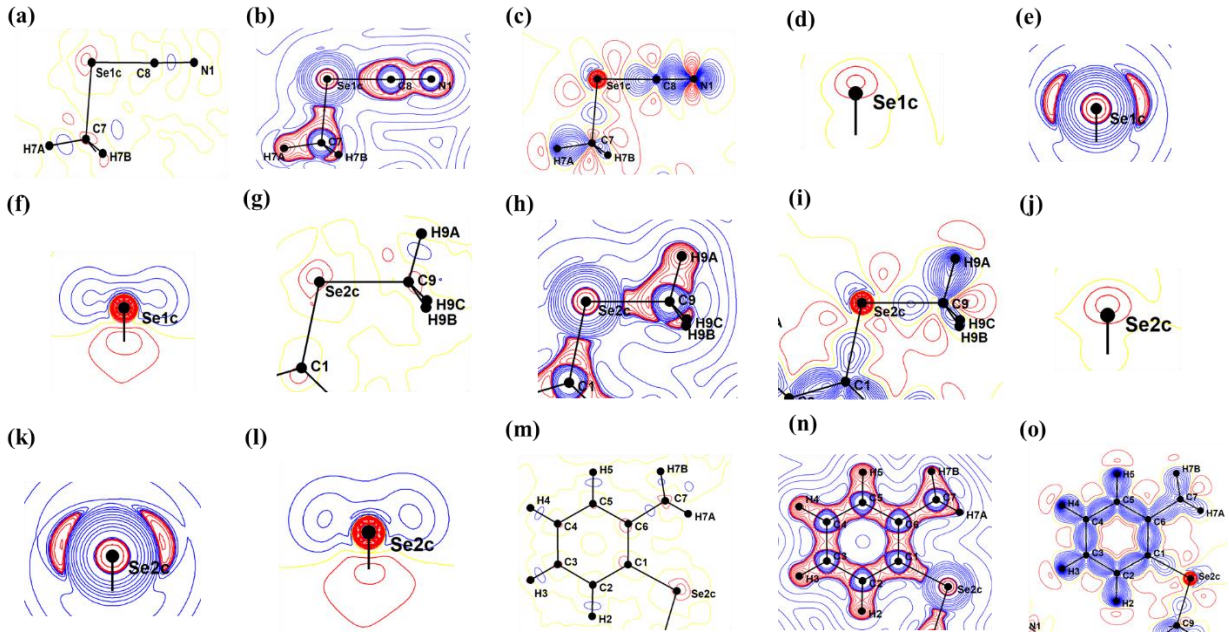

Figure 4.11 Residual, laplacian of electron density and static deformation density maps obtained after TMM-4 of SeCN3 in, (a)-(c), (g)-(i) *plane-1* [containing either C7, Se1 and N1 atoms or C1, Se2 and C9 atoms], (d)-(f), (j)-(l) *plane-2* [plane bisecting either C7-Se1-N1 or C1-Se2-C9 angle] and (m)-(o) plane containing the benzene ring. Contours of residual maps (drawn for the resolution range 0.0 < sinθ/λ < 0.8 Å^{-1}) and static deformation density maps are at ±0.05 eÅ^{-3} level: blue – positive, red – negative. Laplacian of electron density maps contours (eÅ^{-5}) are in logarithmic scale: red – positive, blue – negative.

Note: The atomic co-ordinates file (cif) used for the generation of TMM-4, which correspond to the positional co-ordinates extracted from EMM-3 and the H-atom positions optimized *via* the second periodic theoretical calculation, was further utilized for the crystal packing analysis and subsequent electronic investigations of ChB interactions. Next section will deal with the crystal packing analysis of all three molecules, based on the energetic analysis of intermolecular interactions in molecular dimers performed *via* CrystalExplorer.

4.5.2 Crystal structure description

4.5.2.1 Energetic and electronic analysis of intermolecular interactions

The main goal of this analysis is to study the crystal packing of a molecule as a whole, and to understand the significance of dimers formed by ChB interactions in the overall crystal packing. In addition, dimers connected by other intermolecular interactions are also investigated in order to rationalize the differences observed in packing topologies among the three molecules.

All three molecules crystallize in the monoclinic system ($P2_1/c$ space group, Z=4), with one molecule in the asymmetric unit. The values of unit-cell parameters and volume are found the

same as those previously reported (Maartmann *et al.*, 1984; McWhinnie *et al.*, 1998; Lari *et al.*, 2009). The magnitude of the total interaction energy (E_tot) and its decomposition into electrostatic, polarization, dispersion, and repulsion contributions for all the crystallographically independent molecular dimers found in all three molecules are gathered in **Table 4.4**. During the calculation, a molecular shell of 3.80 Å in radius was created around the central (*x*,*y*,*z*) molecule. With this procedure, SeCN1, SeCN2 and SeCN3 molecules respectively show 9, 8 and 8 crystallographically independent molecular dimers. Further, a ranking scheme has been assigned to these molecular dimers based on the calculated E_tot value, going from most to least significance. The names of the dimers are denoted as *dimerX*, where *X* is the position of the particular dimer in the proposed ranking scheme.

In the first step, molecular dimers formed by ChB interactions involving the strong σ-hole of Se-atom(s) (indicated with red colours in **Table 4.4**) are considered. The corresponding dimer in SeCN1 is ranked 2nd (*dimer2*; **Figure 4.12a**), whereas for SeCN2 and SeCN3, they are respectively ranked as 1st (*dimer1*; **Figure 4.12c**) and 4th (*dimer4*; **Figure 4.12e**). *Dimer2* in SeCN1 display an E_tot of -25.8 kJ/mol, linked through a C(sp)-Se···N(*-1+x*,*y*,*z*) [$d_{Se\cdots N}$ = 3.018 Å (RR = 0.87), $\alpha_{C\text{-}Se\cdots N}$ = 169°] ChB interaction (denoted as **ChB1I**) and a C-H···N(*-1+x*,*y*,*z*) [$d_{H\cdots N}$ = 2.56 Å (RR = 0.93), $\alpha_{C\text{-}H\cdots N}$ = 127°] HB interaction (denoted as **HB1I**), and it is mainly stabilized by the electrostatic component (-29.1 kJ/mol). In the crystal packing, the recurrent formation of the above motifs makes *dimer2* to extend along the crystallographic *a*-axis direction, forming a 1D chain-like motif (**Figure 4.12b**). In this particular **ChB1I** interaction, the lone-pair of N in the CN group of one molecule (acting as the ChB acceptor) is interacting with the strong σ-hole of Se-atom in the other molecule (acting as the ChB donor). At the same time, this N atom is also acting as the HB acceptor in the **HB1I** interaction, thus exhibiting a bifurcated character. The motifs found in *dimer1* of SeCN2 are very similar. The main difference concerns the number of motifs, which are doubled here since this molecule possess two selenocyanate groups (**Figure 4.12c**). This is also evident in the E_tot value, because the value of -54.5 kJ/mol found in SeCN2 is approximately twice the value of -25.8 kJ/mol found in SeCN1 (**Table 4.4**). Here also, the dominant contribution of the E_tot is coming from the electrostatic term (-69.9 kJ/mol). In this dimer, the corresponding C(sp)-Se···N (*x*,*1+y*,*z*) ChB interactions are denoted as **ChB2IA** [$d_{Se\cdots N}$ = 2.921 Å (RR = 0.85), $\alpha_{C\text{-}Se\cdots N}$ = 173°] and **ChB2IB** [$d_{Se\cdots N}$ = 2.916 Å (RR = 0.85), $\alpha_{C\text{-}Se\cdots N}$ = 173°].

Table 4.4 Total interaction energy (E_tot) determined for SeCNi (i=1,2,3) molecular dimers and their decomposition into electrostatic (E_ele), polarization (E_pol), dispersion (E_dis) and repulsion (E_rep) terms. Sym. Op denote the symmetry code of the neighbouring molecule, R is the intermolecular centroid to centroid distance). All energies are given in kJ/mol. Molecular dimers formed by ChB interactions are highlighted with red (involving strong σ-hole of Se) and green (involving weak σ-hole of Se) colours

Molecule	Rank	Sym.Op	R	E_ele	E_pol	E_dis	E_rep	E_tot
SeCN1	1	*1-x,1-y,1-z*	5.75	-25.7	-3.4	-14.1	12.7	-30.5
	2	*-1+x,y,z*	5.99	-29.1	-4.8	-13.9	22.0	-25.8
	3	*-x,1/2+y,1/2-z*	6.28	-9.8	-1.3	-21.4	15.5	-17.1
	4	*1-x,1/2+y,1/2-z*	6.83	-10.9	-1.3	-19.3	14.6	-16.9
	5	*1-x,2-y,1-z*	6.82	-11.7	-1.6	-9.4	9.1	-13.6
	6	*-x,1-y,1-z*	6.09	-3.0	-1.0	-11.3	7.4	-7.9
	7	*1+x,3/2-y,1/2+z*	10.09	-3.0	-0.4	-1.2	0.1	-4.4
	8	*x,3/2-y,1/2+z*	8.79	-2.4	-0.4	-7.1	5.7	-4.2
	9	*-x,2-y,1-z*	7.11	-4.5	-0.2	-5.0	6.5	-3.2
SeCN2	1	*x,1+y,z*	5.90	-69.9	-13.2	-29.6	58.2	-54.5
	2	*1-x,1-y,1-z*	7.53	-29.6	-4.0	-20.6	15.4	-38.8
	3	*2-x,1-y,1-z*	5.73	-24.0	-4.5	-24.0	20.6	-32.0
	4	*2-x,1/2+y,3/2-z*	7.78	-9.5	-2.4	-15.2	11.2	-15.9
	5	*1-x,1/2+y,3/2-z*	8.92	-6.8	-0.7	-15.9	10.9	-12.5
	6	*2-x,2-y,1-z*	7.89	-4.8	-1.4	-11.1	8.2	-9.2
	7	*-1+x,y,z*	7.93	-3.8	-1.1	-12.6	8.5	-9.1
	8	*-1+x,1+y,z*	9.89	2.6	-0.2	-2.6	0.7	0.5
SeCN3	1	*1-x,1-y,1-z*	5.08	-31.0	-1.9	-40.5	31.9	-41.5
	2	*x,3/2-y,-1/2+z*	5.76	-24.7	-5.0	-31.3	31.5	-29.6
	3	*1+x,3/2-y,1/2+z*	9.29	-13.1	-2.6	-7.6	8.0	-15.2
	4	*1-x,1-y,-z*	5.30	-33.7	-1.6	-23.3	45.0	-13.6
	5	1+x,y,z	8.79	-6.4	-0.9	-10.0	7.3	-10.1
	6	*-x,1-y,-z*	9.10	-3.7	-0.7	-8.9	3.7	-9.5
	7	*x,y,-1+z*	7.14	-3.6	-0.5	-14.0	9.8	-8.4
	8	*1+x,y,1+z*	8.95	-2.3	-1.4	-10.0	5.5	-8.2

Similarly to SeCN1, two C-H···N (*x,1+y,z*) HB interactions are also observed here, namely **HB2IA** [$d_{H\cdots N}$ = 2.56 Å (RR = 0.93), $\alpha_{C\text{-}H\cdots N}$ = 109°] and **HB2IB** [$d_{H\cdots N}$ = 2.50 Å (RR = 0.91), $\alpha_{C\text{-}H\cdots N}$ = 120°]. One important point to note down here is that the ChB interactions found in SeCN2 are stronger and more linear than those found in SeCN1, whereas among the two HBs, one is stronger and the other one is very similar to the HB of SeCN1 (in terms of RR, but both HBs are less linear as compared to the case of SeCN1). Very similar to SeCN1, *dimer1* of SeCN2 is also forming an extended network in its crystal packing, with two parallel 1D chains placed along the crystallographic *b*-axis direction (**Figure 4.12d**). On the other hand, *dimer4* of SeCN3 is differently formed and characterized with a comparatively smaller E_tot magnitude of -13.6 kJ/mol. This dimer is formed around an inversion centre, involving the symmetry related ChB and HB interactions: C(sp)-Se···Se(*1-x,1-y,-z*) [$d_{Se\cdots Se}$ = 3.435 Å (RR = 0.90), $\alpha_{C\text{-}Se\cdots Se}$ = 164°] (denoted as **ChB3I**) and C-H···Se(*1-x,1-y,-z*) [$d_{H\cdots Se}$ = 3.07 Å (RR = 0.99), $\alpha_{C\text{-}H\cdots Se}$ = 126°] (denoted as **HB3I**) (**Figure 4.12e**). As compared to the first two molecules SeCN3 exhibits a different ChB acceptor atom (the Se-atom of the Se-CH_3 group), which also induces changes in the associated HB interaction (the Se-atom acts in addition as the HB acceptor). Since the characterized intermolecular interactions are of same kind, a dominant electrostatic term (-33.7 kJ/mol) is again mainly contributing to the stabilization of the dimer (**Table 4.4**). Further, in the crystal packing, *dimer4* exists as a discrete supramolecular dimer rather than an extended 1D chain-like structure, thus exhibiting a different packing topology driven by the changes in the intermolecular interactions (especially concerning the ChB interaction).

In the second set of SeCNi (i=1,2,3) molecular dimers, that is ChB interactions involve a weak σ-hole of the Se-atom (indicated with green colours in **Table 4.4**). The concerned dimer is ranked 5th with SeCN1 (*dimer5*; **Figure 4.13a**), whereas it is ranked 2nd with SeCN2 (*dimer2*; **Figure 4.13b**) and SeCN3 (*dimer2*; **Figure 4.13c**). *Dimer5* with SeCN1 (E_tot = -13.6 kJ/mol) is centrosymmetric and assembled through the ChB interaction C(sp^2)-Se···N(*1-x,2-y,1-z*) [$d_{Se\cdots N}$ = 3.520 Å (RR = 1.02), $\alpha_{C\text{-}Se\cdots N}$ = 164°] (denoted as **ChB1II**). Here, the ChB interaction appears weaker and less linear than the one in *dimer1*, mostly due to the weak nature of the corresponding σ-hole region. Also, in this dimer, both electrostatic (-11.7 kJ/mol) and dispersion (-9.4 kJ/mol) terms are almost equally contributing to the stabilization of the dimer. Similarly, *dimer2* of SeCN2 also shows two such C(sp^2)-Se···N(*1-x,1-y,1-z*) ChB interactions, namely **ChB2IIA** [$d_{Se\cdots N}$ = 3.595 Å (RR = 1.04), $\alpha_{C\text{-}Se\cdots N}$ = 136°] and **ChB2IIB** [$d_{Se\cdots N}$ = 3.636 Å (RR = 1.05), $\alpha_{C\text{-}Se\cdots N}$ = 155°].

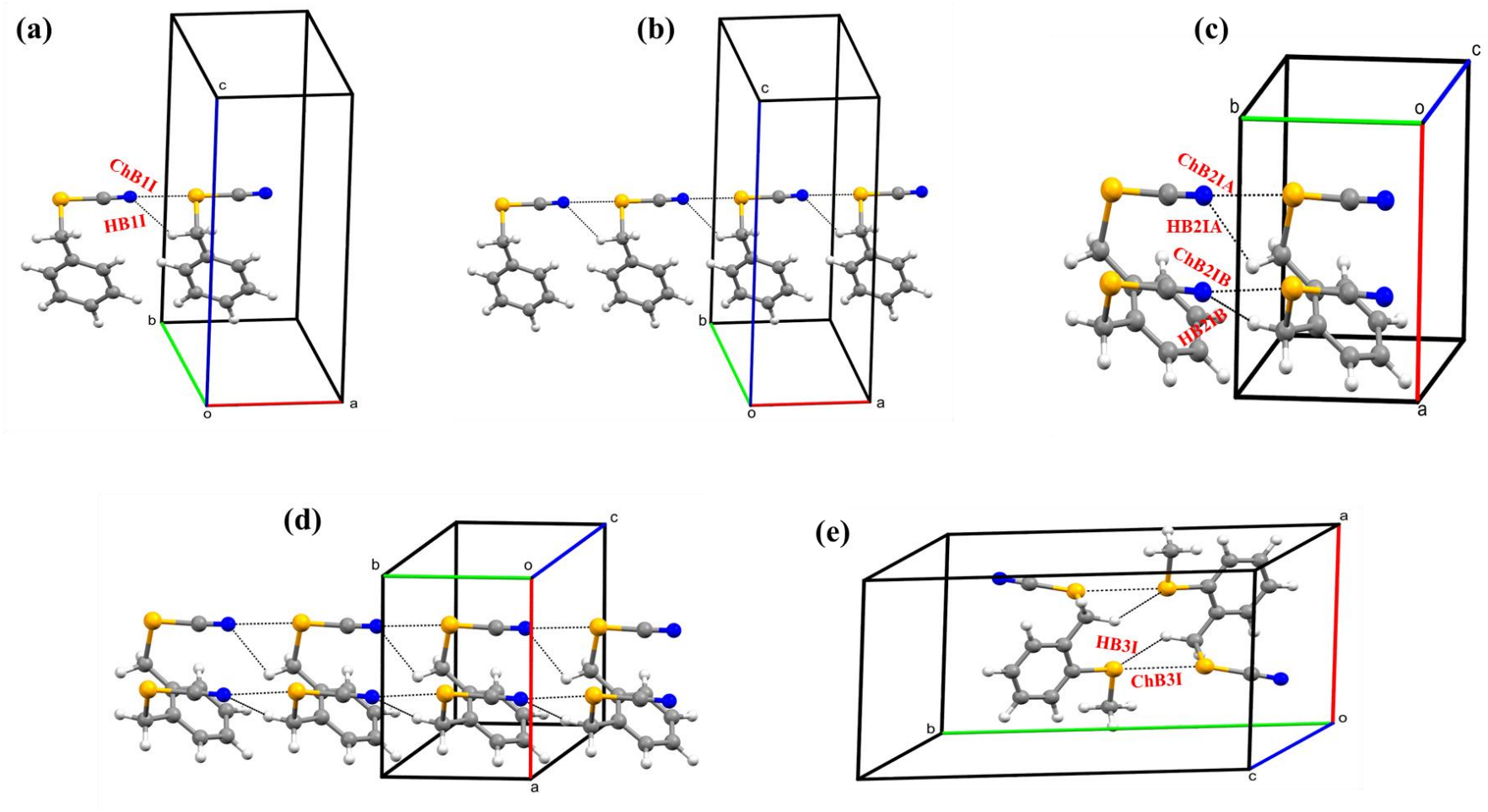

Figure 4.12 (a) *dimer2* of SeCN1 and (b) its extension forming 1D chain-like motifs along crystallographic *a*-axis direction, (c) *dimer1* of SeCN2 and (d) its extension forming two parallel 1D chain-like motifs along crystallographic *b*-axis direction, and (e) *dimer4* of SeCN3 forming discrete centrosymmetric structure. Atoms are shown with colouring scheme, intermolecular interactions are depicted as black dashed lines along with their names given in red colour.

Here also, both ChB interactions are found weaker than the ones in *dimer1* of SeCN2, one of them being less linear (**ChB2IIA**) compared to the other cases (**ChB2IIB, ChB2IA and ChB2IB)**. The total interaction energy of this dimer is -38.8 kJ/mol, with an electrostatic contribution (-29.6 kJ/mol) apparently dominant over the dispersion (-20.6 kJ/mol). Nevertheless, in the crystal packing, both *dimer5* of SeCN1 and *dimer2* of SeCN2 exist as discrete dimeric structures. The case of *dimer2* in SeCN3 is very different, being formed with an E_tot of -29.6 kJ/mol and linked through a strong ChB interaction C(sp^2)-Se···N(*x,3/2-y,-1/2+z*) [$d_{Se\cdots N}$ = 3.080 Å (RR = 0.89), $\alpha_{C\text{-}Se\cdots N}$ = 166°] (denoted as **ChB3II**). Unlike SeCN1 and SeCN2, SeCN3 exhibits a strong ChB interaction involving the weak σ-hole of the Se-atom. In addition, a weak C···H-C(*x,3/2-y,-1/2+z*) [$d_{C\cdots H}$ = 2.86 Å (RR = 0.99), $\alpha_{C\cdots H\text{-}C}$ = 129°] HB interaction and a short C···N(*x,3/2-y,-1/2+z*) [$d_{C\cdots N}$ = 3.072 Å (RR = 0.95)] contact are also found within this dimer. Being different from the first two molecules, this dimer of SeCN3 forms an extended 1D network in the crystal structure along the crystallographic *c*-axis direction, characterised by a zig-zag arrangement of ChB motifs (**Figure 4.13d**).

In short, it has been found that the crystal packing topologies driven by ChB interactions are very similar with SeCN1 and SeCN2 molecules, their ChB interactions being associated to the strong σ-hole of the Se-atom forming a 1D chain-like motif (through strong and linear ChBs) and the weak one forming discrete dimers (through weak and less linear ChBs). Unlike the first two molecules, ChB interactions identified in the crystal structure of SeCN3 are very different, with both σ-holes of the Se-atom forming equally strong ChB interactions in spite of their difference in strength (extent of electron depletion). Thus, with SeCN3, strong σ-hole of the Se-atom is interacting with a Lewis base different than that observed with SeCN1 and SeCN2 to form a discrete centrosymmetric structure in the crystal packing, while the other ChB interaction is found with the weaker σ-hole forming a 1D network. Thus, compared to SeCN1 and SeCN2, rationale behind the changes in ChB interactions with SeCN3 will be investigated in the upcoming sections.

At the same time, it has to be kept in mind that other intermolecular interactions (with the resulting molecular dimers) are also playing a significant role in molecular arrangements, leading altogether the three-dimensional packing of the investigated molecules. For all three molecules of Bz-SeCNs, details of intermolecular interactions involved in other dimers and the resulting three-dimensional packing are given in appendices.

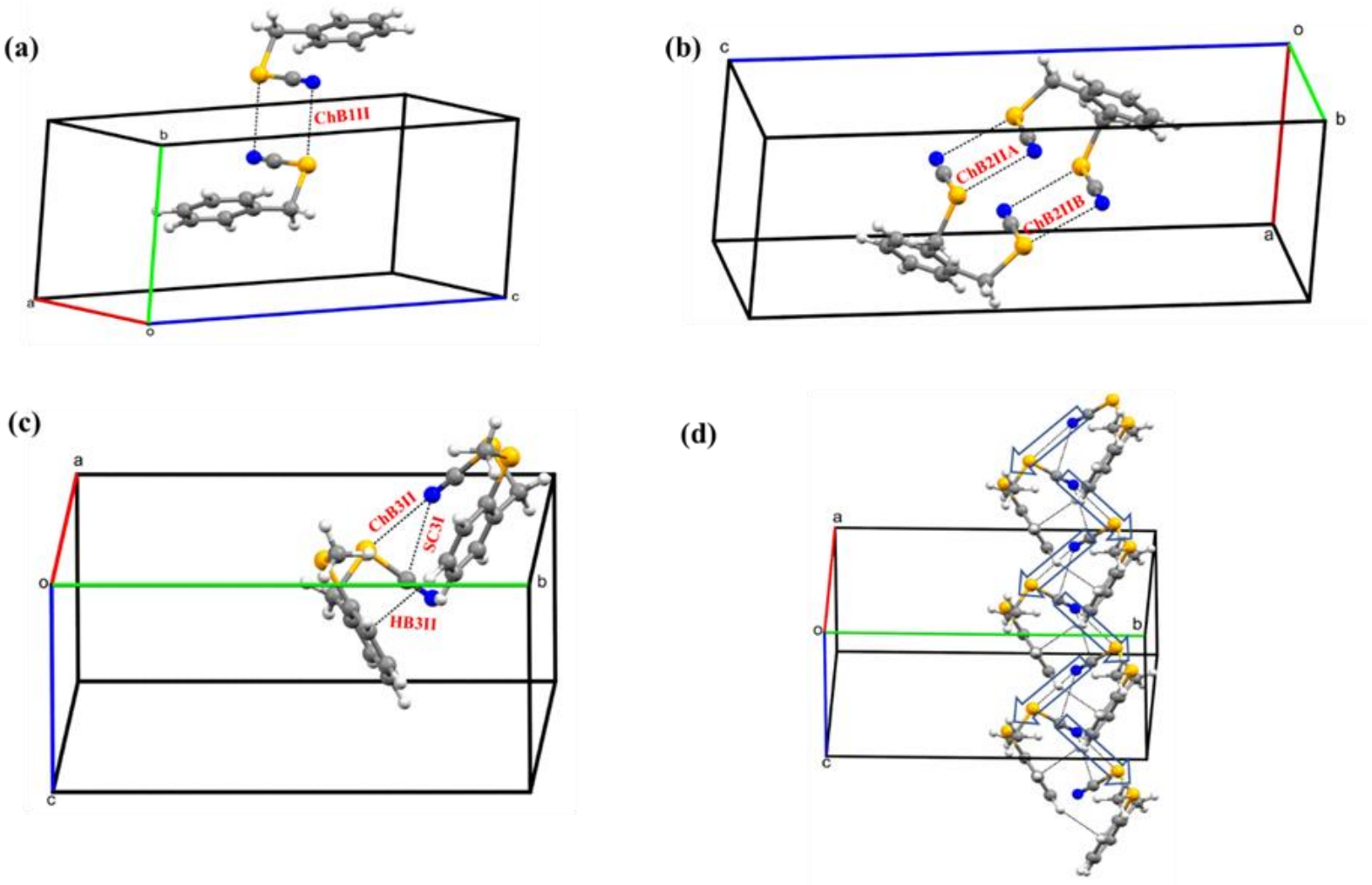

Figure 4.13 (a) *dimer5* of SeCN1 and (b) *dimer2* of SeCN2 forming discrete centrosymmetric structures, (c) *dimer2* of SeCN3 and (d) its extension forming a 1D network along the crystallographic *c*-axis direction (zig-zag arrangements of ChB interactions are indicated with blue transparent arrows, pointing from ChB acceptor to ChB donor atom). Atoms are shown with colouring scheme. Intermolecular interactions are depicted as black dashed lines along with their names given in red colour.

4.5.2.2 Hirshfeld surface analysis and enrichment ratio

The usefulness of Hirshfeld surfaces, 2D fingerprint plots and enrichment ratios (ERs) in analyzing the intermolecular interactions, as a whole-of-molecule approach rather than treating individual interactions separately, has been discussed in **section 2.2.2**. Hirshfeld surfaces generated for the three molecules *via* CrystalExplorer software can be found in **Figure 4AP. 23**, indicating that larger red spots (and therefore shorter contacts) observed in the surfaces correspond to ChB interactions. Molecular dimers or trimers formed through these short ChB interactions are also depicted in **Figure 4AP.23**. With SeCN3, it appears that two such red spots of equivalent size are present. They correspond to both σ-holes of the Se1-atom, referring to the formation of two equally strong ChB interactions, as discussed before. Simultaneously, 2D fingerprint plots generated from the Hirshfeld surfaces are indicating some characteristic differences between each other in terms of the percentage contribution coming from individual atom···atom interactions (**Figure 4AP.23**). Accordingly, the percentage contributions of individual atom···atom interactions to the total Hirshfeld surface and the corresponding ERs values calculated with MoproViewer are given for all three molecules in **Table 4.5**.

For SeCN1, the major contribution of the Hirshfeld surface is coming from C···H interactions (33.5%) followed by H···H (28.5%), N···H (17.8 %) and then Se···H (11.9 %) interactions, whereas the contribution of the Se···N interactions to the Hirshfeld surface is only 5.2%. Interestingly, the Se···N interactions show the largest ER (2.29) among all the atom···atom contacts in SeCN1, revealing that they are the most significant interactions in the construction of the crystal packing. Three other interactions showing ER greater than 1 in SeCN1 are, C···H (1.54), N···H (1.30) and Se···H (1.11). Accordingly, the important roles of Se···N, C···H, N···H and Se···H interactions in the formation of various molecular dimers in SeCN1 discussed earlier are now pointed by their ER values, corroborating their significance in the crystal packing.

Similarly to SeCN1, N···H (23.1%), H···H (22.8%) and C···H (21.4%) interactions contribute to the most significant portion of the Hirshfeld surface of SeCN2 as well, whereas the contribution of the Se···N interactions is almost doubled (12.4%) as compared to SeCN1 (5.2%). This larger proportion of Se···N interactions in the Hirshfeld surface of SeCN2 is actually linked to the presence of one additional selenocyanate functional group within the molecular core, and therefore to the concomitant formation of two parallel 1D chain-like motifs in the crystal structure. As expected from crystal packing similarities, Se···N interactions

display the largest ER (2.06) among all atom···atom contacts in SeCN2 as well, thus being the most significant interactions in the construction of the crystal packing. Considering the magnitude of ER corresponding to Se···N interactions, SeCN2 (2.06) is showing a lower magnitude in comparison to SeCN1 (2.29). This feature can be due to a larger proportion of both Se and N atoms in the molecular surface of SeCN2 (this information is used for the calculation of random contacts). Other interactions showing ER value greater than 1 with SeCN2 are the same than those observed with SeCN1 [C···H (1.58) and N···H (1.28) interactions], except for the case of C···C (1.50) interactions. The smaller ER value observed for C···C interactions with SeCN1 (0.84), as compared to a larger value with SeCN2 (1.50), points a pronounced π···π interaction for the latter.

On the other hand, the percentage contribution of individual atom···atom interactions and the corresponding ERs are very different with SeCN3, as expected from the differences observed in its crystal packing with respect to those of SeCN1 and SeCN2. With SeCN3, the most significant interactions contributing to the Hirshfeld surface are H···H (30.1%), followed by C···H (27.6%), Se···H (20.6%) and then N···H (13.9%) interactions. Meanwhile, the contribution coming of the Se···N (2.1%) interactions is very low, as expected from the

Table 4.5 Percentage contribution of individual atom...atom interactions and their calculated ER values gathered as left/right entries for SeCNi (i=1,2,3). Contacts with ER > 1 are highlighted with red colour.

Contacts	SeCN1/ER	SeCN2/ER	SeCN3/ER
Se···Se	1.2/0.88	3.4/0.95	2.4/1.06
Se···N	5.2/2.29	12.4/2.06	2.1/0.94
Se···C	0.5/0.45	0.3/0.31	0.5/0.82
Se···H	11.9/1.11	11.8/0.99	20.6/1.08
N···C	0.8/0.16	2.3/0.11	2.2/0.51
N···H	17.8/1.30	23.1/1.28	13.9/1.51
C···C	0.6/0.84	2.6/1.50	0.6/0.79
C···H	33.5/1.54	21.4/1.58	27.6/1.32
H···H	28.5/0.50	22.8/0.52	30.1/0.67

absence of 1D chain-like motifs involving Se···N ChB interactions in the crystal structure. The largest ER value is shown by N···H interactions (1.32), followed by C···H (1.32), Se···H (1.08) and Se···Se (1.06) interactions, while the ER value of Se···N interactions reduces to 0.94. This observation points the low propensity of Se and N atoms in SeCN3 to form contacts in the crystalline phase. At the same time, in SeCN3 Se···Se interactions show an ER value greater than 1 (1.06) while for SeCN1 and SeCN2 it was less than 1 (0.88 and 0.95 respectively). This high propensity observed in SeCN3 is linked to the occurrence of strong Se···Se ChB interactions, whereas weak type I Se···Se contacts are only formed with the other two molecules.

In conclusion, the ER analysis reveals that Se···N interactions are most significant in forming the crystal packings of SeCN1 and SeCN2 molecules. This feature is linked to the presence of 1D chain-like motifs assembled through strong and linear Se···N ChB interactions in their respective crystal structures. At the same time, there are no such 1D chain-like motifs observed with SeCN3, leading to a lower ER and to a less significant role of Se···N interactions in the crystal packing of this molecule. Instead, N···H interactions seem to play the most important role in the construction of the SeCN3 crystal packing.

4.5.3 Molecular Electrostatic potential surface analysis

In previous sections, crystal packing and ER analyses have been well established the significant role of Se···N ChB interactions in the solid-state assemblies of both SeCN1 and SeCN2 molecules. However, this is not the case with the SeCN3 molecule, exhibiting a lower ER value for Se···N ChB interactions but a larger one for Se···Se ChB interactions. Also, the molecular arrangements driven by ChB interactions in the crystal packing of SeCN3 are very different from those found with SeCN1 and SeCN2. Therefore, ChB interactions have a strong influence in the solid-state assemblies of the three given molecules. In this respect, it is very important to gather more insight into the characteristics of these interactions. Accordingly, a particular focus is given to study their electronic properties, beyond their simple structural characterization.

ChB interactions are often characterized as an electrostatic interaction between the σ-hole of the chalcogen atom acting as the electrophilic site and the electron rich center of the Lewis base acting as the nucleophilic site. In such cases, the evaluation of molecular electrostatic potential (MESP) surfaces serves the purpose of identifying molecular nucleophilic and electrophilic regions, and to quantitatively estimate the power of nucleophilic···electrophilic interactions

through the extremal values of the ESP function ($V_{s,\,min}$ and $V_{s,\,max}$) determined in those nucleophilic and electrophilic regions (**section 2.1.1.5**). Accordingly, MESP surfaces were generated for all three molecules, along with the quantitative measure of the $V_{s,\,max}$ and $V_{s,\,min}$ values (**Figure 4.14**).

As expected, for all three molecules, the σ-hole observed along the extension of the Se-CN covalent bond (called *region-1* hereafter) appears more depleted in electron density (and therefore with a larger positive ESP value) than that along the extension of Bz-Se covalent bond (called *region-2* hereafter). For SeCN2, there are two such *region-1* (called *region-1A* and *region-1B* hereafter) and *region-2* (called *region-2A* and *region-2B* hereafter). The σ-holes found in *region-1* of SeCN1, and in *region-1A* and *region-1B* of SeCN2, exhibit similar ESP values (respectively 36, 40 and 39 kcal/mol), suggesting a similar electron distribution around the corresponding Se-atoms (**Figure 4.14**). At the same time, the ESP value found in *region-1* of SeCN3 is lower (29 kcal/mol), might be due to the close vicinity of the Se2 lone-pair that brings a negative contribution to the ESP magnitude. From these values one would normally expect a relatively stronger ChB interaction with SeCN1 and SeCN2, as compared to SeCN3. This parallels with the RR values of Se···N/Se···Se ChB interactions determined earlier from the crystal packing analysis [$RR_{(Se\cdots N)}$ = 0.87 in SeCN1, $RR_{(Se1\cdots N1)}$/ $RR_{(Se2\cdots N2)}$ = 0.85/0.85 in SeCN2 and $RR_{(Se\cdots Se)}$ = 0.90 in SeCN3; **section 4.5.2.1**]. It should be pointed out that ChB interactions observed in the crystal structure of SeCN2 are slightly stronger (thus with lower RR) than in SeCN1 (both exhibiting Se···N ChB interactions). Other than a small difference observed in the positive ESP values of the σ-hole regions, this is mainly happening due to the differences found in the $V_{s,\,min}$ values of the nucleophilic sites.

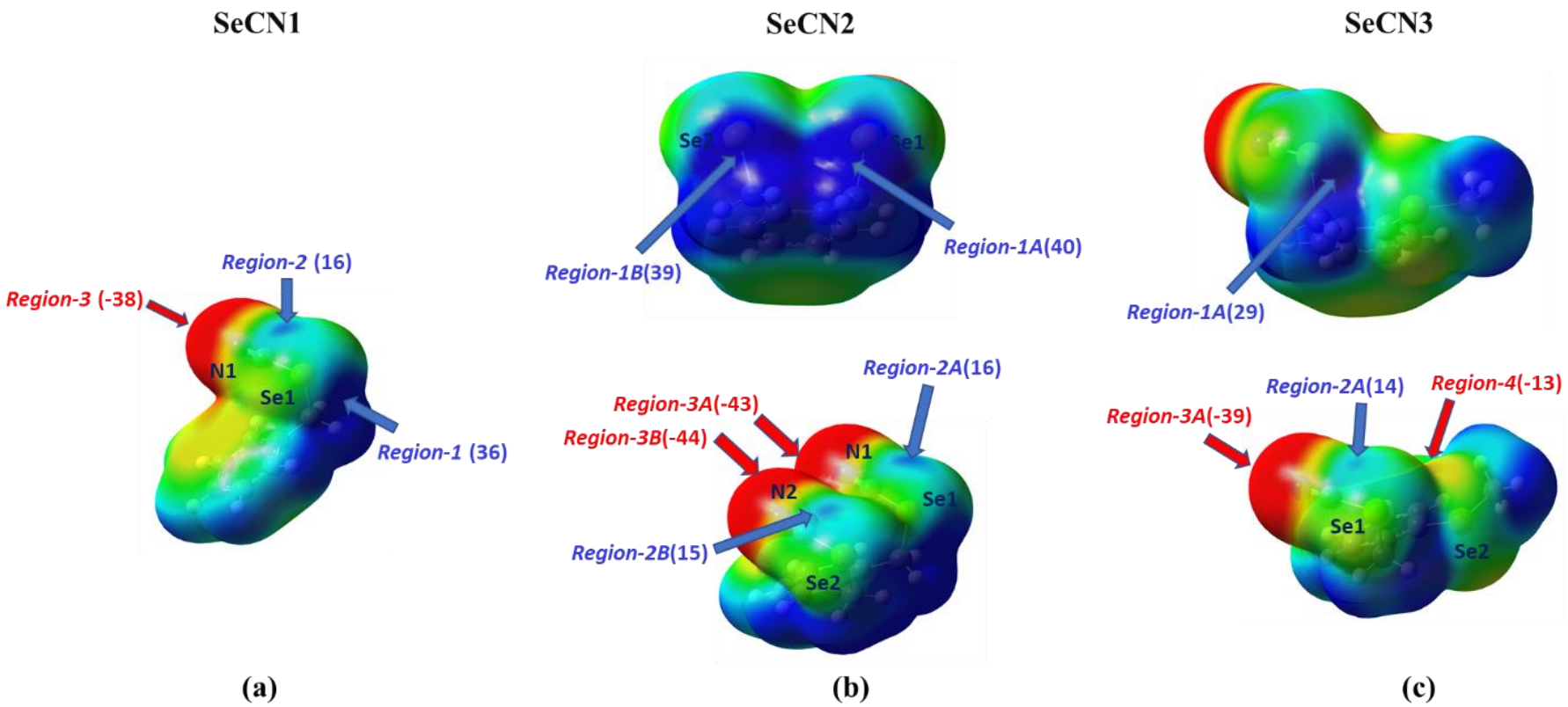

Figure 4.14 MESP maps drawn on the ρ = 0.001 a.u. iso-surface for (a) SeCN1, (b) SeCN2 and (c) SeCN3 molecules. Electrophilic and nucleophilic regions are highlighted with their assigned names (atomic labelling of the associated atom is also given). The corresponding electrostatic potential (ESP) values (in kcal/mol) are given within the bracket. ESP surface colouring: red = -20 kcal/mol to blue = +20 kcal/mol.

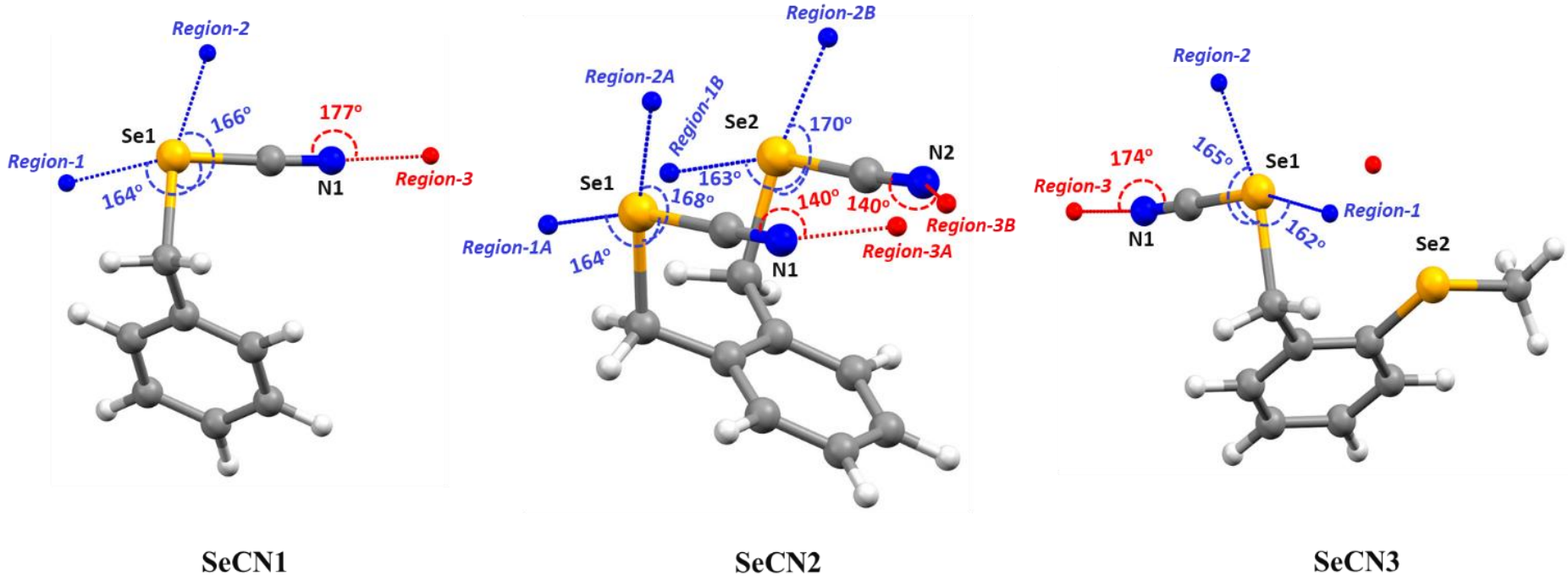

Figure 4.15 Extremal points of the ESP function of the regions discussed in the text for SeCN1, SeCN2 and SeCN3 molecules. Sites with maximal ($V_{s,max}$) and minimal ($V_{s,min}$) values are respectively represented with blue and red coloured spheres. Atomic labels are given for the associated atom. The angles made by the sites of the extremal values with the corresponding covalent bonds are also depicted.

The lone-pair of N in the CN group (called *region-3* hereafter) is acting as a potential nucleophilic site in both SeCN1 and SeCN2. For SeCN2, there are two such *region-3*, called *region-3A* and *region-3B* that show respectively a $V_{s,\,min}$ value of -43 kcal/mol and -44 kcal/mol, being more negative than the $V_{s,\,min}$ value in *region-3* of SeCN1 (-38 kcal/mol). Accordingly, the presence of deeper holes and better nucleophiles resulted to stronger ChB interactions with SeCN2. Another feature that merits to be pointed out here is the different type of ChB interaction observed in the *region-1* of SeCN3 (Se···Se), as compared to the other two molecules (both showing Se···N ChB interactions). A concrete reason for this difference cannot be derived from the MESP analysis. However, it can be argued that the orientation of the ortho group in SeCN3 (Se-CH_3) has an influence on the observed difference, leading to the Se2 lone-pair orientation in the close vicinity of *region-1* and causing a different intermolecular interaction.

Considering the second set of σ-holes (namely those formed in *region-2*), they exhibit a similar ESP value in all three molecules (*region-2* of SeCN1:16 kcal/mol, *region-2A* and *region-2B* of SeCN2:16 and 15 kcal/mol, *region-2* of SeCN3: 14 kcal/mol), therefore pointing a similar electron distribution in those regions (**Figure 4.14**). Furthermore, the same type of Se···N ChB interactions is found in *region-2* of all three molecules, with SeCN3 showing a stronger interaction (in terms of RR) than that of SeCN1 and SeCN2. Also, the Se···N ChB interactions observed in *region-2* of SeCN1, and in *region-2A* and *region-2B* of SeCN2, exhibit a weaker nature (RR values of 1.02, 1.04 and 1.05 respectively) in comparison to the ones observed earlier in *region-1*, *region-1A* and *region-1B* (RR values of 0.87, 0.85 and 0.85 respectively). This difference is actually linked to the ESP values observed in the corresponding σ-holes. Therefore, a deeper σ-hole (with a large positive ESP value) found in *region-1* results to a stronger ChB interaction than in *region-2* with either SeCN1 or SeCN2. On the other hand, a stronger Se···N ChB interaction (with RR of 0.89) is shown by *region-2* of SeCN3, whose interaction strength (in terms of RR) is quite close to the one observed for the Se··Se ChB interaction in *region-1*(RR = 0.90). Even though the nucleophilic (σ-hole in *region-2*) and electrophilic (lone pair of N) centers of this Se···N ChB interaction are very similar to those in SeCN1 and SeCN2, this additional strength observed in SeCN3 might be coming from a better electrostatic complementarity of the interacting regions (discussed below).

In addition, the lone-pair of Se2-atom (*region-4*) in SeCN3 is also acting as a nucleophilic center in a ChB interaction, forming a Se···Se interaction with the strong σ-hole (*region-1*) of

the Se1 atom. A smaller ESP value in *region-4* (-13.6 kcal/mol) in comparison to *region-3* is related to the more diffused nature of the Se lone-pair as compared to the N lone-pair.

Another feature that can be estimated from the MESP surfaces is the electrostatic complementarity of the interacting atoms, that is how well and closely oriented are the interacting nucleophilic and electrophilic sites. This can be understood from the geometrical disposition of $V_{s,\,max}$ and $V_{s,\,min}$ sites with respect to the direction of interacting atoms. For this purpose, maximum and minimum values of the MESP function (extremal points) were calculated on the molecular surfaces of all three molecules and represented as spheres of arbitrary radius (**Figure 4AP. 24**). Spheres corresponding to the above discussed nucleophilic and electrophilic sites are given in **Figure 4.15**, revealing that the σ-holes of Se-atoms are not linearly positioned along the extension of the covalent bonds but with an angle ranging 163°-170°. On the other hand, nucleophilic sites corresponding to the lone-pair of N in CN group are positioned almost linear to the associated covalent bonds in SeCN1 and SeCN3 (177° and 174°, respectively), whereas a clear non-linearity is observed for the same in SeCN2 (140° in *region-3A* and *region-3B*). Since the geometrical disposition of $V_{s,\,max}$ and $V_{s,\,min}$ sites of an atom in space is also dependent on the position of nearby atoms and their electrostatic potential contributions, it will be interesting to see how these sites are placed between ChB donor and acceptor atoms in a ChB interaction. In such a way, this will guide us to understand how good is the electrostatic complementarity in a ChB interaction. A better electrostatic complementarity is achieved when there is a face-to-face and close orientation of associated $V_{s,\,max}$ and $V_{s,\,min}$ sites are present. The geometrical disposition of $V_{s,\,max}$ and $V_{s,\,min}$ sites that correspond to the ChB interactions are shown in **Figure 4.16** for all three molecules (in each figure, only $V_{s,\,max}$ and $V_{s,\,min}$ sites involved in that particular interaction are shown). In **Figure 4.16a** and **c**, ChB interactions involving the *region-1* of SeCN1 and of SeCN2, the $V_{s,\,max}$ and $V_{s,\,min}$ sites of Se and N atoms are very close to each other in space (with kind of a mutual interpenetration). Apart from their mutual interpenetration, the geometrical disposition also suggests a close and face-to-face orientation of $V_{s,\,max}$ and $V_{s,\,min}$ sites. Altogether, it results to a better electrostatic complementarity and to strong ChB interactions in both crystal structures.

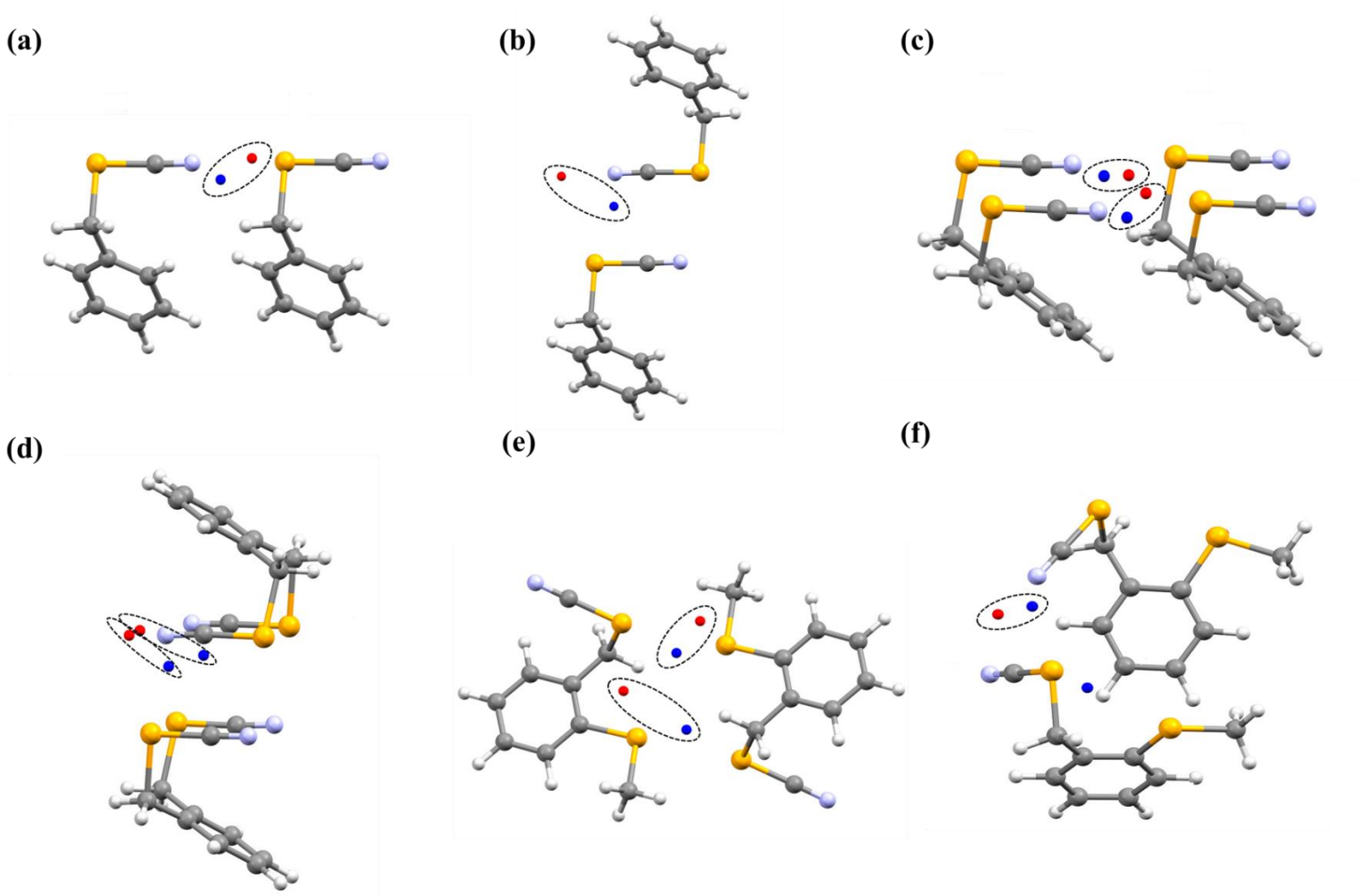

Figure 4.16 Geometrical disposition of $V_{s,\,max}$ (shown as blue spheres) and $V_{s,\,min}$ (shown as red spheres) sites corresponding to ChB interactions in (a)-(b) SeCN1, (c)-(d) SeCN2 and (e)-(f) SeCN3. Interacting sites are encircled inside a dashed oval shape.

On the other hand, the ChB interaction involving *region-1* of SeCN3 is very different. Here, the $V_{s,\,min}$ corresponding to the Se2 lone-pair is not directed towards the $V_{s,\,max}$ corresponding to the strong σ-hole of Se1-atom (**Figure 4.16e**). In SeCN3, in comparison to the previous molecules, this results to a diminished electrostatic complementarity and to a weaker ChB interaction.

Considering the case of ChB interactions involving *region-2*, in SeCN1 and SeCN2 there is a side-on orientation of the $V_{s,\,max}$ and $V_{s,\,min}$ sites (**Figure 4.16b** and **d**). Therefore, this particular orientation is leading to a poor electrostatic complementarity and concomitantly very weak ChB interactions in SeCN1 and SeCN2. Again, the case of SeCN3 is different. Indeed, even though the $V_{s,\,max}$ site displays the same ESP value than in SeCN1 and SeCN2, a close and approximately face-to-face orientation of $V_{s,\,max}$ and $V_{s,\,min}$ sites result to a stronger ChB interaction in *region-2* of SeCN3 (**Figure 4.16f**).

Despite of the previous discussion, it should be remembered that the geometrical disposition of $V_{s,\,max}$ and $V_{s,\,min}$ sites in atoms are dependent on other atoms in their neighborhood. Accordingly, this tool has some limitations in dictating precisely the characteristics of local nucleophilic···electrophilic interactions. For instance, considering the ChB interactions involving *region-1* of SeCN1 and SeCN2, crystal packing analysis shows that the interactions in both crystal structures are very close in terms of their RR and interaction angles. However, a drastic difference can be observed in the geometrical positioning of their $V_{s,\,min}$ sites in MESP surfaces: a linear positioning of *region-3* is found in SeCN1 while a non-linear one is observed for *region-3A* and *region-3B* in SeCN2 (**Figure 4.15**). These features indicate that the analysis of MESP surfaces alone cannot output the precise characteristics of nucleophilic···electrophilic interactions, demanding the need for an alternate characterization tool which deals with a more local function.

4.5.4 Topological analysis of ρ(r) and L(r) functions

It has been well established previously that the characteristics of local nucleophilic···electrophilic interactions can be studied from the local topological and energetic properties of $\rho(\mathbf{r})$ and $L(\mathbf{r})$ functions, derived within the framework of the QTAIM approach (Brezgunova *et al.*, 2012; Brezgunova *et al.*, 2013; Shukla *et al.*, 2020). The rationale behind this approach can be found in **section 2.1.1.4**. The results derived from this method is intended

to enrich the information gathered previously with MESP surfaces, to get a deeper insight into the molecular connectivity directed through nucleophilic···electrophilic interactions.

Significant information that is derived from the topological analysis of $\rho(\mathbf{r})$ is coming from its local properties at (3,-1) BCPs, which help to rationalize the characteristics and strength of individual intermolecular interactions. As discussed earlier, the interaction between any two atoms in a molecular assembly can be identified from the presence of a bond path (BP) and a concomitant BCP. The information obtained at BCPs is not only helpful to understand the nature of individual interactions but also to rank them based on their significance in the overall crystal packing. In such a way, this method provides an alternative understanding to the intermolecular interactions that are most significant in the constitution of the crystal packing. As mentioned earlier, in this particular analysis we will mainly focus on ChB interactions by providing their electronic descriptions. For all the three given molecules, the topological calculation of $\rho(\mathbf{r})$ has been performed in both crystal and gas phases, using the structure(s) obtained either after multipolar modelling or extracted from the crystal geometry (monomer, dimer and trimer). Accordingly, topological and energetic properties determined at BCPs of various ChB interactions are discussed below.

The topological analysis of $L(\mathbf{r})$ function can provide a further perspective to these ChB interactions through the properties and disposition of its critical points, known as laplacian critical points (LCPs). Earlier studies clearly demonstrated the usefulness of this $L(\mathbf{r})$ function in identifying nucleophilic and electrophilic regions in the valence shell of a chalcogen atom (Brezgunova *et al.*, 2012; Brezgunova *et al.*, 2013; Shukla *et al.*, 2020). These nucleophilic and electrophilic regions are associated with LCPs of specific kinds, whose disposition and electronic characteristics provide a quantitative description to local nucleophilic···electrophilic interactions. Accordingly, in all three molecules, LCPs have been searched for chalcogen atoms and the atoms bearing nucleophilic regions (ChB acceptors). Unfortunately, due to some technical barrier the LCPs search is just limited to the structures in gas phase (monomers, dimers and trimers extracted from the crystal geometries). Since the $L(\mathbf{r})$ function fluctuates quickly in space between their positive and negative values, the topological profile of the Se-atom is very complex. Thus, even considering only the valence shell, a large number of LCPs can be observed. So, it is very important to identify and filter the LCPs that are of interest. This also applies for the N atom that is bearing the nucleophilic site, however, its small size results to a less complicated $L(\mathbf{r})$ topology. In the below section, LCPs that are significant for the discussion of ChB interactions are only considered.

Monomers extracted from the crystal geometry exhibit a fully depleted valence shell of the Se-atom (due to the screening made by a large quantity of core electrons) and hence the LCPs of interest are lying in the valence shell charge depleted (VSCD) region (**Figure 4.17**). Types and disposition of LCPs are consistent and closely situated in the VSCD region of the Se-atoms of all three molecules, even when considering the Se-atom belonging to the Se-CH_3 group of SeCN3. This implies that the variation in the electron distribution among the Se-atoms of SeCN1, SeCN2 and SeCN3 molecules is only affecting the properties at LCPs but not their types or disposition in space. The nucleophilic charge concentration (CC) sites of the Se-atoms are identified by (3,-3) LCPs and they correspond to the lone-pair regions. Since these Se-atoms are sp^3 hybridized, two such CC sites (CC1 and CC2) are found in *plane-2* (namely, the plane bisecting the R-Se-R' angle and perpendicular to the R-Se-R' plane; R and R' being the substituents covalently bonded to Se-atom). The disposition of these (3,-3) LCPs along with the corresponding CC1-Se(i)-CC2 angles are given in **Figure 4AP.25**. On the other hand, potential electrophilic charge depletion (CD) sites present in *plane-1* (or positioned very close to this plane; the R-Se-R' plane) are represented in **Figure 4.17**. Four such CD sites can be spotted in the VSCD region of each Se-atom in all three molecules, namely CP1, CP2, CP3 and CP4, or CP6, CP7, CP8 and CP9 (two sets of labelling are given because SeCN2 and SeCN3 molecules possess two Se-atoms; the first set belonging to Se1 and the second set to Se2). In both sets, the first three LCPs are of (3,+1) type while the last one is of (3,-1) type. Also, it is important to note that, CP3, CP4, CP8 and CP9 LCPs are found within the atomic basins of Se-atoms, whereas CP1, CP2, CP6 and CP7 LCPs are positioned close to the interatomic surfaces between Se and C atoms, facing Se-C BCPs. As per the σ-hole notion discussed earlier, these charges depleted electrophilic sites are expected to be observed along the extension of covalent bonds that are connected to the Se-atom. Angles made by theses LCPs with associated covalent bonds are given in **Table 4.6**. Two main observations that can be derived from here are (i) charge depleted LCPs are not positioned linearly to the extension of the covalent bonds, but with an angle and (ii) the magnitude of these angles are more or less consistent in all Se-atoms belonging to -CH_2-Se-CN functional group of all three molecules, while a small difference is found in the case of -Se-CH_3 group of SeCN3 (especially in the positioning of C8 and C9 CPs with respect to C9-Se2 and C1-Se2 covalent bonds).

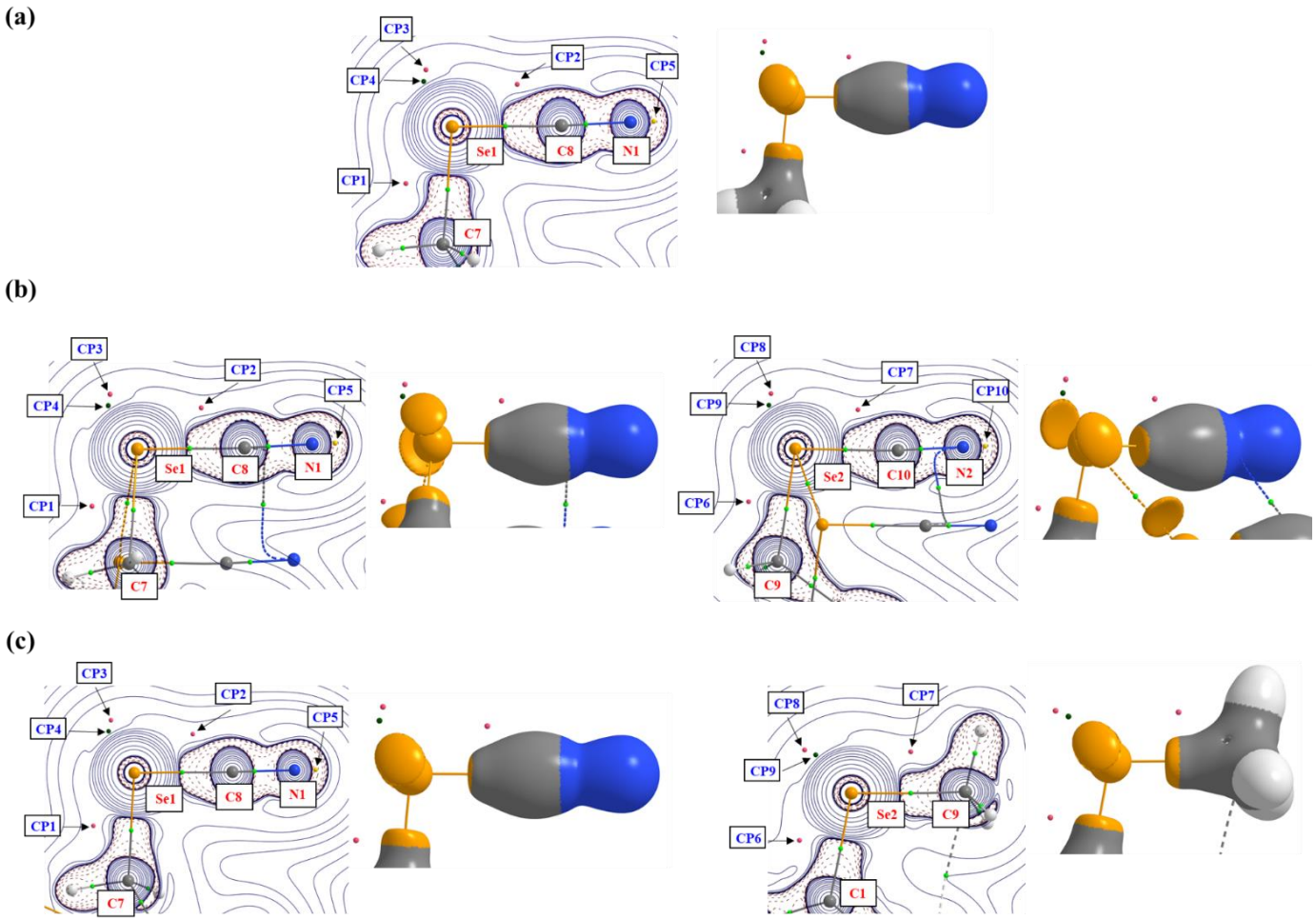

Figure 4.17 (left) $L(r)$ maps [eÅ^{-5}, contours are in logarithmic scale: positive (red) and negative (blue)] drawn in *plane-1* (R-Se-R' plane; R and R' are the substituents covalently bonded to the Se-atom), with relevant CPs of $L(r)$ function represented as spheres of arbitrary radius [(3,−1) LCPs are green and (3,+1) LCPs are pink] in the valence shell of Se and N atoms, and (right) $\nabla^2\rho(r) = 0$ reactivity surfaces for, (a) SeCN1, (b) SeCN2 and (c) SeCN3 molecules. (3, -3) LCPs corresponding to the lone-pairs of Se-atoms are out of the plane in the $L(r)$ maps and hidden by the enclosing surfaces in $\nabla^2\rho(r) = 0$ maps. (3,-1) BCPs are represented with light green spheres of arbitrary radius, bond paths are shown with broken lines, and labelling is given for atoms and LCPs.

Table 4.6 Angles made by the electrophilic charge depleted LCPs with associated covalent bonds in SeCNi (i = 1,2,3).

Angles	SeCN1 (°)	SeCN2 (°)	SeCN3 (°)
C8-Se1-CP1	129.8	129.5	129.0
C7-Se1-CP2	127.9	127.8	127.0
C8-Se1-CP3	113.8	115.3	113.1
C8-Se1-CP4	121.3	122.7	121.1
C7-Se1-CP3	150.9	149.5	152.4
C7-Se1-CP4	143.4	142.1	144.4
C8-N1-CP5	179.4	179.2	179.7
C10-Se2-CP6	-	131.3	-
C9-Se2-CP7	-	130.5	-
C10-Se2-CP8	-	115.2	-
C10-Se2-CP9	-	122.7	-
C9-Se2-CP8	-	146.8	135.7
C9-Se2-CP9	-	139.3	131.5
C10-N2-CP10	-	179.3	-
C9-Se2-CP6	-	-	137.7
C1-Se2-CP7	-	-	136.4
C1-Se2-CP8	-	-	122.5
C1-Se2-CP9	-	-	126.8

Table 4.7 Topological properties at LCPs associated to Se and N atoms in SeCNi (i = 1,2,3). (* *Table continuous to the next page*)

Molecule	Name	Type	Nuclei	Distance to nucleus	ρ (r) ($eÅ^{-3}$)	L(r) ($eÅ^{-5}$)	L/ρ ($eÅ^{-2}$)
SeCN1	CP1	(3,+1)	Se1	1.25	0.34	-2.46	-7.31
	CP2	(3,+1)	Se1	1.31	0.39	-2.40	-6.12
	CP3	(3,+1)	Se1	1.06	0.43	-1.62	-3.81
	CP4	(3,-1)	Se1	0.90	0.72	-1.35	-1.89
	CP5	(3,-3)	N1	0.39	3.72	60.37	16.23
	CC1	(3,-3)	Se1	0.91	0.83	0.92	0.91
	CC2	(3,-3)	Se1	0.90	0.81	0.90	0.90
SeCN2	CP1/CP6	(3,+1)/(3,+1)	Se1/Se2	1.25/1.25	0.33/0.33	-2.44/-2.42	-7.32/-7.37
	CP2/CP7	(3,+1)/(3,+1)	Se1/Se2	1.31/1.31	0.40/0.40	-2.41/-2.47	-6.10/-6.14
	CP3/CP8	(3,+1)/(3,+1)	Se1/Se2	1.06/1.06	0.43/0.42	-1.63/-1.61	-3.81/-3.80
	CP4/CP9	(3,-1)/(3,-1)	Se1/Se2	0.90/0.90	0.72/0.73	-1.35/-1.31	-1.88/-1.81
	CP5/CP10	(3,-3)/(3,-3)	N1/N2	0.39/0.39	3.73/3.73	60.81/60.89	16.30/16.30
	CC1/CC1’	(3,-3)/(3,-3)	Se1/Se2	0.87/0.87	0.91/0.90	0.83/0.80	0.91/0.89

	CC2/CC2’	(3,-3)/(3,-3)	Se1/Se2	0.87/0.87	0.90/0.91	0.80/0.79	0.89/0.87
SeCN3	CP1/CP6	(3,+1)/(3,+1)	Se1/Se2	1.26/1.20	0.33/0.36	-2.38/-2.91	-7.24/-8.13
	CP2/CP7	(3,+1)/(3,+1)	Se1/Se2	1.32/1.24	0.40/0.36	-2.44/-2.60	-6.13/-7.22
	CP3/CP8	(3,+1)/(3,+1)	Se1/Se2	1.06/1.09	0.42/0.41	-1.61/-1.53	-3.81/-3.78
	CP4/CP9	(3,-1)/(3,-1)	Se1/Se2	0.90/0.90	0.72/0.75	-1.33/-1.10	-1.84/-1.46
	CP5/-	(3,-3)/(3,-3)	N1/N2	0.39/-	3.72/-	60.22/-	16.20/-
	CC1/CC1’	(3,-3)/(3,-3)	Se1/Se2	0.87/0.87	0.90/0.90	0.79/0.75	0.88/0.83
	CC2/CC2’	(3,-3)/(3,-3)	Se1/Se2	0.87/0.87	0.91/0.89	0.79/0.70	0.87/0.78

This small difference can be attributed to the change in the functional groups that are covalently bonded (Se-CH_3 or -CH_2-Se-CN) and the subsequent electron density distribution. Furthermore, the non-linear disposition of these charge depleted LCPs in Se-atoms are resulting to the formation of less-linear ChB interactions during the molecular assemblies (discussed below). Another interesting observation that can be made from **Figure 4.17** concerns the $\nabla^2\rho(\mathbf{r}) = 0$ surfaces in the outer valence shell of the atoms, which is defined as the *reactivity surface* of a molecule. From this reactivity surface one could point possible sites of nucleophilic attack in a molecule, which are the regions where the surface exhibit a hole. It is evident from **Figure 4.17** that, the reactivity surface of the Se-atoms is widely open and therefore a large region is available for the nucleophilic attack. In addition, charge depleted LCPs of the Se-atoms are positioned in the widely open region of the reactivity surface, allowing the nucleophiles to approach with non-linear angles with respect to the extension of covalent bonds. However, the charge concentrated regions corresponding to the lone-pairs of Se-atoms can be found within the volume closed by the $\nabla^2\rho(\mathbf{r}) = 0$ surfaces [(3,-3) CPs are embedded within the surface].

Now, considering the topological parameters at LCPs [$\rho(\mathbf{r})$, $L(\mathbf{r})$ and L/ρ] given in **Table 4.7**, it can be observed that CP1/CP6 acts as the most preferred electrophilic site in the Se-atom (CP1 in case of Se1-atoms and CP6 in case of Se2-atoms), as denoted by their more negative L/ρ values as compared to the other three CPs in each set. This is followed by CP2/CP7, CP3/CP8 and then CP4/CP9 LCPs (left entries corresponding to the Se1-atoms and right entries corresponding to the Se2-atoms). The observed trend also follows the general consideration that (3,+1) CPs act as stronger nucleophilic centers in comparison to (3,-1) CPs, because ρ(r) is depleted along two main directions for the former and along one for the latter. These results also support the σ-hole notion discussed earlier that the σ-hole observed along the extension of the Se-CN covalent is expected to show a large depletion of electron density than the one along the extension of the other covalent bond. Thus, CP1/CP6 (with higher L/ρ) corresponds to the strongest σ-hole regions while CP2/CP7 (with comparatively lower L/ρ) corresponds to the weakest σ-hole regions. Considering the values of topological parameters, LCPs of the Se-atoms belonging to the same chemical environment (Se1 of SeCN1, Se1 and Se2 of SeCN2, and Se1 of SeCN3) are exhibiting similar values, whereas a small difference is again observed with the LCPs of the Se2-atom in SeCN3. Accordingly, CP6 and CP7 belonging to Se2 of SeCN3 shows a larger depletion of electron density (L/ρ of -8.13 $Å^{-2}$ and -7.22 $Å^{-2}$ respectively) and CP9 a lower depletion of electron density (L/ρ of -1.46 $Å^2$) in comparison to their counterparts in all

other Se-atoms of all three molecules. Once again, these differences can be attributed to the change in the functional groups and subsequent electron density distribution in Se2 of SeCN3 as compared to the other Se-atoms.

Considering the case of the N-atom that is bearing the nucleophilic site, it appears that the (3,-3) LCP corresponding to its lone-pair is belongs to the valence shell charge concentration (VSCC) region. As expected from the *sp* hybridization of the N-atom, in all three molecules, this (3,-3) CP is positioned almost linear to the extension of the covalent bond with an angle ~180°. Compared to Se-atoms, larger L/ρ values can be found at the (3,-3) LCPs of N-atoms, because the lone-pair is seen in a VSCC region in case of the latter and in a VSCD in case of the former.

Further, analysis of the LCPs also extended to the gas phase optimized structures of SeCN1, SeCN2 and SeCN3 molecules (initial geometries were taken from the corresponding crystal structures). The results obtained from this analysis show very close analogies with the results obtained earlier with the monomers extracted from the crystal geometries (**Figure 4AP.26, Table 4AP.1 and Table 4AP.2**).

4.5.4.1 Analysis of ChB interactions

Following the previous discussion of the topological analysis of monomers extracted from the crystal geometries, the topology of $\rho(\mathbf{r})$ and $L(\mathbf{r})$ functions along with the 3D static deformation density maps $\Delta\rho(\mathbf{r})$ in intermolecular regions exhibiting ChB interactions will be discussed in this section. In the first part, $\Delta\rho(\mathbf{r})$ maps and the topology of $\rho(\mathbf{r})$ with its local properties determined at the (3,-1) BCPs of the ChB interactions are described. In the second part, the topological features of the $L(\mathbf{r})$ function are described to characterize quantitatively the electrostatically favoured ChB interactions through the disposition of LCPs and their associated electronic properties.

4.5.4.1.1 $\Delta\rho(\mathbf{r})$ maps and topology of $\rho(\mathbf{r})$ function

The regions of atoms involved in the ChB interactions can be identified from 3D static deformation density $\Delta\rho(\mathbf{r})$ maps generated after the multipolar modelling. Accordingly, **Figure 4.18** represents these maps drawn after TMM-4 of all three molecules, using the MoProViewer software. In case of SeCN1 and SeCN2 (**Figure 4.18a and Figure 4.18b**), $\Delta\rho(\mathbf{r})$ maps indicate the existence of Se···N ChB interactions, where δ^+ regions of the Se-atoms are facing δ^- regions

coming from the N-atoms of the neighboring molecules. In SeCN1 (**Figure 4.18a**), there are two such δ^+ regions present in the periphery of the Se-atom (*region-1* and *region-2*), each positioned approximately along the extension of a covalent bond (with non-linear disposition), representing the electrophilic σ-hole sites. *Region-1*, which corresponds to the δ^+ region observed along the extension of the Se-CN covalent bond, shows a larger iso-surface than *region-2* seen along the extension of the other covalent bond, paralleling the notion of σ-hole size discussed earlier. Both *region-1* and *region-2* of the Se-atom are electrostatically interacting with a δ^- region coming from the N-atom of the neighboring molecules, simultaneously establishing two $\delta^+\cdots\delta^-$ interactions. In *region-1*, a close and face-to-face orientation of the interacting sites can be observed, whereas in *region-2* δ^+ and δ^- regions interact in a side-on manner with a comparatively larger separation between them. Similar features are also observed in SeCN2, but with two *region-1* and *region-2* instead of only one. Their presence is due to the additional selenocyanate function group in the ortho position, thus establishing four electrostatically favored $\delta^+\cdots\delta^-$ interactions (**Figure 4.18b**).

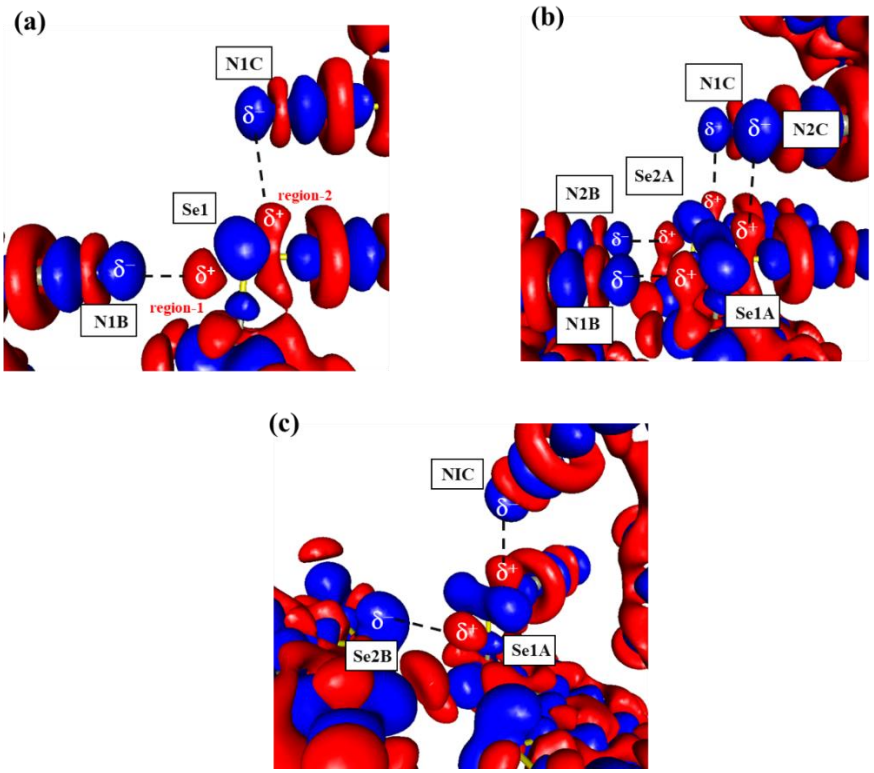

Figure 4.18 3D static deformation density map $\Delta\rho(r)$ plotted in intermolecular regions exhibiting ChB interactions: (a) SeCN1, (b) SeCN2 and (c) SeCN3. Iso-surfaces are drawn at ±0.05 eÅ^{-3} levels: blue – positive, red – negative. δ^+ and δ^- regions of the atoms involved in the ChB interactions are highlighted, with black dashed lines indicating the corresponding ChB interactions. In (a) labels are given for *region-1* and *region-2*, for (b) and (c) the labelling follows the same convention.

On the other hand, significant differences can be found in the $\Delta\rho(\mathbf{r})$ map of SeCN3, where *region-1* of the Se-atom is interacting with a δ^- region coming from other Se-atom (corresponding to its lone-pair) of a neighboring molecule, establishing a Se···Se ChB interaction. Meanwhile in *region-2*, even though the type of atoms involved in the ChB interaction are the same as those of the other two molecules, differently oriented δ^+ and δ^- regions (approximately face-to-face and relatively close to each other) are observed.

In order to quantitatively characterize and rank the above ChB interactions, topological and energetic properties determined at their (3,-1) BCPs are investigated. Accordingly, the results obtained from the topological analysis of $\rho(\mathbf{r})$ carried out in gas and crystal phases, respectively using the dimers extracted from the crystal geometries and structures obtained after multipolar modelling (with TMM-4), are given in **Table 4.8**. Considering the interactions involving *region-1* (BCP1 of SeCN1 and SeCN3, and BCP1A and BCP1B of SeCN2; **Figure 4.19**), it has been revealed that the values of the electron density ρ determined at the BCPs are very close to each other from one molecule to the other ($0.08 < \rho < 0.11$ eÅ^{-3}), with a good agreement between the results obtained from gas and crystal phase calculations. However, a relatively larger magnitude of ρ is shown by the Se···N ChB interactions in SeCN2, paralleling with the trend observed in RR values (the lower the RR the stronger is the interaction, and therefore larger is ρ at the BCP). Also, even though the type of atoms involved in ChB interactions change from SeCN1 to SeCN3 (from Se···N to Se···Se), the values of ρ determined at their BCPs exhibit an almost equivalent value. On the other hand, the values of L show a significant difference from one to the other molecule ($-0.08 < L < -0.31$ eÅ^{-5}), with SeCN2 possessing the largest negative value (and therefore a higher degree of electron depletion) followed by SeCN1 and then SeCN3. Comparing the topological properties of three compounds, larger amount of electron density at the BCP of the ChB interaction is associated with a more depleted character of the electron density (and therefore larger negative value of L). This points to the pure close-shell character of this type of interactions, as corroborated by the $|V|/G < 1$ values observed for SeCN1, SeCN2 and SeCN3. Even though, the individual L values show a small difference from gas to crystalline phase, they follow the same trend (from one molecule to the other). Further, considering the $|V|/G$ descriptor, it shows a similar value in gas and crystalline phases for all the ChB interactions.

Table 4.8 Topological and energetic properties determined at (3,-1) BCPs of ChB interactions in SeCNi (i = 1,2,3). Structural characteristics of the corresponding ChB interactions are also gathered. Values of ρ, L and $|V|/G$ obtained from gas/crystal phases are given as left/right entries. The delocalization index (DI) is just limited to the case of gas phase structures.

Molecule/ region	Interaction	d (Å)/RR	Angle (°)	Topological properties				
				BCPs	ρ (eÅ^{-3})	L(eÅ^{-5})	$\|V\|/G$	DI
SeCN1/ region-1	N1B···Se1A	3.018/0.87	169	BCP1	0.09/0.09	-1.07/-1.04	0.81/0.86	0.11
SeCN1/ region-2	N1C···Se1A	3.521/1.02	164.5	BCP2	0.03/0.04	-0.39/-0.42	0.75/0.72	0.05
SeCN2/ region-1	N1B···Se1A	2.916/0.85	172.8	BCP1A	0.11/0.11	-1.31/-1.25	0.84/0.90	0.12
	N2B···Se2A	2.921/0.85	172.9	BCP1B	0.10/0.11	-1.30/-1.24	0.84/0.89	0.12
SeCN2/ region-2	N2C···Se1A	3.637/1.05	155.4	BCP2A	0.03/0.03	-0.32/-0.35	0.74/0.70	0.04
	N1C···Se2A	3.595/1.04	135.8	BCP2B	0.03/0.04	-0.37/-0.42	0.75/0.71	0.04
SeCN3/ region-1	Se2B···Se1A	3.435/0.90	164.1	BCP1	0.08/0.09	-0.72/-0.68	0.84/0.96	0.12
SeCN3/ region-2	N1C···Se1A	3.080/0.89	166.1	BCP2	0.08/0.08	-0.93/-0.97	0.81/0.83	0.09

The delocalization index (DI) determined at the BCP of a given interaction is considered as a measure of its covalence degree. **Table 4.8** reveals that DI also shows a very similar value for all ChB interactions involving *region-1* of the Se atoms (DI values are only given for gas phase structures since VMoPro software do not output these values for the structures in crystalline phase). In short, all these features are suggesting that ChB interactions involving *region-1* of the Se-atoms are electronically very similar for all three molecules and therefore they are similarly ranked from their close values of ρ, $|V|/G$ and DI parameters.

Further, considering the second set of ChB interactions that involve the *region-2* of Se-atoms (BCP2 of SeCN1 and SeCN3, and BCP2A and BCP2B of SeCN2; **Figure 4.20**), a clear difference is observed with SeCN3 as compared to both SeCN1 and SeCN2. Thus, while all of them exhibit the same type of Se···N ChB interaction, the topological and energetic properties determined at the BCP suggest a stronger ChB interaction in case of SeCN3, as observed from the larger values of ρ, $|V|/G$ and DI parameters with respect to their counterparts in SeCN1 and SeCN2. This observation also follows the trend pointed earlier with their RR values, indicating that the ChB interaction in SeCN3 shows a significantly lower RR than in SeCN1 and SeCN2. In addition, individual values of the parameters determined here for SeCN3 are also quite close to the ones observed earlier for the ChB interaction in *region-1*, paralleling their close RR values found with the structural characterization. For the other two molecules, ChB interactions observed in *region-2* are found to be significantly weaker (exhibiting lower values of ρ, $|V|/G$ and DI parameters) than those of *region-1*.

In summary, it can be concluded that the electronic investigations carried out at the BCPs of the ChB interactions suggest a superior importance for the interactions involving the *region-1* of Se-atoms over the others involving *region-2*. This is evident for SeCN1 and SeCN2, as they show a clear difference in the values of ρ, $|V|/G$ and DI parameters determined in *region-1* and in *region-2*. In case of SeCN3, ChB interactions involving both regions of the Se-atom are however similar in terms of their topological and energetic properties, yet the interaction involving *region-1* is found slightly stronger than the other one. In addition, the conclusions derived from the electronic and energetic properties also closely follow the trend observed earlier with the structural descriptors (in terms of RR).

Investigation of the gas phase structures is also extended to trimers extracted from the crystal geometries, where the central molecule and two neighboring molecules interacting through

ChB interactions are accounted. Results obtained from trimers show very similar topological features as those of dimers discussed above (**Table 4AP.3**).

4.5.4.1.2 Topology of $L(\mathbf{r})$ function

In order to quantitatively measure the local electrostatic intensity of the above ChB interactions, the spatial orientation and the electronic properties of the LCPs associated to the interacting atoms were explored. As mentioned earlier, due to some technical reasons, the topological analysis of the $L(\mathbf{r})$ function is limited to gas phase structures, extracted from the crystal geometries and subjected to SPE calculation. Following the previous discussion with the monomers, the topological features of the $L(\mathbf{r})$ function in dimers and trimers extracted from the crystal geometries and connected by the ChB interactions are discussed in this section. In such a way, a partial effect of the crystalline environment on the geometrical arrangement of the LCPs that are involved in the ChB interactions are investigated in this analysis.

At first, the case of molecular dimers connected by the ChB interactions involving *region-1* of the Se-atoms are described. For all three molecules, a similar spatial disposition of the LCPs in the VSCD region of the Se-atoms can be observed, which is also consistent with the topology observed earlier with the monomers (**Figure 4.19 and 4.20**). This is also found in the case of the charge concentrated (3,-3) LCP corresponding to the lone-pair of N belonging to the CN group, being positioned almost linearly to the extension of the covalent in the VSCC region of the N-atom in the dimers of the three derivatives as in monomers (**Figure 4.19 and 4.20**). Therefore, these features indicate that the effect of the crystalline environment (at least partial), resulting from the presence of neighboring molecules, does not cause any spatial re-agreement of the LCPs that are involved in the ChB interactions in comparison to the case of monomers. Further, as discussed in **section 2.1.1.4.2**, local nucleophilic···electrophilic ChB interactions are alternatively studied as the interaction between CC and CD sites found in the respective nucleophilic and electrophilic regions. For dimers involving *region-1*, three CD sites can be spotted in the VSCD region of the Se-atoms, acting as potential electrophilic sites (**Figure 4.19**). Out of those, two are of (3,+1) and the other is of (3,-1) type [one (3,+1) LCP is observed close to the Se-C_{sp3} BCP and other two LCPs are found close to the perpendicular plane bisecting the R-Se-R' angle]. With both SeCN1 and SeCN2, the (3,-3) LCP located in the VSCC region of the N-atom is acting as the closer nucleophilic site that interacts with the CD sites of the Se-atom to establish Se···N ChB interaction (**Figure 4.19a, b and c**). On the other hand, with SeCN3, it is the lone-pair of the other Se-atom (correspondingly to the Se-CH_3

group) that is interacting with the CD sites of the Se found in *region-1* (**Figure 4.19d**). Simultaneously, the electrostatic intensity of an individual CC···CD interaction has been evaluated by using the descriptor $\Delta(L/\rho)$ [$\Delta(L/\rho) = (L/\rho)_{CC} - (L/\rho)_{CD}$], where the normalized magnitudes of $(L/\rho)_{CC}$ and $(L/\rho)_{CD}$ measure the nucleophilic and electrophilic power per charge density unit of the CC and CD sites. Among the observed ChB interactions, the magnitude of $\Delta(L/\rho)$ vary in the range $2.27 < \Delta(L/\rho) < 23.98$ Å^{-2} (**Table 4.9**). For SeCN1, the larger value of $\Delta(L/\rho)$ is correspond to the CP5b···CP1a interaction (23.66 Å^{-2}), followed by CP5b···CP3a (19.79 Å^{-2}) and then CP5b···CP4a (17.85 Å^{-2}) interactions. Another important parameter that merits attention is the distance between interacting CC and CD sites, denoted as $d_{CC\cdots CD}$. Among the three CC···CD interactions of SeCN1, CP5b···CP1a is showing the shortest distance (1.97 Å), indicating that more powerful nucleophilic···electrophilic interaction leads to a shorter CC···CD separation, and therefore it is considered to be the stronger driving force for the formation of that particular ChB dimer. Altogether, in order to analyze the effective intensity of these CC···CD interactions a modified electrostatic descriptor $(\Delta L/\rho)/d^2_{CC\cdots CD}$ is introduced, which increases with the electrophilic and nucleophilic power of the interacting sites and with a shorter geometrical distance between them. Accordingly, the CP5b···CP1a interaction, which exhibits the largest $\Delta(L/\rho)$ magnitude and the shortest $d_{CC\cdots CD}$, possess the largest $(\Delta L/\rho)/d^2_{CC\cdots CD}$ local nucleophilic···electrophilic intensity (6.10 Å^{-4}) in SeCN1. For the other two interactions, CP5b···CP3a exhibits a larger $d_{CC\cdots CD}$ (2.59 Å) than CP5b···CP4a (2.45 Å), yet a comparatively larger $\Delta(L/\rho)$ magnitude for the former results to a very similar $(\Delta L/\rho)/d^2_{CC\cdots CD}$ magnitude in both cases. Another interesting observation is the possible link between the geometrical arrangement of the LCPs and the structurally characterized ChB angle that deviates from 180^o (169^o in case of SeCN1). It can be argued from this analysis that, a possible reason for this deviation of the ChB angle could be the enhanced CP5b···CP1a interaction over the other two CC···CD interactions. This means a shorter and stronger CP5b···CP1a interaction demands the geometrical position of the N to be below the direction along the extension of the Se-CN covalent bond. Another reason deduced for the geometrical positioning of N is the presence of C-H···N HB interaction within the same dimer, where N is also acting as the HB acceptor (**Figure 4.19a**). This bifurcated character of the N again prefers it to be placed below the extension of the Se-CN covalent bond, so that both interactions could co-exist at the same time. In the C-H···N HB interaction, the (3,-3) LCP of N is interacting with a (3,+1) LCP of H (**Figure 4.19a and Table4AP.4**).

Table 4.9 Structural and topological characteristics of the ChB interactions obtained for dimers extracted from the crystal geometries of SeCNi (i = 1,2,3). α is the angle between atom (ChB acceptor)···atom (ChB donor) and CC···CD directions, except for the CD sites positioned closer to the BCPs of Se-C covalent bonds (CP1, CP2, CP6 and CP7) where α is calculated between atom (ChB acceptor)···BCP and CC···CD directions. $d_{CC\cdots CD}$ corresponds to the distance between CC and CD sites. CC···CD interactions corresponding to Figure 4.19e (see text) are highlighted in red colour. (* *Table continues to the next page*)**

Molecule/ region	Interaction	d (Å)/RR	Angle (°)	LCPs						
				CC···CD	$(L/\rho)_{CC}$ (Å^{-2})	$(L/\rho)_{CD}$ (Å^{-2})	$\Delta(L/\rho)$ (Å^{-2})	$d_{CC\cdots CD}$ (Å)	$\Delta(L/\rho)/d_{CC\cdots CD}^2$ (Å^{-4})	α (°)
SeCN1/ region-1	N1B···Se1A	3.018/0.87	169	CP5b···CP1a	16.00	-7.66	23.66	1.97	6.10	7.3
				CP5b···CP3a	16.00	-3.79	19.79	2.59	2.95	23.9
				CP5b···CP4a	16.00	-1.85	17.85	2.45	2.97	20.6
SeCN1/ region-2	N1C···Se1A	3.521/1.02	164.5	CP5c···CP2a	16.08	-6.24	22.31	2.81	2.83	13.2
				CP5c···CP3a	16.08	-4.00	20.08	2.68	2.80	8.1
				CP5c···CP4a	16.08	-2.00	18.07	2.84	2.24	6.6
SeCN2/ region-1	N1B···Se1A	2.916/0.85	172.8	CP5b···CP1a	16.07	-7.80	23.87	1.83	7.13	7.2
				CP5b···CP3a	16.07	-3.77	19.85	2.52	3.13	25.1
				CP5b···CP4a	16.07	-1.81	17.89	2.36	3.21	21.7
	N2B···Se2A	2.921/0.85	172.9	CP10b···CP6a	16.10	-7.88	23.98	1.8	7.40	7.0
				CP10b···CP8a	16.10	-3.76	19.86	2.53	3.10	24.9
				CP10b···CP9a	16.10	-1.73	17.83	2.37	3.17	21.5
SeCN2/ region-2	N2C···Se1A	3.637/1.05	155.4	CP10c···CP2a	16.15	-6.22	22.36	2.93	2.60	13.1
				CP10c···CP3a	16.15	-4.03	20.18	2.9	2.40	10.0
				CP10c···CP4a	16.15	-1.99	18.14	3.03	1.98	7.8

	N1C···Se2A	3.595/1.04	135.8	CP5c···CP7a	16.11	-6.21	22.31	3.09	2.34	14.7
				CP5c···CP8a	16.11	-3.91	20.02	3.02	2.19	13.4
				CP5c···CP9a	16.11	-1.83	17.94	3.14	1.82	10.5
SeCN3/ region-1	Se2B···Se1A	3.435/0.90	164.1	CC1'B···CP1a	0.79	-7.32	8.10	2.58	1.22	20.2
				CC1'B···CP3a	0.79	-3.84	4.62	2.55	0.71	9.2
				CC1'B···CP4a	0.79	-1.93	2.72	2.45	0.45	5.0
				CC2'B···CP1a	0.84	-7.32	8.16	2.78	1.06	15.0
				CC1A···CP7B	0.92	-7.27	8.19	2.57	1.24	14.7
				CC2A···CP8B	0.89	-3.72	4.60	2.75	0.61	15.8
				CC2A···CP9B	0.89	-1.39	2.27	2.92	0.27	12.5
SeCN3/ region-2	N1C···Se1A	3.080/0.89	166.1	CP5c···CP2a	16.05	-6.51	22.56	1.96	5.87	9.2
				CP5c···CP3a	16.05	-4.07	20.12	2.41	3.46	23.7
				CP5c···CP4a	16.05	-1.96	18.00	2.43	3.05	19.9

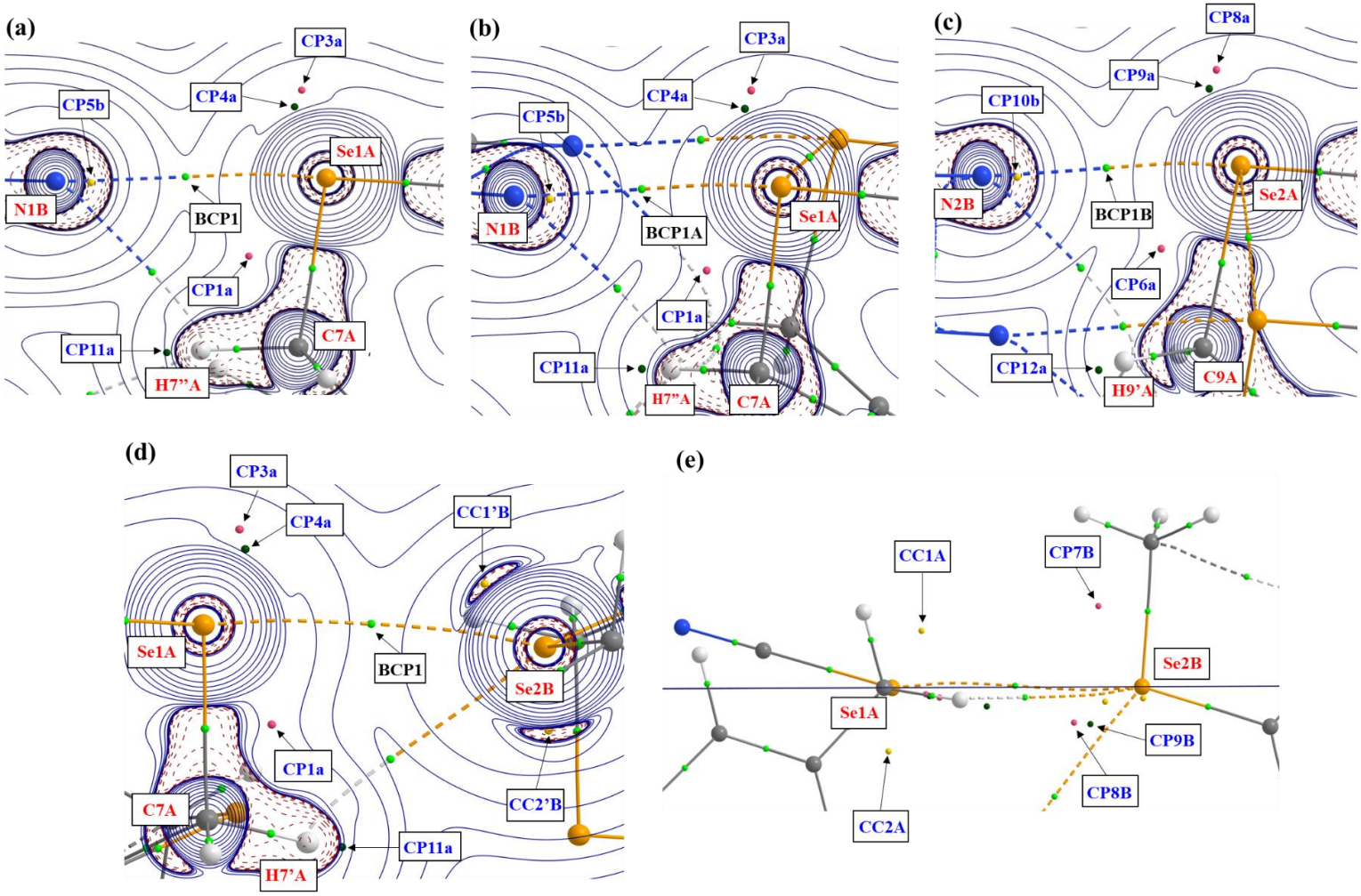

Figure 4.19 Charge concentration (CC) and charge depletion (CD) LCPs [(3,-3) in yellow, (3,+1) in pink and (3,-1) in green coloured spheres] participating in the ChB interactions involving *region-1* of the Se-atoms in (a) SeCN1, (b)-(c) SeCN2 and (d)-(e) SeCN3. Labels are given for the atoms, LCPs and the intermolecular bond critical points (BCPs, light green spheres) corresponding to the ChB interactions of interest (discussed in section 4.5.4.1.1). Intermolecular bond paths are shown with dashed lines.

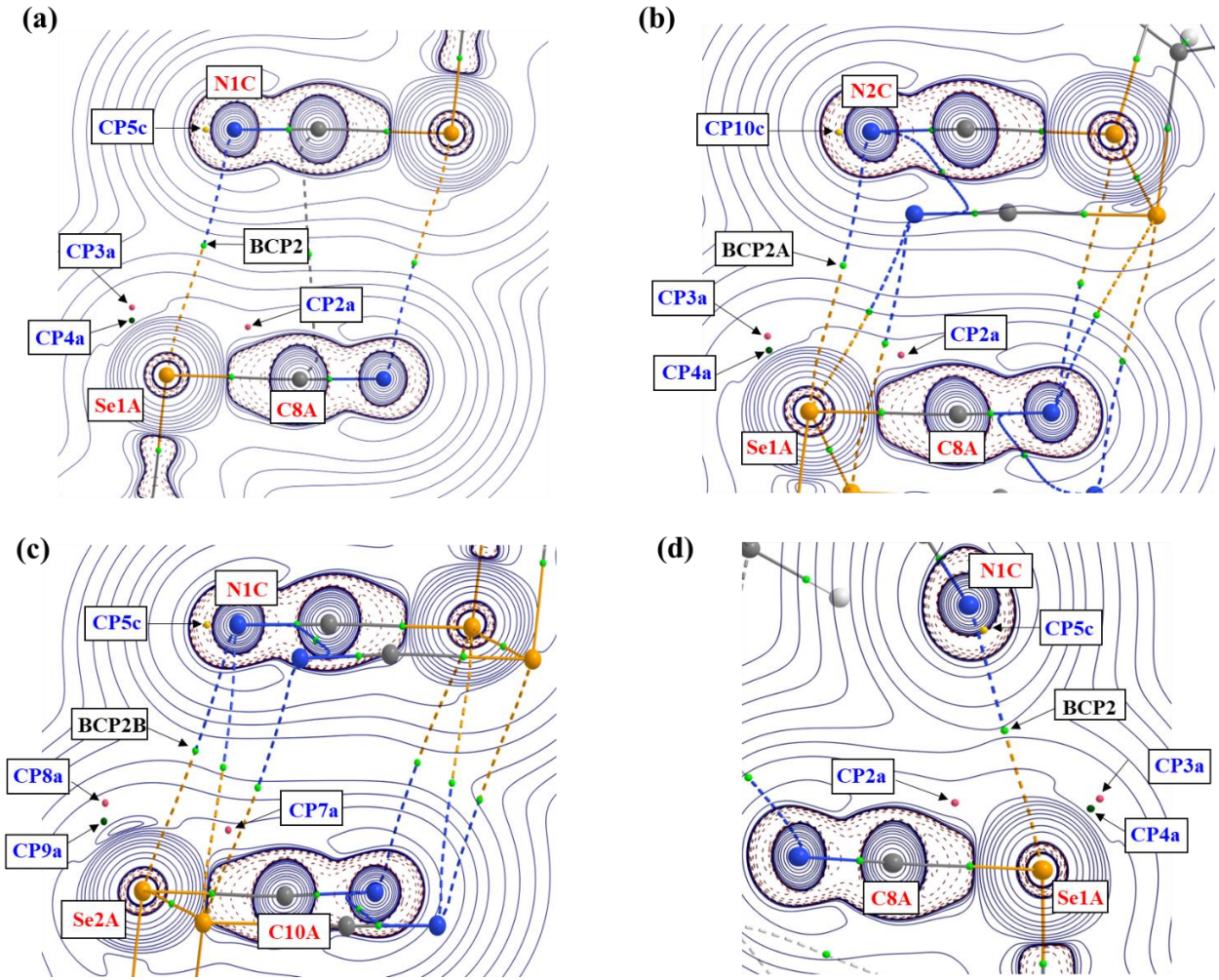

Figure 4.20 Charge concentration (CC) and charge depletion (CD) LCPs [(3,-3) in yellow, (3,+1) in pink and (3,-1) in green coloured spheres] participating in the ChB interactions involving *region-2* of the Se-atoms in (a) SeCN1, (b)-(c) SeCN2 and (d) SeCN3. Labels are given for the atoms, LCPs and the intermolecular bond critical points (BCPs, light green spheres) corresponding to the ChB interactions of interest (discussed in section 4.5.4.1.1). Intermolecular bond paths are shown with dashed lines.

As per previous reports (Brezgunova *et al.*, 2012; Brezgunova *et al.*, 2013; Shukla *et al.*, 2020), stronger nucleophilic···electrophilic interactions [$\Delta(L/\rho) > \sim 5$ Å^{-2}] leads to a low magnitude of the angle α [which is defined as the angle between CC···CD and atom···atom (or sometimes atom···BCP) directions], typically less than 15°. This trend is also found in our case, since the CP5b···CP1a interaction exhibits an angle α considerably less than 15° (7.3°), whereas for the other two interactions it is above 20°. This low magnitude of α also points to CC···CD interactions that are responsible for the geometrical preferences in molecular assemblies, due to their ability to reflect the relative orientation of the atoms (and therefore of their functional groups) in the intermolecular interactions (ChB interactions here). Accordingly, in this dimer, the CP5b···CP1a interaction is the one that mainly drives the geometrical positioning of interacting Se and N atoms (and of SeCN groups per extension).

In SeCN2, there are two such *region-1,* namely *region-1A* and *region-1B* that are respectively associated to Se1 and Se2 atoms. Similar CC···CD interactions than those found in SeCN1 are also observed here in both of these regions, with comparatively larger $(\Delta L/\rho)/d^2_{CC\cdots CD}$ magnitudes (**Figure 4.19b, c, Table 4.9 and Table4AP.4**). These larger magnitudes suggest stronger Se···N ChB interactions in the case of SeCN2 as compared to SeCN1. Hence, these electronic descriptors parallel the earlier observation made during the structural analysis with the RR values of the Se···N ChB interactions in SeCN2, which are found lower than for their counterpart in SeCN1. Also, CP5b···CP1a and CP10b···CP6a interactions in SeCN2 show α values that are significantly less than 15° (7.2 ° and 7 ° respectively), being therefore considered as the CC···CD interactions that are directing the geometrical preferences in the molecular assembly.

As observed from the structural characterization, ChB interactions involving *region-1* of the Se-atom in SeCN3 are differently formed, exhibiting a Se···Se ChB interaction. Here, the lone-pairs of the Se-atom belonging to the Se-CH_3 group are interacting with the CD sites of the Se-atom in *region-1*, with lower $\Delta(L/\rho)$ and $(\Delta L/\rho)/d^2_{CC\cdots CD}$ magnitudes for all those CC···CD interactions in comparison to the previous two molecules (**Figure 4.19d and Table 4.9**). The low magnitudes of $\Delta(L/\rho)$ in SeCN3 are actually linked to the low $(L/\rho)_{CC}$ values (and therefore to the low nucleophilic power) that correspond to the Se lone-pairs, which are more diffused in nature in comparison to the lone-pair of the N-atom. From **Figure 4.19e**, it is also observed that the Se1A atom (namely, the Se-atom providing the CD sites in **Figure 4.19d**) can also act as a ChB acceptor, whose lone-pairs interact with the CD sites of the Se2B atom (namely, the

Se-atom providing the CC sites in **Figure 4.19d**). These interactions are shown with red color in **Table 4.9**. Therefore, in this ChB dimer both Se-atoms can simultaneously act as ChB donor and acceptor to each other. However, it should be pointed out that the CC···CD interactions showing the largest $(\Delta L/\rho)/d^2_{CC\cdots CD}$ magnitudes (CC1'B···CP1a and CC1A···CP7B) exhibit α angles close to or above 15°, indicating that these CC···CD interactions have minor roles in directing the geometrical preferences of atoms in the molecular assembly. This is also supported by the observation made earlier during the intermolecular interaction energy analysis, revealing that this dimer of SeCN3 is positioned 4th in the ranking, with a significantly lower E_tot value (-13.6 kJ/mol) in comparison to the dimers of the other two molecules (E_tot = -25.8 and -54.5 kJ/mol, respectively for SeCN1 and SeCN2), indicating a lesser significance in the construction of the SeCN3 crystal packing.

While exploring the ChB interactions that are involving *region-2* of the Se-atoms, three potential electrophilic CD sites can be found again in the VSCD region of the Se-atoms: one (3,+1) LCP close to the other Se-C$_{sp}$ BCP, and the same (3,+1) and (3,-1) LCPs found close to the perpendicular plane bisecting the R-Se-R' angle (**Figure 4.20**). For all three molecules, one (3,-3) LCP that is found in the VSCC region of the N-atom acts as a potential nucleophilic site, establishing Se···N ChB interactions. Among the three molecules, $\Delta(L/\rho)$ magnitude varies in the range $17.94 < \Delta(L/\rho) < 22.56$ Å^{-2} (**Table 4.9**). For SeCN1 and SeCN2, even though all the CC···CD interactions show α angles less than 15°, their $(\Delta L/\rho)/d^2_{CC\cdots CD}$ magnitudes are found to be < 3 Å^{-4}, indicating a low intensity for these nucleophilic···electrophilic interactions. This feature also parallels the RR values > 1 determined for these Se···N ChB interactions involving *region-2*. On the other hand, the case of SeCN3 is again different, indeed its CP5c···CP2a interaction shows a $(\Delta L/\rho)/d^2_{CC\cdots CD}$ magnitude of 5.87 Å^{-4} while for the other two interactions (CP5c···CP3a and CP5c···CP4a) it is above 3 Å^{-4}. In comparison to the other two molecules, these larger intensities of local nucleophilic···electrophilic (CC···CD) interactions in SeCN3 can be attributed to their short $d_{CC\cdots CD}$ distances, which are arising due to differently oriented ChB acceptor [the N-atom and its associated (3,-3) charge concentrated LCP], as observed earlier from the crystal packing and MESP analyses. Furthermore, this CP5c···CP2a interaction also exhibits an angle α of less than 15° (9.2°), indicating its importance in driving the relative orientation of atoms in the corresponding ChB interaction. These relatively significant intensities of CC···CD interactions in SeCN3 also parallel the lower RR value of the Se···N ChB interaction in comparison to SeCN1 and SeCN2.

Further, investigation of LCPs was extended to trimers extracted from the crystal geometries, the obtained results indicating that trimers exhibit almost the same topological features as those with the dimers (refer to **Table 4AP.5** for further details).

In conclusion, the local nucleophilic···electrophilic intensity of individual ChB interactions has been studied *via* the interaction between CC and CD sites found in the valence-shell of acceptor and donor atoms. Accordingly, the intensity of individual CC···CD interactions was estimated using an electronic descriptor $\Delta(L/\rho)/d_{CC\cdots CD}^2$, which along with the angle α, point most significant CC···CD interactions in driving the relative orientation of the interacting atoms in ChB interactions. For SeCN1 and SeCN2, CC···CD interactions involving *region-1* of the Se-atoms show larger values of $(\Delta L/\rho)/d^2_{CC\cdots CD}$ (and therefore a stronger local nucleophilic···electrophilic intensity) as compared to the ones in *region-2* of the Se-atom. In addition, the CC···CD interactions that show the largest intensity in *region-1* also exhibit lower α values (~7°). Therefore, with SeCN1 and SeCN2, it is concluded that ChB interactions involving *region-1* are more significant in the molecular assemblies than those involving *region-2*. This trend parallels the conclusion made earlier from their RR values. On the other hand, the case of SeCN3 is different, showing larger values of $(\Delta L/\rho)/d^2_{CC\cdots CD}$ for the CC···CD interactions involving *region-2*. One reason invoked for this difference is the involvement of the Se lone-pairs as ChB acceptor sites in *region-1*, which are more diffused in their electron density [and therefore lower $(L/\rho)_{CC}$ magnitudes] than those of the N-atom. Additionally, another reason that can be pointed out for this difference is the differently oriented ChB acceptor atom N [with its (3,-3) LCP] in *region-2*, which leads to a shorter $d_{CC\cdots CD}$ in SeCN3 in comparison to the other two molecules.

4.6 Summary

In this study, both structural and electronic characteristics of the ChB interactions found in the solid-state assemblies of three benzyl selenocyanate derivatives [benzyl selenocyanate (SeCN1), ortho-bis(selenocyanatomethyl) benzene (SeCN2) and 2-(methylselanyl) benzyl selenocyanate (SeCN3)] are explored. Multipolar modelling of the data derived from HR-SCXRD experiments and subsequent crystal structure analysis revealed differently formed ChB interactions in SeCN3 in comparison to the other two molecules. Accordingly, crystal structures of SeCN1 and SeCN2 exhibit 1D chain-like motifs directed by strong and linear Se···N ChB interactions, whereas a discrete centrosymmetric dimer formed *via* strong and less linear Se···Se ChB interactions is found in the crystal packing of SeCN3. All these interactions

are involving the strongest σ-hole belonging to the Se-atom. A clear difference between these three molecules is also shown by their ChB interactions involving the weakest σ-hole of the Se-atom, leading to weak and less linear ChB interactions for SeCN1 and SeCN2 while SeCN3 shows strong and moderately linear Se···N ChB interactions.

The importance of the above ChB interactions in the crystal packing of the respective molecules has been established *via* intermolecular interaction energy analysis, by calculating the E_tot magnitudes for the ChB dimers. A clear difference of the ChB interactions is found in SeCN3, in comparison to SeCN1 and SeCN2, was also revealed by the intermolecular interaction energy analysis. This has been further supported by the enrichment ratio analysis. In order to quantitatively estimate the intensity of these ChB interactions, it has been carried out the investigation of the MESP surfaces and topological descriptors of the $\rho(\mathbf{r})$ and $L(\mathbf{r})$ functions. The disposition of $V_{s,\,max}$ and $V_{s,\,min}$ points of the MESP function in the molecular surface of SeCN3 is very different in comparison to the other two molecules, supporting the difference observed earlier from the structural analysis. Further, the strength of these ChB interactions has been analysed *via* the local topological and energetic properties determined at their (3,-1) BCPs. The results obtained here follow the same trends as pointed earlier from the structural analysis. Also, the ratio $|V|/G < 1$ determined at the BCPs has revealed that these ChB interactions belong to the category of pure closed-shell interaction with weak strength. Later, the intensity of the local nucleophilic···electrophilic ChB interactions has been estimated from the topological analysis of the $L(\mathbf{r})$ function and its associated CPs. The electrostatic descriptors $(\Delta L/\rho)/d^2_{CC\cdots CD}$ and angle α are used to identify the most significant CC···CD interactions, leading the geometrical preferences of the interacting atoms in the ChB interaction. For SeCN1 and SeCN2, CC···CD interactions involving region-*1* of the Se-atoms (that is, involving the strongest σ-hole) exhibit larger values of $(\Delta L/\rho)/d^2_{CC\cdots CD}$ and lower values of α than those observed when involving *region-2*, marking their pronounced importance in the geometrical arrangements of atoms in the molecular assemblies. Meanwhile, an opposite trend is observed with SeCN3, mainly due to a different ChB acceptor atom in *region-1* and to a differently oriented ChB acceptor atom in *region-2*. These results characterized from the electronic analysis of the LCPs also closely follow the conclusions derived earlier from the structural and the energetic analyses.

References

Blessing, R.H. (1986). J. Appl. Cryst. 19, 412.

Brezgunova, M. E., Aubert, E., Dahaoui, S., Fertey, P., Lebègue, S., Jelsch, C., Ángyán, J. G. and Espinosa, E. (2012). Crystal Growth & Design, 12 (11), 5373–5386.

Brezgunova, M. E., Lieffrig, J., Aubert, E., Dahaoui, S., Fertey, P., Lebègue, S., Ángyán, J. G., Fourmigué, M. and Espinosa, E. (2013). Cryst. Growth Des. 13, 3283–3289.

Bruker (2019). APEX3 v2019.11. Bruker AXS Inc., Madison, Wisconsin, USA.

Dennington, R., Keith, T. A. and Millam, J. M. (2016). GaussView, Version 5.0.9, Semichem Inc., Shawnee Mission, KS.

Dolomanov, O.V., Bourhis, L.J., Gildea, R.J., Howard, J.A.K. and Puschmann, H. (2009). J Appl Crystallogr. 42, 339-341.

Dovesi, R., Orlando, R., Civalleri, B., Roetti, C., Saunders, V. R. and Zicovich-Wilson, C. M. (2005). Z. Für Krist. - Cryst. Mater. 220, 571–573.

Farrugia L. J. WinGX (Version 1.80.05). J. Appl. Crystallogr. 1999, 32, 837-838.

Fourmigué, M. and Dhaka, A. (2020). Coord. Chem. Rev. 403, 213084.

Frisch, M.J., Trucks, G.W., Schlegel, H.B., Scuseria, G.E., Robb, M.A., Cheeseman, J.R., Scalmani, G., Barone, V., Mennucci, B., Petersson, G.A., Nakatsuji, H., Caricato, M., Li, X., Hratchian, H.P., Izmaylov, A.F., Bloino, J., Zheng, G., Sonnenberg, J.L., Hada, M., Ehara, M., Toyota, K., Fukuda, R., Hasegawa, J., Ishida, M., Nakajima, T., Honda, Y., Kitao, O., Nakai, H., Vreven, T., Montgomery, J.A., Jr., Peralta, J.E., Ogliaro, F., Bearpark, M., Heyd, J.J., Brothers, E., Kudin, K.N., Staroverov, V.N.. Keith, T., Kobayashi, R., Normand, J., Raghavachari, K., Rendell, A., Burant, J.C., Iyengar, S.S., Tomasi, J., Cossi, M., Rega, N., Millam, J.M., Klene, M., Knox, J.E., Cross, J.B., Bakken, V., Adamo, C., Jaramillo, J., Gomperts, R., Stratmann, R.E., Yazyev, O.A., Austin, J., Cammi, R., Pomelli, C., Ochterski, J.W., Martin, R.L., Morokuma, K., Zakrzewski, V.G., Voth, G.A., Salvador, P., Dannenberg, J.J., Dapprich, S., Daniels, A.D., Farkas, O., Foresman, J.B., Ortiz, J.V., Cioslowski, J. and Fox, D.J. (2013). Gaussian 09, Revision D.01, Gaussian, Inc., Wallingford CT.

Grimme, S., Antony, J., Ehrlich, S. and Krieg, H. (2010). J. Chem. Phys. 132, 154104.

Guillot, B., Jelsch, C. and Macchi, P. (2021). In Complementary Bonding Analysis; Grabowsky, S., Ed., De Gruyter, 2021. pp 235–268.

Huynh, H.-T., Jeannin, O. and Fourmigué, M. (2017). Chem. Commun. 53, 8467–8469.

Jeannin, O., Huynh, H.-T., Riel, A. M. S. and Fourmigué, M. (2018). New J. Chem. 42, 10502–10509.

Jelsch, C., Ejsmont, K. and Huder, L. (2014). IUCrJ, 1 (2), 119–128.

Jelsch C., Guillot B., Lagoutte A., Lecomte C. J. (2005). Appl. Crystallogr. 38, 38-54.

Keith, T. A. AIMAll (Version 19.10.12), TK Gristmill Software, Overland Park KS, USA, (2019).

Lari, A., Bleiholder, C., Rominger, F. and Gleiter, R. (2009a). Eur. J. Org. Chem. 17, 2765–2774.

Lari, A., Gleiter, R. and Rominger, F. (2009b). Eur. J. Org. Chem. 14, 2267–2274.

Lu, T. and Chen, F. (2012). J. Comput. Chem., 33 (5), 580–592.

Maartmann-Moe, K., Sanderud, K. A. and Songstad, J. (1984) Acta Chemica Scandinavica, 38, 187.

Madsen, A. Ø. (2006). J. Appl. Crystallogr. 39, 757–758.

McWhinnie, S. L. W., Brooks, A. B. and Abrahams, I. (1998). Acta Cryst. C54, 126-128.

Nasim, M. J., Witek, K., Kincses, A., Abdin, A. Y., Żesławska, E., Marć, M. A., Gajdács, M., Spengler, G., Nitek, W., Latacz, G., Karczewska, E., Kieć-Kononowicz, K., Handzlik, J. and Jacob, C. (2019). New J. Chem. 43, 6021–6031.

Rigaku Oxford Diffraction (2020). CrysAlis PRO, Rigaku Corporation, Tokyo, Japan.

Sheldrick, G.M. (2015a). Acta Cryst. A71, 3-8.

Sheldrick, G. M. (2008). Acta Cryst. A64, 112-122.

Sheldrick, G.M. (2015b). Acta Cryst. C71, 3–8.

Shukla, R., Dhaka, A., Aubert, E., Vijayakumar-Syamala, V., Jeannin, O., Fourmigué, M. and Espinosa, E. (2020). Crystal Growth & Design 2020, 20 (12), 7704–7725.

Spackman, P. R., Turner, M. J., McKinnon, J. J., Wolff, S. K., Grimwood, D. J., Jayatilaka, D. and Spackman, M. A. (2021). J. Appl. Crystallogr. 2021, 54 (3), 1006–1011.

Turner, M. J., Grabowsky, S., Jayatilaka, D. and Spackman, M. A. (2014). J. Phys. Chem. Lett., 5 (24), 4249–4255.

Turner, M.J., McKinnon, J.J., Wolff, S.K., Grimwood, D.J., Spackman, P.R., Jayatilaka D. and Spackman, M.A. (2017). CrystalExplorer17. University of Western Australia.

5

General conclusions and future perspectives

5.1 General conclusion

Understanding the fundamentals of the formation and stabilization of non-covalent interactions is of paramount importance in the field of crystal engineering. With this respect, in this thesis we have studied a sub-class of non-covalent interactions known as σ-hole interactions. σ-hole interactions are defined as those involving electrophilic sites (also called σ-holes) associated to a covalently bonded atom belonging to either *p*-block (groups 13-18) or d-block (groups 8,11 and 12) of the periodic table, and nucleophilic sites coming from either the same or a different molecule. Depending upon the group of the atom on which the σ-hole is present, the interaction can be further classified into various sub-classes. Out of these, we have given emphasis to the case studies of halogen bond (HaB) and chalcogen bond (ChB) interactions. Considering the fact that the rationale behind the formation and stabilization of HaB and ChB are less explored in comparison to the well-known case of HB, a strong attempt is made throughout this thesis to gather a deeper insight into the structural, energetic and electronic characteristics of HaB and ChB interactions. For this purpose, a series of SCXRD experiments were carried out either at standard ambient conditions of temperature and pressure, low-temperature (100K) or high-pressure generated within a Membrane Diamond Anvil Cell (MDAC). The so-obtained crystal structures were used to derive the electron density distribution in the periodic crystalline phases. Then, the electron distributions of the molecular systems extracted from their crystalline environments were used to calculate the electrostatic potential in molecular surfaces and to carry out the topological analyses of the electron density and its laplacian function within the framework of the Quantum Theory of Atoms in Molecules (QTAIM) methodology. Apart from the understanding of individual interactions, a strong focus has also been given to explore the effect of crystalline environment (role of neighboring secondary non-covalent interactions) in the tuning the properties of σ-hole interactions.

This thesis has mainly covered two mainstream topics of crystallography: (i) high-pressure X-ray diffraction and (ii) charge density analysis. Structural and electronic investigations were undertaken based on data derived from single-crystal X-ray diffraction (SCXRD) experiments carried out either at ambient or extreme conditions. The energetic analysis of intermolecular interactions was conducted in order to dictate the significance of σ-hole interactions in the crystal packing of respective molecules. During the structural investigations, σ-hole interactions were rationalized using the reduction ratio (RR) descriptor and the interatomic interaction angle parameter. On the other hand, the electronic investigations were performed

within the framework of the QTAIM methodology, in order to obtain the partition of the total molecular electron density among individual atoms. Later, the electron density distribution of atoms involved in the σ-hole interactions were analyzed, in particular how their charge concentration (CC) and charge depletion (CD) sites in the valence-shell are placed with respect to each other in case of nucleophilic···electrophilic interactions. The strength of individual interactions was estimated based on the local topological and energetic properties of $\rho(\mathbf{r})$ determined at their (3,-1) BCPs. This also allowed to rank these interactions based on their significance in the constitution of the overall crystal packing. Further, in the case of ChB interactions the electrostatic intensity of local nucleophilic···electrophilic interactions was estimated using $(\Delta L/\rho)/d^2_{CC\cdots CD}$ and α descriptors, derived from the topological analysis of the $L(\mathbf{r})$ function and its associated critical points.

In chapter 3, the evolution of HaB interactions was investigated in molecular crystals under the application of external pressure ranging from 0-5 GPa, generated with a MDAC. Two donor-acceptor co-crystals, composed of NISac as HaB donor and a derivative of pyridine (Py or 4CYP) as HaB acceptor, exhibiting strong $N_{donor}\cdots I\cdots N_{acceptor}$ HaB motif was chosen for this purpose. A series of HP-SCXRD experiments were carried out in order to structurally and electronically characterize the modifications in HaB interactions. At ambient conditions, both co-crystals revealed a neutral co-crystal form of the binary adduct, where I-atom is bound close and stronger to the donor, but with a significant covalent degree at both donor and acceptor sides. This last feature suggests that individual $N_{donor}\cdots I$ and $I\cdots N_{acceptor}$ HaBs are not very different from each other. The results obtained from HP-SCXRD experiments pointed that in both co-crystals the I-atom, initially found closer to the donor, starts its migration towards the acceptor on increasing pressure. This is also observed from theoretical calculations of periodic phases at high-pressure and the electronic properties determined at $N_{donor}\cdots I$ and $I\cdots N_{acceptor}$ BCPs. In such a way, this study reveals that the structural and electronic characteristics of the HaB interactions in a molecular crystal can be effectively modified by applying pressure as an external stimulus. But unfortunately, in both structural and electronic analyses, the different electronic environment of N_{donor} and $N_{acceptor}$ atoms remains as a main hindrance in concluding the exact state of the system (neutral *vs* ionic) at high-pressure. However, considering the uncertainties of HaB distances and the values of the topological properties, it is concluded that both adducts at high-pressure should be considered more as a single molecular unit rather than two separate entities. Interestingly, crystal structures of both binary adducts show a reversible recovery upon the decompression process, which also permits the reversibility in the position

of I-atom within the adduct, endorsing the possibility of a reversible halogen shift in these donor-acceptor complexes. These variations in the halogen atom position are also found to be partially driven by secondary non-covalent interactions, marking the importance of neighboring crystalline environment. However, the shift of the halogen atom in the studied binary adducts is not sufficiently pronounced to conclude about the state of system at high-pressure. With this respect, it should be kept in mind that interatomic distances within the $N_{donor}\cdots I\cdots N_{acceptor}$ HaB motif are difficult to characterize accurately using the experimental data. In such a situation, DFT periodic calculations performed by applying isotropic external pressures can be used as a complementary tool, considering a good geometrical agreement between the theoretically calculated and the experimentally determined crystal structures. It has been shown previously that, in these donor-acceptor co-crystals the position of the halogen atom can be can modulated by modifying the electronic properties of the constituents, however, this study reveals that the same purpose can also be achieved through applying pressure as an external constraint. Also, in these complexes one can expect to drive the electronic properties of the solid in a switch on/off manner upon increasing/decreasing pressure (or with any other external stimuli), playing with the reversible modification of the halogen atom position as well as the crystalline environment.

In chapter 4, the characteristics of Se···N and/or Se···Se ChB interactions that are responsible for the molecular organization of benzyl selenocyanate derivatives in solid-state were explored. Investigations were carried out with three different derivatives of benzyl selenocyanate family, (1) benzyl selenocyanate (SeCN1), (2) ortho-bis(selenocyanatomethyl) benzene (SeCN2) and 2-(methylselanyl) benzyl selenocyanate (SeCN3). The crystal structures of SeCN1 and SeCN2 exhibit a 1D chain-like topology directed by the formation of recurrent ···NC(R)Se···NC(R)Se···NC(R)Se··· ChB interactions. Meanwhile, in SeCN3, an additional Lewis base in the form of the Se lone-pair belonging to the –(R)Se-CH_3 group results to the formation of two strong ChB motifs in the crystal structure: (R)Se···Se and (R)Se···N. These motifs lead to different packing topologies in SeCN3, as compared to the first two molecules. Previous studies involving the crystal packing of these three given molecules have mainly focused on the structural characterization of the ChB interactions (in terms of RR and interatomic interaction angles), while the electronic characteristics have been largely unexplored. In this way, the main focus of this study has been to characterize electronically those ChB interaction, by exploring the regions of atoms that are interacting to each other and also to understand how significant are these interactions in regard to the overall crystal

packings. The energetic analysis of intermolecular interactions revealed the importance of these ChB interactions to the overall crystal packings, considering the significant E_tot values displayed by ChB dimers in all three molecules. Simultaneously, the energetic analysis also indicated a clear difference in the ChB interactions of SeCN3, in comparison to the other two molecules, corroborating the dissimilarities observed earlier from the structural characterization. A change in the preferential atom···atom interaction that is involved in the crystal packing of SeCN3 was also observed by the enrichment ratio analysis. Further, attempts were made to quantitatively characterize the strength of these ChB interactions, first from the inspection of molecular electrostatic potential (MESP) surfaces and then from the topological analyses of the $\rho(\mathbf{r})$ and $L(\mathbf{r})$ functions of the associated atoms. Investigation of $V_{s,\,max}$ and $V_{s,\,min}$ points of the MESP function in the molecular surfaces of all three molecule revealed the different electrophilic and nucleophilic regions involved in the ChB interactions. Also, among the three molecules, differences in the structural distances of their ChB interactions were rationalized in terms of the geometrical positioning, and therefore of the electrostatic complementarity, of the interacting sites. Later, local nucleophilic···electrophilic ChB interactions were alternatively studied as the interaction between CC and CD sites obtained from the topological analysis of the $L(\mathbf{r})$ function. The electrostatic power of individual CC···CD interactions has been evaluated *via* the $\Delta(L/\rho)$ parameter. With the consideration of the distance between interacting CC and CD sites, the intensity is measured by the descriptor $(\Delta L/\rho)/d^2_{CC\cdots CD}$, which along with the angle α indicate the most relevant CC···CD interactions to the geometrical preferences of the interacting atoms in the ChB interactions. The analysis has revealed that larger $(\Delta L/\rho)/d^2_{CC\cdots CD}$ values and lower α angles for the CC···CD interactions are correspond to the ChB interactions involving the strong σ-hole of Se-atoms, at difference of those involving the weak σ-holes. Also, the electronic properties derived from the topological analyses of $\rho(\mathbf{r})$ and $L(\mathbf{r})$ functions follows the trend and supports the results seen earlier from the structural characterizations.

In such a way, in addition to the structural characterization carried out in terms of the RR values and interatomic interaction angles, the electronic investigations performed within the framework of the QTAIM methodology provide a deeper and richer insight into the characteristics of ChB interactions. Accordingly, these electronic investigations allowing a better understanding of the crystal packing. Also, extending this study of electronic descriptors to other electrostatically driven intermolecular interactions in the crystal packing allow one to rank the intermolecular interactions based on their local intensities.

5.2 Future perspectives

Below, we have listed some future perspectives of the studies carried out in Chapter3 and Chapter4 of this thesis. They are intended to either enrich current information or tackle a potential problem faced during the analysis.

Concerning the high-pressure studies,

1. An interesting feature found with *NISac.4CYP* at high-pressure is the single-crystal to single-crystal 2nd order structural phase transition happened at ~ 4.0(2) GPa, very close to the pressure at which the PTM (Daphne oil 7474) solidifies. This kind of behaviour has been observed in some previous reports as well. It will be interesting to investigate if there is any possible link between the phase transition pressure and the solidification limit of the PTM. This can be verified by carrying out HP-SCXRD experiments with a new PTM that possess a relatively higher solidification limit, permitting to cross-check if the phase transition pressure stays the same or changes in value.
2. Another interesting feature to investigate with both binary adducts *NISac.Py* and *NISac.4CYP* is the closeness of the $N_{donor}\cdots I\cdots N_{donor}$ HaB motif to a 3center-4 electron bond. It has been shown from the structural and electronic analysis that both HaB interactions are not very different from each other and show partial covalent characters, as indicated by the $1 < |V|/G < 2$ at their BCPs. All these features resemblance with the case of halonium ions (which is an example of 3center-4 electron bond) discussed earlier in the introduction chapter (**Section 1.3.1.4.**).
3. The information regarding the halogen atom shift in a donor-acceptor co-crystal system under evolving pressure can be expanded by increasing the library of compounds. For example, one potential study could be undertaken by choosing a much better Lewis base [for example, 4-dimethylaminopyridine] as the co-former molecule with NISac. Accordingly, the resulting binary adduct will have stronger HaB interactions and will be interesting to observe to what extend the I-atom position shifts under pressure.

Concerning the studies with benzyl selenocyanate derivatives,

1. During this study, even after many attempts of crystal growth and data collection we could not generate a good quality experimental multipolar model for any of the three molecules, mainly due to the large residues seen around the Se-atoms. One possible argument for this problematic situation is the flexibility of the selenocyanate group

within the molecule, where the Se-atom is bonded to the CN group and to a sp^3 hybridized C-atom. This permits a large degree of freedom for the movement of the Se-atoms in space, which might result to significant thermal vibrations even at 100K. One potential solution for this issue is to choose some another derivative, where Se-CN group is directly linked to the benzene core. In such a way, this will reduce the degree of freedom of the Se-atom up to an extent. In this direction, we tried to collect HR-SCXRD data for phenyl selenocyanate and ortho-nitrophenyl selenocyanate derivatives. But, their poor crystalline quality did not give any fruitful results.

2. One important feature still to investigate is the spatial orientation and electronic properties of the LCPs corresponding to the molecular structures obtained in the crystalline phase. Unfortunately, due to some technical problems with the VMoPro software we could not perform this analysis. In the future it will be interesting to compare these results with those obtained from the gas phase of monomers and dimers.

Appendices – Chapter 3

Table 3AP.1 Crystallographic information for the data collected at ambient conditions for crystal-2 outside MDAC

Crystal data	
Chemical formula	$C_{12}H_9IN_2O_3S$
M_r (g/mol)	388.17
Crystal system, space group	Monoclinic, $B2_1/e$
Temperature (K)	298
a, b, c (Å)	27.272 (5), 7.8156 (9), 12.6155 (16)
β (°)	88.703 (3)
V (Å^3)	2688.3 (7)
Z	8
Radiation type	Mo K_α (λ=0.7107 Å)
μ (mm^{-1})	2.54
Crystal size (mm)	0.110 × 0.091 × 0.048
Data collection	
Diffractometer	Bruker APEX-III CCD
Absorption correction	Numerical (face indexing)
No. of measured, independent, observed [I >2σ(I)] reflections	67239, 2738, 2670
Completeness (%)	100
R_{int}	0.049
$(\sin\theta/\lambda)_{max}$ (Å^{-1})	0.625
Refinement	
R [$F^2 > 2\sigma(F^2)$], $wR(F^2)$, S	0.063, 0.155, 1.16
No. of reflections	2738
No. of parameters	173
$\Delta\rho_{max}$, $\Delta\rho_{min}$ (e Å^{-3})	2.49, -1.41

These comparatively larger agreement factors and residual density indicator obtained for crystal-2 might be linked with a poorer crystalline quality, happened after a full cycle of compression-decompression inside the MDAC.

Table 3AP.2 Crystallographic information for the data collected at 100 K for crystal-1.

Crystal data	
Chemical formula	$C_{12}H_9IN_2O_3S$
M_r (g/mol)	388.17
Crystal system, space group	Monoclinic, $B2_1/e$
Temperature (K)	100
a, b, c (Å)	27.085 (5), 7.6524 (9), 12.5325 (14)
β (°)	88.571 (2)
V (Å^3)	2596.7 (6)
Z	8
Radiation type	Mo $K\alpha$ (λ=0.7107 Å)
μ (mm^{-1})	2.63
Crystal size (mm)	0.149 × 0.122 × 0.053
Data collection	
Diffractometer	Bruker APEX-II CCD
Absorption correction	Numerical (face indexing)
No. of measured, independent, observed [I >2σ(I)] reflections	104622, 3643, 3587
Completeness (%)	100
R_{int}	0.031
$(\sin\theta/\lambda)_{max}$ (Å^{-1})	0.694
Refinement	
R [$F^2 > 2\sigma(F^2)$], $wR(F^2)$, S	0.015, 0.038, 1.13
No. of reflections	3643
No. of parameters	173
H-atom treatment	H-atom parameters constrained
$\Delta\rho_{max}$, $\Delta\rho_{min}$ (e Å^{-3})	1.04, -0.32

Table 3AP.3 Variation of intermolecular distances and angles involving I1(*x,y,z*) and atoms of neighbouring adducts, as a function of pressure for the high-pressure experimental dataset. Values within brackets are the standard deviations of the corresponding values. Distance and reduction ratio (RR) values are gathered as left/right entries. RR is defined as the ratio between the internuclear distance and the sum of van der Waals radii of interacting atoms. A ranking is assigned based on RR values determined at 4.5(2) GPa, sorted from smaller to larger values. Δ(RR) = $RR_{0.00(5)\ GPa} - RR_{4.5(2)\ GPa}$. The distances are given in Å and the angles are given in degrees (º).

Pressure (GPa)	*1/2-x,-1/2+y,1-z*					*1/2-x,1-y,3/2-z*			*x,1/2-y,1/2+z*	*1/2-x,1/2+y,1-z*			
	I1···C8/ RR	I1···I1/ RR	I1···N2/ RR	I1···H8/ RR	<I1···H8-C8	I1···C11/ RR	I1···H11/ RR	<I1···H11-C11	I1···O3/ RR	I1···C12/ RR	I1···N2/ RR	I1···H12/ RR	<I1···H12-C12
0.00(5)	3.671(9)/1.00	4.3683(14)/1.10	4.097(7)/1.16	3.39/1.07	96.0	4.024(9)/1.09	3.46/1.09	113.9	4.016(8)/1.15	3.938(8)/1.07	3.912(7)/1.11	3.88/1.22	85.4
0.00(5)	3.671(14)/1.00	4.372(2)/1.10	4.119(10)/1.17	3.35/1.05	98.4	4.028(14)/1.09	3.47/1.09	112.9	4.031(11)/1.15	3.935(12)/1.07	3.901(10)/1.11	3.88/1.22	85.1
0.05(5)	3.666(13)/1.00	4.362(2)/1.10	4.111(10)/1.16	3.35/1.05	98.0	4.023(13)/1.09	3.48/1.09	112.3	4.012(11)/1.15	3.948(11)/1.07	3.892(10)/1.10	3.92/1.23	83.8
0.20(5)	3.632(11)/0.99	4.3149(17)/1.09	4.063(8)/1.15	3.35/1.05	96.2	4.003(11)/1.09	3.45/1.08	113.3	3.979(9)/1.14	3.913(10)/1.06	3.865(8)/1.09	3.85/1.21	85.0
0.4(1)	3.613(13)/0.98	4.2589(19)/1.08	4.012(10)/1.14	3.35/1.05	94.8	3.957(13)/1.08	3.37/1.06	115.2	3.950(11)/1.13	3.882(10)/1.05	3.831(9)/1.09	3.81/1.20	85.6
0.5(1)	3.599(11)/0.98	4.2145(15)/1.06	3.976(8)/1.13	3.38/1.06	92.6	3.932(11)/1.07	3.36/1.06	113.9	3.91(1)/1.12	3.87(9)/1.05	3.793(8)/1.07	3.84/1.21	83.3
0.5(1)	3.603(12)/0.98	4.2358(18)/1.07	4.010(9)/1.14	3.32/1.04	96.1	3.950(12)/1.07	3.39/1.07	113.6	3.926(10)/1.12	3.871(10)/1.05	3.801(9)/1.08	3.82/1.20	84.3
0.8(1)	3.555(12)/0.97	4.1529(17)/1.05	3.941(9)/1.12	3.29/1.03	95.2	3.897(13)/1.06	3.31/1.04	115.0	3.865(11)/1.10	3.823(10)/1.04	3.740(9)/1.06	3.77/1.19	84.3
0.9(1)	3.543(11)/0.96	4.120(15)/1.04	3.899(8)/1.10	3.3/1.04	93.6	3.853(12)/1.05	3.25/1.02	116.0	3.851(10)/1.10	3.808(9)/1.03	3.729(8)/1.06	3.76/1.18	84.4
1.3(2)	3.501(16)/0.95	4.079(2)/1.03	3.864(12)/1.09	3.26/1.03	93.8	3.822(15)/1.04	3.20/1.01	117.3	3.808(13)/1.09	3.784(13)/1.03	3.703(11)/1.05	3.71/1.17	85.3
1.5(2)	3.485(14)/0.95	4.0421(18)/1.02	3.836(10)/1.09	3.23/1.02	94.4	3.799(13)/1.03	3.17/1.00	117.1	3.782(11)/1.08	3.767(11)/1.02	3.672(10)/1.04	3.72/1.17	84.3
1.9(2)	3.430(16)/0.93	3.993(2)/1.01	3.786(12)/1.07	3.14/0.99	96.4	3.760(15)/1.02	3.14/0.99	117.0	3.724(13)/1.06	3.725(13)/1.01	3.647(12)/1.03	3.64/1.14	86.0
2.0(2)	3.431(16)/0.93	3.984(2)/1.01	3.782(12)/1.07	3.15/0.99	95.9	3.748(16)/1.02	3.10/0.97	119.0	3.712(14)/1.06	3.717(13)/1.01	3.630(12)/1.03	3.61/1.14	87.3
2.4(2)	3.413(14)/0.93	3.947(2)/1.00	3.744(11)/1.06	3.11/0.98	96.6	3.738(14)/1.02	3.11/0.98	117.1	3.676(12)/1.05	3.694(11)/1.00	3.613(11)/1.02	3.59/1.13	86.8
3.3(2)	3.386(8)/0.92	3.8644(11)/0.98	3.691(5)/1.05	3.12/0.98	94.6	3.690(7)/1.00	3.11/0.98	113.9	3.603(6)/1.03	3.641(5)/0.99	3.562(5)/1.01	3.59/1.13	83.7
4.5(2)	3.350(11)/0.91	3.7902(15)/0.96	3.641(8)/1.03	3.06/0.96	95.6	3.643(10)/0.99	3.07/0.97	113.3	3.533(8)/1.01	3.602(8)/0.98	3.530(8)/1.00	3.53/1.11	85.2
Rank	1	2	9	3	-	6	4	-	8	5	7	10	-
Δ(RR)	0.09	0.14	0.13	0.11	-	0.10	0.12	-	0.14	0.09	0.11	0.11	-

Table 3AP.4 Variation of intermolecular distances and angles involving I1(*x,y,z*) and atoms of neighbouring adducts, as a function of pressure for the high-pressure theoretical dataset. Distance and reduction ratio (RR) values are gathered as left/right entries. A ranking is assigned based on RR values determined at 4.72 GPa, sorted from smaller to larger values. Δ(RR) = $RR_{-0.03\ GPa} - RR_{4.72\ GPa}$. The distances are given in Å and the angles are given in degrees (º).

Pressure[a] (GPa)	*1/2-x,-1/2+y,1-z*					*1/2-x,1-y,3/2-z*			*x,1/2-y,1/2+z*	*1/2-x,1/2+y,1-z*			
	I1···C8/ RR	I1···I1/ RR	I1···N2/ RR	I1···H8/ RR	<I1···H8-C8	I1···C11/ RR	I1···H11/ RR	<I1···H11-C11	I1···O3/ RR	I1···C12/ RR	I1···N2/ RR	I1···H12/ RR	<I1···H12-C12
-0.03	3.658/0.99	4.336/1.09	4.087/1.16	3.35/1.05	97.7	4.059/1.10	3.50/1.10	113.5	4.003/1.14	3.928/1.07	3.913/1.11	3.82/1.20	87.7
0.22	3.602/0.98	4.284/1.08	4.026/1.14	3.30/1.04	97.2	4.055/1.10	3.51/1.10	112.9	3.966/1.13	3.865/1.05	3.859/1.09	3.75/1.18	87.7
0.47	3.553/0.97	4.200/1.06	3.955/1.12	3.26/1.02	96.5	3.965/1.08	3.40/1.07	113.8	3.891/1.11	3.833/1.04	3.789/1.07	3.74/1.18	86.7
0.72	3.529/0.96	4.160/1.05	3.920/1.11	3.24/1.02	96.0	3.922/1.07	3.35/1.05	113.9	3.841/1.10	3.816/1.04	3.758/1.06	3.73/1.17	86.3
0.97	3.504/0.95	4.110/1.04	3.882/1.10	3.22/1.01	96.8	3.877/1.05	3.30/1.04	114.1	3.790/1.08	3.810/1.04	3.729/1.06	3.73/1.17	85.9
1.22	3.479/0.95	4.077/1.03	3.850/1.09	3.20/1.01	95.5	3.852/1.05	3.28/1.03	114.1	3.760/1.07	3.788/1.03	3.699/1.05	3.71/1.17	85.7
1.47	3.470/0.94	4.030/1.02	3.824/1.08	3.20/1.01	94.8	3.799/1.03	3.21/1.01	114.8	3.721/1.06	3.779/1.03	3.665/1.04	3.71/1.17	85.4
1.72	3.448/0.94	3.996/1.01	3.792/1.07	3.19/1.00	94.3	3.781/1.03	3.19/1.00	114.9	3.684/1.05	3.759/1.02	3.655/1.04	3.67/1.15	86.4
1.97	3.432/0.93	3.978/1.00	3.755/1.06	3.18/1.00	94.2	3.760/1.02	3.17/1.00	114.8	3.662/1.05	3.753/1.02	3.633/1.03	3.68/1.16	85.5
2.22	3.420/0.93	3.949/1.00	3.754/1.06	3.17/1.00	93.9	3.734/1.01	3.14/0.99	114.9	3.639/1.04	3.741/1.02	3.618/1.02	3.66/1.15	85.9
2.47	3.398/0.92	3.920/0.99	3.723/1.05	3.16/0.99	93.2	3.734/1.01	3.15/0.99	114.6	3.632/1.04	3.682/1.00	3.594/1.02	3.57/1.12	87.3
2.72	3.384/0.92	3.902/0.99	3.704/1.05	3.15/0.99	93.0	3.717/1.01	3.13/0.98	114.6	3.613/1.03	3.670/1.00	3.579/1.01	3.56/1.12	87.2
2.97	3.370/0.92	3.879/0.98	3.688/1.04	3.13/0.98	93.0	3.696/1.00	3.11/0.98	114.3	3.587/1.02	3.663/1.00	3.566/1.01	3.55/1.12	87.2
3.22	3.363/0.91	3.865/0.98	3.675/1.04	3.13/0.98	93.0	3.677/1.00	3.10/0.97	114.2	3.571/1.02	3.656/0.99	3.559/1.01	3.54/1.11	87.2
3.47	3.352/0.91	3.848/0.97	3.662/1.04	3.11/0.98	93.0	3.655/0.99	3.08/0.97	113.7	3.554/1.02	3.642/0.99	3.550/1.01	3.52/1.11	87.5
3.72	3.341/0.91	3.835/0.97	3.650/1.03	3.11/0.98	92.7	3.648/0.99	3.07/0.97	113.8	3.533/1.01	3.642/0.99	3.539/1.00	3.53/1.11	87.1
3.97	3.329/0.90	3.817/0.96	3.636/1.03	3.09/0.97	92.9	3.636/0.99	3.07/0.97	113.0	3.525/1.01	3.609/0.98	3.526/1.00	3.48/1.09	87.8
4.22	3.318/0.90	3.803/0.96	3.623/1.03	3.08/0.97	92.7	3.624/0.98	3.06/0.96	112.9	3.513/1.00	3.598/0.98	3.512/0.99	3.47/1.09	87.7
4.47	3.313/0.90	3.789/0.96	3.613/1.02	3.08/0.97	92.7	3.610/0.98	3.05/0.96	112.9	3.487/1.00	3.595/0.98	3.509/0.99	3.47/1.09	87.8
4.72	3.303/0.90	3.777/0.95	3.601/1.02	3.07/0.97	92.5	3.599/0.98	3.04/0.95	112.8	3.473/0.99	3.584/0.97	3.495/0.99	3.46/1.09	87.6
Rank	1	2	9	4	-	6	3	-	8	5	7	10	-
Δ(RR)	0.09	0.14	0.14	0.08	-	0.12	0.15	-	0.15	0.10	0.12	0.11	-

Table 3AP.5 Variation of interatomic distances and angles involving atoms of the reference (*x,y,z*) adduct and atoms of neighbouring symmetry generated adducts, as a function of pressure for the *NISac.Py* high-pressure theoretical dataset. Distance and reduction ratio (RR) values are gathered as left/right entries. A ranking is assigned based on the RR values determined at 4.72 GPa, sorted from smaller to larger values. Δ(RR) = $RR_{-0.03\ GPa} - RR_{4.72\ GPa}$. The distances are given in Å and the angles are given in degree (º). Centroids of the rings are defined as: cen_1= centroid of the ring formed by atoms C1-C6, cen_2= centroid of the ring formed by atoms C5,C6,C7,N1,S1, and cen_3= centroid of the ring formed by atoms C8-C12,N2. (* *Table continues to the next pages*)**

Pressure (GPa)	*1/2-x,-1/2+y,1-z*						*-1/2+x, y,1/2+z*				*1/2-x,1-y,3/2-z*					
	$cen_3\cdots cen_2$/ RR	C8···O1/ RR	<C8···O1-S1	O2···H9/ RR	<O2···H9-C9	$cen_2\cdots cen_3$/ RR	H9···C3/ RR	<C9-H9···C3	H10···C3/ RR	<C10-H10···C3	$cen_3\cdots cen_3$/ RR	C12···C12/ RR	H10···O1/ RR	<C10-H10···O1	H11···O1/ RR	<C11-H11···O1
-0.03	3.822/1.14	3.407/1.06	121.25	2.61/0.96	137.4	4.886/1.45	2.92/1.01	130.6	3.24/1.12	117.6	4.955/1.48	3.634/1.07	2.47/0.91	131.0	2.91/1.07	112.3
0.22	3.783/1.12	3.392/1.05	120.84	2.53/0.93	138.2	4.826/1.43	2.91/1.00	130.3	3.23/1.11	117.7	4.946/1.48	3.633/1.07	2.45/0.90	131.5	2.93/1.08	111.5
0.47	3.717/1.10	3.281/1.02	120.72	2.51/0.92	136.8	4.737/1.41	2.87/0.99	129.8	3.18/1.09	117.4	4.895/1.46	3.527/1.04	2.42/0.89	130.6	2.86/1.05	112.0
0.72	3.682/1.09	3.227/1.00	120.76	2.50/0.92	136.1	4.696/1.40	2.84/0.98	129.3	3.14/1.08	117.3	4.862/1.45	3.476/1.02	2.40/0.88	130.0	2.83/1.04	112.0
0.97	3.643/1.08	3.177/0.99	120.39	2.47/0.91	135.0	4.648/1.38	2.79/0.96	129.1	3.10/1.07	116.7	4.829/1.44	3.418/1.01	2.38/0.87	129.1	2.78/1.02	112.0
1.22	3.617/1.07	3.148/0.98	120.26	2.44/0.90	134.7	4.611/1.37	2.78/0.96	129.0	3.08/1.06	116.8	4.812/1.44	3.391/1.00	2.36/0.87	129.0	2.77/1.02	112.0
1.47	3.568/1.06	3.067/0.95	119.87	2.46/0.90	132.7	4.577/1.36	2.74/0.94	128.4	3.04/1.05	116.3	4.781/1.43	3.333/0.98	2.35/0.86	127.9	2.71/1.00	112.4
1.72	3.547/1.05	3.006/0.93	121.07	2.44/0.90	131.8	4.535/1.35	2.69/0.93	128.0	3.00/1.03	116.0	4.770/1.42	3.318/0.98	2.33/0.86	126.4	2.65/0.98	112.9
1.97	3.530/1.05	2.998/0.93	120.42	2.43/0.90	131.7	4.521/1.34	2.69/0.93	127.7	2.99/1.03	116.1	4.746/1.42	3.286/0.97	2.32/0.85	126.7	2.66/0.98	112.5
2.22	3.510/1.04	2.965/0.92	120.45	2.42/0.89	131.1	4.487/1.33	2.66/0.92	127.5	2.96/1.02	115.8	4.735/1.41	3.264/0.96	2.30/0.85	125.8	2.62/0.96	112.7
2.47	3.495/1.04	2.924/0.91	121.57	2.39/0.88	130.2	4.455/1.32	2.66/0.92	126.5	2.92/1.01	116.5	4.719/1.41	3.261/0.96	2.29/0.84	125.0	2.58/0.95	112.7
2.72	3.482/1.03	2.909/0.90	121.42	2.38/0.87	130.0	4.434/1.32	2.65/0.91	126.4	2.91/1.00	116.4	4.709/1.41	3.243/0.95	2.28/0.84	124.9	2.57/0.95	112.5
2.97	3.464/1.03	2.886/0.90	121.40	2.37/0.87	129.4	4.410/1.31	2.64/0.91	126.1	2.89/1.00	116.4	4.683/1.40	3.217/0.95	2.27/0.83	124.5	2.56/0.94	112.5
3.22	3.455/1.03	2.870/0.89	121.56	2.37/0.87	128.9	4.393/1.31	2.62/0.90	125.9	2.87/0.99	116.0	4.673/1.39	3.198/0.94	2.26/0.83	124.2	2.54/0.93	112.5
3.47	3.442/1.02	2.847/0.88	121.88	2.36/0.87	128.5	4.375/1.30	2.60/0.90	125.7	2.86/0.98	115.8	4.653/1.39	3.178/0.93	2.25/0.83	123.6	2.52/0.93	112.6
3.72	3.427/1.02	2.828/0.88	121.73	2.36/0.87	128.0	4.365/1.30	2.61/0.90	125.5	2.85/0.98	116.1	4.641/1.39	3.166/0.93	2.25/0.83	123.6	2.52/0.93	112.6
3.97	3.421/1.02	2.814/0.87	122.25	2.35/0.86	127.6	4.341/1.29	2.59/0.89	124.8	2.82/0.97	116.1	4.625/1.38	3.159/0.93	2.23/0.82	123.4	2.50/0.92	112.3
4.22	3.410/1.01	2.805/0.87	122.04	2.34/0.86	127.5	4.326/1.29	2.59/0.89	124.9	2.82/0.97	116.2	4.618/1.38	3.148/0.93	2.22/0.82	123.3	2.49/0.92	112.2

4.47	3.401/1.01	2.784/0.86	122.41	2.34/0.86	126.8	4.308/1.28	2.57/0.89	124.6	2.80/0.97	116.0	4.602/1.37	3.129/0.92	2.22/0.81	122.8	2.47/0.91	112.4
4.72	3.388/1.01	2.771/0.86	122.15	2.33/0.86	126.6	4.297/1.28	2.56/0.88	124.4	2.79/0.96	116.0	4.596/1.37	3.119/0.92	2.21/0.81	122.7	2.46/0.91	112.2
Rank	20	7	-	8	-	25	10	-	18	-	26	16	4	-	14	-
ΔRR	0.13	0.20	-	0.10	-	0.17	0.13	-	0.16	-	0.11	0.15	0.10	-	0.16	-

Continuation of Table 3AP.5

Pressure (GPa)	***1/2-x,1-y,1/2-z***				***1-x, 1/2+y,1/2-z***							***x,1/2-y,1/2+z***					
	O3··H8/ RR	**<O3···H8-C8**	**H1···H8/ RR**	**H1···H9/ RR**	**cen$_1$··· cen$_1$/ RR**	**H2···O2/ RR**	**<C2-H2···O2**	**H3···O2/ RR**	**<C3-H3···O2**	**H3···C6/ RR**	**<C3-H3···C6**	**O2···C1/ RR**	**<S1-O2···C1**	**H12···O3/ RR**	**<C12-H12···O3**	**H11···C8/ RR**	**<C11-H11···C8**
-0.03	2.42/0.89	174.5	2.29/0.96	2.29/0.95	4.510/1.33	2.63/0.97	128.5	2.89/1.06	117.5	2.85/0.98	134.2	3.377/1.05	159.09	2.43/0.89	166.6	3.39/1.17	160.8
0.22	2.38/0.87	173.7	2.25/0.94	2.25/0.94	4.461/1.31	2.57/0.95	128.5	2.84/1.05	117.1	2.81/0.97	134.1	3.314/1.03	157.86	2.39/0.88	167.2	3.34/1.15	161.5
0.47	2.36/0.87	174.7	2.23/0.93	2.21/0.92	4.380/1.29	2.57/0.94	129.0	2.87/1.06	116.4	2.75/0.95	133.5	3.234/1.00	159.23	2.35/0.86	165.8	3.29/1.14	160.2
0.72	2.33/0.86	175.0	2.20/0.92	2.18/0.91	4.341/1.28	2.56/0.94	129.2	2.88/1.06	115.9	2.73/0.94	133.0	3.196/0.99	159.48	2.32/0.85	164.9	3.26/1.12	159.6
0.97	2.31/0.85	175.1	2.20/0.92	2.16/0.90	4.289/1.26	2.51/0.92	129.5	2.86/1.05	115.1	2.68/0.92	132.6	3.147/0.98	160.30	2.29/0.84	163.3	3.23/1.11	159.0
1.22	2.29/0.84	174.8	2.18/0.91	2.14/0.89	4.257/1.25	2.50/0.92	129.6	2.85/1.05	114.8	2.66/0.92	132.4	3.113/0.97	160.22	2.27/0.84	163.1	3.2/1.1	158.9
1.47	2.28/0.84	174.5	2.19/0.91	2.14/0.89	4.205/1.24	2.49/0.92	130.3	2.89/1.06	113.9	2.62/0.90	131.8	3.093/0.96	161.89	2.26/0.83	161.9	3.18/1.1	157.8
1.72	2.23/0.82	173.5	2.18/0.91	2.12/0.88	4.172/1.23	2.48/0.91	131.4	2.93/1.08	112.8	2.58/0.89	131.9	3.083/0.96	163.19	2.26/0.83	161.7	3.17/1.09	156.9
1.97	2.23/0.82	173.8	2.15/0.90	2.11/0.88	4.151/1.22	2.48/0.91	131.0	2.91/1.07	113.0	2.58/0.89	131.2	3.051/0.95	162.95	2.24/0.82	160.9	3.15/1.08	157.0
2.22	2.21/0.81	173.3	2.17/0.90	2.10/0.88	4.123/1.21	2.45/0.90	132.0	2.93/1.08	112.1	2.54/0.88	131.6	3.038/0.94	163.81	2.24/0.82	160.6	3.13/1.08	156.6
2.47	2.13/0.78	172.4	2.19/0.91	2.10/0.87	4.088/1.20	2.48/0.91	134.1	3.04/1.12	110.8	2.52/0.87	130.9	3.035/0.94	166.60	2.25/0.83	161.2	3.13/1.08	156.3
2.72	2.12/0.78	172.1	2.18/0.91	2.09/0.87	4.068/1.20	2.47/0.91	134.2	3.04/1.12	110.5	2.51/0.87	130.7	3.015/0.94	166.58	2.24/0.82	160.9	3.12/1.08	156.2
2.97	2.11/0.78	171.7	2.17/0.90	2.08/0.87	4.052/1.19	2.47/0.91	134.6	3.06/1.12	110.4	2.50/0.86	130.7	2.997/0.93	167.02	2.22/0.81	160.4	3.11/1.07	156.1
3.22	2.09/0.77	171.5	2.17/0.90	2.07/0.86	4.031/1.19	2.46/0.90	134.8	3.06/1.13	109.9	2.48/0.86	130.3	2.987/0.93	167.49	2.22/0.82	160.0	3.1/1.07	156.0
3.47	2.07/0.76	171.0	2.18/0.91	2.06/0.86	4.013/1.18	2.46/0.90	135.3	3.09/1.13	109.4	2.47/0.85	130.1	2.981/0.93	168.44	2.22/0.82	159.6	3.09/1.07	156.2
3.72	2.07/0.76	170.8	2.15/0.90	2.05/0.85	4.005/1.18	2.47/0.91	135.3	3.09/1.13	109.6	2.47/0.85	129.8	2.963/0.92	168.20	2.19/0.81	159.1	3.07/1.06	155.9
3.97	2.04/0.75	170.5	2.19/0.91	2.06/0.86	3.976/1.17	2.48/0.91	137.1	3.17/1.16	108.5	2.45/0.84	129.5	2.956/0.92	170.16	2.20/0.81	159.4	3.07/1.06	156.3

4.22	2.03/0.75	170.3	2.18/0.91	2.06/0.86	3.962/1.17	2.47/0.91	137.1	3.16/1.16	108.3	2.44/0.84	129.4	2.941/0.91	170.11	2.19/0.81	159.3	3.06/1.05	156.3
4.47	2.02/0.74	169.9	2.17/0.91	2.05/0.85	3.950/1.16	2.47/0.91	137.5	3.18/1.17	108.0	2.42/0.84	129.3	2.935/0.91	170.60	2.18/0.80	158.6	3.05/1.05	156.0
4.72	2.01/0.74	169.9	2.17/0.90	2.04/0.85	3.933/1.16	2.46/0.90	137.4	3.18/1.17	107.8	2.41/0.83	128.9	2.921/0.91	170.72	2.17/0.80	158.4	3.04/1.05	156.0
Rank	1	-	12	6	23	13	-	24	-	5	-	15	-	3	-	21	-
ΔRR	0.15	-	0.06	0.10	0.17	0.07	-	0.11	-	0.15	-	0.14	-	0.09	-	0.12	-

Continuation of Table 3AP.5

Pressure (GPa)	***x,3/2-y,1/2+z***					***1-x, 1-y, 1-z***		***1-x, 1-y, -z***	
	H4⋯H2/ RR	**O1··C1/ RR**	**<S1-O1⋯C1**	**O1⋯H1**	**<S1-O1⋯H1**	**H4⋯O2/RR**	**<C4-H4⋯O2**	**H1⋯H2/ RR**	**H2⋯H2/ RR**
-0.03	2.86/1.19	3.288/1.02	153.38	2.98/1.10	151.6	2.36/0.87	164.3	3.20/1.33	2.49/1.04
0.22	2.81/1.17	3.231/1.00	153.31	2.92/1.07	151.0	2.32/0.85	164.9	3.23/1.34	2.50/1.04
0.47	2.75/1.15	3.140/0.98	152.98	2.83/1.04	151.5	2.28/0.84	163.7	3.14/1.31	2.40/1.00
0.72	2.71/1.13	3.093/0.96	152.51	2.78/1.02	151.3	2.24/0.82	163.2	3.12/1.30	2.37/0.99
0.97	2.68/1.12	3.069/0.95	151.68	2.75/1.01	150.4	2.23/0.82	162.6	3.02/1.26	2.33/0.97
1.22	2.65/1.11	3.036/0.94	151.48	2.72/1.00	150.3	2.21/0.81	162.5	3.01/1.25	2.31/0.96
1.47	2.61/1.09	2.992/0.93	150.75	2.67/0.98	150.1	2.19/0.81	160.8	2.92/1.22	2.27/0.95
1.72	2.54/1.06	2.971/0.92	148.78	2.64/0.97	148.8	2.16/0.79	158.6	2.83/1.18	2.27/0.95
1.97	2.55/1.06	2.945/0.91	149.32	2.62/0.96	149.3	2.14/0.79	159.6	2.86/1.19	2.24/0.93
2.22	2.51/1.05	2.931/0.91	148.41	2.60/0.96	148.4	2.14/0.79	157.2	2.78/1.16	2.25/0.94
2.47	2.47/1.03	2.917/0.91	146.15	2.56/0.94	146.5	2.14/0.79	152.3	2.71/1.13	2.27/0.95
2.72	2.45/1.02	2.896/0.90	146.05	2.54/0.94	146.4	2.12/0.78	152.3	2.70/1.12	2.26/0.94
2.97	2.44/1.01	2.881/0.89	145.75	2.53/0.93	146.2	2.12/0.78	151.4	2.68/1.12	2.25/0.94
3.22	2.41/1.01	2.865/0.89	145.42	2.51/0.92	146.0	2.1/0.77	150.9	2.65/1.10	2.25/0.94
3.47	2.39/0.99	2.849/0.88	144.71	2.49/0.92	145.5	2.1/0.77	149.0	2.60/1.08	2.25/0.94

3.72	2.39/0.99	2.836/0.88	144.75	2.48/0.91	145.6	2.09/0.77	149.8	2.63/1.09	2.23/0.93
3.97	2.37/0.99	2.834/0.88	143.79	2.46/0.91	144.8	2.09/0.77	145.8	2.55/1.06	2.26/0.94
4.22	2.36/0.98	2.819/0.88	143.70	2.45/0.90	144.6	2.09/0.77	145.7	2.55/1.06	2.25/0.94
4.47	2.34/0.97	2.812/0.87	143.20	2.44/0.90	144.3	2.09/0.77	144.7	2.53/1.05	2.26/0.94
4.72	2.33/0.97	2.794/0.87	143.10	2.42/0.89	144.1	2.07/0.76	144.7	2.52/1.05	2.24/0.93
Rank	19	9	-	11	-	2	-	22	17
ΔRR	0.22	0.15	-	0.21	-	0.11	-	0.28	0.11

Table 3AP.6 Variation of intermolecular distances and angles involving atoms of the reference(*x,y,z*) adduct and atoms of neighbouring symmetry generated adducts, as a function of pressure for the *NISac.Py* high-pressure experimental dataset. Values within brackets are the standard deviations of the corresponding values. Distance and reduction ratio (RR) values are gathered as left/right entries. The ranking is assigned based on the RR values determined at 4.5(2) GPa, sorted from smaller to larger values. Δ(RR) = $RR_{0.00(5)\,GPa} - RR_{4.5(2)\,GPa}$. The distances are given in Å and the angles are given in degree (º). Centroids of the rings are defined as: cen_1= centroid of the ring formed by atoms C1-C6, cen_2= centroid of the ring formed by atoms C5,C6,C7,N1,S1, and cen_3= centroid of the ring formed by atoms C8-C12,N2. (* *Table continues to the next pages*)**

Pressure (GPa)	*1/2-x,-1/2+y,1-z*						*-1/2+x,y,1/2+z*				*1/2-x,1-y,3/2-z*					
	$cen_3\cdots cen_2$/ RR	C8···O1/ RR	<C8···O1-S1	O2···H9/ RR	<O2···H9-C9	$cen_2\cdots cen_3$/ RR	H9···C3/ RR	<C9-H9···C3	H10···C3/ RR	<C10-H10···C3	$cen_3\cdots cen_3$/ RR	C12···C12/ RR	H10···O1/ RR	<C10-H10···O1	H11···O1/ RR	<C11-H11···O1
0.00(5)	3.834(6)/1.14	3.429(15)/1.06	120.6(5)	2.72/1.00	135.7	4.913(7)/1.46	3.08/1.06	131.1	3.31/1.14	121.5	4.899(13)/1.46	3.6(2)/1.06	2.48/0.91	131.8	2.95/1.08	112.7
0.00(5)	3.842(9)/1.14	3.47(2)/1.08	120.1(7)	2.71/0.99	135.6	4.912(10)/1.46	3.07/1.06	130.5	3.32/1.14	121.3	4.884(19)/1.46	3.61(3)/1.06	2.47/0.91	131.9	2.91/1.07	113.5
0.05(5)	3.825(8)/1.14	3.45(2)/1.07	119.9(7)	2.69/0.99	135.9	4.895(10)/1.45	3.04/1.05	129.8	3.25/1.12	121.6	4.888(18)/1.46	3.57(3)/1.05	2.48/0.91	130.9	2.90/1.07	113.6
0.20(5)	3.798(7)/1.13	3.398(18)/1.06	119.9(6)	2.65/0.97	135.9	4.854(8)/1.44	3.04/1.05	130.7	3.26/1.13	121.5	4.877(16)/1.46	3.57(3)/1.05	2.47/0.91	131.4	2.92/1.07	112.9
0.4(1)	3.743(8)/1.11	3.31(2)/1.03	120.5(7)	2.60/0.96	134.6	4.785(9)/1.42	2.97/1.02	130.0	3.21/1.11	120.6	4.883(19)/1.46	3.53(3)/1.04	2.44/0.90	129.8	2.84/1.04	113.5
0.5(1)	3.716(7)/1.10	3.237(18)/1.01	121.2(6)	2.55/0.94	134.8	4.752(8)/1.41	2.95/1.02	129.5	3.20/1.10	119.7	4.835(16)/1.44	3.44(3)/1.01	2.40/0.88	129.8	2.83/1.04	113.1
0.5(1)	3.733(8)/1.11	3.301(19)/1.03	120.6(6)	2.60/0.96	133.9	4.780(9)/1.42	2.96/1.02	129.0	3.19/1.10	120.4	4.85(16)/1.45	3.5(3)/1.03	2.43/0.89	129.5	2.81/1.03	113.7
0.8(1)	3.668(8)/1.09	3.214(19)/1	120.4(6)	2.54/0.94	132.4	4.703(9)/1.40	2.92/1.01	129.1	3.16/1.09	120.2	4.806(16)/1.43	3.44(3)/1.01	2.38/0.88	128.9	2.76/1.02	113.6
0.9(1)	3.650(7)/1.08	3.151(18)/0.98	121.1(6)	2.54/0.93	129.9	4.664(8)/1.39	2.86/0.99	129.7	3.16/1.09	119.4	4.776(16)/1.43	3.37(3)/0.99	2.37/0.87	129.6	2.71/1.00	114.4
1.3(2)	3.626(10)/1.08	3.15(2)/0.98	120.3(8)	2.49/0.91	132.5	4.627(11)/1.38	2.90/1.00	129.1	3.14/1.08	119.7	4.74(2)/1.41	3.35(4)/0.99	2.35/0.86	128.4	2.75/1.01	112.7
1.5(2)	3.606(9)/1.07	3.09(2)/0.96	121.3(7)	2.51/0.92	129.1	4.591(10)/1.36	2.84/0.98	129.0	3.10/1.07	119.1	4.712(19)/1.41	3.3(3)/0.97	2.33/0.86	128.3	2.69/0.99	113.8
1.9(2)	3.573(10)/1.06	3.08(2)/0.96	121.2(8)	2.51/0.92	126.9	4.537(11)/1.35	2.82/0.97	128.4	3.07/1.06	119.7	4.69(2)/1.40	3.3(4)/0.97	2.31/0.85	127.6	2.65/0.97	113.8
2.0(2)	3.579(11)/1.06	3.08(3)/0.96	120.8(8)	2.47/0.91	129.5	4.538(12)/1.35	2.84/0.98	128.2	3.07/1.06	119.1	4.66(2)/1.39	3.31(4)/0.97	2.30/0.85	127.7	2.70/0.99	112.4
2.4(2)	3.538(9)/1.05	3.02(2)/0.94	121.2(7)	2.47/0.91	127.2	4.485(10)/1.33	2.79/0.96	126.2	2.98/1.03	118.8	4.69(2)/1.4	3.29(4)/0.97	2.28/0.84	126.4	2.65/0.98	112.6
3.3(2)	3.468(5)/1.03	2.908(11)/0.9	121.7(3)	2.43/0.89	125.9	4.396(5)/1.31	2.69/0.93	126.9	2.91/1.00	118.0	4.656(10)/1.39	3.167(17)/0.93	2.23/0.82	125.2	2.57/0.95	112.8
4.5(2)	3.416(6)/1.02	2.854(15)/0.89	121.7(5)	2.41/0.89	124.0	4.322(7)/1.28	2.58/0.89	126.5	2.84/0.98	117.2	4.621(15)/1.38	3.15(2)/0.93	2.21/0.81	123.0	2.44/0.90	114.1

Rank	20	6	-	7	-	25	8	-	18	-	26	14	4	-	10	-
ΔRR	0.12	0.17	-	0.11	-	0.18	0.17	-	0.16	-	0.08	0.13	0.10	-	0.18	-

Continuation of Table 3AP.6

Pressure (GPa)	***1/2-x,1-y,1/2-z***				***1-x, 1/2+y,1/2-z***							***x,1/2-y,1/2+z***					
	O3··H8/ RR	**<O3···H8-C8**	**H1···H8/ RR**	**H1···H9/ RR**	**cen$_1$··· cen$_1$/ RR**	**H2···O2/ RR**	**<C2-H2···O2**	**H3···O2/ RR**	**<C3-H3···O2**	**H3···C6/ RR**	**<C3-H3···C6**	**O2···C1/ RR**	**<S1-O2···C1**	**H12···O3/ RR**	**<C12-H12···O3**	**H11···C8/ RR**	**<C11-H11···C8**
0.00(5)	2.51/0.92	174.2	2.31/0.96	2.31/0.96	4.54(1)/1.34	2.78/1.02	129.9	3.05/1.12	118.1	2.88/0.99	135.6	3.401(11)/1.06	157.6(8)	2.42/0.89	165.2	3.36/1.16	161.4
0.00(5)	2.55/0.94	174.7	2.35/0.98	2.31/0.96	4.554(13)/1.34	2.78/1.02	129.4	3.03/1.12	119.1	2.88/0.99	136.3	3.406(15)/1.06	157.1(11)	2.44/0.90	164.3	3.39/1.17	163.8
0.05(5)	2.54/0.93	175.2	2.36/0.98	2.32/0.97	4.541(13)/1.34	2.77/1.02	128.7	3.03/1.12	117.6	2.91/1	134.8	3.424(15)/1.06	157.3(11)	2.45/0.90	162.4	3.38/1.16	164.4
0.20(5)	2.49/0.92	173.4	2.3/0.96	2.31/0.96	4.494(11)/1.32	2.74/1.01	130.2	3.05/1.12	117.9	2.87/0.99	134.2	3.373(13)/1.05	159.1(10)	2.40/0.88	163.5	3.35/1.16	162.1
0.4(1)	2.45/0.90	173.3	2.23/0.93	2.28/0.95	4.450(13)/1.31	2.77/1.02	129.4	3.03/1.11	118.5	2.8/0.97	135.8	3.323(15)/1.03	159.7(11)	2.40/0.88	163.4	3.32/1.14	159.5
0.5(1)	2.42/0.89	171.6	2.21/0.92	2.26/0.94	4.407(11)/1.30	2.73/1.01	130.3	3.06/1.12	117.3	2.78/0.96	135.6	3.289(12)/1.02	161.5(10)	2.37/0.87	160.5	3.29/1.13	160.4
0.5(1)	2.45/0.90	175.1	2.32/0.97	2.25/0.94	4.415(12)/1.30	2.72/1.00	130.2	3.04/1.12	117.5	2.78/0.96	134.9	3.311(13)/1.03	160.1(10)	2.40/0.88	161.5	3.31/1.14	162.2
0.8(1)	2.40/0.88	173.1	2.27/0.94	2.22/0.93	4.354(12)/1.28	2.71/1.00	131.1	3.08/1.13	116.6	2.73/0.94	136.7	3.238(14)/1.01	163.1(10)	2.36/0.87	160.5	3.28/1.13	159.7
0.9(1)	2.37/0.87	171.9	2.22/0.93	2.22/0.92	4.328(12)/1.27	2.70/0.99	131.8	3.09/1.14	116.0	2.71/0.94	135.5	3.219(13)/1.00	163.5(10)	2.33/0.86	160.4	3.26/1.12	158.0
1.3(2)	2.34/0.86	171.1	2.22/0.93	2.21/0.92	4.294(15)/1.26	2.69/0.99	132.2	3.11/1.14	115.9	2.66/0.92	137.6	3.185(18)/0.99	164.2(13)	2.31/0.85	160.5	3.26/1.12	155.4
1.5(2)	2.33/0.86	170.0	2.2/0.92	2.18/0.91	4.248(13)/1.25	2.67/0.98	133.3	3.12/1.15	115.1	2.63/0.91	135.3	3.159(15)/0.98	165.8(12)	2.29/0.84	158.7	3.25/1.12	155.9
1.9(2)	2.28/0.84	168.4	2.2/0.92	2.15/0.9	4.200(15)/1.24	2.68/0.99	133.5	3.13/1.15	115.6	2.58/0.89	136.3	3.131(18)/0.97	166.1(14)	2.25/0.83	158.6	3.23/1.11	155.5
2.0(2)	2.29/0.84	167.4	2.21/0.92	2.16/0.9	4.174(16)/1.23	2.65/0.97	134.5	3.13/1.15	115.2	2.58/0.89	134.5	3.125(18)/0.97	166.7(14)	2.26/0.83	158.1	3.26/1.12	152.6
2.4(2)	2.25/0.83	167.1	2.2/0.92	2.1/0.87	4.146(14)/1.22	2.64/0.97	135.1	3.15/1.16	113.9	2.57/0.89	133.1	3.087(16)/0.96	166.6(13)	2.27/0.83	157.9	3.23/1.11	154.4
3.3(2)	2.17/0.80	166.0	2.16/0.9	2.12/0.88	4.067(7)/1.20	2.64/0.97	136.0	3.23/1.19	111.6	2.48/0.86	133.1	3.030(8)/0.94	169.7(6)	2.19/0.80	156.3	3.13/1.08	156.8
4.5(2)	2.14/0.79	164.2	2.2/0.92	2.13/0.89	3.995(10)/1.18	2.58/0.95	138.0	3.26/1.20	110.1	2.42/0.83	132.5	2.988(12)/0.93	170.9(9)	2.15/0.79	154.8	3.11/1.07	157.6
Rank	1	-	12	9	23	16	-	24	-	5	-	15	-	2	-	22	-
ΔRR	0.13	-	0.04	0.07	0.16	0.07	-	0.08	-	0.16	-	0.13	-	0.10	-	0.09	-

Continuation of Table 3AP.6

Pressure (GPa)	*x,3/2-y,1/2+z*					*1-x, 1-y, 1-z*		*1-x, 1-y, -z*	
	H4··H2/ RR	**O1··C1/** RR	**<S1-O1···C1**	**O1···H1**	**<S1-O1···H1**	**H4···O2/RR**	**<C4-H4···O2**	**H1···H2/ RR**	**H2···H2/ RR**
0.00(5)	2.93/1.22	3.323(13)/1.03	154.7(9)	3.00/1.10	152.3	2.33/0.86	159.2	3.32/1.38	2.51/1.05
0.00(5)	2.95/1.23	3.335(17)/1.04	154.5(12)	3.01/1.11	152.3	2.32/0.85	160.3	3.36/1.40	2.52/1.05
0.05(5)	2.93/1.22	3.31(18)/1.03	155.1(12)	2.97/1.09	153.0	2.32/0.85	159.5	3.33/1.39	2.50/1.04
0.20(5)	2.86/1.19	3.26(15)/1.01	155.5(10)	2.94/1.08	153.3	2.31/0.85	159.2	3.30/1.37	2.54/1.06
0.4(1)	2.83/1.18	3.226(17)/1.00	154.4(12)	2.89/1.06	152.8	2.27/0.83	157.9	3.25/1.36	2.42/1.01
0.5(1)	2.79/1.16	3.19(15)/0.99	152.5(11)	2.86/1.05	151.6	2.28/0.84	156.4	3.16/1.32	2.41/1.01
0.5(1)	2.80/1.17	3.225(16)/1.00	152.3(11)	2.90/1.07	151.2	2.25/0.83	158.2	3.19/1.33	2.45/1.02
0.8(1)	2.76/1.15	3.155(16)/0.98	151.9(11)	2.83/1.04	150.5	2.27/0.83	154.4	3.05/1.27	2.34/0.97
0.9(1)	2.72/1.13	3.124(15)/0.97	150.1(11)	2.79/1.02	149.6	2.27/0.84	154.0	3.03/1.26	2.34/0.98
1.3(2)	2.69/1.12	3.09(2)/0.96	151.4(14)	2.76/1.02	150.2	2.25/0.83	153.1	2.97/1.24	2.30/0.96
1.5(2)	2.65/1.10	3.048(18)/0.95	149.2(12)	2.71/1.00	148.9	2.24/0.82	151.6	2.93/1.22	2.34/0.97
1.9(2)	2.63/1.10	3.01(2)/0.93	149.5(14)	2.66/0.98	149.3	2.19/0.81	150.7	2.93/1.22	2.31/0.96
2.0(2)	2.57/1.07	3.01(2)/0.93	149.5(15)	2.67/0.98	149.5	2.18/0.80	150.6	2.90/1.21	2.35/0.98
2.4(2)	2.57/1.07	2.98(19)/0.93	148.6(13)	2.63/0.97	148.8	2.17/0.80	148.3	2.85/1.19	2.32/0.97
3.3(2)	2.52/1.05	2.914(10)/0.90	146.8(6)	2.52/0.93	147.3	2.18/0.80	144.0	2.72/1.13	2.25/0.94
4.5(2)	2.44/1.02	2.893(14)/0.90	145.2(9)	2.50/0.92	145.9	2.18/0.80	139.6	2.54/1.06	2.28/0.95
Rank	19	11	-	13	-	3	-	21	17
ΔRR	0.20	0.13	-	0.18	-	0.06	-	0.32	0.10

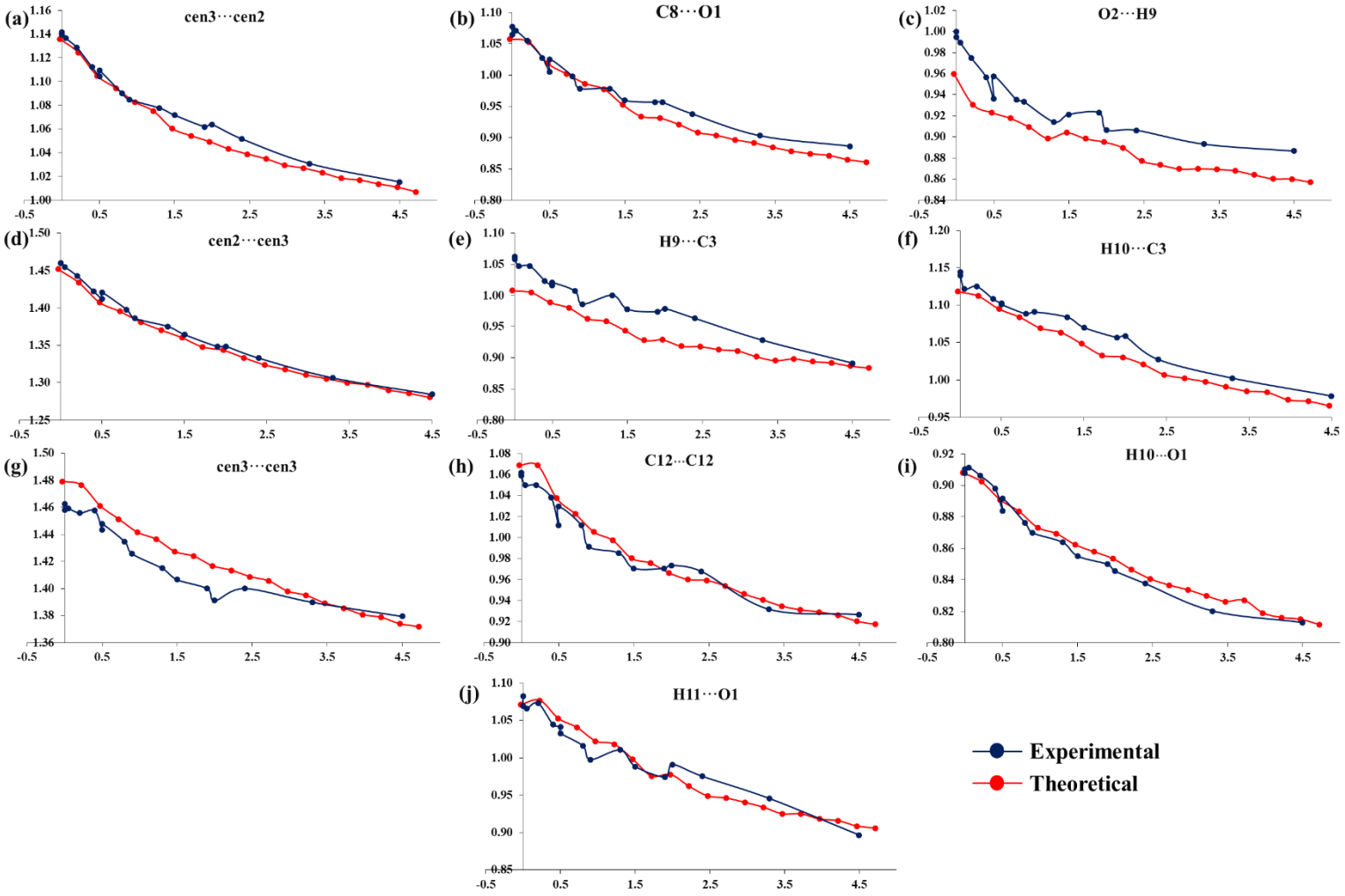

Figure 3AP.1 Variation of the Reduction Ratio (RR), calculated for interatomic contacts involving atoms of the reference (*x,y,z*) adduct and atoms of neighbouring symmetry generated adducts, as a function of pressure for *NISac.Py*. The neighbouring atom belong to: (a)-(d) (*1/2-x,-1/2+y,1-z*), (e)-(f) (*-1/2+x, y,1/2+z*) and (g)-(j) (*1/2-x,1-y,3/2-z*), symmetry generated adducts.

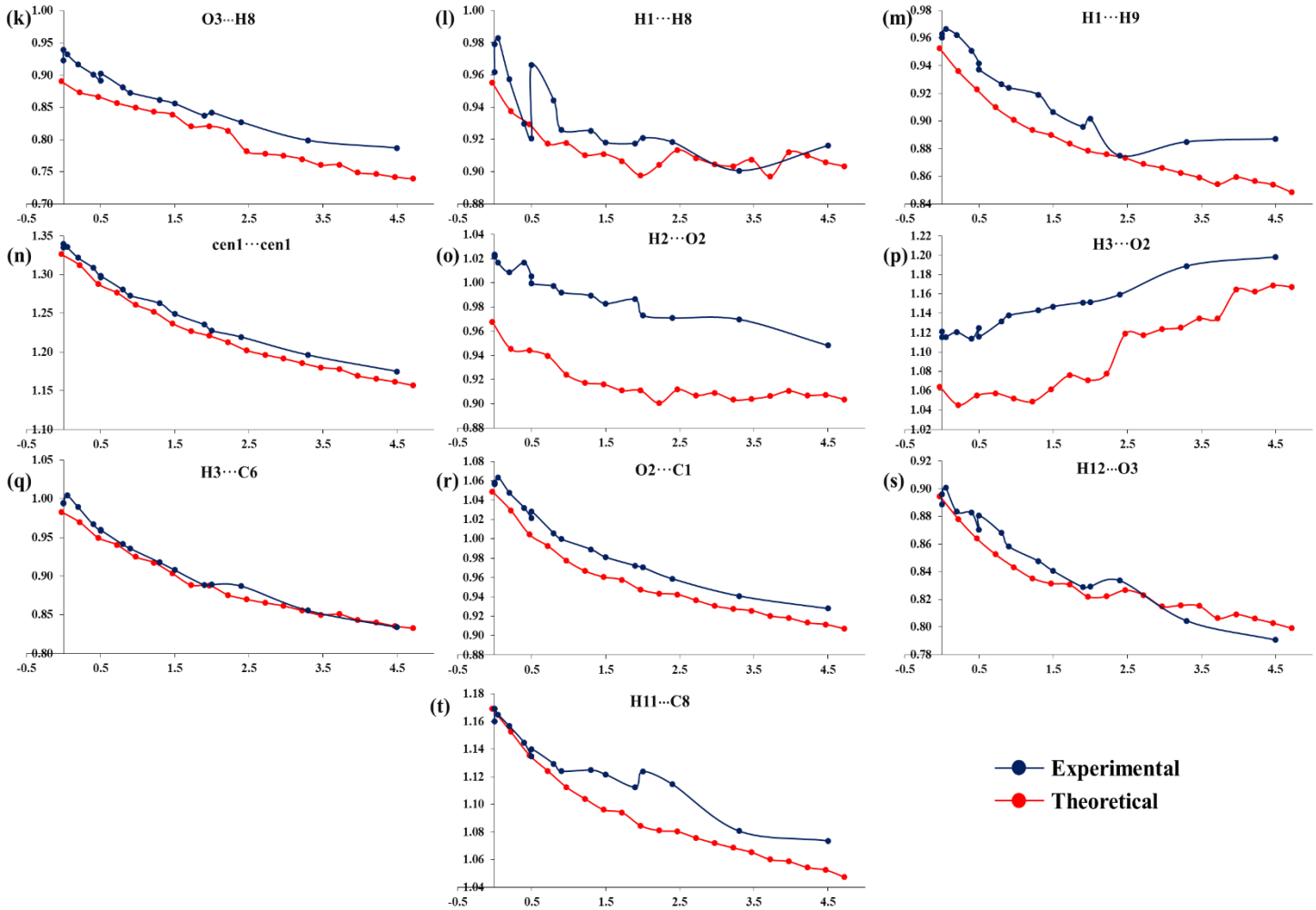

Figure 3AP.2 Variation of the Reduction Ratio (RR), calculated for interatomic contacts involving atoms of the reference (*x,y,z*) adduct and atoms of neighbouring symmetry generated adducts, as a function of pressure for *NISac.Py*. The neighbouring atom belong to: (k)-(m) (*1/2-x,1-y,1/2-z*), (n)-(q) (*1-x, 1/2+y,1/2-z*) and (r)-(t) (*x,1/2-y,1/2+z*), symmetry generated adducts.

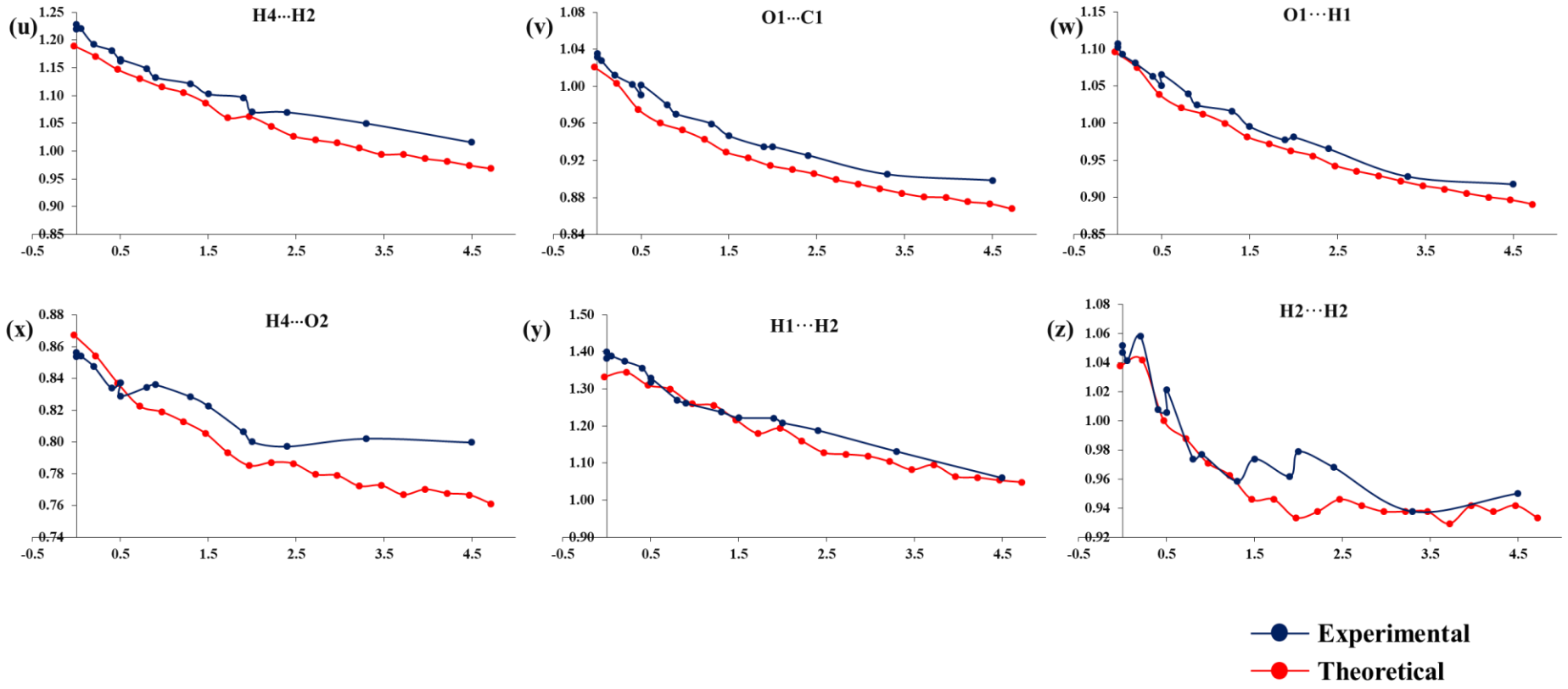

Figure 3AP.3 Variation of the Reduction Ratio (RR), calculated for interatomic contacts involving atoms of the reference (*x,y,z*) adduct and atoms of neighbouring symmetry generated adducts, as a function of pressure for *NISac.Py*. The neighbouring atom belong to: (u)-(w) (*x,3/2-y,1/2+z*), (x) (*1-x, 1-y,1-z*) and (y)-(z) (*1-x, 1-y,-z*), symmetry generated adducts.

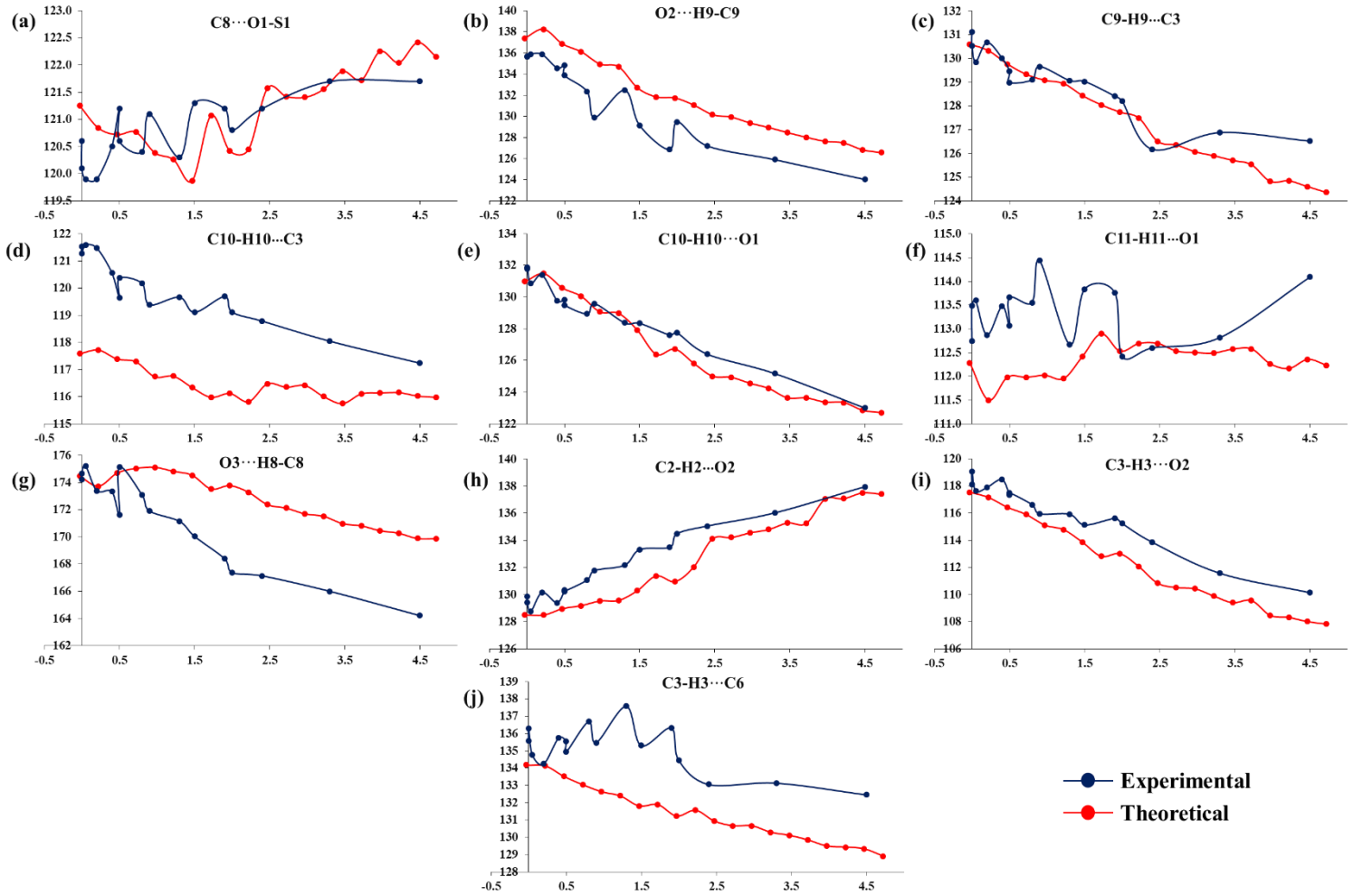

Figure 3AP.4 Variation of the interatomic interaction angle, involving the atoms of the reference (*x,y,z*) adduct and atoms of neighbouring symmetry generated adducts, as a function of pressure for *NISac.Py*. The neighbouring atoms belong to: (a)-(b) (*1/2-x,-1/2+y,1-z*), (c)-(d) (*-1/2+x,y,1/2+z*), (e)-(f) (*1/2-x,1-y,3/2-z*), (g) (*1/2-x,1-y,1/2-z*) and (h)-(j) (*1-x,1/2+y,1/2-z*), symmetry generated adducts.

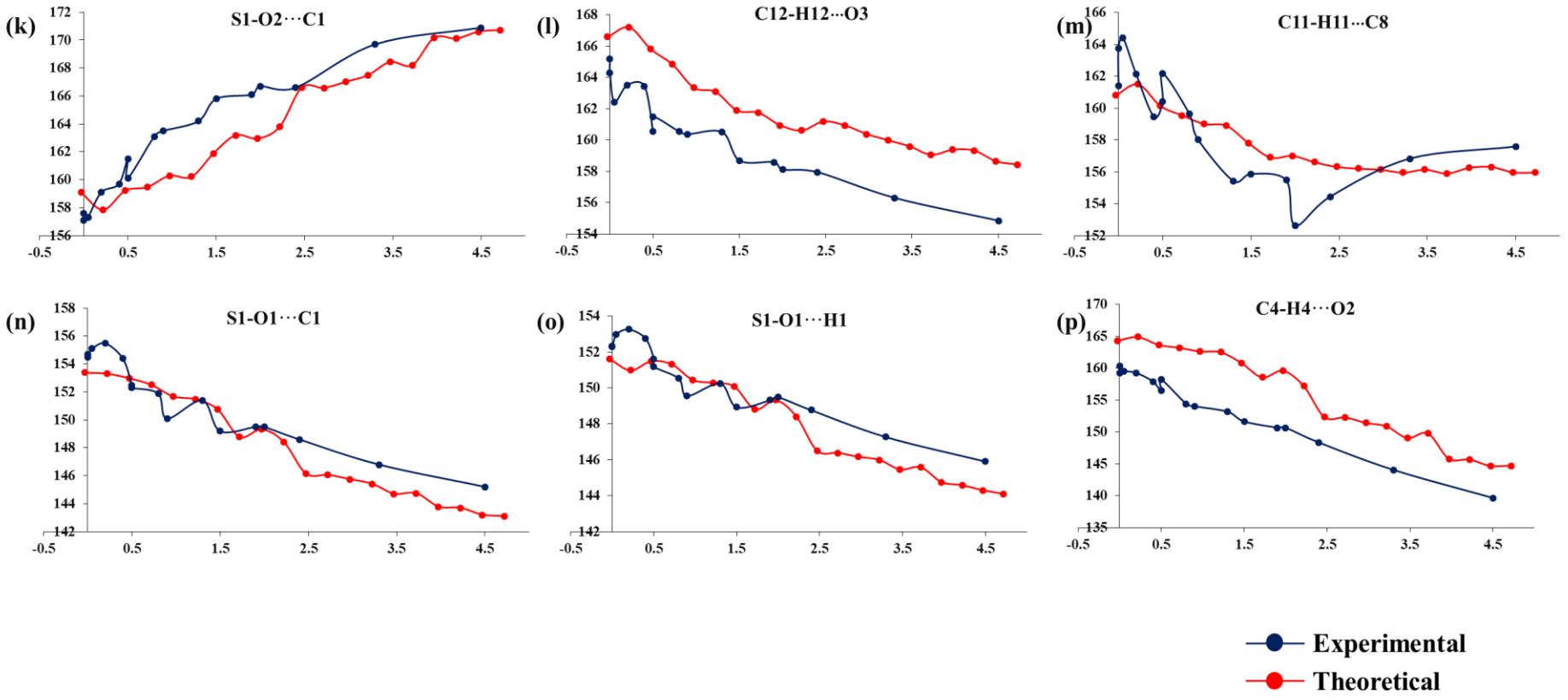

Figure 3AP.5 Variation of the interatomic interaction angle, involving the atoms of the reference (*x,y,z*) adduct and atoms of neighbouring symmetry generated adducts, as a function of pressure for *NISac.Py*. The neighbouring atoms belong to: (k)-(m) (*x,1/2-y,1/2+z*), (n)-(o) (*x,3/2-y,1/2+z*) and (p) (*1-x, 1-y,1-z*), symmetry generated adducts.

Table 3AP.7 Total intermolecular interaction energies obtained from the theoretical high-pressure structures. All energies are given in kJ/mol. Total interaction energy and ΔE are shown as left/right entries. $\Delta E = E_{x\ GPa} - E_{0.00(5)\ GPa}$, whereas for the binary adducts that are coming into the molecular shell at high pressure Y only, $\Delta E = E_{X\ GPa} - E_{Y\ GPa}$.

Pressure (GPa)	**-0.03**	**0.22**	**0.72**	**1.22**	**1.72**	**2.22**	**2.72**	**3.22**	**3.72**	**4.22**	**4.72**
1/2-x,-1/2+y,1-z	-82.6/0.0	-85.8/-3.2	-90/-7.4	-93.2/-10.6	-95.4/-12.8	-96.3/-13.7	-97.6/-15.0	-97.9/-15.3	-98.1/-15.5	-98/-15.4	-97.6/-15.0
1/2-x,1-y,1/2-z	-29.6/0.0	-30.9/-1.3	-31.2/-1.6	-31.9/-2.3	-33.2/-3.6	-33.2/-3.6	-36/-6.4	-35.8/-6.2	-35.4/-5.8	-36.8/-7.2	-36.1/-6.5
x,1/2-y,-1/2+z	-22.1/0.0	-23.3/-1.2	-25/-2.9	-26.2/-4.1	-26.3/-4.2	-26.5/-4.4	-25.9/-3.8	-25.8/-3.7	-25.8/-3.7	-25.0/-2.9	-24.6/-2.5
x,3/2-y,-1/2+z	-0.6/0.0	-0.9/-0.3	-1.3/-0.7	-1.2/-0.6	-0.8/-0.2	-0.8/-0.2	-0.4/0.2	-0.4/0.2	-0.2/0.4	0.0/0.6	0.1/0.7
1/2-x,1-y,3/2-z	-80.3/0.0	-80.7/-0.4	-85.2/-4.9	-87.8/-7.5	-91.4/-11.1	-92.5/-12.2	-94.3/-14	-95/-14.7	-95.4/-15.1	-96/-15.7	-95.9/-15.6
1-x,1-y,1-z	-27.3/0.0	-27.7/-0.4	-29/-1.7	-29.3/-2.0	-30.3/-3.0	-30.5/-3.2	-31.4/-4.1	-31.6/-4.3	-31.9/-4.6	-32.4/-5.1	-32.6/-5.3
1-x,-1/2+y,1/2-z	-24/0.0	-24.7/-0.7	-25.5/-1.5	-26.1/-2.1	-26.2/-2.2	-26.3/-2.3	-26.3/-2.3	-26.2/-2.2	-26.2/-2.2	-25.9/-1.9	-25.7/-1.7
1-x,1-y,-z	-5.7/0.0	-5.8/-0.1	-5.9/-0.2	-6.1/-0.4	-6.2/-0.5	-6.3/-0.6	-6.4/-0.7	-6.4/-0.7	-6.4/-0.7	-6.4/-0.7	-6.5/-0.8
-1/2+x,y,1/2+z	-5.3/0.0	-5.4/-0.1	-5.4/-0.1	-5.6/-0.3	-5.5/-0.2	-5.3/0	-5/0.3	-4.6/0.7	-4.4/0.9	-4/1.3	-3.5/1.8
-x+1/2, -y, -z+3/2								-15.8/0.0	-16.1/-0.3	-16.5/-0.7	-16.8/-1.0
x+1/2, -y+3/2, z											-3.4/0.0

Table 3AP.8 Results obtained from the topological calculations of the isolated *NISac.Py* adduct, extracted from the crystal structure at each applied pressure for the experimental high-pressure dataset of *NISac.Py*. N1···I1/I1···N2 distances are shown as left/right entries. The gathered QTAIM topological and energetic properties of ρ(r) at both N1···I1/I1···N2 BCPs are given as left/right values: the electron density (ρ), its laplacian ($\nabla^2\rho$), the total energy density ($H=V+G$) as well as the ratio between the electron potential (V) and kinetic (G) densities ($|V|/G$), and its values normalized to ρ. The delocalization index at BCPs is denoted as DI. ΔX (X=ρ, $\nabla^2\rho$, $|V|/G$, DI) is the difference between left and right values.

Pressure (GPa)	Distance (Å)	ρ(r) (eÅ^{-3})	$\nabla^2\rho$(r) (eÅ^{-5})	$\nabla^2\rho$(r)/ρ(r) (Å^{-2})	$\|V\|/G$	H(a.u.)	H/ρ (a.u.)	D.I	$\Delta\rho$ (eÅ^{-3})	$\Delta(\nabla^2\rho$(r)) (eÅ^{-5})	$\Delta(\|V\|/G)$	Δ (DI)
0.00(5)	2.240/2.295	0.574/0.502	2.725/3.038	4.744/6.056	1.498/1.401	-0.028/-0.021	-0.330/-0.283	0.746/0.617	0.073	-0.313	0.098	0.128
0.00(5)	2.23/2.252	0.585/0.518	2.801/3.216	4.786/6.210	1.501/1.402	-0.029/-0.022	-0.337/-0.292	0.751/0.624	0.067	-0.415	0.099	0.127
0.05(5)	2.21/2.258	0.590/0.518	2.851/3.219	4.830/6.214	1.501/1.402	-0.030/-0.022	-0.34/-0.293	0.754/0.624	0.072	-0.368	0.099	0.130
0.20(5)	2.231/2.26	0.572/0.525	2.732/3.226	4.773/6.139	1.496/1.409	-0.028/-0.023	-0.329/-0.298	0.741/0.634	0.047	-0.494	0.087	0.108
0.4(1)	2.21/2.256	0.580/0.524	2.770/3.224	4.777/6.157	1.499/1.407	-0.029/-0.023	-0.333/-0.296	0.747/0.631	0.056	-0.454	0.092	0.116
0.5(1)	2.214/2.235	0.577/0.542	2.788/3.346	4.829/6.174	1.495/1.416	-0.028/-0.025	-0.332/-0.308	0.741/0.645	0.036	-0.558	0.079	0.096
0.5(1)	2.231/2.245	0.572/0.532	2.748/3.278	4.806/6.167	1.494/1.411	-0.028/-0.024	-0.329/-0.301	0.739/0.636	0.040	-0.529	0.083	0.102
0.8(1)	2.233/2.219	0.572/0.563	2.798/3.505	4.893/6.225	1.490/1.424	-0.028/-0.027	-0.328/-0.320	0.733/0.660	0.009	-0.707	0.066	0.073
0.9(1)	2.220/2.203	0.574/0.569	2.832/3.556	4.936/6.251	1.488/1.425	-0.028/-0.027	-0.330/-0.324	0.732/0.664	0.005	-0.724	0.063	0.068
1.3(2)	2.22/2.192	0.568/0.586	2.815/3.663	4.955/6.254	1.485/1.433	-0.027/-0.029	-0.326/-0.334	0.726/0.677	-0.018	-0.848	0.052	0.049
1.5(2)	2.23/2.181	0.565/0.600	2.819/3.791	4.988/6.321	1.481/1.436	-0.027/-0.030	-0.324/-0.342	0.720/0.688	-0.035	-0.972	0.046	0.032
1.9(2)	2.25/2.17	0.560/0.604	2.779/3.810	4.961/6.312	1.481/1.438	-0.027/-0.031	-0.321/-0.344	0.717/0.690	-0.043	-1.031	0.043	0.027
2.0(2)	2.26/2.14	0.552/0.626	2.761/4.038	5.003/6.455	1.474/1.440	-0.026/-0.033	-0.316/-0.356	0.708/0.707	-0.074	-1.277	0.034	0.000
2.4(2)	2.26/2.168	0.550/0.611	2.717/3.905	4.938/6.387	1.477/1.438	-0.026/-0.032	-0.315/-0.348	0.711/0.697	-0.061	-1.188	0.039	0.014
3.3(2)	2.248/2.218	0.558/0.584	2.751/3.560	4.933/6.091	1.481/1.440	-0.026/-0.029	-0.320/-0.335	0.719/0.679	-0.027	-0.810	0.041	0.040
4.5(2)	2.249/2.162	0.572/0.641	2.914/4.110	5.093/6.413	1.480/1.449	-0.028/-0.035	-0.329/-0.365	0.716/0.713	-0.069	-1.196	0.031	0.003

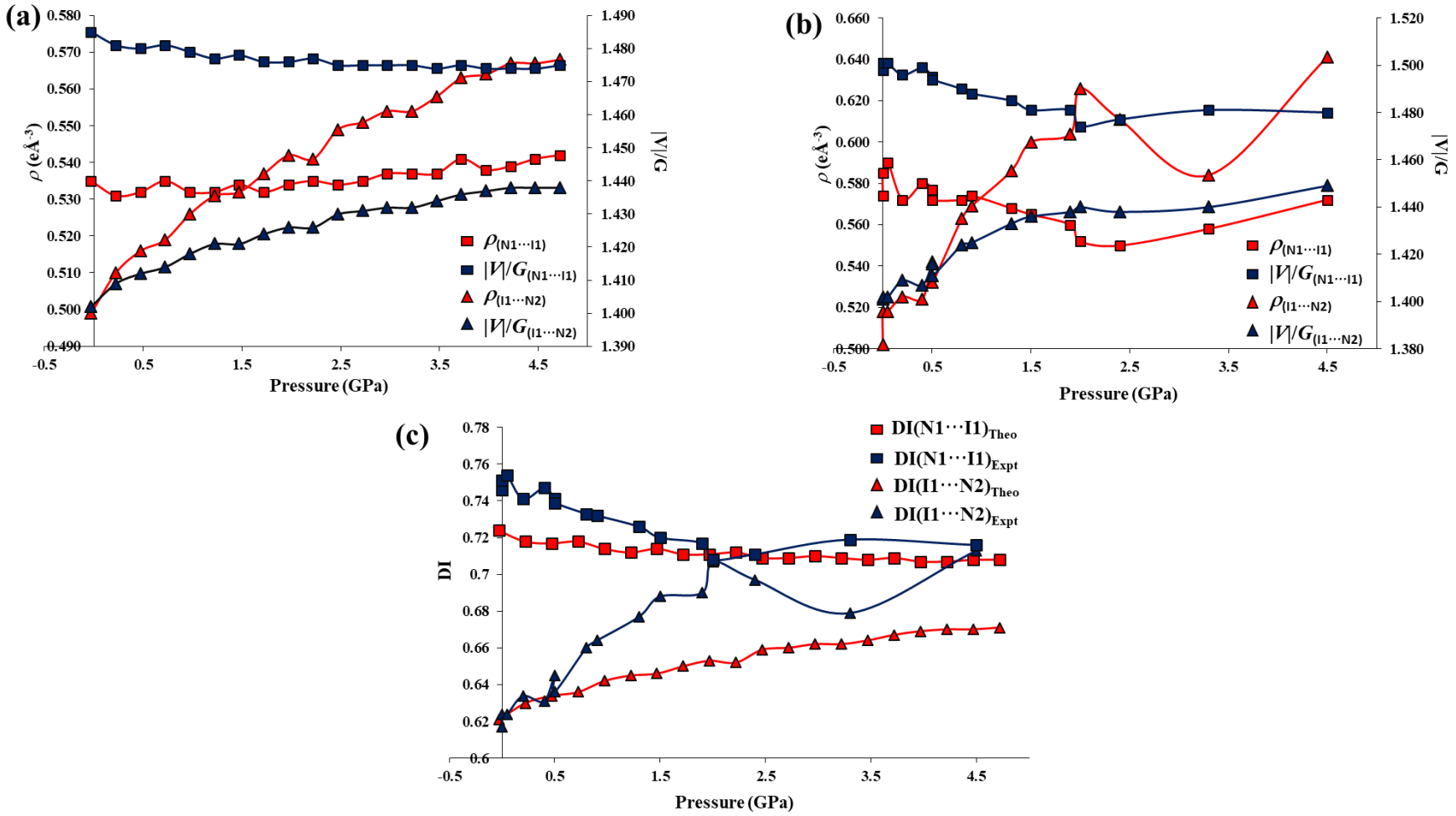

Figure 3AP.6 Topological parameters calculated at N1···I1 and I1···N2 BCPs: ρ and $|V|/G$ for (a) theoretical (b) experimental datasets, (c) delocalization index (DI) for theoretical and experimental datasets.

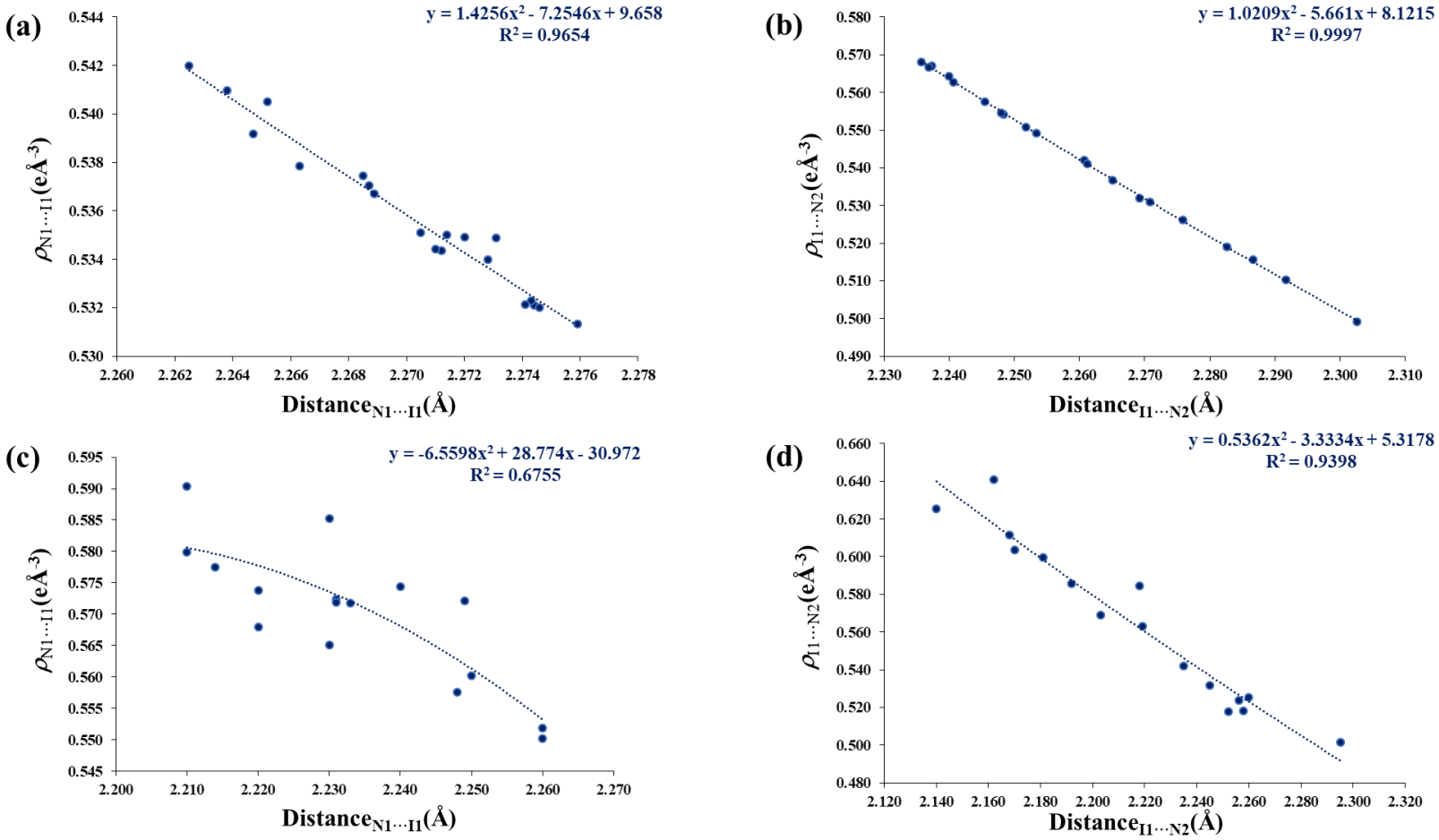

Figure 3AP.7 Plots of: $\rho_{N1\cdots I1}$ vs $Distance_{N1\cdots I1}$ for (a) theoretical (c) experimental datasets, $\rho_{I1\cdots N2}$ vs $Distance_{I1\cdots N2}$ for (b) theoretical (d) experimental datasets. Data points were fitted with a 2nd order polynomial function. The corresponding polynomial equation and statistical R^2 values are shown within each plot.

Section 3AP.1 Variation of charges with pressure

The variation in the charges of the atomic/molecular entities were also extracted as a function of pressure. Charges of the molecular entities are obtained from the summation of Bader's atomic charges (B3LYP/Def2TZVPP) in the isolated *NISac.Py* adduct extracted from the crystal structure at each applied pressure (**Table 3AP.9**). The total charge of the saccharinate (Nsac) moiety, which is acting as the donor entity in the HaB motif, is found to be almost unaffected with pressure. On the other hand, the I atom becomes slightly more positive with increasing pressure, showing an overall change of +0.03 *e* between -0.03 GPa and 4.72 GPa. At the same time, the pyridine moiety (Py), which acts as the acceptor entity in the HaB motif becomes slightly negative with pressure, showing an overall change of -0.03 *e* between -0.03 GPa and 4.72 GPa. Altogether, these features indicate only slight modifications in the net charges of atomic and molecular entities involved in the HaB interaction upon the action of the external pressure. A similar observation can be also drawn from the topological calculations performed with the experimental dataset (**Table 3AP.10**).

Table 3AP.9 Charges of atomic and molecular entities as a function of pressure for the theoretical high-pressure dataset of *NISac.Py*. Charges of the molecular entities are obtained from the summation of Bader's atomic charges (B3LYP/Def2TZVPP) with the *NISac.Py* isolated adduct extracted from the crystal structure at each calculated pressure. Nsac- saccharinate molecular entity, Py- pyridine molecular entity, I- iodine atom.

Pressure (GPa)	**-0.03**	**0.22**	**0.47**	**0.72**	**0.97**	**1.22**	**1.47**	**1.72**	**1.97**	**2.22**	**2.47**	**2.72**	**2.97**	**3.22**	**3.47**	**3.72**	**3.97**	**4.22**	**4.47**	**4.72**
Nsac (*e*)	0.19	0.19	0.19	0.19	0.19	0.19	0.19	0.19	0.19	0.19	0.19	0.19	0.19	0.19	0.19	0.19	0.19	0.19	0.19	0.19
I (*e*)	0.46	0.47	0.47	0.47	0.47	0.47	0.47	0.48	0.48	0.48	0.48	0.48	0.48	0.48	0.48	0.49	0.49	0.49	0.49	0.49
Py (*e*)	-0.65	-0.65	-0.66	-0.66	-0.66	-0.66	-0.66	-0.66	-0.67	-0.67	-0.67	-0.67	-0.67	-0.67	-0.67	-0.68	-0.68	-0.68	-0.68	-0.68

Table 3AP.10 Charges of atomic and molecular entities as a function of pressure for the experimental high-pressure dataset of *NISac.Py*. Charges of the molecular entities are obtained from the summation of Bader's atomic charges (B3LYP/Def2TZVPP) with the *NISac.Py* isolated adduct extracted from the crystal structure at each applied pressure. Nsac-saccharinate molecular entity, Py- pyridine molecular entity, I- iodine atom.

Pressure (GPa)	**0.00 (5)**	**0.00 (5)**	**0.05 (5)**	**0.20 (5)**	**0.4 (1)**	**0.5 (1)**	**0.5 (1)**	**0.8 (1)**	**0.9 (1)**	**1.3 (2)**	**1.5 (2)**	**1.9 (2)**	**2.0 (2)**	**2.4 (2)**	**3.3 (2)**	**4.5 (2)**
Nsac (*e*)	0.18	0.17	0.17	0.18	0.18	0.18	0.18	0.18	0.17	0.18	0.17	0.18	0.17	0.17	0.18	0.18
I (*e*)	0.47	0.48	0.49	0.48	0.48	0.49	0.49	0.49	0.50	0.50	0.51	0.50	0.51	0.51	0.49	0.52
Py (*e*)	-0.66	-0.66	-0.66	-0.66	-0.66	-0.66	-0.66	-0.67	-0.67	-0.68	-0.68	-0.68	-0.69	-0.68	-0.68	-0.69

Section 3AP.2 Non-covalent interaction (NCI) plots analysis

Modifications in the non-covalent interactions formed within different dimers of adduct were visualized as a function of pressure *via* non-covalent interactions (NCI) plots and reduced density gradient (RDG) scatter plots generated using the Multiwfn software (Lu & Chen, 2012) in conjunction with the VMD tool (version 1.9.3). This will provide a visual track of either the stabilizing or destabilizing behaviour of intermolecular interactions at any given pressure, simply through the analysis of iso-surfaces coloured according to the sign(λ_2)ρ values (**section 2.2.3**). Iso-surfaces can give a clear distinction between different types of intermolecular interactions, where blue colour indicates a strong attractive interaction, green colour indicates a van der Waals interaction and red colour indicates a repulsive or steric interaction. In addition, ρ(**r**) values corresponding to the troughs in 2D RDG scatter plot can give further insight into the enhancing or diminishing strength of an intermolecular interactions under varying pressure.

To simplify the discussion, and to avoid the repetition of information, the results obtained for two calculated structures, at the lowest (-0.03 GPa) and the highest (4.72 GPa) pressure, are only discussed here. Accordingly, **Figure 3AP.8**, **9** and **10** represents the 2D scatter plots and 3D NCI plots for the nine crystallographically independent dimers of adducts obtained from the *NISac.Py* crystal structure (at -0.03GPa and 4.72GPa). As described **in section 2.2.3,** the regions or troughs observed on the negative side of sign(λ_2)ρ represent attractive non-covalent interactions, whereas those on the positive side represent a non-bonded repulsive interaction between the atoms. Iso-surfaces are coloured according to the sign(λ_2)ρ (a.u.) values, from -0.035 to 0.020 a.u. A clear modification of the iso-surfaces is evident from low to high pressure, with formation of additional short contacts [both attractive and repulsive; on negative and positive sides of sign(λ_2)ρ]. Red iso-surfaces observed in the middle of rings, and at the periphery of N1···I1 and I1···N2 BCPs, correspond to steric effects present in the system. Other observations that can be drawn from the analysis of scatter and the NCI plots are given below:

(1) At the highest pressure 4.72 GPa [for (a)-(i)], the intermolecular interactions formed between the *NISac.Py* adducts are still in the stabilizing zone. They do not show the appearance of any additional red iso-surfaces that could correspond to repulsive interactions or to a destabilization of the molecular pairs.
(2) Contribution of van der Waals interactions between the molecular adducts [for (a)-(i)] increase from -0.03GPa to 4.72 GPa, as observed from the enlargement of green (light and

dark green) iso-surfaces. This is expected because dimers approach each other in space upon increasing the pressure and as a consequence the void volume diminishes.

(3) Troughs corresponding to red iso-surfaces (observed at the middle of rings, and at the periphery of N1···I1 and I1···N2 BCPs) in the 2D scatter plots [for (a)-(i)] are largely unaffected under pressure. Only a minor fraction of shift towards more positive values of $\text{sign}(\lambda_2)\rho$ is observed from low to high-pressure, indicating that molecular dimers are still in the stabilizing zone with a minor increase of the steric effect.

(4) The contribution of the repulsive component between molecular dimers increases with pressure [for (a)-(i)]. This is evident from the presence of additional dark green troughs observed from 2D scatter plots at 4.72 GPa, as compared to -0.03 GPa. This is also occurring due to the approach of the molecular adducts to each other in space while increasing pressure.

(5) The peaks corresponding to the non-covalent intermolecular interactions (light green) shift towards a more negative value of $\text{sign}(\lambda_2)\rho$ at high-pressure [for (a)-(i)]. This feature indicates an increase in the electron density $\rho(\mathbf{r})$ at BCP, suggesting the strengthening of non-covalent interactions with pressure.

(6) In case of (c) and (d) some blue regions are appearing on the iso-surfaces at 4.72 GPa with $\rho(\mathbf{r}) > 0.02$ a.u. (shown with blue circles on the corresponding NCI plots). The corresponding troughs can be also observed from scatter plots. These regions correspond to the C-H···O HB interactions, which become strengthened and more stabilized upon the application of pressure. These HB interactions were also present at -0.03 GPa, but with light green iso-surfaces and $\rho(\mathbf{r}) \sim 0.01$ a.u.

Thus, the comparison of RDG scatter plots and NCI plots at different applied pressures can guide us to a qualitative idea about the stabilizing or destabilizing situation of the molecular pairs upon increasing the pressure. This can be understood from the modification of iso-surfaces (along with their colouring scheme) and from the changes in the $\rho(\mathbf{r})$ values that correspond to the troughs observed in the 2D scatter plots. From the same features, the enhancing or diminishing behaviour of intermolecular interactions with pressure can be also identified. A similar analysis was also carried out for the experimental dataset, comparing the adduct dimers formed at 0.00(5) GPa and 4.5(2) GPa. It gives similar results as that observed from the theoretical dataset.

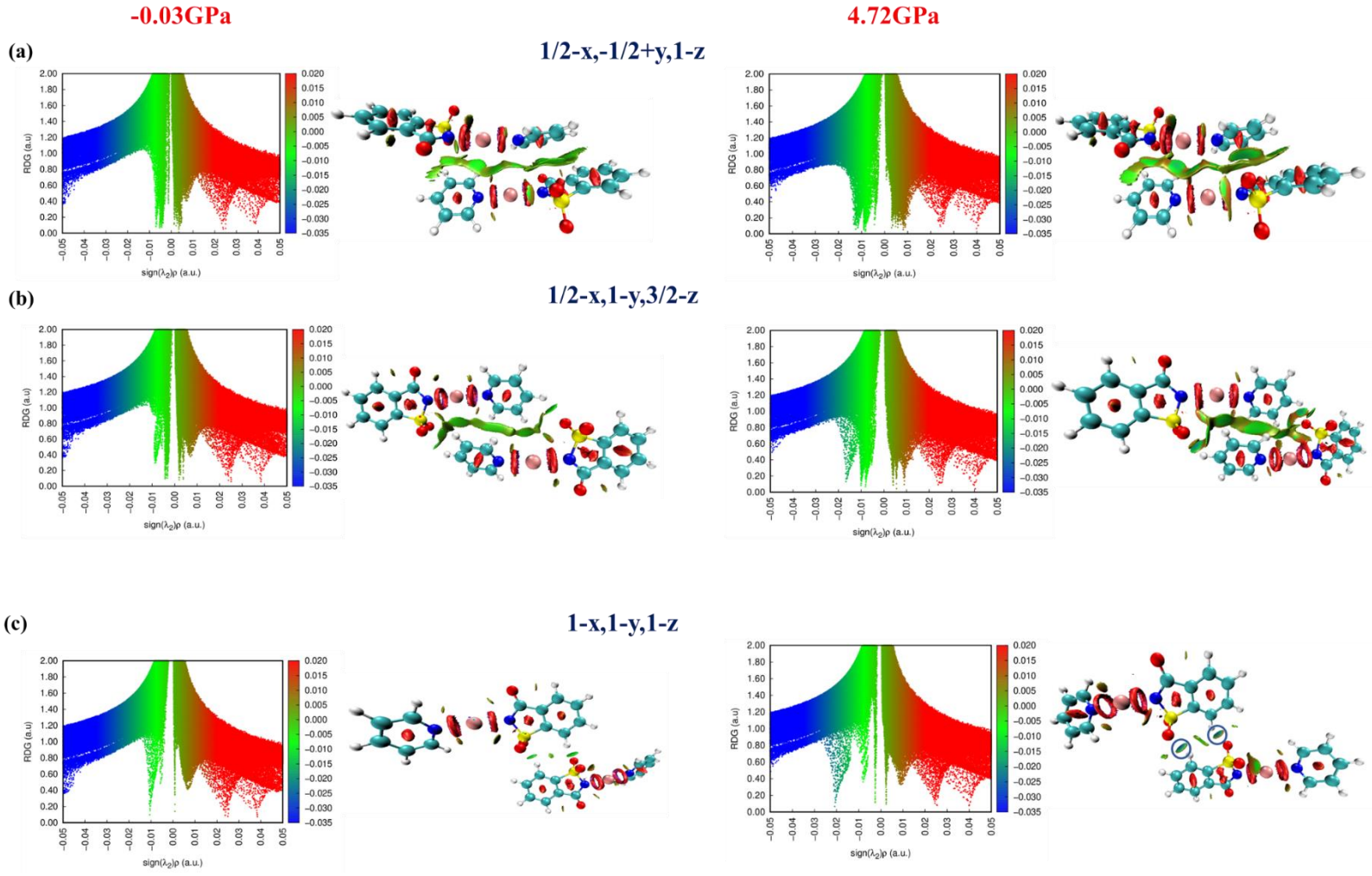

Figure 3AP.8 Dimer formed between the central (*x,y,z*) adduct and (a) (*1/2-x,-1/2+y,1-z*), (b) (*1/2-x,1-y,3/2-z*) and (c) (*1-x,1-y,1-z*), symmetry generated adducts for the theoretically calculated lowest (-0.03 GPa) and highest(4.72 GPa) pressure. RDG scatter plot (left) and non-covalent interactions (NCI) plots generated for $s(\rho)$=0.7a.u. (right) are shown. Iso-surfaces are coloured according to sign(λ_2)ρ values, from -0.035 to 0.020 a.u.

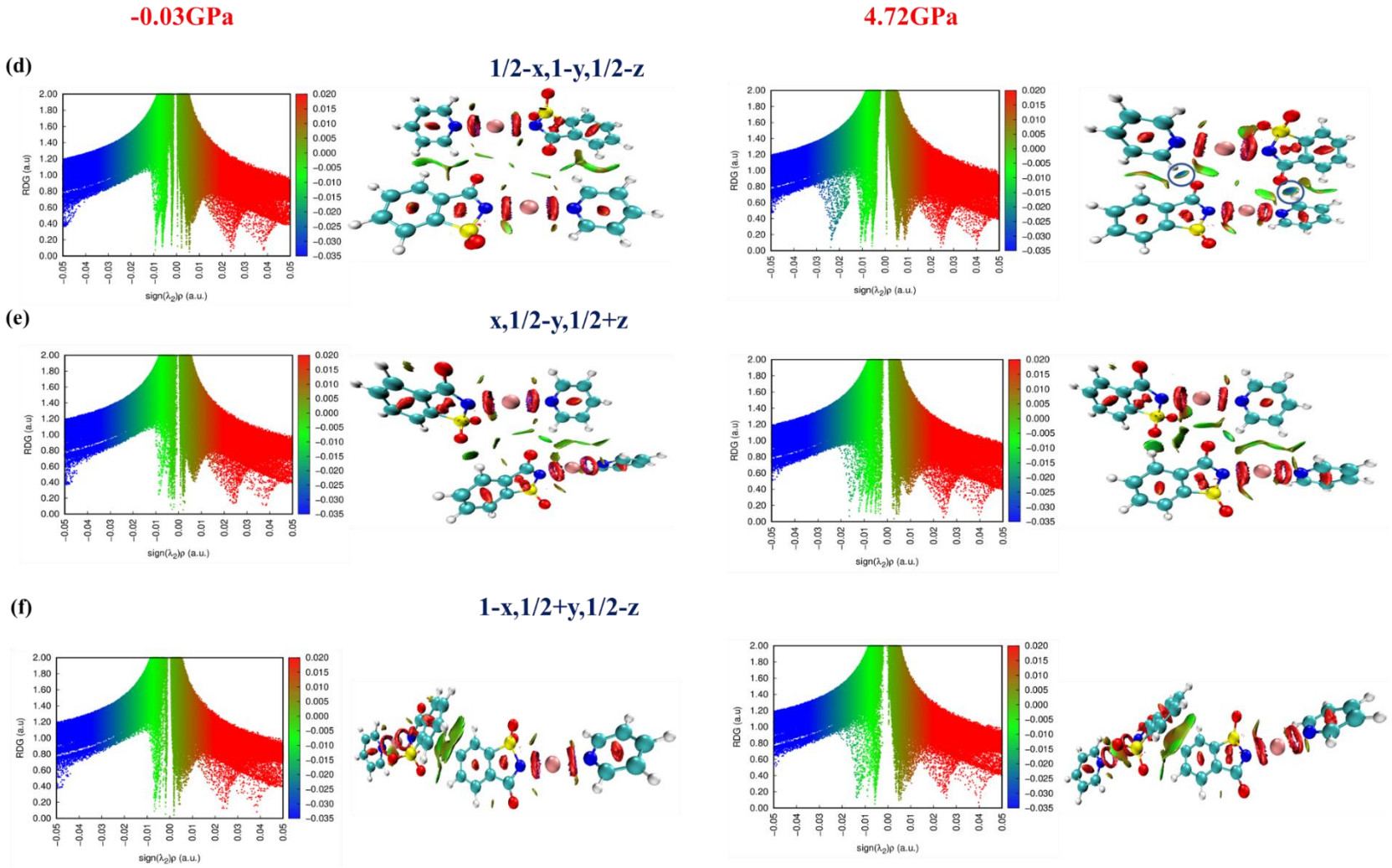

Figure 3AP.9 Dimer formed between the central (*x,y,z*) adduct and (d) (*1/2-x,1-y,1/2-z*), (e) (*x,1/2-y,1/2+z*) and (f) (*1-x,1/2+y,1/2-z*), symmetry generated adducts for the theoretically calculated lowest (-0.03 GPa) and highest (4.72 GPa) pressure. RDG scatter plot (left) and non-covalent interactions (NCI) plots generated for $s(\rho)$=0.7a.u. (right) are shown. Iso-surfaces are coloured according to sign(λ_2)ρ values, from -0.035 to 0.020 a.u.

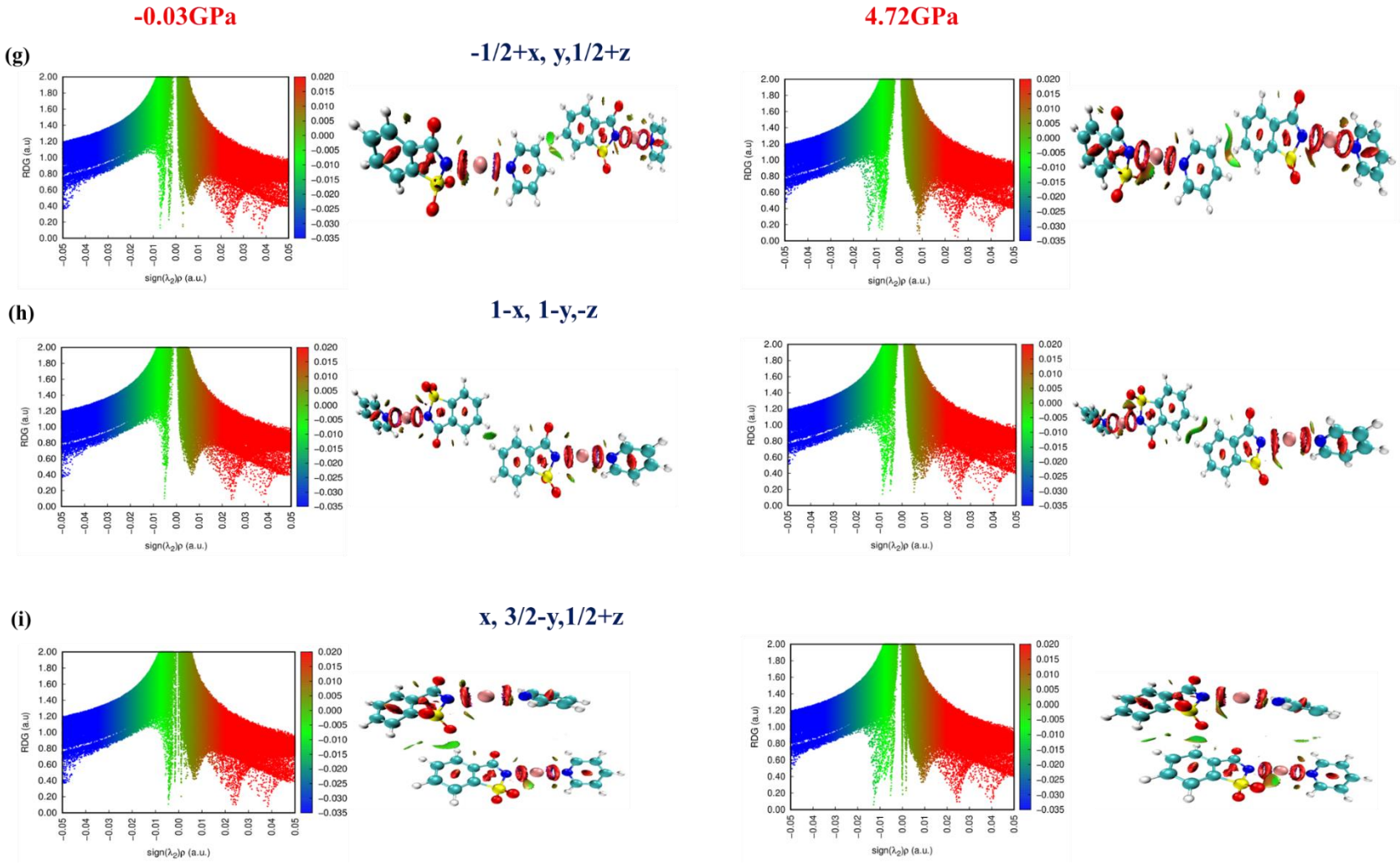

Figure 3AP.10 Dimer formed between the central (*x,y,z*) adduct and (g) (*-1/2+x, y,1/2+z*) , (h) (*1-x,1-y,-z*) and (i) (*x,3/2-y,1/2+z*), symmetry generated adduct for the theoretically calculated lowest (-0.03 GPa) and highest (4.72 GPa) pressure. RDG scatter plot (left) and non-covalent interactions (NCI) plots generated for $s(\rho)$ = 0.7a.u. (right) are shown. Iso-surfaces are coloured according to sign(λ_2)ρ values, from -0.035 to 0.020 a.u.

Section 3AP.3 Hirshfeld surface analysis

A quantitative measure of the variation in intermolecular interactions from low to high pressure can also be obtained from the analysis of Hirshfeld surfaces (**section 2.2.2**). **Figure 3AP.11** and **12** show the Hirshfeld surfaces (mapped with d_{norm}) and the corresponding 2D fingerprint plots ($d_{\mathrm{e}}\ vs\ d_{\mathrm{i}}$) generated for the crystal structures respectively calculated at -0.03 GPa and 4.72 GPa. On Hirshfeld surfaces mapped with d_{norm}, the extent of intermolecular interactions is displayed with a red-white-blue coloring scheme. Regions on the surface with red color point shorter contacts, whereas a white color points contacts around the van der Waals separation and a blue color points longer contacts. It is evident from the d_{norm} surfaces that the number of shorts contacts formed between the reference *NISac.Py* adduct with that of the neighboring adducts increases while going from low to high pressure. This is suggested by a greater number of red spots observed on the d_{norm} surface at 4.72GPa, as compared to -0.03GPa. This is occurring because of the approach of adducts to each other in space during compression. Consequently, more atoms are coming close to each other, in favor to form additional short contacts. Due to the same reason, the percentage of the white color region also increases whereas the blue color region decreases on the d_{norm} surfaces at 4.72GPa.

In addition, the percentage of interatomic interactions contributing to the total Hirshfeld surfaces can be quantitatively measured using 2D fingerprint plots, drawn between d_{e} and d_{i}. These distances $d_{\mathrm{e}}\ and\ d_{\mathrm{i}}$ correspond respectively to the nearest neighbor outside and inside of the Hirshfeld surface. While comparing the total fingerprint plots of **Figure 3AP.11** and **12**, it is evident that the overall plot is shifted towards a lower $(d_{\mathrm{e}}, d_{\mathrm{i}})$ region at high-pressure. Also, at 4.72 GPa, there are several points in the plot represented with dark green color (indicating a larger contribution to the Hirshfeld surface), which were light green or blue color at -0.03 GPa (indicating a smaller contribution to the Hirshfeld surface). This trend indicates once again the decrease of interatomic distances upon increasing the pressure. The percentage contribution of various interatomic interactions to the total surface are shown in **Table 3AP.11**, where the major contribution is coming from O···H short contacts. It is also interesting to look at the 2D fingerprint plots that correspond to different interatomic interactions, in particular the one corresponding to the O···H hydrogen bonding HB interaction. HB interactions are generally known to show characteristic spikes in the 2D fingerprint plot, which is true in our case as well. It has been found that these characteristic spikes are shifted to lower $(d_{\mathrm{e}}, d_{\mathrm{i}})$ values going from -0.03 GPa to 4.72 GPa, thus represents the shortening of O···H distances under pressure.

Another interesting region to look at is the one corresponding to C···H HB interactions. These interatomic interactions do not show any characteristic spikes at -0.03 GPa (but only a beginning of spikes), whereas clear evident spikes are present at 4.72 GPa. The appearance of these spikes indicates the dominance of C···H HB interactions at high-pressure. Another interesting region to look at is the one corresponds C···C interaction, which shows a variation in the percentage contribution from 5.1 to 6.9 upon increasing the pressure. Several points corresponding to this region are represented with green color at 4.72 GPa, which were mostly blue colored at -0.03 GPa. This is coming from the enhancement of π···π stacking motifs at high pressure with carbon atoms coming closer to each other in space.

Table 3AP.11 Percentage contribution of different interatomic interactions to the total Hirshfeld surface. The values obtained at -0.03 GPa/4.72 GPa are shown as left/right entries.

Interaction	%contribution
I···I	0.3/0.6
I···S	0.0/00
I···N	1.7/1.9
I···O	0.2/0.4
I···C	1.1/1.0
I···H	7.3/8.0
N···N	0.3/0.5
N···O	0.3/0.3
N···C	2.3/3.2
N···H	3.1/3.0
O···O	0.6/0.8
O···C	4.0/4.7
O···H	36.6/33.8
C···C	5.1/6.9
C···H	14.8/14.1
H···H	22.1/20.9

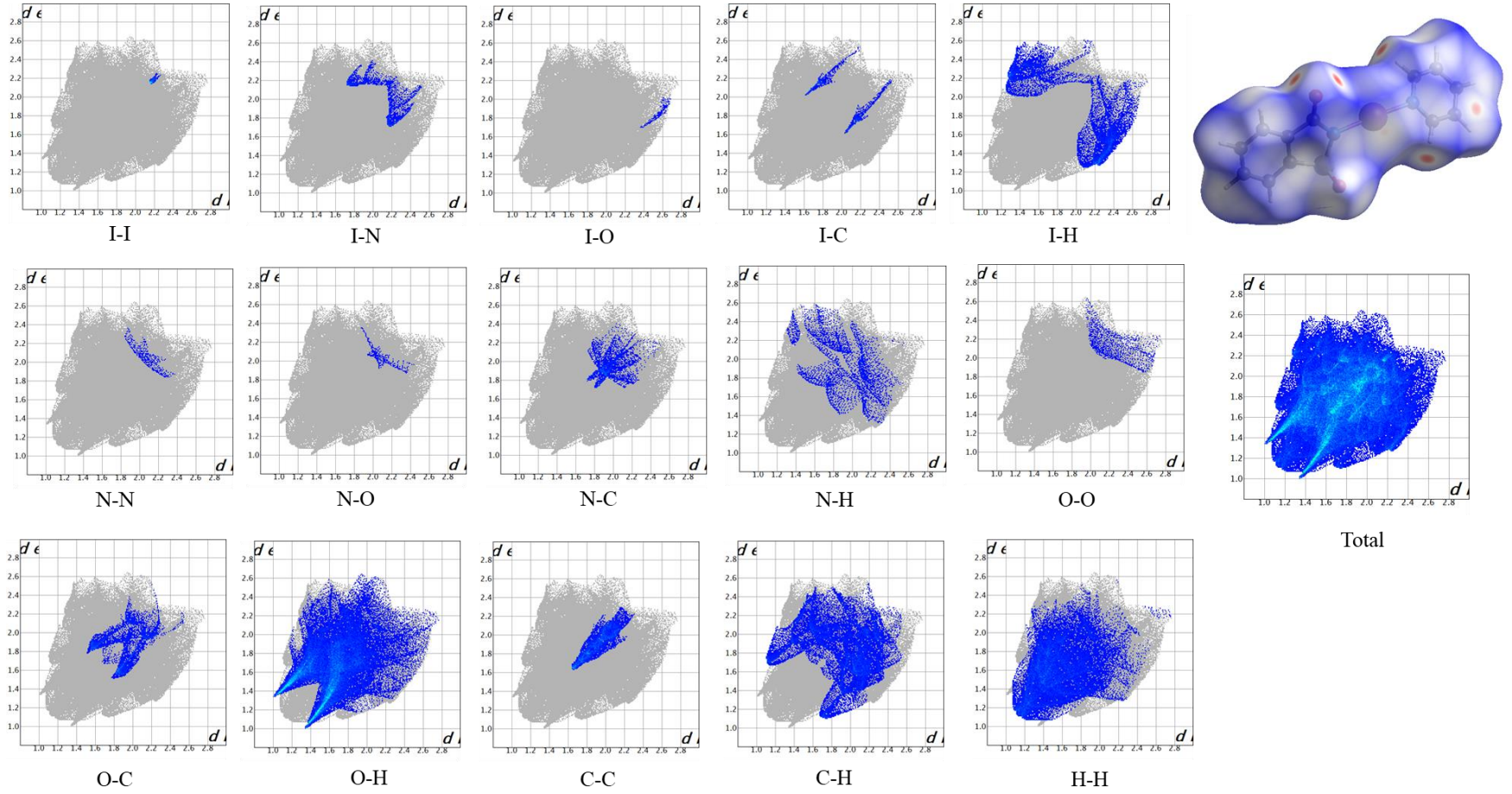

Figure 3AP.11 Hirshfeld surface (mapped with d_{norm}) and 2D fingerprint plots (d_e *vs* d_i) for the crystal structure determined at -0.03 GPa. Different atomic interactions contributing to the total interaction are shown seperately.

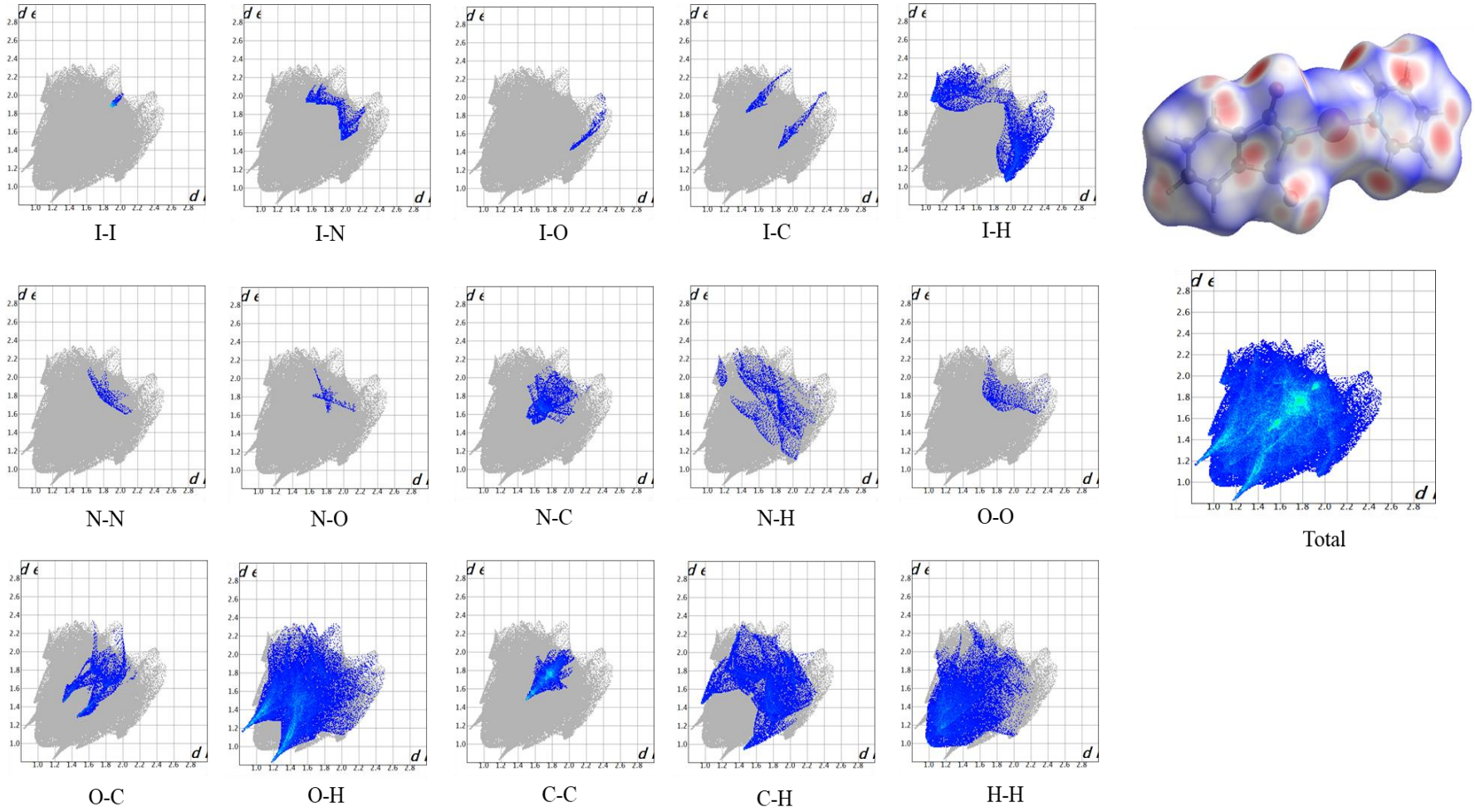

Figure 3AP.12 Hirshfeld surface (mapped with d_{norm}) and 2D fingerprint plots (d_e *vs* d_i) for the crystal structure determined at 4.72 GPa. Different atomic interactions contributing to the total interaction are shown seperately.

Table 3AP.12 Bader's atomic charges (B3LYP /Def2TZVPP) for the *NISac.4CYP* isolated adduct, and for NISac and 4CYP isolated molecules extracted from the crystal structure at ambient conditions.

	NISac.4CYP	**NISac**	**4CYP**
Atom label	**Q (*e*)**	**Q (*e*)**	**Q (*e*)**
C8	0.57		0.58
H8	0.08		0.04
C9	0.03		0.01
H9	0.07		0.05
C10	0.08		0.07
C11	0.03		0.01
H11	0.07		0.05
C12	0.53		0.54
H12	0.07		0.04
N2	-1.20		-1.14
C13	0.94		0.94
N3	-1.16		-1.19
I1	0.48	0.44	
C1	0.02	0.03	
H1	0.06	0.07	
C2	0.01	0.01	
H2	0.02	0.03	
C3	0.01	0.02	
H3	0.02	0.03	
C4	0.03	0.04	
H4	0.05	0.06	
C5	-0.18	-0.17	
C6	0.00	0.01	
C7	1.44	1.43	
O3	-1.17	-1.14	
N1	-1.37	-1.32	
S1	3.15	3.15	
O1	-1.36	-1.34	
O2	-1.36	-1.34	

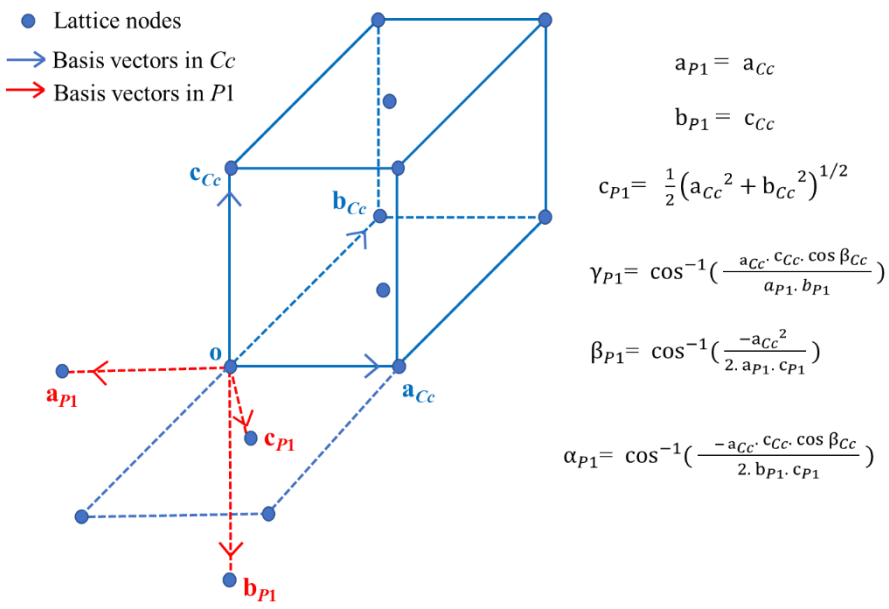

Figure 3AP.13 Lattice transformation from *Cc* to *P*1 space group. Equations relating the *Cc* and *P*1 unit cell parameters are also shown in the figure.

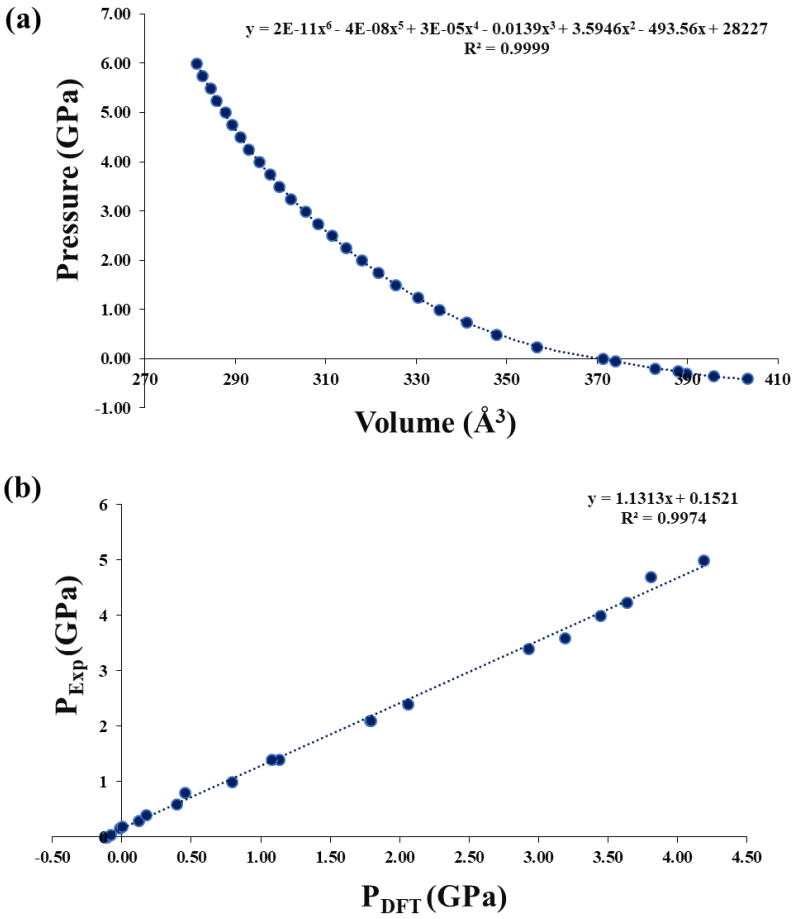

Figure 3AP.14 Plot of: (a) pressure *vs* volume per adduct drawn for the theoretical dataset, fitted with a 6th order polynomial function (b) P_{Exp} vs P_{DFT} fitted with a linear equation. Equation fitting parameters and corresponding R^2 values are given in each plot.

Section 3AP.4 Validation of phase transition process

At 4.2(2) GPa, the data reduction software (APEX3) assigned the space group of *NISac.4CYP* crystal as *P*1, while the attempt to index in the *Cc* space group setting was unsuccessful. This space group symmetry can be verified in (1) reciprocal space and (2) real space. In case of (1), the indexes of the Bragg reflection *hkl* were transformed from *P*1 to *Cc* setting using the transformation matrix **B** obtained from the Bilbao crystallographic server (**Equation AP1**).

$$(h\ k\ l)_{P1}\mathrm{B} = (h\ k\ l)_{Cc} \quad \text{Where B} = \begin{bmatrix} 1 & -1 & 0 \\ 0 & 0 & 1 \\ 0 & -2 & 0 \end{bmatrix} \qquad AP1$$

For a structure actually indexed in *Cc* space group, the *h*0*l* set of Bragg reflections (where *l* = 2n+1; odd number) should be symmetry forbidden. Therefore, these reflections should be either absent in the transformed *hkl* list or the corresponding intensities should be very close to zero within standard deviation. In the transformed *hkl* list, it is observed that the Bragg reflections corresponding to *h*0*l* (where *l* = 2n+1) are present, even in some cases with an intensity $I > 10\ \sigma(I)$. **Figure 3AP.15** shows some representative examples of such reflections, where the peak intensity appears high as compared to the background noise observed in the diffraction frames. Thus, this examination reveals that the actual space group of the crystal at 4.2(2) GPa pressure is *P*1, as suggested by the data reduction software.

In case of (2), that is in order to confirm the change in space group in the real space, the following procedures were followed,

(i) The unit cell parameters obtained in *P*1 (either after phase transition or by re-integrating the structures initially obtained in the *Cc* space group) were transformed quasi-monoclinic space group (similar to *Cc* space group obtained in region-1) using the following equations,

$$a_{Cc} = a_{P1}$$

$$c_{Cc} = b_{P1}$$

$$b_{Cc} = \left({a_{P1}}^2 + 4.{c_{P1}}^2 + 4.a_{P1}.c_{P1}.\cos\beta_{P1}\right)^{1/2}$$

$$\alpha_{Cc} = \cos^{-1}\left(\frac{a_{P1}.b_{P1}.\cos\gamma_{P1} + 2.b_{P1}.c_{P1}.\cos\alpha_{P1}}{b_{Cc}.c_{Cc}}\right)$$

$$\beta_{Cc} = \cos^{-1}\left(\frac{a_{P1}.b_{P1}.\cos\gamma_{P1}}{a_{Cc}.c_{Cc}}\right)$$

$$\gamma_{Cc} = \cos^{-1}\left(\frac{{a_{Cc}}^2 + 2.a_{Cc}.c_{Cc}.\cos\beta_{P1}}{a_{Cc}.b_{Cc}}\right)$$

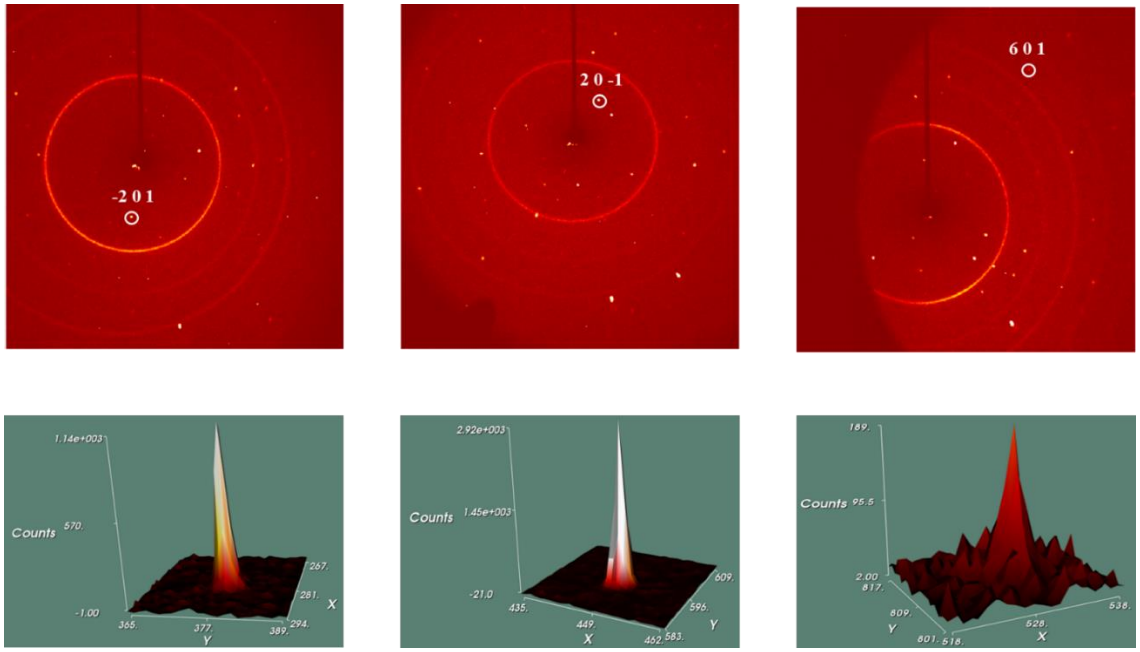

Figure 3AP.15 Representative examples of Bragg reflection *h0l* (where *l* = 2n+1) in diffraction frames obtained from data collected at 4.2(2) GPa. Selected reflections are shown encircled along with their *hkl* labels. The corresponding 3D intensity maps are shown at bottom. Labels given are corresponding to the transformed *hkl* indexes in the *Cc* space group, the corresponding indexes in *P*1 space group, are respectively from left to right -2 1 1, 2 -1 -1 and 6 1 -3.

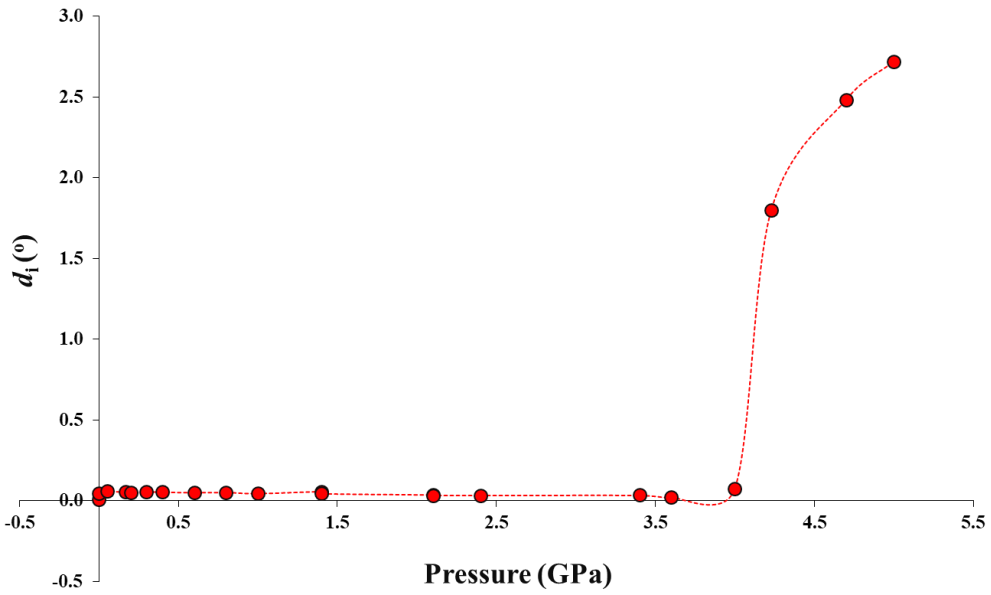

Figure 3AP.16 Plot of d_i vs Pressure

(ii) Later, a parameter d_i was calculated for each pressure i as $d_i = [(\alpha_i - 90)^2 + (\gamma_i - 90)^2]^{1/2}$, indicating the measure of deviation of α and γ angles from 90° in the transformed *Cc* unit cell setting. For an actual monoclinic space group, both α and γ should correspond to 90°.

The d_i value is very close to zero from 0.00(5) GPa to 4.0(2) GPa (**Figure 3AP.16**). This trend points that the angles α and γ are very close to 90^0 and is consistent with the fact that the data reduction software suggests the *Cc* space group until 4.0(2) GPa (largest pressure measured before the change of symmetry). At the next increased pressure [4.2(2) GPa; in region-2] d_i shows a comparatively larger value of 1.8°, indicating that α and γ angles start their deviation from 90° and the crystal structure is not anymore monoclinic. This is also consistent with the software suggestion that the space group of the crystal changes into *P*1 above 4.0(2) GPa. Afterwards, the value of d_i increases gradually with pressure, suggesting that the angles α and γ deviate more from 90° with the increasing pressure. Overall, this analysis in direct space confirms once again that the space group of *NISac.4CYP* changes from *Cc* to *P*1 above 4.0(2) GPa.

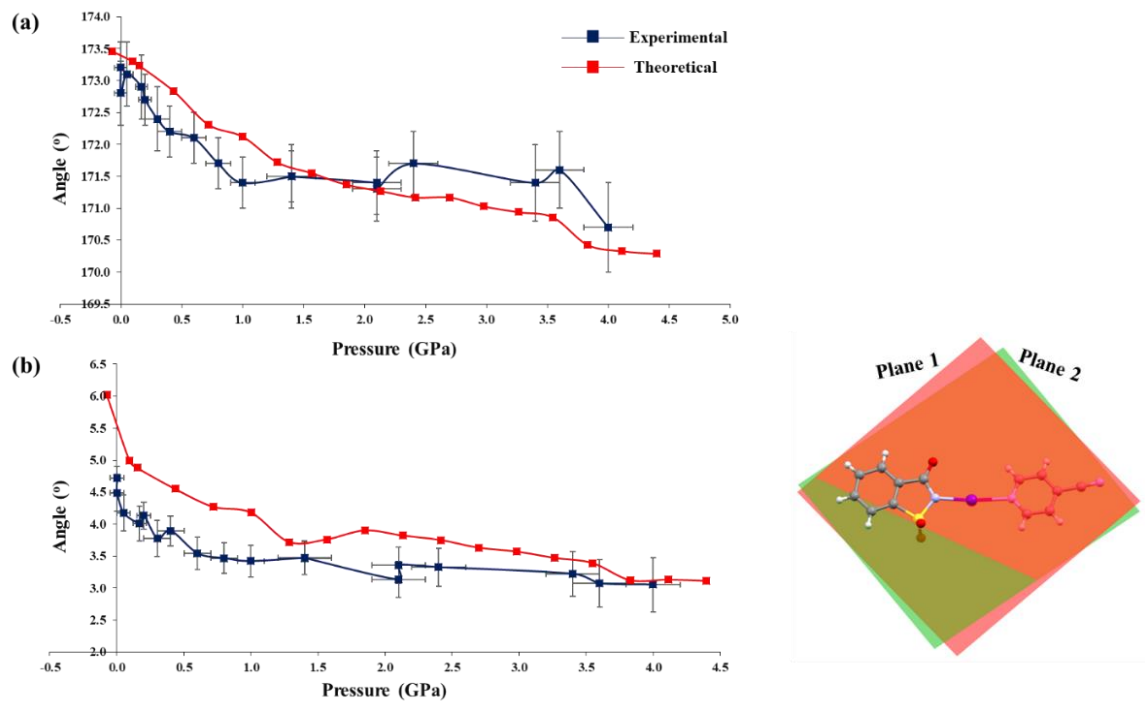

Figure 3AP.17 Variations as a function of pressure for: (a) N1···I1···N2 angle and (b) angle between molecular planes. Molecular planes are formed by the saccharinate ring – Plane 1 (excluding I and H-atoms) and the 4-cyano pyridine ring – Plane 2 (excluding H-atoms). They are shown respectively with red and green colours. Error bars are shown for experimental data. Lines connecting data are plotted for guiding eye.

Table 3AP.13 Variation of interatomic distances and angles involving I1(*x,y,z*) and atoms of neighbouring adducts, as a function of pressure for the experimental high-pressure datasets. Values within brackets are the standard deviations of the corresponding values. Distance and RR values are gathered as left/right entries. A ranking is assigned based on the RR value determined at 4.0(2) GPa, sorted from smaller to larger values. Δ(RR)= $RR_{0.00(5)\,GPa}$ - $RR_{4.0(2)\,GPa}$. The distances are given in Å and the angles are given in degrees (º).

Pressure (GPa)	*x,y,-1+z*		*x,y,1+z*		*-1/2+x,3/2-y,-1/2+z*			
	I1···C3	**I1···C2**	**N3 ···I1**	**< N3 ···I1-N1**	**I1···O2**	**< I1···O2-S1**	**I1···O1**	**<I1···O1-S1**
0.00(5)	3.903(7)/1.06	3.911(7)/1.06	4.159(9)/1.18	82.9(3)	4.309(11)/1.23	96.6(3)	4.261(11)/1.22	98.6(5)
0.00(5)	3.914(10)/1.06	3.914(9)/1.06	4.174(15)/1.18	83.3(4)	4.326(17)/1.24	96.4(6)	4.267(18)/1.22	99.0(8)
0.05(5)	3.904(10)/1.06	3.909(9)/1.06	4.169(15)/1.18	83.2(4)	4.290(16)/1.23	96.9(5)	4.243(17)/1.21	99.1(7)
0.17(5)	3.872(9)/1.05	3.887(8)/1.06	4.152(14)/1.18	83.3(4)	4.235(15)/1.21	97.3(5)	4.221(16)/1.21	98.1(7)
0.20(5)	3.866(7)/1.05	3.880(7)/1.05	4.142(10)/1.17	83.0(3)	4.230(11)/1.21	96.9(4)	4.206(12)/1.20	97.8(5)
0.3(1)	3.814(9)/1.04	3.844(8)/1.04	4.128(13)/1.17	83.6(3)	4.137(14)/1.18	97.9(5)	4.147(16)/1.18	97.4(7)
0.4(1)	3.801(7)/1.03	3.845(7)/1.04	4.115(11)/1.17	83.4(3)	4.109(11)/1.17	97.6(4)	4.129(13)/1.18	96.6(5)
0.6(1)	3.741(7)/1.02	3.807(7)/1.03	4.093(11)/1.16	84.1(3)	4.003(12)/1.14	98.4(4)	4.061(14)/1.16	95.9(6)
0.8(1)	3.725(7)/1.01	3.799(7)/1.03	4.081(10)/1.16	83.9(3)	3.981(11)/1.14	98.2(4)	4.055(12)/1.16	95.0(5)
1.0(1)	3.674(7)/1.00	3.758(8)/1.02	4.048(11)/1.15	84.6(3)	3.884(11)/1.11	98.9(4)	3.997(13)/1.14	94.1(5)
1.4(2)	3.624(7)/0.98	3.725(8)/1.01	4.020(11)/1.14	85.0(3)	3.807(11)/1.09	98.8(4)	3.935(13)/1.12	93.3(5)
1.4(2)	3.639(7)/0.99	3.735(8)/1.01	4.026(11)/1.14	84.8(3)	3.821(11)/1.09	99.0(4)	3.953(13)/1.13	93.2(6)
2.1(2)	3.552(8)/0.97	3.674(8)/1.00	3.968(11)/1.12	86.0(3)	3.691(12)/1.05	99.6(4)	3.866(14)/1.1	91.9(6)
2.1(2)	3.559(8)/0.97	3.671(8)/1.00	3.977(11)/1.13	86.3(3)	3.694(12)/1.06	99.8(4)	3.881(14)/1.11	91.5(6)
2.4(2)	3.528(8)/0.96	3.654(9)/0.99	3.959(11)/1.12	86.5(3)	3.661(12)/1.05	99.5(4)	3.840(14)/1.10	91.4(6)
3.4(2)	3.456(9)/0.94	3.601(10)/0.98	3.924(14)/1.11	87.2(4)	3.568(14)/1.02	99.8(5)	3.792(17)/1.08	89.5(7)
3.6(2)	3.443(10)/0.94	3.586(10)/0.97	3.92(14)/1.11	87.6(4)	3.548(14)/1.01	99.7(5)	3.792(18)/1.08	88.7(7)
4.0(2)	3.420(11)/0.93	3.570(11)/0.97	3.905(17)/1.11	88.4(4)	3.521(16)/1.01	100.0(5)	3.78(2)/1.08	88.5(9)
Rank	1	2	5	-	3	-	4	-
Δ(RR)	0.13	0.09	0.07	-	0.22	-	0.14	-

Table 3AP.14 Variation of interatomic distances and angles involving I1(*x,y,z*) and atoms of neighbouring adducts, as a function of pressure for the theoretical high-pressure datasets. Distance and RR values are gathered as left/right entries. A ranking is assigned based on the RR value determined at 4.0(2) GPa, sorted from smaller to larger values. Δ(RR)= $RR_{-0.07\,GPa} - RR_{4.39\,GPa}$. The distances are given in Å and the angles are given in degrees (º).

Pressure (GPa)	*x,y,-1+z*		*x,y,1+z*		*-1/2+x,3/2-y,-1/2+z*			
	I1···C3	I1···C2	N3···I1	<N3···I1-N1	I1···O2	<I1···O2-S1	I1···O1	<I1···O1-S1
-0.07	3.907/1.06	3.869/1.05	4.118/1.17	82.4	4.420/1.26	97.0	4.351/1.24	99.9
0.10	3.809/1.04	3.804/1.03	4.072/1.15	82.8	4.374/1.25	97.1	4.325/1.24	99.1
0.15	3.793/1.03	3.795/1.03	4.055/1.15	82.8	4.348/1.24	97.1	4.306/1.23	98.9
0.43	3.754/1.02	3.782/1.03	4.032/1.14	83.7	4.134/1.18	98.3	4.168/1.19	96.9
0.72	3.703/1.01	3.752/1.02	4.016/1.14	83.9	4.013/1.15	99.0	4.098/1.17	95.4
1.00	3.662/1.00	3.723/1.01	3.985/1.13	83.9	3.962/1.13	99.1	4.065/1.16	94.9
1.28	3.623/0.98	3.705/1.01	4.033/1.14	84.4	3.872/1.11	99.6	4.007/1.14	94.0
1.57	3.599/0.98	3.687/1.00	4.013/1.14	84.8	3.816/1.09	99.7	3.969/1.13	93.4
1.85	3.576/0.97	3.675/1.00	3.982/1.13	85.3	3.738/1.07	100.2	3.928/1.12	92.3
2.13	3.555/0.97	3.660/0.99	3.956/1.12	85.5	3.709/1.06	100.2	3.909/1.12	91.9
2.41	3.532/0.96	3.645/0.99	3.935/1.11	85.7	3.680/1.05	100.2	3.888/1.11	91.6
2.70	3.512/0.95	3.635/0.99	3.925/1.11	86.1	3.641/1.04	100.2	3.860/1.10	91.2
2.98	3.492/0.95	3.622/0.98	3.904/1.11	86.4	3.619/1.03	100.2	3.847/1.10	90.8
3.26	3.472/0.94	3.611/0.98	3.890/1.10	87.0	3.585/1.02	100.2	3.823/1.09	90.4
3.55	3.453/0.94	3.597/0.98	3.876/1.10	87.4	3.563/1.02	100.4	3.814/1.09	90.0
3.83	3.406/0.93	3.567/0.97	3.872/1.10	90.0	3.518/1.01	100.6	3.802/1.09	89.0
4.11	3.393/0.92	3.554/0.97	3.852/1.09	90.2	3.500/1.00	100.6	3.790/1.08	88.7
4.39	3.382/0.92	3.543/0.96	3.840/1.09	90.5	3.482/0.99	100.7	3.782/1.08	88.4
Rank	1	2	5	-	3	-	4	-
Δ(RR)	0.14	0.09	0.08	-	0.27	-	0.16	-

Table 3AP.15 Variation of interatomic distances and angles involving atoms of reference (*x,y,z*) adduct and atoms of neighbouring symmetry generated adducts as a function of pressure for the *NISac.4CYP* experimental dataset. Values within brackets are the standard deviations of the corresponding values. Distance and RR values are shown as left/right entries. A ranking is assigned based on the RR values determined at 4.0(2) GPa, sorted from smaller to larger values. Δ(RR) = $RR_{0.00(5)\ GPa}$ - $RR_{4.0(2)\ GPa}$. The distances are given in Å and the angles are given in degree (º). centroid of the rings are defined as, cen_1= centroid of the ring formed by atoms C1-C6, cen_2= centroid of the ring formed by atoms C5,C6,C7,N1,S1 and cen_3= centroid of the ring formed by atoms C8- C12,N2. (* *Table continues to next page)***

Pressure (GPa)	*-1+x,y,-1+z*				*x,y,-1+z*					*-1+x,y,-2+z*			
	cen3···cen1	C13···O1	H11···O1	<C11-H11···O1	cen3···cen2	cen3···cen1	H11···O2	<C11-H11···O2	C13···O3	N3···H2	<N3···H2-C2	N3···H3	<N3···H3-C3
0.00(5)	3.681(4)/1.09	3.28(2)/1.02	2.75/1.01	109.5	3.755(4)/1.12	3.865(4)/1.14	2.91/1.07	107.7	3.390(12)/1.05	2.80/1.02	125.2	2.83/1.03	124.1
0.00(5)	3.693(6)/1.09	3.30(3)/1.02	2.75/1.01	110.6	3.753(6)/1.12	3.860(6)/1.14	2.93/1.08	107.2	3.397(18)/1.05	2.80/1.02	126.3	2.85/1.04	124.3
0.05(5)	3.679(6)/1.09	3.29(3)/1.02	2.72/1.00	111.3	3.739(5)/1.11	3.854(6)/1.14	2.94/1.08	105.7	3.390(17)/1.05	2.80/1.02	125.9	2.84/1.03	123.9
0.17(5)	3.662(5)/1.09	3.25(3)/1.01	2.73/1.01	108.8	3.715(5)/1.10	3.841(5)/1.14	2.89/1.06	106.9	3.369(16)/1.05	2.79/1.01	124.7	2.81/1.02	124.2
0.20(5)	3.650(4)/1.08	3.23(2)/1.00	2.74/1.01	108.5	3.712(4)/1.10	3.841(4)/1.14	2.87/1.06	107.7	3.371(12)/1.05	2.79/1.01	124.9	2.81/1.02	124.3
0.3(1)	3.623(5)/1.07	3.21(3)/1.00	2.71/1.00	108.1	3.677(5)/1.09	3.822(5)/1.13	2.87/1.06	107.1	3.338(16)/1.04	2.77/1.01	123.8	2.76/1.00	124.6
0.4(1)	3.607(4)/1.07	3.19(3)/0.99	2.69/0.99	107.9	3.659(4)/1.09	3.816(4)/1.13	2.86/1.05	107.3	3.317(13)/1.03	2.79/1.01	123.0	2.74/1.00	124.9
0.6(1)	3.567(4)/1.06	3.16(3)/0.98	2.63/0.97	108.4	3.616(4)/1.07	3.791(4)/1.12	2.86/1.05	106.0	3.278(14)/1.02	2.77/1.01	122.1	2.69/0.98	125.6
0.8(1)	3.558(4)/1.05	3.13(2)/0.97	2.64/0.97	107.4	3.600(4)/1.07	3.783(4)/1.12	2.83/1.04	106.8	3.262(13)/1.01	2.77/1.01	121.8	2.66/0.97	125.8
1.0(1)	3.513(4)/1.04	3.09(3)/0.96	2.58/0.95	107.9	3.547(4)/1.05	3.759(4)/1.11	2.84/1.04	105.3	3.210(13)/1.00	2.73/0.99	120.7	2.61/0.95	126.1
1.4(2)	3.477(5)/1.03	3.07(3)/0.95	2.55/0.94	107.7	3.505(4)/1.04	3.735(4)/1.11	2.81/1.03	104.7	3.171(14)/0.98	2.71/0.98	120.1	2.57/0.94	125.8
1.4(2)	3.477(5)/1.03	3.07(3)/0.95	2.55/0.94	107.8	3.510(4)/1.04	3.745(4)/1.11	2.82/1.04	104.8	3.186(14)/0.99	2.71/0.99	120.6	2.59/0.94	125.6
2.1(2)	3.425(5)/1.01	3.02(3)/0.94	2.49/0.91	107.3	3.436(5)/1.02	3.702(5)/1.10	2.79/1.02	103.5	3.123(14)/0.97	2.67/0.97	119.0	2.51/0.91	126.2
2.1(2)	3.420(5)/1.01	3.01(3)/0.93	2.48/0.91	107.4	3.440(5)/1.02	3.708(5)/1.10	2.80/1.03	103.5	3.115(14)/0.97	2.66/0.97	119.7	2.53/0.92	125.8
2.4(2)	3.404(5)/1.01	2.99(3)/0.93	2.47/0.91	107.1	3.414(5)/1.01	3.693(5)/1.09	2.77/1.02	103.6	3.098(14)/0.96	2.65/0.96	119.3	2.51/0.91	125.5
3.4(2)	3.338(6)/0.99	2.94(3)/0.91	2.39/0.88	108.7	3.357(6)/1.00	3.671(6)/1.09	2.78/1.02	102.1	3.069(17)/0.95	2.61/0.95	119.2	2.47/0.90	124.8
3.6(2)	3.318(6)/0.98	2.88(3)/0.89	2.37/0.87	109.5	3.346(6)/0.99	3.666(6)/1.08	2.79/1.03	101.3	3.067(17)/0.95	2.58/0.94	119.6	2.47/0.90	124.0
4.0(2)	3.312(8)/0.98	2.90(4)/0.90	2.37/0.87	108.4	3.322(7)/0.99	3.654(7)/1.08	2.76/1.02	101.7	3.035(19)/0.94	2.56/0.93	119.3	2.47/0.90	123.6
Rank	15	7	6	-	13	18	17	-	11	10	-	8	-
Δ(RR)	0.11	0.12	0.14	-	0.13	0.06	0.05	-	0.11	0.09	-	0.13	-

Continuation of Table 3AP.15

Pressure (GPa)	*-1/2+x,3/2-y,-1/2+z*						*x,1-y,-1/2+z*					
	O2···H3	**<O2···H3-C3**	**O2···H4**	**<O2···H4-C4**	**H12···O1**	**<C12-H12···O1**	**N3···H9**	**<N3···H9-C9**	**H8···O3**	**<C8-H8···O3**	**O3···H1**	**<O3···H1-C1**
0.00(5)	3.02/1.11	107.0	2.25/0.83	137.3	2.28/0.84	154.1	2.66/0.97	135.1	2.40/0.88	124.5	2.51/0.92	122.9
0.00(5)	3.04/1.12	107.0	2.26/0.83	137.1	2.30/0.85	153.4	2.68/0.97	134.1	2.41/0.89	123.1	2.47/0.91	123.7
0.05(5)	3.02/1.11	107.5	2.27/0.84	136.7	2.29/0.84	151.3	2.64/0.96	136.2	2.40/0.88	122.7	2.44/0.90	123.5
0.17(5)	3.01/1.11	107.5	2.26/0.83	136.2	2.27/0.83	152.4	2.63/0.96	137.4	2.40/0.88	123.9	2.46/0.90	122.4
0.20(5)	2.99/1.10	107.4	2.25/0.83	136.0	2.26/0.83	152.7	2.63/0.96	136.5	2.41/0.89	123.1	2.45/0.90	122.5
0.3(1)	2.97/1.09	107.2	2.23/0.82	135.8	2.23/0.82	152.2	2.60/0.94	137.6	2.40/0.88	122.1	2.42/0.89	122.0
0.4(1)	2.95/1.09	107.3	2.23/0.82	134.9	2.23/0.82	151.6	2.60/0.95	136.8	2.38/0.88	122.4	2.40/0.88	122.1
0.6(1)	2.93/1.08	106.9	2.20/0.81	135.2	2.18/0.80	149.2	2.54/0.92	136.7	2.37/0.87	120.2	2.37/0.87	120.3
0.8(1)	2.92/1.07	106.6	2.20/0.81	134.0	2.17/0.80	149.9	2.54/0.92	137.5	2.36/0.87	121.1	2.36/0.87	120.8
1.0(1)	2.89/1.06	106.4	2.16/0.79	134.0	2.13/0.78	148.5	2.48/0.90	138.6	2.33/0.86	120.5	2.33/0.86	119.0
1.4(2)	2.85/1.05	106.6	2.15/0.79	133.0	2.08/0.77	148.2	2.44/0.89	138.3	2.30/0.85	121.2	2.31/0.85	118.7
1.4(2)	2.84/1.04	106.7	2.15/0.79	133.0	2.08/0.77	149.1	2.46/0.89	138.4	2.29/0.84	121.6	2.32/0.85	118.9
2.1(2)	2.80/1.03	106.4	2.11/0.78	131.8	2.01/0.74	147.4	2.41/0.88	139.0	2.30/0.84	120.3	2.29/0.84	117.0
2.1(2)	2.80/1.03	106.4	2.11/0.78	132.1	2.02/0.74	148.6	2.38/0.86	139.1	2.28/0.84	120.8	2.28/0.84	117.5
2.4(2)	2.78/1.02	106.5	2.11/0.77	131.6	1.98/0.73	147.9	2.37/0.86	139.2	2.30/0.85	120.9	2.28/0.84	117.0
3.4(2)	2.73/1.00	106.2	2.09/0.77	130.2	1.93/0.71	146.9	2.30/0.84	138.5	2.27/0.84	120.0	2.21/0.81	117.0
3.6(2)	2.71/0.99	106.4	2.10/0.77	129.2	1.95/0.72	146.1	2.26/0.82	138.6	2.28/0.84	119.4	2.20/0.81	116.9
4.0(2)	2.69/0.99	106.4	2.07/0.76	129.4	1.90/0.70	147.3	2.24/0.82	138.8	2.26/0.83	120.2	2.20/0.81	116.0
Rank	14	-	2	-	1	-	4	-	5	-	3	-
Δ(RR)	0.12	-	0.07	-	0.14	-	0.15	-	0.05	-	0.11	-

Table 3AP.16 Variation of interatomic distances and angles involving atoms of reference (*x,y,z*) adduct and atoms of neighbouring symmetry generated adducts as a function of pressure for the *NISac.4CYP* theoretical dataset. Distance and RR values are shown as left/right entries. A ranking is assigned based on the RR values determined at 4.39 GPa, sorted from smaller to larger values. Δ(RR) = $RR_{-0.07\ GPa}$ - $RR_{4.39\ GPa}$. The distances are given in Å and the angles are given in degree (º). centroid of the rings are defined as, cen_1= centroid of the ring formed by atoms C1-C6, cen_2= centroid of the ring formed by atoms C5,C6,C7,N1,S1 and cen_3= centroid of the ring formed by atoms C8- C12,N2. (* *Table continues to next page*)**

Pressure (GPa)	*-1+x,y,-1+z*				*x,y,-1+z*					*-1+x,y,-2+z*			
	cen3···cen1	C13···O1	H11···O1	<C11-H11···O1	cen3···cen2	cen3···cen1	H11···O2	<C11-H11···O2	C13···O3	N3···H2	<N3···H2-C2	N3···H3	<N3···H3-C3
-0.07	3.659/1.08	3.33/1.03	2.71/1.00	110	3.746/1.11	3.876/1.15	2.87/1.06	109	3.345/1.04	2.72/0.99	124	2.73/0.99	124
0.10	3.592/1.06	3.28/1.02	2.69/0.99	111	3.668/1.09	3.830/1.13	2.82/1.04	108	3.332/1.03	2.75/1.00	125	2.76/1.00	124
0.15	3.573/1.06	3.27/1.02	2.68/0.98	111	3.652/1.09	3.815/1.13	2.80/1.03	108	3.317/1.03	2.75/1.00	125	2.76/1.00	124
0.43	3.505/1.04	3.20/0.99	2.62/0.96	109	3.597/1.07	3.812/1.13	2.79/1.03	108	3.249/1.01	2.69/0.98	122	2.62/0.95	124
0.72	3.466/1.03	3.13/0.97	2.60/0.96	108	3.554/1.06	3.776/1.12	2.76/1.01	108	3.197/0.99	2.72/0.99	121	2.60/0.95	125
1.00	3.425/1.01	3.10/0.96	2.57/0.94	109	3.515/1.04	3.747/1.11	2.73/1.01	108	3.164/0.98	2.7/0.98	121	2.58/0.94	125
1.28	3.401/1.01	3.07/0.95	2.54/0.93	109	3.482/1.03	3.744/1.11	2.75/1.01	107	3.152/0.98	2.68/0.98	120	2.56/0.93	125
1.57	3.377/1.00	3.06/0.95	2.51/0.92	109	3.459/1.03	3.729/1.10	2.75/1.01	106	3.127/0.97	2.68/0.97	120	2.54/0.92	125
1.85	3.365/1.00	3.02/0.94	2.50/0.92	108	3.438/1.02	3.726/1.10	2.76/1.02	106	3.104/0.96	2.68/0.97	119	2.51/0.91	125
2.13	3.343/0.99	3.01/0.93	2.49/0.91	109	3.416/1.02	3.711/1.10	2.75/1.01	106	3.092/0.96	2.67/0.97	119	2.50/0.91	125
2.41	3.322/0.98	2.99/0.93	2.47/0.91	109	3.395/1.01	3.698/1.09	2.73/1.00	106	3.078/0.96	2.66/0.97	119	2.48/0.90	125
2.70	3.310/0.98	2.97/0.92	2.46/0.91	108	3.38/1.00	3.699/1.09	2.74/1.01	105	3.075/0.95	2.65/0.97	118	2.46/0.90	125
2.98	3.293/0.98	2.96/0.92	2.45/0.90	109	3.361/1.00	3.689/1.09	2.73/1.00	105	3.065/0.95	2.64/0.96	118	2.45/0.89	125
3.26	3.281/0.97	2.94/0.91	2.44/0.90	109	3.346/0.99	3.688/1.09	2.73/1.00	105	3.061/0.95	2.63/0.96	118	2.44/0.89	125
3.55	3.268/0.97	2.93/0.91	2.43/0.89	109	3.331/0.99	3.683/1.09	2.73/1.00	104	3.054/0.95	2.62/0.95	118	2.42/0.88	125
3.83	3.268/0.97	2.90/0.90	2.42/0.89	109	3.328/0.99	3.726/1.10	2.79/1.03	104	3.079/0.96	2.60/0.95	118	2.41/0.88	125
4.11	3.251/0.96	2.89/0.90	2.41/0.88	109	3.314/0.98	3.716/1.10	2.78/1.02	104	3.070/0.95	2.59/0.94	118	2.40/0.87	125
4.39	3.241/0.96	2.88/0.89	2.40/0.88	109	3.304/0.98	3.714/1.10	2.78/1.02	103	3.067/0.95	2.58/0.94	117	2.39/0.87	124
Rank	12	8	7	-	14	20	17	-	11	10	-	6	-
Δ(RR)	0.12	0.14	0.12	-	0.13	0.05	0.04	-	0.09	0.05	-	0.12	-

Continuation of Table 3AP.16

Pressure (GPa)	*-1/2+x,3/2-y,-1/2+z*						*x,1-y,-1/2+z*					
	O2···H3	**<O2···H3-C3**	**O2···H4**	**<O2···H4-C4**	**H12···O1**	**<C12-H12···O1**	**N3···H9**	**<N3···H9-C9**	**H8···O3**	**<C8-H8···O3**	**O3···H1**	**<O3···H1-C1**
-0.07	3.17/1.16	106	2.29/0.84	142	2.41/0.88	159	2.65/0.96	137	2.34/0.86	127.3	2.48/0.91	125
0.10	3.11/1.14	107	2.28/0.84	141	2.36/0.87	159	2.62/0.95	138	2.35/0.86	127.4	2.45/0.90	125
0.15	3.08/1.13	107	2.27/0.83	140	2.34/0.86	159	2.61/0.95	138	2.33/0.86	127.5	2.44/0.90	124
0.43	3.02/1.11	106	2.20/0.81	140	2.27/0.83	156	2.50/0.91	140	2.33/0.86	125.4	2.39/0.88	123
0.72	2.99/1.10	106	2.20/0.81	138	2.21/0.81	155	2.46/0.90	141	2.32/0.85	123.5	2.36/0.87	122
1.00	2.96/1.09	107	2.18/0.80	138	2.18/0.80	155	2.42/0.88	141	2.30/0.85	123.6	2.33/0.86	121
1.28	2.94/1.08	106	2.17/0.80	137	2.15/0.79	153	2.39/0.87	142	2.30/0.85	123.2	2.32/0.85	121
1.57	2.91/1.07	107	2.16/0.79	136	2.13/0.78	153	2.36/0.86	142	2.29/0.84	122.8	2.30/0.85	121
1.85	2.87/1.05	107	2.15/0.79	135	2.09/0.77	153	2.33/0.85	142	2.28/0.84	122.0	2.28/0.84	120
2.13	2.84/1.05	107	2.14/0.79	135	2.07/0.76	153	2.31/0.84	142	2.27/0.83	122.0	2.26/0.83	119
2.41	2.82/1.04	107	2.13/0.78	134	2.05/0.75	152	2.29/0.83	142	2.25/0.83	121.9	2.25/0.83	119
2.70	2.79/1.03	107	2.12/0.78	133	2.03/0.74	152	2.27/0.83	142	2.25/0.83	121.5	2.24/0.82	118
2.98	2.77/1.02	107	2.12/0.78	133	2.01/0.74	152	2.26/0.82	143	2.23/0.82	121.5	2.23/0.82	117
3.26	2.75/1.01	107	2.11/0.78	132	1.99/0.73	152	2.24/0.81	143	2.23/0.82	121.5	2.22/0.82	117
3.55	2.73/1.00	107	2.10/0.77	131	1.98/0.73	152	2.22/0.81	143	2.21/0.81	121.5	2.21/0.81	117
3.83	2.71/0.99	107	2.11/0.78	129	1.97/0.72	152	2.18/0.79	144	2.23/0.82	122.0	2.20/0.81	117
4.11	2.69/0.99	107	2.10/0.77	129	1.95/0.72	152	2.17/0.79	144	2.23/0.82	122.0	2.18/0.80	117
4.39	2.67/0.98	107	2.10/0.77	129	1.94/0.71	153	2.16/0.79	144	2.22/0.82	122.0	2.17/0.80	116
Rank	15	-	2	-	1	-	3	-	5	-	4	-
Δ(RR)	0.18	-	0.07	-	0.17	-	0.17	-	0.04	-	0.11	-

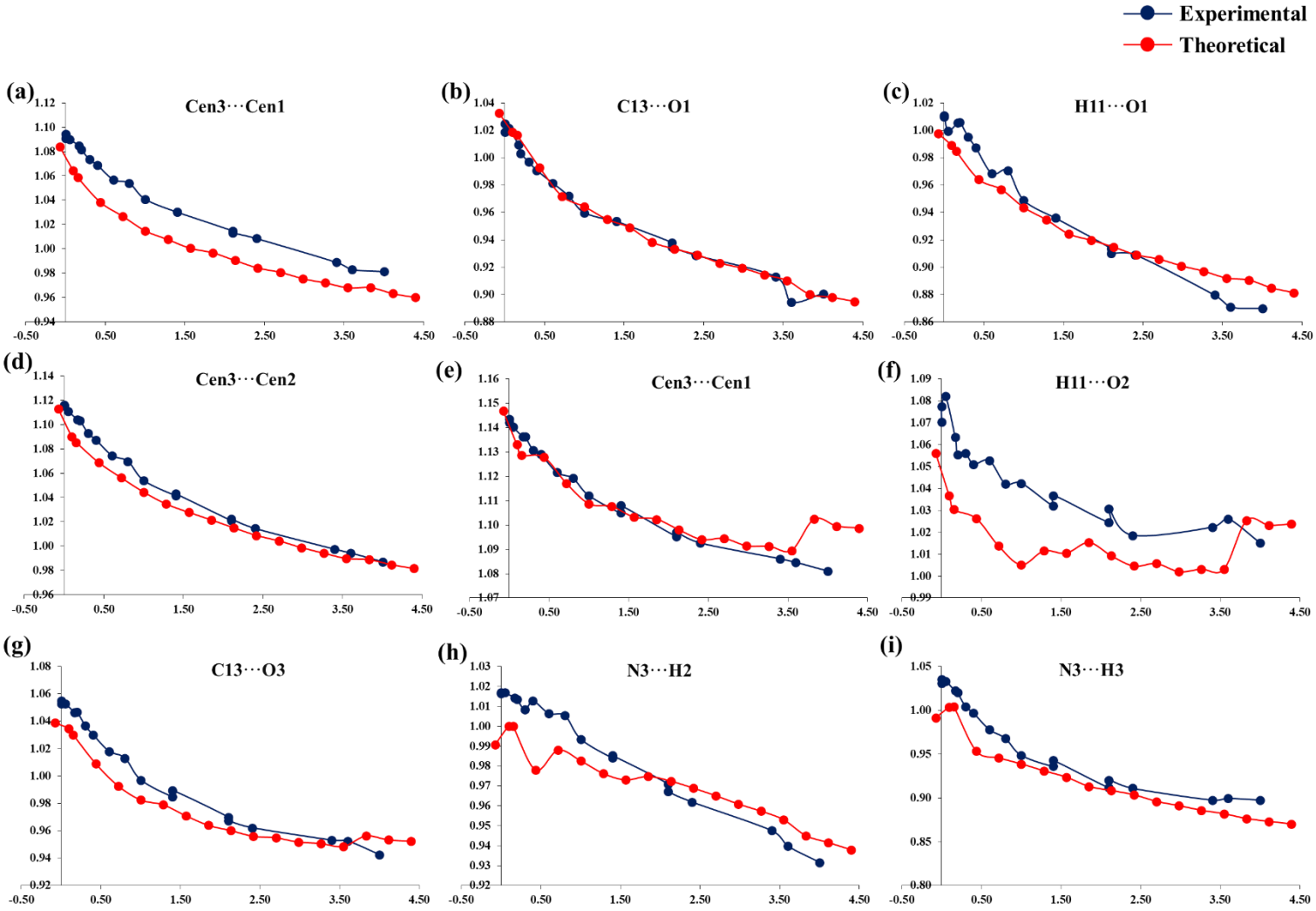

Figure 3AP.18 Variation of RR values, determined for interatomic contacts involving atoms of the reference adduct (*x,y,z*) and atoms of neighbouring symmetry generated adducts, as a function of pressure for *NISac.4CYP*: neighbouring atom belong to: (a)-(c) (*-1+x,y,-1+z*), (d)-(g) (*x,y,-1+z*) and (h)-(i) (*-1+x, y,-2+z*), symmetry generated adducts.

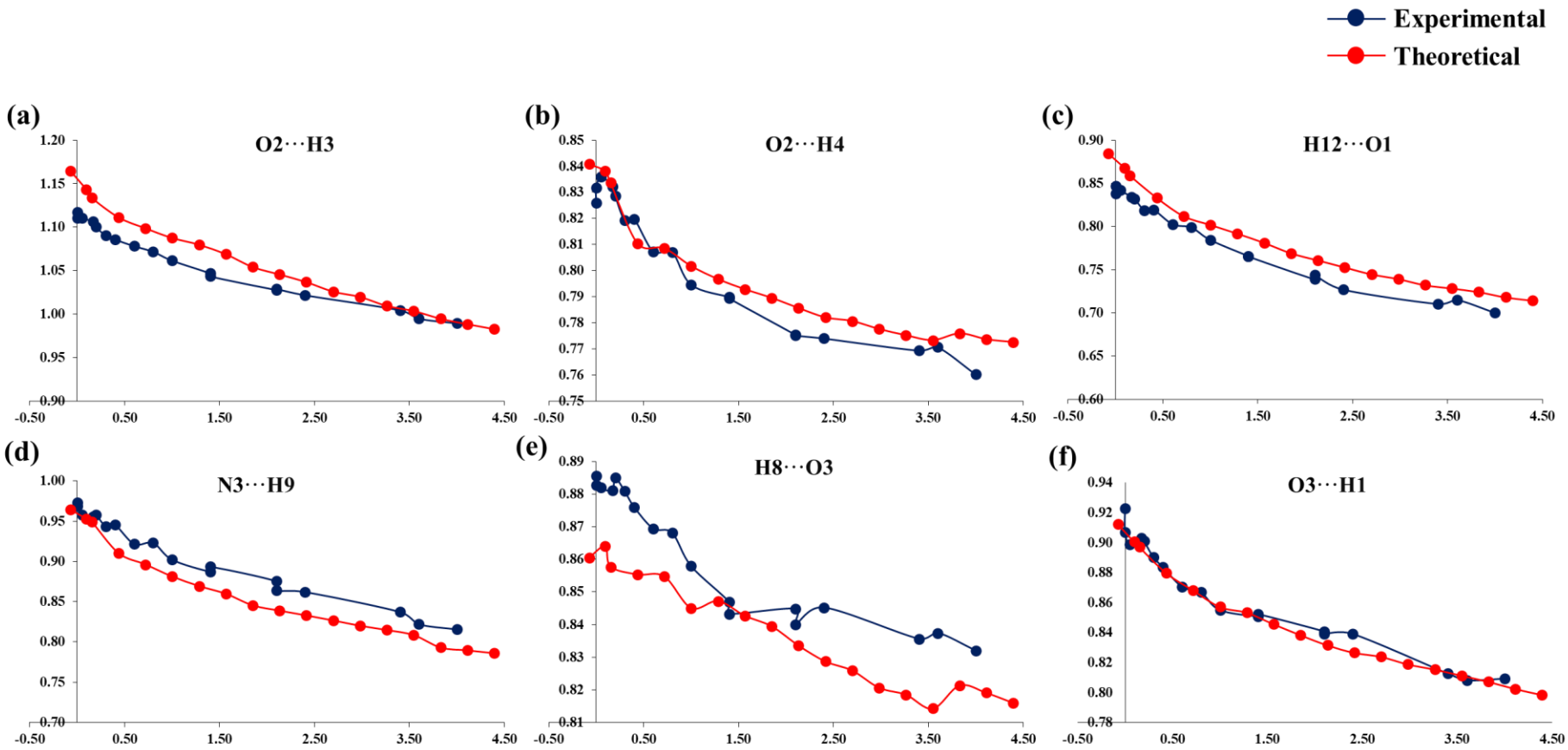

Figure 3AP.19 Variation of RR values, determined for interatomic contacts involving atoms of the reference adduct (*x,y,z*) and atoms of neighbouring symmetry generated adducts, as a function of pressure for *NISac.4CYP*: neighbouring atom belong to: (a)-(c) (*-1/2+x,3/2-y,-1/2+z*) and (d)-(f) (x,1-y,-1/2+z), symmetry generated adducts.

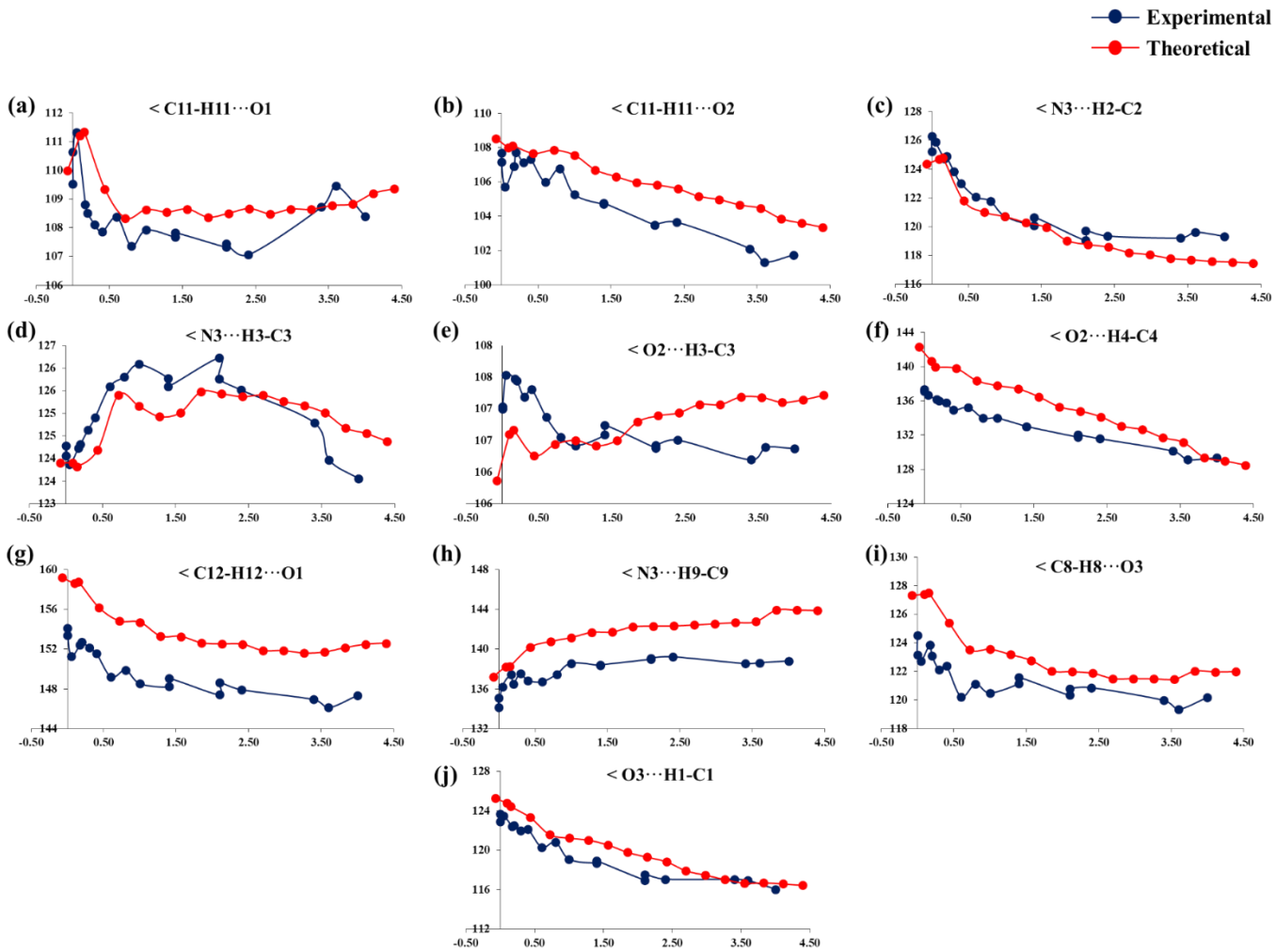

Figure 3AP.20 Variation of the HB angles, involving atoms of the reference adduct (*x,y,z*) and atoms of neighbouring symmetry generated adducts, as a function of pressure for *NISac.4CYP*: neighbouring atom belong to (a) (*-1+x,y,-1+z*) (b) (*x,y,-1+z*) (c)-(d) (*-1+x,y,-2+z*) (e)-(g) (*-1/2+x,3/2-y,-1/2+z*) and (h)-(j) (*x,1-y,-1/2+z*), symmetry generated adducts.

Table 3AP.17 Intermolecular interaction energies calculated using the structures obtained at each experimentally applied pressure. All energies are given in kJ /mol. Total interaction energy and ΔE values are shown as left/right entries. $\Delta E = E_{x\ GPa} - E_{0.00(5)\ GPa}$, whereas for the adducts that are coming into the molecular shell at a high-pressure Y, $\Delta E = E_{X\ GPa} - E_{Y\ GPa}$.

Sl. No	Pressure (GPa)	0.00(5)	0.00(5)	0.05(5)	0.17(5)	0.20(5)	0.3(1)	0.4(1)	0.6(1)	0.8(1)	1.0(1)	1.4(2)	1.4(2)	2.1(2)	2.1(2)	2.4(2)	3.4(2)	3.6(2)
1	*x,y,-1+z*	-58.9/ 0.0	-58.0/ 0.9	-58.7/ 0.2	-59.6/ -0.7	-60.3/ -1.4	-62.0/ -3.1	-62.9/ -4.0	-65.6/ -6.7	-66.1/ -7.2	-68.4/ -9.5	-70.3/ -11.4	-70.3/ -11.4	-72.6/ -13.7	-72.1/ -13.2	-73.4/ -14.5	-75.4/ -16.5	-75.2/ -16.3
2	*-1/2+x,3/2-y,-1/2+z*	-46.8/ 0.0	-45.5/ 1.3	-46.0/ 0.8	-45.9/ 0.9	-46.4/ 0.4	-47.1/ -0.3	-47.1/ -0.3	-48.9/ -2.1	-48.8/ -2.0	-50.1/ -3.3	-50.5/ -3.7	-51.4/ -4.6	-51.8/ -5.0	-51.7/ -4.9	-51.9/ -5.1	-51.2/ -4.4	-50.9/ -4.1
3	*x,1-y,-1/2+z*	-45.9/ 0.0	-45.6/ 0.3	-46.3/ -0.4	-46.1/ -0.2	-46.3/ -0.4	-47.0/ -1.1	-47.8/ -1.9	-48.0/ -2.1	-48.2/ -2.3	-48.4/ -2.5	-48.3/ -2.4	-48.6/ -2.7	-47.4/ -1.5	-47.3/ -1.4	-46.9/ -1.0	-46.8/ -0.9	-45.7/ 0.2
4	*-1+x,y,-1+z*	-40.8/ 0.0	-40.5/ 0.3	-41.5/ -0.7	-41.8/ -1.0	-41.8/ -1.0	-43.1/ -2.3	-43.3/ -2.5	-45.2/ -4.4	-44.9/ -4.1	-46.7/ -5.9	-47.8/ -7.0	-47.7/ -6.9	-49.4/ -8.6	-49.7/ -8.9	-50.3/ -9.5	-50.9/ -10.1	-51.0/ -10.2
5	*-1+x,y,-2+z*	-8.3/ 0.0	-8.1/ 0.2	-8.0/ 0.3	-8.1/ 0.2	-8.3/ 0.0	-8.4 /-0.1	-8.4/ -0.1	-8.6/ -0.3	-8.6/ -0.3	-8.7/ -0.4	-8.7/ -0.4	-8.7/ -0.4	-8.7/ -0.4	-8.7/ -0.4	-8.5/ -0.2	-8.1/ 0.2	-8.0/ 0.3
6	*-1+x,1-y,-3/2+z*	-0.4/ 0.0	-0.5/ -0.1	-0.4/ 0.0	-0.6/ -0.2	-0.5/ -0.1	-0.6/ -0.2	-0.6/ -0.2	-0.9/ -0.5	-0.9/ -0.5	-1.1/ -0.7	-1.2/ -0.8	-1.1/ -0.7	-1.5/ -1.1	-1.3/ -0.9	-1.5/ -1.1	-1.3/ -0.9	-1.3/ -0.9
7	*-1/2+x,3/2-y,-3/2+z*	0.0/ 0.0	-0.1/ -0.1	-0.2/ -0.2	-0.1/ -0.1	0.0/ 0.0	-0.2/ -0.2	-0.1/ -0.1	-0.4/ -0.4	-0.3/ -0.3	-0.6/ -0.6	-0.8/ -0.8	-0.6/ -0.6	-0.9/ -0.9	-1.1/ -1.1	-1.2/ -1.2	-1.4/ -1.4	-1.5/ -1.5
8	*1/2+x,3/2-y,-1/2+z*																4.9/ 0.0	4.8/ -0.1

Table 3AP.18 Intermolecular interaction energies calculated using the theoretically obtained high-pressure structures. All energies are given in kJ/mol. Total interaction energy and ΔE values are shown as left/right entries. $\Delta E = E_{x\ GPa} - E_{0.00(5)\ GPa}$, whereas for the adducts that are coming into the molecular shell at a high-pressure Y, $\Delta E = E_{X\ GPa} - E_{Y\ GPa}$.

Sl. No	Pressure (GPa)	-0.07	0.10	0.15	0.43	0.72	1.00	1.28	1.57	1.85	2.13	2.41	2.70	2.98	3.26	3.55
1	*x,y,-1+z*	-60.7/ 0.0	-63.6/ -2.9	-64.2/ -3.5	-67.0/ -6.3	-69.2/ -8.5	-70.5/ -9.8	-71.6/ -10.9	-72.3/ -11.6	-73.0/ -12.3	-73.6/ -12.9	-74.1/ -13.4	-74.5/ -13.8	-74.8/ -14.1	-75.1/ -14.4	-75.1/ -14.4
2	*-1/2+x,3/2-y,-1/2+z*	-45.9/ 0.0	-47.5/ -1.6	-48.0/ -2.1	-50.0/ -4.1	-51.6/ -5.7	-52.4/ -6.5	-53.1/ -7.2	-53.7/ -7.8	-54.6/ -8.7	-55.0/- 9.1	-55.4/ -9.5	-55.6/ -9.7	-55.8/ -9.9	-56.1/ -10.2	-56.2/ -10.3
3	*x,1-y,-1/2+z*	-46.7/ 0.0	-46.5/ 0.2	-46.7/ 0.0	-47.5/ -0.8	-47.5/ -0.8	-47.9/ -1.2	-47.4/ -0.7	-47.3/ -0.6	-46.9/ -0.2	-46.8/ -0.1	-46.5/ 0.2	-45.9/ 0.8	-45.4/ 1.3	-44.8/ 1.9	-44.2/ 2.5
4	*-1+x,y,-1+z*	-42.6/ 0.0	-43.5/ -0.9	-43.8/ -1.2	-46.4/ -3.8	-47.5/ -4.9	-48.4 /-5.8	-49.3/ -6.7	-49.6/ -7.0	-49.7/ -7.1	-49.8/ -7.2	-49.9/ -7.3	-49.8/ -7.2	-49.8/ -7.2	-49.6/ -7.0	-49.5/ -6.9
5	*-1+x,y,-2+z*	-8.5/ 0.0	-8.3/ 0.2	-8.3/ 0.2	-8.5/ 0.0	-8.5/ 0.0	-8.5/ 0.0	-8.4/ 0.1	-8.3/ 0.2	-8.2/ 0.3	-8.2/ 0.3	-8.1/ 0.4	-8.0/ 0.5	-7.9/ 0.6	-7.8/ 0.7	-7.7/ 0.8
6	*-1+x,1-y,-3/2+z*	0.2/ 0.0	0.0/ -0.2	-0.1/ -0.3	-0.3/ -0.5	-0.5/ -0.7	-0.6/ -0.8	-0.8/ -1.0	-0.8/ -1.0	-0.8/ -1.0	-0.8/ -1.0	-0.8/ -1.0	-0.9/ -1.1	-0.9/ -1.1	-0.9/ -1.1	-0.9/ -1.1
7	*-1/2+x,3/2-y,-3/2+z*	-0.8/ 0.0	-0.6/ 0.2	-0.6/ 0.2	-1.0/ -0.2	-1.1/ -0.3	-1.1/ -0.3	-1.6/ -0.8	-1.6/ -0.8	-1.7/ -0.9	-1.7/ -0.9	-1.7/ -0.9	-1.7/ -0.9	-1.7/ -0.9	-1.7/ -0.9	-1.7/ -0.9
8	*1/2+x,3/2-y,-1/2+z*											6.5/ 0.0	6.6/ 0.1	6.7/ 0.2	6.8/ 0.3	6.9/ 0.4

Table 3AP.19 Topological parameters obtained for the isolated *NISac.4CYP* adduct, extracted from the crystal structure at each applied pressure using the experimental dataset. N1-I1/I1-N2 distances are given as left/right values. The gathered QTAIM topological and energetic properties of $\rho(r)$ at both N1-I1/I1-N2 BCPs are given as left/right values. They are electron density (ρ), its Laplacian ($\nabla^2\rho$), the total energy density ($H=V+G$) and the ratio between the electron potential (V) and kinetic (G) densities ($|V|/G$), as well as their values normalized to ρ. The delocalization index at BCPs is denoted as DI. ΔX (X=ρ, L, |V|/G, DI) is the difference between left and right values. The values of the properties for data collected in region-2 ($P1$ space group) are highlighted with red colour.

Pressure (GPa)	Distance (Å)	$\rho(r)$ (eÅ^{-3})	$\nabla^2\rho(r)$ (eÅ^{-5})	$\nabla^2\rho(r)/\rho(r)$ (Å^{-2})	|V|/G	H(a.u.)	H/ρ (a.u.)	DI	Δ$\rho(r)$ (eÅ^{-3})	Δ$\nabla^2\rho(r)$ (eÅ^{-5})	Δ($\nabla^2\rho(r)/\rho(r)$) (Å^{-2})	Δ(|V|/G)	Δ(DI)
0.00(5)	2.162/2.390	0.651/0.410	2.899/2.746	4.454/6.702	1.547/1.316	-0.036/-0.013	-0.376/-0.217	0.821/0.524	0.241	0.153	-2.248	0.230	0.297
0.00(5)	2.173/2.40	0.662/0.416	3.060/2.790	4.625/6.706	1.541/1.321	-0.037/-0.014	-0.381/-0.222	0.822/0.529	0.246	0.271	-2.081	0.220	0.294
0.05(5)	2.176/2.401	0.647/0.408	2.892/2.720	4.470/6.661	1.544/1.317	-0.036/-0.013	-0.374/-0.217	0.818/0.525	0.239	0.172	-2.191	0.227	0.293
0.17(5)	2.168/2.397	0.656/0.413	2.955/2.755	4.504/6.679	1.546/1.319	-0.037/-0.013	-0.379/-0.219	0.823/0.526	0.243	0.199	-2.175	0.226	0.297
0.20(5)	2.161/2.391	0.666/0.415	3.057/2.795	4.592/6.728	1.544/1.319	-0.038/-0.014	-0.384/-0.221	0.827/0.526	0.250	0.262	-2.136	0.225	0.301
0.3(1)	2.166/2.393	0.656/0.415	3.002/2.762	4.575/6.660	1.542/1.322	-0.037/-0.014	-0.378/-0.221	0.820/0.527	0.241	0.241	-2.085	0.220	0.293
0.4(1)	2.163/2.392	0.662/0.416	3.056/2.782	4.618/6.684	1.541/1.322	-0.037/-0.014	-0.381/-0.222	0.822/0.528	0.246	0.274	-2.066	0.220	0.294
0.6(1)	2.170/2.387	0.651/0.421	3.011/2.770	4.625/6.577	1.537/1.329	-0.036/-0.014	-0.375/-0.226	0.813/0.537	0.230	0.241	-1.952	0.207	0.276
0.8(1)	2.168/2.383	0.655/0.423	3.023/2.806	4.612/6.626	1.539/1.329	-0.037/-0.014	-0.378/-0.227	0.817/0.536	0.232	0.217	-2.014	0.210	0.280
1.0(1)	2.172/2.376	0.649/0.430	2.993/2.833	4.615/6.595	1.536/1.334	-0.036/-0.015	-0.374/-0.231	0.811/0.543	0.219	0.160	-1.981	0.202	0.267
1.4(2)	2.175/2.362	0.645/0.440	3.002/2.894	4.657/6.581	1.533/1.341	-0.035/-0.016	-0.371/-0.239	0.805/0.553	0.205	0.108	-1.924	0.191	0.251
1.4(2)	2.172/2.358	0.648/0.443	3.014/2.920	4.653/6.585	1.534/1.343	-0.036/-0.016	-0.373/-0.241	0.806/0.554	0.204	0.094	-1.932	0.191	0.252
2.1(2)	2.170/2.350	0.650/0.450	3.063/2.954	4.716/6.565	1.531/1.348	-0.036/-0.016	-0.374/-0.246	0.805/0.560	0.200	0.109	-1.850	0.183	0.245
2.1(2)	2.174/2.348	0.644/0.453	3.011/2.961	4.673/6.540	1.531/1.351	-0.035/-0.017	-0.371/-0.248	0.802/0.562	0.192	0.050	-1.867	0.180	0.240
2.4(2)	2.176/2.339	0.641/0.460	3.010/3.008	4.692/6.541	1.529/1.355	-0.035/-0.017	-0.369/-0.253	0.797/0.570	0.182	0.002	-1.849	0.174	0.228
3.4(2)	2.180/2.316	0.636/0.480	3.003/3.142	4.720/6.545	1.526/1.367	-0.035/-0.019	-0.366/-0.266	0.789/0.586	0.156	-0.140	-1.826	0.159	0.203
3.6(2)	2.183/2.317	0.633/0.479	2.962/3.127	4.680/6.534	1.527/1.367	-0.034/-0.019	-0.365/-0.265	0.790/0.585	0.154	-0.166	-1.854	0.160	0.205
4.0(2)	2.169/2.319	0.649/0.478	3.138/3.117	4.833/6.528	1.525/1.366	-0.036/-0.019	-0.373/-0.264	0.796/0.583	0.172	0.021	-1.695	0.158	0.212
4.2(2)	2.160/2.317	0.666/0.481	3.180/3.125	4.777/6.502	1.534/1.369	-0.038/-0.019	-0.383/-0.266	0.812/0.578	0.185	0.056	-1.725	0.165	0.234
	2.186/2.308	0.624/0.489	3.229/3.010	5.174/6.151	1.497/1.390	-0.033/-0.020	-0.358/-0.275	0.768/0.588	0.135	0.219	-0.977	0.107	0.180
4.7(2)	2.149/2.312	0.681/0.486	2.342/3.190	4.906/6.566	1.532/1.369	-0.038/-0.019	-0.391/-0.269	0.820/0.581	0.195	0.152	-1.660	0.163	0.239
	2.20/2.314	0.613/0.481	3.110/3.012	5.070/6.265	1.498/1.379	-0.032/-0.019	-0.352/-0.268	0.767/0.581	0.133	0.098	-1.195	0.118	0.187
5.0(2)	2.166/2.329	0.607/0.494	3.030/3.058	4.988/6.186	1.500/1.390	-0.031/-0.019	-0.349/-0.277	0.763/0.592	0.113	-0.028	-1.198	0.109	0.171
	2.200/2.302	0.663/0.471	3.080/3.052	4.645/6.483	1.540/1.363	-0.038/-0.018	-0.382/-0.259	0.816/0.571	0.192	-0.029	-1.837	0.177	0.245

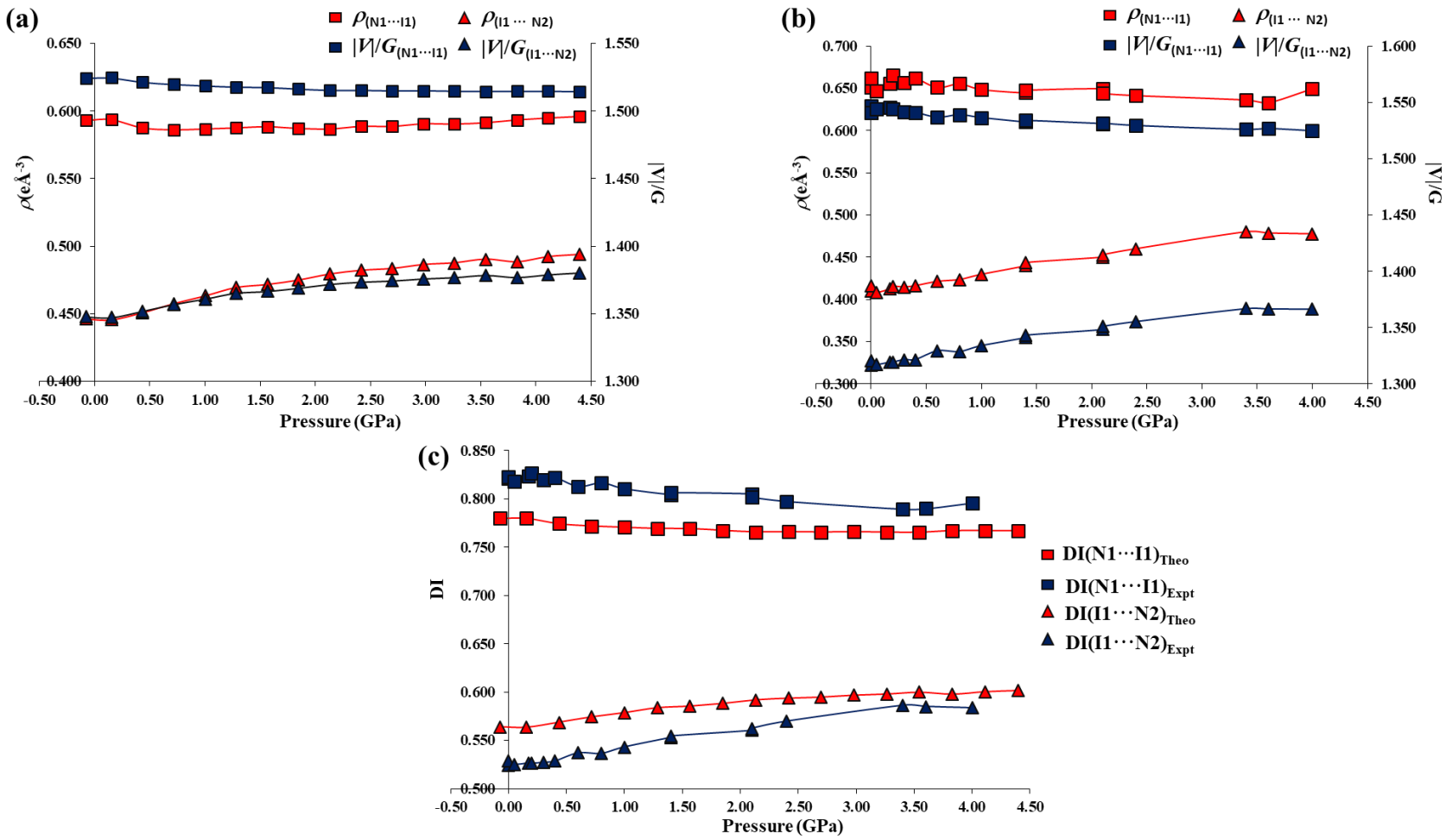

Figure 3AP.21 Topological parameters ρ and $|V|/G$ calculated at N1···I1 and I1···N2 BCPs for (a) theoretical and (b) experimental datasets. The delocalization index DI is represented in (c) for theoretical and experimental datasets.

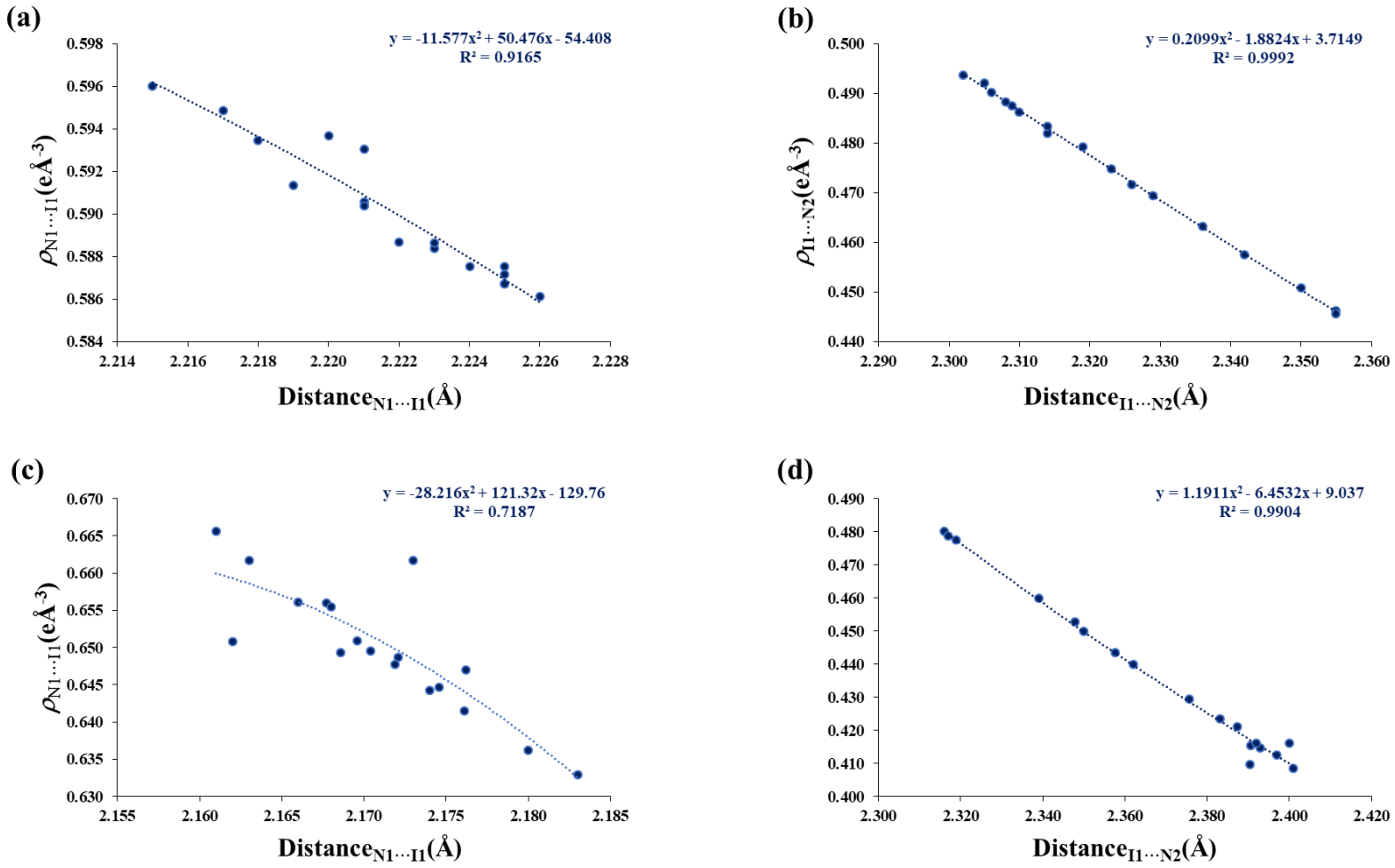

Figure 3AP.22 Plot of $\rho_{N1\cdots I1}$ vs Distance$_{N1\cdots I1}$ for (a) theoretical and (c) experimental datasets. Plot of $\rho_{I1\cdots N2}$ vs Distance$_{I1\cdots N2}$ for (b) theoretical and (d) experimental datasets. Data are fitted with a 2nd order polynomial function. The corresponding polynomial equation and R^2 values are shown within each plot.

Table 3AP.20 Charges of atomic and molecular entities as a function of pressure for the high-pressure theoretical dataset of *NISac.4CYP*. Molecular charges are obtained from the summation of topological atomic charges (B3LYP/Def2TZVPP) with the *NISac.4CYP* isolated adduct extracted from the crystal structure at each applied pressure. N_{sac} reads for the saccharinate molecular entity, 4CYP for the 4-cyanopyridine molecular entity and I for the iodine atom.

Pressure (GPa)	-0.07	0.10	0.15	0.43	0.72	1.00	1.28	1.57	1.85	2.13	2.41	2.70	2.98	3.26	3.55	3.83	4.11	4.39
4CYP(*e*)	0.15	0.15	0.15	0.15	0.15	0.15	0.15	0.15	0.15	0.15	0.15	0.15	0.15	0.15	0.15	0.15	0.15	0.15
I(*e*)	0.47	0.47	0.47	0.47	0.47	0.48	0.48	0.48	0.48	0.48	0.48	0.48	0.48	0.48	0.49	0.49	0.49	0.49
N_{Sac}(*e*)	-0.62	-0.62	-0.62	-0.62	-0.62	-0.63	-0.63	-0.63	-0.63	-0.63	-0.63	-0.63	-0.63	-0.64	-0.64	-0.64	-0.64	-0.64

Table 3AP.21 Charges of atomic and molecular entities as a function of pressure for the high-pressure experimental dataset of *NISac.4CYP*. Molecular charges are obtained from the summation of topological atomic charges (B3LYP/Def2TZVPP) with the *NISac.4CYP* isolated adduct extracted from the crystal structure at each applied pressure. N_{sac} reads for the saccharinate molecular entity, 4CYP for the 4-cyanopyridine molecular entity and I for the iodine atom.

Pressure (GPa)	0.00(5)	0.00(5)	0.05(5)	0.17(5)	0.20(5)	0.3(1)	0.4(1)	0.6(1)	0.8(1)	1.0(1)	1.4(2)	1.4(2)	2.1(2)	2.1(2)	2.4(2)	3.4(2)	3.6(2)	4.0(2)
4CYP(*e*)	0.14	0.14	0.14	0.14	0.14	0.14	0.14	0.15	0.14	0.14	0.14	0.14	0.14	0.15	0.15	0.14	0.14	0.14
I(*e*)	0.48	0.47	0.47	0.47	0.48	0.47	0.48	0.48	0.48	0.48	0.48	0.48	0.49	0.48	0.49	0.49	0.49	0.50
N_{Sac}(*e*)	-0.62	-0.61	-0.61	-0.61	-0.61	-0.62	-0.62	-0.62	-0.62	-0.62	-0.63	-0.63	-0.63	-0.63	-0.63	-0.64	-0.64	-0.64

Appendices – Chapter 4

For all the multipolar models contours of residual maps (drawn for the resolution range $0.0 < \sin\theta/\lambda < 0.8$ Å^{-1}) and static deformation density maps are at ±0.05 eÅ^{-3} level: blue - positive, red - negative. Laplacian of electron density maps contours (eÅ^{-5}) are in logarithmic scale: red - positive, blue - negative.

TMM-2 of SeCN1

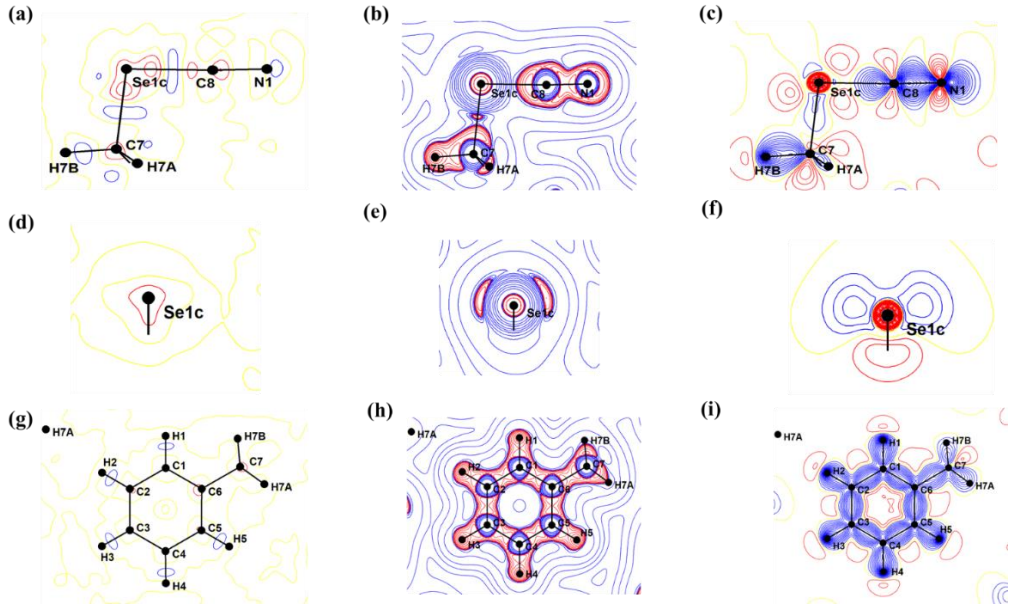

Figure 4AP.1 Residual, laplacian of electron density and static deformation density maps drawn after TMM-2 of SeCN1 in, (a)-(c) *plane-1* [containing C7, Se1 and N1 atoms], (d)-(f) *plane-2* [plane bisecting C7-Se1-N1 angle], (g)-(i) plane containing benzene ring.

TMM-3 of SeCN1

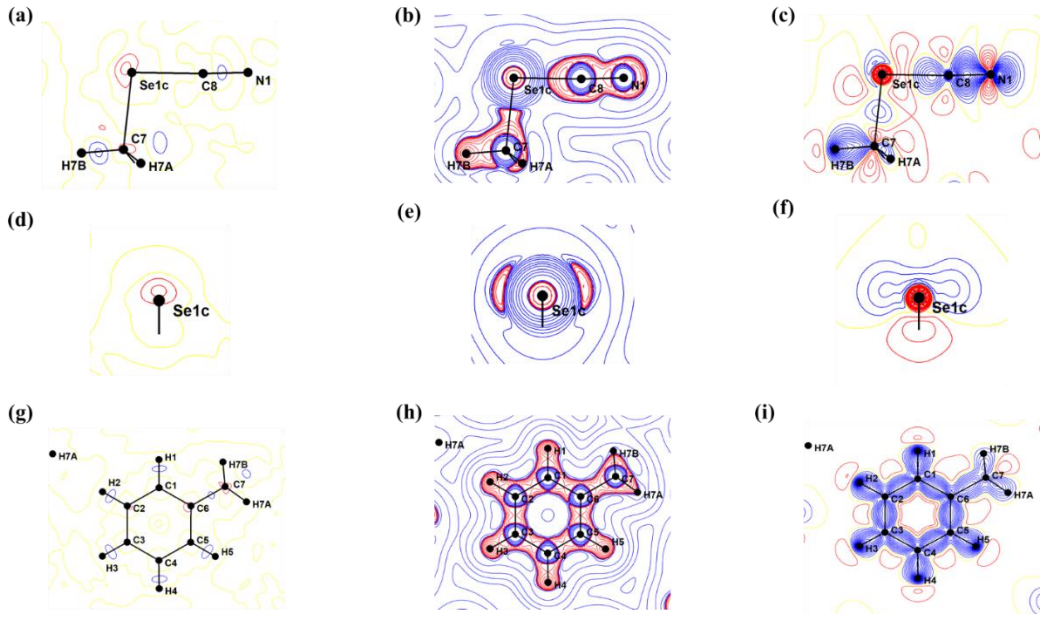

Figure 4AP.2 Residual, laplacian of electron density and static deformation density maps drawn after TMM-3 of SeCN1 in, (a)-(c) *plane-1* [containing C7, Se1 and N1 atoms], (d)-(f) *plane-2* [plane bisecting C7-Se1-N1 angle], (g)-(i) plane containing benzene ring.

EMM-2 of SeCN1

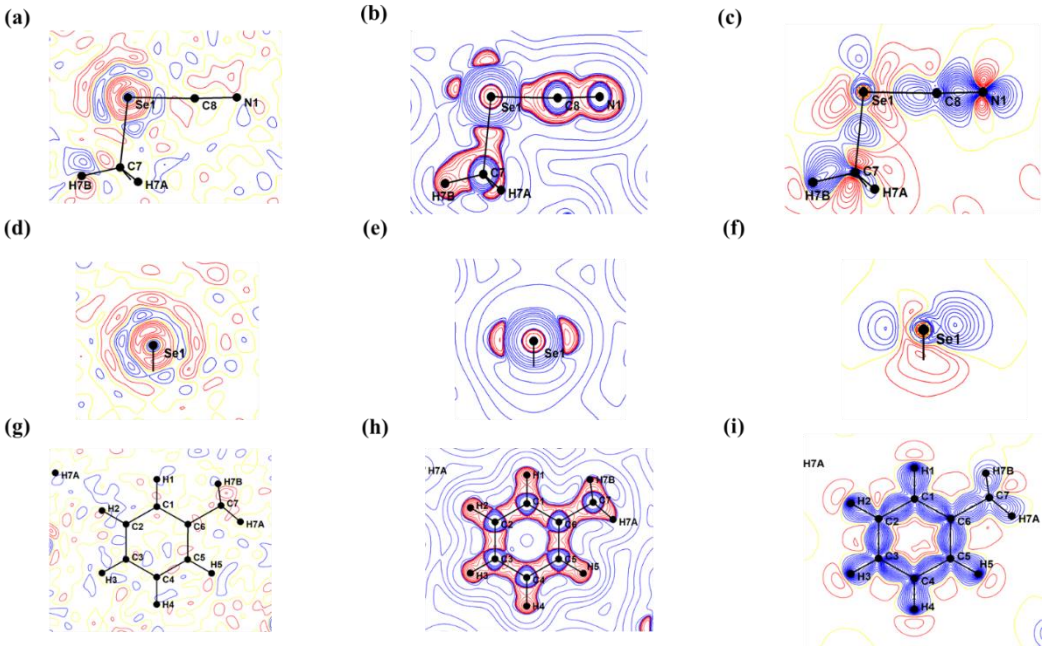

Figure 4AP.3 Residual, laplacian of electron density and static deformation density maps drawn after EMM-2 of SeCN1 in, (a)-(c) *plane-1* [containing C7, Se1 and N1 atoms], (d)-(f) *plane-2* [plane bisecting C7-Se1-N1 angle], (g)-(i) plane containing benzene ring.

EMM-3 of SeCN1

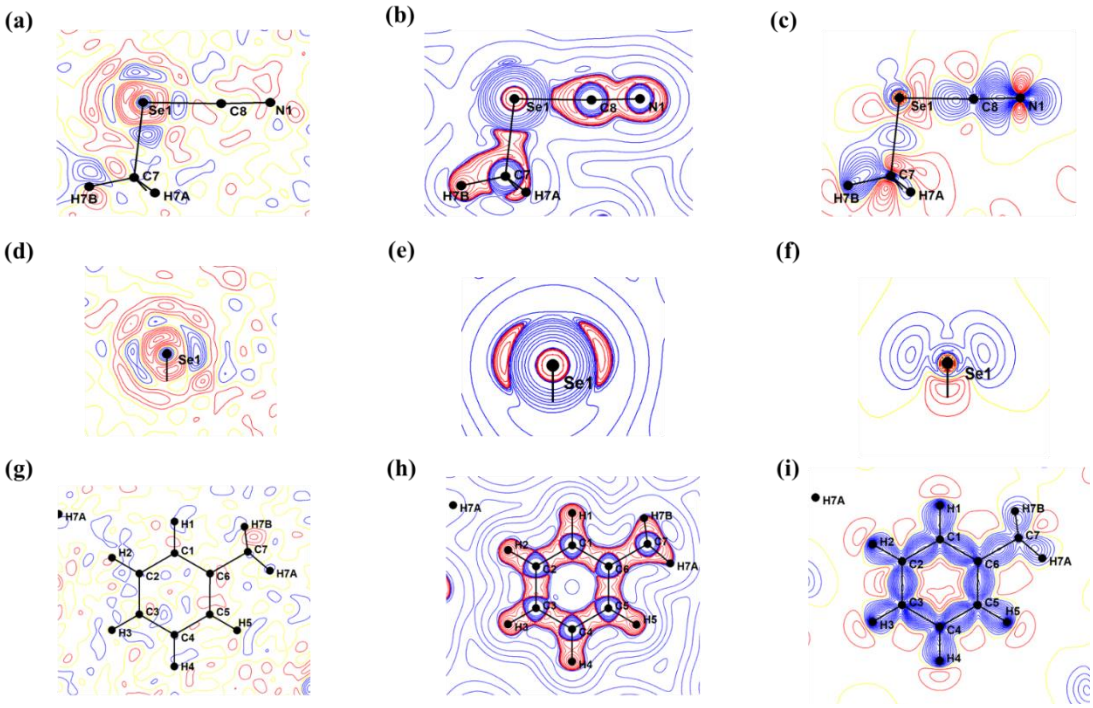

Figure 4AP.4 Residual, laplacian of electron density and static deformation density maps drawn after EMM-3 of SeCN1 in, (a)-(c) *plane-1* [containing C7, Se1 and N1 atoms], (d)-(f) *plane-2* [plane bisecting C7-Se1-N1 angle], (g)-(i) plane containing benzene ring.

EMM-1 of SeCN2

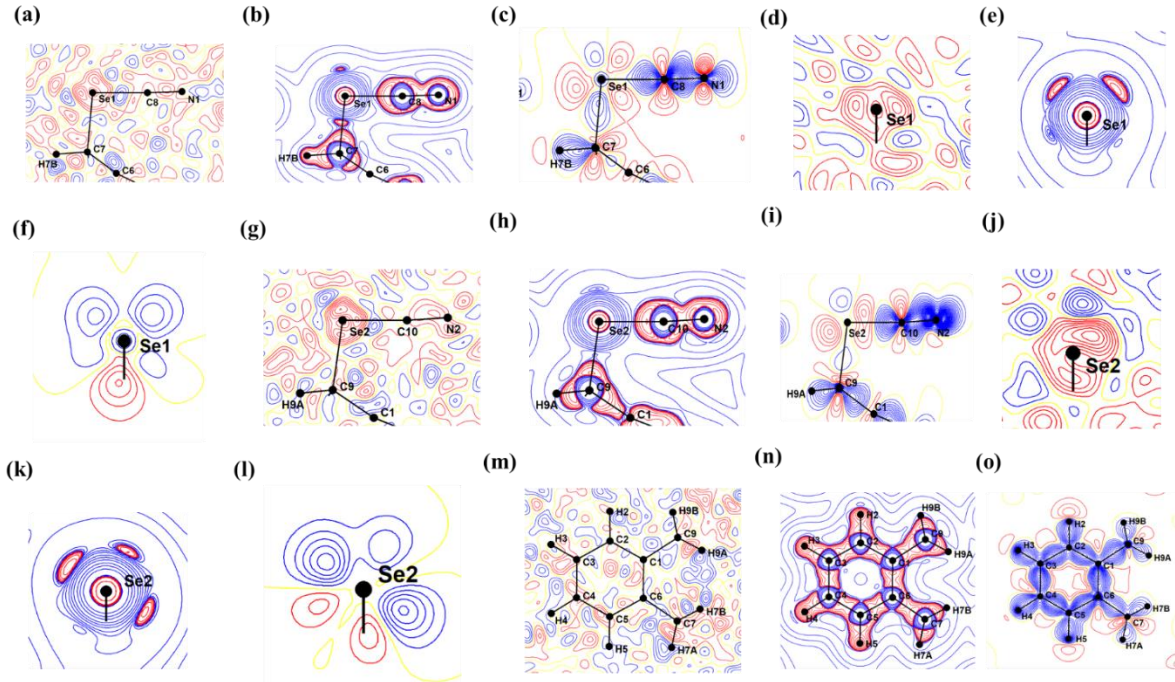

Figure 4AP.5 Residual, laplacian of electron density and static deformation density maps obtained after EMM-1 of SeCN2 in, (a)-(c), (g)-(i) *plane-1* [containing either C7, Se1 and N1 atoms or C9, Se2 and N2 atoms], (d)-(f), (j)-(l) *plane-2* [plane bisecting either C7-Se1-N1 or C9-Se2-N2 angle] and (m)-(o) plane containing benzene ring.

TMM-1 of SeCN2

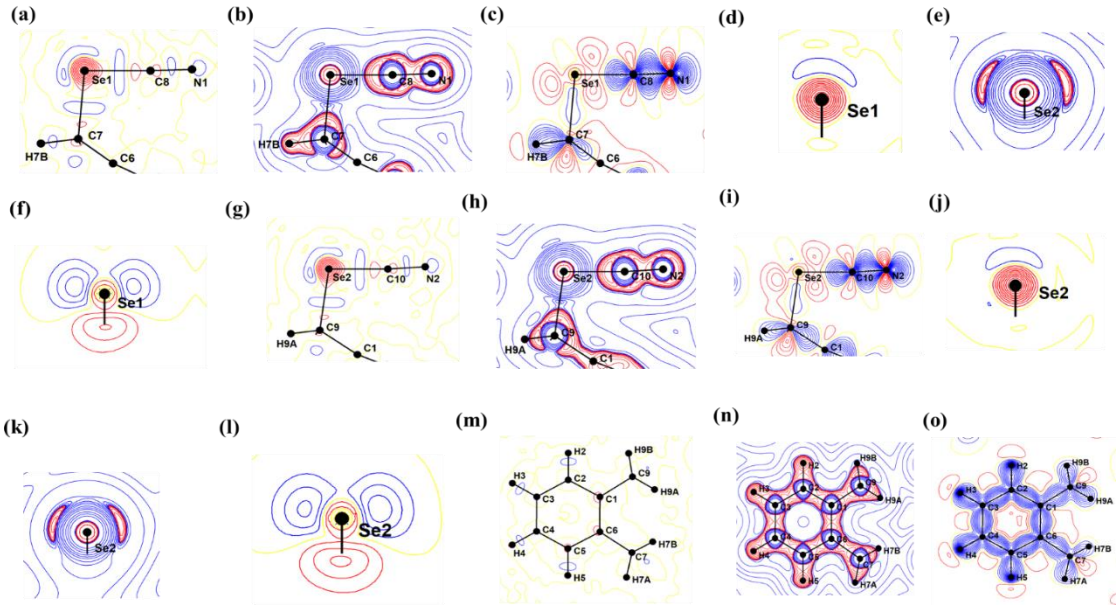

Figure 4AP.6 Residual, laplacian of electron density and static deformation density maps obtained after TMM-1 of SeCN2 in, (a)-(c), (g)-(i) *plane-1* [containing either C7, Se1 and N1 atoms or C9, Se2 and N2 atoms], (d)-(f), (j)-(l) *plane-2* [plane bisecting either C7-Se1-N1 or C9-Se2-N2 angle] and (m)-(o) plane containing benzene ring.

TMM-2 of SeCN2

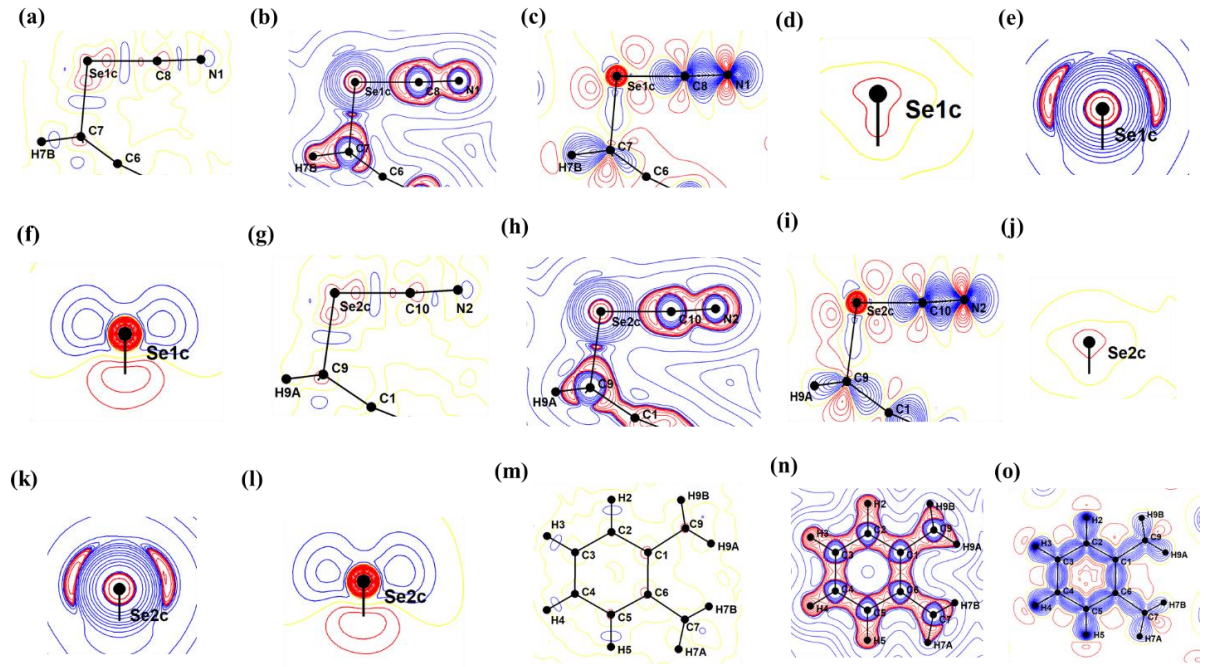

Figure 4AP.7 Residual, laplacian of electron density and static deformation density maps obtained after TMM-2 of SeCN2 in, (a)-(c), (g)-(i) *plane-1* [containing either C7, Se1 and N1 atoms or C9, Se2 and N2 atoms], (d)-(f), (j)-(l) *plane-2* [plane bisecting either C7-Se1-N1 or C9-Se2-N2 angle] and (m)-(o) plane containing benzene ring.

TMM-3 of SeCN2

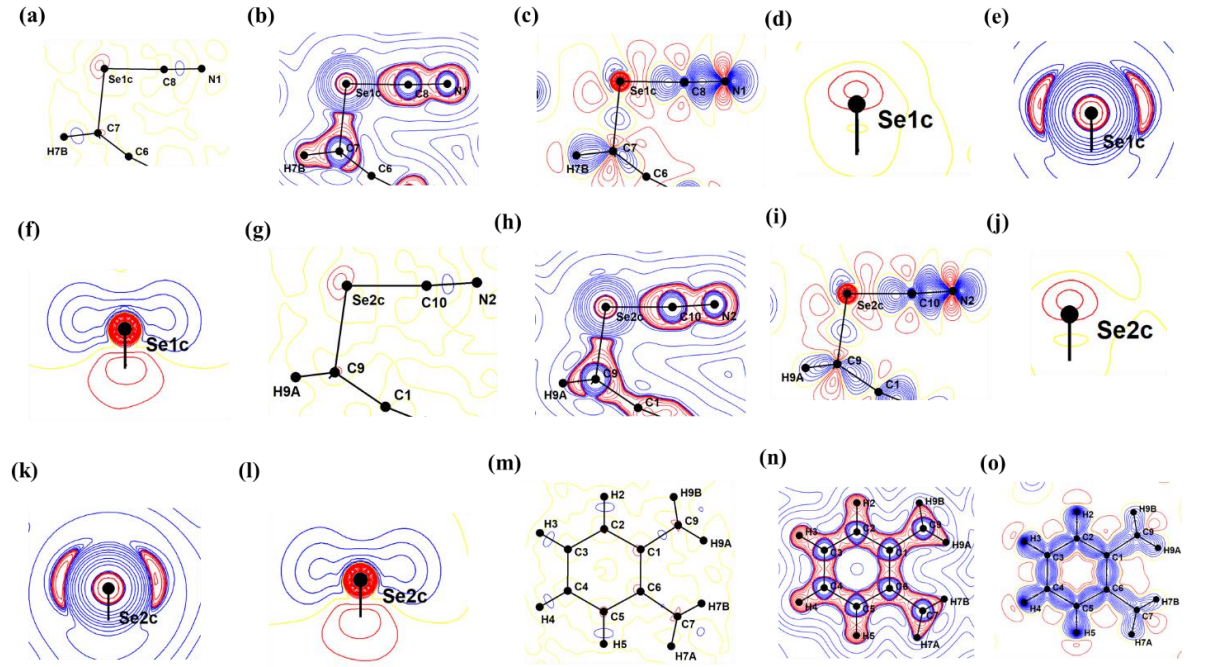

Figure 4AP.8 Residual, laplacian of electron density and static deformation density maps obtained after TMM-3 of SeCN2 in, (a)-(c), (g)-(i) *plane-1* [containing either C7, Se1 and N1 atoms or C9, Se2 and N2 atoms], (d)-(f), (j)-(l) *plane-2* [plane bisecting either C7-Se1-N1 or C9-Se2-N2 angle] and (m)-(o) plane containing benzene ring.

EMM-2 of SeCN2

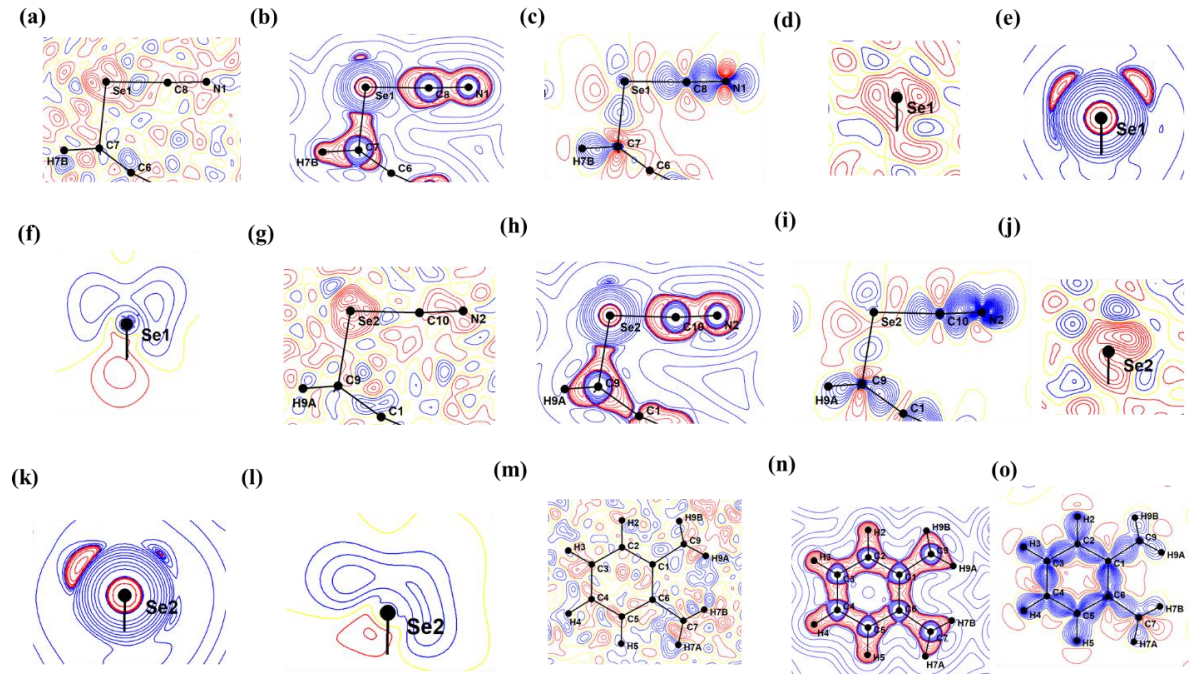

Figure 4AP.9 Residual, laplacian of electron density and static deformation density maps obtained after EMM-2 of SeCN2 in, (a)-(c), (g)-(i) *plane-1* [containing either C7, Se1 and N1 atoms or C9, Se2 and N2 atoms], (d)-(f), (j)-(l) *plane-2* [plane bisecting either C7-Se1-N1 or C9-Se2-N2 angle] and (m)-(o) plane containing benzene ring.

EMM-3 of SeCN2

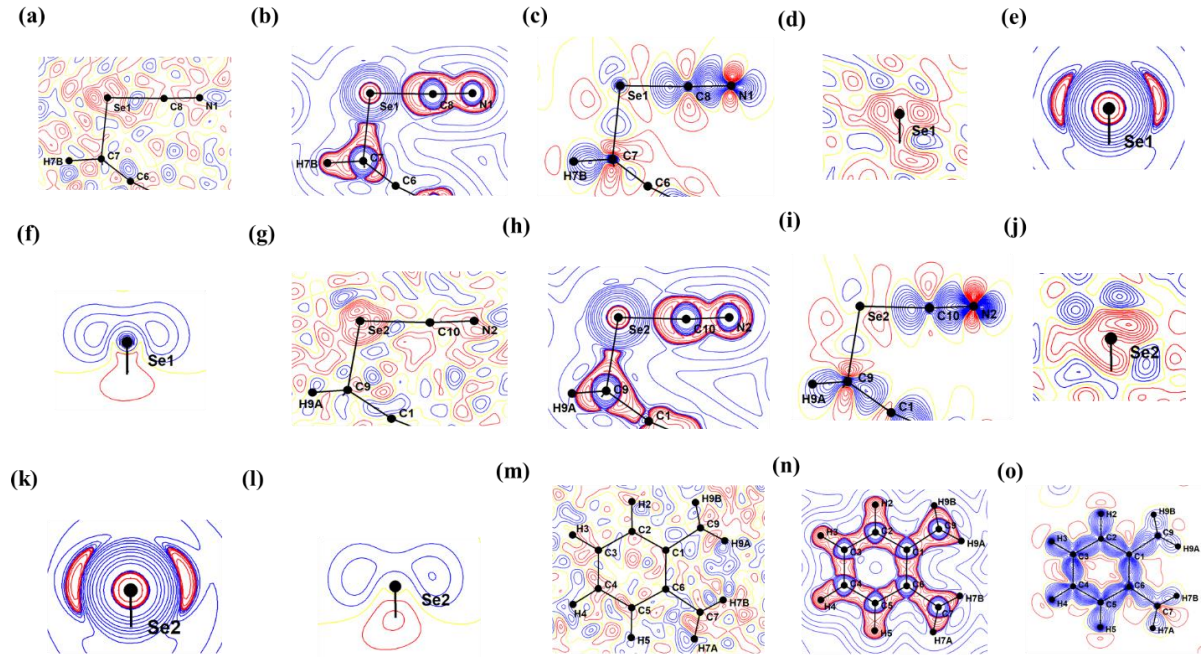

Figure 4AP.10 Residual, laplacian of electron density and static deformation density maps obtained after EMM-3 of SeCN2 in, (a)-(c), (g)-(i) *plane-1* [containing either C7, Se1 and N1 atoms or C9, Se2 and N2 atoms], (d)-(f), (j)-(l) *plane-2* [plane bisecting either C7-Se1-N1 or C9-Se2-N2 angle] and (m)-(o) plane containing benzene ring.

EMM-1 of SeCN3

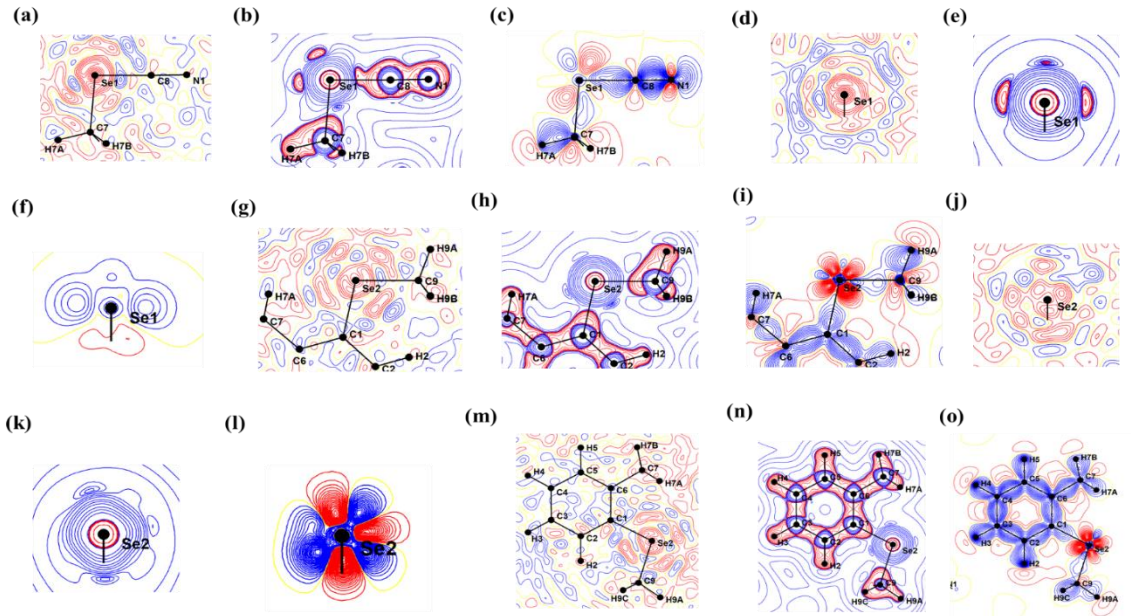

Figure 4AP.11 Residual, laplacian of electron density and static deformation density maps obtained after EMM-1 of SeCN3 in, (a)-(c), (g)-(i) *plane-1* [containing either C7, Se1 and N1 atoms or C1, Se2 and C9 atoms], (d)-(f), (j)-(l) *plane-2* [plane bisecting either C7-Se1-N1 or C1-Se2-C9 angle] and (m)-(o) plane containing benzene ring.

TMM-1 of SeCN3

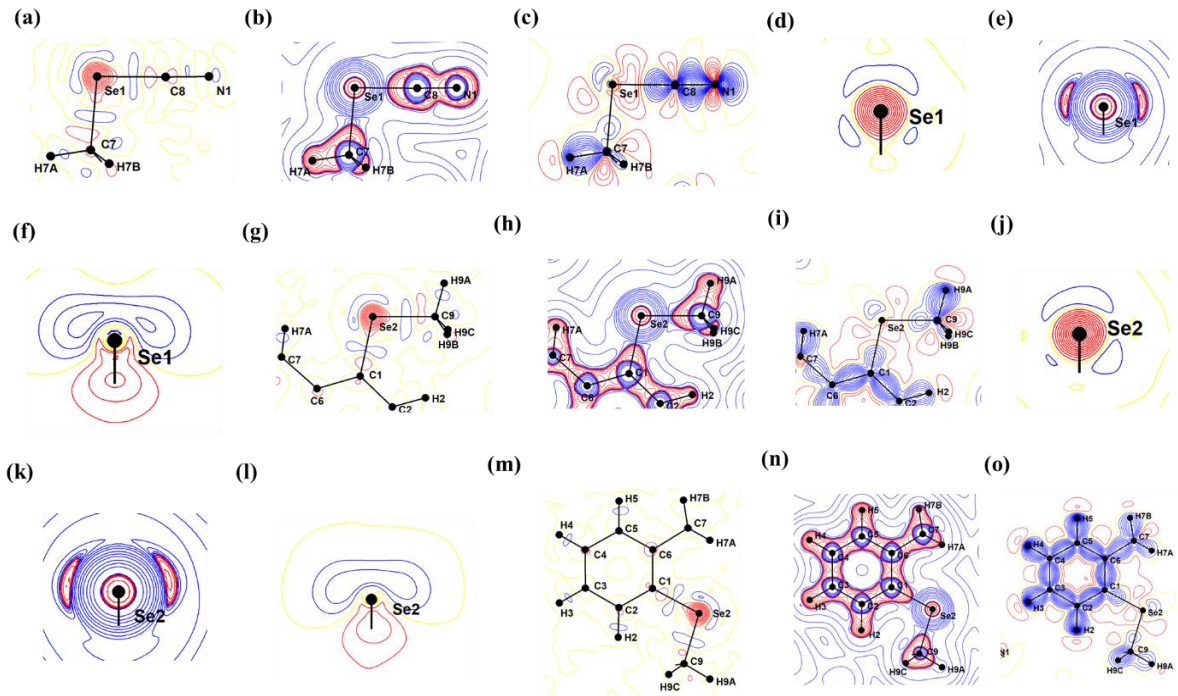

Figure 4AP.12 Residual, laplacian of electron density and static deformation density maps obtained after TMM-1 of SeCN3 in, (a)-(c), (g)-(i) *plane-1* [containing either C7, Se1 and N1 atoms or C1, Se2 and C9 atoms], (d)-(f), (j)-(l) *plane-2* [plane bisecting either C7-Se1-N1 or C1-Se2-C9 angle] and (m)-(o) plane containing benzene ring.

TMM-2 of SeCN3

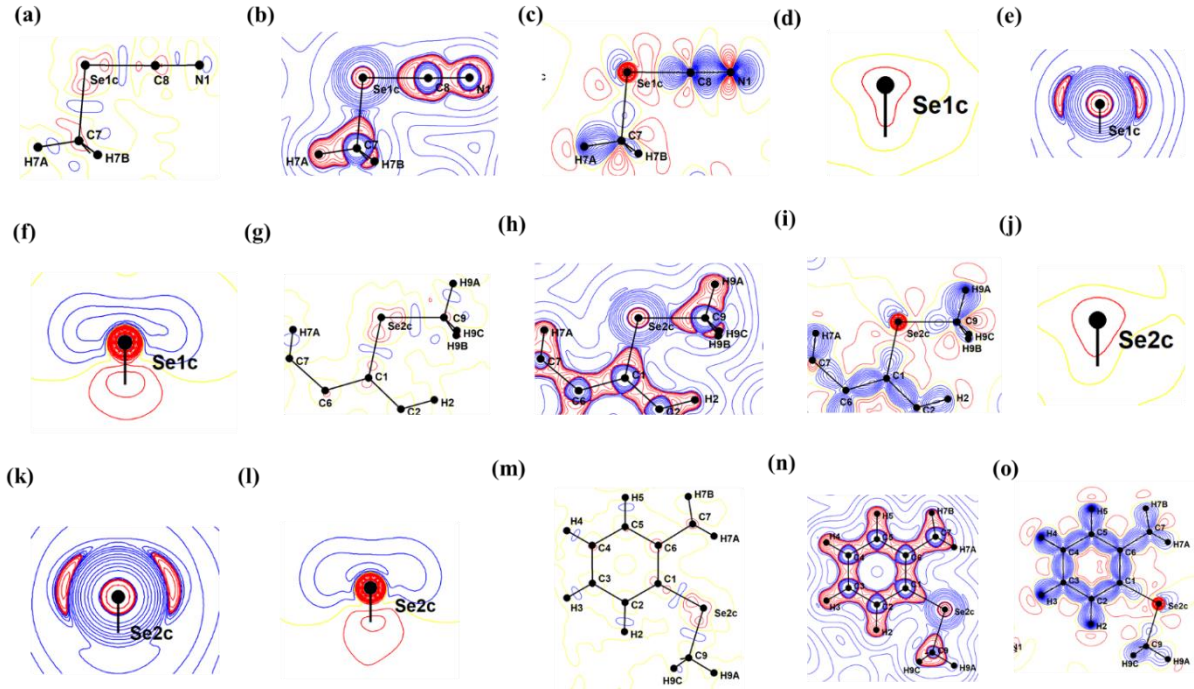

Figure 4AP.13 Residual, laplacian of electron density and static deformation density maps obtained after TMM-2 of SeCN3 in, (a)-(c), (g)-(i) *plane-1* [containing either C7, Se1 and N1 atoms or C1, Se2 and C9 atoms], (d)-(f), (j)-(l) *plane-2* [plane bisecting either C7-Se1-N1 or C1-Se2-C9 angle] and (m)-(o) plane containing benzene ring.

TMM-3 of SeCN3

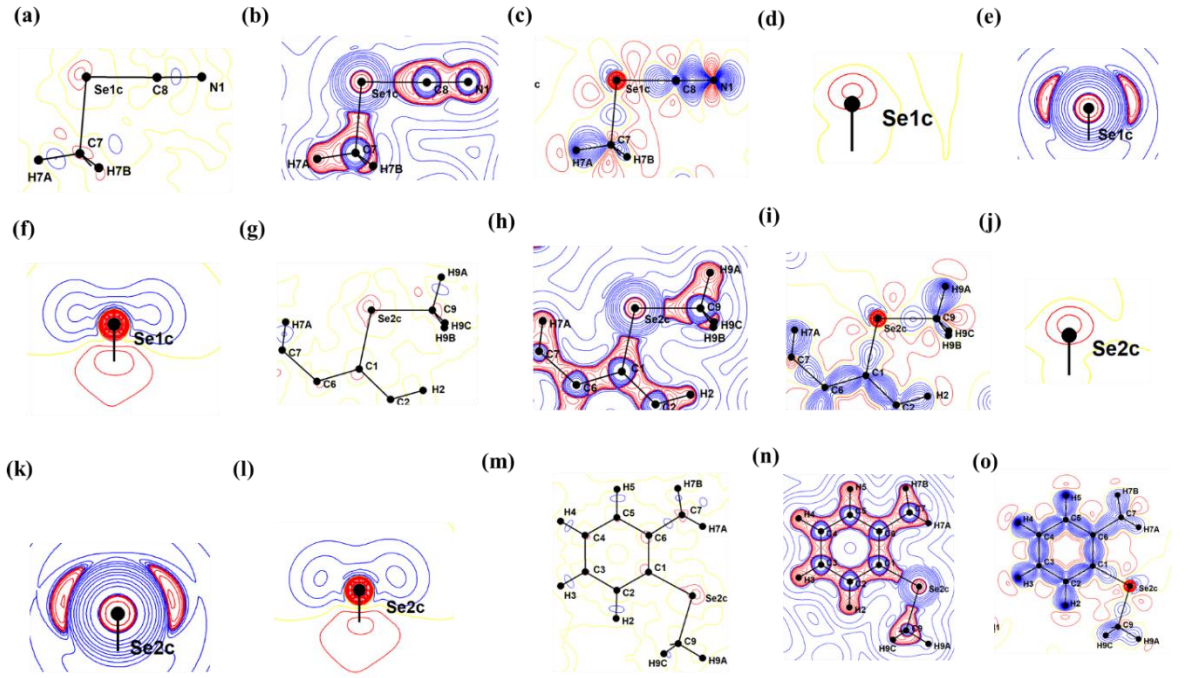

Figure 4AP.14 Residual, laplacian of electron density and static deformation density maps obtained after TMM-3 of SeCN3 in, (a)-(c), (g)-(i) *plane-1* [containing either C7, Se1 and N1 atoms or C1, Se2 and C9 atoms], (d)-(f), (j)-(l) *plane-2* [plane bisecting either C7-Se1-N1 or C1-Se2-C9 angle] and (m)-(o) plane containing benzene ring.

EMM-2 of SeCN3

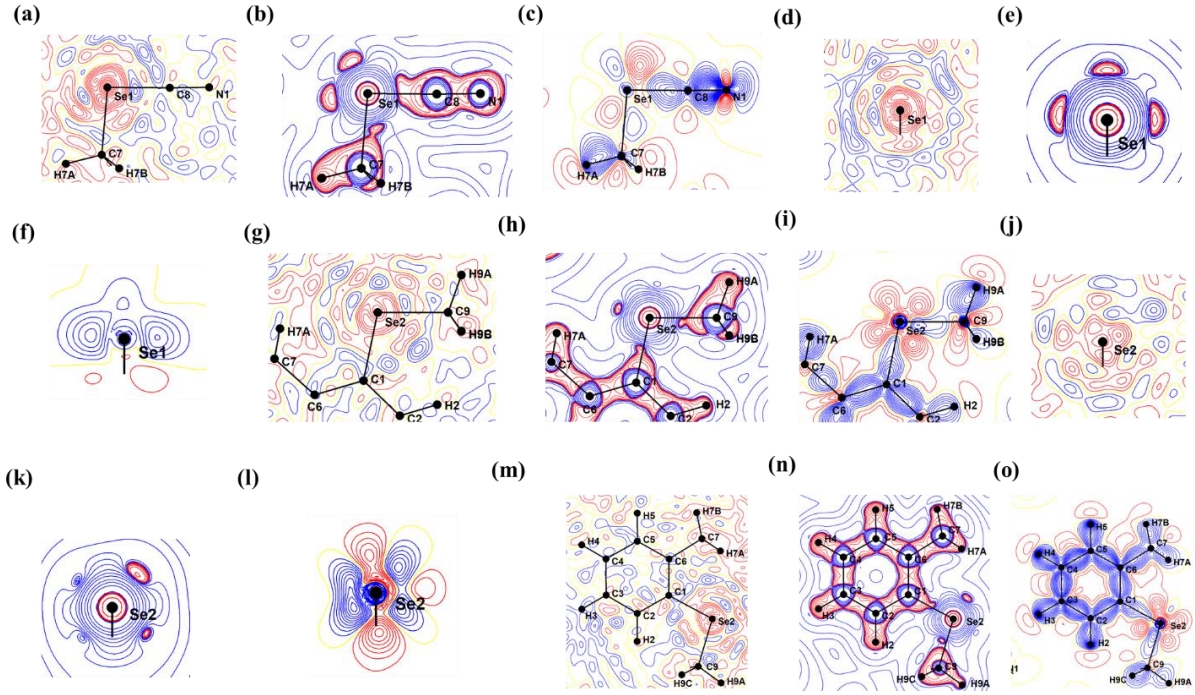

Figure 4AP.15 Residual, laplacian of electron density and static deformation density maps obtained after EMM-2 of SeCN3 in, (a)-(c), (g)-(i) *plane-1* [containing either C7, Se1 and N1 atoms or C1, Se2 and C9 atoms], (d)-(f), (j)-(l) *plane-2* [plane bisecting either C7-Se1-N1 or C1-Se2-C9 angle] and (m)-(o) plane containing benzene ring.

EMM-3 of SeCN3

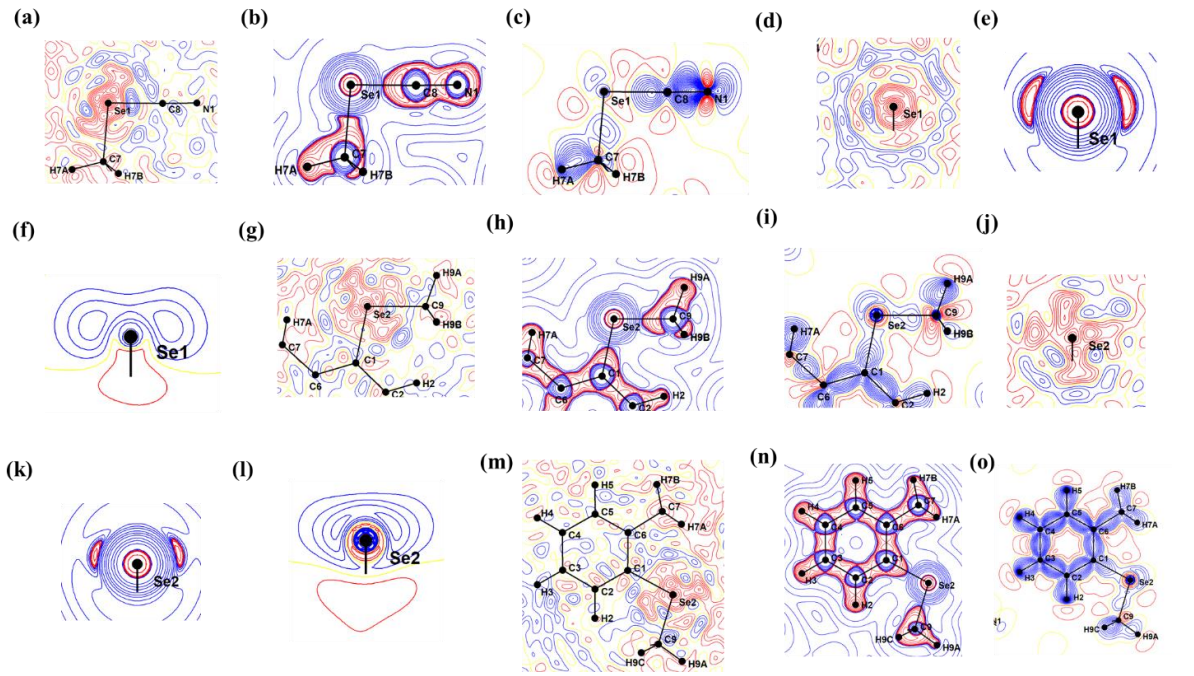

Figure 4AP.16 Residual, laplacian of electron density and static deformation density maps obtained after EMM-3 of SeCN3 in, (a)-(c), (g)-(i) *plane-1* [containing either C7, Se1 and N1 atoms or C1, Se2 and C9 atoms], (d)-(f), (j)-(l) *plane-2* [plane bisecting either C7-Se1-N1 or C1-Se2-C9 angle] and (m)-(o) plane containing benzene ring.

Section 4AP.1 Other intermolecular interactions in SeCNi (i = 1,2,3)

SeCN1

Exploring other intermolecular interactions constituting the crystal packing of SeCN1, the most significant dimer among all is formed with (*1-x,1-y,1-z*) symmetry generated molecule (*dimer1*). This is a centrosymmetric dimer formed through a symmetry related strong and linear C-H···N(*1-x,1-y,1-z*) [$d_{H\cdots N}$ = 2.48 Å (RR = 0.90), $\alpha_{C\text{-}H\cdots N}$ = 176°] HB interaction (**Figure 4AP.17a** and **Figure 4AP.18b**). Therefore, the most dominant contribution of the E_tot of -30.5 kJ/mol is coming from the electrostatic term (-25.7 kJ/mol). In the crystal structure, this *dimer1* is connected through *dimer2* and *dimer6* interactions to form a tightly held supramolecular 1D structure placed along the crystallographic *a*-axis (**Figure 4AP.18c**). The motifs involved in *dimer2* is already discussed, whereas *dimer6* (E_tot = -7.9 kJ/mol) is another centrosymmetric dimer in which the molecules are connected through a weak symmetry related C-H···Se (*-x,1-y,1-z*) short contact [$d_{H\cdots Se}$ = 3.29 Å (RR = 1.06), $\alpha_{C\text{-}H\cdots Se}$ = 122°] (**Figure 4AP.17b**). This 1D supramolecular structure is then prolongated along the crystallographic *b*-axis direction through *dimer3*, *dimer4*, *dimer7* and *dimer8* interactions (**Figure 4AP.18d**). Considering each dimer separately, *dimer3* (E_tot = -17.1 kJ/mol) is mainly constituted by a C-H···Cen_1(*-x,1/2+y,1/2-z*) [$d_{H\cdots Cen_1}$ = 2.761 Å (RR = 0.95), $\alpha_{C\text{-}H\cdots Cen_1}$ = 130°; Cen is defined as the centroid of the ring] HB interaction (**Figure 4AP.17c**). A similar Cen_2···H-C(*1-x,1/2+y,1/2-z*) [$d_{Cen_2\cdots H}$ = 2.757 Å (RR = 0.95), $\alpha_{Cen_2\cdots H\text{-}C}$ = 134°] HB interaction is also found in *dimer4* (E_tot = -16.9 kJ/mol) in addition to a weak N···H-C(*1-x,1/2+y,1/2-z*) [$d_{N\cdots H}$ = 2.76 Å (RR = 1.00), $\alpha_{N\cdots H\text{-}C}$ = 126°] HB interaction (**Figure 4AP.17d**). In the crystal structure, this *dimer3* and *dimer4* forms a 1D network along the crystallographic *b*-axis direction (**Figure 4AP.17c** and **d**). On the other hand, *dimer7* and *dimer8* are comparatively less significant in the overall crystal packing, as they show an E_tot of only -4.4 and -4.2 kJ/mol, respectively. There are no short contacts identified connecting the two molecules in *dimer7* while *dimer8* exhibit a weak Se···H-C (*x,3/2-y,1/2+z*) short contact [$d_{Se\cdots H}$ = 3.15 Å (RR = 1.02), $\alpha_{Se\cdots H\text{-}C}$ = 131°] that later advances along crystallographic *c*-axis to form a 1D network (**Figure 4AP.17e** and **f**). This supramolecular network is further extending through *dimer5* and *dimer9* interactions, altogether constituting the three-dimensional crystal packing of SeCN1 molecule (**Figure 4AP.18e**). The case of *dimer5* is already discussed and *dimer9* is the weakest molecular dimer among all (E_tot = -3.2 kJ/mol), composed mainly of a type I Se···Se [$d_{Se\cdots Se}$ = 3.780 Å (RR = 0.99)] interaction (**Figure 4AP.17g**).

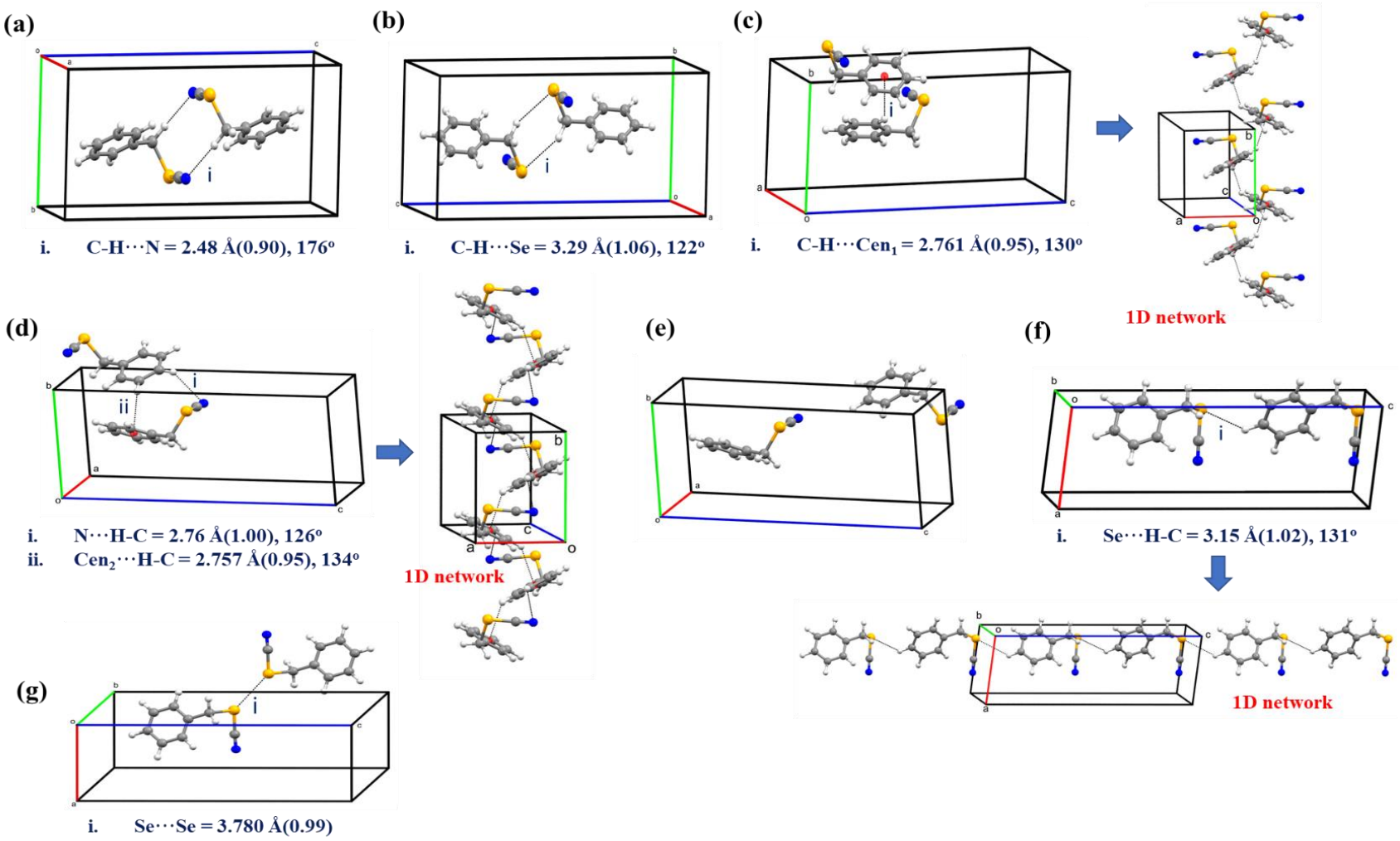

Figure 4AP.17 (a) *dimer1*, (b) *dimer6*, (c) *dimer3*, (d) *dimer4*, (e) *dimer7*, (f) *dimer8* and (g) *dimer9* of SeCN1. In (c) and (d) 1D network respectively formed by *dimer3* and *dimer4* along the crystallographic *b*-axis, and in (f) 1D network formed by *dimer9* along the crystallographic *c*-axis are also shown. Atoms are shown with colouring scheme, intermolecular interactions are depicted as black dashed lines along with roman numbering whose details are given below in each figure, values within the bracket corresponds to RR.

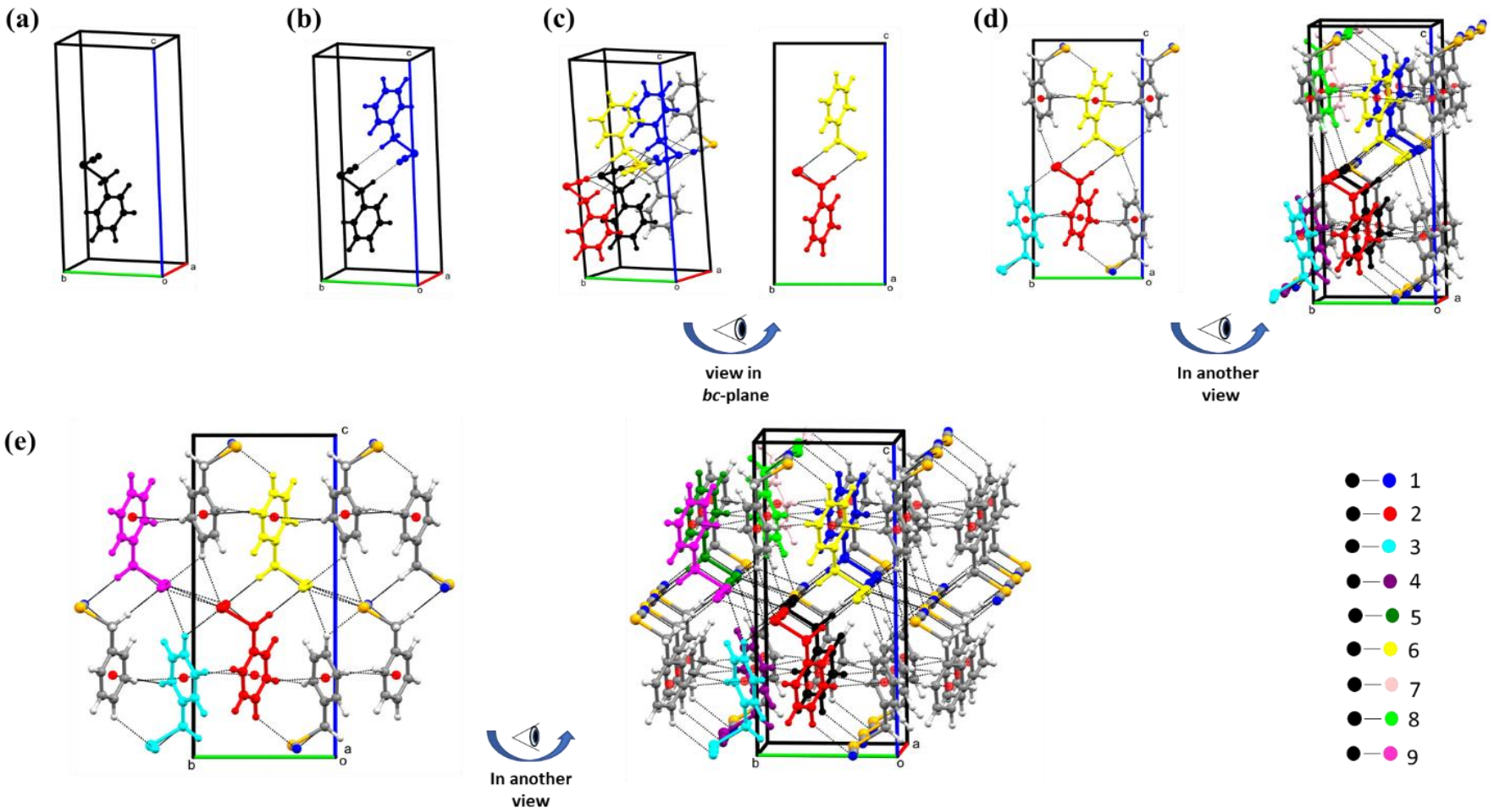

Figure 4AP.18 Three-dimensional packing of SeCN1 molecule: (a) central reference (*x,y,z*) molecule found in the asymmetric unit, (b) *dimer1* where (*x,y,z*) is interacting with the (*1-x,1-y,1-z*) symmetry generated molecule to form a discrete centrosymmetric dimer, (c) 1D supramolecular structure formed along crystallographic *a*-axis through *dimer1*, *dimer2* and *dimer6* interactions, (d) this supramolecular structure extending along crystallographic *b*-axis to form a network through *dimer3*, *dimer4*, *dimer7* and *dimer8* interactions and (e) the whole three dimensional packing of SeCN1 constituted through additional *dimer5* and *dimer9* interactions. Molecules forming *dimer1-9* with (*x,y,z*) are shown with specific colouring, while in other molecules atomic colouring scheme is given. In (c), (d) and (e) two different views of the packing are given for better understanding.

SeCN2

The crystal packing of SeCN2 shows close similarities with that of SeCN1, but doubling the number of selenocyanate functional group and thus the number of motifs causes the molecular dimers to be ranked in a different order. As discussed above, *dimer1* in SeCN2 is composed of two ChB and HB interactions that extending along the crystallographic *b*-axis direction to form two parallel 1D chain-like motifs (**Figure 4AP.20b**). Two such supramolecular structures are then connected through *dimer2* (comprising weak ChB interactions; discussed above) interactions to form a tightly held anti-parallel arrangement of molecules along crystallographic *b*-axis (**Figure 4AP.20c**). Also, the motifs seen in *dimer1* and *dimer2* of SeCN2 is same as those of *dimer2* and *dimer5* of SeCN1. Further, this tightly held supramolecular structure is mainly prolongated along the crystallographic *a*-axis through *dimer3*, *dimer6*, *dimer7* and *dimer8* interactions (**Figure 4AP.20d**). The *dimer3* is a centrosymmetric dimer that composed of a symmetry related C-H···N(*2-x,1-y,1-z*) [$d_{H\cdots N}$ = 2.65 Å (RR = 0.96), $\alpha_{C\text{-}H\cdots N}$ = 157°] HB interaction (**Figure 4AP.19a**), very similar to *dimer1* of SeCN1 since both are characterized with same kind of intermolecular interactions and are showing very close E_tot values (-32.0 kJ/mol in SeCN1 and -30.5 kJ/mol in SeCN1; **Table 4.4**). But unlike SeCN1, here the dimer is equally stabilized by both electrostatic and dispersion terms (-24 kJ/mol each) while in SeCN1 it was electrostatic term that was more dominant (might be linked with the more strong and linear nature of HB interaction in SeCN1 than SeCN2). The features of *dimer6* (E_tot = -9.2 kJ/mol) is also seemed very similar in both molecules, a centrosymmetric dimer composed of a symmetry related C-H···Se(*2-x,2-y,1-z*) [$d_{H\cdots Se}$ = 3.13 Å (RR = 1.01), $\alpha_{C\text{-}H\cdots Se}$ = 140°] short contact (**Figure 4AP.19b**). At the same time, *dimer7* and *dimer8* is differently formed in this molecule. In *dimer7* the molecules are connected through weak N···H-C(*-1+x,y,z*) [$d_{N\cdots H}$ = 2.94 Å (RR = 1.07), $\alpha_{N\text{-}H\cdots C}$ = 115°] and C···H-C(*-1+x,y,z*) [$d_{C\cdots H}$ = 2.97 Å (RR = 1.02), $\alpha_{C\text{-}H\cdots C}$ = 108°] short contacts, displaying an E_tot of -9.1 kJ/mol (**Figure 4AP.19c**). A similar dimer (*dimer8*) in SeCN1 exhibit a different type of interaction and a lower E_tot value of -4.2 kJ/mol. The more energetic stabilization of *dimer7* in SeCN2 is mainly coming from the dispersion contribution (-12.6 kJ/mol), which might be a consequence of close proximity of aromatic rings in this molecule. Also, in the crystal packing, this *dimer7* extends along the crystallographic *a*-axis direction to form a 1D network (**Figure 4AP.19c**). On the other hand, *dimer8* in SeCN2 do not exhibit any short contact between the molecules, very similar to case of *dimer7* in SeCN1 (**Figure 4AP.19d**).

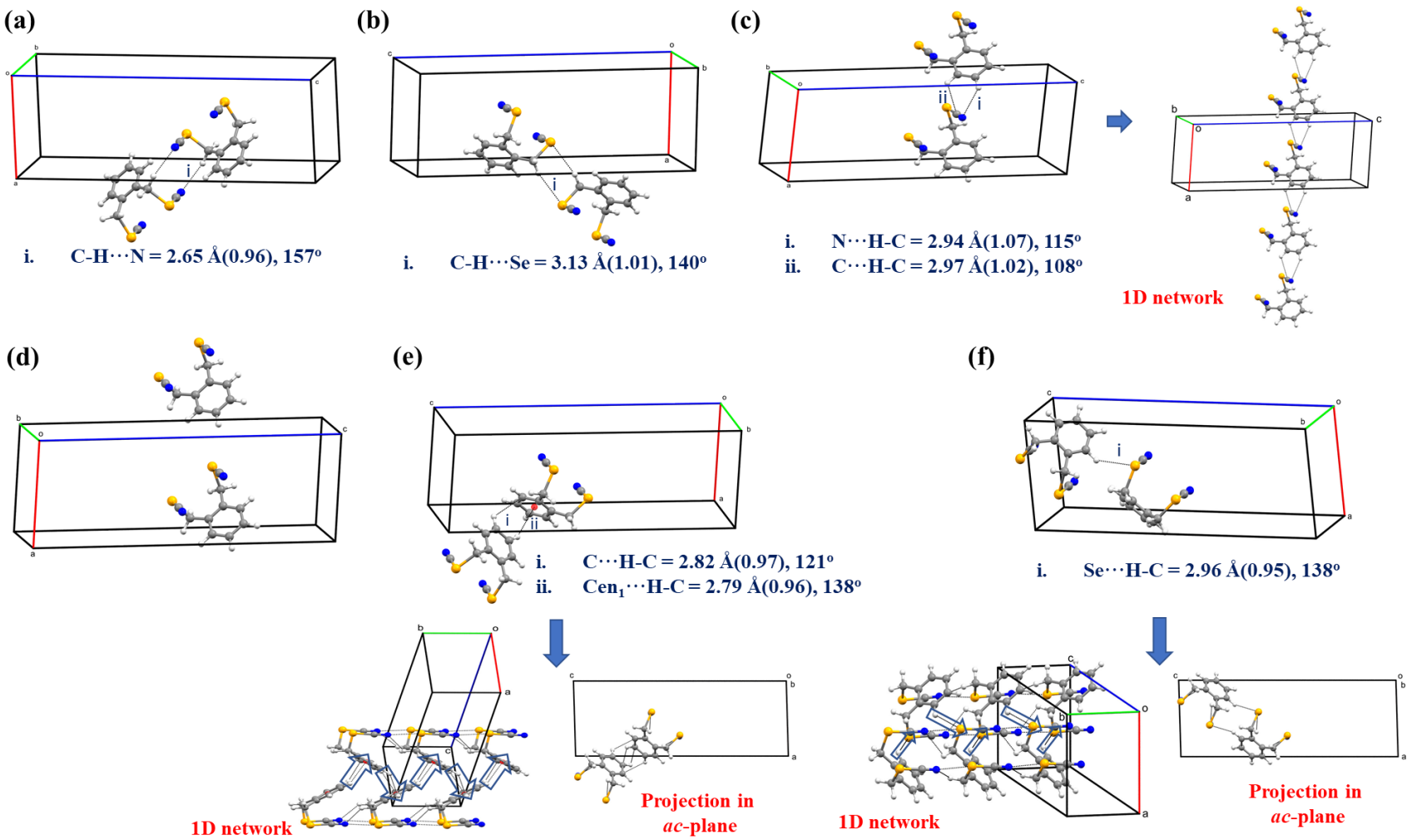

Figure 4AP.19 (a) *dimer3*, (b) *dimer6*, (c) *dimer7*, (d) *dimer8*, (e) *dimer4* and (f) *dimer5* of SeCN2. In (c) 1D network formed by *dimer7* along the crystallographic *a*-axis, and in (e) and (f) 1D network formed respectively by *dimer4* and *dimer5* along the crystallographic *b*-axis are also shown. Atoms are shown with colouring scheme, intermolecular interactions are depicted as black dashed lines along with roman numbering whose details are given below in each figure, values within the bracket corresponds to RR.

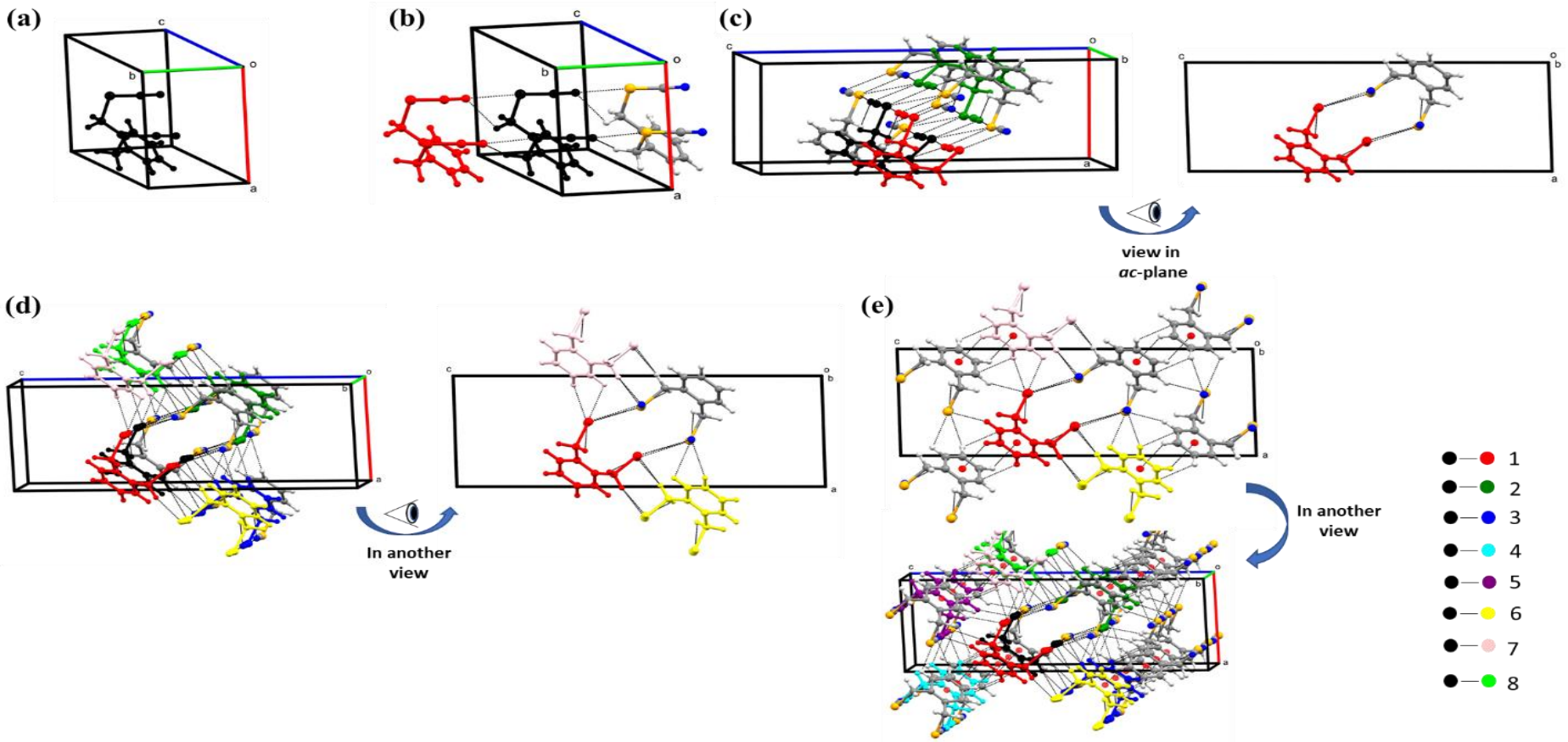

Figure 4AP.20 Three-dimensional packing in SeCN2 molecule: (a) central reference (*x,y,z*) molecule found in the asymmetric unit, (b) *dimer1* where (*x,y,z*) is interacting with (*x,1+y, z*) symmetry generated molecule to form two parallel 1D chain-like motifs along crystallographic *b*-axis, (c) supramolecular structure with anti-parallel arrangement of molecules along crystallographic *b*-axis through *dimer1* and *dimer2* interactions, (d) this supramolecular structure mainly extending along crystallographic *a*-axis through *dimer3*, *dimer6*, *dimer7* and *dimer8* interactions and (e) the whole three dimensional packing of SeCN2 molecule constituted through additional *dimer4* and *dimer5* interactions. Molecules forming *dimer1-8* with (*x,y,z*) are shown with specific colouring, while in other molecules atomic colouring scheme is given. In (c), (d) and (e) two different views of the packing are given for better understanding.

But the difference in SeCN2 is that, *dimer8* is not supposed to play any decisive role in crystal packing of the molecules since it possesses an E_tot of just 0.5 kJ/mol whereas *dimer7* of SeCN1 exhibit an E_tot of -4.4 kJ/mol. Further, the supramolecular network shown in **Figure 4AP.20d** extends through additional *dimer4* and *dimer5* interactions to constitute the whole three-dimensional packing of SeCN2 molecule in space (**Figure 4AP.20e**). Here, *dimer4* (E_tot = -15.9 kJ/mol) is a molecular dimer mainly composed of $Cen_1\cdots$H-C(*2-x,1/2+y,3/2-z*) [$d_{Cen_1\cdots H}$ = 2.79 Å (RR = 0.96), $\alpha_{Cen_1\cdots H\text{-}C}$ = 138°] and C$\cdots$H-C(*2-x,1/2+y,3/2-z*) [$d_{C\cdots H}$ = 2.82 Å (RR = 0.97), $\alpha_{C\cdots H\text{-}C}$ = 121°] HB interactions (**Figure 4AP.19e**), while *dimer5* (E_tot = -12.5 kJ/mol) is characterized with a Se$\cdots$H-C(*1-x,1/2+y,3/2-z*) [$d_{Se\cdots H}$ = 2.96 Å (RR = 0.95), $\alpha_{Se\cdots H\text{-}C}$ = 138°] HB interaction (**Figure 4AP.19f**). In the crystal packing, this *dimer4* and *dimer5* are then extends to form of a 1D network which is mainly oriented along the crystallographic *b*-axis (**Figure 4AP.19e** and **f**).

SeCN3

The crystal packing of SeCN3 is differently formed as compared to other two molecules. Here, both the strong and the weak σ-hole of the Se1-atom (which is the Se-atom of -CH_2-SeCN group) are making equally strong ChB interaction (in terms of RR; respectively with the lone-pairs of Se2 and N atoms), whereas a strong and a weak ChB interaction was found corresponding to the strong and the weak σ-hole of the Se-atom in the first two molecules (both interactions are forming with the N -tom). Another striking difference was seen in the ranking hierarchy of molecular dimers formed through ChB interactions. In SeCN3, the dimer formed through ChB interaction involving the strong σ-hole of the Se-atom is placed lower in the ranking (*dimer4*) than the other dimer involving the weak σ-hole of Se-atom (*dimer2*), while an opposite order was found in the first two molecules. All these observations are pointing that the characteristics of ChB interactions are quite different in SeCN3 than in SeCN1 and SeCN2.

Now, considering other molecular dimers that constituting the crystal packing, the most significant one (*dimer1*) among all is formed with the (*1-x,1-y,1-z*) symmetry generated molecule. This dimer is formed around an inversion center and are linked through a symmetry related C-H$\cdots Cen_1$(*1-x,1-y,1-z*) [$d_{H\cdots Cen_1}$ = 2.78 Å (RR = 0.96), $\alpha_{C\text{-}H\cdots Cen_1}$ = 138°] HB interaction (**Figure 4AP.21a** and **b**). This dimer exhibits an E_tot of -41.5 kJ/mol, where the most significant contribution is coming from the dispersion term (-40.5 kJ/mol) followed by a non-negligible electrostatic term (-31.0 kJ/mol). At the same time, it was the electrostatic term that was more dominant in the *dimer1* of both SeCN1 and SeCN2. Motifs connecting the

dimer2 of SeCN3 are already discussed, which along with *dimer1* constitute a strong trimeric unit within the crystal structure (**Figure 4AP.22c**). This trimeric unit is then expanding through *dimer4* and *dimer7* interactions to constitute a 2D network (**Figure 4AP.22d**). In *dimer4* the molecules are connected through a combination of ChB and HB interactions (details are already discussed), whereas in *dimer7* (E_tot = -8.4 kJ/mol) they are connected through a weak Se···H-C(*x,y,-1+z*) short contacts [$d_{Se\cdots H}$ = 3.29 Å (RR = 1.06), $\alpha_{Se\cdots H\text{-}C}$ = 119°] (**Figure 4AP.21b**). Also, this molecular dimer is forming an extended 1D network in the crystal packing along the crystallographic *c*-axis (**Figure 4AP.21b**). Exploring the molecular arrangement in other directions, the 2D network shown earlier in **Figure 4AP.22d** is further expanding along crystallographic *a*-axis through *dimer3*, *dimer5*, *dimer6* and *dimer8* interactions (**Figure 4AP.22e**). In *dimer3* (E_tot = -15.2 kJ/mol) the molecules are connected through one strong N···H-C(*1+x,3/2-y,1/2+z*) [$d_{N\cdots H}$ = 2.56 Å (RR = 0.93), $\alpha_{N\cdots H\text{-}C}$ = 144°] and one weak N···H-C(*1+x,3/2-y,1/2+z*) [$d_{N\cdots H}$ = 2.77 Å (RR = 1.01), $\alpha_{N\cdots H\text{-}C}$ = 123°] HB interactions (**Figure 4AP.21c**). A similar N···H-C(*1+x,y,z*) [$d_{N\cdots H}$ = 2.67 Å (RR = 0.97), $\alpha_{N\cdots H\text{-}C}$ = 153°] motif is also found in *dimer5* (**Figure 4AP.21d**). Both these dimers are forming an extended 1D network in the crystal structure as shown respectively in **Figure 4AP.21c** and **d**. At the same time, *dimer6* (E_tot = -9.5 kJ/mol) exist as a discrete centrosymmetric dimer in the crystal structure and a H···H(*-x,1-y,-z*) [$d_{H\cdots H}$ = 2.40 Å (RR = 1.00)] short contact is only identified in between the molecules (**Figure 4AP.21e**). And, *dimer8* is the molecular dimer that shows lowest E_tot (-8.2 kJ/mol) among all, where a N···H-C(*1+x,y,1+z*) [$d_{N\cdots H}$ = 2.88 Å (RR = 1.05), $\alpha_{N\cdots H\text{-}C}$ = 123°] short is identified connecting two molecules together and it later extend as a 1D network in the crystal packing (**Figure 4AP.21f**). Finally, all these molecular dimers altogether construct the three-dimensional packing of the SeCN3 molecule (**Figure 4AP.22f**).

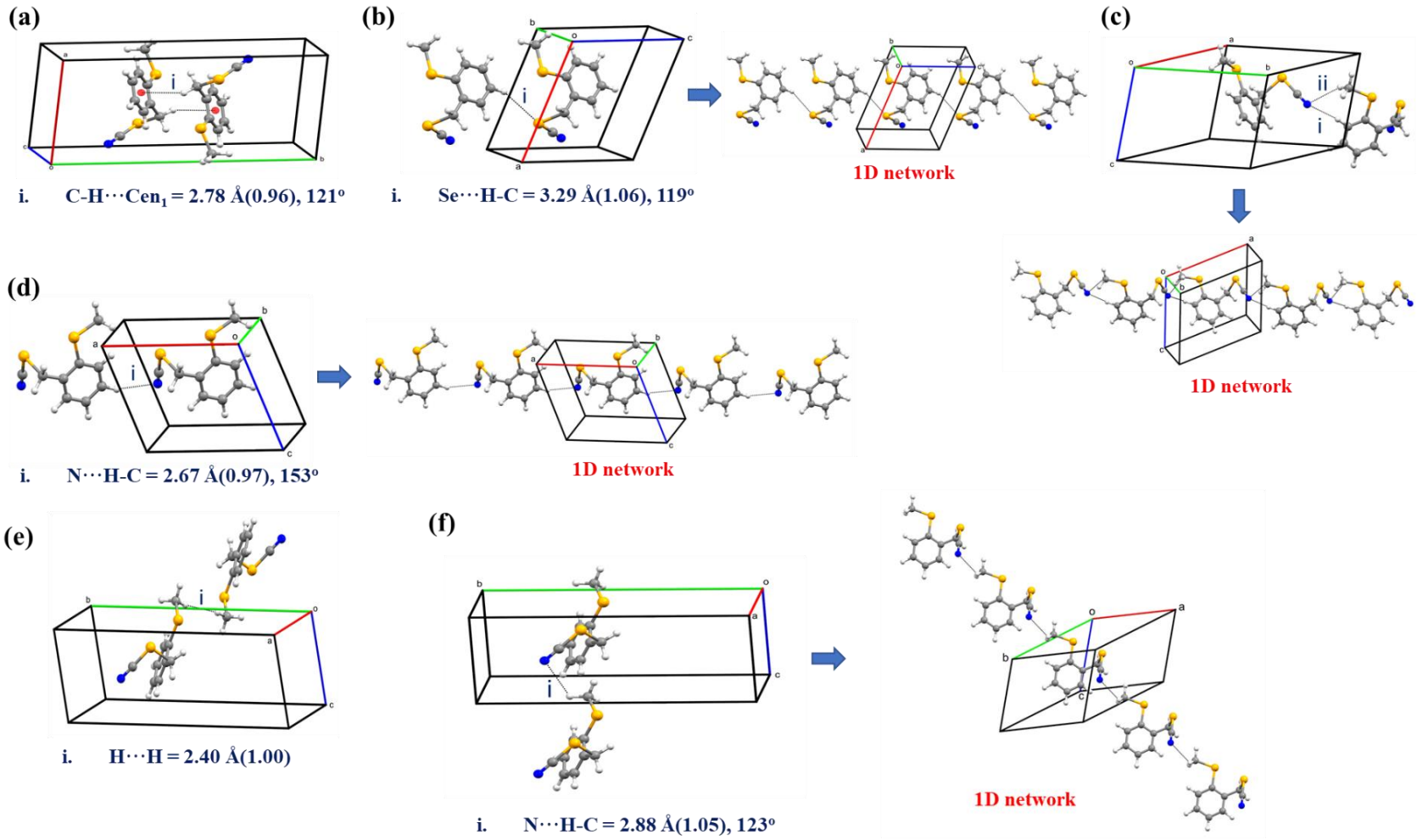

Figure 4AP.21 (a) *dimer1*, (b) *dimer7*, (c) *dimer3*, (d) *dimer5*, (e) *dimer6* and (f) *dimer8* of SeCN3. In (c), (d) and (f) extended 1D network formed by *dimer3*, *dimer5* and *dimer8* respectively along (*a*+*c*), *a* and (*b*+*c*) crystallographic directions are also shown. Atoms are shown with colouring scheme, intermolecular interactions are depicted as black dashed lines along with roman numbering whose details are given below in each figure, values within the bracket corresponds to RR.

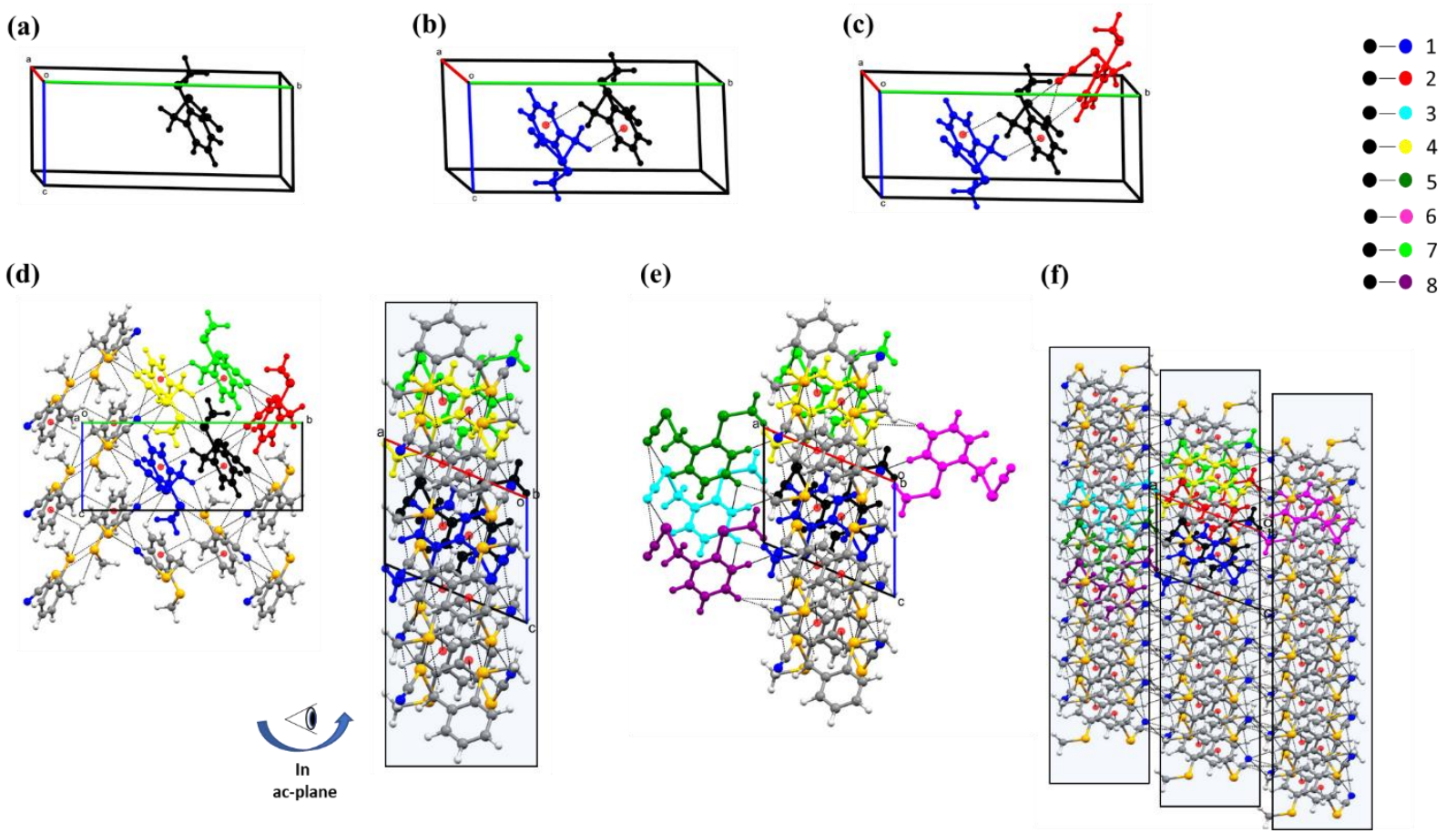

Figure 4AP.22 Three-dimensional packing of SeCN3 molecule: (a) central reference (*x,y,z*) molecule found in the asymmetric unit, (b) *dimer1* where reference (*x,y,z*) molecule is interacting with (*1-x,1-y,1-z*) symmetry generated molecule to form a discrete centrosymmetric dimer, (c) a trimeric structure constituted by *dimer1* and *dimer2* interactions, (d) a 2D network formed by *dimer1*, *dimer2*, *dimer4* and *dimer7* interactions (e) expansion of this 2D network along crystallographic *a*-axis direction through additional *dimer3*, *dimer5*, *dimer6* and *dimer8* interactions and (f) projection of 3D packing of SeCN3 in *ac*-plane. Molecules forming *dimer1-8* with (*x,y,z*) are shown with specific colouring, while in other molecules atomic colouring scheme is given. In (d) two different views of the packing is given for better understanding, the 2D network formed in (d) is shown inside a transparent square box to indicate how these are arranged in the 3D packing in (f).

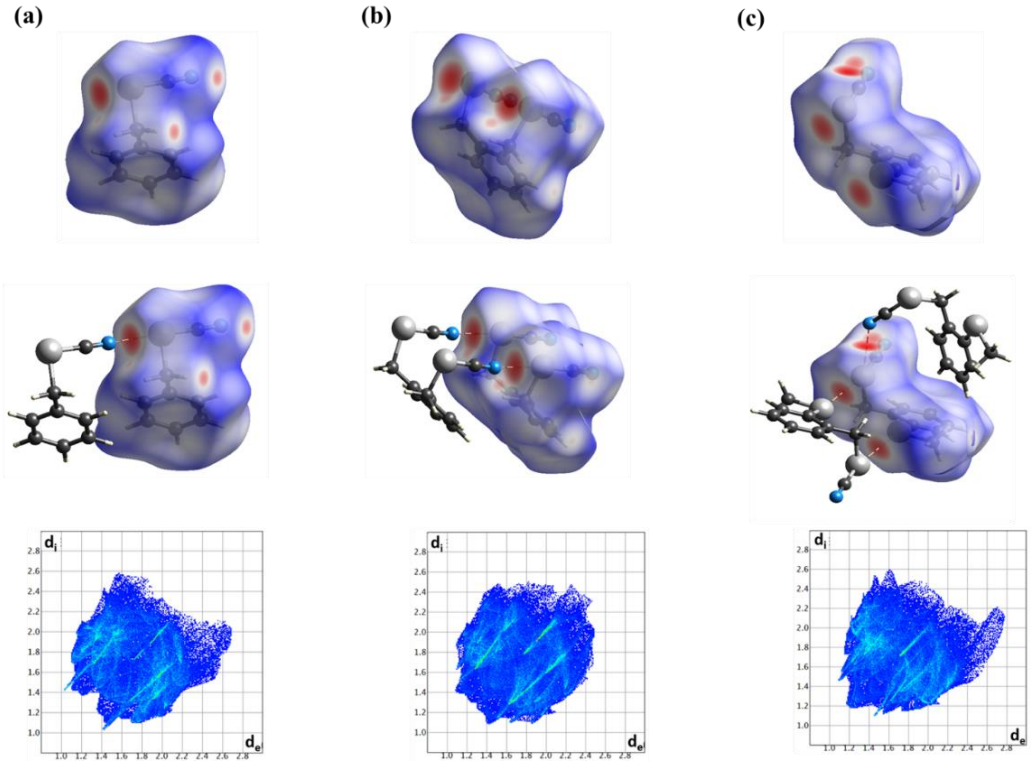

Figure 4AP.23 Hirshfeld surfaces mapped with d_{norm} (top), strong ChB interaction(s) formed with the neighbouring symmetry generated molecule (middle) and the 2D fingerprint plots (bottom), for (a) SeCN1, (b) SeCN2 and (c) SeCN3 molecules.

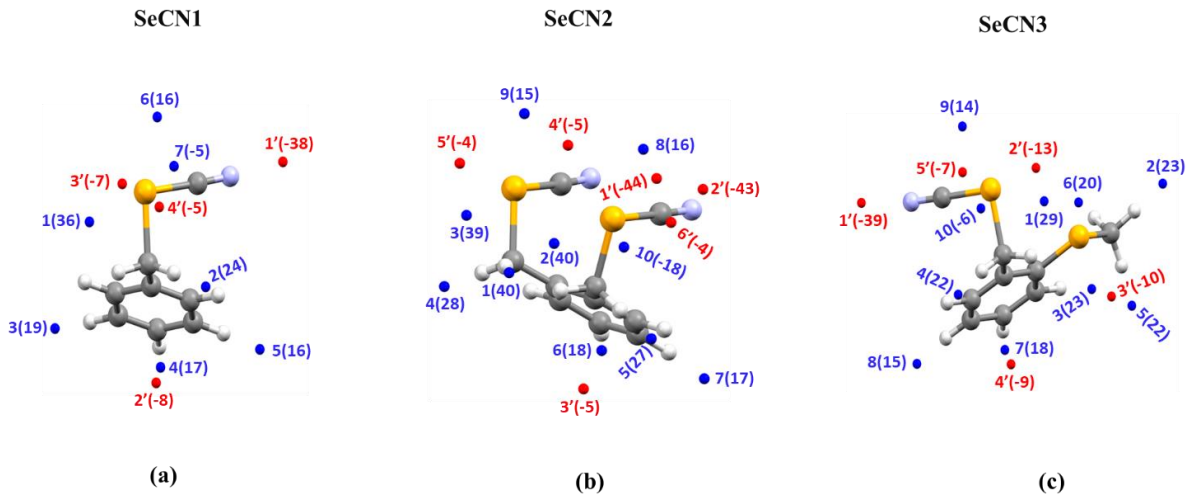

Figure 4AP.24 Extremal points of the ESP function calculated on 0.001 a.u. molecular iso-electron density surface of (a) SeCN1, (b) SeCN2 and (c) SeCN3. Maximal and minimal points are respectively represented with blue and red spheres of arbitrary radius. A numbering scheme is assigned based on the ESP values (separately for maximal and minimal points), with corresponding ESP value (in kcal/mol) given in bracket.

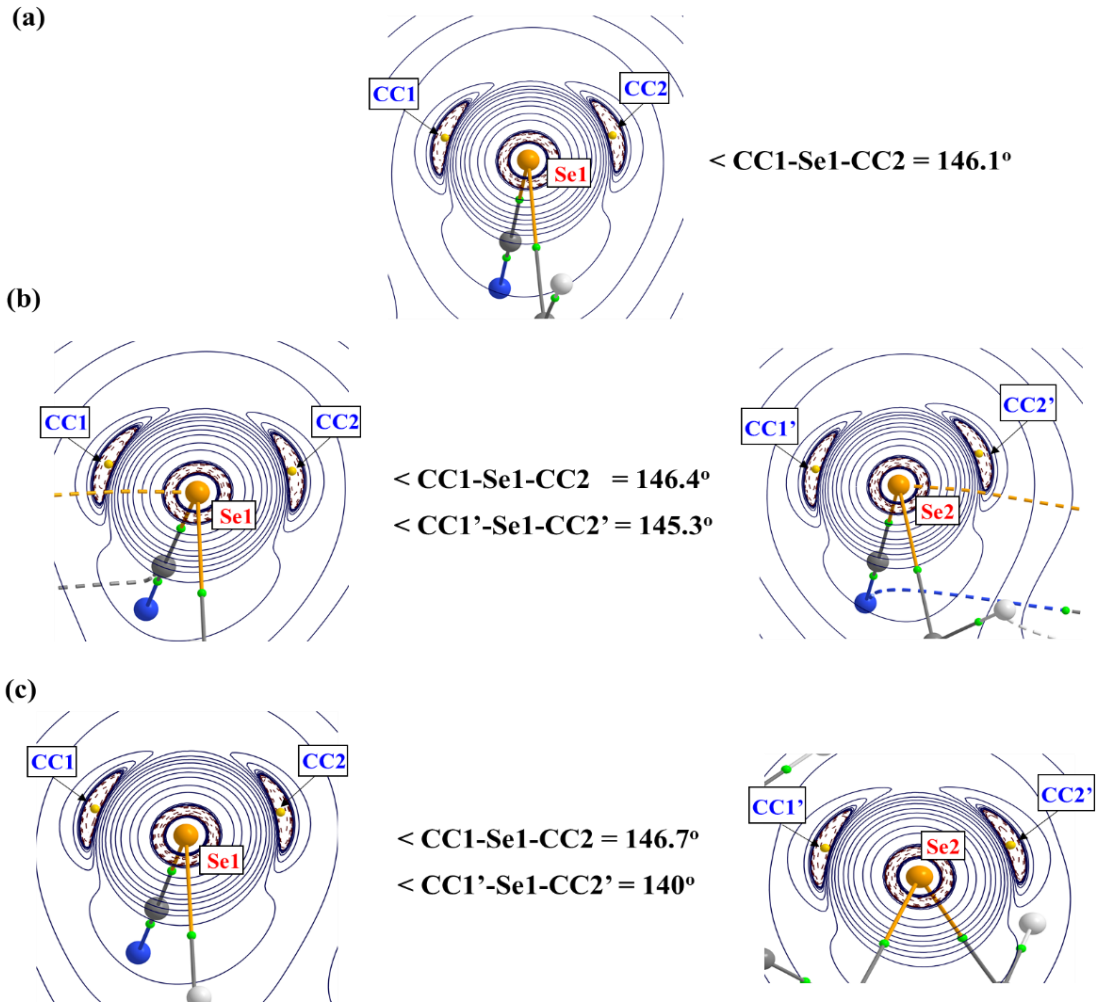

Figure 4AP.25 ***L*(r) maps [eÅ^{-5}, contours are in logarithmic scale: positive (red) and negative (blue)] drawn in *plane-2* (plane containing Se lone-pairs) and (3,-3) CPs of *L*(r) represented as yellow spheres with CC1-Se(i)-CC2 angles for (a) SeCN1, (b) SeCN2 and (c) SeCN3 molecules. (3,-1) BCPs are represented as light green spheres, bond paths are shown with broken lines and labelling is given for Se-atoms and associated LCPs.**

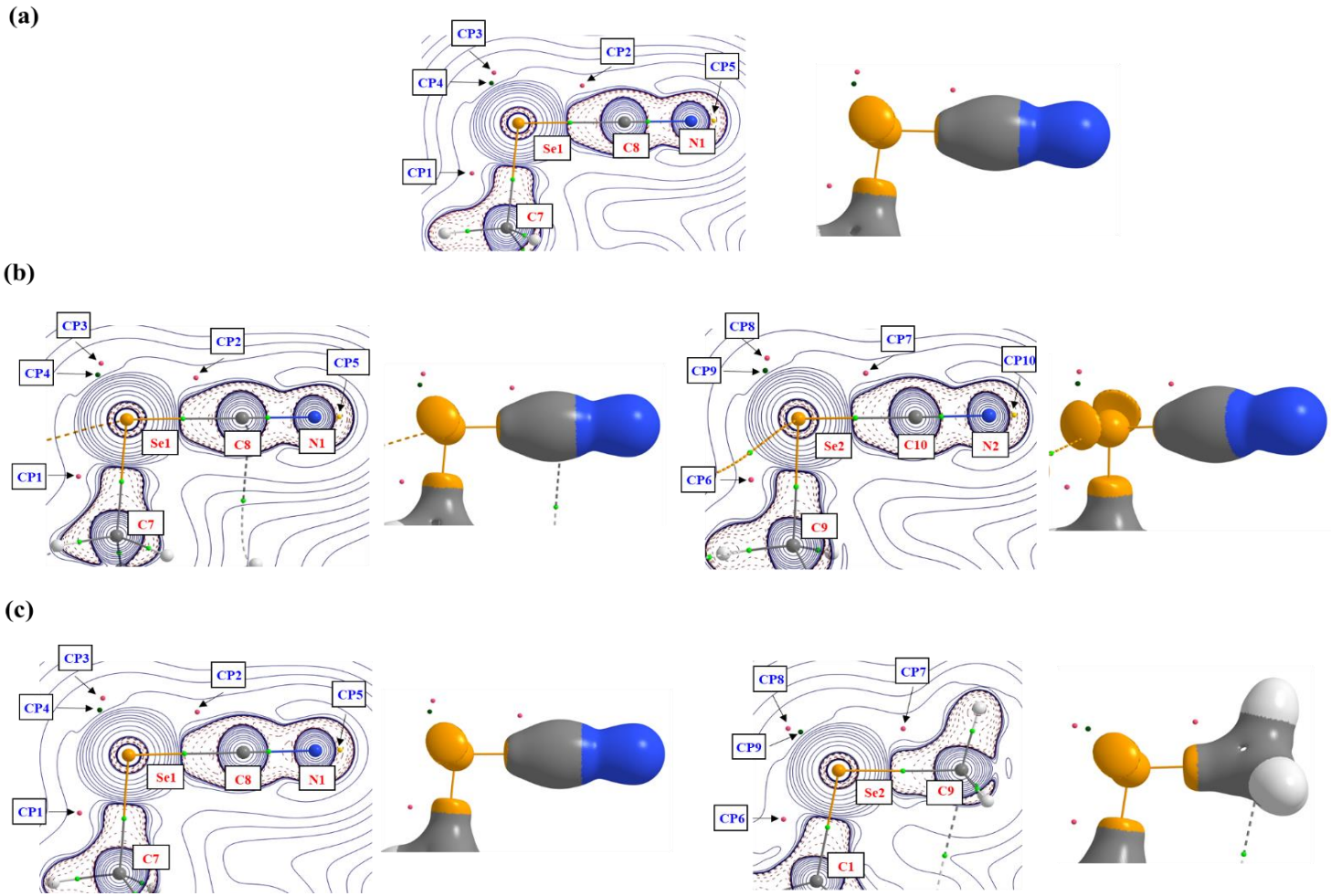

Figure 4AP.26 (left) *L*(r) maps [eÅ^5, contours are in logarithmic scale: positive (red) and negative (blue)] drawn in *plane-1* (R-Se-R' plane; R and R' are the substituents covalently bonded to the Se-atom), with relevant CPs of *L*(r) function represented as spheres of arbitrary radius [(3,−1) CPs are green and (3,+1) CPs are pink] in the valence shell of Se and N atoms, and (right) $\nabla^2\rho(r) = 0$ reactivity surfaces, for (a) SeCN1, (b) SeCN2 and (c) SeCN3 monomers optimized in gas phase. (3, -3) CPs corresponding to the lone-pairs of Se-atoms are out of the plane in the *L*(r) maps and hidden by the enclosing surfaces in $\nabla^2\rho(r) = 0$ maps. (3,-1) BCPs are represented with light green spheres of arbitrary radius, bond paths are shown with broken lines, and labelling is given for atoms and associated LCPs.

Table 4AP.1 Angles made by the electrophilic charge depleted LCPs with associated covalent bonds in SeCNi (i = 1,2,3).

Angles	SeCN1 (°)	SeCN2 (°)	SeCN3 (°)
C8-Se1-CP1	130	128.2	
C7-Se1-CP2	128.7	127.8	127.6
C8-Se1-CP3	113.1	112	112
C8-Se1-CP4	120.9	120.2	120
C7-Se1-CP3	150.7	152.6	152.8
C7-Se1-CP4	142.9	144.4	144.8
C8-N1-CP5	180	180	180
C10-Se2-CP6	-	130.5	-
C9-Se2-CP7	-	129.1	-
C10-Se2-CP8	-	113.5	-
C10-Se2-CP9	-	121.1	-
C9-Se2-CP8	-	150	138.1
C9-Se2-CP9	-	142.4	132.4
C10-N2-CP10	-	180	-
C9-Se2-CP6	-	-	136.7
C1-Se2-CP7	-	-	135.3
C1-Se2-CP8	-	-	121.1
C1-Se2-CP9	-	-	126.8

Table 4AP.2 Topological properties at LCPs associated to Se and N atoms in SeCNi (i = 1,2,3).

Molecule	Name	Type	Nuclei	Distance to Nucleus	ρ (r) (eÅ^{-3})	L(r) (eÅ^{-5})	L/ρ (eÅ^{-2})
SeCN1	CP1	(3,+1)	Se1	1.26	0.32	-2.35	-7.25
	CP2	(3,+1)	Se1	1.02	0.39	-2.41	-6.11
	CP3	(3,+1)	Se1	1.06	0.42	-1.61	-3.79
	CP4	(3,-1)	Se1	0.90	0.72	-1.33	-1.86
	CP5	(3,-3)	N1	0.39	3.72	60.43	16.23
	CC1	(3,-3)	Se1	0.87	0.91	0.81	0.89
	CC2	(3,-3)	Se1	0.87	0.90	0.80	0.88
SeCN2	CP1/CP6	(3,+1)/(3,+1)	Se1/Se2	1.27/1.26	0.32/0.32	-2.27/-2.38	-7.15/-7.32
	CP2/CP7	(3,+1)/(3,+1)	Se1/Se2	1.32/1.32	0.39/0.39	-2.41/-2.40	-6.13/-6.09
	CP3/CP8	(3,+1)/(3,+1)	Se1/Se2	1.06/1.06	0.43/0.42	-1.63/-1.61	-3.81/-3.80
	CP4/CP9	(3,-1)/(3,-1)	Se1/Se2	0.90/0.90	0.72/0.72	-1.36/-1.33	-1.91/-1.85
	CP5/CP10	(3,-3)/(3,-3)	N1/N2	0.39/0.39	3.72/3.74	60.40/60.95	16.22/16.31
	CC1/CC1’	(3,-3)/(3,-3)	Se1/Se2	0.87/0.87	0.91/0.90	0.82/0.77	0.90/0.85
	CC2/CC2’	(3,-3)/(3,-3)	Se1/Se2	0.87/0.87	0.90/0.91	0.81/0.88	0.90/0.97
SeCN3	CP1/CP6	(3,+1)/(3,+1)	Se1/Se2	1.26/1.21	0.32/0.35	-2.30/-2.79	-7.17/-8.05
	CP2/CP7	(3,+1)/(3,+1)	Se1/Se2	1.32/1.25	0.39/0.35	-2.41/-2.48	-6.11/-7.17
	CP3/CP8	(3,+1)/(3,+1)	Se1/Se2	1.06/1.08	0.42/0.41	-1.61/-1.55	-3.79/-3.77
	CP4/CP9	(3,-1)/(3,-1)	Se1/Se2	0.90/0.90	0.72/0.74	-1.34/-1.16	-1.86/-1.56
	CP5/-	(3,-3)/(3,-3)	N1/N2	0.39/-	3.72/-	60.30/-	16.20/-
	CC1/CC1’	(3,-3)/(3,-3)	Se1/Se2	0.87/0.87	0.90/0.90	0.79/0.74	0.88/0.82
	CC2/CC2’	(3,-3)/(3,-3)	Se1/Se2	0.87/0.87	0.91/0.89	0.79/0.73	0.87/0.81

Table 4AP.3 Topological and energetic properties determined at (3,-1) BCPs of ChB interactions in gas phase structures (trimers) of SeCNi (i = 1,2,3).

Molecule/ region	Interaction	d (Å)/RR	Angle (°)	Topological properties			
				ρ (eÅ^{-3})	L (eÅ^{-5})	$\|V\|/G$	DI
SeCN1/ region-1	N1B···Se1A	3.018/0.87	169	0.09	-1.07	0.81	0.11
SeCN1/ region-2	N1C···Se1A	3.521/1.02	164.5	0.03	-0.39	0.74	0.05
SeCN2/ region-1	N1B···Se1A	2.916/0.85	172.8	0.11	-1.31	0.84	0.12
	N2B···Se2A	2.921/0.85	172.9	0.10	-1.30	0.84	0.12
SeCN2/ region-2	N2C···Se1A	3.637/1.05	155.4	0.03	-0.32	0.74	0.04
	N1C···Se2A	3.595/1.04	135.8	0.03	-0.37	0.75	0.04
SeCN3/ region-1	Se2B···Se1A	3.435/0.90	164.1	0.08	-0.72	0.84	0.11
SeCN3/ region-2	N1C···Se1A	3.080/0.89	166.1	0.08	-0.93	0.81	0.09

Table 4AP.4 Structural and topological characteristics of the HB interactions obtained from the dimers and trimers extracted from the crystal geometries in SeCNi (i = 1,2,3). α is the angle between atom (ChB acceptor)···atom(ChB donor) and CC···CD directions, $d_{CC\cdots CD}$ corresponds to the distance between CC and CD sites. Topological parameters from dimers/trimers are gathered as left/right entries.

Molecule	Interaction	d (Å)/RR	Angle (°)	LCPs						
				CC···CD	$(L/\rho)_{CC}$ (Å^{-2})	$(L/\rho)_{CD}$ (Å^{-2})	$\Delta(L/\rho)$ (Å^{-2})	$d_{CC\cdots CD}$ (Å)	$\Delta(L/\rho)/d_{CC\cdots CD}^2$ (Å^{-4})	α (°)
SeCN1	N1B···H7''A	2.56/0.93	126.9	CP5b···CP11a	16.00/ 16.03	-3.95/ -3.92	19.95/ 19.95	2.18/ 2.18	4.20/ 4.20	16.4/ 16.5
SeCN2	N1B···H7''A	2.50/0.91	120	CP5b···CP11a	16.07/ 16.12	-3.83/ -3.81	19.91/ 19.92	2.18/ 2.18	4.19/ 4.19	17.0/ 17.0
	N2B···H9'A	2.56/0.93	109.1	CP10b···CP12a	16.10/ 16.12	-3.88/ -3.89	19.98/ 20.01	2.33/ 2.33	3.68/ 3.69	16.1/ 16.1
SeCN3	Se2B···H7'A	3.07/0.99	125.6	CC2'B···CP11a	0.84/ 0.85	-3.97/ -3.90	4.82/ 4.74	2.36/ 2.37	0.86/ 0.84	10.4/ 10.3

Table 4AP.5 Structural and topological characteristics of the ChB interactions obtained fore trimers extracted from the crystal geometries of SeCNi (i = 1,2,3). α is the angle between atom (ChB acceptor)···atom(ChB donor) and CC···CD directions, except for the CD sites positioned closer to the BCPs of Se-C covalent bonds (CP1, CP2, CP6 and CP7) where α is calculated between atom(ChB acceptor)···BCP and CC···CD directions. $d_{CC\cdots CD}$ corresponds to the distance between CC and CD sites. (* *Table continues to next page*)**

Molecule/ region	Interaction	d (Å)/RR	Angle (°)	LCPs						
				CC···CD	$(L/\rho)_{CC}$ (Å^{-2})	$(L/\rho)_{CD}$ (Å^{-2})	$\Delta(L/\rho)$ (Å^{-2})	$d_{CC\cdots CD}$ (Å)	$\Delta(L/\rho)/d_{CC\cdots CD}^2$ (Å^{-4})	α (°)
SeCN1/ region-1	N1B···Se1A	3.018/0.87	169	CP5b···CP1a	16.03	-7.67	23.69	1.97	6.11	7.5
				CP5b···CP3a	16.03	-3.99	20.02	2.56	3.05	24.0
				CP5b···CP4a	16.03	-1.98	18.01	2.42	3.07	20.6
	N1C···Se1A	3.521/1.02	164.5	CP5c···CP2a	16.11	-6.24	22.35	2.82	2.81	13.4
				CP5c···CP3a	16.11	-3.99	20.10	2.59	3.00	6.6
				CP5c···CP4a	16.11	-1.98	18.09	2.79	2.32	5.9
SeCN2/ region-1	N1B···Se1A	2.916/0.85	172.8	CP5b···CP1a	16.12	-7.81	23.92	1.84	7.07	7.3
				CP5b···CP3a	16.12	-4.00	20.12	2.48	3.27	25.2
				CP5b···CP4a	16.12	-1.94	18.06	2.34	3.30	21.7
	N2B···Se2A	2.921/0.85	172.9	CP10b···CP6a	16.12	-7.88	24.00	1.8	7.41	7.1
				CP10b···CP8a	16.12	-3.87	19.99	2.52	3.15	25.0
				CP10b···CP9a	16.12	-1.77	17.89	2.36	3.21	21.4
	N2C···Se1A	3.637/1.05	155.4	CP10c···CP2a	16.17	-6.21	22.38	2.93	2.61	13.2
				CP10c···CP3a	16.17	-4.00	20.17	2.78	2.61	9.1

				CP10c···CP4a	16.17	-1.94	18.11	2.95	2.08	7.3
	N1C···Se2A	3.595/1.04	135.8	CP5c···CP7a	16.14	-6.21	22.35	3.1	2.33	14.8
				CP5c···CP8a	16.14	-3.87	20.02	2.95	2.30	13.7
				CP5c···CP9a	16.14	-1.77	17.91	3.1	1.86	10.8
SeCN3/ region-1	Se2B···Se1A	3.435/0.90	164.1	CC1'B···CP1a	0.76	-7.32	8.08	2.59	1.21	20.4
				CC1'B···CP3a	0.76	-4.19	4.95	2.37	0.88	7.7
				CC1'B···CP4a	0.76	-2.08	2.84	2.36	0.51	3.7
				CC2'B···CP1a	0.85	-7.32	8.16	2.79	1.05	14.7
				CC1A···CP7B	0.96	-7.27	8.24	2.56	1.26	14.4
				CC2A···CP8B	0.93	-3.74	4.66	2.74	0.62	15.2
				CC2A···CP9B	0.93	-1.39	2.31	2.92	0.27	12.2
SeCN3/ region-2	N1C···Se1A	3.080/0.89	166.1	CP5c···CP2a	16.04	-6.50	22.54	1.96	5.87	9.2
				CP5c···CP3a	16.04	-4.19	20.23	2.25	4.00	22.3
				CP5c···CP4a	16.04	-2.08	18.12	2.39	3.17	19.5

List of publications

(1) Vijayakumar-Syamala, V., Aubert, E., Deutsch, M., Wenger, E., Dhaka, A., Fourmigué, M., Nespolo, M., Espinosa, E. N-iodosaccharin-Pyridine Co-crystal System under Pressure: Experimental Evidence of Reversible Twinning. Acta Crystallogr B Struct Sci Cryst Eng Mater. 2022, 78 (3). https://doi.org/10.1107/S2052520622002542.

(2) Shukla, R., Dhaka, A., Aubert, E., Vijayakumar-Syamala, V., Jeannin, O., Fourmigué, M., Espinosa, E. Understanding Reactivity and Assembly of Dichalcogenides: Structural, Electrostatic Potential, and Topological Analyses of 3*H*-1,2-Benzodithiol-3-One and Selenium Analogs. Cryst. Growth Des. 2020, 20 (12), 7704–7725. https://doi.org/10.1021/acs.cgd.0c00961.